The spalling mechanism of fire exposed concrete

Lottman, Bas

DOI
10.4233/uuid:5b78d71b-708f-405f-b3b3-ca664b141ce0

Publication date
2017

Document Version
Final published version

Citation (APA)
Lottman, B. (2017). *The spalling mechanism of fire exposed concrete*. [Dissertation (TU Delft), Delft University of Technology]. https://doi.org/10.4233/uuid:5b78d71b-708f-405f-b3b3-ca664b141ce0

The spalling mechanism of fire exposed concrete

Proefschrift

ter verkrijging van de graad van doctor
aan de Technische Universiteit Delft,
op gezag van de Rector Magnificus prof. ir. K.C.A.M. Luyben,
voorzitter van het College voor Promoties,
in het openbaar te verdedigen op
1 mei 2017 om 15:00 uur
door

Bastiaan Bernardus Gerardus LOTTMAN

civiel ingenieur
geboren te Zwolle

Dit proefschrift is goedgekeurd door de promotor:
Prof. dr. ir. Dr.-Ing. E.h. J.C. Walraven

en de tweede promotor:
Prof. dr. ir. E.A.B. Koenders

Samenstelling promotiecommissie:

Rector Magnificus,	voorzitter
Prof. dr. ir. Dr.-Ing. E.h. J.C. Walraven,	Technische Universiteit Delft, promotor
Prof. dr. ir. E.A.B. Koenders,	Technische Universität Darmstadt, promotor

Onafhankelijke leden:

Prof. Dr.-Ing. F. Dehn,	Universität Leipzig
Prof. Dr. Ing. R. Felicetti,	Politecnico di Milano
Prof. dr. ir. H.E.J.G. Schlangen,	Technische Universiteit Delft
Dr. ir. L. Pel,	Technische Universiteit Eindhoven

Overige leden:

Dr. ir. C.B.M. Blom,	Technische Universiteit Delft
Prof. dr. ir. D.A. Hordijk,	Technische Universiteit Delft, reservelid

Cover design by M.A.J. Lottman

Printed in the Netherlands by Ipskamp Printing, Enschede
First printing, 2017
ISBN 978-94-028-0623-6

Keywords: concrete, fire, (explosive) spalling, pore pressure, fracture mechanics, finite element method, thermal buckling mechanism

Email: bbglottman@icloud.com

Acknowledgements

The research that is reported in this thesis was performed at the group Concrete Structures at Delft University of Technology, Faculty of Civil Engineering and Geosciences, Department of Structural and Building Engineering. I first would like to express my utmost gratitude to my promoter, Prof. Joost Walraven, for giving me the opportunity of doing this research. His guidance and patience allowed me to explore many aspects surrounding this topic and eventually obtain the work presented. His ability to understand and discuss all sorts of concrete related issues I admire and his critical comments and careful reading were also greatly appreciated.

I am also grateful to my second promoter, Prof. Eddie Koenders, for guiding me through the most part of my scientific work. As my daily supervisor he helped me establish new ideas, improve my scientific writing and deal with all sorts of matters. I also thank him for accompanying me to the workshops regarding my topic as well as arranging for me to visit several research institutes and experience firsthand spalling of fire exposed concrete. I also express my gratitude to Dr. Kees Blom, for his contributions in establishing the mechanical part of the finite element model and dealing with the fracture behaviour. Also our discussions, especially outside my topic and dating back to my master thesis, helped my professional development for which I thank you.

The Dutch National Science Foundation (STW) I would like to thank for funding the research project DCB-7045 of which this thesis is a part. The (financial) contributions by all governmental and commercial parties involved, amongst others, Rijkswaterstaat, TNO, Gemeentewerken Rotterdam, Strukton and Efectis, also requires acknowledgement. I am as well thankful to their representatives present during the progress meetings for their input and critical questions. The additional financial contribution by the stichting Stimulering Onderwijs en Onderzoek Betonconstructies (SOOB) is also appreciated. Moreover, I was given the opportunity to attend various meetings of the RILEM technical workgroup dealing with high performance concrete at high temperatures. These provided me at the beginning of my work with an overview of the current state of art for which I thank the chairman and the members.

The promotion committee has to be thanked for their time and effort spent in reading of my PhD thesis as well as formulating questions during my public defence. In particular I mention the critical remarks by Prof. Roberto Felicetti, regarding the influence of the pore pressure, and Prof. Erik Schlangen, reflecting on the time-dependent aspects in mechanics. The discussions I had with each of the committee members, especially during the international workshops on concrete spalling due to fire exposure, were also greatly appreciated. Furthermore, I would like to point out that the multi-disciplinary approach adopted in this research is reflected as well in the various areas of expertise of the committee members.

The possibility to visit several institutes active in the field of fire-induced spalling of concrete turned out to be a valuable contribution to my work. I therefore would like to acknowledge Efectis and in particular thank Dr. Kees Both and Ir. Arnoud Breunese for allowing me to observe and assist several concrete fire tests. I especially appreciated the opportunity to visit a real-life fire test in the Runehamar tunnel in Norway. During my visit to the CSTB I experienced a scientific approach to spalling for which I especially thank Dr. Pierre Pimienta and Dr. Jean-Christophe Mindeguia. The possibility to witness both material- and fire testing as well as our discussions regarding the topic proved particular helpful in identifying the main processes to be considered. The most memorable full-scale fire tests I observed were performed at the MFPA. I am therefore thankful to Prof. Frank Dehn and Dipl.-Ing. Michael Juknat for allowing me the opportunity to visit the institute. During the analyses of the spalling simulations these observations frequently came to mind.

Several persons have also contributed to my research among whom I first would like to thank Dr. Fred Vermolen. His help in understanding and deriving the numerical approximation of the physical part of the finite element model was very helpful. The critical comments by Dr. Leo Pel regarding the forced drying process and the pore pressure development in fire exposed concrete were also appreciated. I also mention here the help by Prof. Erik Schlangen in getting started with the lattice-based fracture mechanics model. The Dutch research project consisted of two additional PhD students with which I cooperated. To Gijs van der Heijden, thanks for our discussions regarding the role of the pore pressure and the movement of moisture. To Zhang Qi, thanks for your contributions in identifying the changes in the microstructure of the cement paste during heating.

And of course I thank my former and current colleagues at the university. You supported me in more than my research and provided a pleasant atmosphere which I will not forget. To my friends, former roommates in the student housing and the members of the soccer team I was a part of, thanks for remembering me that there is more to life than work.

To my family and above all my mother and sister, I will never forget your love and support which only strengthened my resolve to succeed and helped me to obtain this result. This thesis is therefore not only the product of the education I have received throughout my life, but also my closest family has played an invaluable role.

Bas Lottman

Contents

Notations

General

Roman upper case

A	[mm^2]	Cross-sectional area of the structural element / cross-sectional area defined perpendicular to an axis
D	[mm]	Unit thickness in depth direction of the structural element
H	[mm]	Height of the structural element
W	[mm]	Width of the structural element

Roman lower case

e_{tot}	[-]	Total number of elements distributed across the domain
h	[mm]	Internal height governing the cross-sectional area
l	[m], [mm]	Length defined parallel to an axis (based on ref. system)
n_S	[-]	Number of nodes with imposed Dirichlet conditions
n_{tot}	[-]	Total number of nodes across the domain
r	[mm]	Radius in the polar coordinate system
t	[s]	Time or duration of fire exposure
t_0	[s]	Initial or start time before fire exposure develops
x, y	[m], [mm]	Cartesian coordinate defined by the x-axis, y-axis

Greek upper case

Γ	[-]	Boundary of the discretised domain
Δ	[-]	Increment of a property
Δt	[s]	Incremental time step size
Δx	[m], [mm]	Constant element size (based on ref. system)
Ω	[-]	Discretised domain

Greek lower case

α	[rad]	Angle defined relative to a coordinate system
ϵ	[-]	Arbitrary parameter governing the variation
θ	[rad]	Angle in the polar coordinate system
ξ	[m], [mm]	Natural coordinate system defined by the element discretisation (based on ref. system)

Vectors

$\boldsymbol{n}$	[-]	Unit outward normal vector
$\boldsymbol{x}$	[m], [mm]	Coordinate system vector
$\boldsymbol{\eta}$	[var.]	Variation or test function vector

Matrices

$\boldsymbol{A}$	[mm^2]	Matrix containing the cross-sectional areas
$\boldsymbol{B}$	[1/m], [1/mm]	Gradient matrix of shape functions (based on ref. system)
$\boldsymbol{N}$	[m], [mm]	Matrix of shape functions (based on ref. system)
$\boldsymbol{l}$	[m], [mm]	Matrix containing the lengths (based on ref. system)

Subscriptions

$\cdots_{ag}$	Indication for the aggregate particles
$\cdots_{avg}$	Indication for an averaged property
$\cdots_{c}$	Indication for the variables, temperature and capillary pressure
$\cdots_{cr}$	Indication for a cracked property
$\cdots_{i}, \cdots_{j}$	Indication for the node number
$\cdots_{i_d}, \cdots_{j_d}$	Indication for the node number at edge 'd' of the triangular element
$\cdots_{itz}$	Indication for the interfacial (transition) zone
$\cdots_{k}$	Indication for the incremental (crack) step
$\cdots_{m}$	Indication for the surrounding mortar
$\cdots_{max}$	Indication for a maximum property
$\cdots_{ref}$	Indication for the reference or initial state of a property
$\cdots_{sys}$	Indication for a property defined for the system to be solved
$\cdots_{tot}$	Indication for a combined or total property
$\cdots_{u}$	Indication for the variables, horizontal and vertical displacements
$\cdots_{z}$	Indication for a zone in width direction of the structural element
$\cdots_{1}, \cdots_{2}, \cdots_{3}$	Indications for the nodes of the triangular element

Superscriptions

$\ldots^{e}$	Indication for the element number
$\ldots^{e_d}$	Indication for edge 'd' of the triangular element
$\ldots^{s}$	Indication for an inner or outer section of the structural element
$\ldots^{t}$	Indication for the incremental time step
$\hat{\ldots}$	Indication for an approximate solution
$\ldots'$	Indication for a local definition
$\ldots^{I}, \ldots^{II}, \ldots^{III}$	Indications for the edges of the triangular element

Temperature and pore pressure

Roman upper case

C	[J/kgK]	Specific heat capacity of the material
E_{kin}	[var.]	Kinetic energy across the domain associated with fluxes
H_{vap}	[J/kg]	Enthalpy of vaporization per unit of mass
$H_{vap_{ref}}$	[J/kg]	Reference enthalpy of vaporization of water defined as 2260 kJ/kg
J	[var.]	Functional contribution based on conservation of a density
K	[m^2]	Permeability of the material
K_{xx}, K_{yy}	[m^2]	Principal directions of permeability
K_{cr}	[m^2]	Permeability defined by opening of the crack
$K_{cr_{max}}$	[m^2]	Maximum permeability of the crack
K_{rel_g}, K_{rel_w}	[-]	Relative permeability of the gas, liquid phase based on the saturation level
M_a	[kg/mol]	Molar mass of dry air defined as 0.02897 kg/mol
M_w	[kg/mol]	Molar mass of water defined as 0.018015 kg/mol
P_{atm}	[Pa]	Atmospheric pressure defined at 101325 Pa (1 atm)
P_c	[Pa]	Capillary pressure across the meniscus between the water phases
$P_{c_{max}}$	[Pa]	Maximum capillary pressure defined at 1.72E9 Pa
P_{crit}	[Pa]	Critical vapour pressure defined at 22.09 MPa
P_g, P_w	[Pa]	Pressure of the gas, liquid phase
P_{ga}, P_{gw}	[Pa]	Partial pressure of dry air, water vapour in the gas phase
P_{ref}	[Pa]	Reference vapour pressure defined at 101325 Pa (1 atm)
P_{sat}	[Pa]	Saturated water vapour pressure
Q_A	[var.]	Source of energy related to density exchange along the boundary
R	[J/molK]	Universal gas constant defined as 8.3144 J/molK
RH	[-]	Relative humidity of the material
S_g, S_w	[-]	Saturation level of the gas, liquid phase
T	[K]	Temperature
T_{crit}	[K]	Critical temperature defined at 647.3 K (374.15 ^oC)
T_{ref}	[K]	Reference temperature defined at 373.15 K (100 ^oC)
U	[var.]	Internal energy across the domain associated with a density change
U_{vap}	[J/kg]	Internal energy related to the vaporization process
V_g, V_w	[m^3]	Volume of the gas, liquid phase
V_{pore}	[m^3]	Pore volume
V_{tot}	[m^3]	Total volume
W_{vap}	[J/kg]	Work produced at constant pressure to change the volume

Roman lower case

k	[W/mK]	Thermal conductivity of the material
m_{ga}	[m^3]	Mass of the dry air phase
m_{gw}, m_w	[m^3]	Mass of the water vapour, liquid water phase
n	[-]	Porosity of the material
n_w	[-]	Parameter used to characterise the desorption isotherm
t_{cr}	[s]	Time of fracture
w	[m]	Crack width

Greek lower case

α_A	[W/m^{2}K]	Convective heat transfer coefficient of the material
α_{cr}	[-]	Parameter governing the crack permeability development
α_w	[1/Pa]	Parameter used to characterise the desorption isotherm
β_A	[m/s]	Convective mass transfer coefficient of the material
β_{cr}	[-]	Flux factor governing the permeability perpendicular to the crack
μ_g, μ_w	[kg/ms]	Dynamic viscosity of the gas, liquid phase
ρ	[kg/m^3]	Density of the material
ρ_{ga}	[kg/m^3]	Density of the dry air phase
ρ_{gw}, ρ_w	[kg/m^3]	Density of the water vapour, liquid water phase
ρ_T	[J/m^3]	Density of the thermal energy
ρ_{vap}	[kg/m^3]	Mass density of water vapour produced by evaporation

Vectors

$\boldsymbol{Q_{bc}}$	[var.]	Vector reflecting the contributions by the Neumann boundary conditions
$\boldsymbol{c}$	[var.]	Temperature and capillary pressure vector
$\boldsymbol{q_{gw}}, \boldsymbol{q_w}$	[kg/m^{2}s]	Mass flux vector of the water vapour, liquid water phase
$\boldsymbol{q_T}$	[J/m^{2}s]	Heat flux vector of thermal energy
$\boldsymbol{v_{gw}}, \boldsymbol{v_w}$	[m/s]	Velocity vector driving the water vapour, liquid water mass flux

Matrices

$\boldsymbol{K}$	[m^2]	Permeability tensor (second order)
$\boldsymbol{M}$	[var.]	Mass matrix of partial derivatives with respect to variables
$\boldsymbol{S}$	[var.]	Stiffness matrix based on the fluxes
$\boldsymbol{S_{bc}}$	[var.]	Stiffness matrix reflecting the contributions by the Neumann boundary conditions
$\boldsymbol{T_{ag}}$	[-]	Transformation matrix used to reduce the definition
$\boldsymbol{T_\alpha}$	[-]	Coordinate transformation tensor (second order)
$\boldsymbol{T_\nabla}$	[-]	Transformation matrix for modification of the gradient
$\boldsymbol{k}$	[W/mK]	Thermal conductivity tensor (second order)

Subscriptions

$\cdots_A$	Indication for definition at the surface exposed to the environment
$\cdots_T, \cdots_P$	Indication for a contribution with respect to temperature, capillary pressure
$\cdots_{ag}$	Indication for a contribution based on an aggregate particle
$\cdots_{bc}$	Indication for a contribution based on the Neumann boundary conditions
$\cdots_\alpha$	Indication for the property conserved
$\cdots_\infty$	Indication for definition of a property at distance from the surface
$\cdots_I$	Indication for the conservation equations without considering the coupling based on the process of evaporation
$\cdots_{II}$	Indication for the coupling, reflecting the influence of evaporation on the conservation of thermal energy

Superscriptions

$\overline{\cdots}$	Indication for an averaged property
$\cdots^*$	Indication for reduced properties based only on thermal energy conservation
$\cdots^{**}$	Indication for reduced properties by omitting the material characterisation

(Fracture) mechanics

Roman upper case

E	[MPa]	Modulus of elasticity or Young's modulus of the material
E_{cr}	[MPa]	Young's modulus of the cracked material
EA	[N]	Extensional stiffness of the cross-section
EI	[Nmm^2]	Bending stiffness of the cross-section
F_x, F_y	[N]	Horizontal, vertical force
F_{y_S}, F_{φ_S}	[N], [Nmm]	External load through axial force, moment at the support
$F_{y_{S_{tot}}}, F_{\varphi_{S_{tot}}}$	[N], [Nmm]	Total vertical force, moment at the support
I	[mm^4]	Moment of inertia of the cross-section
J_σ	[J]	Functional based on the balance of linear momentum
K_{y_S}	[N/mm]	Translational spring stiffness at the support
K_{φ_S}	[Nmm/rad]	Rotational spring stiffness at the support
M	[Nmm]	Moment at the cross-section
M_T	[Nmm]	Total thermal moment acting on the cross-section
N	[N]	Normal force at the cross-section
N_T	[N]	Total thermal normal force acting on the cross-section
P_{gw}, P_{atm}	[MPa]	Water vapour, atmospheric pressure
P_{pore}	[MPa]	Pore pressure governed by the uniform gas pressure
$R_{y_{S_{tot}}}, R_{\varphi_{S_{tot}}}$	[N], [Nmm]	Total vertical force, moment reaction at the support
S	[mm^3]	Static moment of the cross-section
U_ε	[J]	Elastic strain energy across the domain
W_F	[J]	Work produced by forces
W_S	[J]	Work produced at the supports by imposed stress concentrations

Roman lower case

d_{rel}	[mm]	Relative distance along the edge relative to the support
d_{rel_T}	[mm]	Temperature elongation defined relative to the support
f_t	[MPa]	Axial tensile strength of the material
f_x, f_y	[MPa]	Body force acting along the x-axis, y-axis
r_i, r_o	[mm]	Inner, outer radius of the surrounding material
s_i, s_o	[-]	Inner, outer section in height direction of the structural element
u_x, u_y	[mm]	Horizontal, vertical displacement
u_{x_κ}, u_{x_T}	[mm]	Horizontal displacement due to curvature, temperature strain
u_{y_S}	[mm]	Vertical displacement of the support
w	[mm]	Crack width
x_{NC}	[mm]	Location of the NC in the cross-section
x_{rel}	[mm]	Internal distance defined relative to the NC
x_{max}	[mm]	Distance from the cross-sectional centre to an exterior edge

Greek lower case

γ_B	[-]	Bending factor governing the influence of the beam
ε	[-]	Total extensional strain
ε_0	[-]	Uniform extensional strain
ε_m	[-]	Mechanical strain inducing stress
ε_T	[-]	Temperature-induced elongation strain
$\varepsilon_{xx}, \varepsilon_{yy}$	[-]	Extensional strain acting along the x-axis, y-axis
γ_{xy}	[-]	Shearing strain
κ	[1/mm]	Curvature
ν	[-]	Poisson's ratio of the material
σ	[MPa]	Stress
σ_{cr}	[MPa]	Axial stress governing the redistribution of the normal force present at fracture
σ_T	[MPa]	Thermal stress in case of restrained expansion based on a uniform temperature increase
σ_P	[MPa]	Pressure-induced stress
σ_{max}	[MPa]	Stress at the cross-section at the exterior edge
σ_{xx}, σ_{yy}	[MPa]	Extensional stress acting along the x-axis, y-axis
σ_{xy}	[MPa]	Shear stress
φ	[rad]	Rotation
φ_S	[rad]	Rotation of the support
ϕ	[var.]	Airy's stress function

Vectors

$\boldsymbol{F}$	[N]	Force vector
$\boldsymbol{F_{bc}}$	[var.]	Force vector governing the prescribed thermal elongation along the rigid body edge
$\boldsymbol{F_T}, \boldsymbol{F_P}$	[var.]	Force vector representing the temperature, pressure induced stresses
$\boldsymbol{F_{cr}}$	[var.]	Force vector representing the redistribution at fracture
$\boldsymbol{F_S}$	[var.]	External load defined as force vector at the support
$\boldsymbol{N}$	[N]	Normal force vector
$\boldsymbol{P_{gw}}, \boldsymbol{P_{atm}}$	[MPa]	Water vapour, atmospheric pressure vector
$\boldsymbol{f}$	[MPa]	Body force vector
$\boldsymbol{t}$	[MPa]	Traction or tension vector applied along the boundary
$\boldsymbol{u}$	[mm]	Displacement vector
$\boldsymbol{u_T}$	[mm]	Displacement vector based on the temperature strain
$\boldsymbol{u_S}$	[mm]	Imposed displacement vector at the supports
$\boldsymbol{\varepsilon}$	[-]	Total strain vector
$\boldsymbol{\varepsilon_T}$	[-]	Temperature-induced strain vector
$\boldsymbol{\sigma}$	[MPa]	Stress vector
$\boldsymbol{\sigma_p}$	[MPa]	Pressure-induced stress vector

Matrices

$\boldsymbol{C}$	[MPa]	Elasticity tensor (fourth order)
$\boldsymbol{D}$	[MPa]	Elasticity tensor using engineering notation (fourth order)
$\boldsymbol{K}$	[var.]	Stiffness matrix
$\boldsymbol{K_S}$	[var.]	Spring stiffness matrix governing the structural interaction
$\boldsymbol{T_{rb}}$	[var.]	Transformation tensor based on coupling conditions along the rigid body edge (second order)
$\boldsymbol{T_\alpha}$	[-]	Coordinate transformation tensor (second order)
$\boldsymbol{T_\gamma}$	[-]	Transformation matrix to define the shearing strain
$\boldsymbol{T_\varepsilon}$	[-]	Strain transformation tensor (fourth order)
$\boldsymbol{T_\sigma}$	[-]	Stress transformation tensor (fourth order)
$\boldsymbol{T_\varphi}$	[-]	Transformation matrix used to extent the nodal variables
$\underline{\boldsymbol{\varepsilon}}$	[-]	Total strain tensor (second order)
$\underline{\boldsymbol{\varepsilon_m}}$	[-]	Mechanical strain tensor inducing stresses (second order)
$\underline{\boldsymbol{\varepsilon_T}}$	[-]	Temperature-induced strain tensor (second order)
$\underline{\boldsymbol{\sigma}}$	[MPa]	Stress tensor (second order)

Subscriptions

$\cdots_S$	Indication for definition at a support
$\cdots_{S_D}, \cdots_{S_N}$	Indication for imposed Dirichlet, Neumann conditions at a support
$\cdots_a, \cdots_b$	Indication for a contribution
$\cdots_{bc}$	Indication for a contribution to impose the thermal elongation of a rigid body edge
$\cdots_{cr}$	Indication for a contribution at a crack edge
$\cdots_{rb}$	Indication for definition at the rigid body boundary condition
$\cdots_{i_{rb}}$	Indication for the node number situated along the rigid body
$\cdots_{u_M}, \cdots_{u_G}$	Indication for a material, geometrical contribution with respect to the horizontal and vertical displacements
$\cdots_{u_B}$	Indication for a bending contribution with respect to the vertical displacement and rotation
$\underline{\cdots}$	Indication for a tensor property

Superscriptions

$\cdots^*$	Indication for definition expressed in half of the shearing strain

Abbreviations

BC	boundary condition(s)
BLEVE	boiling liquid expanding vapour explosion
CG	conjugate gradient
CH	calcium hydroxide
CSH	calcium silicate hydroxide
EPS	expandable polystyrene
FDM	finite difference method
FEM	finite element method
HC	hydrocarbon
HGV	heavy goods vehicle
HRR	heat release rate
HSC	high strength concrete
LITS	load-induced thermal strain
LPG	liquefied petroleum gas
LS	limestone
LWC	light weight concrete
NC	normal force centre
NMR	nuclear magnetic resonance
NSC	normal strength concrete
PDE	partial differential equation
PP	polypropylene
PTM	pressure, temperature and mass
REV	representative elementary volume
RG	river gravel
RH	relative humidity
SCC	self-compacting concrete
UHSC	ultra high strength concrete
W/C	water to cement

1 Introduction

Spalling is first introduced by giving a definition on the specific type of damage referred to. Subsequently a historical overview reflects on several severe fires that occurred in concrete structures and the coinciding development of new fields in research. Practical relevance is established by the damage observed after several tunnel and building fires. Thereafter, the focus is on full-scale experiments and in particular the nature of the spalling process, varying in time of occurrence and level of damage. The concept of fire safety design is introduced, consisting of prevention and mitigation measures as well as methods to assess the fire resistance. This chapter is concluded by an overview of the contents of this thesis.

1.1 Definition of fire-induced spalling of concrete

The subject of this thesis is the damage that occurs to concrete structures in case of exposure to a severe fire. The focus is especially on the phenomenon commonly referred to as fire-induced (explosive) spalling of concrete. In other languages spalling of concrete is known as 'Abplatzungen von Beton' (in German), 'éclatement / écaillage du béton' (in French) and 'spatten van beton' (in Dutch).

Spalling of concrete can be defined as the breaking off of layers or pieces of concrete from the heated surface of a structural element during the rapidly increasing temperatures as experienced in fires (Khoury & Anderberg, 2000). The term explosive spalling is commonly used to indicate that the delamination process is sometimes characterised by a sudden ejection of concrete layers or pieces from the heated surface.

1.2 Historical perspective

Around 1900 several severe fires in buildings focused the attention on the fire resistance and prompted the first fire tests on structural elements (Davey & Ashton, 1953). A committee was established to advice architects and engineers about the fire resistance of materials and to assist public authorities in formulating regulations for buildings (Davey & Ashton, 1953).

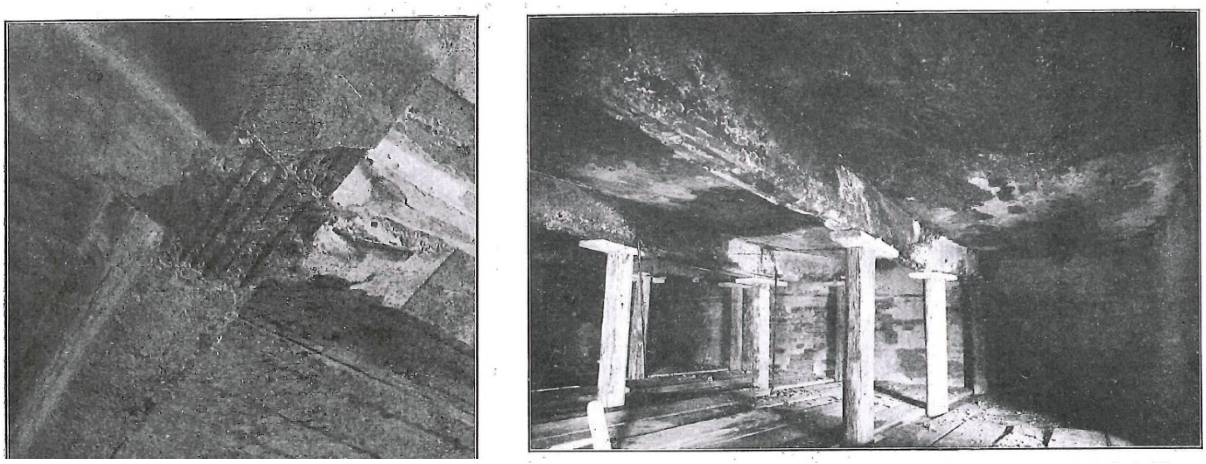

Fig. 1.1 *Spalling of concrete in a building in Dresden, Germany after a fire on August, 13th 1911 (left) and damage to the concrete structure of a building in Vienna, Austria after a fire on January, 8th 1913* (Emperger, 1921).

In the 1920's one of the first reports about fire-induced spalling of concrete observed in several building fires was published (Emperger, 1921). In Fig. 1.1 the damage after the building fires in Dresden, Germany in 1911 and Vienna, Austria in 1913 are shown respectively (Emperger, 1921). In both cases spalling of the concrete surface was observed which exposed the reinforcement to the fire. The fire-induced damage to the building in Vienna resulted in large deformations (Emperger, 1921). The first research into spalling of concrete provided insight into the fire resistance mostly based on the type of material (Probst, 1917). For concrete this included the type of aggregate and the provision of sufficient cover on the reinforcement (Probst, 1917).

In the 1930's the first standardisation for full-scale testing was implemented describing the fire curve, element dimensions and external conditions in order to validate the fire resistance of a structural element (Davey & Ashton, 1953). After the second World War, in the 1950's and 1960's, more elaborate full-scale testing with load application on the specimen during fire exposure were conducted (Davey & Ashton, 1953). This included slabs and columns and provided externally applied loads and possible partial restraint (Davey & Ashton, 1953; Thomas & Webster, 1953). The models that were used had a fundamental character focussing on the temperature development (Kordina, 1963) and resulting thermal stress state. The first theories on pressure development in the concrete due to evaporation of moisture were established (Harmanthy, 1965). Interestingly, the first basic calculations on pressure development were also made (Waubke, 1966).

Around the 1970's and the 1980's the research into spalling of concrete intensified (Khoury & Anderberg, 2000). This was also triggered by the observed damage to the concrete structure in several severe fires such as the Moorfleet tunnel in Hamburg, Germany in 1968 (Haack, 2002), as shown in Fig. 1.2, and the Velser tunnel near IJmuiden, the Netherlands in 1978 (Biersma, 2000). The research was conducted on normal strength concrete (NSC) for which it was observed that spalling can occur in various ways (Khoury & Anderberg, 2000).

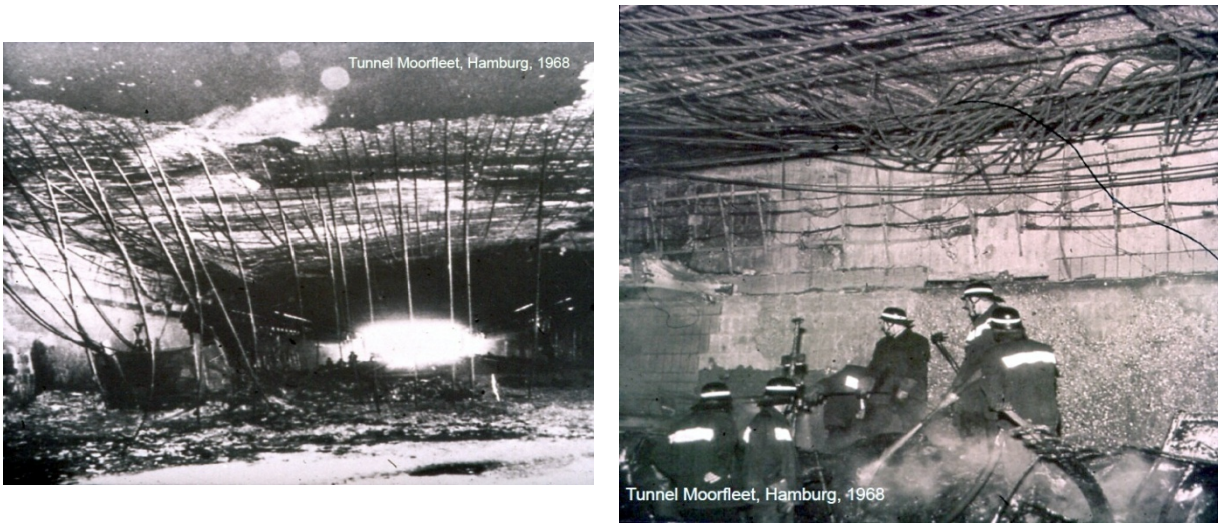

Fig. 1.2 *Damage to the concrete structure of the Moorfleet tunnel in Hamburg, Germany after a fire on August, 31st 1968* (pictures by the fire department of Hamburg).

The influence of the moisture content, thickness and compressive stress were investigated (Meyer-Ottens, 1972; Copier, 1979). This increased the perception and the theory on pressure development in the concrete combined with the thermal stress state as well as possible external loading (Meyer-Ottens, 1975; Zhukov, 1976). The influence of the degradation with temperature of the material also became a focus for experimental research, especially concerning the mechanical properties. This included compressive strength, Young's modulus and tensile strength as well as deformation behaviour at high temperatures (RILEM TC-HTC, 2004). Advances in computational capabilities also allowed models to be based on the finite element method (FEM) (Kordina & Klingsch, 1983).

In the 1990's and the 2000's the research into the behaviour of concrete at elevated temperatures continued also focussing on new concrete types such as high strength concrete (HSC) and self-compacting concrete (SCC) which became more common (fib WP-4.3-1, 2007; Phan, 1996). However, these new types of concrete, with an improved performance, also indicated a higher tendency for spalling during fire exposure (fib WP-4.3-1, 2007; Phan, 1996). Special attention was also given to the behaviour of reactor vessels for nuclear power plants (Schneider, 1991). Several severe fires in the infrastructure occurred, such as in the Channel tunnel between France and England in 1996 (CTSA, 1997) and in the Gotthard tunnel between Italy and Switzerland in 2001 (TCRP & NCHRP, 2006), as illustrated by Fig. 1.3 and Fig. 1.4 respectively. This increased the demand for improved fire safety and the development of spalling resistant concrete structures (Haack, 2002; fib WP-4.3-1, 2007). Fire protection systems with enhanced performance such as boards or panels, sprayed shotcrete or inclusion of polypropylene (PP) fibres in the concrete mixture were developed (Khoury & Anderberg, 2000; fib WP-4.3-1, 2007). Furthermore, also design recommendations indicating the influence of moisture content, aggregate type and reinforcement were established (Khoury & Anderberg, 2000; fib WP-4.3-1, 2007).

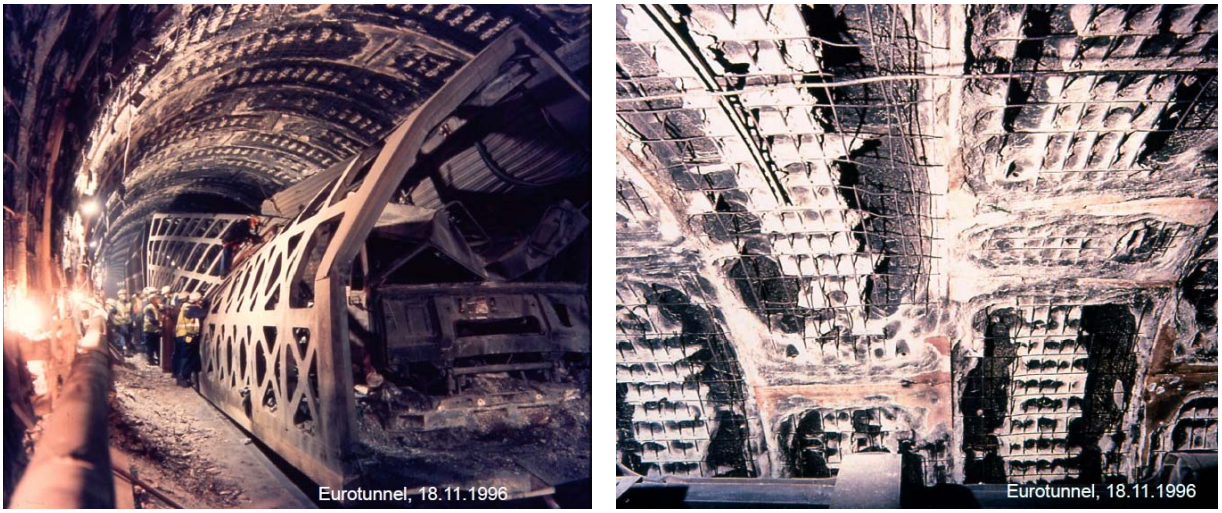

Fig. 1.3 *Damage to the Channel tunnel between France and England after the fire on November, 18th 1996 indicating severe spalling of the concrete lining and exposure of the reinforcement* (pictures by Eurotunnel).

The experimental research into the material behaviour was extended to include chemical investigations into the microstructure of concrete (Alonso & Fernandez, 2004; Castellote, et al., 2004). Additional focus was on the development with temperature of physical properties such as porosity, permeability (IREX, 2005) and the desorption behaviour (Baroghel-Bouny, et al., 1999). New measuring techniques allowed investigation of (pore) pressure build-up (Kalifa, et al., 2000) and the influence of crack development on the thermal deformations (RILEM TC-HTC, 2004; fib WP-4.3-1, 2007). This coincided with the development of numerical models aimed at describing concrete at elevated temperatures using the existing theories for pore pressure and thermal stresses (Gawin, et al., 2003; Tenchev, et al., 2001).

1.3 Practical relevance

1.3.1 Recent fire scenarios

Channel tunnel fire on November, 18th 1996

A well known severe tunnel fire occurred in the Channel tunnel between France and England on November, 18th 1996. This tunnel has a length of 50 kilometres and consists of two main tubes and a smaller service tunnel in the centre interconnected by crossover passages (TCRP & NCHRP, 2006). The fire started at the end of the train in a heavy goods vehicle (HGV) shuttle filling the tunnel with smoke and reaching temperatures of about 1000 °C (TCRP & NCHRP, 2006; CTSA, 1997). The passengers of the train were evacuated through the centre service tunnel and about 30 people suffered injuries from smoke inhalation (TCRP & NCHRP, 2006). The HGV was loaded with expandable polystyrene (EPS) which is inflammable, but was nevertheless allowed to be transported through the tunnel (TCRP & NCHRP, 2006). The fire lasted for 2.5 hours (Lönnermark, 2005) and caused severe damage along 50 metres of the concrete tunnel lining (CTSA, 1997). The lining with a thickness of 400 mm suffered severe spalling and was reduced on average to 170 mm, exposing the reinforcement as shown in Fig. 1.3 (CTSA, 1997).

Fig. 1.4 *Fire in the Gotthard tunnel between Italy and Switzerland on October, 24th 2001 with partial collapse of the concrete roof* (pictures by EPA (left) and by Ti-Press (right)).

In some places only 20 mm remained (CTSA, 1997). The zone with extensive damage to the lining was situated in a rock ground layer (CTSA, 1997) which prohibited water from entering the tunnel. This allowed the possibility to rebuilt the lining afterwards, closing the tunnel tube for the duration of 1 month for repair works (TCRP & NCHRP, 2006).

Gotthard tunnel fire on October, 24th 2001

One of the most severe tunnel fires occurred in the Gotthard tunnel between Italy and Switzerland on October, 24th 2001. This tunnel has a single tube with a length of 17 kilometres with traffic in both directions (TCRP & NCHRP, 2006). The fire started by the collision of 2 trucks, from which one was loaded with tyres, and ultimately destroyed 13 HGV's and 10 cars (Lönnermark, 2005; TCRP & NCHRP, 2006). The fire reached a temperature of 1000 ^{o}C and lasted for 24 hours (TCRP & NCHRP, 2006). In total 11 people died and part of the roof of the concrete structure collapsed as shown in Fig. 1.4. The tunnel was closed for 2 months to allow for repair (Lönnermark, 2005; TCRP & NCHRP, 2006).

Fig. 1.5 *Damage to the concrete structure of a car park in Rotterdam, the Netherlands after a fire on October, 1st 2007 showing severe damage to the roof and spalling of the wall* (pictures by Efectis).

Fig. 1.6 *Damage to the concrete multi-storey building of the Faculty of Architecture at Delft University of Technology in the Netherlands after the fire on May, 13th 2008* (pictures by ANP).

Car park in the Harbour Edge building in Rotterdam on October, 1st 2007

A possible fire scenario for a car park occurred on October, 1st 2007 in the multi-storey building Harbour Edge in Rotterdam, the Netherlands. The fire started in a parked car and spread around, eventually destroying and damaging 7 cars (de Feijter & Breunese, 2007). During the fire the inhabitants were evacuated through the staircases (de Feijter & Breunese, 2007). The discolouring of the concrete wall gave an indication for an obtained maximum temperature of around 1000 ^{o}C (de Feijter & Breunese, 2007). Extensive damage to the hollow core slab roof of the car park occurred as well as spalling of the concrete walls exposing the reinforcement (de Feijter & Breunese, 2007) as seen in Fig. 1.5.

Faculty of Architecture, Delft University of Technology on May, 13th 2008

An example of a large scale fire in a multi-storey building occurred in Delft on May, 13th 2008 as illustrated in Fig. 1.6. A very large fire, starting from a coffee machine, developed in the building of the Faculty of Architecture on the campus of Delft University of Technology (COT, 2008). The fire extinction work was obstructed by temporarily bad accessibility due to construction works as well as the development of multiple fires on several floors. Fortunately, all the occupants were safely evacuated before the fire fully developed (COT, 2008). Part of the building collapsed as a consequence of the prolonged fire exposure (COT, 2008). The building was demolished afterwards (COT, 2008).

Channel tunnel fire on September, 11th 2008

A second fire in the Channel tunnel occurred on September, 11th 2008 onboard of a train (BEA-TT & RAIB, 2010). After detection of the fire the train was stopped and the passengers were evacuated through the central service tunnel with only 6 persons suffering slight injuries (BEA-TT & RAIB, 2010). The train was carrying 25 lorries and 2 vans and the fire fighting operations lasted for 19 hours (BEA-TT & RAIB, 2010). The concrete tunnel lining was damaged due to severe spalling along 16 meters, coinciding with a freight shuttle carrying a HGV with a high fire load (BEA-TT & RAIB, 2010). Heavy spalling had occurred along 284 meters, representing a large part of the train length (BEA-TT & RAIB, 2010).

Fig. 1.7 *Damage and repair works to the Channel tunnel between France and England after the fire on September, 11th 2008* (pictures by AFP).

The depth of the spalling varied and in some cases extended to almost the thickness of the lining (BEA-TT & RAIB, 2010). The service disruption cost the Eurotunnel operator 22 million Euro (Wright, 2008a). The repair works of the tunnel lining involved blasting off of the damaged concrete (Wright, 2008b). A new reinforcement mesh and fresh concrete layer were placed (Wright, 2008b) as shown in Fig. 1.7. The repair costs for the damaged tunnel lining amounted to 60 million Euro and took 5 months (Wright, 2008b). In this period only limited service through one tube was possible resulting in a loss in revenue of 190 million Euro (Wright, 2008a).

1.3.2 Fire development in concrete structures based on full-scale testing

The fire development in several concrete structures has indicated to lead to a severe thermal loading. During full-scale testing measurements on the temperature development as a function of distance to various types of fire were performed (Lönnermark, 2005). For road tunnels, the maximum measured temperature can range from 200 °C for an incended car to 1000 °C for an incended truck as illustrated in Fig. 1.8 (Richter, 1993). An interesting fact is that the fire load of modern cars, due to the usage of plastics, increases resulting in a higher maximum temperature of 400 °C (Richter, 1993). For railway tunnels, the measured maximum temperature ranges from 400 °C to 1000 °C dependent on the type of incended railway carries (Richter, 1993). In both graphs the maximum temperatures are obtained at the roof and at the level of the wall where the windows of the vehicles/carries are located (Richter, 1993).

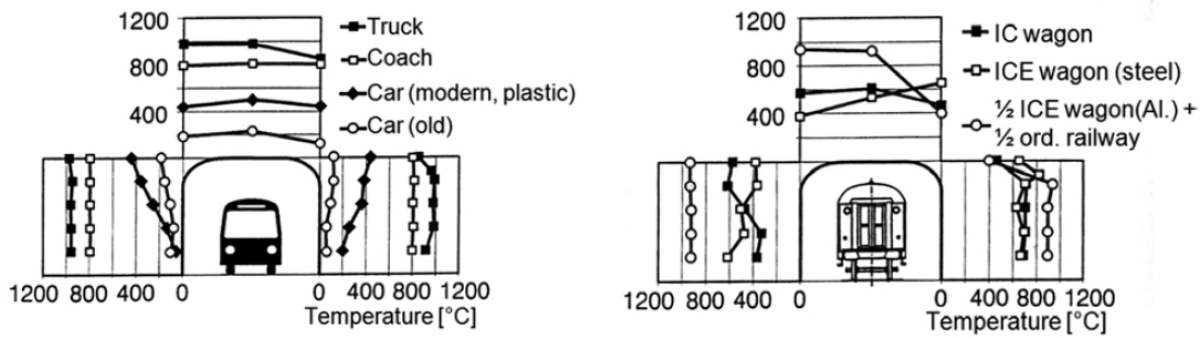

Fig. 1.8 *Maximum temperatures in transverse direction at the tunnel walls and roof for road vehicles (left) and railway carries (right)* (Richter, 1993).

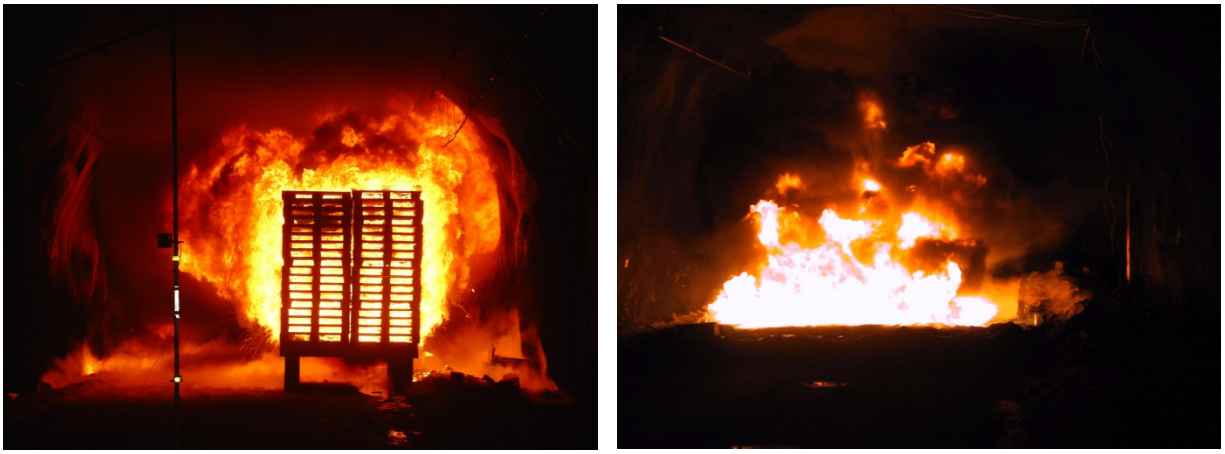

Fig. 1.9 *Full-scale fire testing to determine the temperature development in a tunnel due to a 50 MW solid wood pallet fire (left) and a 200 MW diesel fuel pool fire (right)* (pictures by SINTEF NBL and Aquasys[1]).

The intensity of the fire is expressed by the heat release rate (HRR) and is governed by the fire load corresponding to the material available as fuel. A single car has a HRR of 2.5 - 5 MW dependent on the size (Lönnermark, 2005). A bus or lorry has a HRR of 20 MW and a truck or HGV has a HRR of 20 - 30 MW dependent on the load (Lönnermark, 2005). A tanker truck with fuel can reach a HRR of 100 - 200 MW (Lönnermark, 2005). In actual scenarios the various fire loads are combined dependent on the time of development. During full-scale testing the representative fire load, expressed by the HRR, is commonly based on solid fires consisting of stacked wooden or plastic pallets and liquid fires in which a pan or pool with fuel is used (Lönnermark, 2005).

An example of possible full-scale fire testing was performed in the Runehamar test tunnel in Andalsnes, Norway (Lemaire & Meeussen, 2008). The aim was to determine the suppressing and extinguishing effect of a water-mist system on fully developed fires inside the tunnel. Furthermore, measurements to determine the possibility of a boiling liquid expanding vapour explosion (BLEVE) of a tanker truck as well as temperature and survivability were performed (Lemaire & Meeussen, 2008). The solid fires of 50 MW (180 stacked pallets) and 200 MW (720 stacked pallets) represented possible truck loads and the 200 MW liquid fires in a 100 m^2 pool of diesel fuel represented a tanker truck (Lemaire & Meeussen, 2008) as shown in Fig. 1.9. The temperature in the vicinity of the fire increased for the 50 MW solid fire in 400 seconds to a temperature of 500 ^oC (Lemaire & Meeussen, 2008). For the 200 MW solid fire the temperature increased to 800 ^oC in 300 seconds, reaching a temperature of 1000 ^oC after 400 seconds (Lemaire & Meeussen, 2008). The 200 MW liquid fires were characterised by a very rapid temperature increase to 1000 ^oC in around 100 seconds (Lemaire & Meeussen, 2008). This first rapid temperature increase, referred to as the heating rate, combined with the maximum temperature is commonly used to characterise the development of the fire.

[1] Full-scale fire testing by SINTEF NBL and Aquasys in December 2007 at the Runehamar test tunnel in Andalsnes, Norway on request of Rijkswaterstaat with participation of TNO and Efectis. The author attended these tests as part of his visit to Efectis in Rijswijk, The Netherlands from October to December 2007.

1.3.3 Possible types of fire damage to a concrete structure

(Explosive) spalling of concrete

Spalling of concrete is the most important type of thermal damage and is characterised by a sudden removal of pieces or layers from the heated surface of the structural element (Khoury & Anderberg, 2000; Copier, 1979; fib WP-4.3-1, 2007; Horvath, et al., 2004). This phenomenon is commonly reported to occur during the first 7 to 30 minutes of fire exposure (Khoury & Anderberg, 2000; fib WP-4.3-1, 2007). An important aspect is the repetitive nature in which the spalling process can continue in time removing several layers of concrete (Horvath, et al., 2004). The spalled pieces can have a length varying between 1 and 30 centimetres and a thickness varying between 1 or several centimetres (Mindeguia, 2009; Horvath, et al., 2004). The temperature at the depth at which spalling occurs is in the range of 150 ^{o}C - 250 ^{o}C (Horvath, et al., 2004). The observations made during full-scale fire testing are sometimes used to characterise the different types of spalling. The continuous removal of relatively small layers from the concrete surface is due to the continuous sound effects sometimes referred to as popcorn to describe the spalling process (Khoury & Anderberg, 2000; Mindeguia, 2009). The removal of a relatively large layer is commonly accompanied by a loud bang which illustrates the violent nature and is referred to as explosive spalling (Khoury & Anderberg, 2000; Mindeguia, 2009).

The thickness of the removed layers governs the influence of the spalling process on the structural safety as illustrated by Fig. 1.10. In case of surface spalling (Jansson & Boström, 2008), the protective concrete layer on the reinforcement is only partially reduced. This could, during continued fire exposure, cause a faster temperature increase of the reinforcement. The strength and stiffness reduction of the reinforcement starts at a temperature of about 100 ^{o}C and is commonly not allowed to exceed 250 ^{o}C or 350 ^{o}C (Eurocode 2, 2011b; RWS, 2011).

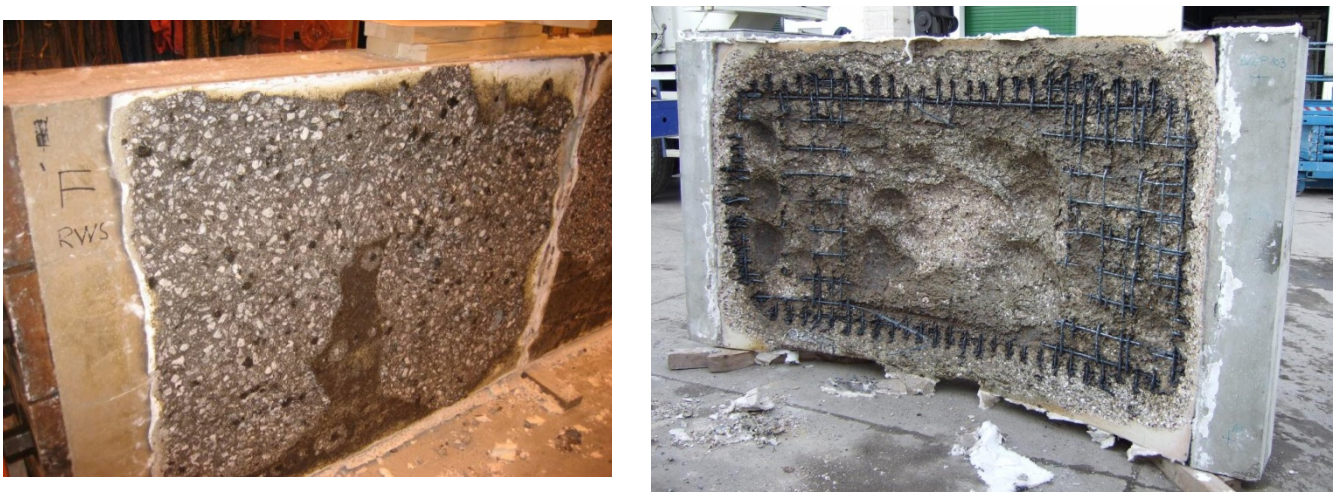

Fig. 1.10 *Spalling of concrete can be limited to the surface as illustrated by the concrete slab after full-scale fire testing (left)* (Jansson & Boström, 2008). *The most severe spalling reduces the thickness and exposes the reinforcement as illustrated by the tunnel lining segment after the full-scale fire test (right)* (picture taken at the MFPA[2]).

[2] Observation by the author after full-scale fire testing of a tunnel lining segment while visiting the MFPA Institute in Leipzig, Germany in February 2009.


Fig. 1.11 *The high temperatures reached during the fire test can cause the exposed reinforcement to melt (left)* (picture by MFPA[3]). *After the fire test a partially detached surface layer was observed at the centre of the tunnel lining segment* (picture taken at the MFPA[4]).

In case of severe spalling the concrete cross-section is reduced and the protective layer on the reinforcement is partially or complete removed (Khoury & Anderberg, 2000; Horvath, et al., 2004). In this last worst case scenario the reinforcement becomes directly exposed to the fire and could possibly melt as indicated in the left picture of Fig. 1.11. In some cases, after the fire test, an indication for the thickness of a spalled layer is possible as shown in the right picture of Fig. 1.11. A surface layer was observed to be partially detached from the cross-section of the tunnel lining segment.

The consequences for the structural safety could possibly be severe dependent on the remaining load bearing capacity of the reduced cross-section and the strength and stiffness of the reinforcement (Khoury & Anderberg, 2000; Horvath, et al., 2004). The structural capacity of the cross-section, the load level and the possible capabilities for redistribution of forces determine the influence of the spalling process. In case of severe spalling, based on single or continued removal of layers, the concrete cross-section could ultimately become sufficiently weakened to allow structural failure of the element (Khoury & Anderberg, 2000; Horvath, et al., 2004). Another possible consequence of spalling is the failure of the separation function of an element. In case of severe spalling holes could develop in the member which therefore no longer fulfils the function as a fire separation barrier (Khoury & Anderberg, 2000; Horvath, et al., 2004).

In literature also some additional specific types of spalling are mentioned such as corner spalling or aggregate spalling (Khoury & Anderberg, 2000; fib WP-4.3-1, 2007; Horvath, et al., 2004). Corner spalling occurs at the edges of the structural element. This type of spalling follows a similar process as described and is influenced by the varying conditions in

[3] Observation by the MFPA Institute in Leipzig, Germany during full-scale fire testing of a tunnel lining segment in February 2009.
[4] Observation by the author after full-scale fire testing of a tunnel lining segment while visiting the MFPA Institute in Leipzig, Germany in February 2009.

temperature and stresses at the edges. The damage and consequences can therefore be similar. Aggregate spalling occurs at the surface of the structural element and is caused by the thermal instability of the aggregate particles (fib WP-4.3-1, 2007; Mindeguia, 2009). This type of spalling is mostly characterised during fire testing by cracking sounds.

Sloughing off of concrete at high temperatures
This type of thermal damage occurs after prolonged fire exposure and is characterised as a continuous falling off of concrete pieces from the heated surface (Copier, 1979; fib WP-4.3-1, 2007; Horvath, et al., 2004). This process occurs at high temperatures which weaken the concrete by degradation of the material until the pieces can no longer remain part of the cross-section and fall off. Dependent on the temperature and duration of fire exposure can this process slowly continue in time and gradually reduce the concrete cross-section (Copier, 1979).

Post-cooling damage to the concrete
After the full-scale tests the concrete specimens can appear to have survived the thermal exposure with a certain extent of damage. Additional damage can occur due to the cooling down of the structural element which could induce additional stresses in a weakened cross-section (fib WP-4.3-1, 2007; Horvath, et al., 2004). Furthermore, the ingress of moisture from the ambient air by the dried concrete can also result in additional damage (fib WP-4.3-1, 2007).

1.4 Fire safety design in current practice

1.4.1 The total concept approach

Fire safety design of a concrete structure incorporates more than only the structural fire safety. Commonly four different categories are distinguished (Heijboer, et al., 2004):

- Pro-action starts in the design phase and aims to reduce the possible occurrence of a fire (Heijboer, et al., 2004). For buildings this could be reached by the use of materials with reduced inflammability. In a tunnel for instance opposite traffic movements in a single tunnel tube are to be avoided possibly combined with a transport restriction for highly dangerous goods such as liquefied petroleum gas (LPG) (Heijboer, et al., 2004; FHWA, 2006).

- Prevention measures aim to reduce the development and the consequences of a fire (Heijboer, et al., 2004). Possible solutions are monitoring, fire and smoke detectors and applying a fire protective board or cladding (Heijboer, et al., 2004; FHWA, 2006).

- Rescue measures provide users with the possibility to take action themselves (Heijboer, et al., 2004). These measures could be alarm buttons combined with fire extinguishing equipment (Heijboer, et al., 2004; FHWA, 2006). For escape staircases or tunnels the possibility for usage in case of smoke and reduced visibility is to be ensured (Heijboer, et al., 2004; FHWA, 2006).

- Repression measures focus on making emergency assistance possible by detection and suppressing of the fire (Heijboer, et al., 2004). This is implemented by for instance sprinklers in buildings. In tunnels a water-mist system, using high pressure sprinklers to extinguish and suffocate the fire, could be used (FHWA, 2006). Smoke extraction by overhead fans and ducts is also possible (Heijboer, et al., 2004; FHWA, 2006).

The design codes, regulations and different parties involved in the construction of the building or tunnel determine the criteria which the fire safety measures have to comply with. The choice for a specific type of fire safety measure can be based on financial considerations (Heijboer, et al., 2004). The investment required for fire safety provisions is weighed by a risk-based analysis (Heijboer, et al., 2004; den Drijver, et al., 2003). In Table 1.1 an overview of the estimated costs for various types of fire safety measures for the Betuwe cargo railway line in the Netherlands is given (den Drijver, et al., 2003). This railway line extends from Rotterdam to the border with Germany and is used to transport cargo from the sea port further into Europe (Bouwdienst Rijkswaterstaat, 2003). The risk-based analysis for each tunnel is based on the possibility for occurrence multiplied by the financial consequences of a severe fire (den Drijver, et al., 2003). However, the choice for fire safety provisions is often based on more than only financial considerations. The established criteria also take into account the public demand for providing the safe usage of a building or tunnel.

1.4.2 Structural fire safety design of concrete structures

In current practise of fire safety design and engineering for concrete structures the applicable European design codes are Eurocode 2, part 1-1 dealing with general rules (Eurocode 2, 2011a) and Eurocode 2, part 1-2 dealing with structural fire design (Eurocode 2, 2011b).

	Heat resistant cladding [*10^6 Euro]	Smoke ventilation [*10^6 Euro]	Fire detection and sprinklers [*10^6 Euro]
Tunnel Giessen Type: open cofferdam Dimensions: 500 m / 2X 1 railway track	1.4	0.3	1.5
Tunnel Zevenaar Type: cut and cover Dimensions: 1500 m / 2X 1 railway track	4.3	0.7	4.6
Tunnel Pannerdensch channel Type: bored tunnel Dimensions: 1615 m / 2X 1 railway track	5.8	1.0	6.2
Tunnel Botlek Type: bored tunnel Dimensions: 1835 m / 2X 1 railway track	7.2	1.2	7.8
Tunnel Sophia Type: bored tunnel Dimensions: 4000 m / 2X 1 railway track	17.3	3.1	18.5

Table 1.1 *Estimation of costs, in June 2003, for fire protection measures in the tunnels of the Betuwe cargo railway line in the Netherlands* (den Drijver, et al., 2003; Bouwdienst Rijkswaterstaat, 2003).

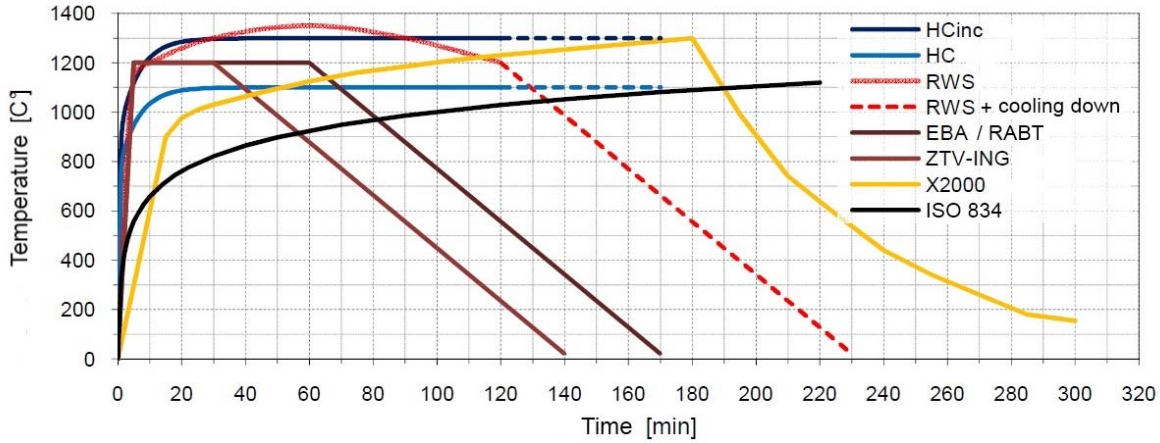

Fig. 1.12 *Various fire curves describing the temperature development in time* (Dehn, et al., 2010) (graph translated from German).

In the Netherlands also guidelines for design of infrastructural structures from Rijkswaterstaat (RWS, 2011) as well as regulations for construction, use and demolishment of structures from the national government (Bouwbesluit 2012, 2011) are in use. In these codes provisions are established to which a concrete structure has to comply. The most important regulations are the fire resistance class, avoidance of spalling of concrete, protection of structural reinforcement and maintaining the separation function.

Design fire curves used in practice

The obtained temperature development from full-scale testing has led to the definition of fire design curves (Eurocode 1, 2011a; Eurocode 1, 2011b) which are shown in Fig. 1.12 (Dehn, et al., 2010). The representative fire loads depend on the type of structure and use. Compared to buildings the assumed fire load for tunnels is higher corresponding to a faster temperature development and a higher level of the maximum temperature. Most fire curves are based on a worst case scenario with relatively high fire loads. The following fire curves are most commonly used:

- The basic fire curve is the ISO 834 or standard fire curve as mentioned in Eurocode 1, part 1-2 dealing with temperature loading on structures (Eurocode 1, 2011a). This curve describes a fully developed fire and is commonly used as standard fire for various structural elements in for instance buildings (Dehn, et al., 2010; Horvath, et al., 2004; Eurocode 1, 2011a). The heating rate is 50 ^{o}C/min in the first 5 minutes after which the heating rate steadily decreases. The temperature is 300 ^{o}C after 6 minutes and 500 ^{o}C after 22 minutes.

- The ZTV and RABT fire curves are used in Germany for road and railway tunnels (Dehn, et al., 2010; Horvath, et al., 2004). In the first 5 minutes the temperature increases to 1200 ^{o}C which corresponds with a heating rate of 236 ^{o}C/min. Dependent on the type of tunnel the temperature is constant during 25 or 55 minutes after which cooling down occurs (Horvath, et al., 2004).

- The hydrocarbon fire curves are for instance used in France and have two possible scenarios (Dehn, et al., 2010; Horvath, et al., 2004; Eurocode 1, 2011a). The increased hydrocarbon fire (HCinc) has the highest heating rate in the first minute reaching a temperature of almost 900 ^{o}C and obtains a maximum temperature of 1300 ^{o}C (Horvath, et al., 2004). The standard hydrocarbon fire (HC) is also given in Eurocode 1, part 1-2 as a severe fire design curve with a maximum temperature of 1100 ^{o}C (Eurocode 1, 2011a).

- The RWS fire curve is developed by Rijkswaterstaat in the Netherlands and is the most severe fire scenario used (Horvath, et al., 2004; RWS, 2011; Eurocode 1, 2011b). This curve is based on the complete burning down of the content of a fuel tank truck. This corresponds with a fire of 2 hours reaching a temperature of 1350 ^{o}C (Horvath, et al., 2004). The maximum heating rate in the first 3 minutes is almost 300 ^{o}C/min.

Structural design for fire resistance

The fire safety design of a structure is based on maintaining sufficient load bearing capacity to withstand a prescribed fire curve for a specified duration (Eurocode 2, 2011b). For buildings commonly the ISO 834 standard fire curve is to be maintained for a specified duration of 30, 60 or 90 minutes on which the fire resistance class is based (Eurocode 2, 2011b; Eurocode 1, 2011a). For a tunnel the possibility of severe fire scenarios is reflected by the requirement to maintain the load bearing capacity during for instance the HCinc, RABT or RWS fire curves (Eurocode 2, 2011b; Eurocode 1, 2011a; Eurocode 1, 2011b). The fire safety design is required at both the component level and the structural level in which also the external loading present during the service life has to be taken into account (Eurocode 2, 2011b).

Actual fire safety design in practice can be based on design tables or graphs, numerical calculations and full-scale testing as stated (Eurocode 2, 2011b):

- The design tables or graphs are mostly based on full-scale testing of standardised concrete elements for which a fire resistance class under certain conditions of heating and loading is determined. This leads to a first indication of the fire resistance and can be the basis for the structural fire design (Eurocode 2, 2011b).

- The numerical calculations are mostly based on mechanical models in which the diminishing fire resistance capacity is incorporated by using temperature-dependent material properties for the strength and stiffness of concrete and reinforcement (Eurocode 2, 2011b). The ultimate load bearing capacity is checked against the imposed loading (Eurocode 2, 2011b). However, also more advanced FEM models can be used to check the load bearing capacity.

- The most expensive solution is full-scale testing of standardised structural elements according to one of the fire curves (Horvath, et al., 2004; Dehn, et al., 2010; Jansson & Boström, 2008). These tests can also incorporate the external load by using dead loads, applying prestressing or using hydraulic jacks (Horvath, et al., 2004; Dehn, et al., 2010; Jansson & Boström, 2008).

Fig. 1.13 *Fire protection boards in the Elb tunnel in Hamburg, Germany* (Promat International N.V., 2003).

Fig. 1.14 *Tunnel lining segment with PP-fibres after full-scale fire testing* (picture taken at the MFPA[5]).

Fig. 1.15 *Spraying of heat resistant cladding in the Western Scheldt tunnel in the Netherlands* (Heijboer, et al., 2004).

The design codes also impose that spalling of concrete is not allowed and that the temperature of the structural reinforcement may not exceed 250 ^{o}C or 350 ^{o}C (Eurocode 2, 2011b; RWS, 2011). These criteria are related with each other and have to ensure that the integrity and load bearing capacity of the structure is maintained (Eurocode 2, 2011b; RWS, 2011).

Fire protection measures for concrete structures

The first type of measures are applied to protect the concrete structure from (spalling) damage and maintain the load bearing capacity. The principle is to mitigate the temperature development by placing an insulation material with sufficient thickness and low thermal conductivity in front of the concrete cross-section. This ensures that spalling of the concrete does not occur and that the temperature increase of the reinforcement is kept within the defined boundaries. The reduced temperatures at the cross-section also ensure that the degradation of the concrete at high temperatures does not occur and that the load bearing capacity is maintained. However, as already indicated in Table 1.1, these protective measures require a financial investment which can be quite substantial.

[5] Observation by the author after full-scale fire testing of a tunnel lining segment while visiting the MFPA Institute in Leipzig, Germany in February 2009.

There are several different types of fire or heat protective measures which can be applied:

- Rectangular panels or boards made of calcium silicate can have a thickness ranging from 12 to 40 mm dependent on the required fire performance as illustrated by Fig. 1.13 (Promat International N.V., 2003).

- Sprayed cladding or plaster is a mixture of vermiculite (wet silicate mineral) and cement sprayed on the concrete surface on which a reinforcement mesh is installed to anchor the cladding (CBBN fire proofing int., 2005). The thickness is determined by the fire protection requirements resulting in a layer of 45 mm in the Western Scheldt tunnel shown in Fig. 1.15 (Heijboer, et al., 2004).

The second type of measures are aimed at reducing the spalling sensitivity. These measures are mostly limited to modifying the concrete mixture since the design fire curve, the moisture content and the structural loading are defined by the building or tunnel project. This may lead to a more cost effective solution than the usage of fire protective measurements. However, the design criterion of avoidance of spalling combined with the complex nature of the phenomenon currently leads to full-scale fire testing to be the only feasible method to ensure fulfilment. It is important to also consider that these measures still allow the temperature to progress into the cross-section and affect the material by degradation and thermal stress development.

There are several methods to modify the concrete mixture in order to possibly reduce the spalling sensitivity. In the guidelines for design of infrastructural structures from Rijkswaterstaat an indication for a concrete mixture with a limited spalling sensitivity is given (RWS, 2011). This NSC is based on limiting the strength class to a C28/35 by defining the maximum cement content of 340 kg/m^3 of CEM III (blast furnace slag cement). The maximum allowable compressive stress is defined as 10 N/mm^2 (RWS, 2011). These provisions are based on the observed limited spalling after exposure to the RWS fire curve of an externally prestressed slab made of a similar concrete mixture with a water to cement (W/C) ratio of 0.5 (Both, 2001).

Addition of PP-fibres to the concrete mixture is also indicated, in these guidelines, to have a beneficial effect on the spalling sensitivity (RWS, 2011). This is attributed to the melting of these fibres at high temperatures (Khoury & Anderberg, 2000). It is believed that this reduces the possibility of unwanted pore pressures and could thereby mitigate the development of spalling (Khoury & Anderberg, 2000). The addition of these fibres has indeed proven beneficial in reducing spalling damage (Brekelmans, et al., 2008; Dehn, et al., 2010) as illustrated by Fig. 1.14. However, conflicting results have also been obtained for ultra high strength concrete (UHSC) (Khoury & Anderberg, 2000; Horvath, et al., 2004). This could possibly be attributed to an insufficient amount and/or type of PP-fibres added to the concrete mixture. The possible dosage of the PP-fibres is limited by the required workability of the concrete mixture (Horvath, et al., 2004).

1.5 STW funded research project

This thesis is written as part of the research project DCB-7045 entitled 'explosive spalling of concrete: towards a model for fire resistant design of concrete elements' (Koenders & Pel, 2004) funded by the Dutch National Science Foundation (STW). Several other governmental and commercial parties, amongst others, Rijkswaterstaat, TNO, Gemeentewerken Rotterdam, Strukton and Efectis, were co-financiers and involved in this research project.

This Dutch research project was a joint effort of Eindhoven University of Technology and Delft University of Technology consisting of 3 PhD sub-projects:

1. *The study of the development of the dehydration processes in the microstructure of the cement paste.* This position was carried out by Q. Zhang at the Microlab group at Delft University of Technology, Faculty of Civil Engineering and Geosciences, Department of Materials and Environment (Zhang, 2013).

2. *The development of an experimental test set-up to measure the moisture distribution in heated concrete using nuclear magnetic resonance (NMR).* This part was carried out by G.H.A. van der Heijden at the group Transport in Permeable Media at Eindhoven University of Technology, Department of Applied Physics (van der Heijden, 2011).

3. *The development of a model that describes the spalling process by taking material aspects such as dehydration and pore pressure development into account as well as structural aspects such as the fire scenario and the external loading.* This investigation was carried out by the author of this thesis at the group Concrete Structures at Delft University of Technology, Faculty of Civil Engineering and Geosciences, Department of Structural and Building Engineering.

1.6 Overview of this thesis

This thesis consists of 4 different parts, as seen in Fig. 1.16, where any part is subdivided in several chapters. The **first part** consists of this introduction (**chapter 1**) followed by a state of art study presented in **chapter 2**. These findings are used, in **chapter 3**, to state the problem description and the objectives of this thesis. The adopted solution approach focuses mainly on the derivation of a FEM-based model, implemented for a 2D cross-section representing part of a fire exposed concrete structural element. A coupled heterogeneous material description is proposed, aimed at temperature and pore pressure as well as fracture mechanics behaviour.

The **second part** starts with the basic theories and relationships used to describe fire exposed concrete. In **chapter 4** first the relationship between temperature and gas pressure development is clarified by using a simplified closed system. Using a similar approach allows to examine the gas pressure development during crack opening. Subsequently, an open system is defined based on an averaged material description governed by the partial differential equation (PDE) for the conservation of a property. This general PDE is extended to conserve the thermal energy or the mass of the water phases in a porous material. In both cases the PDE is solved using the finite difference method (FDM).

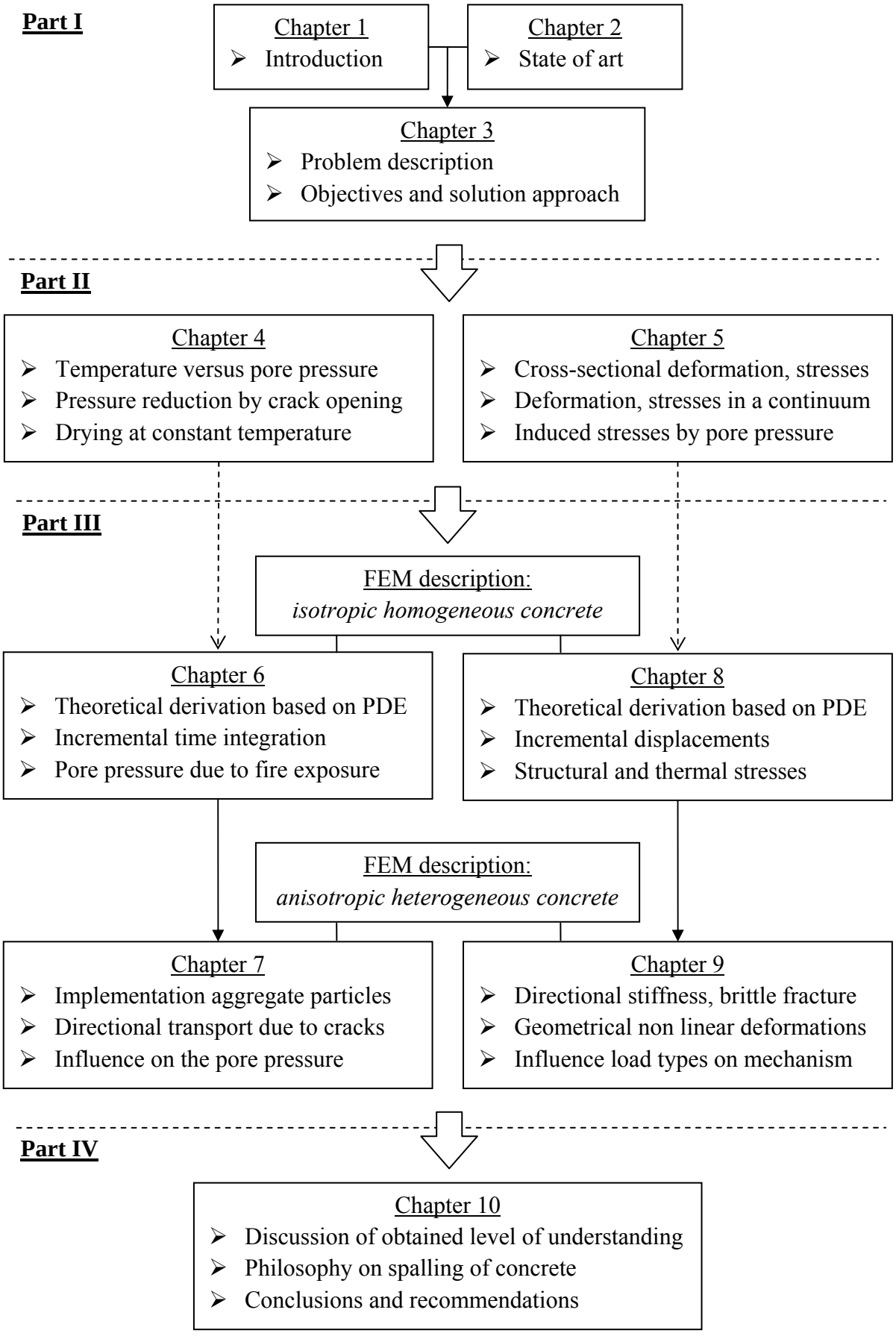

Fig. 1.16 *Schematic overview of the various parts and chapters presented in this thesis.*

In the next chapter, **chapter 5**, the stress state in the cross-section is determined based on the numerical approximation of the equilibrium conditions. Basic mechanical relationships governing a symmetrical structural element are presented. Thereafter the definition of a mechanical continuum is stated, taking into account the initial temperature elongation strain. This chapter is concluded by discussing the mechanical consequences of pressure development in a porous material. For this purpose the PDE that governs the continuum is restated in polar coordinates to determine the elastic stresses in the material.

Derivation of two coupled FEM models are the topic of the **third part** which consist of four chapters. The first two chapters focus on temperature and pore pressure. In **chapter 6** an isotropic and homogeneous material description for a 2D cross-section is stated by extending and coupling of the conservation equations derived in chapter 4. This averaged porous material description characterises the process of forced drying while the Neumann boundary conditions reflect exchange with the environment. Periodical conditions are imposed along the top and bottom boundary. Subsequent, Galerkin's method is used to numerically approximate this coupled system of PDE's in order to define a random 2D triangular element. The FEM system is obtained by using an Euler backward time integration scheme with an incremental definition of the nodal variables. In the remainder of this chapter the FEM definition is validated by comparisons with the results of chapter 4. Fire exposure of the cross-section allows to indicate the forced drying process and the gas pressure development.

In **chapter 7** the FEM definition is extended to first include heterogeneity. The aggregate particles are assumed to be impermeable and surrounded by mortar and interfacial zones. This introduces a solid material description which only allows for thermal conductivity. Secondly, anisotropy is introduced by the definition of directional dependence in the transport properties along the crack. The orientation and opening characterises the influence of the crack pattern as will be obtained through a fracture mechanics approach as presented in chapter 9. Also attention is given to numerical stability issues related to the boundary conditions and the sudden permeability increase upon crack opening. Several numerical results are presented, allowing to assess the influence of the aggregate particles on the pore pressure development. A simplified cracked cross-section is used to indicate key aspects of the drying process caused by the localised increased flow capability of the material.

The next two chapters deal with the mechanical behaviour in which **chapter 8** also describes an isotropic and homogeneous material. The linear elastic continuum definition from chapter 5 forms the starting point, with only temperature strains imposed as internal loading. A plane strain approximation is used to characterise the out-of-plane direction. Structural boundary conditions are imposed along the top and bottom edges through the definition of rigid bodies with central supports. The PDE is numerically approximated through Galerkin's method to obtain the FEM definition, discretised by similar random 2D triangular elements. An incremental approach is used to define the displacements. This approximation is validated through comparison with results stated in chapter 5. Thereafter, the influence of structural boundary conditions and fire exposure is discussed. Attention is also given to the chosen approximation for the out-of-plane direction.

The FEM definition, presented in **chapter 9,** aims to approximate the fracture mechanics behaviour through an anisotropic definition. The triangular area is characterised by 1D bars which only allow for axial force transfer. This directional deformation characterisation is used to approximate the global strains. Initial temperature strains as well as pressure-induced stresses are assumed to load the cross-section. Furthermore, heterogeneity is implemented through characterisation for each bar of the stiffness and temperature strain development. A brittle fracture mechanics approach is used to simulate the development of the crack pattern. Extensional fracture and subsequent removal of bars forces the localisation of deformation in opening of the crack. The possible development of large strains and rotations is addressed through an additional geometrical stiffness definition. Furthermore, in order to distribute to fracture forces along the crack edges Bernoulli-Euler beams are implemented. This chapter is concluded by presenting numerical results aimed at the development of the crack pattern. The influence of temperature and pore pressure development as well as structural loading is discussed. The results reflect the formation of a fracture mechanism characterised by the removal or spalling of heated surface layers.

This thesis is concluded by the **fourth part,** consisting of a philosophical view on the fire-induced spalling mechanism of concrete. The differences between the dominant processes such as temperature and pore pressure as well as internal and external loading are discussed in relation to experimental results. It is argued that spalling might be seen as a form of thermal buckling which develops due to partially restrained deformation of the heated surface layer. Finally, the conclusions and recommendations for the scientific and engineering field are presented.

2 State of art

In this chapter first a survey of experimental results regarding concrete at elevated temperatures is presented. The chemical dehydration processes that develop in the microstructure of the cement paste are identified based on thermal investigations. Thereafter, attention is given to the physical processes, reflecting mainly (pore) pressure measurements and results obtained by NMR. The influence of elevated temperatures on the mechanical behaviour of concrete is elaborated based on strength and stiffness measurements as well as thermal deformations. In the second part of this chapter the focus is on fire tests conducted to assess the spalling sensitivity of concrete. Various results are discussed in relationship to the main existing theories of pore pressure and thermal stresses. In the final part an overview of numerical models aimed at describing concrete at elevated temperatures is provided.

2.1 Thermal chemical degradation processes

2.1.1 Concrete as a heterogeneous material

The material concrete consists of aggregates, distributed in its volume, forming the skeleton. These particles are 'glued' together by the mixture of hardened cement paste and sand, commonly referred to as mortar (Fischer, 2009; Mehta & Monteiro, 2006). The latter is the first main component of this heterogeneous material as seen in the left picture of Fig. 2.1. The hydrated cement paste is the product of several chemical reactions of cement powder and water. The W/C ratio governs the compressive strength development and defines the concrete strength class using cylinders or cubes according to (Eurocode 2, 2011a). A W/C ratio of 0.5 results in a NSC with a compressive strength of 30 to 40 MPa (Li, 2011). A HSC generally has a W/C ratio of about 0.3 leading to a compressive strength of 60 to 70 MPa (Koenders, 1997).

Portland cement powder consists of calcium oxide (CaO) or lime, silicon oxide (SiO_2) or silica and aluminium oxide (Al_2O_3) or alumina (Fischer, 2009). Upon mixing the water is chemically bound by hydration with the cement powder forming almost instantaneously the first product commonly referred to as ettringite (Mehta & Monteiro, 2006). Subsequently, two additional hydration products are formed which are calcium silicate hydroxide (CSH) and calcium hydroxide ($Ca(OH)_2$) or portlandite (CH) (Mehta & Monteiro, 2006).

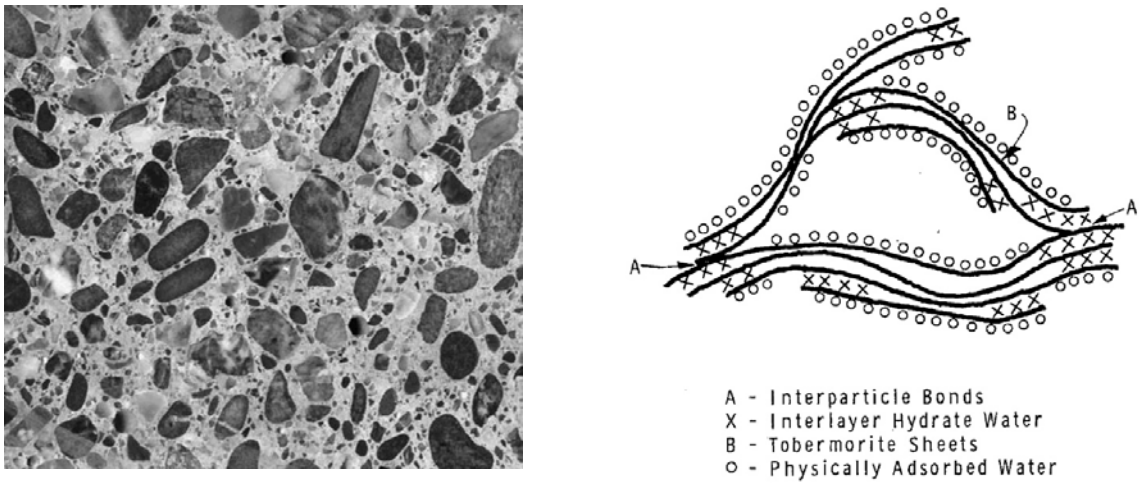

Fig. 2.1 *Concrete consisting of aggregate particles surrounded by the mortar mixture of hydrated cement paste and sand (left)* (Mehta & Monteiro, 2006). *The porous microstructure of cement paste, schematically represented by the layered CSH gel and the various states of liquid water (right)* (Feldman & Sereda, 1968).

The CSH gel or tobermorite gel (Mehta & Monteiro, 2006) has a layered structure with relatively small gel pores or interlayer spaces filled by gel water or interlayer water (Mehta & Monteiro, 2006; Feldman & Sereda, 1968). Water is also absorbed to the surfaces of the microstructure (Mehta & Monteiro, 2006) as is schematically shown in Fig. 2.1 (Feldman & Sereda, 1968). The gel pores have the smallest pore sizes in the range of 0.5 nm to 3 nm (Mehta & Monteiro, 2006; Baroghel-Bouny, 1994b) and form an interconnected network. The strength and stiffness of the cement paste is largely governed by Van der Waals forces acting across the relatively high surface area in the CSH structure (Mehta & Monteiro, 2006).

The remaining space, not filled by the hydration products, is commonly referred to as the volume of capillary pores (Mehta & Monteiro, 2006). The capillary pores are voids in the solid hydration product with a negative influence on the strength and stiffness of the cement paste (Mehta & Monteiro, 2006). The capillary pores display larger pore sizes, in the range of 3 nm to as large as 3 µm, (Mehta & Monteiro, 2006; Baroghel-Bouny, 1994b) and tend to be not fully interconnected. The degree of filling with capillary water is for the pore sizes lower than 50 nm determined by capillary suction (Mehta & Monteiro, 2006). This is governed by atmospheric conditions such as the temperature and the RH. The larger capillary pores are not influenced by the environment and filled with 'free' water (Mehta & Monteiro, 2006).

The aggregate particles are the second main component of concrete. Various types are used which differ in geological history (Krebs, 2003). In the Netherlands glacial river gravel is commonly used which is a sedimentary rock consisting mainly of quartz (SiO_2) (Krebs, 2003; fib WP-4.3-1, 2007). In other European countries also limestone aggregate is used which is a sedimentary rock formed by the consolidation of calcite ($CaCO_3$) (Krebs, 2003; fib WP-4.3-1, 2007). With respect to concrete both are commonly referred to as siliceous or calcareous aggregate types (fib WP-4.3-1, 2007). Other types of aggregates used are granite or basalt, both igneous rock formed by cooling of magma (Krebs, 2003). Finally, also lightweight aggregates, such as expanded slag from blast furnaces, are used (fib WP-4.3-1, 2007).

The third main component are the interfacial transition zones governing the connection between the surface of the aggregate particle and the surrounding mortar (Mehta & Monteiro, 2006). The microstructure of the interfacial zones is generally less well developed due to the liquid water film surrounding the aggregates causing a higher W/C ratio (Mehta & Monteiro, 2006). The increased porosity of the formed microstructure combined with micro cracking during hydration leads to a reduced strength (Mehta & Monteiro, 2006).

2.1.2 Dehydration of the cement paste microstructure

The exposure of concrete to elevated temperatures has the largest impact on the microstructure of the cement paste. Several chemical processes develop which affect the cement paste by removal of the liquid water present in various forms in the microstructure. At temperatures below 100 ^{o}C the evaporation process of the capillary water defines the first phase of the forced drying of the microstructure (Mehta & Monteiro, 2006; Alonso & Fernandez, 2004), starting with the largest pore sizes (Pel & Huinink, 2007). The energy consumption and relative mass loss, shown in Fig. 2.2 and Fig. 2.3, illustrate a process that gradually develops with temperature (Khoury, 2006a; Alonso & Fernandez, 2004). As the temperature reaches the interval of 100 ^{o}C to 250 ^{o}C the evaporation of the capillary water could still be ongoing (Liu, 2006).

In the temperature interval from 200 ^{o}C to 400 ^{o}C the liberation of gel water occurs, contributing to the drying of the microstructure (Alonso & Fernandez, 2004; Liu, 2006). The dehydration process of the CSH also develops in which chemically bound water is removed from the formed hydration product causing a continued degradation (Liu, 2006; Castellote, et al., 2004). Around a temperature of 450 ^{o}C the energy consumption of the cement paste indicates a relatively short but distinctive energy peak. This is governed by the rapid dehydration of the CH creating calcium oxide (CaO) or lime (Alonso & Fernandez, 2004; Liu, 2006). The degradation of the microstructure continues slowly to a temperature of 600 ^{o}C after which the remaining CH has dehydrated (Liu, 2006).

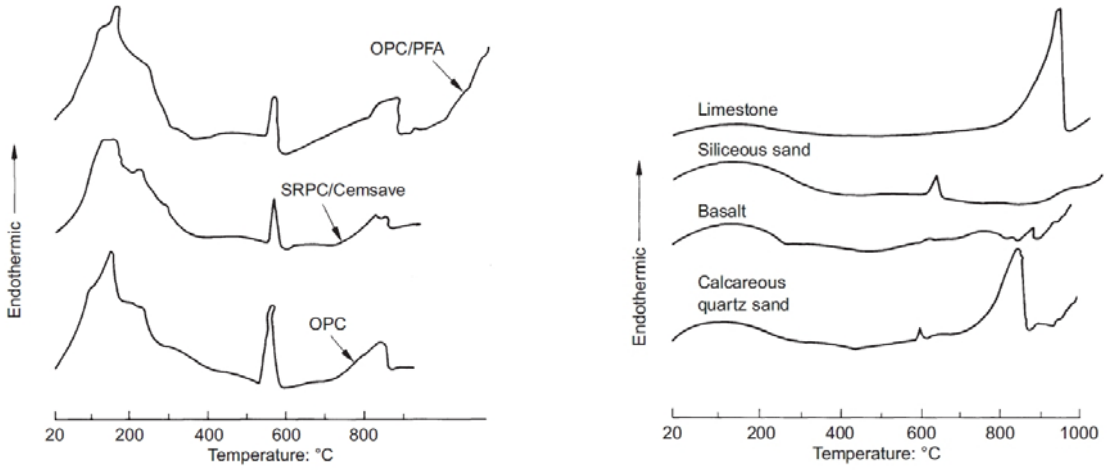

Fig. 2.2 *Consumption of energy as governed by the dehydration processes for cement pastes with a W/C ratio of 0.45 (left). Aggregates and sand types only exhibit energy consumption at high temperatures (right)* (Khoury, 2006a).

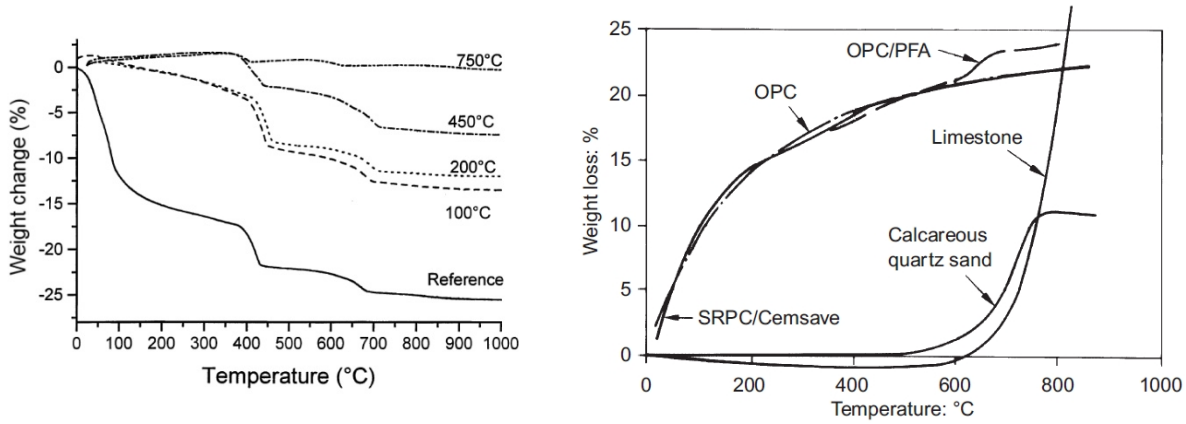

Fig. 2.3 *Relative mass loss illustrating drying and dehydration of pre-heated cement paste samples with a W/C ratio of 0.4 (left)* (Alonso & Fernandez, 2004). *Decarbonation and α-β quartz inversion develop at temperatures of 600 °C (right)* (Khoury, 2006a).

A final chemical reaction occurs in the temperature interval of 650 °C to 750 °C, characterised by the decarbonation of calcium carbonate ($CaCO_3$) or calcite (Alonso & Fernandez, 2004; Liu, 2006; Castellote, et al., 2004). Calcium oxide (CaO) or lime and carbon dioxide (CO_2) are formed (Alonso & Fernandez, 2004; Liu, 2006; Castellote, et al., 2004). This process marks the final chemical reaction for the microstructure of the cement paste. Further temperature increase will only lead to small additional changes.

2.1.3 Degradation processes in aggregate and sand types

The decarbonation reaction is also observed in the energy consumption of limestone aggregate and calcareous quartz sand as a distinctive peak around a temperature of 800 °C (fib WP-4.3-1, 2007). This causes a relatively large mass loss for the aggregates as seen in Fig. 2.3 (Khoury, 2006a). Siliceous sand only exhibits one distinctive energy consumption reaction as shown in Fig. 2.2 (Khoury, 2006a). At a temperature of 573 °C the transformation of the crystalline structure of sand from α-quartz to β-quartz occurs (Cruz & Gillen, 1980). Some siliceous aggregate types, such as Thames river gravel and French flint, are reported to fracture under a sudden thermal expansion and are referred to as thermally unstable as shown in Fig. 2.4 (fib WP-4.3-1, 2007; Mindeguia, 2009).

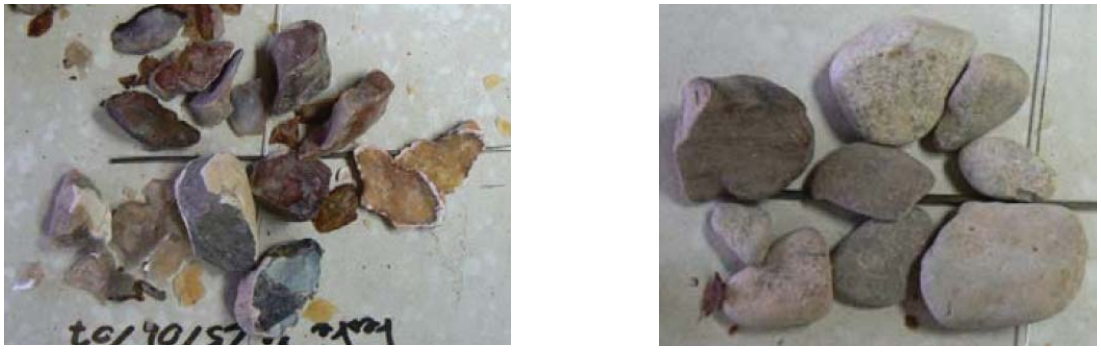

Fig. 2.4 *Thermal instability of French flint (left), a siliceous aggregate type, compared to calcareous aggregates (right) after heating to a temperature of 200 °C* (Mindeguia, 2009).

Limestone aggregate is considered to have a higher thermal stability (fib WP-4.3-1, 2007; Mindeguia, 2009) based on the reduced and more controlled thermal expansion compared to quartz (Flynn, 1999). Basalt is thermally stable and exhibits no distinctive energy consumption process since this type of aggregate originates from cooled magma (fib WP-4.3-1, 2007). For lightweight aggregates the presence of moisture in the microstructure could lead to evaporation and possible pressures causing thermal instability (fib WP-4.3-1, 2007).

2.2 Thermal physical processes causing gas pressure development

2.2.1 The relationship between temperature and pore pressure

Exposure of a concrete specimen or structure to a heat source increases the surface temperature. The transmission of thermal energy through the material is for the most part characterised by the thermal conductivity of the mortar and aggregate particles based on the temperature gradients (Hassanizadeh & Gray, 1979b; Bear & Bachmat, 1986). The thermal energy is also transported through the mortar by the flow of heated gas and liquid phases referred to as convection (Hassanizadeh & Gray, 1979b; Bear & Bachmat, 1986). Elevated temperatures also cause forced drying of the cement paste (Alonso & Fernandez, 2004; Liu, 2006) governed by evaporation of liquid water. The resultant gas pressure increase in the confined pore space is commonly referred to as the pore pressure.

Gradual thermal exposure of C40/50 and C60/75 specimens indicates the development of the temperature and gas pressure in the cross-section as illustrated in Fig. 2.5 (Mindeguia, 2009). These pressure, temperature and mass (PTM) measurements (Kalifa, et al., 2000) are performed at various depths as indicated (Mindeguia, 2009). The temperature development gradually progresses into the cross-section. Directly behind the heated surface temperature plateau's are observed coinciding with the maximum gas pressure measurements at the same depths (Mindeguia, 2009). This behaviour is attributed to the evaporation process since it was not observed in similar concrete specimens predried at 80 ^{o}C (Mindeguia, 2009). The continued temperature increase coincides with a gradual reduction of the gas pressure.

The temperature gradient combined with the varying stages of the evaporation process results in the development of gas pressure gradients driving the transport of the liquid and especially the gas phases through the cross-section (Hassanizadeh & Gray, 1980; Couture, et al., 1996). The influence of the relatively high gas pressure gradient outweighs the slow process of diffusion governed by gradients in the phase concentrations (Bear & Bachmat, 1986). The uniform thermal exposure causes a predominately 1D flow perpendicular to the heated surface. The vapour transported towards the heated surface can directly escape into the ambient atmosphere (Kalifa, et al., 2000; Zeiml, et al., 2006). However, in the opposite direction, into the cross-section, the reduction of the temperature leads to condensation of vapour into liquid water which increases the local moisture level (Kalifa, et al., 2000; Zeiml, et al., 2006). With time the drying front progresses into the cross-section, thereby increasing the distance to the heated surface. This enables the gas pressure to reach higher values governed by the volume of liquid water available, the temperature and the type of concrete (Kalifa, et al., 2000; Zeiml, et al., 2006).

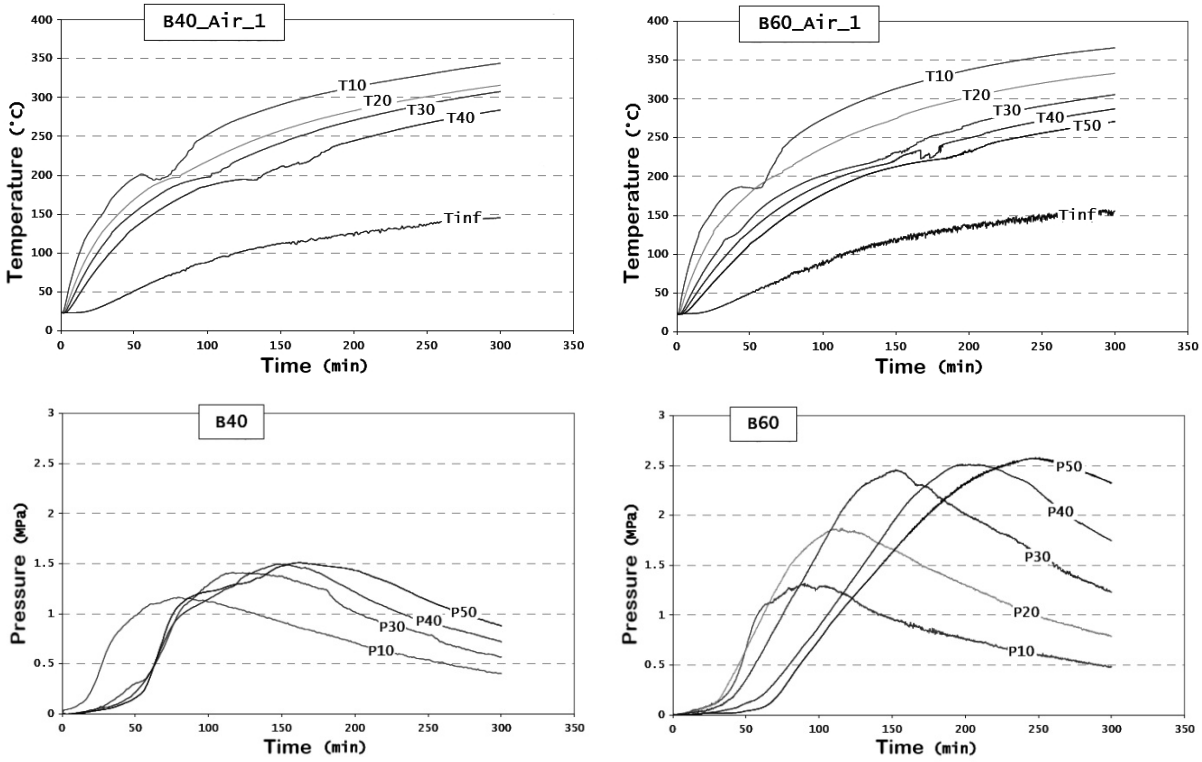

Fig. 2.5 *The behaviour of gradually heated B40 or C40/50 (left) and B60 or C60/75 (right), characterised by increasing temperatures and coinciding gas pressures as measured at various depths* (Mindeguia, 2009) (graphs translated from French).

2.2.2 Comparison between NSC and HSC

It is commonly stated that in HSC the pore pressure reaches higher values than in NSC (Mindeguia, 2009; Phan, 2008). This is illustrated by comparing the maximum gas pressures which reach 1.5 MPa in C40/50 and increase to 2.5 MPa in C60/75 as shown in Fig. 2.5 (Mindeguia, 2009). The comparison between the gas pressure distributions furthermore indicates that the drying process in C60/75 develops at a lower rate. This is reflected by the gas pressures, measured at the various depths, indicating a mitigation in the development (Mindeguia, 2009). The differences in gas pressure build-up increase with the distance relative to the heated surface. The highest gas pressures are obtained for the HSC, illustrated in the right graph of Fig. 2.6, reaching almost 4.0 MPa (Kalifa, et al., 2000). This concrete, characterised as C95/110, reflects the unfavourable influence of the concrete strength in the pore pressure development (Kalifa, et al., 2000; Mindeguia, 2009).

This difference in gas pressure development is mainly attributed to the permeability of the concrete (Kalifa, et al., 2000; Phan, 2008) as illustrated in Fig. 2.7 (IREX, 2005). The reduced pore space and connectivity, reflected by the lower permeability of HSC, mitigates the possibility for the formed vapour to escape. This allows for higher gas pressures which are sustained due to the increased strength of the material. This also influences the progress of the drying front which for HSC needs more time to develop. Interestingly, for the displayed concrete types, the maximum gas pressure is observed to be roughly constant in time. This suggests that at a sufficient distance from the heated surface the evaporation process results in a similar gas pressure dependent on the concrete strength.

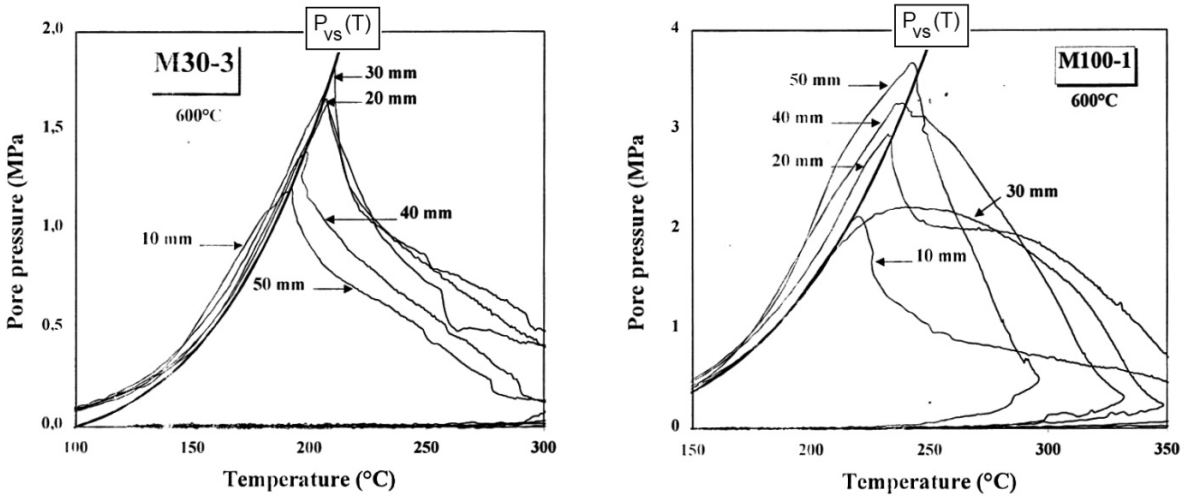

Fig. 2.6 *The lower permeability of M100 or C95/110 (right) compared to M30 or C35/45 (left) mitigating the possibility for the water vapour to escape to the heated surface. This causes the gas pressure to increase with depth* (Kalifa, et al., 2000).

In Fig. 2.6 also the relationship between the gas pressure and the saturated water vapour pressure or $P_{vs}(T)$ is represented (Kalifa, et al., 2000). This equilibrium pressure describes the saturated state of the vapour and increases with temperature (Kotz, et al., 2009). The overall gas pressure is determined by the partial pressures of the water vapour and dry air phases (Moran & Shapiro, 2004). The maximum gas pressures for C35/45 and C95/110 are found in Fig. 2.6 for temperatures of 200 ^{o}C and 250 ^{o}C respectively (Kalifa, et al., 2000). This directly influences the attained vapour pressure. The gas pressure in C95/110 is also observed to reach higher values than the saturated water vapour pressure. This is attributed to the dry air phase being trapped in the microstructure due to the low permeability (Kalifa, et al., 2000).

2.2.3 The relationship between temperature and moisture content

The actual development of the drying process is demonstrated by NMR experiments, obtaining the temperature and moisture distributions in time as shown in Fig. 2.8 for gradually heated C40/50 cylinders (van der Heijden, 2011). The graphs are based on preconditioned specimens, at various RH's, governing the initial moisture level (van der Heijden, 2011).

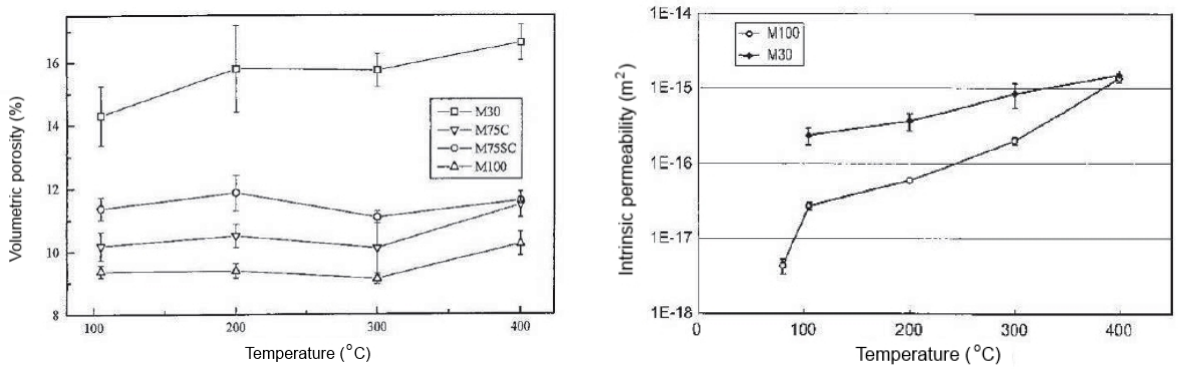

Fig. 2.7 *Porosity (left) and especially permeability (right), indicated for M30 or C35/45 and M100 or C95/110, govern gas pressures by characterising the pore space and the flow capability respectively* (IREX, 2005) (graphs translated from French).

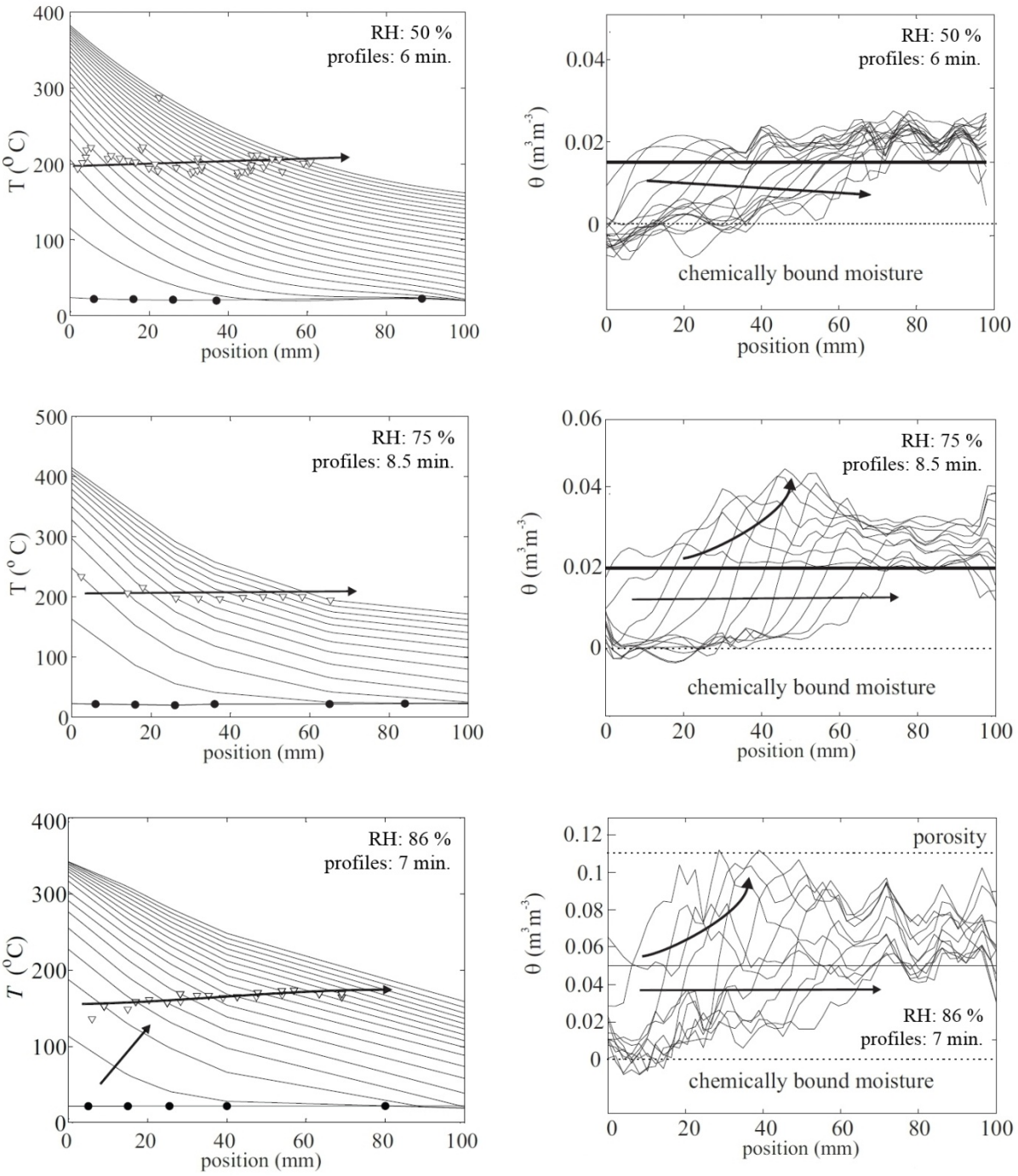

Fig. 2.8 *Distributions of temperature (left) and moisture level (right) illustrating the drying of gradually heated C40/50 cylinders preconditioned at various RH's. Across the temperature profiles the boiling front is indicated* (van der Heijden, 2011).

From the heated left surface the reduced moisture level reflects the dried state of the material (van der Heijden, 2011). In this layer the capillary water is evaporated and the gas pressure is no longer sustained. The contribution of the dehydration processes by continued liberation of chemically bound water is indicated to be limited due to the gradual nature (Alonso & Fernandez, 2004). The permeability of the dried material governs the transport of vapour to the heated surface (Kalifa, et al., 2000; Zeiml, et al., 2006).

The progress of evaporation, or boiling, into the cylinders is marked by the gradients in the moisture content indicating the drying and possibly wetting of the material (van der Heijden, 2011). Drying of concrete at temperatures higher than 100 ^{o}C corresponds to water vapour pressures exceeding atmospheric conditions, assuming a saturated state (van der Heijden, 2011). For the specimens with an initial relative humidity (RH) of 50 % and 75 % the boiling temperatures indicate a vapour pressure between 1.5 and 1.9 MPa (van der Heijden, 2011). At an initial RH of 86 % the pressures were only between 0.6 and 0.8 MPa (van der Heijden, 2011).

At the drying front the gas pressure increases with temperature, causing the flow of vapour and coinciding increasing moisture levels into the cylinder (van der Heijden, 2011). This is especially observed for the concrete cylinders with a high initial moisture level imposed by the preconditioned RH. The highest moisture levels are observed in Fig. 2.8 for the cylinder preconditioned at a RH of 86 %. An almost saturated state is reached, commonly referred to as moisture clogging (van der Heijden, 2011; Zeiml, et al., 2006).

2.2.4 Mitigation of gas pressures

Addition of PP-fibres to the concrete mixture

In some concrete mixtures PP-fibres are added aimed at reduction of unwanted pore pressures. These PP-fibres as for instance shown in Fig. 2.9 (Hager, 2004) are very small, with a diameter of around 18 μm and a length between 6 and 12 mm (Mindeguia, 2009; Zeiml, et al., 2008a; Brekelmans, et al., 2008; Dehn, et al., 2010). The dosage of the PP-fibres varies commonly between 1.0 kg/m^3 and 2.0 kg/m^3 of concrete with incidentally even 3.0 kg/m^3 (Mindeguia, 2009; Zeiml, et al., 2008a; Brekelmans, et al., 2008; Dehn, et al., 2010). The PP-fibres are added to the mixture during casting and reduce workability (Hager, 2004).

PP-fibres are believed to already affect the permeability of the concrete at ambient temperatures. This is attributed to the poor adhesion between the PP-fibres and the cement paste as well as micro cracking (Khoury, 2008b). The PP-fibres melt at a temperature of 160 ^{o}C to 170 ^{o}C and evaporate at a temperature of 340 ^{o}C to 365 ^{o}C (Zeiml, et al., 2008a; Brekelmans, et al., 2008; Khoury & Willoughby, 2008).

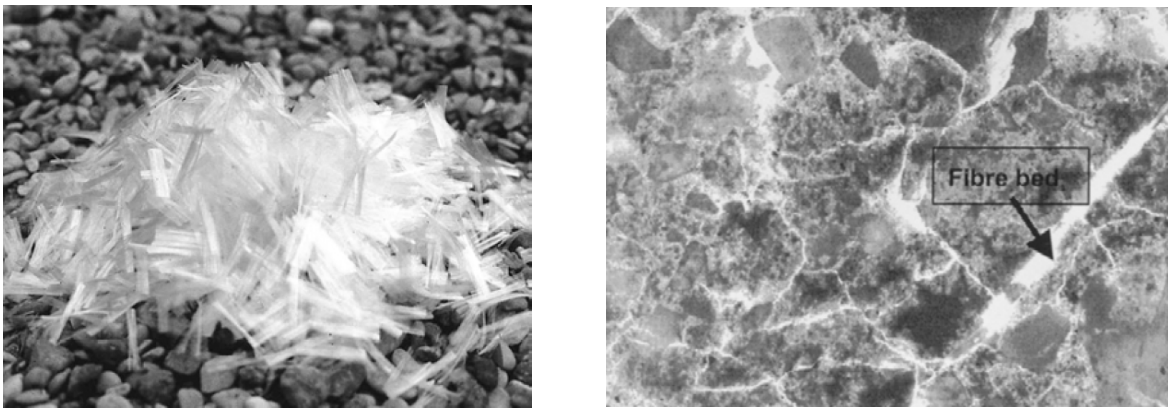

Fig. 2.9 *The relatively small PP-fibres (left)* (Hager, 2004) *melt during heating as indicated for a concrete mixture exposed to a temperature of 400 ^{o}C (right)* (Kalifa, et al., 2001).

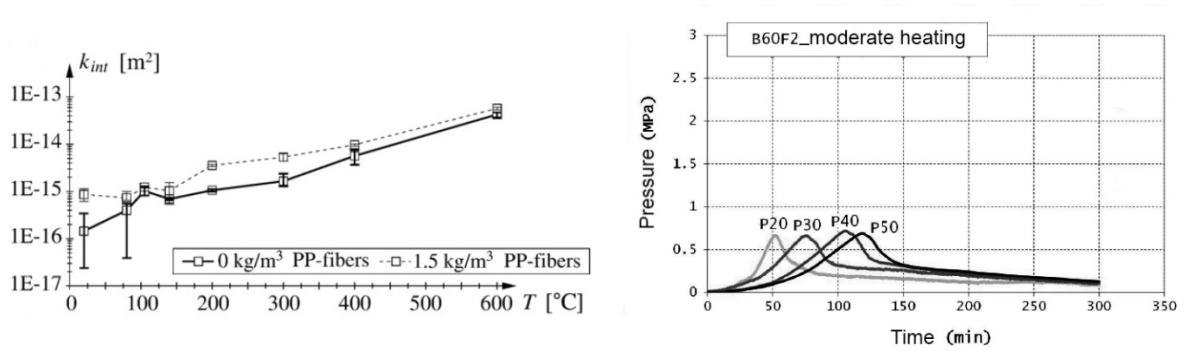

Fig. 2.10 *Permeability increase of C25/30 by melting of the PP-fibres (left)* (Zeiml, et al., 2008a). *Mitigated gas pressures in heated B60 or C60/75 with 2.0 kg/m³ of PP-fibres (right)* (Mindeguia, et al., 2012) (right graph translated from French).

This influences especially the permeability of the concrete, as illustrated for C25/30 in the left graph of Fig. 2.10 (Zeiml, et al., 2008a). The dissolution of the PP-fibres leads to the creation of new channels and enhances the interconnectivity of the microstructure (Bentz, 2000). The beneficial influence on the gas pressure development is indicated for C60/75 specimens with 2.0 kg/m³ of PP-fibres by comparing Fig. 2.5 (Mindeguia, 2009) with Fig. 2.10 (Mindeguia, et al., 2012).

Crack development due to thermal stresses

At increased heating rates a steeper temperature gradient develops in the cross-section which could allow for a faster build-up of the gas pressure. However, the temperature and the gas pressure development, obtained at various depths relative to the heated surface as shown in Fig. 2.11, indicates a different behaviour (Mindeguia, 2008). The exposure of this C40/50 slab to the ISO fire curve only leads to gas pressures slightly above atmospheric conditions (Mindeguia, 2008). The occurrence of spalling, referred to as instabilities, is indicated by a sudden increase in the temperature at a depth of 10 mm. (Mindeguia, 2008). This is probably caused by exposure of the thermocouple to the fire. The limited gas pressures are believed to be attributed to cracking of the slab, leading to a substantial increase in the transport capabilities (Mindeguia, 2009). The crack pattern forms a partially connected network which allows the vapour to directly escape, mitigating the gas pressure (Bažant, 1997).

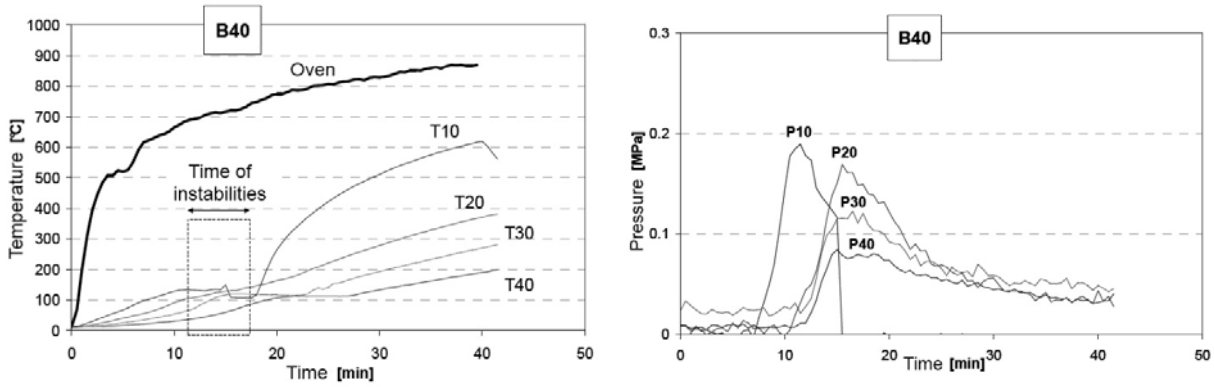

Fig. 2.11 *Exposure of B40 or C40/50 to the ISO fire curve causing spalling, as reflected by the sudden temperature increase (left). Gas pressures were reported to be limited, attributed to cracking (right)* (Mindeguia, 2008) (graphs translated from French).

During fire exposure of concrete slabs commonly large quantities of vapour are observed to escape from the furnace or oven (Horvath, et al., 2004; FSV, 2004) as can for instance be seen in Fig. 2.19. At the unexposed topside and along the outer edges liquid water is also seen to gradually flow out of cracks. These observations confirm the forced drying and the presence of pressure driven flow in the cross-section.

2.3 Thermal mechanical material behaviour and crack development

2.3.1 Thermal mismatch between aggregates and the surrounding mortar

During most of the mechanical experiments the heating rate is in the range of 0.1 to 10 ^{o}C/min (RILEM TC-HTC, 2004). However, even at these relatively low heating rates the differences in thermal expansion of the concrete components affect the local deformations. For instance, quartz aggregate has a higher thermal expansion than mortar, influenced by the dehydration processes in the cement paste (Diederichs, et al., 1987; Flynn, 1999). In siliceous sand and aggregates the α-β quartz inversion, at a temperature of around 600 ^{o}C, coincides with a rapid increase in the thermal expansion loading the surrounding mortar (Cruz & Gillen, 1980). In contrary, limestone aggregates have a similar thermal expansion as mortar (Flynn, 1999), reducing the thermal mismatch and resulting stresses.

Thermal loading of the cross-section is furthermore determined by the differences in strength and stiffness development with temperature. The stiffness distribution, established at ambient conditions, changes due to the chemical and physical degradation processes that develop in the microstructure of the mortar (RILEM TC-HTC, 2004). However, the aggregates only exhibit a small reduction in stiffness (Dmitriyev, et al., 1969/1972). These particles tend to impose a higher thermal load on the weaker surrounding mortar (Schneider, 1982).

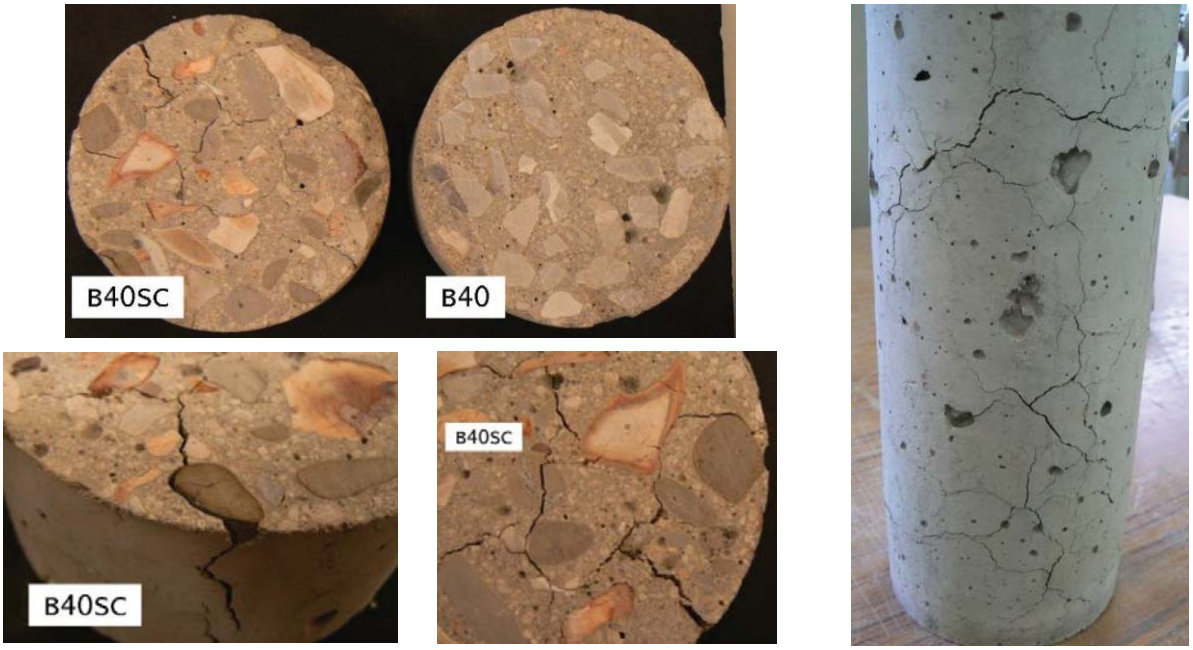

Fig. 2.12 *Thermal expansion differences between aggregates and mortar causing cracking in the interfacial zones of B40 or C40/50 specimens heated to a temperature of 400 ^{o}C (left). This also affects the state of specimens (right)* (Mindeguia, 2009).

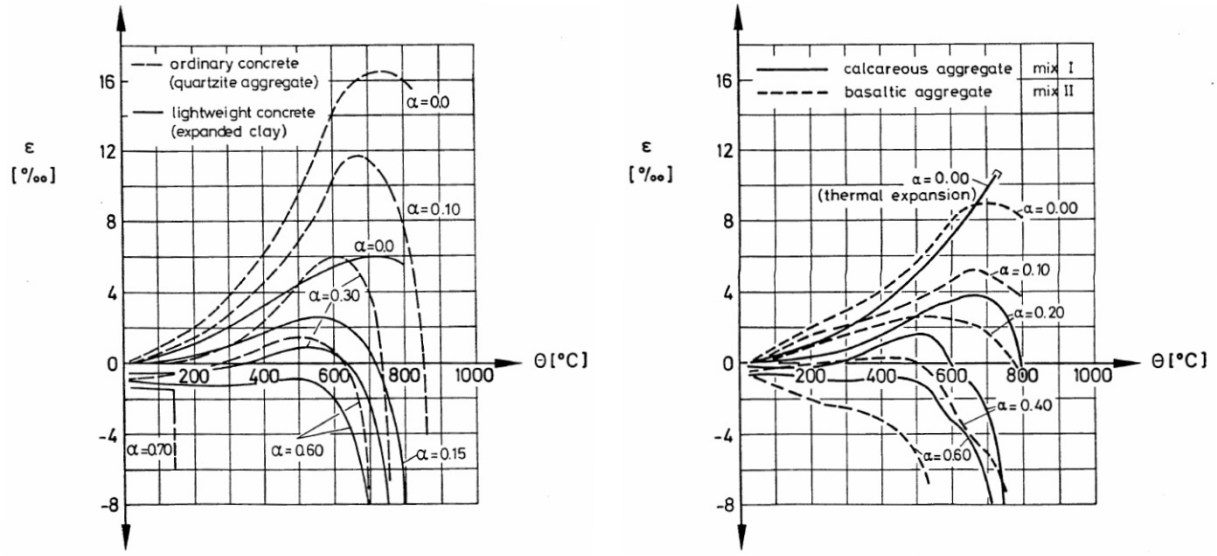

Fig. 2.13 *Deformation or transient creep as characterised by thermal expansion of the aggregate type as well as the initial compressive load level, illustrated for NSC* (RILEM TC-HTC, 2004).

Local stresses develop, especially in the interfacial zone of NSC, which leads to cracking and becomes more susceptible with temperature. The pictures in Fig. 2.12 show the crack pattern that developed in the C40/50 cross-section, extending between the siliceous aggregates (French flint). The cross-section with calcareous aggregates (limestone) remains largely undisturbed (Mindeguia, 2009).

2.3.2 Unloaded and loaded thermal deformation at low heating rates

Deformation behaviour of concrete with temperature is predominately determined by the aggregate type (Schneider, 1982). This is illustrated in Fig. 2.13 by NSC specimens exposed to a constant heating rate without load application (RILEM TC-HTC, 2004). The differences in thermal expansion between quartz and limestone aggregate concrete indicate the importance of the particles, especially at temperatures higher than 400 ^{o}C (RILEM TC-HTC, 2004).

By initially loading the concrete in compression, the thermal mechanical behaviour changes. This is also reflected in Fig. 2.13, indicating the thermal deformation during heating under constant load referred to as transient creep (RILEM TC-HTC, 2004; van Breugel, et al., 1998). The level of thermal restraint is thereby dependent on the compressive load (RILEM TC-HTC, 2004). Dependent on the aggregate type and the load level also a reduction in the deformation with temperature is reported (RILEM TC-HTC, 2004). At load levels higher than 0.5 the thermal expansion of the specimen is not able to overcome the initial compression deformation (RILEM TC-HTC, 2004).

The application of a compression load causes an initial crack pattern to be present in the specimen. During heating the virgin state is no longer present and additional thermal cracking extends the existing pattern (Mindeguia, 2009). This could explain the observed sudden reduction in the thermal deformation as the onset of failure of the specimen (RILEM TC-

HTC, 2004). This behaviour becomes more pronounced for ordinary siliceous concrete compared to calcareous concrete as well as at higher load levels (RILEM TC-HTC, 2004). At the highest load levels the specimens already indicate failure at a temperature of 500 ^{o}C.

2.3.3 Strength and deformation of heated concrete

The development of compressive and tensile strengths as well as Young's modulus are characterised by a gradual reduction with temperature (RILEM TC-HTC, 2004; van Breugel, et al., 1998). The continued dehydration of the cement paste as well as the thermal expansion of especially the aggregate particles cause the Young's modulus and tensile strength to reduce to 10 % or 20 % of the initial values as shown in Fig. 2.14 (RILEM TC-HTC, 2004; Thelandersson, 1971).

This behaviour is also reflected by the development of the ultimate compressive strength and subsequent softening deformation as shown by the stress-strain relationships in Fig. 2.15 (Schneider, et al., 1980). The reference behaviour is established at a temperature of 20 ^{o}C and reflects the basic relationship obtained at a constant strain rate (RILEM TC-HTC, 2004). The initial linear elastic behaviour, characterised by a constant Young's modulus, is influenced by crack development during loading (van Mier, 1997).

The maximum load carrying capacity is reached as soon as the vertically orientated pattern of relatively small cracks has sufficiently weakened the member (van Mier, 1997). The descending branch is obtained through controlling the deformation (van Mier, 1997; RILEM TC-HTC, 2004). This behaviour is commonly referred to as (compression) softening and reflects stable fracture propagation by removal of the load (van Mier, 1997).

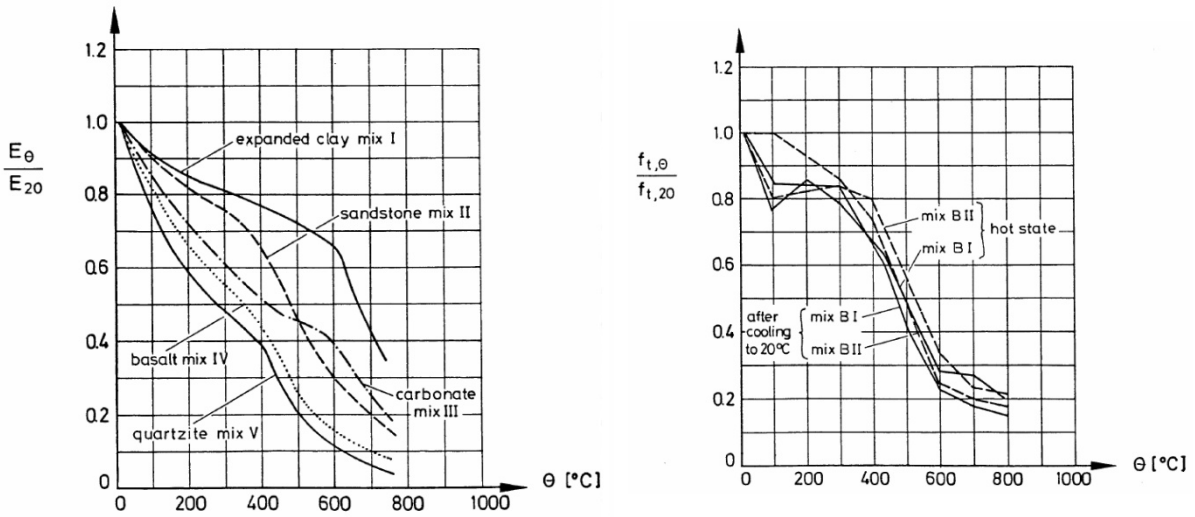

Fig. 2.14 *Development of Young's modulus (left)* (RILEM TC-HTC, 2004) *and tensile strength (right)* (Thelandersson, 1971) *with temperature for various NSC types indicating a gradual reduction with temperature until 800 ^{o}C.*

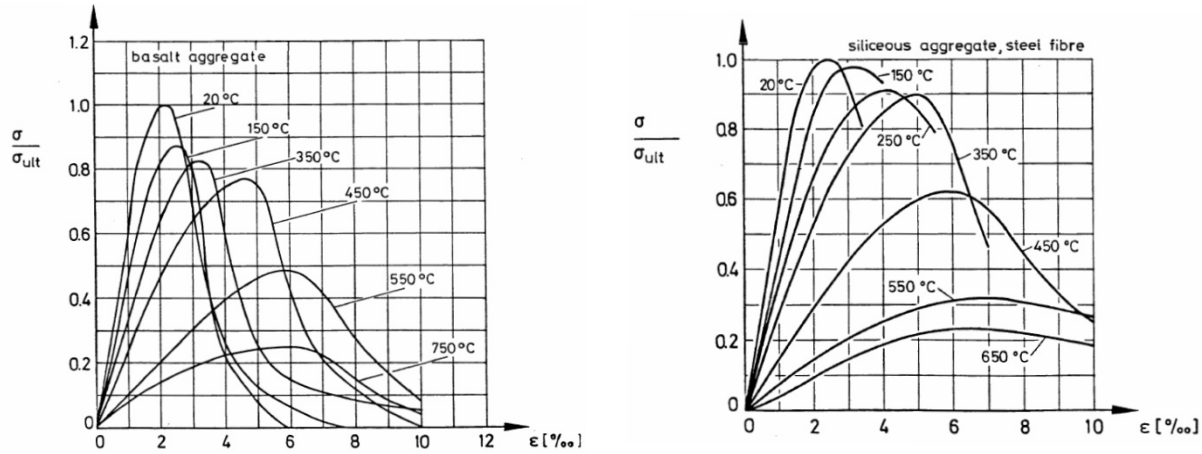

Fig. 2.15 *Stress-strain development of NSC in compression exhibiting a reduction of the maximum load and increased softening* (Schneider, et al., 1980).

Temperature dependence as shown in Fig. 2.15 (Schneider, et al., 1980) is based on heating of unloaded specimens until a constant state is reached. Subsequently the compression load is applied with a constant strain rate (RILEM TC-HTC, 2004). Degradation of the cement paste is observed to affect the maximum compressive strength and increase the deformations under sustained loading (Schneider, et al., 1980). At temperatures until 350 °C the concrete with siliceous aggregates and steel fibres shows a small strength reduction (Schneider, et al., 1980). However, the reduction at higher temperatures could be caused by the loss of bond between the weakened cement paste and the steel fibres as seen in right graph of Fig. 2.15 (RILEM TC-HTC, 2004).

A similar thermal behaviour is observed for C70/85 specimens loaded in tension as shown in the left graph of Fig. 2.16 (Felicetti & Gambarova, 1998). The maximum tensile stress under these circumstances is reached by failure of the cross-section due to a dominating horizontal crack (van Mier, 1997). The descending branch, after the peak load, is commonly referred to as (tension) softening (van Mier, 1997). With increasing temperature a progressive reduction of the tensile strength is observed with only 20 % remaining at 400 °C (Felicetti & Gambarova, 1998).

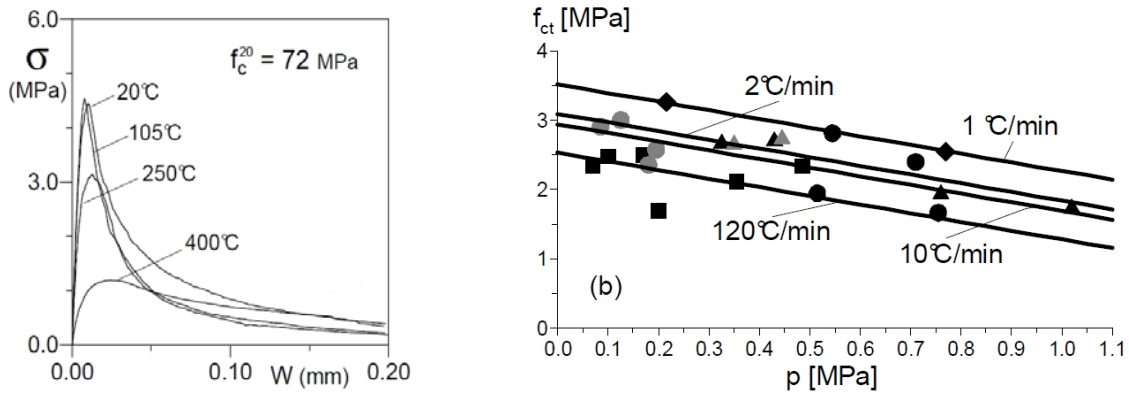

Fig. 2.16 *Stress-displacement distributions for C70/85 reflecting tensile strength reduction with temperature (left)* (Felicetti & Gambarova, 1998). *Possible relationships between pressure and tensile strength for C40/50 (right)* (Felicetti, et al., 2012).

2.3.4 Possible influence of gas pressure on strength

The influence of gas pressures on the tensile strength of concrete is investigated by exposure of C40/50 specimens to various heating rates followed by tensile splitting tests (Felicetti, et al., 2012). The relationship with the gas pressure, shown in Fig. 2.16, seems to indicate a reduction of the tensile strength (Felicetti, et al., 2012). However, mitigation of the gas pressures is observed at the highest heating rates, caused by cracking of the specimens. The lowest heating rates caused gradual drying of the material. The maximum pressure is obtained by limited cracking at the highest possible heating rate (Felicetti, et al., 2012).

2.3.5 Time-dependent deformations of heated concrete

The steady state creep measurement of concrete at temperature is commonly limited to 150 ^{o}C (RILEM TC-HTC, 2004). The specimens are slowly heated until a constant temperature has been reached. Subsequent application of a constant compression load is used to measure the creep based on gradually increasing deformations (RILEM TC-HTC, 2004; van Breugel, et al., 1998) as shown for NSC in the left graph of Fig. 2.17 (Gross, 1973). This time-dependent behaviour is influenced by moisture movement in the porous microstructure, the temperature and the load level (RILEM TC-HTC, 2004). The speed at which creep develops increases with temperature.

Additionally, the heated specimens can also be subjected to a constant compressive strain allowing the stress to decrease indicating relaxation (RILEM TC-HTC, 2004; van Breugel, et al., 1998). This is illustrated by the right graph in Fig. 2.17 which is derived for light weight concrete (LWC) with expanded clay aggregate (Schneider, 1979). Relaxation is closely related to creep, but develops faster (RILEM TC-HTC, 2004).

2.3.6 Crack development in practical situations

In case of fire exposure the heating rate increases to 50 ^{o}C/min or even 200 ^{o}C/min which results in a rapid development of the temperature gradient in the cross-section. Substantial thermal stresses develop, causing cracks to develop (van Breugel, et al., 1998; Lottman, 2007). An example of the crack pattern that could develop during fire exposure of a concrete specimen is shown in Fig. 2.18.

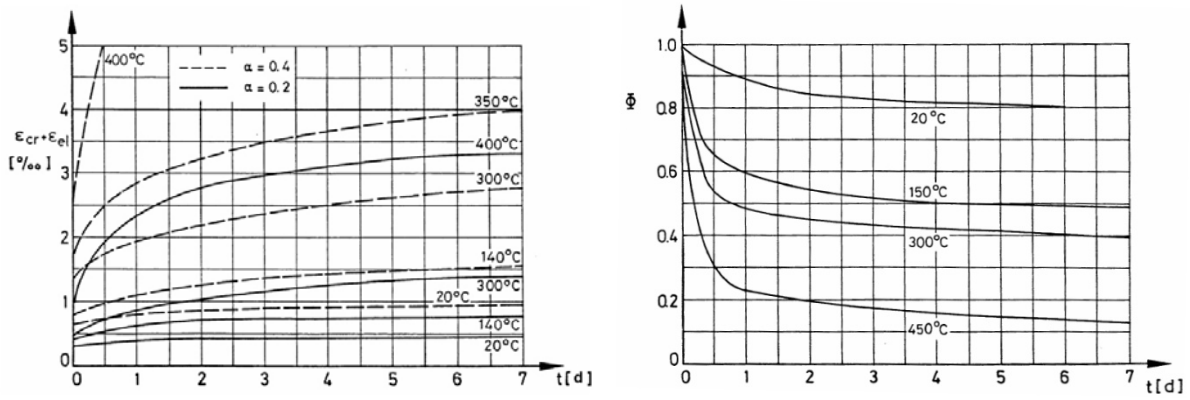

Fig. 2.17 *Deformation of NSC specimens, indicating steady state creep influenced by the temperature and the compressive load (left)* (Gross, 1973). *Relaxation under sustained strain for LWC with expanded clay aggregate (right)* (Schneider, 1979).

Fig. 2.18 *Thermal expansion of the heated surface layer leading to a circular crack in the cross-section. In the centre a radial crack pattern developed* (pictures taken at Efectis[6]).

In this test specimens were placed inside the furnace and exposed to high heating rates (Brekelmans, et al., 2008). The partial restraint of the heated surface layer by the cross-section eventually caused the development of an almost continuous circular crack. In the centre of the cross-section also some cracking in radial direction was observed. Both types of cracking are caused by imposed deformations and in some cases led to partial separation of the heated surface layer.

An example of a large scale fire test is shown in Fig. 2.19. This concrete tunnel lining segment was initially loaded by a steel frame with horizontal and vertical hydraulic jacks in order to obtain a representative stress state for service life conditions (Dehn, et al., 2010). During fire testing this representative load was maintained (Dehn, et al., 2010). The curved shape of the segment allowed to observe the crack pattern that developed at the concrete surface during fire exposure. These cracks were orientated perpendicular to the heated surface, extending across the width of the segment. These reflect the stress state acting in the member caused by the initial loading and the subsequent restraint of the steep temperature gradient that developed in the cross-section. Additional influencing aspects are the curved geometry and restraint of the segment during testing by maintaining the load. Furthermore, the process of forced drying is reflected by vapour escaping from the oven and the flow of liquid water from cracks visible at the concrete surface.

[6] Observations by the author after full-scale fire testing of concrete cylinders as part of the European research project NewCon while visiting Efectis in Rijswijk, The Netherlands from October to December 2007.

Fig. 2.19 *Crack development observed during full scale fire testing of a tunnel lining segment with applied external loading* (pictures by MFPA[7]).

2.4 Spalling of concrete due to fire exposure

2.4.1 Historic nomograms for spalling of concrete

Based on experimental research the nomograms, shown in Fig. 2.20, were developed, indicating areas as 'spalling or no spalling' (Meyer-Ottens, 1972; Zhukov, 1975). These graphs already recognised the relationship between moisture content and applied stress, but are independent of the type of concrete and the heating rate. Both graphs are well known and still used today to obtain an indication of the spalling sensitivity (fib WP-4.3-1, 2007).

2.4.2 Basic theories with respect to spalling of concrete

Pore pressure spalling

In this theory pore pressure build-up is identified as the main reason for spalling of concrete (Shorter & Harmathy, 1961; Harmanthy, 1965). The high heating rate of the cross-section and the rapid evaporation of liquid water results in pore pressures (Harmanthy, 1965). A progressive partially saturated layer with liquid water, referred to in the left picture of Fig. 2.21 as a 'moisture clog', develops causing the pore or gas pressure to build-up (Harmanthy, 1965). This process is intensified for high moisture levels and in the dense microstructure of HSC (Harmanthy, 1965). Spalling of the layer in front of the pore pressure peak occurs by surpassing the strength of the concrete (Harmanthy, 1965; Waubke, 1966).

[7] Observations by the MFPA Institute in Leipzig, Germany during full-scale fire testing of a loaded tunnel lining segment in February 2009.

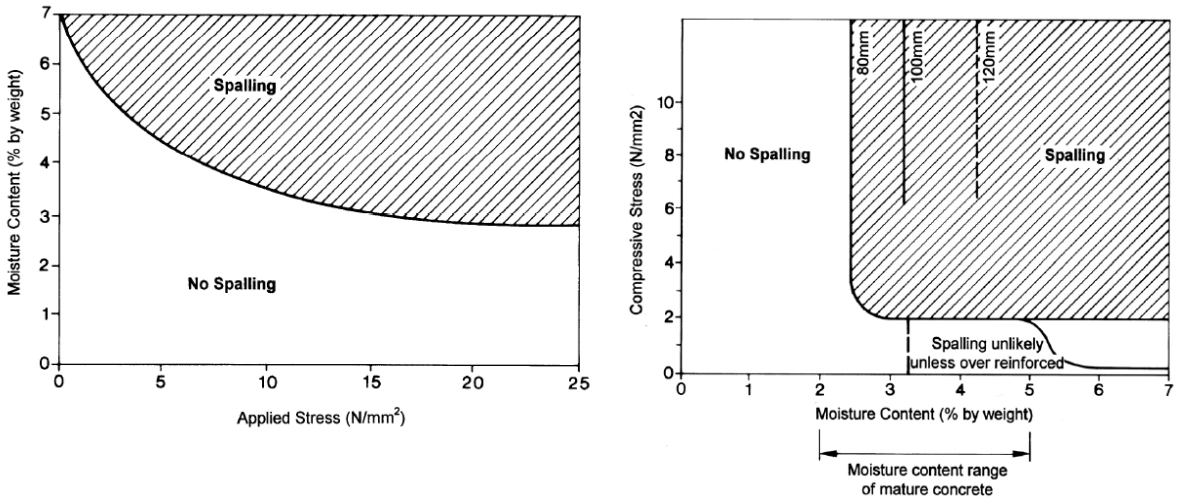

Fig. 2.20 *Nomograms indicating areas of spalling sensitivity based on moisture content and applied stress* (Meyer-Ottens, 1972; Zhukov, 1975).

Thermal stress spalling

The main assumption in this theory is that the thermal stress state is the reason for spalling of concrete (Dougill, 1972; Saito, 1965). The high heating rate of the cross-section and the resultant steep temperature gradient cause a thermally restrained surface layer to develop (Meyer-Ottens, 1975). The resulting high compressive stresses cause cracks which weaken this surface layer (Dougill, 1972; Saito, 1965). Additional external compressive loading or partial restraint increases the stress state (Saito, 1965). The loss of thermal stability under compression loading leads to spalling of the surface layer (Dougill, 1972).

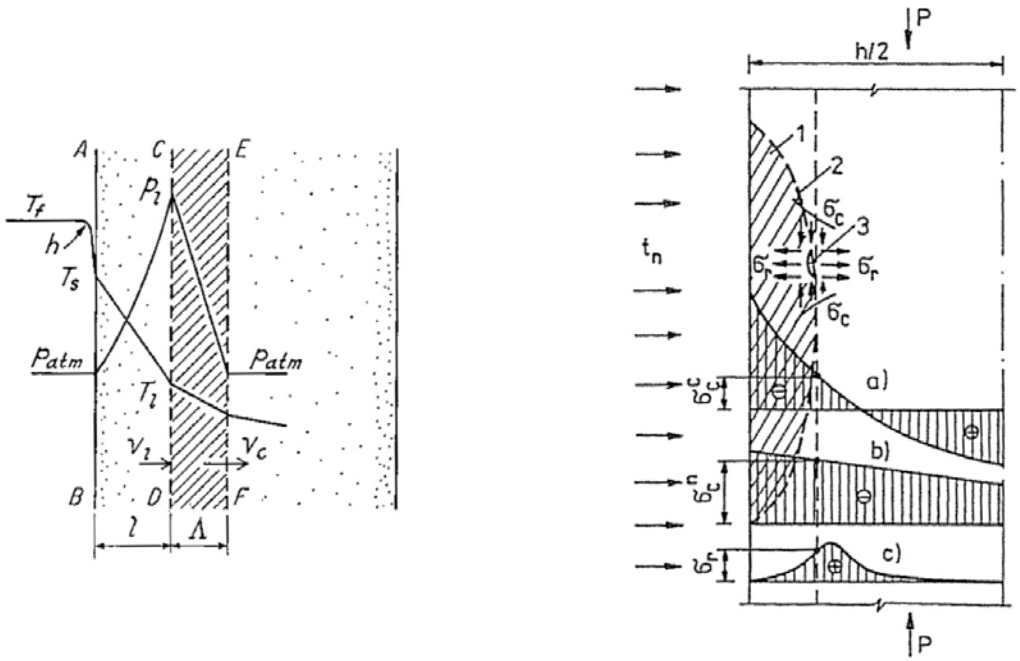

Fig. 2.21 *Schematic representation of the temperature gradient (T), the build-up of the pore pressure (P) and the formation of a moisture clog (C-F) (left)* (Harmanthy, 1965). *Spalled piece of concrete (1) due to a crack (2) initiated (3) by stresses based on temperature (a), loading (b) and pore pressures (c) (right)* (Zhukov, 1976).

Combined pore pressure and thermal stress spalling

According to this theory the simultaneous development of pore pressures and thermal stresses is the reason for spalling of concrete (Zhukov, 1976). The resulting stress state is a combination of internal temperature stresses, stresses by external loading and stresses induced by pore pressure build-up as shown in the right picture of Fig. 2.21 (Zhukov, 1976). Spalling of a piece of concrete is determined by development of the crack pattern (Zhukov, 1976).

2.4.3 Influencing factors governing the spalling sensitivity of concrete

The spalling sensitivity is not as straightforward as implied by these theories, as illustrated by several full-scale fire tests on concrete slabs as subsequently discussed. Most reported observations are also limited to assessing the damage after fire exposure (Jansson & Boström, 2008). Additional information about the spalling process can be obtained during testing by observations (FSV, 2004) and possibly acoustic emission measurements (Richter, et al., 2013). Moreover, using cylinders or cubes to indicate spalling is more practical, but less informative (Brekelmans, et al., 2008; Dehn, et al., 2010). The size and geometry leads to heating from multiple sides, making analyses more difficult.

Influence of the concrete strength, type of aggregate and reinforcement

It is commonly believed that HSC has a higher sensitivity for spalling than NSC (Khoury & Anderberg, 2000). The reduced permeability, caused by the denser microstructure, leads to a higher pore pressure development promoting the occurrence of spalling (Khoury & Anderberg, 2000). This seems to be confirmed by the observed spalling damage to a C85/100 slab with quartz aggregate, as shown in Fig. 2.22, after fire exposure according to the RWS curve (Horvath, et al., 2004). The slab was stored under water until testing in order to promote the development of pore pressures (Horvath, et al., 2004). The sustained damage was on average 32 mm in depth with a maximum of 41 mm (Horvath, et al., 2004). During testing, severe cracking was observed causing the surface layer to partially detach (Horvath, et al., 2004). The spalling tendency is also believed to be influenced by the type of aggregate in which the higher thermal expansion of quartz aggregates has a negative influence (Khoury & Anderberg, 2000).

Fig. 2.22 *Cracking of a slab during thermal exposure according to the RWS fire curve (left) and resulting spalling damage (right). The C85/100 concrete was made with quartz aggregates and stored under water before testing* (Horvath, et al., 2004).

Fig. 2.23 *Spalling occurring in C25/30 stored at ambient conditions before exposure to the Lainz fire curve (left). Drying of a similar slab before testing under compression according to the RWS fire curve did not prevent spalling (right)* (FSV, 2004).

An improvement in the spalling behaviour could possibly be obtained by using limestone aggregates combined with a reduction of the moisture level. This is the case for the C25/30 slab, shown in the left picture of Fig. 2.23, stored at ambient conditions before testing (FSV, 2004; Zeiml, et al., 2008a). Fire exposure corresponding to the Lainz curve resulted in repetitive spalling occurring between 4 and 13 minutes after the start of the test (FSV, 2004). This exposed the reinforcement and was followed by a single occurence after 19 minutes (FSV, 2004). The spalling depth was on average 50 mm with a maximum of 80 mm (FSV, 2004) also indicating the limited influence of reinforcement in mitigating spalling.

Influence of the moisture level

To establish that spalling of concrete is dominated by the presence of moisture, full-scale tests have been conducted on predried slabs (FSV, 2004; Mindeguia, 2009). The drying of concrete slabs commonly takes considerable time and is only feasible for a limited thickness (Mindeguia, 2009). The influence of the moisture level on the spalling process seems to be confirmed by exposure of limestone aggregate C40/50 and C60/75 slabs dried at 80 ^{o}C to the ISO fire curve (Mindeguia, 2009). No spalling was observed, possibly to be attributed to the reduction in the pore pressure development.

The exposure of a C25/30 slab made with limestone aggregates conditioned by drying at a temperature of 50 ^{o}C should allow for a mitigation in the spalling behaviour (FSV, 2004). Such as slab was externally loaded during the test by hydraulic jacks to a compressive stress of 1.16 MPa (FSV, 2004). Exposure to a fire according to the RWS curve resulted in continued spalling in the first 4 to 15 minutes after starting the test (FSV, 2004). This exposed the reinforcement, as shown in the right picture of Fig. 2.23, after which the spalling process continued with a lower frequency (FSV, 2004). After 37 and 40 minutes larger pieces of concrete were spalled off, reaching a maximum depth of 200 mm after 55 minutes (FSV, 2004). Under these circumstances the dried state of the slab did not prevent spalling and the applied compressive stress seemed to increase the spalling sensitivity (Khoury & Anderberg, 2000).

Fig. 2.24 *Exposure of a water stored C25/30 (left)* (Horvath, et al., 2004) *and an air stored B40 or C40/50 (right)* (Mindeguia, 2009) *slab to an ISO type of fire indicating only for the latter one limited surface spalling, attributed to the flint aggregates.*

Influence of the heating rate and external loading

Mitigation of the heating rate as well as the absence of external loading and/or restraint reduces the thermal stresses and could reduce spalling (Khoury & Anderberg, 2000). This seems to be confirmed by full-scale testing according to the ISO fire curve of unloaded concrete slabs (Horvath, et al., 2004; Mindeguia, 2009). Storage of limestone aggregate type C40/50 and C60/75 slabs at ambient conditions or under water resulted in, on average, limited spalling with a depth of about 10 mm (Mindeguia, 2009). Usage of siliceous aggregates, such as quartz (Horvath, et al., 2004) or flint (Mindeguia, 2009), in C40/50 slabs resulted only in limited spalling for the latter as shown in Fig. 2.24. However, by application of a compressive stress of 15 MPa on C40/50 slabs, exposed both to an ISO type of fire, the spalling damage increased to an average depth of about 20 mm and a maximum of 40 mm (Carré, et al., 2013).

The spalling behaviour is found to intensify in case the heating rate reflects the RWS fire curve while a compressive stress is applied (Jansson & Boström, 2008). The granite aggregate C35/45 slabs, shown in the left picture of Fig. 2.25, were stored at ambient conditions and externally compressed by a stress of 7.1 MPa using post tensioning of bars (Jansson & Boström, 2008). The spalling process started after 2.5 minutes with the slabs cracked in the direction of the bars after 20 minutes (Jansson & Boström, 2008). Exposure of the bars to these high temperatures also caused relaxtion of the initially applied compression stress.

Fig. 2.25 *Spalling as observed during exposure of compression loaded C35/45 slabs to a RWS type of fire (left)* (Jansson & Boström, 2008). *Exposure of a B60 or C60/75 slab to a low heating rate still causing spalling (right)* (Mindeguia, 2009).

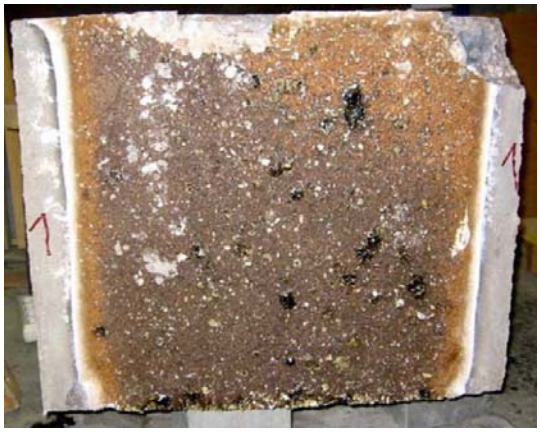


Fig. 2.26 *Preventing spalling by addition of 2.0 kg/m^3 of PP-fibres to the C85/100 mixture (left)* (Horvath, et al., 2004). *No damage occurred during testing of a compression loaded C25/30 slab made with 3.0 kg/m^3 of PP-fibres (right)* (FSV, 2004) *Both slabs were stored under water before fire testing according to the RWS curve.*

Contrary, a reduction in the heating rate ought to improve the spalling behaviour. Exposure of a C60/75 slab to a relatively low heating rate resulted in spalling of a large piece of concrete after 106 minutes of fire exposure (Mindeguia, 2009). In the next 14 minutes spalling occurred by smaller pieces of concrete leading to a depth of on average 35 mm with a maximum of 61 mm (Mindeguia, 2009). This behaviour indicated that even at these low heating rates spalling can still occur. However, the positioning of the slab on top of the oven between two refractory concrete blocks (Mindeguia, 2009) could possibly have resulted in partial restraint, influencing the thermal stress state.

Influence of addition of polypropylene fibres

The beneficial influence of adding PP-fibres to the concrete mixture to mitigate or prevent spalling is commonly investigated (Khoury & Anderberg, 2000). For instance, the addition of 1.5 kg/m^3 of PP-fibres to the concrete mixture of the slab shown in the left picture of Fig. 2.25 resulted in a reduction of the spalling damage to an average depth of 6 mm with a maximum of 35 mm (Jansson & Boström, 2008). The spalling process started after 4.8 minutes and, similar to the concrete mixture without PP-fibres, the slab cracked after 12.5 minutes during which a reduction in the compressive load was observed (Jansson & Boström, 2008).

No spalling was observed for an addition of 2.0 kg/m^3 of PP-fibres to the mixture of the C85/100 slab shown in Fig. 2.22 (Horvath, et al., 2004). The discolouring, shown in the left picture of Fig. 2.26, is caused by melting of the siliceous sand at high temperatures (Khoury, 2008a). A higher dosages of 3.0 kg/m^3 of PP-fibres was added to the mixture of the C25/30 slab shown in the right picture of Fig. 2.23 (FSV, 2004). However, this slab was stored under water before testing and a compressive stress of 6.5 MPa was applied through external loading (FSV, 2004). No spalling was observed as illustrated by the right picture in Fig. 2.26 (FSV, 2004). This enhanced spalling resistance is commonly attributed to the increase of permeability by melting of the PP-fibres (Zeiml, et al., 2006; Khoury & Anderberg, 2000).

Fig. 2.27 *Spalling damage of B60 or C60/75 slabs after exposure to a fire corresponding to the HCinc curve. The slabs were stored at ambient conditions without (left) and with addition of 1.84 kg/m^3 PP-fibres (middle) or predried at 80 ^{o}C (right)* (Pictures by Mindeguiea[8]).

Influence of partial restraint and external loading

The results presented indicate that spalling of unloaded concrete is mostly observed for high heating rates for which the influence of the moisture level is still not completely understood. This has also been the focus of several full-scale tests, according to the HCinc fire curve, on C60/75 slabs combined by a steel frame to form a single plate (Mindeguia, 2009). The influence of the moisture level is illustrated in Fig. 2.27. The average spalling depth of the slabs stored in ambient conditions, without and with addition of PP-fibres, was limited to roughly the diameter of the largest aggregates (Mindeguia, 2009). Only the dried slab did not show spalling (Mindeguia, 2009). However, the test set-up could have partially restrained the thermal expansion of the various slabs. The addition of PP-fibres did not completely eliminate spalling (Mindeguia, 2009). This could have been caused by the dosage and type of fibres which are known to influence the effectiveness (FSV, 2004; Khoury & Anderberg, 2000).

Another example are the C30/37 tunnel lining segments made with limestone aggregates (Dehn, et al., 2010). These segments were during testing, based on a ZTV-ING type of fire, unloaded or hydraulically loaded (Dehn, et al., 2010).

Fig. 2.28 *Observed spalling damage to C30/37 tunnel lining segments made with limestone aggregate, without (left) and with (right) addition of 2.0 kg/m^3 of PP-fibres. Both members were exposed to a ZTV-ING type of fire* (Dehn, et al., 2010).

[8] Pictures by J.C. Mindeguia taken during experimental work for his PhD thesis (Mindeguia, 2009) at the CSTB institute in Paris, France.

Fig. 2.29 *Spalling damage to similar segments, without (left) and with (right) 2.0 kg/m^3 of PP-fibres added to the C30/37 mixture. Both members were loaded to service life conditions during testing according to the ZTV-ING curve* (Dehn, et al., 2010).

A representative loading scenario with total horizontal and vertical forces of 3600 kN and 1900 kN respectively was maintained during the test (Dehn, et al., 2010). The segments with 2.0 kg/m^3 of PP-fibres experienced only limited spalling as seen in Fig. 2.28 and Fig. 2.29 (Dehn, et al., 2010). However, the segments without PP-fibres indicated severe spalling, exposing the reinforcement after 7.5 minutes (Dehn, et al., 2010). For the unloaded segment an average spalling depth of 67 mm with a maximum of 110 mm was observed (Dehn, et al., 2010). External loading increased the damage to an average depth of 110 mm and a maximum of 271 mm (Dehn, et al., 2010).

2.5 Numerical methods for describing the behaviour of heated concrete

2.5.1 Temperature and pore pressure development

Simplified models describing the temperature and pore pressure relationship

In the most basic 1D models temperature and pore pressure development are uncoupled (van der Heijden, 2011; Lottman, 2007). The temperature development is commonly based on an analytical or numerical solution of the Fourier differential equation for thermal conductivity (van der Heijden, 2011; Lottman, 2007). The temperature distribution obtained is subsequently used to determine the pore or gas pressure based on the saturated water vapour pressure (van der Heijden, 2011; Lottman, et al., 2007). This neglects the influence of the dry air phase and characterises the flow of the vapour by Darcy's law (van der Heijden, 2011; Lottman, et al., 2007). The direction of transport is assumed to be 1D, perpendicular to the heated surface, resulting in the build-up of the pore pressure with temperature at the drying front (van der Heijden, 2011; Lottman, et al., 2007). These simplified models include the moisture content, heating rate and permeability (van der Heijden, 2011; Lottman, et al., 2008).

Coupled models describing the transfer of heat and moisture

More insight is obtained by the numerical solution of a system of PDE's, representing a 1D or 2D cross-section. Conservation of energy is combined with the mass balance of free water (Bažant, et al., 1981; Ichikawa & England, 2004; Ožbolt, et al., 2011).

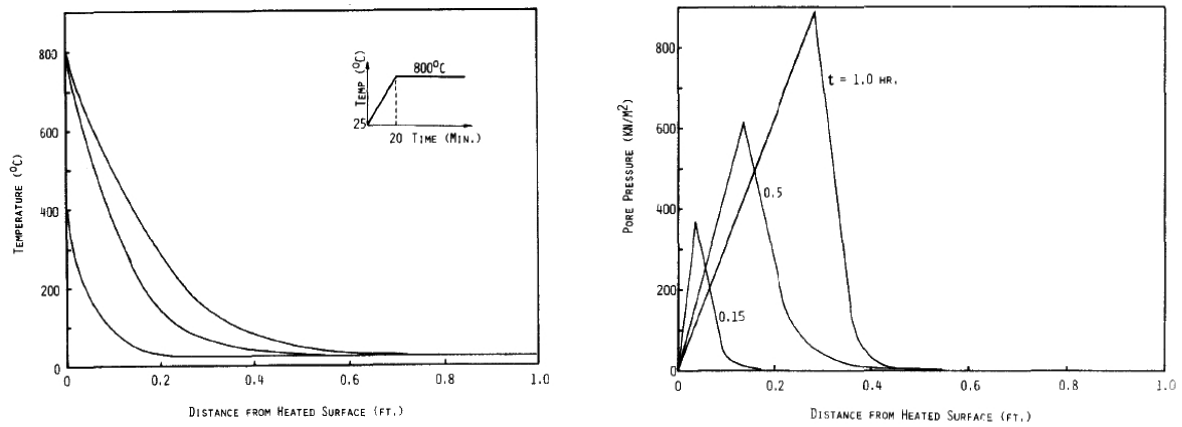

Fig. 2.30 *Typical temperature and pore pressure distributions obtained using FEM-based porous material descriptions* (Bažant, et al., 1981).

This balance equation is based on transport according to Darcy's law and the release of bound water by dehydration (Bažant, et al., 1981; Ichikawa & England, 2004; Ožbolt, et al., 2011). These models can be uncoupled and solved by the FDM (Ichikawa & England, 2004) or coupled and solved by the FEM (Bažant, et al., 1981; Ožbolt, et al., 2011). The temperature and the mass of free water determine the thermodynamic state and the gas pressure (Bažant, et al., 1981; Ichikawa & England, 2004; Ožbolt, et al., 2011). The distributions shown in Fig. 2.30 are based on drying of the material according to desorption isotherms (Bažant, et al., 1981). The permeability is temperature-dependent (Bažant, et al., 1981; Ichikawa & England, 2004) and in some models also the aggregates are included (Ožbolt, et al., 2011).

Fully coupled models describing the heated multi-phase porous material

Approximation based on a system of three or four coupled PDE's, characterised by a more elaborated material description (van der Heijden, 2011; Erich, et al., 2008), is commonly solved by the FEM (Gawin, et al., 2003; Davie, et al., 2006; Dal Pont, 2004). The PDE's govern the conservation of thermal energy and the mass balances for an averaged porous material (Hassanizadeh & Gray, 1979a; Bachmat & Bear, 1986). Several phases are defined such as water in liquid or vapour form and possibly dry air, assuming that thermodynamic equilibrium is maintained (Hassanizadeh & Gray, 1979b; Bear & Bachmat, 1986).

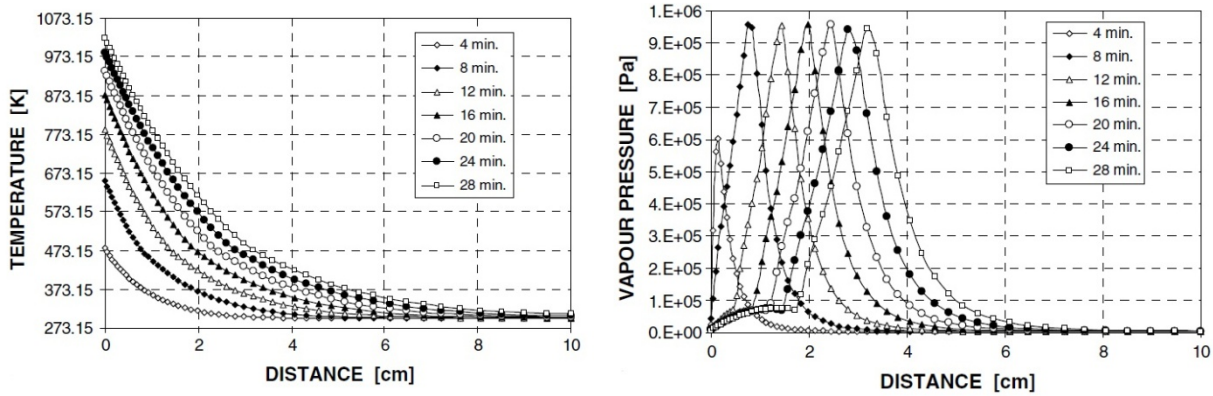

Fig. 2.31 *More elaborate FEM approximations are based on a coupled system of PDE's describing an averaged multi-phase porous material* (Gawin, et al., 2006).

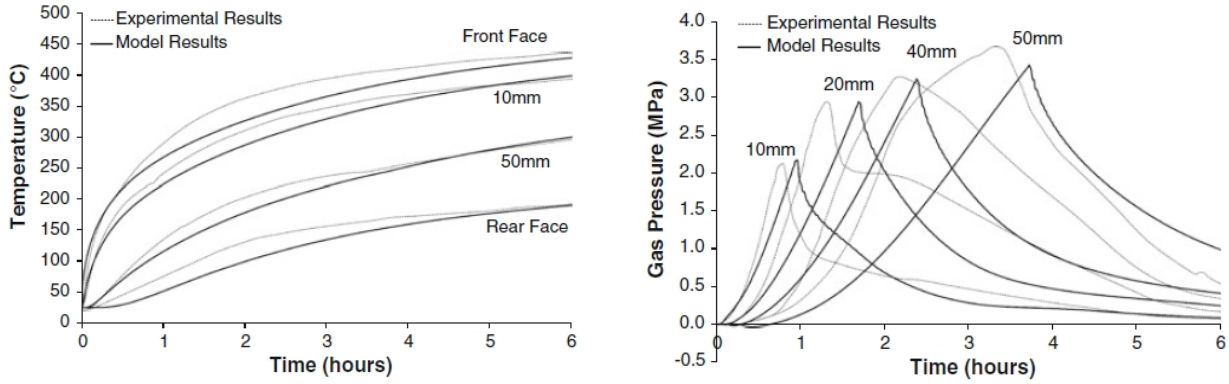

Fig. 2.32 *Time-dependent temperature and gas pressure distributions obtained by means of the FEM compared to experimental measurements* (Davie, et al., 2010).

The desorption isotherms characterise the process of drying and are based on theoretical equations (Genuchten, 1980; Erich, et al., 2008) extended by experimental measurements performed after heating on concrete specimens (Tenchev, et al., 2001; Dal Pont, 2004). The capillary pressure governs the water phases (Gawin, et al., 2003; Tenchev, et al., 2001) and the evaporation/condensation process is assumed to develop instantaneously (Gawin, et al., 2003; Tenchev, et al., 2001). Transmission of thermal energy is governed by thermal conductivity and convection (Gawin, et al., 2003; Tenchev, et al., 2001). Transport of phases is driven by pressure and concentration gradients (Gawin, et al., 2003; Tenchev, et al., 2001). The temperature and gas pressure obtained are illustrated in Fig. 2.31 for C80/95 exposed to a ISO type of fire (Gawin, et al., 2006). Similar distributions are shown in Fig. 2.32 for C85/100 exposed to prolonged temperature of 600 ^{o}C (Davie, et al., 2010).

2.5.2 Thermal stresses and crack development

Continuum models based on elasticity

In the most basic 1D models a temperature distribution is used to obtain the thermal deformation. The total strain definition is governed by the elastic mechanical strain and the temperature-induced strain (Hartsuijker & Welleman, 2007; van Breugel, et al., 1998). Equilibrium of forces determines the deformation and the stress distribution (Hartsuijker & Welleman, 2007; van Breugel, et al., 1998). These models are also extended to include load combinations, partial restraint and the cross-sectional shape (Taerwe, 2007). Design recommendations and calculation methods (Eurocode 2, 2011b) allows to obtain insight into the member and the structural behaviour (Taerwe, 2007). These simplified models reflect the influence of thickness, heating rate, structural loading and restraint (Lottman, 2007).

Differences between elastic and measured deformation during heating of specimens has lead to more elaborate total strain definitions (Anderberg & Thelandersson, 1976; Khoury, 2006c). In the left graph of Fig. 2.33 the largest component is defined at increasing temperatures as the transient strain (Anderberg & Thelandersson, 1976). Creep strains are defined at constant temperature (RILEM TC-HTC, 2004). The strain difference during first heating without and with load is identified in the right graph as the load-induced thermal strain (LITS), based mainly on the transient strain or creep (Schrefler, et al., 2002; Khoury, 2006c).

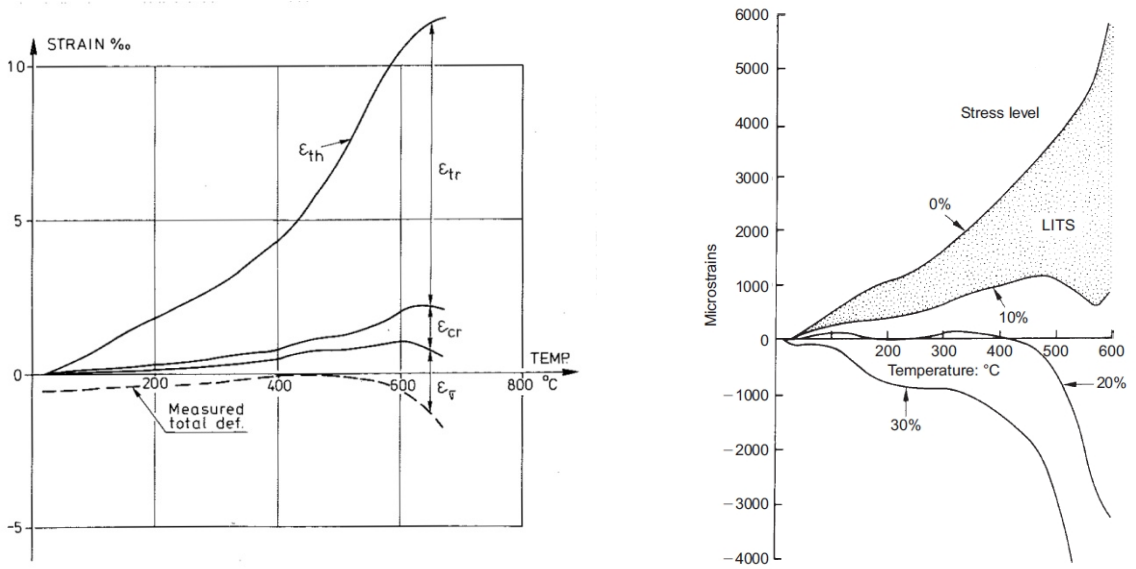

Fig. 2.33 *Total strain definition (left) of heated concrete based on the thermal strain (ε_{th}), transient strain (ε_{tr}), creep strain (ε_{cr}) and stress related strain (ε_{σ})* (Anderberg & Thelandersson, 1976). *Thermal strain development of concrete at various load levels indicating the LITS contribution (right)* (Khoury, 2006a).

Continuum models based on elastic-plastic behaviour

These models are based on a yield criterion (Vonk, 1992; Feenstra, 1993) such as Rankine-Drucker-Prager (Breunese, 2001; Fellinger, 2004) or Willam-Warnke (Ulm, et al., 1999a). Reversible linear strains and irreversible non-linear plastic strains are included in which the latter characterises softening during cracking (Vonk, 1992; Feenstra, 1993). Failure of the material is based on the principal stress directions, resulting in cracking in tension (Vonk, 1992; Feenstra, 1993) distributed across the width of the element (Breunese, 2001). Compression failure is based on yielding (Vonk, 1992; Feenstra, 1993) and incorporates shear retention governing the load transfer across the crack (Breunese, 2001; Fellinger, 2004). The material is assumed to remain isotropic or direction-independent (Fellinger, 2004) which neglects fixation of the plastic strain in the direction of initiation.

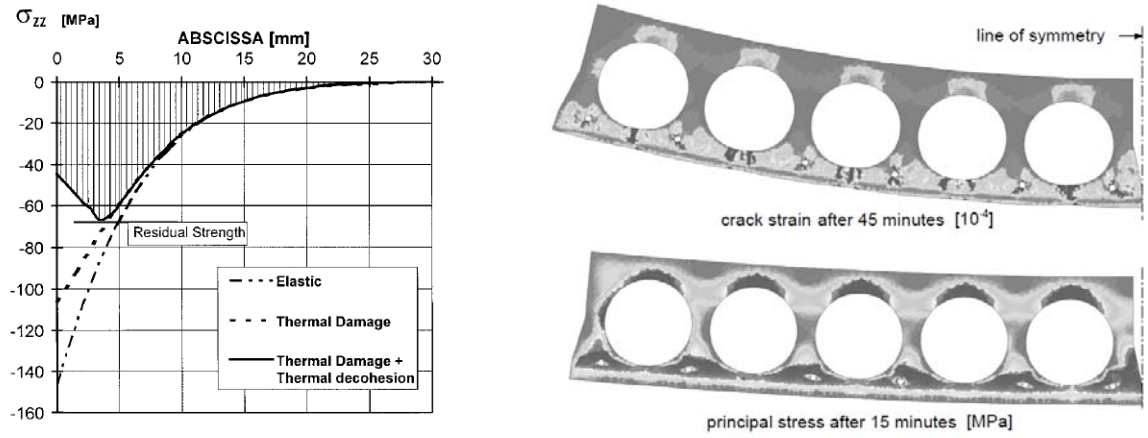

Fig. 2.34 *Stresses in the lining of the Channel tunnel during the fire in 1996 using elastic-plastic behaviour (left)* (Ulm, et al., 1999b). *Principal stress and crack strain in a fire exposed hollow core slab (right)* (Fellinger, 2004).

Commonly, a homogeneous material description is used leading to stress and/or crack strain distributions as seen in Fig. 2.34. These represent stress analysis of the lining of the Channel tunnel during the fire in 1996 (Ulm, et al., 1999b) or a fire exposed hollow core slab (Fellinger, 2004). Aggregates can be included for a heterogeneous material (Breunese, 2001).

Fracture mechanics models based on a smeared approach

The focus on the localisation of deformations in opening of the crack has led to the development of smeared crack fracture mechanics models. These commonly describe a 2D homogeneous material (Vonk, 1992). The total strain is decomposed into the strain of the solid material and the crack strain (de Borst, 1986; Rots, 1988). Mode I fracture by tension softening characterises the stress-crack strain relationship (de Borst, 1986; Rots, 1988). This description governs the crack propagation in the cohesive zone (Hillerborg, et al., 1976) or the process zone (Bažant & Oh, 1983) as illustrated in Fig. 2.35. The crack is fixed in the direction of initiation (de Borst, 1986; Rots, 1988) which makes the material anisotropic and influences the principal stress directions (de Borst, 1986; Rots, 1988).

Implementation of local softening can lead to stress variations that counteract localization or cause stiffening by locking (Rots, 1988). This especially occurs in case the mesh is not aligned with the direction of crack development, resulting in mode II fracture based on tension and shear loading (Rots, 1988). More elaborate models use a multi-directional fixed basis which allows the crack strain to be decomposed across several cracks (de Borst, 1986; Rots, 1988). Another possibility is the rotational smeared crack approach in which the crack is continuously aligned with the principal strain direction (Rots, 1988). Shear retention governs the possibility for aggregate interlock between the crack faces (de Borst, 1986; Rots, 1988).

Fracture mechanics models based on discrete fracture

In discrete fracture mechanics each crack is modelled separately (Vonk, 1992; Schlangen, 1993). The most basic models are characterised by a preliminary known crack path which is explicitly included in the material description of the 2D continuum (Vonk, 1992; Schlangen, 1993). Another possibility is to determine crack propagation based on the stress field combined with a mesh refinement at the crack tip (Vonk, 1992; Schlangen, 1993). These models include a stress-crack opening relationship or use more commonly genuine separation by a discontinuity in the material (Vonk, 1992; Rots, 1988; Schlangen, 1993).

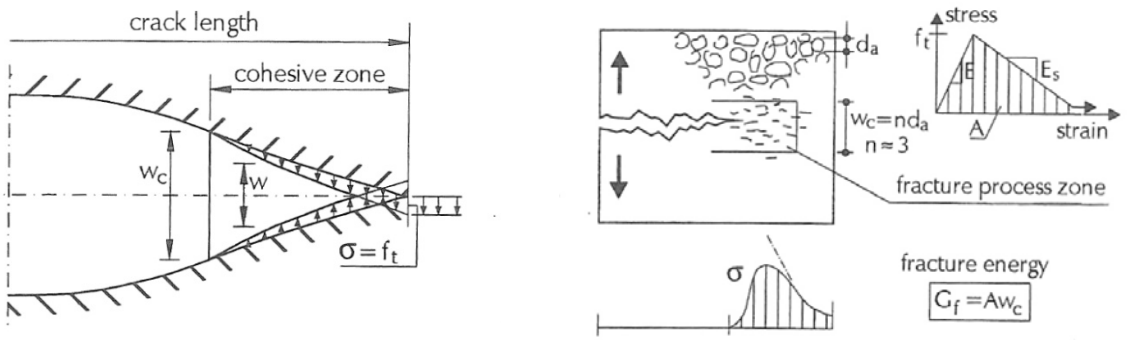

Fig. 2.35 *Schematisation of crack development in concrete in the cohesive zone (left)* (Hillerborg, et al., 1976) *or the process zone (right)* (Bažant & Oh, 1983).

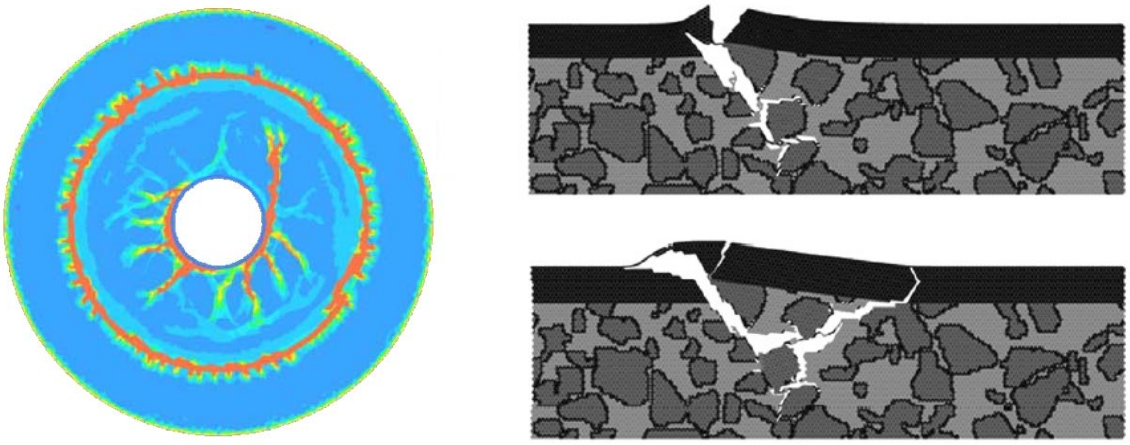

Fig. 2.36 *Crack strain development in the cross-section of a heated concrete cylinder (left)* (Fellinger & Breunese, 2005). *Damage caused by frost salt scaling determined by means of a lattice model (right)* (Çopuroğlu & Schlangen, 2008).

A special type are the lattice models which schematise the 2D continuum by linear elastic 1D beam elements (Schlangen, 1993; Vervuurt, 1997). Cracks are included by incremental brittle fracture of individual beams based on the stress field (Schlangen, 1993; Vervuurt, 1997). This explicit type of cracking is determined for a detailed, possibly random, network description of a heterogeneous material. The fractured beams no longer contribute to the stiffness of the material which allows localisation of deformations in opening of the crack (Schlangen, 1993; Vervuurt, 1997). The relatively long calculation times commonly restricts this model to small scale mechanical problems such as tensile tests (Schlangen, 1993; Vervuurt, 1997) or frost salt scaling as illustrated in the right picture of Fig. 2.36 (Çopuroğlu & Schlangen, 2008).

2.5.3 Coupling between temperature, pore pressure and thermal stresses

The most basic approach obtains an indication for the mechanical consequences of gas pressure development. The porous microstructure is schematised as a plate with holes as shown in the left picture of Fig. 2.37 (Ichikawa & England, 2004). The tensile stress at the edge of a hole in the surrounding material indicates a direct relationship with the gas pressure and the pore volume (Ichikawa & England, 2004). However, the coupling is more commonly implemented by a mechanical equilibrium equation added to the porous material description (Gawin, et al., 2003; Davie, et al., 2010; Ožbolt, et al., 2011; Zeiml, et al., 2008b). An effective stress approach is used to relate the pore pressure to the solid stress, taking the deformability of the microstructure into account by Biot's constant (Gray & Schrefler, 2001; Gawin, et al., 2006). The pore pressure is based on a combination of the gas and water pressure influenced by the liquid water saturation level (Gray & Schrefler, 2001).

The influence of the temperature and the crack development on the permeability and Young's modulus can be implemented by chemical and mechanical damage parameters (Gawin, et al., 2003; Davie, et al., 2010). Chemical damage is based on the degradation of the concrete due to dehydration (Gawin, et al., 2003; Davie, et al., 2010). Mechanical damage is for the permeability taken into account by several constants describing the increase through cracking (Gawin, et al., 2003). Young's modulus is based on loaded stress-strain relationships (Gawin, et al., 2003) or governed by the fracture energy (Davie, et al., 2010).

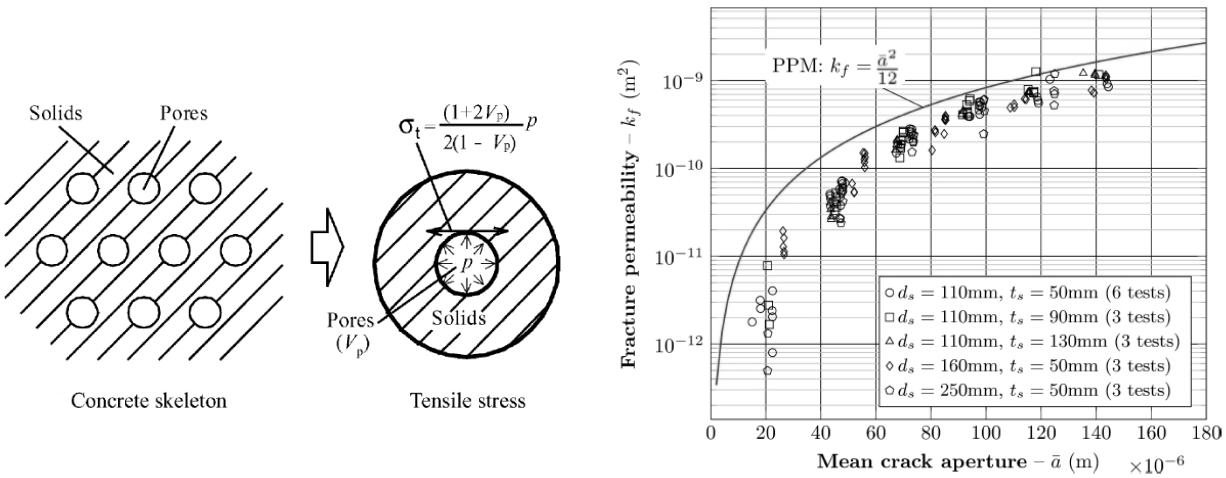

Fig. 2.37 *Simplified model for determining the stress at the pore edge (left)* (Ichikawa & England, 2004). *The parallel plate model estimates the crack permeability based on its width* (Neuzil & Tracy, 1981) *as validated by experiments* (Rastiello, et al., 2013).

An alternative method to determine the influence on the permeability of a local crack is to use the parallel plate model (Neuzil & Tracy, 1981). The laminar flow at low velocity between two plates is used to relate the permeability to the crack width (Neuzil & Tracy, 1981). Validation by experiments seems to suggest a sufficient representation as shown in the right graph of Fig. 2.37 (Rastiello, et al., 2013). This relationship neglects tortuosity, varying crack width and the roughness along the edges.

2.5.4 Thermal stability of heated concrete

Most of the models described are focused on the description of heated concrete rather than the thermal instability that characterises the spalling process. An example of such a model is based on rigid body springs and has a dynamic basis (Nakamura, et al., 2011). The equation of motion is extended by simplified temperature, pore pressure and mechanical relationships (Nakamura, et al., 2011). Instability of the heated surface layer is governed by the sudden increase in the spring deformations, indicating spalling of the rigid bodies as shown in Fig. 2.38 (Nakamura, et al., 2011).

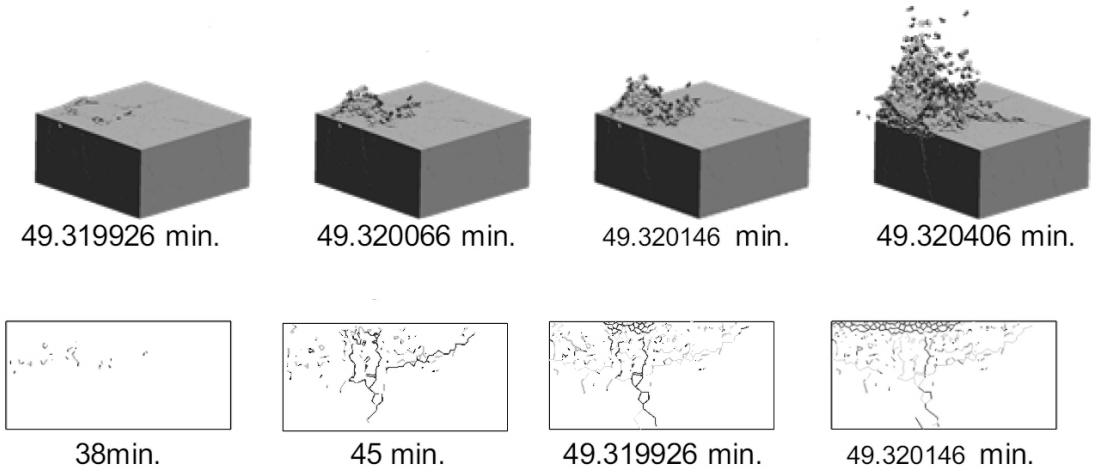

Fig. 2.38 *Rigid body spring model focused on the thermal instabilities which characterises spalling by temperature and pore pressure* (Nakamura, et al., 2011).

3 Problem description, objectives and solution approach

3.1 Problem description

Coupled development of chemical, physical and mechanical processes

The exposure of a concrete element to a fire leads to the development of several interacting processes which have a chemical, physical and mechanical basis. The characterisation of heated concrete is further complicated by the multi-scale nature of the problem as represented by the schematic overview in Fig. 3.1 (Lottman, et al., 2009; Lottman, et al., 2011).

- The chemical degradation of the material develops with temperature in the cement paste. The forced drying and the dehydration processes weaken and open the microstructure of the cement paste (Alonso & Fernandez, 2004; Liu, 2006). This increases the porosity and permeability (IREX, 2005) and reduces the strength and stiffness (RILEM TC-HTC, 2004). These properties govern the temperature and pore pressure as well as the deformations and stresses that develop in heated concrete.

- The development of the temperature gradient and the rapid evaporation of liquid water leads to gas pressures in the pores of the microstructure (Kalifa, et al., 2000). The resultant flow of the gas and liquid phases progressively changes the moisture distribution (van der Heijden, 2011). The gas or pore pressure increases by penetrating into the cross-section affected by the low permeability of concrete (Kalifa, et al., 2000). Ultimately, a layer partially saturated with liquid water could be formed which further enhances the gas pressure (van der Heijden, 2011; Zeiml, et al., 2006).

- The temperature gradient also causes the development of thermal stresses in the cross-section (van Breugel, et al., 1998) based on the differences in thermal expansion between the aggregate particles and the surrounding mortar (Diederichs, et al., 1987; Flynn, 1999). This stress state is extended by possible external structural restraint and loading (fib WP-4.3-1, 2007) causing a distinctive crack pattern. The pore pressure build-up further extends the internal loading, acting between the aggregate particles and is mitigated by local cracking (Bažant, 1997).

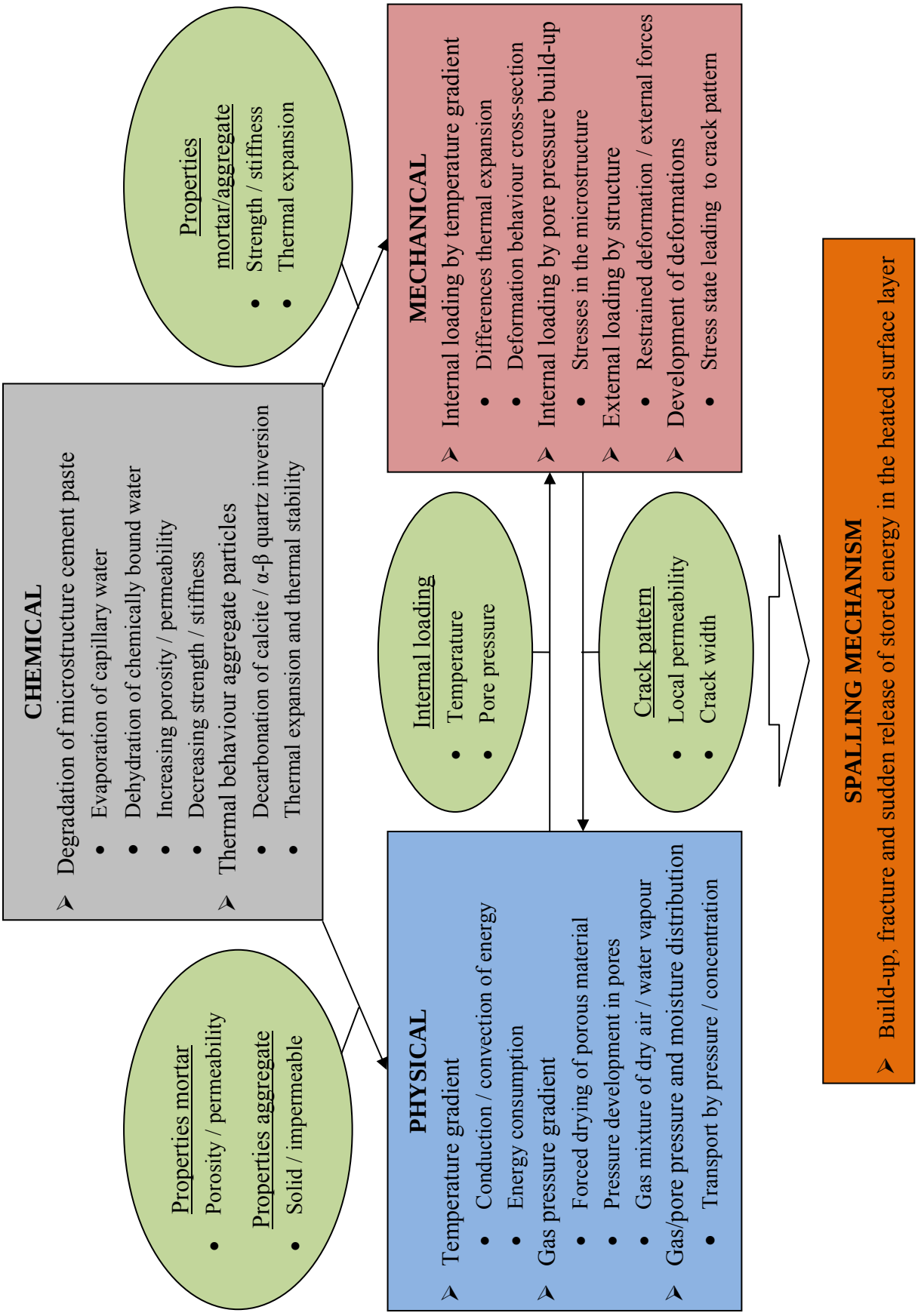

Fig. 3.1 *Schematic overview of the main chemical, physical and mechanical processes that develop in heated concrete as well as the possible resultant spalling mechanism.*

Experimental research into the material behaviour and properties

The experimental determination of material behaviour and properties of heated concrete is difficult, especially at high temperatures. The traditional material properties, such as Young's modulus, compressive and tensile strength, are determined by hot or residual testing at room temperature (RILEM TC-HTC, 2004). Advances made in measuring techniques have allowed to obtain better insight into specific areas such as pore pressure development (Kalifa, et al., 2000) and unloaded or loaded thermal deformations (RILEM TC-HTC, 2004). However, certain testing procedures, aimed at determining the porosity or permeability, can still only be performed at ambient conditions. The preheated and subsequent cooled down samples allow for the possibility of rehydration of the microstructure which should be avoided. Other important material characterisations, such as desorption isotherms (Poyet, 2009) and softening behaviour under load (Felicetti & Gambarova, 1998), are difficult to measure from samples at elevated temperatures.

The emphasis in these experiments is mainly on concrete specimens. Experimental research into the high temperature behaviour of the various components of concrete is currently mainly focussed on cement paste (Alonso & Fernandez, 2004). The measurements often include the development of energy, relative weight loss and the microstructure of cement paste (Alonso & Fernandez, 2004; Zhang, 2013). Various other basic parameters such as the porosity, pore size distribution (Castellote, et al., 2004; Liu, 2006) and stiffness are also determined experimentally. Research into the other components, such as the aggregate particles, is limited especially to high temperatures. For all heating and testing procedures it should be noted that the samples used, or obtained, always reflect the state of development of the main processes.

Full-scale experimental research into spalling of concrete

The dynamical environment, to which the concrete element is exposed, is characterised by high heating rates and rapidly developing processes. This makes understanding of the material behaviour and the observed spalling damage even more difficult. Through extensive testing the most dominant factors that influence the spalling process have been established (Khoury & Anderberg, 2000):

- The heating rate, temperature and duration of the fire exposure are the driving factors for all processes (Horvath, et al., 2004; Mindeguia, 2009).

- The material factors believed to influence the behaviour are the moisture content and the concrete mixture mainly characterised by W/C ratio and type of aggregate (Horvath, et al., 2004; Mindeguia, 2009).

- The addition of PP-fibres to the mixture has shown a beneficial effect in reducing the spalling sensitivity (Jansson & Boström, 2008; Dehn, et al., 2010). Also of importance are the presence and distribution of reinforcing bars (FSV, 2004).

- The structural influence is considered to consists of especially compressive external loading and restraint (FSV, 2004; Dehn, et al., 2010). The geometry is characterised by the cross-section and single or multiple side exposure (Brekelmans, et al., 2008).

The quantity and interaction of these dominating processes and factors are not conclusively determined yet. This makes spalling of concrete a still somewhat illusive phenomenon. This is further underlined by the observation of seemingly contradictory results in observed spalling damage (FSV, 2004; Pimienta, et al., 2010). Important in this regard are the concrete mixture (Horvath, et al., 2004) and the sample geometry (Brekelmans, et al., 2008). The test set-up, involving factors such as temperature development control (Dehn, et al., 2010) and possible partial restraint (Mindeguia, 2009), is also to be considered. Furthermore, it should be ensured that the external load is sustained during the test. This turned out to be difficult for post tensioned systems in which the heating of the bars relaxes the applied force (Jansson & Boström, 2008). It should also be noted that the duration of conditioning or storage of the samples (Horvath, et al., 2004; Mindeguia, 2009) determines the extent of uniformity in the moisture content of the surface layers.

The observed development of the spalling process further complicates the understanding. This process ranges from repetitive spalling of small layers to relatively isolated single occurrences of more explosive nature resulting in spalling of larger layers (FSV, 2004; Mindeguia, 2009). The damage can range from superficial, affecting only the concrete surface (Jansson & Boström, 2008), to exposure of the reinforcement (Dehn, et al., 2010). Spalling of concrete is therefore often characterised as an almost random behaviour making analyses and predictions based solely on experiments difficult. However, the current state of the fire design codes only states that spalling is not allowed (Eurocode 2, 2011b). Since guidelines and calculation methods are not present yet, the only feasible solution is the usages of expensive full-scale testing in order to determine the spalling sensitivity.

Theoretical and numerical description of heated concrete and spalling

In order to obtain more insight into the behaviour of heated concrete and the spalling process the focus has also been on the statement of theories. The most basic theories focus on pore pressure (Harmanthy, 1965) and thermal stress development (Dougill, 1972) as being individually, or in combination (Zhukov, 1976), the main driving forces behind the spalling process. These theories are commonly accepted as to influence the spalling sensitivity of heated concrete. However, the interaction and the extent of the influence of these theories is currently not sufficiently understood.

These theories have also formed the basis for development of numerical models mostly aimed at derivation of the physical behaviour characterised by the drying process (Bažant, et al., 1981; Gawin, et al., 2003; Tenchev, et al., 2001). These models capture the main behaviour such as temperature and gas or pore pressure development. However, the main material characterisation and properties, such as the desorption isotherms and the permeability, have already been indicated to be difficult to determine at high temperatures. The drying behaviour is further complicated by the cross-section in which the distribution of the aggregate particles influences the transport behaviour. Furthermore, measurements of gas pressure build-up in heated concrete slabs has indicated the relatively large mitigation effect by crack development (Mindeguia, 2009). The current state of the physical models, with mainly a 1D homogeneous material description, proved to be insufficient to capture these localised 2D effects.

In the field of mechanics the focus has, for the most part, been on the application of existing models. The application ranges from 1D linear elastic models to determine the stress state in a cross-section (Ulm, et al., 1999b) to 2D fracture mechanics models focussing on the crack development (Fellinger, 2004). These models capture the main mechanical behaviour mostly based on the temperature distribution acting as internal loading. The possible influence of gas pressure development on the mechanical behaviour of a porous material is thereby still not fully understood (Gawin, et al., 2006; Felicetti, et al., 2012). Furthermore, elaborate strain definitions are used to include non-linear aspects observed in the thermal deformation behaviour (Anderberg & Thelandersson, 1976; fib WP-4.3-1, 2007). However, the interaction of the main processes and the level of cracking makes statement of separated material laws difficult. The fracture mechanics behaviour is also complicated by the key parameters, such as strain softening (de Borst, 1986; Rots, 1988), being difficult to determine at high temperatures. Important is also that the structural behaviour should be taken into account by factors such as the geometry, external loading and partial restraint.

Through the physical and mechanical models the comprehension of the behaviour of heated concrete has increased. However, the current state of these models has also proven to be insufficient in assessing the quantity and interaction in the dominant processes in spalling of concrete. The involvement of chemical, physical and mechanical processes at high temperatures makes understanding and coupling difficult, also by combining various disciplinary fields of research.

Spalling of concrete as an instability mechanism

The focus on the characterisation of material behaviour and especially pore pressure development has shifted attention away from the actual instability mechanism. The commonly observed occurrence of spalling of concrete during full-scale testing, yet varying in geometry and nature, seems to indicate that a certain mechanism frequently develops. This mechanism develops in the heated surface layer of a concrete cross-section and is characterised by the build-up of energy. The separation of layers by sudden localised fracture occurs in case sufficient energy has developed which can no longer be contained. The formed instabilities are ejected off the heated surface by release of the stored energy observed in tests as spalling.

3.2 Problem definition

From the problem description it becomes clear that two aspects are dominant:

- The first is the material behaviour of heated concrete. The development of the various interacting chemical, physical and mechanical processes in a 2D heterogeneous cross-section driving the spalling process are difficult to comprehend and to schematise.

- The second is the instability mechanism of spalling of concrete. The build-up of energy followed by a sudden release characterised as spalling of a layer of the heated surface is insufficiently understood. The lack of knowledge on the dominant processes, that lead to the development of a spalling mechanism, is extended by insufficient focus on the instability itself.

3.3 Objectives of this thesis

This thesis aims to fulfil the following objectives:

- The first objective is to obtain a better understanding of the coupled main chemical, physical and mechanical processes that develop in heated concrete. The approach followed in this thesis is based on the derivation of a conceptual FEM model. The temperature and pore pressure as well as the thermal deformations and stresses are to be characterised based on a simplified approach.

- The second objective is to couple both the physical and mechanical processes by taking the local effect of the pore pressure into account. This should also allow for mitigation of the pore pressure by local crack development.

- The third objective is to determine the dominating processes responsible for the occurrence of a spalling mechanism. The focuses is to be on the crack pattern, allowing for the possibility of formation of instabilities in the heated surface layer.

3.4 Layout of the solution approach

Coupled temperature, pore pressure and fracture mechanics approach
In this thesis a conceptual FEM model is derived which focuses on temperature and pore pressure as well as fracture mechanics. The influence of the main chemical processes is reflected by the temperature-dependent behaviour of the material properties. The physical and mechanical processes are each represented by a separate FEM model based on simplified material descriptions. The interaction between both processes is reflected by coupling of the two FEM models in key aspects such as the internal loading and the crack development.

The 2D structural cross-section characterised by the concrete components
Schematisation of the model is based on a 2D cross-section representing part of the concrete structural element as shown in Fig. 3.2. This element is exposed to a single sided fire assumed constant in height direction. Development of the temperature and pore pressure distribution is numerically approximated by the first FEM model. The physical behaviour is, under these circumstances, assumed to be continuous in depth direction and develops predominantly in width direction of the cross-section. The fracture mechanics behaviour, numerically approximated by the second FEM model, is characterised by restraint and loading imposed by the surrounding structure. This leads to the development of stresses based on deformation of the element. In depth direction the cross-section is assumed constant, represented by a unit thickness, governed by a plane strain assumption (Timoshenko & Goodier, 1970).

The material schematisation is based on the concrete components. The aggregate particles are distributed in the cross-section and connected to the surrounding mortar by interfacial (transition) zones. This allows to combine the overall structural loading with the local material behaviour. The material description also allows for cracking in the heterogeneous material to influence both the deformations and the pore pressure development.

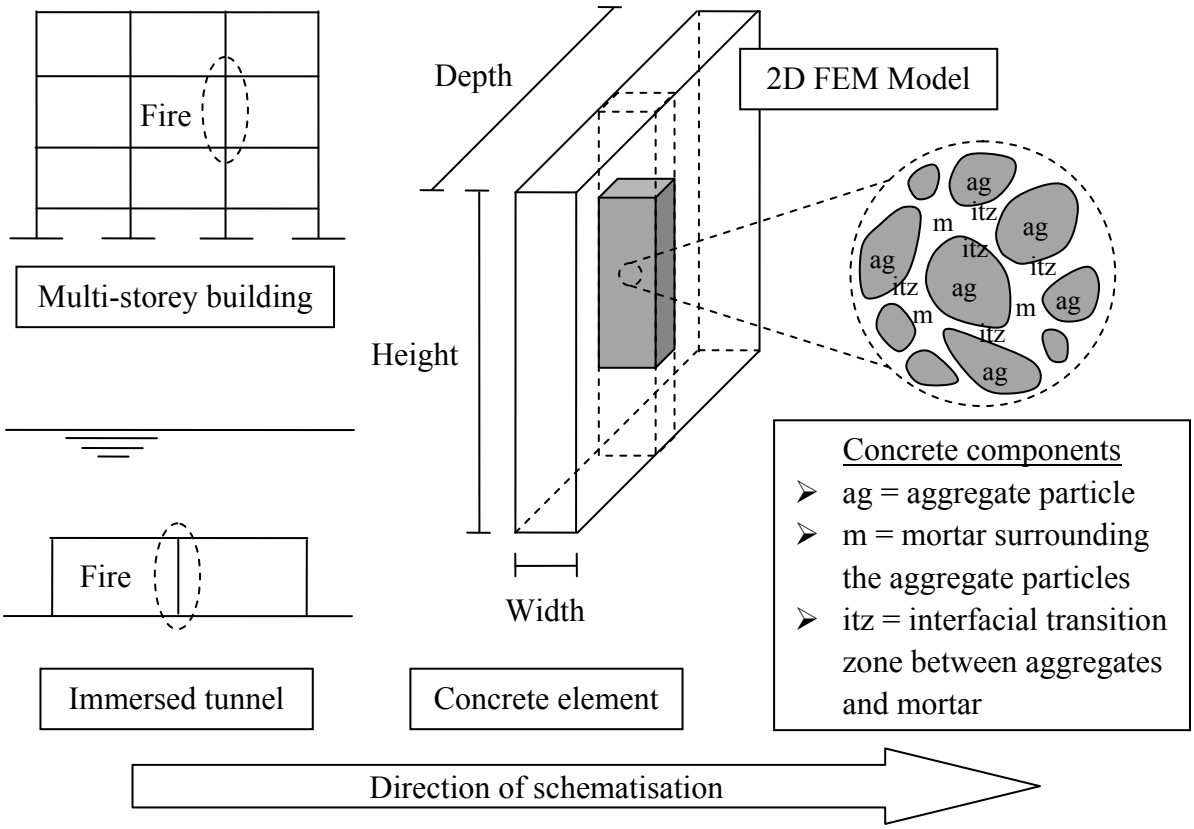

Fig. 3.2 *Conceptual FEM model based on schematisation of a part of the structural element, characterised by a 2D cross-section based on the concrete components.*

Both models are implemented for a representative cross-section in order to obtain a FEM discretisation which balances the structural and material requirements:

- The height of the cross-section is chosen several times larger than the width. This allows to maintain the structural characterisation as an element and overcomes possible disturbances at the top and bottom edges by the surrounding structure.

- The local detail level is chosen several times smaller than the aggregate particles. This ensures sufficient detail in the material to also capture the local tortuosity of the crack path. Important aspects are the localised permeability increase and stiffness reduction.

The first FEM model - temperature and pore pressure

Exposure of the element to a fire causes the rapid propagation of heat across the concrete components. This leads to pressure development in the gas phase based on the evaporation of liquid water which develops in the porous structure of only the mortar and interfacial zones. Transport of the gas and liquid phases is assumed to be driven, predominately, by the gas pressure build-up for which the aggregate particles are assumed to form impermeable obstacles.

In this thesis, the FEM model is based on a multi-phase porous material description (Hassanizadeh & Gray, 1979b; Bear & Bachmat, 1986) taking the local aggregates or solid material into account. Forced drying of the mortar and interfacial zones is characterised by the material-dependent desorption isotherm and the capillary pressure (Pel & Huinink, 2007). The

2D cross-section is represented by a continuum based on the conservation of thermal energy and mass of the water phases, both coupled by a system of PDE's (Hassanizadeh & Gray, 1979b; Bear & Bachmat, 1986). The local material is averaged in order to obtain a representative behaviour (Hassanizadeh & Gray, 1979a; Bachmat & Bear, 1986).

The FEM definition is completed by boundary conditions at the left and right edges of the cross-section reflecting the single sided fire exposure. The top and bottom edges are governed by continuous boundary conditions to ensure a mainly 1D behaviour perpendicular to the heated surface as shown in Fig. 3.3.

This 2D continuum is extended by including local material directions, resulting in an anisotropic description (Bear, 1972/1988). This allows to include the orientation of the crack pattern obtained by means of the facture mechanics model. The simplified parallel plate model is used to estimate the local permeability increase based on the crack width (Bear, 1972/1988; Neuzil & Tracy, 1981).

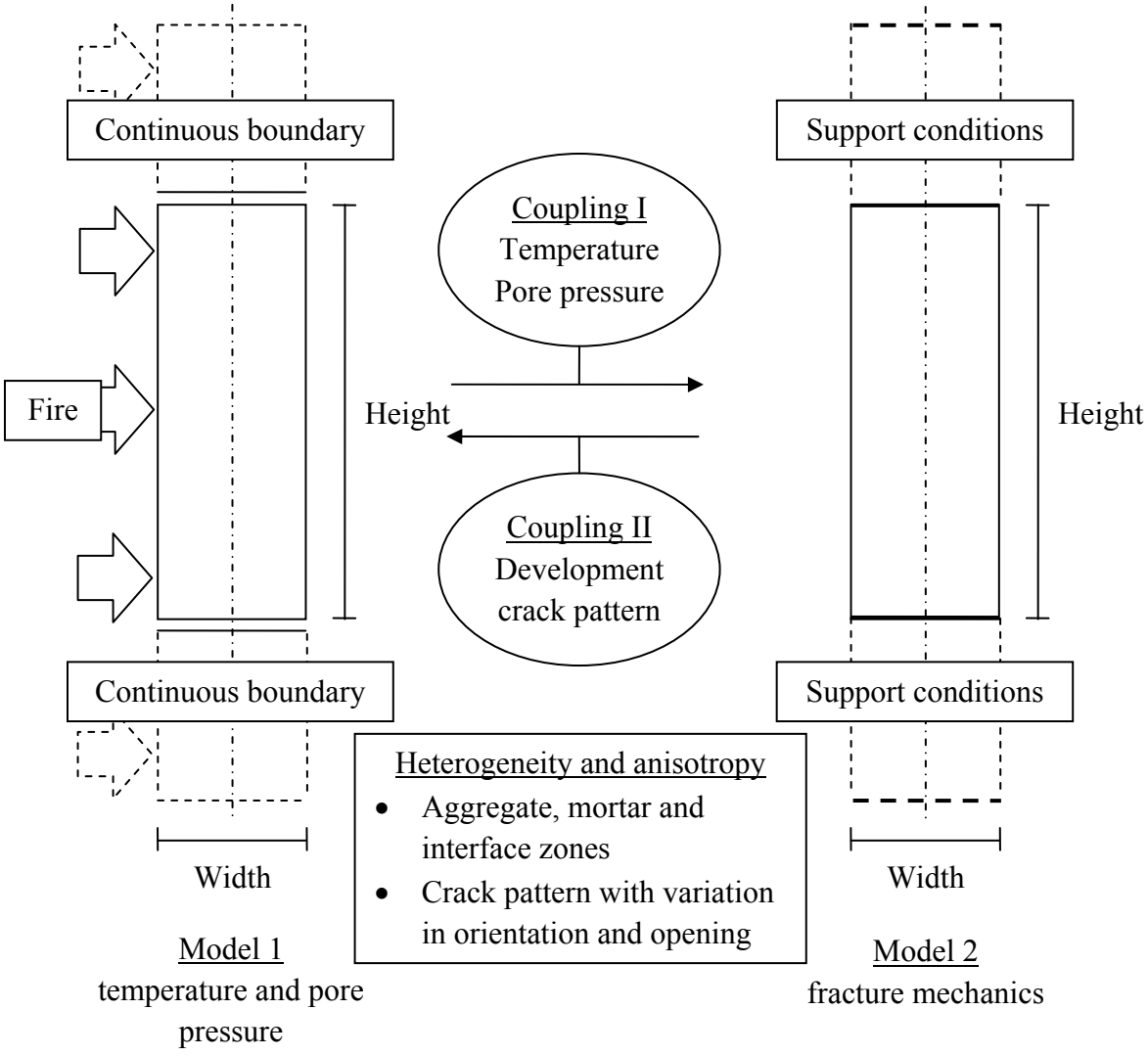

Fig. 3.3 *Schematic overview of the FEM models based on the representative cross-section of the element with indication of materials, boundary conditions and couplings.*

The second FEM model - fracture mechanics

The deformation and stress distribution of the element result from various types of loading. The temperature and pore pressure distribution, obtained by the first model, are imposed as internal loading based on the concrete components. The support conditions govern the structural restraint and possible external forces, present at the top and bottom edges. This in-time varying stress state leads to a pattern of cracks having different orientations and crack widths.

In this thesis, the FEM model is based on the mechanical description of the material characterised by the concrete components. Internal loading is imposed as an initial elongation strain reflecting temperature development (Timoshenko & Goodier, 1970; Prezemieniecki, 1968/1985). The influence of the gas pressure build-up is included as initial load based on the induced linear elastic stress state in the material surrounding the pores (Timoshenko & Goodier, 1970). The 2D cross-section is represented by a continuum based on the balance of forces governed by a single PDE (Felippa, 2004a; Felippa, 2004b; Wells, 2006).

The FEM definition is completed by the support conditions at the top and bottom edges. These impose Bernoulli's hypothesis (Hartsuijker & Welleman, 2007) governing the cross-sectional deformation. Interaction with the surrounding structure is reflected by a combination of fixed and spring support conditions as shown in Fig. 3.3.

This 2D continuum is approximated by local extensional strains schematised as bars leading to an anisotropic material description (Prezemieniecki, 1968/1985; Blaauwendraad, 2004). This simplification allows for initiation of a crack to be based on the analogy of local extensional fracture of fibres, capturing the relatively low tensile strength of concrete (Schlangen, 1993; Vervuurt, 1997). Deformation of the continuum tends to be localised in opening of the cracks, relaxing stresses in the surrounding material. A geometric non-linear material description is added to reflect these deformations (Bathe, 1986; Gavin, 2014). Furthermore, to improve the redistribution of fracture forces Bernoulli-Euler beams are added, obtaining a traditional lattice approach (Schlangen, 1993; Vervuurt, 1997).

Characterisation of concrete

Throughout this thesis both NSC and HSC are used to characterise the main material properties. With respect to the temperature and especially the pore pressure development the desorption isotherms, porosity and permeability are the most important. Young's modulus, tensile strength and temperature strain govern the displacements, stresses and the crack development. These properties and several others are presented throughout the coming chapters based on definition of the constitutive relationships.

Both concrete strength classes are governed by typical values with the NSC serving as reference. This C25/30 is mainly characterised by a relatively low Young's modulus (van Breugel, et al., 1998) and tensile strength for the mortar and especially the interfacial zones (Müller & Rubner, 1994). The HSC reflects a C90/105 which is characterised by a reduced porosity and especially permeability (IREX, 2005). Compared to the reference NSC is also the mortar assumed stiffer and stronger with the interfacial zones having similar properties.

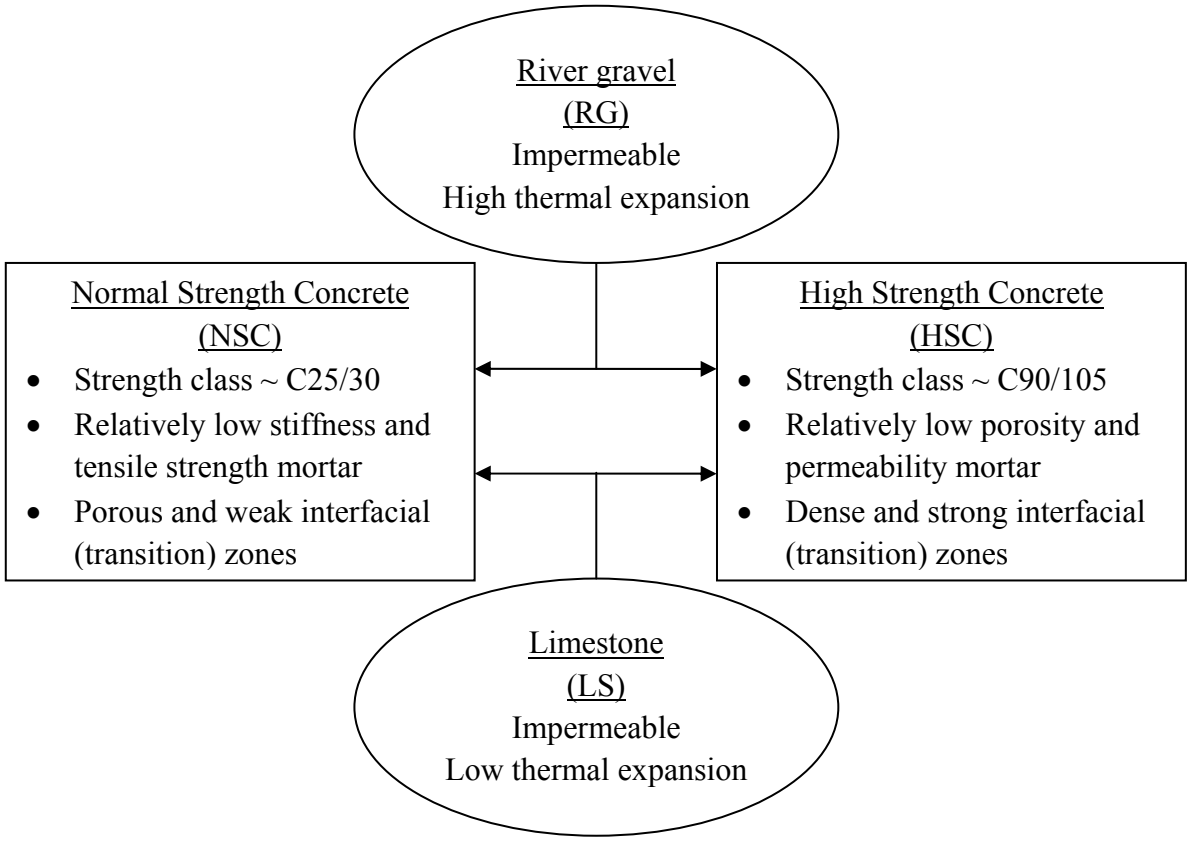

Fig. 3.4 *Overview of the various concrete strength classes and aggregate types, indicating the main behaviour considered in the various material schematisations.*

Both concrete strength classes can be made with river gravel (RG) or limestone aggregate (LS). These particles are considered impermeable with the former characterised by a higher thermal expansion (Eurocode 2, 2011b). The various considerations are schematically indicated in Fig. 3.4 with the mortar characterised according to the concrete strength class.

Initially the material is schematised as homogeneous and isotropic in order to determine the main influencing parameters. Aspects considered are the concrete strength class, the type of fire exposure and the environmental conditions as well as the level of structural restraint and the possibility for external loading. Subsequent a heterogeneous schematisation is adopted to reflect the local material behaviour by introducing the aggregate particles, the surrounding mortar and the interfacial zones. Anisotropy is included to especially focus on the local crack development, characterised by aspects such as orientation, opening and connectivity throughout the crack pattern.

4 Temperature and pore pressure basics for fire exposed concrete

In this chapter the physical relationships governing fire exposed concrete are elaborated and discussed. These will form the basis for the derivation of the FEM model, presented in chapters 6 and 7. First, the relationship between temperature and pressure development is clarified based on an infinitely stiff and strong closed system. This allows to elaborate the constitutive relationships governing the mixture of water vapour and dry air above liquid water. Furthermore, the gas pressure development during crack opening is discussed using a similar approach. The inherent limitations are overcome by definition of an open system for which the general conservation of a property across a representative volume is stated. This is subsequently applied to the thermal energy and the mass of the water phases across the continuum. Additional constitutive relationships such as Fourier's law and Darcy's law as well as the characterisation by a desorption isotherm are introduced. The obtained PDE's are numerically approximated using the FDM extended by Neumann boundary conditions. Several numerical results are presented, indicating key aspects in the material behaviour. This chapter is concluded by defining the permeability of a simplified crack.

4.1 Relationship between temperature and pore pressure in a closed system

The development of the pore pressure is the first main theory used to characterise the behaviour of concrete at elevated temperatures and to explain the spalling mechanism (Harmanthy, 1965). The forced drying of the porous microstructure of cement paste is governed by the evaporation process between the liquid and vapour phases of water. In order to clarify the physical theory governing the observed pore pressure development (Kalifa, et al., 2000) first a simplified closed system is defined reflecting the porous material (Hettema, 1996) as shown in Fig. 4.1. The conservation of mass governing the water phases is used to describe the drying process and to determine the gas pressure commonly referred to as the pore pressure (Hettema, et al., 1998). The uniform increase of the temperature causes the gas pressure in the closed system to increase based on evaporation of liquid water (Hettema, et al., 1998; Clement, 2010). This forms the basis for understanding the processes governing the forced drying of fire exposed concrete.

4.1.1 Basic assumptions used in the definition of the closed system

With respect to the definition of the closed system the following assumptions are stated:

1. The closed system is assumed to have a constant volume and an infinite stiffness and strength. This implies that the degradation of the cement paste with temperature is neglected. Furthermore, the development of the gas pressure is assumed not to deform or fracture the system.

2. The closed system is characterised by not allowing for transport of the phases across the boundaries and no additional sources are present.

3. The thermal energy is assumed sufficient to uniformly increase the temperature in the system and imposes no restrictions on the instantaneous evaporation process. This assumes thermodynamic equilibrium across the water phases (Hassanizadeh & Gray, 1979b; Bear & Bachmat, 1986) and neglects possible time-dependent behaviour.

4. A desorption isotherm, describing equilibrium between the vapour and the liquid phases of water (Bear, 1972/1988), is for the moment neglected. The water vapour phase thus remains saturated during drying. Furthermore, the influence of the capillary pressure (Pel & Huinink, 2007) is neglected by assuming a flat surface between the gas and liquid phases characterised by a uniform pressure.

5. Liquid water is assumed incompressible whereas the gas phase is a compressible mixture of dry air and water vapour (Moran & Shapiro, 2004). The dry air phase is assumed to be dependent on the reference state since no exchange within the closed system is possible. The resultant gas pressure defines the pore pressure.

6. Above the critical temperature liquid water no longer exists as a distinctive phase (Whitten, et al., 2010). Only the gas phase remains which is assumed to still be characterised as a perfect compressible mixture.

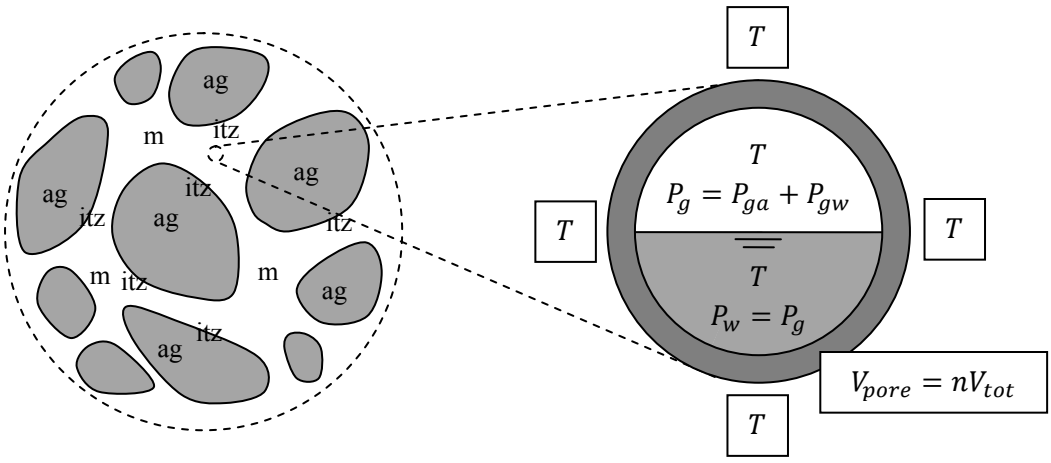

Fig. 4.1 *A schematic illustration of a porous material simplified through definition of the closed system. Uniform temperature across the constant volume leads to gas pressure development based on a mixture of dry air and water vapour.*

4.1.2 Schematisation of the closed system

A porous material is schematically represented by the closed system governed by a constant volume as shown in Fig. 4.1 (Hettema, 1996). The pore volume is assumed characterised by liquid and gas phases which are not miscible. For both phases the saturation level is stated based on the also assumed constant pore volume (Bear, 1972/1988):

$$S_w = \frac{V_w}{V_{pore}} = \frac{V_w}{nV_{tot}}$$
$$S_g = \frac{V_g}{V_{pore}} = \frac{V_{pore} - V_w}{V_{pore}} = 1 - \frac{V_w}{V_{pore}} = 1 - S_w \quad (4.1)$$

where

n	[-]	Porosity of the material
V_{tot}, V_{pore}	[m^3]	Total, pore volume of the closed system
V_g, V_w	[m^3]	Volume of the gas, liquid phase
S_g, S_w	[-]	Saturation level of the gas, liquid phase

Characterisation of the gas phase

The compressible gas mixture is assumed to exhibit a perfect behaviour based on the miscible water vapour and dry air phases. The partial pressure of the water vapour phase above liquid water is defined by the RH and the saturated water vapour pressure (Kotz, et al., 2009; Pel & Huinink, 2007) with the latter shown in the left graph of Fig. 4.2. This equilibrium pressure is temperature-dependent and defined by Clausius-Clapeyron's equation (Kotz, et al., 2009). The following characteristic points are of importance:

- The saturated water vapour pressure is equal to the atmospheric pressure at a temperature of 100 ^{o}C, marking the normal boiling point of liquid water (Whitten, et al., 2010; Moran & Shapiro, 2004). Boiling at increasing temperature occurs by ensuring that the environmental pressure remains equal to the saturation pressure as is the case in a closed system (Whitten, et al., 2010; Moran & Shapiro, 2004). Pressures will increase until no more liquid water is available (van der Heijden, 2011).

- The maximum saturated water vapour pressure of 22.09 MPa is reached at a temperature of 374.15 ^{o}C (Whitten, et al., 2010; Moran & Shapiro, 2004). At this critical point liquid water no longer exists as a distinctive phase (Whitten, et al., 2010). Near the critical temperature the assumed perfect behaviour of the water vapour phase also deviates as illustrated in the right graph of Fig. 4.2 (Moran & Shapiro, 2004).

The gas mixture is characterised by stating the ideal gas law for each phase separately (Moran & Shapiro, 2004) with the water vapour phase assumed saturated (Hettema, 1996; Lottman, 2007). This neglects the desorption behaviour, governing the drying process in a porous material, and assumes a RH of 100 %. The overall pressure of the gas phase is governed by Dalton's law of partial pressures (Moran & Shapiro, 2004):

$$P_g = P_{ga} + P_{gw} \quad (4.2)$$

with

$$P_{ga} = \frac{\rho_{ga} R T}{M_a} \qquad P_{gw} = \frac{\rho_{gw} R T}{M_w} = \overset{=1}{\widetilde{\widetilde{RH}}}\, P_{sat}$$

$$P_{sat} = P_{ref} e^{\frac{H_{vap_{ref}} M_w}{R}\left(\frac{1}{T_{ref}} - \frac{1}{T}\right)}$$

where

T	[K]	Overall temperature
P_g	[Pa]	Overall pressure of the gas phase
P_{ga}, P_{gw}	[Pa]	Partial pressure of dry air, water vapour in the gas phase
RH	[-]	Relative humidity of the material
P_{atm}	[Pa]	Atmospheric pressure defined at 101325 Pa (1 atm)
P_{sat}	[Pa]	Saturated water vapour pressure
R	[J/molK]	Universal gas constant defined as 8.3144 J/molK
M_a	[kg/mol]	Molar mass of dry air defined as 0.02897 kg/mol
M_w	[kg/mol]	Molar mass of water defined as 0.018015 kg/mol
$H_{vap_{ref}}$	[J/kg]	Reference enthalpy of vaporization of water defined as 2260 kJ/kg
P_{ref}	[Pa]	Reference vapour pressure defined at 101325 Pa (1 atm)
T_{ref}	[K]	Reference temperature defined at 373.15 K (100 ^{o}C)
P_{crit}	[Pa]	Critical vapour pressure defined at 22.09 MPa
T_{crit}	[K]	Critical temperature defined at 647.3 K (374.15 ^{o}C)

Characterisation of the liquid phase

The liquid phase of water is assumed incompressible and exhibits a non-linear development of the density as illustrated in the right graph of Fig. 4.2. In a porous material the liquid phase is commonly characterised by the capillary pressure or alternatively the RH (Bear, 1972/1988; Pel & Huinink, 2007). The capillary pressure governs the pressure difference between the gas and liquid phases across the concave interface or meniscus (Bear, 1972/1988; Pel & Huinink, 2007).

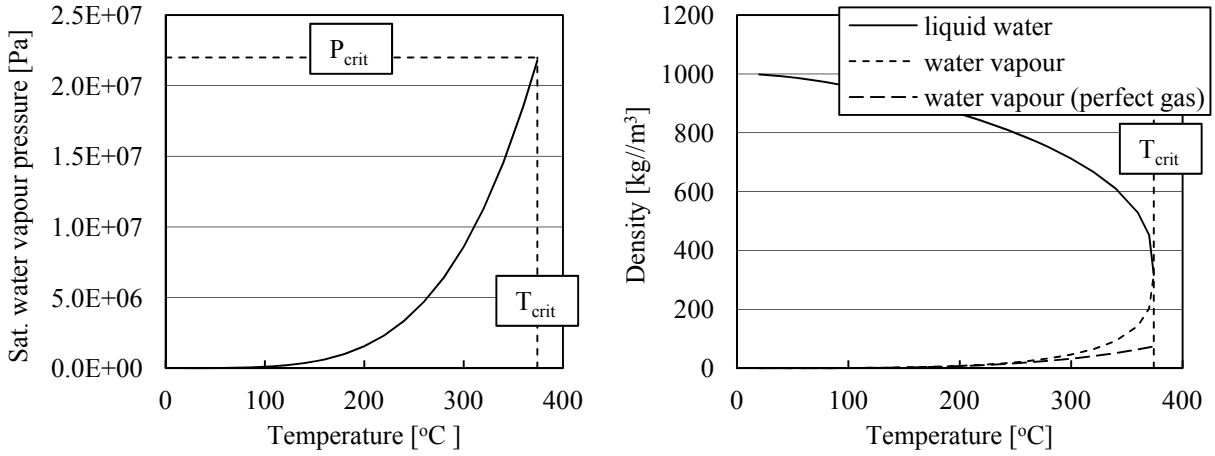

Fig. 4.2 *The saturated water vapour pressure defines the maximum pressure above liquid water as stated by Clausius-Clapeyron's equation (left). The critical point indicates temperature and pressure at which distinction between both liquid and vapour phases of water can no longer be made (right)* (Moran & Shapiro, 2004).

However, in this closed system the liquid water surface is assumed flat, leading to a uniform pressure across the liquid and gas phases:

$$P_c = P_g - P_w = 0 \rightarrow P_w = P_g \tag{4.3}$$

where

P_c	[Pa]	Capillary pressure across the meniscus between the water phases
P_w	[Pa]	Pressure of the liquid phase

4.1.3 Conservation of mass for the dry air and water phases

Development of the gas pressure is based on conservation of mass for the dry air and the water phases. The liquid and vapour phases of water are combined in a single conservation equation to reflect the interaction characterised by the evaporation process (Hettema, 1996). The dry air phase is stated by a separate conservation equation.

Conservation of the dry air phase

The mass of the dry air phase remains constant during temperature development since no exchange is present in the closed system:

$$\begin{aligned} m_{ga} &= \rho_{ga} V_g = \rho_{ga}(1 - S_w) n V_{tot} \\ \frac{m_{ga}}{n V_{tot}} &= \rho_{ga}(1 - S_w) \end{aligned} \tag{4.4}$$

where

m_{ga}	[m^3]	Mass of the dry air phase in the closed system
ρ_{ga}	[kg/m^3]	Density of the dry air phase in the closed system

Through definition of a closed system with a constant volume the temperature-dependent development is related to the initial or reference state using the conservation equation:

$$\begin{aligned} \left(\frac{m_{ga}}{n V_{tot}}\right)_T &= \left(\frac{m_{ga}}{n V_{tot}}\right)_{ref} \\ \rho_{ga}(1 - S_w) &= \rho_{ga_{ref}}\left(1 - S_{w_{ref}}\right) \end{aligned} \tag{4.5}$$

The density of dry air is, according to Eq. (4.2), governed by the partial pressure and the temperature. The initial state of the system is characterised by the reference saturation level with liquid water, the reference and thus atmospheric pressure and the coinciding saturated vapour pressure. The partial pressure of the dry air phase omitting the gas constants becomes:

$$\begin{aligned} \frac{P_{ga} M_a}{RT}(1 - S_w) &= \frac{P_{ga_{ref}} M_a}{R T_{ref}}\left(1 - S_{w_{ref}}\right) \\ P_{ga} &= \frac{P_{ga_{ref}}\left(1 - S_{w_{ref}}\right) T}{(1 - S_w) T_{ref}} \end{aligned} \tag{4.6}$$

with

$$P_{ga_{ref}} = P_{atm} - P_{sat_{ref}}$$

Conservation of the water phases

The definition of a closed system implies that conservation of mass for the water phases is determined by the temperature-dependent evaporation process. The total mass of water, present in liquid or vapour form, remains constant (Hettema, 1996):

$$m_{w_{tot}} = m_w + m_{gw} = \rho_w V_w + \rho_{gw} V_g = \rho_w S_w n V_{tot} + \rho_{gw}(1 - S_w) n V_{tot}$$
$$\frac{m_{w_{tot}}}{nV_{tot}} = \rho_w S_w + \rho_{gw}(1 - S_w) \tag{4.7}$$

where

$m_{w_{tot}}$	[m^3]	Total mass of the water phases in the closed system
m_{gw}, m_w	[m^3]	Mass of the water vapour, liquid water phase in the closed system
ρ_{gw}, ρ_w	[kg/m^3]	Density of the water vapour, liquid water phase in the system

Again the conservation equation is expressed with respect to the reference state:

$$\left(\frac{m_{w_{tot}}}{nV_{tot}}\right)_T = \left(\frac{m_{w_{tot}}}{nV_{tot}}\right)_{ref}$$
$$\rho_w S_w + \rho_{gw}(1 - S_w) = \rho_{w_{ref}} S_{w_{ref}} + \rho_{gw_{ref}}\left(1 - S_{w_{ref}}\right) \tag{4.8}$$

Conservation of mass for the water phases is defined by the densities and the reference liquid water saturation level (Hettema, 1996). The development of the saturation level is obtained through the density of the saturated water vapour phase as stated in Eq. (4.2):

$$\rho_w S_w + \frac{P_{sat} M_w}{RT}(1 - S_w) = \rho_{w_{ref}} S_{w_{ref}} + \frac{P_{sat_{ref}} M_w}{RT_{ref}}\left(1 - S_{w_{ref}}\right)$$
$$S_w = \frac{\rho_{w_{ref}} S_{w_{ref}} + \frac{P_{sat_{ref}} M_w}{RT_{ref}}\left(1 - S_{w_{ref}}\right) - \frac{P_{sat} M_w}{RT}}{\rho_w - \frac{P_{sat} M_w}{RT}} \tag{4.9}$$

4.1.4 Possible limit states in the closed system

The development of the liquid water saturation level has a lower and upper limit reflecting the dried or saturated state of the system respectively (Hettema, et al., 1998; Clement, 2010). The limit states are defined using Eq. (4.9) and the critical temperature and pressure.

Lower limit state - superheated vapour

This state corresponds to the evaporation process transforming the available liquid water into vapour. The maximum reference saturation level with liquid water that reaches a dried state is defined by the critical temperature and pressure based on Eq. (4.2) (Hettema, 1996). Lower reference liquid water saturation levels will result in the formation of a superheated vapour (Moran & Shapiro, 2004; Hettema, 1996):

$$S_w \leq 0 \rightarrow \frac{\rho_{w_{ref}} S_{w_{ref}} + \rho_{gw_{ref}} \left(1 - S_{w_{ref}}\right) - \rho_{gw_{crit}}}{\rho_{w_{crit}} - \rho_{gw_{crit}}} \leq 0$$

$$S_{w_{ref}} \left(\rho_{w_{ref}} - \rho_{gw_{ref}}\right) \leq \rho_{gw_{crit}} - \rho_{gw_{ref}} \tag{4.10}$$

$$S_{w_{ref}} \leq \frac{\rho_{gw_{crit}} - \rho_{gw_{ref}}}{\rho_{w_{ref}} - \rho_{gw_{ref}}} = \frac{\frac{P_{crit}}{T_{crit}} - \frac{P_{sat_{ref}}}{T_{ref}}}{\rho_{w_{ref}} \frac{R}{M_w} - \frac{P_{sat_{ref}}}{T_{ref}}} = 0.07$$

Subsequently the gas pressure continuously develops with the contribution of the dry air phase defined by the reference state through Eq. (4.6). However, the partial pressure of the water vapour phase is determined by the temperature and the saturated vapour pressure at which the system reached a dried state, marking the completion of the evaporation process:

$$\left(\frac{m_{gw}}{nV_{tot}}\right)_T = \left(\frac{m_{gw}}{nV_{tot}}\right)_{dry} \neq \left(\frac{m_{gw}}{nV_{tot}}\right)_{ref}$$

$$\rho_{gw} \left(1 - \overset{=0}{\overbrace{\widetilde{S_w}}}\right) = \rho_{gw_{dry}} \left(1 - \overset{=0}{\overbrace{\widetilde{S_w}}}\right) \tag{4.11}$$

Using Eq. (4.2) the water vapour pressure is defined as linearly dependent on the temperature:

$$\frac{P_{gw} M_w}{RT} = \frac{P_{sat_{dry}} M_w}{RT_{dry}}$$

$$P_{gw} = P_{sat_{dry}} \frac{T}{T_{dry}} \tag{4.12}$$

Upper limit state - compressed liquid

This corresponds to the evaporation process reaching a state of saturation with liquid water with no pore volume available for the gas phase. The minimal reference saturation level with liquid water that reaches the saturated state is again based on the critical point (Hettema, 1996). Higher reference liquid water saturation levels will result in the formation of a compressed liquid (Moran & Shapiro, 2004; Hettema, 1996):

$$S_w \geq 1 \rightarrow \frac{\rho_{w_{ref}} S_{w_{ref}} + \rho_{gw_{ref}} \left(1 - S_{w_{ref}}\right) - \rho_{gw_{crit}}}{\rho_{w_{crit}} - \rho_{gw_{crit}}} \geq 1$$

$$S_{w_{ref}} \left(\rho_{w_{ref}} - \rho_{gw_{ref}}\right) \geq \rho_{w_{crit}} - \rho_{gw_{ref}} \tag{4.13}$$

$$S_{w_{ref}} \geq \frac{\rho_{w_{crit}} - \rho_{gw_{ref}}}{\rho_{w_{ref}} - \rho_{gw_{ref}}} = \frac{\rho_{w_{crit}} - \frac{P_{sat_{ref}} M_w}{RT_{ref}}}{\rho_{w_{ref}} - \frac{P_{sat_{ref}} M_w}{RT_{ref}}} = 0.41$$

The pressure development is under these circumstances dependent on the saturated water vapour phase and the reference state of the dry air phase through Eq. (4.6).

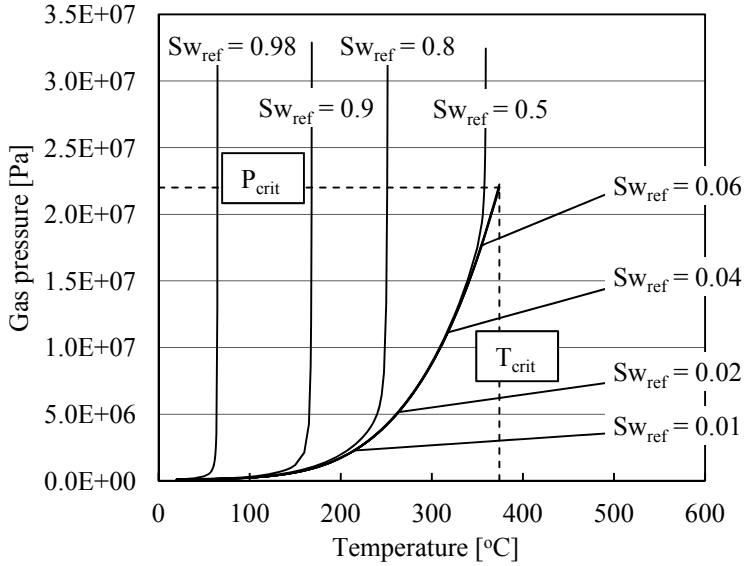

Fig. 4.3 *Development of the gas pressure with temperature in the closed system is based on the reference saturation level with liquid water. Three different states can develop, a superheated vapour (I), a compressed liquid (III) or the partially saturated state remains until the critical temperature is reached (II).*

4.1.5 Gas pressure development based on the reference saturation level

The gas pressure is determined for a closed system characterised by a constant volume with an infinite stiffness and strength. This allows to obtain gas pressures far surpassing the strength of the material. The results in this section are therefore only used to characterise the basic behaviour of a multi-phase system with exchange between phases. Important is to consider that the actual gas pressure is based on an open system including phase transport.

The development of the gas pressure is a function of the temperature and the reference saturation level. In the closed system three possible states can develop as seen in Fig. 4.3:

- A superheated vapour, defined as the first state, is reached in the closed system for relatively low reference liquid water saturation levels. All the liquid water is evaporated to maintain the saturated vapour state. The closed system is dried and the superheated vapour is characterised by a linear development of the gas pressure.

- For intermediate reference liquid water saturation levels, ranging from 0.07 to 0.41, the closed system remains partially saturated, defining the second state.

- A third state is formed for high reference saturation levels, characterised by a compressed liquid. The gas pressure rapidly increases based on the closed system reaching a state of almost full saturation with liquid water. The dry air phase is forced or trapped in a relatively small volume, causing this partial pressure to rapidly increase towards infinity as illustrated by Fig. 4.4. The water vapour phase remains saturated until complete saturation by the liquid phase.

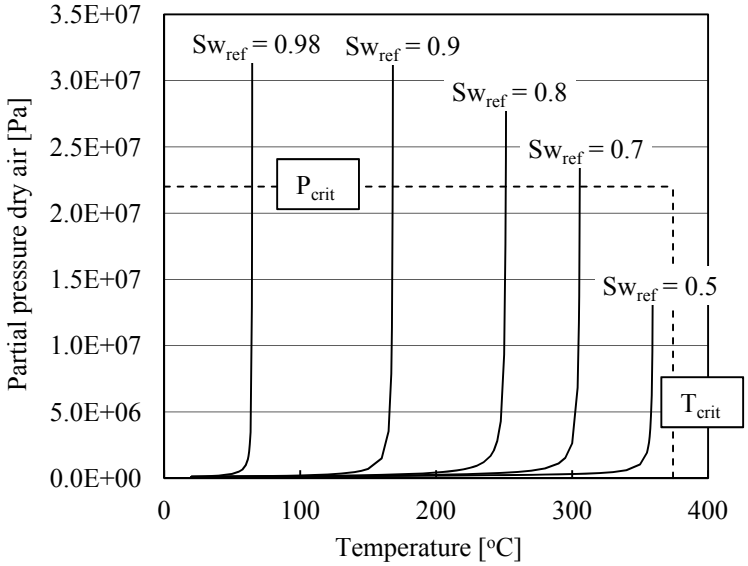

Fig. 4.4 *At reference saturation levels higher than 0.41 a compressed liquid is formed, causing the partial dry air pressure to rapidly increase.*

The development of the saturation level with liquid water is determined by the reference value and the density of liquid water as illustrated by Fig. 4.5. At low reference saturation levels, between 0.1 and 0.2, the influence of the non-linear density of liquid water becomes apparent. The forced drying process is assumed to maintain the saturated water vapour state in the gas phase. However, this is seen not to reduce the saturation level especially at higher reference values. For these saturation levels the compressed liquid is formed and the coinciding rapid increase in gas pressure is determined. The pressure of the closed system initially at a reference level of 0.4 is indicated to surpass the critical pressure, but not reach a state of full saturation as previously determined.

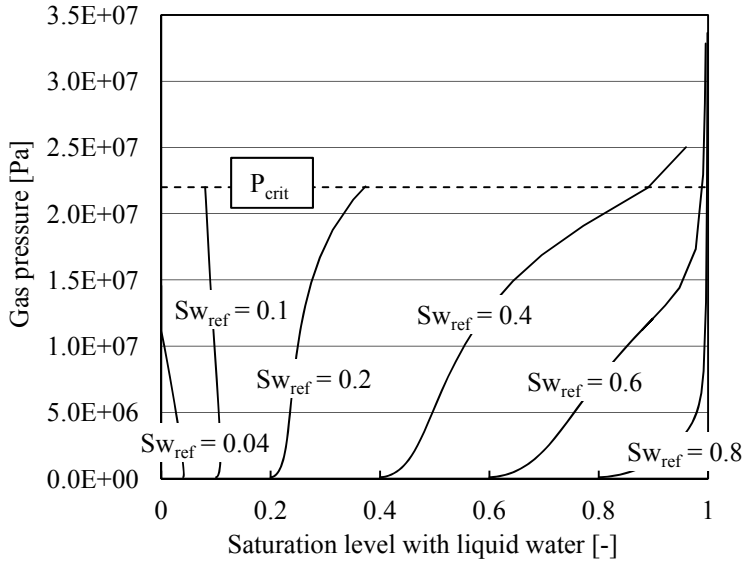

Fig. 4.5 *Development of the saturation level in the system based on evaporation which at reference values lower than 0.07 results in a dried state. At higher values the saturation level increases, caused by the assumed restricted transport.*

4.1.6 Conclusions with respect to the closed system

From the closed system the following conclusions and remarks can be drawn:

- The closed system is based on a constant, infinitely stiff and strong volume allowing the gas pressure to surpass the tensile strength of concrete. This simplified model only allows to obtain insight into the reasons for gas pressure build-up (Hettema, 1996).

- The gas phase is a compressible mixture based on the dry air and the assumed saturated water vapour phases. Both gas phases are characterised by the ideal gas law and define through partial pressures the overall gas pressure (Moran & Shapiro, 2004).

- Development of the gas pressure is governed by the non-linear temperature-dependent saturated water vapour pressure (Kotz, et al., 2009). The assumption of a closed system causes the gas pressure to always increase with temperature. Only at reference liquid water saturation levels lower than 0.07 the system is dried before the critical temperature is reached, forming a superheated vapour.

- The influence of the dry air phase only becomes apparent at reference liquid water saturation levels higher than 0.41. The reference mass of dry air, initially present in the system, becomes trapped by almost full saturation with liquid water, forming a compressed liquid.

- The non-linear density causes the liquid water saturation to increase which is indicated to already occur at relatively low levels. Of importance is also the critical temperature after which liquid water as a distinct phase no longer exists (Whitten, et al., 2010).

4.2 Gas pressure based on crack opening

The influence of gas pressures on the spalling process and in general for a porous material are insufficiently understood. The pore pressure is believed to influence the strength of the concrete (Felicetti, et al., 2012) by formation of micro cracks. However, the question remains if the gas pressure is able to contribute to the initiation and opening of cracks. The possible influence on crack initiation is related to mechanics and discussed in the next chapter. In this section the gas pressure development during crack opening is assessed.

4.2.1 Basic assumptions governing mass conservation of the gas phase

With respect to the conservation of mass the following assumptions are defined:

1. The relationship between gas pressure development and opening of the crack is defined for a closed system. This implies that no flow of gas across the boundaries occurs, attributed to the low permeability of concrete (Bažant, 1997).

2. Opening of the crack increases the volume of the system. This is one of the key aspects considered. However, the presented relationships are simplified and do not allow for influence of the gas pressure itself on the volume of the system.

3. The system is assumed to define the state upon crack opening. The total mass of water vapour present in the fractured pores is instantaneously distributed across the volume, resulting in a drop in gas pressure across the crack width (Bažant, 1997).

4.2.2 Conservation of mass governing the gas phase

The gas phase is mainly based on water vapour, assumed saturated upon opening of the crack, and liquid water is assumed not present to simplify the relationship. The volume of the system is defined by the surface area of the crack being assumed plane in depth direction. Upon crack opening, the volume is based on the porosity and the average pore diameter assumed constant in depth direction. This determines the mass of water vapour being distributed during opening, governed by the initial pore volume and the crack width. The temperature is assumed constant to characterise the instantaneous development. The following mass balance governs the gas pressure development:

$$\begin{gathered}\left(m_{gw}\right)_{cr} = \left(m_{gw}\right)_{pore} \rightarrow \rho_{gw} V_{cr} = \rho_{gw_{sat}} V_{pore} \\ \rho_{gw}\left(nD_{cap} + w_{cr}\right)A_{cr} = \rho_{gw_{sat}} nD_{cap} A_{cr} \\ \frac{P_{gw} M_w}{RT_{cr}}\left(nD_{cap} + w_{cr}\right) = \frac{P_{sat_{cr}} M_w}{RT_{cr}} nD_{cap} \rightarrow P_{gw} = P_{sat_{cr}} \frac{nD_{cap}}{\left(nD_{cap} + w_{cr}\right)}\end{gathered} \tag{4.14}$$

where

V_{cr}	[m^3]	Fracture volume
A_{cr}	[m^2]	Fracture surface area
D_{cap}	[m]	Average capillary pore diameter
w_{cr}	[m]	Crack width assumed constant across the fracture surface

This relationship indicates the rapid reduction of the water vapour pressure during opening based on the scale difference between the capillary pores and the crack width. The overall gas pressure is based on the partial pressures of the water vapour and dry air phases. The latter is governed by the surrounding environment and assumed to remain at atmospheric conditions:

$$P_g = P_{ga} + P_{gw} \approx P_{atm} + P_{sat_{cr}} \frac{nD_{cap}}{\left(nD_{cap} + w_{cr}\right)} \tag{4.15}$$

4.2.3 Gas pressure development based on crack opening

This previous relationship is used to determine the possibility for the gas pressure to be sustained during crack opening. Two scenarios are examined which differ by initial capillary pore space defined through the porosity and average pore diameter as provided in Table 4.1.

Crack opening scenarios		
Calculation	**4.1A**	**4.1B**
Porosity	0.1	0.2
Average diameter capillary pores	1.0 μm	3.0 μm

Table 4.1 *Gas pressure development during crack opening in a closed system based on the initial capillary pore space.*

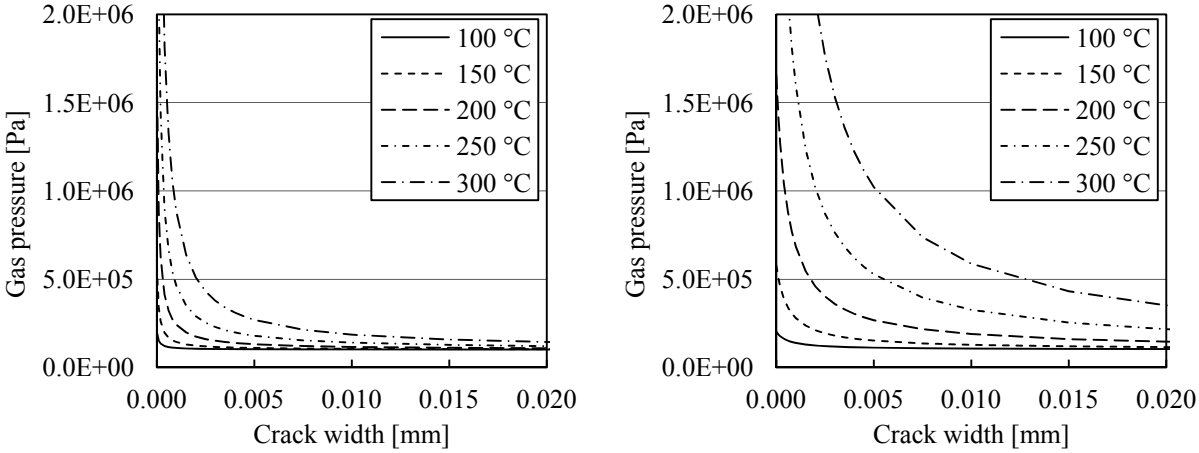

Fig. 4.6 *Opening of the crack causes the gas pressure to almost instantaneously reduce to atmospheric conditions. Pressures remain limited by increasing the capillary pore diameter from 1 μm (left) to 3 μm (right).*

The scale difference between the pore sizes and the crack width causes the gas pressure to rapidly reduce during crack opening. Only at the onset of crack opening and at temperatures higher than 200 ^{o}C does the gas pressure remain above atmospheric conditions. Examination of Fig. 4.6 also indicates an influence by the initial pore space. However, this simplified model indicates that the possibility for the gas pressure to be sustained during crack opening seems unlikely (Bažant, 1997). This would require additional vapour to be transported into the crack which due to the relatively low permeability of concrete and the sudden nature of initiation and opening seems less likely (Bažant, 1997). In this respect opening of the crack is probably attributed to the thermal stresses (Bažant, 1997). However, the possibility for the gas pressure to contribute to the initiation of the crack is still possible, considering the closed nature of the microstructure. The resultant internal loading is discussed in the next chapter.

4.3 Definition of an open system characterised by a continuum

The main restriction of the closed system is that it neglects the ability of transport across the material based on for instance the gradient of the temperature or pressure. This is generally not valid for a porous material and is addressed through definition of an open system, commonly characterised by a representative elementary volume (REV) (Hassanizadeh & Gray, 1979a; Bachmat & Bear, 1986). Across this continuum properties are conserved governed by a general conservation equation reflecting time-dependent development, transport and sources (Hassanizadeh & Gray, 1979b; Bear & Bachmat, 1986). This PDE is subsequently used to define the conservation of thermal energy and mass of the water phases as presented in the remainder of this chapter.

4.3.1 Basic assumptions for the open system

In comparison with the closed system the following assumptions are stated:

1. The system is again assumed to have a constant volume and an infinite stiffness and strength. This implies that the continuum cannot deform and only the material properties influence the behaviour.

2. The open system is characterised by allowing for transport or fluxes across the boundaries. Additional contributions to the conserved property are possible by sources or sinks defined across the continuum.

3. The general conservation equation is stated for a REV, characterised by an averaged porous material description (Hassanizadeh & Gray, 1979a; Bachmat & Bear, 1986). This defines the local material as homogeneous, neglecting variations.

4.3.2 Schematisation of an open system represented by the REV

The open system is represented as a REV across which a property is averaged characterised as a density (Hassanizadeh & Gray, 1979a; Bachmat & Bear, 1986). The property can for instance be the stored thermal energy or the mass of a phase defined relative to the total volume. The REV is chosen to obtain a representative behaviour while remaining sufficiently small (Hassanizadeh & Gray, 1979a; Bachmat & Bear, 1986). The obtained continuum definition is based in the 3D Euclidean space as indicated in Fig. 4.7 (van Kan, et al., 2008). Important is the sign convention regarding the principal axes and the integrals with respect to the boundary and across the domain.

The continuum description can be based on several approaches which are subdivided into the following options:

- The description of the movement of individual particles referred to as an Lagrangian approach (Bear, 1972/1988).

- The more commonly used Eulerian approach defining a fixed field across which transport of a property occurs (Bear, 1972/1988).

The Eulerian description of the general conservation across the REV is determined by the time derivative, the flow and possible sources of the averaged property (Bear, 1972/1988). Transport or flow is governed by the flux across the boundaries, defined positive by the unit outward normal vector, causing a reduction in the property. The flux itself is characterised by the averaged property and the velocity (Bear, 1972/1988). Sources are defined across the continuum as an addition.

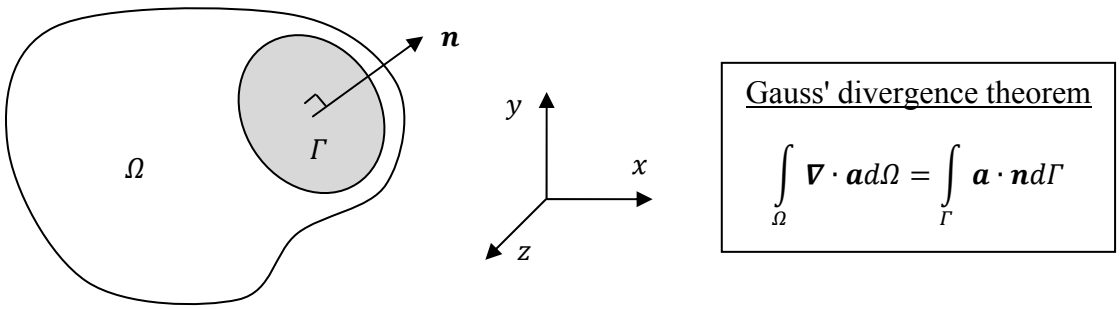

Fig. 4.7 *Schematic representation of a continuum defined in the 3D Euclidean space* ($\mathbb{R}^3$). *The volume or domain* (Ω), *the boundary edge* (Γ) *and the unit outward normal vector* ($\boldsymbol{n}$) *govern the description. Gauss's divergence theorem is commonly used to relate domain and boundary integrals of a vector* ($\boldsymbol{a}$) (van Kan, et al., 2008).

The resultant conservation equation takes the following form:

$$\int_{\Omega} \frac{\partial \overline{\rho_\alpha}}{\partial t} d\Omega = -\int_{\Gamma} \boldsymbol{q_\alpha} \cdot \boldsymbol{n} d\Gamma + \int_{\Omega} H_\alpha d\Omega \tag{4.16}$$

with

$\boldsymbol{q_\alpha} = \overline{\rho_\alpha} \boldsymbol{v_\alpha}$

$$\boldsymbol{q_\alpha} = \begin{bmatrix} q_{\alpha_x} \\ q_{\alpha_y} \\ q_{\alpha_z} \end{bmatrix} \qquad \boldsymbol{v_\alpha} = \begin{bmatrix} v_{\alpha_x} \\ v_{\alpha_y} \\ v_{\alpha_z} \end{bmatrix} \qquad \boldsymbol{n} = \begin{bmatrix} n_x \\ n_y \\ n_z \end{bmatrix}$$

where

$\cdots_\alpha$		Indication for the property conserved
t	[s]	Time or duration of fire exposure
$\overline{\rho_\alpha}$	[var./m^3]	Density of the property averaged across the REV
H_α	[var./m^3]	Source of the property
$\boldsymbol{q_\alpha}$	[var./m^{2}s]	Flux vector of the property
$\boldsymbol{v_\alpha}$	[m/s]	Velocity vector driving the flux
$\boldsymbol{n}$	[-]	Unit outward normal vector

The boundary or surface integral of the flux is redefined across the domain using Gauss' divergence theorem stated in Fig. 4.7 (van Kan, et al., 2008):

$$\int_{\Omega} \frac{\partial \overline{\rho_\alpha}}{\partial t} d\Omega + \int_{\Gamma} \boldsymbol{q_\alpha} \cdot \boldsymbol{n} d\Gamma = \int_{\Omega} H_\alpha d\Omega$$

$$\int_{\Omega} \frac{\partial \overline{\rho_\alpha}}{\partial t} + \boldsymbol{\nabla} \cdot \boldsymbol{q_\alpha} d\Omega = \int_{\Omega} H_\alpha d\Omega \tag{4.17}$$

Eq (4.17) must also hold for all sub-domains allowing the removal of the integrals leading to the general conservation equation while introducing the phase flux (Bear, 1972/1988):

$$\frac{\partial \overline{\rho_\alpha}}{\partial t} + \boldsymbol{\nabla} \cdot \boldsymbol{q_\alpha} = H_\alpha$$

$$\frac{\partial \overline{\rho_\alpha}}{\partial t} + \boldsymbol{\nabla} \cdot (\overline{\rho_\alpha} \boldsymbol{v_\alpha}) = H_\alpha \tag{4.18}$$

This PDE is extended by the definition of boundary conditions which can take several forms:

- Prescribed variables are commonly referred to as Dirichlet or essential boundary conditions (van Kan, et al., 2008). The variables are explicitly imposed on the domain which reduces the number of unknowns.

- Alternatively, Neumann of natural boundary conditions can be imposed (van Kan, et al., 2008). These describe the gradient at the boundary allowing for interaction between the variables and surrounding environment.

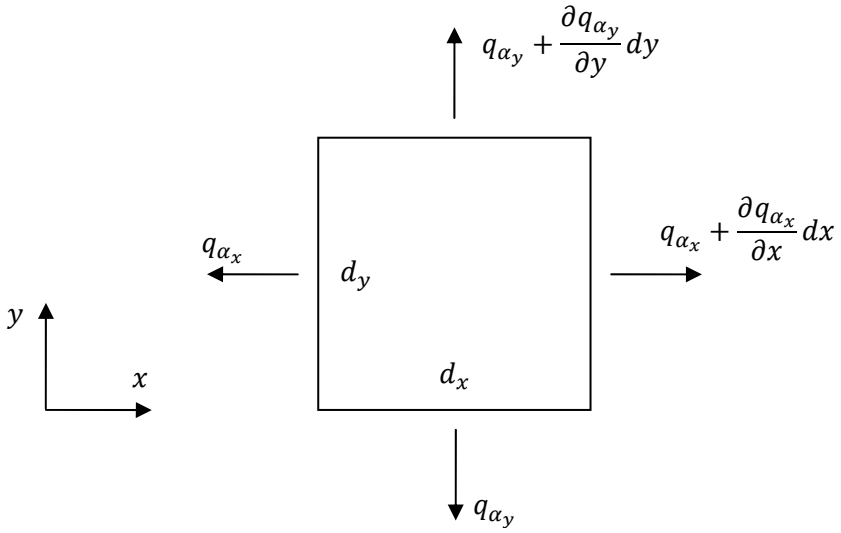

Fig. 4.8 *Schematic representation of the horizontal and vertical fluxes in the continuum defined in the 2D Euclidean space* ($\mathbb{R}^2$) *governing the time-dependent development of the conserved property.*

For a 2D continuum, the outward horizontal and vertical resultant fluxes are based on equilibrium considerations as shown in Fig. 4.8. Both fluxes are defined to act parallel to the principal axes based on a first order approximation. Fluxes are not defined parallel to the edges of the continuum since these do not contribute to conservation of the property (van Kan, et al., 2008). The resultant flux contribution becomes expressed by:

$$\frac{\partial q_{\alpha_x}}{\partial x} + \frac{\partial q_{\alpha_y}}{\partial y} = \boldsymbol{\nabla} \cdot \boldsymbol{q_\alpha} \tag{4.19}$$

4.4 Progress of temperature into the cross-section

During fire exposure of a cross-section commonly a temperature gradient develops based on the relatively low thermal conductivity of concrete (Kordina, 1963). This is governed by the conservation of thermal energy and leads to the basic Fourier differential equation found in literature (Kordina, et al., 1975; van Breugel, et al., 1998).

4.4.1 Conservation of thermal energy

The conservation of thermal energy is based on the following assumption:

1. Thermal energy is transported by heat flux, characterised by the thermal conductivity and the temperature gradient as stated by Fourier's law (Bear, 1972/1988). This neglects convection of energy by flow of heated gases and liquids (Bear, 1972/1988).

The influence of the surrounding environment is included through:

2. Exchange as governed by conservation of thermal energy along the boundary of the domain. Convection of heat is assumed to be the main process and is characterised by a Neumann boundary condition (Kordina, et al., 1975). A thermal energy contribution by radiation is not considered in this simplified approach (Kordina, et al., 1975; Eurocode 1, 2011a), improving stability especially for the models to be presented.

Conservation of energy

The property conserved across the REV is the thermal energy density based on the density, the specific heat capacity and the temperature of the material (Bear, 1972/1988). The material is assumed to be homogeneous allowing to use the thermal properties:

$$\overline{\rho_T} = \rho C T \tag{4.20}$$

where

$\overline{\rho_T}$	[J/m^3]	Thermal energy density averaged across the REV
ρ	[kg/m^3]	Density of the material
C	[J/kgK]	Specific heat capacity of the material

The PDE governing the conservation of thermal energy is obtained by inserting Eq. (4.20) into Eq. (4.18). The energy flux or heat flux is defined by Fourier's law and governed by the thermal conductivity and based on the temperature gradient (Bear, 1972/1988):

$$\frac{\partial(\rho C T)}{\partial t} + \boldsymbol{\nabla} \cdot \boldsymbol{q_T} = 0 \tag{4.21}$$

with

$$\boldsymbol{q_T} = -k\boldsymbol{\nabla} T$$

where

k	[W/mK]	Thermal conductivity of the material
$\boldsymbol{q_T}$	[J/m^{2}s]	Heat flux vector of thermal energy

The density and the specific heat capacity are assumed constant according to (Eurocode 2, 2011b). However, the thermal conductivity varies with temperature (Eurocode 2, 2011b) as is reflected by expanding the term governing the heat flux. The first contribution is governed by the gradient of both the material property and the temperature. The Laplacian operator with respect to the temperature (van Kan, et al., 2008) defines the second contribution while considering a constant thermal conductivity. The resulting PDE describes the conservation of energy based on the temperature as variable (Bear, 1972/1988):

$$\begin{aligned} \rho C \frac{\partial T}{\partial t} - (\boldsymbol{\nabla} k \cdot \boldsymbol{\nabla} T + k \boldsymbol{\nabla} \cdot \boldsymbol{\nabla} T) = 0 \\ \rho C \frac{\partial T}{\partial t} - \boldsymbol{\nabla} k \cdot \boldsymbol{\nabla} T - k \boldsymbol{\Delta} T = 0 \end{aligned} \tag{4.22}$$

This PDE is simplified by assuming a 1D behaviour perpendicular to the heated surface of the cross-section (Kordina, et al., 1975; van Breugel, et al., 1998):

$$\frac{\partial T}{\partial t} = \frac{1}{\rho C}\left(\frac{\partial k}{\partial x}\frac{\partial T}{\partial x} + k\frac{\partial^2 T}{\partial x^2}\right) \tag{4.23}$$

Boundary condition

The definition is completed by the statement of the Neumann boundary condition (Tenchev, et al., 2001; Gawin, et al., 2003). This relationship allows to impose the time-dependent temperature curve reflecting fire exposure (Eurocode 1, 2011a) or the reference ambient conditions. For a positive outward orientated heat flux the following relationship is defined:

$$\begin{aligned} \boldsymbol{q_T}|_{\Gamma_A} &= \alpha_A(T - T_\infty) \\ -k\frac{\partial T}{\partial x}\Big|_{\Gamma_A} &= \alpha_A(T - T_\infty) \\ \frac{\partial T}{\partial x}\Big|_{\Gamma_A} &= -\frac{\alpha_A}{k}(T - T_\infty) \end{aligned} \tag{4.24}$$

where

α_A	[W/m^{2}K]	Convective heat transfer coefficient of the material
T_∞	[K]	Temperature defined at distance from the surface

4.4.2 Numerical solution by FDM including boundary conditions

The 1D cross-section is divided into equal elements with points located at the centres. The time derivative is approximated using an explicit forward Euler integration scheme being conditionally stable (Vermolen, 2005). The first and second order spatial derivatives are approximated by Taylor expansion or using the central difference scheme (van Kan, et al., 2008). Both central difference schemes are second order approximations and are defined as follows (van Kan, et al., 2008):

$$\begin{aligned} \frac{\partial T}{\partial t} &\approx \frac{{T_i}^{t+1} - {T_i}^t}{\Delta t} \\ \frac{\partial T}{\partial x} &\approx \frac{{T_{i+1}}^t - {T_{i-1}}^t}{2\Delta x} \\ \frac{\partial^2 T}{\partial x^2} = \frac{\partial}{\partial x}\left(\frac{\partial T}{\partial x}\right) &\approx \frac{\left(\frac{{T_{i+1}}^t - {T_i}^t}{\Delta x}\right) - \left(\frac{{T_i}^t - {T_{i-1}}^t}{\Delta x}\right)}{\Delta x} = \frac{{T_{i+1}}^t - 2{T_i}^t + {T_{i-1}}^t}{\Delta x^2} \end{aligned} \tag{4.25}$$

where

$\ldots^t$		Indication for the incremental time step
$\cdots_i$		Indication for the node number
Δt	[s]	Incremental time step size
Δx	[m]	Constant element size distributed across the width

The material gradient is also approximated using the central difference scheme:

$$\frac{\partial k}{\partial x} \approx \frac{{k_{i+1}}^t - {k_{i-1}}^t}{2\Delta x} \tag{4.26}$$

Material (homogeneous)	
Strength class	independent
Density	2300 kg/m^3
Specific heat capacity	900 J/kgK

Table 4.2 *Constant material properties used to characterise homogeneous concrete, independent of the strength class* (Eurocode 2, 2011b).

Hence, the numerical approximation is obtained through inserting Eq. (4.25) and Eq. (4.26) into Eq. (4.23) stating the PDE (van Breugel, et al., 1998). After rearranging the following is obtained:

$$T_i^{t+1} = T_i^t + \frac{\Delta t}{\Delta x^2}\frac{1}{\rho C}\left(\left(\left(k_{i+1}^t - k_{i-1}^t\right)\left(\frac{T_{i+1}^t - T_{i-1}^t}{4}\right)\right) + \left(k_i^t\left(T_{i+1}^t - 2T_i^t + T_{i-1}^t\right)\right)\right) \tag{4.27}$$

In addition, the boundary condition requires an approximation based on additional points located outside of the cross-section (Kordina, et al., 1975). The central difference scheme based on these points while using forward Euler time integration leads to:

$$\left.\frac{\partial T}{\partial x}\right|_{\Gamma_A} \approx \frac{T_{i+1}^t - T_{i-1}^t}{2\Delta x} = -\frac{\alpha_A}{k_i^t}\left(T_i^t - T_\infty^t\right)$$
$$\rightarrow T_{i+1}^t = T_{i-1}^t - \frac{2\Delta x \alpha_A}{k_i^t}\left(T_i^t - T_\infty^t\right) \tag{4.28}$$

4.4.3 Temperature development based on various fire scenarios

The development of the temperature gradient is determined for a homogeneous cross-section with a width of 150 mm discretised by elements of 2.5 mm. The assumed constant density and specific heat capacity are stated in Table 4.2 and based on (Eurocode 2, 2011b). However, the thermal conductivity is, as shown in Fig. 4.9, dependent on temperature (Eurocode 2, 2011b). All material properties are independent of the concrete strength class.

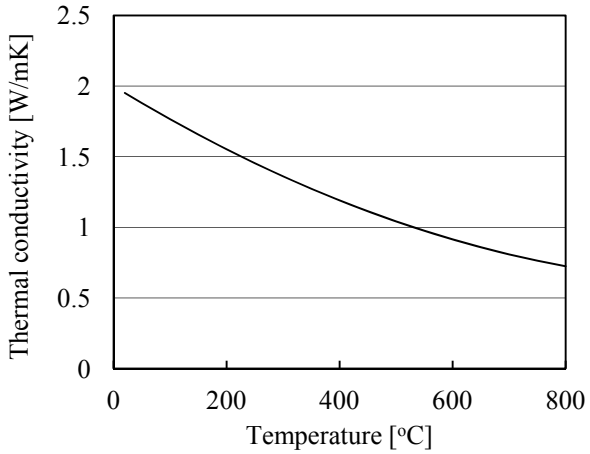

Fig. 4.9 *Development of the thermal conductivity of concrete with temperature according to* (Eurocode 2, 2011b).

Fire scenarios			
Calculation	**4.2A**	**4.2B**	**4.2C**
Reference temperature	20 °C	20 °C	20 °C
Duration	1800 sec	1800 sec	1800 sec
Incremental time step size	2.5 sec	2.5 sec	2.5 sec
Material (homogeneous)			
Strength class	independent	independent	independent
Boundary conditions			
Fire curve	**ISO 834**	**ISO 834**	**HC**
Convective heat transfer coeff.	**25 W/m^{2}K**	**50 W/ m^{2}K**	**50 W/ m^{2}K**

Table 4.3 *Temperature development in the cross-section based on several fire scenarios governed by the design fire curve and the transfer coefficient.*

Single sided fire exposure, at the left edge, is based on the time-dependent temperature development according to two different fire scenarios, the ISO 834 and the HC respectively (Eurocode 1, 2011a). Both fire scenarios are characterised by a significant heating rate as shown in Fig. 4.10. The HC fire curve indicates an air temperature development which, especially in the first minutes, is around 1.5 times faster than the ISO 834 scenario. However, it should be noted that these heating rates are not directly prescribed to the cross-section. Interaction at the surface is defined by the Neumann boundary condition based on the convective heat transfer coefficient as indicated in Table 4.3. It is important to consider also that both fire scenarios are characterised by a substantial reduction in air temperature development after the first minutes of exposure.

The resultant development of the temperature gradient in the cross-section is shown in Fig. 4.11. The differences in imposed thermal energy directly become apparent. The surface temperature of the cross-section exposed to the HC fire scenario experiences a rapid increase. This is mostly caused by the time-dependent development of the air temperature as defined by the fire curve. However, the higher convective heat transfer coefficient, as stated in (Eurocode 1, 2011a), extends the thermal loading.

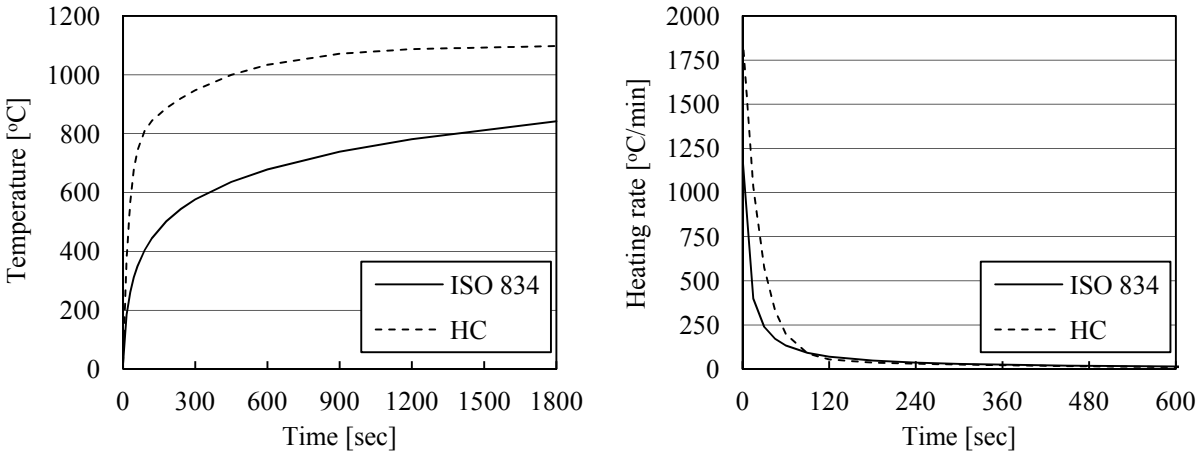

Fig. 4.10 *The scenarios used are based on exposure according to a standard fire (ISO 834) or a hydro carbon fire (HC). Development of the air temperature at the surface of the cross-section characterises the thermal exposure* (Eurocode 1, 2011a).

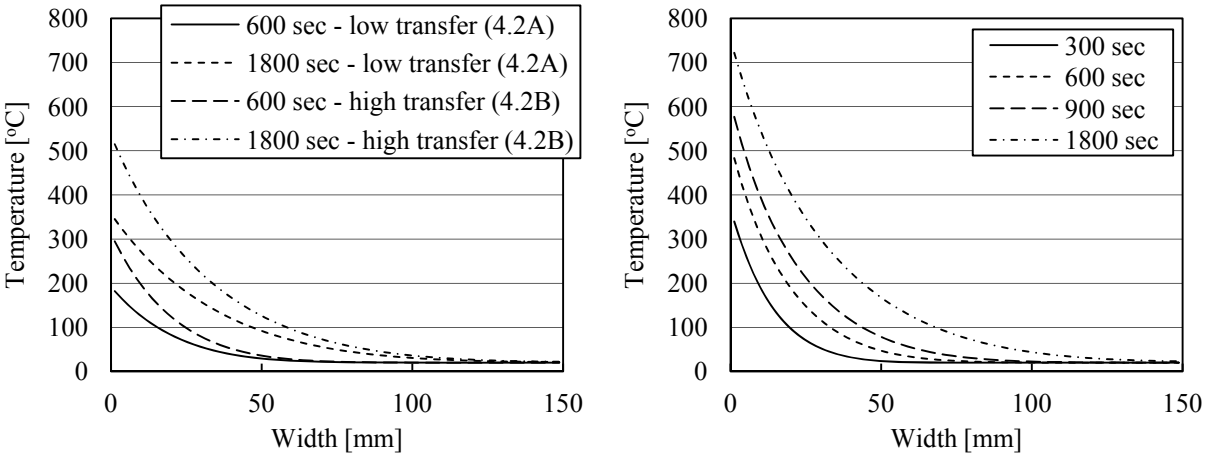

Fig. 4.11 *Exposure according to the HC fire scenario (right) causes the surface temperature to rapidly exceed 400 °C. The ISO 834 fire scenario (left) leads to a more moderate development, reflecting the influence of the transfer coefficient.*

The relatively low thermal conductivity of concrete governs the steep temperature gradient (Kordina, 1963) which is again especially pronounced for the HC fire scenario. Large temperature differences develop between the surrounding environment and the cross-section. For instance, after 15 min the air temperature, according to the HC fire curve, exceeds 1000 °C. However, at the concrete surface the temperature is already halved, reaching around 575 °C. Into the cross-section, at a depth of 45 mm, the temperature has dropped below 100 °C.

4.5 Drying of the cross-section at constant temperature

The temperature-dependent development of the gas pressure in a porous material leads to transport of mainly water vapour based on the relatively low permeability of concrete (Harmanthy, 1965). Moreover, the assumed saturated state of the water vapour phase is also commonly not present. Drying of a porous material is characterised by the capillary pressure and the desorption isotherm (Bear, 1972/1988). This behaviour is both characterised by the conservation of mass defined for the liquid and vapour phases of water.

4.5.1 Basic assumptions for conservation of mass governing the water phases

Several assumptions are stated to characterise the drying behaviour of the continuum:

1. The temperature across the material is assumed constant. This implies that the instantaneous evaporation process does not affect the temperature and thermodynamic equilibrium is present (Hassanizadeh & Gray, 1979b; Bear & Bachmat, 1986).

2. Equilibrium between the water phases is characterised by the desorption isotherm based on the capillary pressure (Bear, 1972/1988). Liquid water is assumed incompressible and water vapour is defined as a perfect gas (Moran & Shapiro, 2004).

3. The dry air phase is neglected based on the limited influence since no exchange process or source is present. The pore or gas pressure is only defined by the partially saturated water vapour phase.

4. The mass fluxes governing the water phases are pressure driven according to Darcy's law (Bear, 1972/1988). The flow is assumed characterised as laminar and viscous under isotropic or direction-independent conditions (Bear, 1972/1988). Transport by diffusion, driven by concentration gradients and governed by Fick's law (Bear, 1972/1988), is not included since this process develops gradually in time.

The surrounding environment influences the continuum by:

5. Drainage as governed by stating mass conservation of the water phases along the boundary of the domain (Tenchev, et al., 2001; Gawin, et al., 2003). The main process is assumed to be convection of mass also characterised by a Neumann boundary condition (Tenchev, et al., 2001; Gawin, et al., 2003).

4.5.2 Conservation of mass governing the water phases

In the pores of the REV the total mass of water is defined by the temperature-dependent equilibrium between the liquid and vapour phases (Tenchev, et al., 2001; Gawin, et al., 2003). Each phase is characterised by a conservation equation based on the averaged density.

Conservation of water vapour

The gas pressure is based, contrary to the closed system, on partially saturated water vapour (Bear, 1972/1988; Pel & Huinink, 2007) neglecting the dry air phase. Under these conditions is the vapour phase characterised by the RH defined through the Kelvin equation based on the temperature and the capillary pressure as shown in the left graph of Fig. 4.13 (Pel & Huinink, 2007). This relationship states the pressure difference across the concave meniscus as present in a porous material compared to a flat liquid water surface (Pel & Huinink, 2007):

$$P_g = \overset{\approx 0}{\overbrace{P_{ga}}} + P_{gw} = RHP_{sat} \tag{4.29}$$

with

$$RH = e^{\frac{-P_c M_w}{\rho_w RT}}$$

The averaged water vapour density is determined by the mass defined relative to the total volume using parts of Eq. (4.7) and Eq. (4.2) (Tenchev, et al., 2001; Gawin, et al., 2003):

$$\overline{\rho_{gw}} = \frac{m_{gw}}{V_{tot}} = n(1 - S_w)\rho_{gw} = n(1 - S_w)\frac{RHP_{sat}M_w}{RT} \tag{4.30}$$

where

$\overline{\rho_{gw}}, \rho_{gw}$	[kg/m^3]	Mass density of the water vapour phase (averaged) across the REV
m_{gw}	[m^3]	Mass of the water vapour phase across the REV

The assumed viscous mass flux of the vapour phase is based on the density and the relatively low velocity in which the latter is characterised by a laminar, parabolic distribution described by Darcy's law (Bear, 1972/1988). This distribution is characterised by shear stresses based on the dynamic viscosity (Bear, 1972/1988) shown in Fig. 4.12 (Gawin, et al., 1999). The material is considered isotropic, or independent of direction (Bear, 1972/1988), while also neglecting gravitational effects by assuming an initial state of equilibrium.

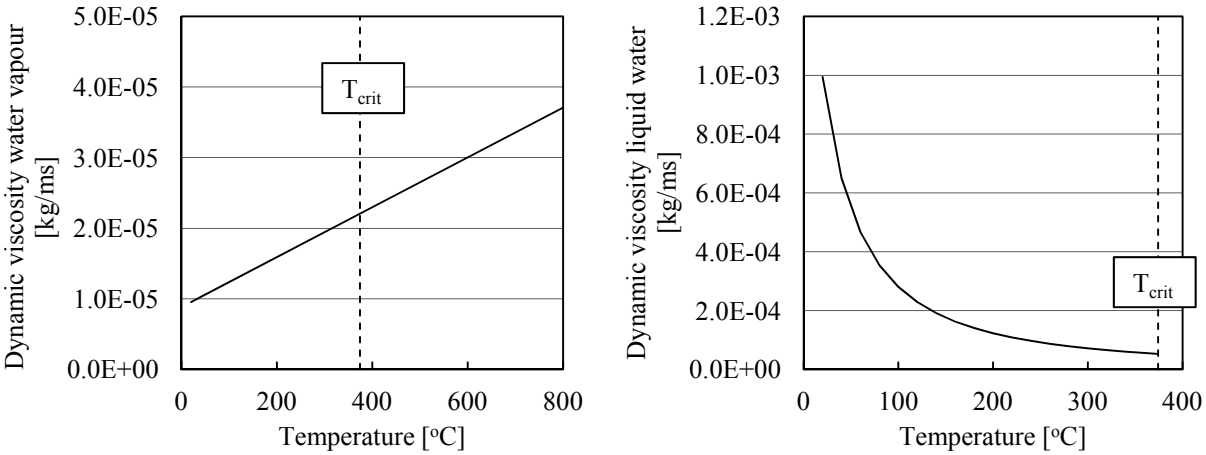

Fig. 4.12 *Differences in velocity of the vapour mass flux (left) compared to the liquid mass flux (right) are characterised by the dynamic viscosity* (Gawin, et al., 1999).

The mass flux is characterised by the permeability and the gas or in this case water vapour pressure gradient. The partially saturated state affects the flow of vapour as reflected by the relative permeability dependent on the liquid water saturation level (Couture, et al., 1996; Bear, 1972/1988). The slip phenomenon or Klinkenberg effect governing the faster flow at relatively low pressures is not included (Bear, 1972/1988). Conservation of the water vapour phase is thus defined by Eq. (4.18) with the source term representing addition through evaporation:

$$\frac{\partial\left(n(1-S_w)\rho_{gw}\right)}{\partial t} + \boldsymbol{\nabla}\cdot\boldsymbol{q_{gw}} = \frac{\partial\overline{\rho_{vap}}}{\partial t} \tag{4.31}$$

with

$$\rho_{gw} = \frac{RHP_{sat}M_w}{RT}$$

$$\boldsymbol{q_{gw}} = \overline{\rho_{gw}}\boldsymbol{v_{gw}} = -n(1-S_w)\rho_{gw}\left(\frac{K_{rel_g}K}{\mu_g}\boldsymbol{\nabla}P_{gw}\right)$$

where

$\overline{\rho_{vap}}$	[kg/m^3]	Mass density of water vapour produced by evaporation in the REV
K_{rel_g}	[-]	Relative permeability of the gas phase based on the saturation level
K	[m^2]	Permeability of the material
μ_g	[kg/ms]	Dynamic viscosity of the gas phase
$\boldsymbol{q_{gw}}$	[kg/m^{2}s]	Mass flux vector of the water vapour phase
$\boldsymbol{v_{gw}}$	[m/s]	Velocity vector driving the mass flux

Conservation of liquid water

The incompressible liquid water phase is governed by the capillary pressure (Bear, 1972/1988; Pel & Huinink, 2007). Especially at low saturation levels the coinciding relatively high capillary pressure defines the liquid water pressure as negative (Bear, 1972/1988; Pel &

Huinink, 2007). The liquid water phase tends to be sucked into the material, referred to as capillary rise, starting with the smallest gel pores (Bear, 1972/1988; Pel & Huinink, 2007):

$$P_c = P_g - P_w = P_{gw} - P_w$$
$$\rightarrow P_w = P_{gw} - P_c \tag{4.32}$$

The averaged liquid water density is also defined by the mass relative to the total volume (Tenchev, et al., 2001; Gawin, et al., 2003):

$$\overline{\rho_w} = \frac{m_w}{V_{tot}} = nS_w\rho_w \tag{4.33}$$

where

$\overline{\rho_w}$	[kg/m^3]	Mass density of the liquid water phase averaged across the REV
m_w	[m^3]	Mass of the liquid water phase across the REV

In addition, the mass flux of liquid water is also characterised by Darcy's law (Bear, 1972/1988) using similar considerations as for the vapour phase. The influence of the evaporation process is included by the removal of liquid water which combined leads to:

$$\frac{\partial(nS_w\rho_w)}{\partial t} + \boldsymbol{\nabla}\cdot\boldsymbol{q_w} = -\frac{\partial\overline{\rho_{vap}}}{\partial t} \tag{4.34}$$

with

$$\boldsymbol{q_w} = \overline{\rho_w}\boldsymbol{v_w} = -nS_w\rho_w\left(\frac{K_{rel_w}K}{\mu_w}\boldsymbol{\nabla}P_w\right)$$

where

K_{rel_w}	[-]	Relative permeability of the liquid phase based on the saturation
μ_w	[kg/ms]	Dynamic viscosity of the liquid phase
$\boldsymbol{q_w}$	[kg/m^{2}s]	Mass flux vector of the liquid water phase
$\boldsymbol{v_w}$	[m/s]	Velocity vector driving the mass flux

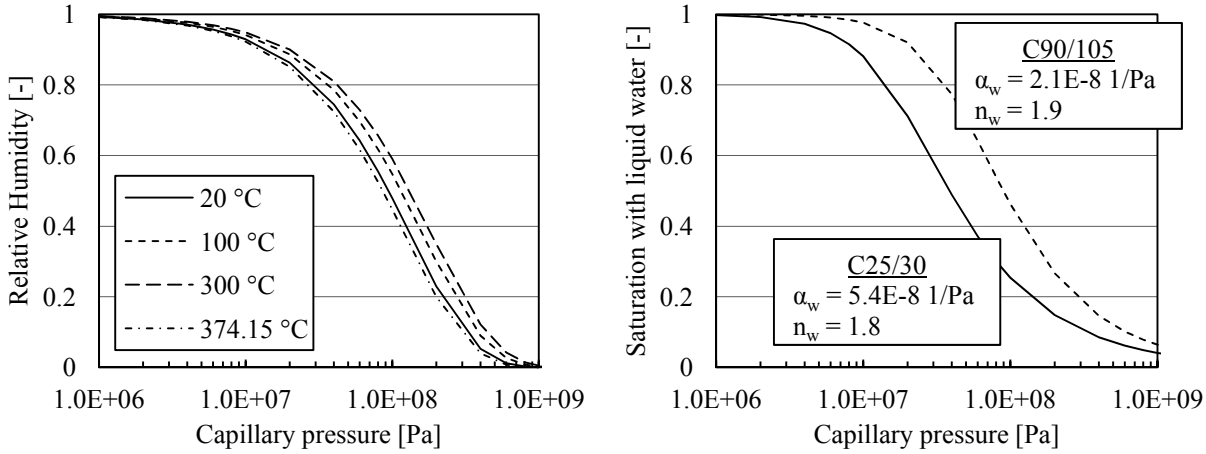

Fig. 4.13 *Kelvin equation describing the equilibrium state across the meniscus between the water phases* (Pel & Huinink, 2007) *(left). Desorption isotherms characterising drying by increase of capillary pressure* (Baroghel-Bouny, 1994a) *(right).*

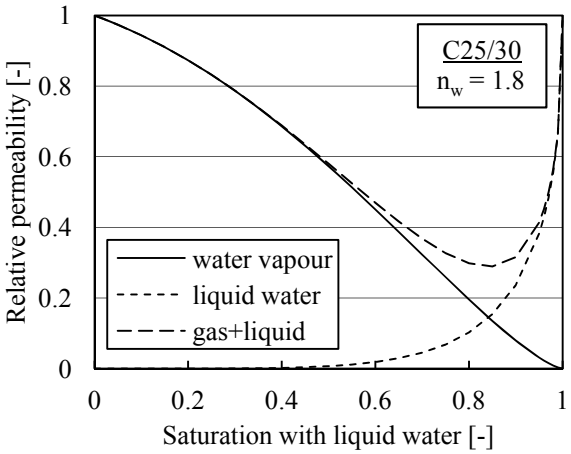

Fig. 4.14 *The saturation level influences both mass fluxes, governed by relative or effective permeability* (Genuchten, 1980; Bear, 1972/1988; Dal Pont, 2004).

Characterisation of the drying process

The capillary pressure is used to characterise drying of the porous material by a desorption isotherm (Pel & Huinink, 2007). A typical behaviour is stated by Genuchten's equation expressed in the pressure head or more commonly in the capillary pressure as defined by the inverse of the RH taken from Eq. (4.29) (Genuchten, 1980). Drying develops from the largest capillary pores to the smallest gel pores by increasing the capillary pressure (Pel & Huinink, 2007). This relationship defines the thermodynamic equilibrium in the evaporation process between both water phases and is expressed as follows:

$$S_w = ((\alpha_w P_c)^{n_w} + 1)^{\frac{1}{n_w}-1} \tag{4.35}$$

with

$$P_c = -\ln(RH)\frac{\rho_w RT}{M_w}$$

where

α_w, n_w [1/Pa], [-] Parameters used to characterise the desorption isotherm

The temperature dependence of desorption isotherms is difficult to obtain (Poyet, 2009). Therefore, in this thesis the isotherms defined are temperature-independent as shown for both strength classes in the right graph of Fig. 4.13 (Baroghel-Bouny, 1994a). Drying of C90/105 is indicated at higher capillary pressures due to the smaller pore sizes (Pel & Huinink, 2007).

Partially saturated flow of the water phases

During drying a partially saturated state develops in which the presence of both water phases influences the respective flow capabilities (Bear, 1972/1988; Pel & Huinink, 2007). The liquid phase becomes increasingly disconnected due to the drying process emptying first the largest capillary pores (Pel & Huinink, 2007; Couture, et al., 1996). Flow of the gas phase occurs across the dried pore space which by continued drying forms a connected network (Bear, 1972/1988). This is commonly represented by relative permeability relationships as shown in Fig. 4.14 based on (Genuchten, 1980; Dal Pont, 2004; Bear, 1972/1988):

$$K_{rel_g} = \sqrt{(1-S_w)}\left(1-S_w^{\frac{n_w}{n_w-1}}\right)^{2-\frac{2}{n_w}}$$
$$K_{rel_w} = \sqrt{S_w}\left(1-\left(1-S_w^{\frac{n_w}{n_w-1}}\right)^{1-\frac{1}{n_w}}\right)^2 \tag{4.36}$$

Partial derivatives and the gradient

The averaged water phases densities are governed by time derivatives with respect to the main variable, the capillary pressure. The partial derivatives are based on Eq. (4.29) and (4.35) and reflect the dependence on the RH and the liquid water saturation level respectively:

$$\frac{\partial\left(n(1-S_w)\rho_{gw}\right)}{\partial t} = \frac{\partial\left(n(1-S_w)\frac{RHP_{sat}M_w}{RT}\right)}{\partial P_c}\frac{\partial P_c}{\partial t} = -\left(RH\frac{\partial S_w}{\partial P_c} - (1-S_w)\frac{\partial RH}{\partial P_c}\right)n\frac{P_{sat}M_w}{RT}\frac{\partial P_c}{\partial t}$$
$$\frac{\partial(nS_w\rho_w)}{\partial t} = \frac{\partial(nS_w\rho_w)}{\partial P_c}\frac{\partial P_c}{\partial t} = n\rho_w\frac{\partial S_w}{\partial P_c}\frac{\partial P_c}{\partial t} \tag{4.37}$$

with

$$\frac{\partial RH}{\partial P_c} = -\frac{M_w}{\rho_w RT}e^{\frac{-P_c M_w}{\rho_w RT}}$$

$$\frac{\partial S_w}{\partial P_c} = (1-n_w)((\alpha_w P_c)^{n_w}+1)^{\frac{1}{n_w}-2}(\alpha_w P_c)^{n_w-1}\alpha_w$$

Both pressure gradients driving the mass fluxes are also expressed using the variable. This introduces the partial derivative of the Kelvin equation and the capillary pressure gradient:

$$\boldsymbol{\nabla} P_{gw} = \boldsymbol{\nabla}(RHP_{sat}) = \frac{\partial RH}{\partial P_c}P_{sat}\boldsymbol{\nabla} P_c$$
$$\boldsymbol{\nabla} P_w = \boldsymbol{\nabla}\left(P_{gw}-P_c\right) = \boldsymbol{\nabla}(RHP_{sat}) - \boldsymbol{\nabla} P_c = \left(\frac{\partial RH}{\partial P_c}P_{sat}-1\right)\boldsymbol{\nabla} P_c \tag{4.38}$$

Coupled conservation of the water phases

The interaction between both conservation equations is reflected by the mass density of water vapour produced by evaporation. This term is commonly exploited to combine both conservation equations in order to assume an instantaneous development of thermodynamic equilibrium between the water phases (Tenchev, et al., 2001; Gawin, et al., 2003). Inserting Eq. (4.31) into Eq. (4.34) and using Eq. (4.38) obtains the coupled conservation equation:

$$\frac{\partial\overline{\rho_w}}{\partial t} + \boldsymbol{\nabla}\cdot\boldsymbol{q_w} = -\left(\frac{\partial\overline{\rho_{gw}}}{\partial t} + \boldsymbol{\nabla}\cdot\boldsymbol{q_{gw}}\right)$$

$$\frac{\partial(nS_w\rho_w)}{\partial t} + \frac{\partial\left(n(1-S_w)\frac{RHP_{sat}M_w}{RT}\right)}{\partial t} - \boldsymbol{\nabla}\cdot\left(nS_w\rho_w\left(\frac{K_{rel_w}K}{\mu_w}\right)\left(\frac{\partial RH}{\partial P_c}P_{sat}-1\right)\boldsymbol{\nabla} P_c\right) \tag{4.39}$$
$$-\boldsymbol{\nabla}\cdot\left(n(1-S_w)\frac{RHP_{sat}M_w}{RT}\left(\frac{K_{rel_g}K}{\mu_g}\right)\frac{\partial RH}{\partial P_c}P_{sat}\boldsymbol{\nabla} P_c\right) = 0$$

The third and fourth terms represent the mass fluxes and are expanded using the product rule while rearranging the constants. The remaining terms depend directly or indirectly through the saturation level on the capillary pressure. From this, two terms are deduced for each mass flux representing the gradient of the material and the Laplacian of the capillary pressure:

$$\begin{aligned} & n\rho_w \frac{K}{\mu_w} \boldsymbol{\nabla} \cdot \left(S_w K_{rel_w} \left(\frac{\partial RH}{\partial P_c} P_{sat} - 1 \right) \boldsymbol{\nabla} P_c \right) \\ &= n\rho_w \frac{K}{\mu_w} \left(\boldsymbol{\nabla} \left(S_w K_{rel_w} \left(\frac{\partial RH}{\partial P_c} P_{sat} - 1 \right) \right) \cdot \boldsymbol{\nabla} P_c + \left(S_w K_{rel_w} \left(\frac{\partial RH}{\partial P_c} P_{sat} - 1 \right) \right) \boldsymbol{\nabla} \cdot \boldsymbol{\nabla} P_c \right) \\ & \frac{n {P_{sat}}^2 M_w}{RT} \frac{K}{\mu_g} \boldsymbol{\nabla} \cdot \left((1 - S_w) K_{rel_g} RH \frac{\partial RH}{\partial P_c} \boldsymbol{\nabla} P_c \right) \\ &= \frac{n {P_{sat}}^2 M_w}{RT} \frac{K}{\mu_g} \left(\boldsymbol{\nabla} \left((1 - S_w) K_{rel_g} RH \frac{\partial RH}{\partial P_c} \right) \cdot \boldsymbol{\nabla} P_c + \left((1 - S_w) K_{rel_g} RH \frac{\partial RH}{\partial P_c} \right) \boldsymbol{\nabla} \cdot \boldsymbol{\nabla} P_c \right) \end{aligned} \tag{4.40}$$

The final expression for the coupled conservation equation is obtained by inserting Eq. (4.37) and Eq. (4.40) into Eq. (4.39) which leads to:

$$\begin{aligned} & \left(n\rho_w \frac{\partial S_w}{\partial P_c} - \left(RH \frac{\partial S_w}{\partial P_c} - (1 - S_w) \frac{\partial RH}{\partial P_c} \right) \frac{n P_{sat} M_w}{RT} \right) \frac{\partial P_c}{\partial t} \\ & - n\rho_w \frac{K}{\mu_w} \left(\boldsymbol{\nabla} \left(S_w K_{rel_w} \left(\frac{\partial RH}{\partial P_c} P_{sat} - 1 \right) \right) \cdot \boldsymbol{\nabla} P_c + \left(S_w K_{rel_w} \left(\frac{\partial RH}{\partial P_c} P_{sat} - 1 \right) \right) \boldsymbol{\Delta} P_c \right) \\ & - \frac{n {P_{sat}}^2 M_w}{RT} \frac{K}{\mu_g} \left(\boldsymbol{\nabla} \left((1 - S_w) K_{rel_g} RH \frac{\partial RH}{\partial P_c} \right) \cdot \boldsymbol{\nabla} P_c + \left((1 - S_w) K_{rel_g} RH \frac{\partial RH}{\partial P_c} \right) \boldsymbol{\Delta} P_c \right) = 0 \end{aligned} \tag{4.41}$$

This PDE is also simplified assuming a 1D behaviour perpendicular to the surface:

$$\begin{aligned} \frac{\partial P_c}{\partial t} = & \frac{1}{\left(n\rho_w \frac{\partial S_w}{\partial P_c} - \left(RH \frac{\partial S_w}{\partial P_c} - (1 - S_w) \frac{\partial RH}{\partial P_c} \right) \frac{n P_{sat} M_w}{RT} \right)} \\ & \left(\left(n\rho_w \frac{K}{\mu_w} \left(\frac{\partial}{\partial x} \left(S_w K_{rel_w} \left(\frac{\partial RH}{\partial P_c} P_{sat} - 1 \right) \right) \frac{\partial P_c}{\partial x} + \left(S_w K_{rel_w} \left(\frac{\partial RH}{\partial P_c} P_{sat} - 1 \right) \right) \frac{\partial^2 P_c}{\partial x^2} \right) \right) \right. \\ & \left. + \left(\frac{n {P_{sat}}^2 M_w}{RT} \frac{K}{\mu_g} \left(\frac{\partial}{\partial x} \left((1 - S_w) K_{rel_g} RH \frac{\partial RH}{\partial P_c} \right) \frac{\partial P_c}{\partial x} + \left((1 - S_w) K_{rel_g} RH \frac{\partial RH}{\partial P_c} \right) \frac{\partial^2 P_c}{\partial x^2} \right) \right) \right) \end{aligned} \tag{4.42}$$

Boundary conditions

The definition is finalised by the Neumann boundary condition reflecting the exchange with the surrounding environment (Tenchev, et al., 2001; Gawin, et al., 2003). The mass fluxes of the vapour and liquid phases of water are obtained from Eq. (4.31) and Eq. (4.34)

respectively. The ambient conditions are governed by the density or alternatively by the pressure of the water vapour phase using again Eq. (4.2). So, for positive outward orientated mass fluxes the following relation is stated:

$$\begin{aligned}\left(\boldsymbol{q_w} + \boldsymbol{q_{gw}}\right)\big|_{\Gamma_A} &= \beta_A\left(\rho_{gw} - \rho_{gw_\infty}\right)\\ -\left(nS_w\rho_w\left(\frac{K_{rel_w}K}{\mu_w}\right)\left(\frac{\partial RH}{\partial P_c}P_{sat} - 1\right) + n(1-S_w)\frac{RHP_{sat}M_w}{RT}\left(\frac{K_{rel_g}K}{\mu_g}\right)\frac{\partial RH}{\partial P_c}P_{sat}\right)\frac{\partial P_c}{\partial x}\bigg|_{\Gamma_A} &= \beta_A\frac{M_w}{RT}\left(RHP_{sat} - P_{gw_\infty}\right)\end{aligned} \tag{4.43}$$

where

β_A	[m/s]	Convective mass transfer coefficient of the material
ρ_{gw_∞}	[kg/m^3]	Density of the water vapour phase at distance from the surface
P_{gw_∞}	[Pa]	Pressure of the water vapour phase at distance from the surface

4.5.3 Numerical solution by FDM including boundary conditions

The same element discretisation is used to determine drying of the cross-section. For the derivatives of the capillary pressure the basic numerical approximations are stated using the conditionally stable forward Euler time integration (van Kan, et al., 2008; Vermolen, 2005):

$$\begin{aligned}\frac{\partial P_c}{\partial t} &\approx \frac{{P_c}_i^{\,t+1} - {P_c}_i^{\,t}}{\Delta t}\\ \frac{\partial P_c}{\partial x} &= \frac{{P_c}_{i+1}^{\,t} - {P_c}_{i-1}^{\,t}}{2\Delta x}\\ \frac{\partial^2 P_c}{\partial x^2} &= \frac{{P_c}_{i+1}^{\,t} - 2{P_c}_i^{\,t} + {P_c}_{i-1}^{\,t}}{\Delta x^2}\end{aligned} \tag{4.44}$$

Both material gradients are approximated using the central difference scheme expressing the various contributions at the surrounding points:

$$\begin{aligned}&\frac{\partial}{\partial x}\left(S_wK_{rel_w}\left(\frac{\partial RH}{\partial P_c}P_{sat} - 1\right)\right)\\ &\approx \frac{{S_w}_{i+1}^{\,t}{K_{rel_w}}_{i+1}^{\,t}\left(\left[\frac{\partial RH}{\partial P_c}\right]_{i+1}^{t}P_{sat} - 1\right) - {S_w}_{i-1}^{\,t}{K_{rel_w}}_{i-1}^{\,t}\left(\left[\frac{\partial RH}{\partial P_c}\right]_{i-1}^{t}P_{sat} - 1\right)}{2\Delta x}\\ &\frac{\partial}{\partial x}\left((1-S_w)K_{rel_g}RH\frac{\partial RH}{\partial P_c}\right)\\ &\approx \frac{\left(1-{S_w}_{i+1}^{\,t}\right){K_{rel_g}}_{i+1}^{\,t}RH_{i+1}^{\,t}\left[\frac{\partial RH}{\partial P_c}\right]_{i+1}^{t} - \left(1-{S_w}_{i-1}^{\,t}\right){K_{rel_g}}_{i-1}^{\,t}RH_{i-1}^{\,t}\left[\frac{\partial RH}{\partial P_c}\right]_{i-1}^{t}}{2\Delta x}\end{aligned} \tag{4.45}$$

Combination of the previous relationships in Eq. (4.42) obtains the numerical approximation which becomes quite elaborate. Both mass fluxes contribute two terms based on the approximation of the material gradient and the Laplacian of the capillary pressure gradient:

$$
\begin{aligned}
{P_c}_i^{\,t+1} = {P_c}_i^{\,t} + \frac{\Delta t}{\Delta x^2} \frac{1}{\left(n\rho_w \left[\frac{\partial S_w}{\partial P_c}\right]_i^{\,t} - \left(RH_i^{\,t}\left[\frac{\partial S_w}{\partial P_c}\right]_i^{\,t} - \left(1-{S_w}_i^{\,t}\right)\left[\frac{\partial RH}{\partial P_c}\right]_i^{\,t}\right)\frac{nP_{sat}M_w}{RT}\right)} \\
\left(n\rho_w \frac{K}{\mu_w}\left({S_w}_{i+1}^{\,t}{K_{rel_w}}_{i+1}^{\,t}\left(\left[\frac{\partial RH}{\partial P_c}\right]_{i+1}^{\,t} P_{sat} - 1\right)\right.\right. \\
\left.\left. - {S_w}_{i-1}^{\,t}{K_{rel_w}}_{i-1}^{\,t}\left(\left[\frac{\partial RH}{\partial P_c}\right]_{i-1}^{\,t} P_{sat} - 1\right)\right)\left(\frac{{P_c}_{i+1}^{\,t} - {P_c}_{i-1}^{\,t}}{4}\right)\right. \\
+ n\rho_w \frac{K}{\mu_w} {S_w}_i^{\,t}{K_{rel_w}}_i^{\,t}\left(\left[\frac{\partial RH}{\partial P_c}\right]_i^{\,t} P_{sat} - 1\right)\left({P_c}_{i+1}^{\,t} - 2{P_c}_i^{\,t} + {P_c}_{i-1}^{\,t}\right) \\
+ \frac{{nP_{sat}}^2 M_w}{RT}\frac{K}{\mu_g}\left(\left(1-{S_w}_{i+1}^{\,t}\right){K_{rel_g}}_{i+1}^{\,t} RH_{i+1}^{\,t}\left[\frac{\partial RH}{\partial P_c}\right]_{i+1}^{\,t}\right. \\
\left. - \left(1-{S_w}_{i-1}^{\,t}\right){K_{rel_g}}_{i-1}^{\,t} RH_{i-1}^{\,t}\left[\frac{\partial RH}{\partial P_c}\right]_{i-1}^{\,t}\right)\left(\frac{{P_c}_{i+1}^{\,t} - {P_c}_{i-1}^{\,t}}{4}\right) \\
\left. + \frac{{nP_{sat}}^2 M_w}{RT}\frac{K}{\mu_g}\left(1-{S_w}_i^{\,t}\right){K_{rel_g}}_i^{\,t} RH_i^{\,t}\left[\frac{\partial RH}{\partial P_c}\right]_i^{\,t}\left({P_c}_{i+1}^{\,t} - 2{P_c}_i^{\,t} + {P_c}_{i-1}^{\,t}\right)\right)
\end{aligned}
\tag{4.46}
$$

The Neumann boundary is stated by a central difference scheme using again exterior points:

$$
\begin{aligned}
\left.\frac{\partial P_c}{\partial x}\right|_{\Gamma_A} &\approx \frac{{P_c}_{i+1}^{\,t} - {P_c}_{i-1}^{\,t}}{2\Delta x} \\
&= -\frac{\beta_A \frac{M_w}{RT}\left(RH_i^{\,t} P_{sat} - {P_{gw}}_\infty^{\,t}\right)}{n{S_w}_i^{\,t}\rho_w\left(\frac{{K_{rel_w}}_i^{\,t}K}{\mu_w}\right)\left(\left[\frac{\partial RH}{\partial P_c}\right]_i^{\,t} P_{sat} - 1\right) + n\left(1-{S_w}_i^{\,t}\right)\frac{RH_i^{\,t}P_{sat}M_w}{RT}\frac{{K_{rel_g}}_i^{\,t}K}{\mu_g}\left[\frac{\partial RH}{\partial P_c}\right]_i^{\,t} P_{sat}}
\end{aligned}
\tag{4.47}
$$

$$
\rightarrow {P_c}_{i+1}^{\,t} = {P_c}_{i-1}^{\,t} - \frac{2\Delta x \beta_A \frac{M_w}{RT}\left(RH_i^{\,t} P_{sat} - {P_{gw}}_\infty^{\,t}\right)}{n{S_w}_i^{\,t}\rho_w\left(\frac{{K_{rel_w}}_i^{\,t}K}{\mu_w}\right)\left(\left[\frac{\partial RH}{\partial P_c}\right]_i^{\,t} P_{sat} - 1\right) + n\left(1-{S_w}_i^{\,t}\right)\frac{RH_i^{\,t}P_{sat}M_w}{RT}\frac{{K_{rel_g}}_i^{\,t}K}{\mu_g}\left[\frac{\partial RH}{\partial P_c}\right]_i^{\,t} P_{sat}}
$$

4.5.4 Temperature-dependent drying of the cross-section

The capillary pressure gradient is numerically approximated for the same homogeneous cross-section as previously used. The results obtained, based on Table 4.4, reflect drying at a constant temperature of 150 °C or 250 °C which defines the properties for both water phases. These conditions also allow to omit the heat fluxes as is the case for this uncoupled model.

Drying scenarios			
Calculation	**4.3A**	**4.3B**	**4.3C**
Reference temperature	**150 °C**	**250 °C**	**250 °C**
Reference RH	80 %	80 %	80 %
Duration	3 hrs	1.5 hrs	0.5 hrs
Incremental time step size	**0.5 sec**	**0.05 sec**	**0.075 sec**
Material (homogeneous)			
Strength class	**C25/30**	**C25/30**	**C90/105**
Initial saturation level	**49 %**	**46 %**	**75 %**
Boundary conditions			
Exterior vapour pressure (dry)	1000 Pa	1000 Pa	1000 Pa
Exterior vapour pressure (ref)	**3.8E+5 Pa**	**3.2E+6 Pa**	**3.2E+6 Pa**
Convective mass transfer coeff.	0.03 m/s	0.03 m/s	0.03 m/s

Table 4.4 *Drying of the cross-section, determined based on several scenarios governed by a constant temperature and the concrete strength class.*

The initial liquid water saturation levels are governed by the reference RH and the desorption isotherms, according to Eq. (4.35), dependent on the strength class (Baroghel-Bouny, 1994a). Simplified relationships for the temperature-dependent porosity and permeability of C25/30 and C90/105 are used based on (IREX, 2005) as seen in the left and right graphs of Fig. 4.15 respectively. The exterior environment is defined by the reference water vapour pressure which for the left edge decreases linearly in 600 seconds to the dried state. Numerical stability is thus improved by avoiding a sudden pressure change imposed by the Neumann boundary condition. The mass transfer coefficient is constant for all scenarios (Gawin, et al., 2003).

The progress of the steep capillary pressure gradient reflects drying of the cross-section as is indicated in Fig. 4.16. The reduction of the liquid water saturation level coincides with an increase in the capillary pressure. Simultaneously, the water vapour pressure reduces based on the RH and the constant saturated vapour pressure as can be seen in Fig. 4.17. However, the uniform temperature has a direct influence on the drying process, taking more time to develop at 150 °C, attributed to the reduced saturation pressure governing the vapour phase.

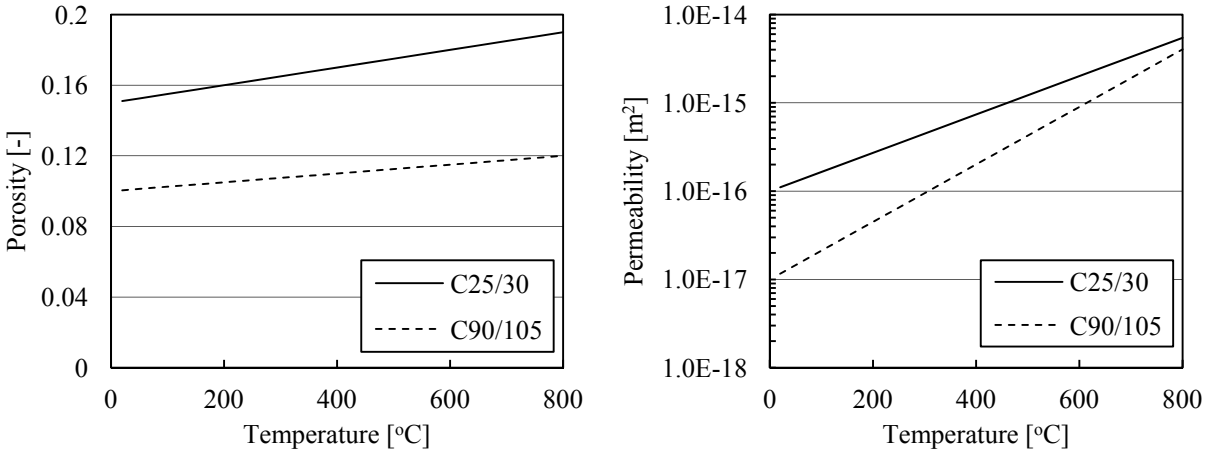

Fig. 4.15 *Concrete porosity (left) and permeability (right) development with temperature as defined through consideration of experimental data by* (IREX, 2005).

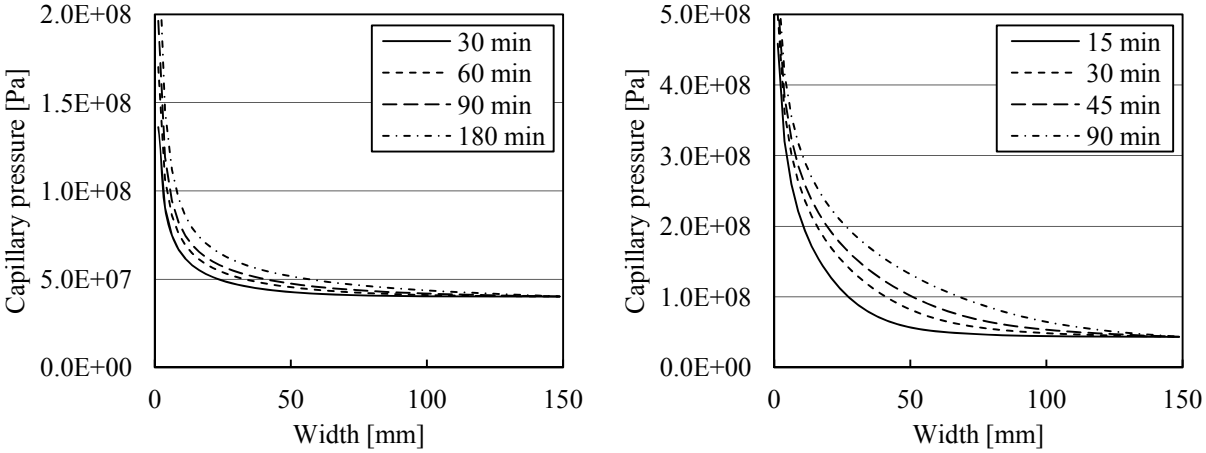

Fig. 4.16 *The capillary pressure gradient characterising the drying process, mainly influenced by the temperature. The progress through the C25/30 cross-section dried at 150 °C (left) is more moderate compared to 250 °C (right).*

The process of drying is mainly characterised by evaporation and subsequent transport of vapour. Only a limited contribution due to the liquid water flux is present, governed by reduction of the corresponding relative permeability. Into the cross-section also no increase in liquid water saturation is observed since the pressure gradient is only directed towards the left surface. This is attributed to the constant temperature which into the cross-section does not affect the equilibrium state between the water phases. It should also be noted that the assumed infinite strength and stiffness implies that no deformations occur due to gas pressures.

The denser pore structure of C90/105 leads to a higher reference saturation level and takes more time to dry as reflected by Fig. 4.18. The constant temperature of 250 °C leads to the same reference water vapour pressure as present in the C25/30 cross-section. However, the reduced permeability imposes higher restrictions on the flow of the formed water vapour towards the left surface. The water vapour pressure at the dried surface reduces in time, reflecting the exchange with the surrounding environment. In time, the drying front progresses slowly into the cross-section eventually forming a steady state.

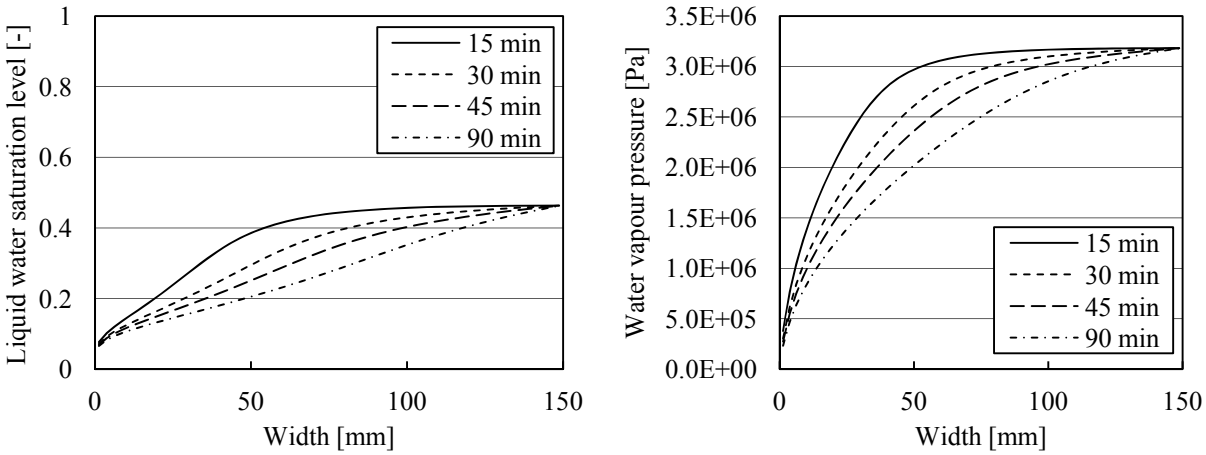

Fig. 4.17 *Reduction of the saturation in the C25/30 cross-section dried at a temperature 250 °C is governed by a steep capillary pressure gradient (left). Simultaneous reduction in RH causes a gas pressure gradient towards the left surface (right).*

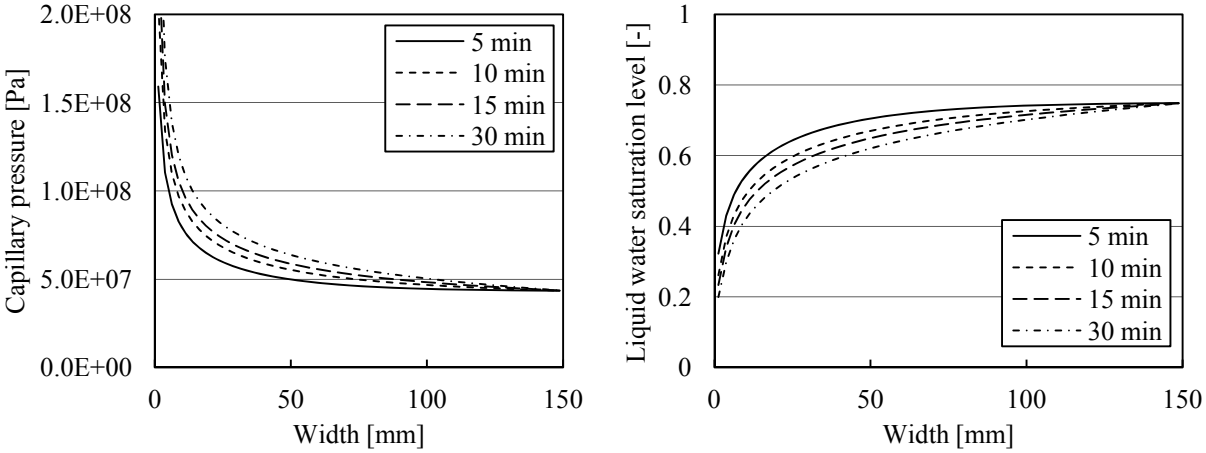

Fig. 4.18 *Drying of the C90/105 cross-section, even at a temperature of 250 ^{o}C, develops relatively slowly (left). This is governed by the higher reference saturation level (right) and especially by the lower permeability.*

For each concrete type and uniform temperature a steady state solution exists which not necessarily defines a completely dried material. The progress of the drying front into the cross-section eventually mitigates by forming an equilibrium based on the boundary conditions and the physical material description. This steady state is defined by considering the time derivative as zero in the coupled PDE stated in Eq. (4.42). Under these circumstances the mass fluxes do not constitute any changes to the capillary pressure gradient. However, additional types of transport, such as based on concentration gradients characterised by Fick's law, could influence the steady state to be formed (Bear, 1972/1988).

A final remark is concerned with the size of the incremental time step which needs to be reduced in case of higher temperatures to maintain numerical stability. This indicates the non-linear nature of the drying characterisation and the permeability-based velocity of especially the water vapour mass flux. It is important to also consider the conditional stability of the Euler forward time integration scheme (Vermolen, 2005).

4.6 Conclusions with respect to the continuum

The definition of a physical continuum is based on:

- The PDE reflecting the general conservation of an averaged property in a REV (Hassanizadeh & Gray, 1979a; Bachmat & Bear, 1986) as stated in Eq. (4.18). The time derivative of this property is governed by development across the volume including fluxes across the boundaries and additional sources (Bear, 1972/1988).

From the conservation of thermal energy and the temperature progress in the cross-section the following conclusions and remarks are deduced:

- Conservation of thermal energy governs the temperature development based mainly on gradients according to Fourier's law and characterised by the thermal conductivity (Bear, 1972/1988). Progress of energy by convection, the flow of heated gases and liquids, is commonly not included (Kordina, et al., 1975; van Breugel, et al., 1998).

- The time-dependent temperature development used to characterise a fire scenario (Eurocode 1, 2011a) can best be included through a Neumann boundary condition (van Kan, et al., 2008). This allows for interaction between the surface of the cross-section and the exterior environment rather than imposing directly the air temperature.

- Fire scenarios and in particular the HC are characterised by a substantial heating rate, present especially in the first minutes of exposure. Development of the actual surface temperature also depends on the convective heat transfer characterisation.

With respect to mass conservation of the water phases governing drying of the cross-section the following is stated:

- The conservation equations for the liquid and vapour phases of water are combined or coupled to obtain the overall behaviour (Tenchev, et al., 2001; Gawin, et al., 2003). This assumes an instantaneous thermodynamic equilibrium based on the Kelvin equation and the desorption isotherm (Bear, 1972/1988; Pel & Huinink, 2007).

- The relatively low velocities of the viscous gas and liquid phase flows are both characterised as laminar and isotropic governed by Darcy's law based on pressure gradients (Bear, 1972/1988). Diffusion through concentration gradients, expressed by Fick's law (Bear, 1972/1988), is not included based on the gradual development.

- Drying or drainage is also best imposed by definition of a Neumann boundary condition governed by the exterior water vapour state (Tenchev, et al., 2001; Gawin, et al., 2003). This allows for equilibration at the dried surface rather than imposing a fixed variable.

- A steep capillary pressure gradient develops which reflects the reduction in the liquid water saturation level. This coincides with a reduction in the RH and the water vapour pressure. This pressure gradient drives the vapour towards the dried surface.

- The imposed constant temperature has a significant influence on the drying characteristic. In the temperature interval, from 150 ^{o}C to 250 ^{o}C, the saturated water vapour pressure increases almost 10 times. This determines the possible gas pressure gradient and the ability for water vapour to escape from the cross-section.

- The density of the porous material also determines the time required to dry the cross-section. This is partially due to the smaller pore sizes and the coinciding desorption isotherm as indicated for C90/105. However, the largest influence is governed by the permeability, reflecting the transport capability of the material.

- Drying of the cross-section is characterised by the capillary pressure and several constitutive relationships. These non-linear relationships govern the reduction of the incremental time step size in case the temperature and the velocity of the phase flow across the material increases.

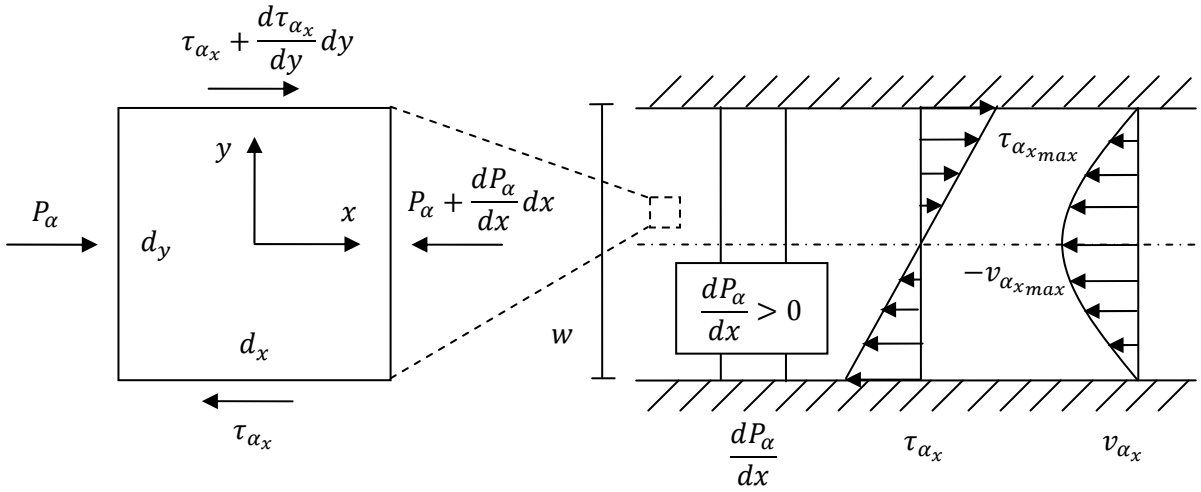

Fig. 4.19 *Flow of a viscous fluid, for instance in* $\mathbb{R}^2$*, is at relatively low velocities based on deformation simplified as sliding of layers due to shear stresses. The dynamic viscosity governs the ability of the fluid to withstand deformation* (Granger, 1985/1995; Bear, 1972/1988).

4.7 Permeability of a simplified crack

The pressure-driven flow across a porous material is characterised by the permeability (Bear, 1972/1988). This experimentally determined property is a measure for the connectivity of the pore structure. However, during fracture a local and sudden change in material behaviour occurs which largely affects the permeability. The formation of a channel is commonly used to estimate the fluid flow (Granger, 1985/1995; Bear, 1972/1988).

Flow between parallel plates

This flow condition is schematically represented in Fig. 4.19 with a pressure gradient driving the viscous fluid between the parallel plate edges (Granger, 1985/1995; Bear, 1972/1988). Along the crack path and in the out-of-plane direction the pressure gradient is assumed constant. The flow at relatively low velocity is schematised as deformation based on sliding of fluid layers due to shear stresses (Granger, 1985/1995; Bear, 1972/1988). For this fluid continuum horizontal equilibrium is stated by (Nakayama & Boucher, 1998/2000):

$$\frac{dP_\alpha}{dx} = \frac{d\tau_{\alpha_x}}{dy} \tag{4.48}$$

where

P_α	[Pa]	Pressure acting in the fluid
τ_{α_x}	[Pa]	Shear stress acting across the fluid, parallel to the crack

These shear stresses are characterised by the dynamic viscosity of the fluid and the gradient of the velocity using Newton's law of viscosity (Bear, 1972/1988):

$$\tau_{\alpha_x} = \mu_\alpha \frac{dv_{\alpha_x}}{dy} \tag{4.49}$$

where

μ_α	[kg/ms]	Dynamic viscosity of the fluid
v_{α_x}	[m/s]	Velocity of the fluid, parallel to the crack

Combination of Eq. (4.48) and Eq. (4.49) leads to the following differential equation, commonly referred to as Poiseuille flow (Neuzil & Tracy, 1981; Granger, 1985/1995):

$$\mu_\alpha \frac{d^2 v_{\alpha_x}}{dy^2} = \frac{dP_\alpha}{dx} \tag{4.50}$$

At the plate edges the velocity of the flow is assumed zero commonly referred to as the no-slip condition (Granger, 1985/1995; Bear, 1972/1988). The differential equation is integrated twice which after fulfilment of the boundary conditions leads to the parabolic velocity distribution (Bear, 1972/1988). It is important to notice the opposite direction compared to the positive pressure gradient:

$$\left\{ \begin{matrix} \mu_\alpha \dfrac{d^2 v_{\alpha_x}}{dy^2} = \dfrac{dP_\alpha}{dx} \\ v_{\alpha_x}|_{y=\frac{w}{2}} = 0 \\ v_{\alpha_x}|_{y=-\frac{w}{2}} = 0 \end{matrix} \right\} \rightarrow v_{\alpha_x} = \frac{1}{2\mu_\alpha} \frac{dP_\alpha}{dx} \left(y^2 - \frac{w^2}{4} \right) \tag{4.51}$$

where

w	[m]	Crack width defined perpendicular to the plate edges

The shear stress distribution, using Eq. (4.51), is linearly dependent on the pressure gradient as shown in Fig. 4.19:

$$\tau_{\alpha_x} = \mu_\alpha \frac{dv_{\alpha_x}}{dy} = \frac{dP_\alpha}{dx} y \tag{4.52}$$

Determination of the average velocity across the crack leads to Darcy's law expressed in the crack permeability (Bear, 1972/1988):

$$v_{\alpha_x avg} = \frac{1}{w} \int_{-\frac{w}{2}}^{\frac{w}{2}} v_{\alpha_x} dy = \int_{-\frac{w}{2}}^{\frac{w}{2}} \frac{1}{2\mu_\alpha} \frac{dP_\alpha}{dx} \left(y^2 - \frac{w^2}{4} \right) dy = -\frac{w^2}{12} \frac{1}{\mu_\alpha} \frac{dP_\alpha}{dx} = -K_{cr} \frac{1}{\mu_\alpha} \frac{dP_\alpha}{dx} \tag{4.53}$$

with

$$K_{cr} = \frac{w^2}{12}$$

where

$v_{\alpha_x avg}$	[m/s]	Average velocity of the fluid across the width, parallel to the crack
K_{cr}	[m^2]	Permeability of the crack defined parallel to the plate edges

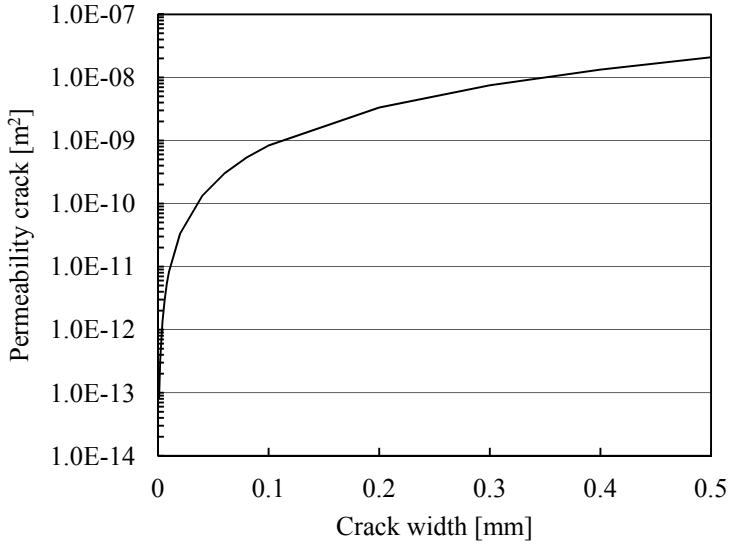

Fig. 4.20 *Permeability due to crack opening, increasing by several orders of magnitude compared to the surrounding material* (Bear, 1972/1988; Neuzil & Tracy, 1981; Rastiello, et al., 2013).

Relationship of permeability and crack width

The permeability development during crack opening is considerable, increasing by several orders of magnitude compared to the surrounding material as indicated by Fig. 4.20 (Neuzil & Tracy, 1981; Rastiello, et al., 2013). Using the permeability of C25/30, presented in Fig. 4.15, allows to quantify this substantial increase. Even at relatively small crack openings of around 0.1 mm, the permeability increases by an order of 8.3E+6. A factor of 1.0E+8 is reached for a crack width of 0.35 mm. The permeability increase of larger crack openings, measured as is more common in millimetres, becomes even higher. However, the flow is under these circumstances still assumed to develop according to the parabolic velocity distribution shown in Fig. 4.19. This requires sufficient mass to be present which is perhaps no longer applicable to the liquid water phase based on the limited permeability of the material surrounding the crack.

5 Deformation and stress basics for fire exposed concrete

The mechanical basis is formed by the relationships describing the deformation and resulting stresses in a fire exposed concrete structural element. These are extended in chapters 8 and 9 dealing with the FEM-based models. First, the stress state acting on the cross-section of the structural element is determined based on equilibrium of forces reflecting the external partial restraint and loading. The cross-sectional forces are based on the total strain definition extended by the imposed temperature strain. The resultant deformation of the element is characterised by extension and curvature, determined through numerical approximation. Several numerical results are presented which state the stresses in the cross-section based on fire exposure and structural interaction. Thereafter, the extension is made to the mechanical continuum by stating the PDE governing the balance of linear momentum. The deformation, characterised by extension and shear, is elaborated as well as the imposed temperature elongation strain. Furthermore, the linear elastic relationship between stresses and strains, governing the material, is stated. This chapter is concluded by using the continuum definition to estimate the stresses that arise in a pressure loaded porous material.

5.1 Relationship between imposed temperature strain, deformation and stresses

The development of the thermal stress state is the second main theory used to characterise the behaviour of concrete at elevated temperatures and to explain the spalling mechanism (Dougill, 1972). Exposure of the concrete element to a fire leads to the development of a temperature gradient causing thermal expansion of the material (van Breugel, et al., 1998). This imposes an internal load which deforms the element characterised by extension and curvature (Hartsuijker & Welleman, 2007) as shown in Fig. 5.1. However, this strains the material and causes stresses to develop in the cross-section. This is elaborated by first stating the strain definition at the cross-section (Hartsuijker & Welleman, 2007; Lagace, 2001). The definition of force equilibrium for the element allows to include the possibilities for restraint and external loading. The resulting stresses are governed by the imposed deformation, assuming a linear elastic material (Hartsuijker & Welleman, 2007). This will form the basis for understanding the mechanical behaviour as well as cracking of fire exposed concrete.

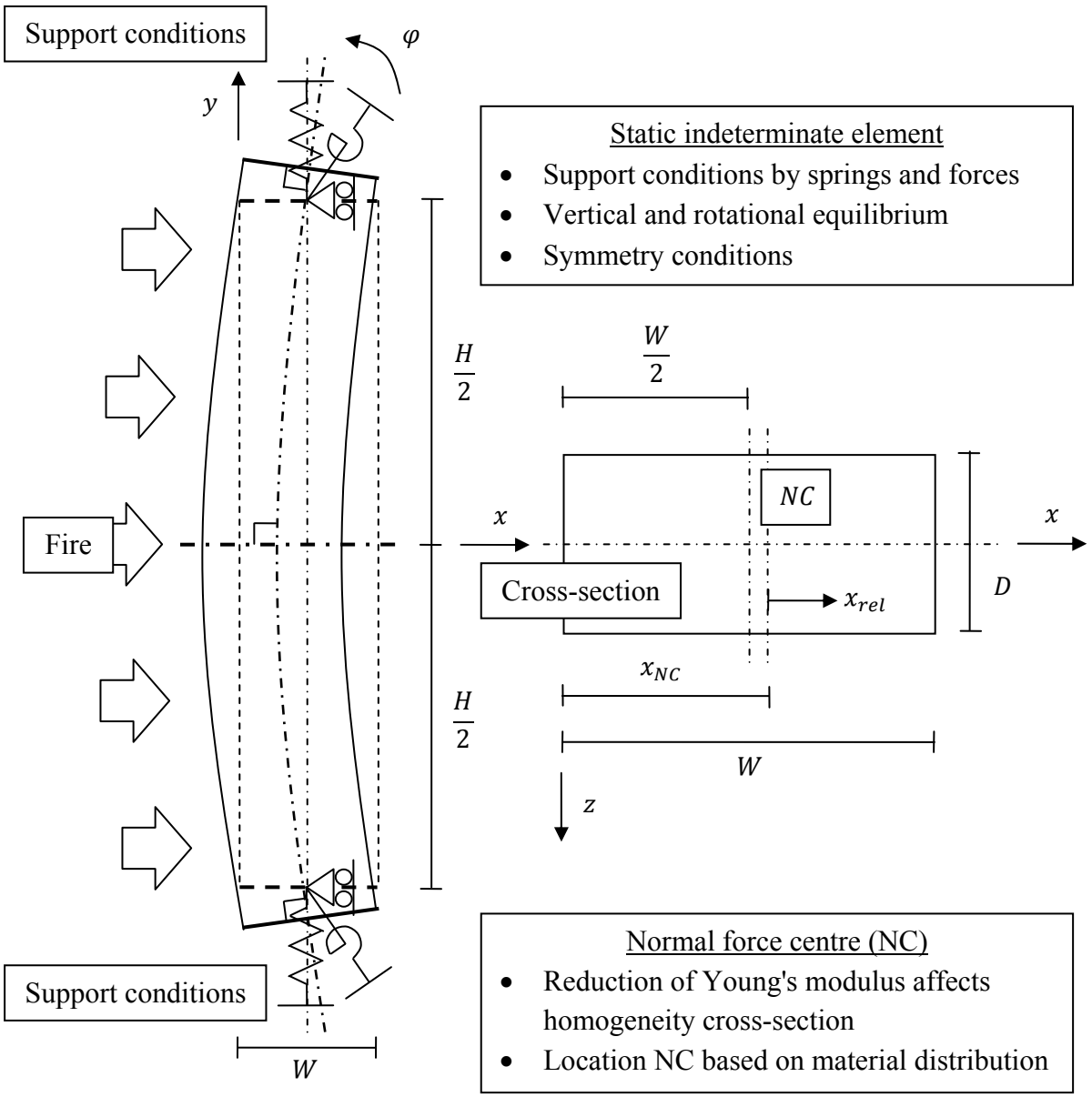

Fig. 5.1 *Schematisation of the fire exposed element characterised as a 2D statically indeterminate structure. In the cross-section the change of the NC is indicated.*

5.1.1 Basic assumptions used to define the structural behaviour

With respect to the structural behaviour the following assumptions are stated:

1. Concrete is characterised based on linear elasticity through Hooke's law and the assumption of small strains (Hartsuijker & Welleman, 2007). The influence of cracking is, at the moment, neglected reflected by an infinite strength.

2. The element is partially restrained by axial and rotational springs with constant stiffness as well as loaded by constant axial forces and moments (Bouma, 2000). Fire exposure is assumed constant across the height and depth of the element. This imposes an instantaneous temperature gradient perpendicular to the heated surface.

3. The internal loading is based on temperature-induced elongation of the material. Self-weight is neglected based on the limited influence in these accidental load scenarios.

4. Deformation of the element is characterised by a linear strain definition across the width based on Bernoulli's hypothesis (Hartsuijker & Welleman, 2007). The cross-sections in height direction of the element remain plane and perpendicular to the vertical axis during deformation. Deformation is a combination of vertical elongation and curvature of the element neglecting the shear contribution (Bouma, 2000).

5.1.2 Schematisation of the cross-section by strain definition

Concrete is described as a homogeneous material for which the linear elastic assumption of reversible strains induced by stresses applies (Hartsuijker & Welleman, 2007). This relationship is reflected by Hooke's law (Hartsuijker & Welleman, 2007):

$$\sigma = E\varepsilon \tag{5.1}$$

where

σ	[MPa]	Stress in the material based on imposed strain
E	[MPa]	Modulus of elasticity or Young's modulus of the material
ε	[-]	Strain in the material

The deformation of the element is characterised by Bernoulli's hypothesis, stating that cross-sections remain plane during deformation (Hartsuijker & Welleman, 2007). The total strain at the cross-section is determined by the uniform extensional strain and the linear strain governed by the curvature (Hartsuijker & Welleman, 2007). The contribution of the linear strain is based on the internal distance relative to the normal force centre (NC) (Hartsuijker & Welleman, 2007):

$$\varepsilon = \varepsilon_0 + \kappa x_{rel} \tag{5.2}$$

with

$$x_{rel} = x - x_{NC}$$

where

ε	[-]	Total extensional strain defined at the cross-section
ε_0	[-]	Uniform extensional strain at the cross-section
κ	[1/mm]	Curvature at the cross-section
x_{rel}	[mm]	Internal distance defined relative to the NC
x_{NC}	[mm]	Location of the NC relative to the left edge of the cross-section

The NC is the location in the cross-section at which the resultant normal force acts (Hartsuijker & Welleman, 2007). In a homogeneous symmetric cross-section the NC coincides with the centroidal axis (Hartsuijker & Welleman, 2007). However, whereas the cross-section remains symmetrical, the thermal degradation reduces the Young's modulus affecting the homogeneity. This causes the location of the NC to change, as indicated in Fig. 5.1, based on the internal material distribution (Hartsuijker & Welleman, 2007):

$$x_{NC} = \frac{\int_A ExdA}{\int_A EdA} = \frac{EAx}{EA} = \frac{ES}{EA} \tag{5.3}$$

where

A	[mm^2]	Cross-sectional area of the structural element
S	[mm^3]	Static moment of the cross-section defined relative to the left edge

The temperature strain development depends on the distribution of the temperature and the thermal expansion of the material (Hartsuijker & Welleman, 2007; Noda, et al., 2003; Lagace, 2001). Especially the steep temperature gradient that develops during fire exposure is only partially accommodated by deformation of the element. This leads to the development of mechanical strains based on the total strain definition taking the initial temperature elongation strain into account (Hartsuijker & Welleman, 2007; Lagace, 2001; Fellinger, 2004):

$$\varepsilon = \varepsilon_m + \varepsilon_T \tag{5.4}$$

where

ε_T	[-]	Temperature-induced elongation strain imposed at the cross-section
ε_m	[-]	Mechanical strain inducing stress at the cross-section

Thermal stress state at the cross-section

The development of mechanical strains cause stresses governed by combination of Eq. (5.2) and (5.4) while assuming a linear elastic material as stated in Eq. (5.1) (Hartsuijker & Welleman, 2007; Lagace, 2001):

$$\sigma = E\varepsilon_m = E(\varepsilon - \varepsilon_T) = E(\varepsilon_0 + \kappa x_{rel} - \varepsilon_T) \tag{5.5}$$

This relationship is schematically shown in Fig. 5.2 and reflects the mechanical strain based on the imposed temperature strain gradient at the cross-section. The total strain governs the deformation of the cross-section whereas the mechanical strain determines the stresses (Hartsuijker & Welleman, 2007; Lagace, 2001). The stress state is characterised by variation between restrained and imposed deformation with at the transition points no straining and thus no loading of the material.

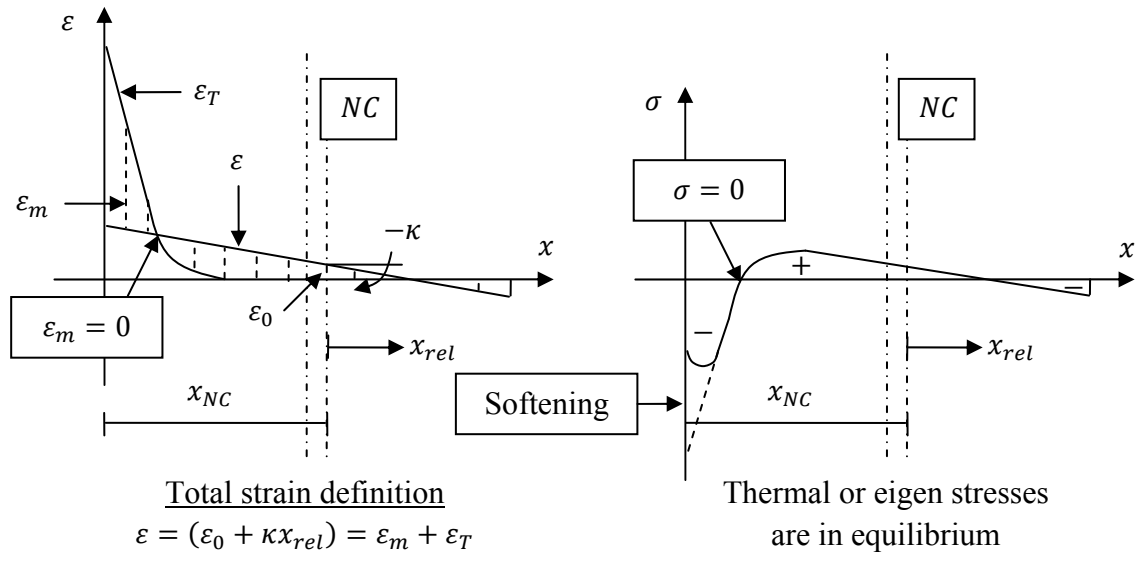

Fig. 5.2 *Linear total strain governing the cross-sectional deformation. Stresses develop from the mechanical strain caused by the imposed temperature strain.*

This stress state is self-equilibrating and governed by the thermal elongation of the material without applying any load to the element. Hence the name eigen stresses, from the German 'Eigenspannungen', is sometimes used (van Breugel, et al., 1998). The assumed constant fire exposure across the height of the element implies that the strain development and thus the stresses are both constant in vertical direction. Furthermore, the stresses are indicated to reduce in the heated surface layer. This behaviour is commonly referred to as softening and occurs due to the stiffness reduction at high temperatures (van Breugel, et al., 1998).

5.1.3 Structural behaviour and boundary conditions

The deformation of the element is based on the definition of static equilibrium in vertical and rotational direction (Hartsuijker & Welleman, 2007; Lagace, 2001). The axial force and moment are constant across the element as indicated by Fig. 5.3. Furthermore, the constant stress state and in particular the constant moment implies that shear forces are not present (Hartsuijker & Welleman, 2007) and horizontal equilibrium is directly fulfilled. The resultant forces at the cross-section are determined using the stress state represented by Eq. (5.5). The definition of the internal distance relative to the NC allows to remove the static moment contributions (Hartsuijker & Welleman, 2007):

$$N = \int_A \sigma dA = \int_A E\varepsilon_m dA = \int_A E\left(\varepsilon_0 + \overbrace{\kappa x_{rel}}^{=0} - \varepsilon_T\right) dA$$

$$M = \int_A \sigma x_{rel} dA = \int_A E\varepsilon_m x_{rel} dA = \int_A E\left(\overbrace{\varepsilon_0}^{=0} + \kappa x_{rel} - \varepsilon_T\right) x_{rel} dA \tag{5.6}$$

where

N	[N]	Normal force at the cross-section defined positive if tension
M	[Nmm]	Moment at the cross-section defined positive by rotational direction

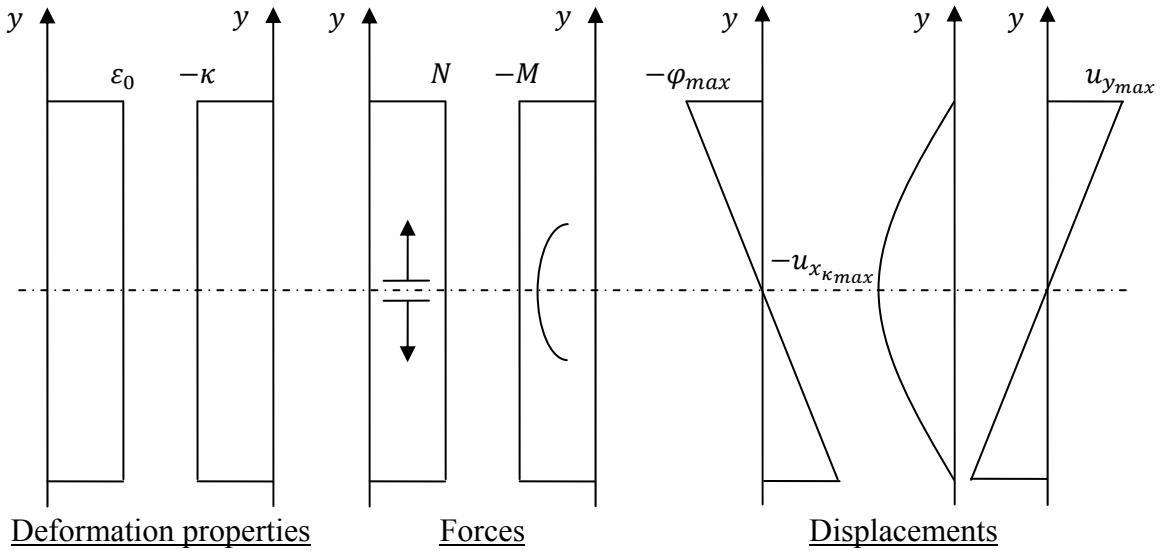

Fig. 5.3 *Schematic representation of the deformation properties, force and displacement distributions across the height of the structural element, assuming symmetry.*

Thermal deformations

This static indeterminate element requires, besides equilibrium conditions, kinematic requirements to define the deformation (Hartsuijker & Welleman, 2006). The symmetry of the element, with respect to the horizontal axis, is used to define the displacements and the rotation. The kinematic relationships, commonly used in mechanics (Hartsuijker & Welleman, 2007), are stated in accordance with Fig. 5.1. Integration and ensuring fulfilment of the boundary conditions allows to obtain the displacement relationships (Hartsuijker & Welleman, 2007). For instance, the constant curvature across the element causes a linear rotation in height direction:

$$\left.\begin{matrix} \kappa = \dfrac{d\varphi}{dy} \\ \varphi|_{y=0} = 0 \end{matrix}\right\} \rightarrow \varphi = \kappa y \tag{5.7}$$

where

φ	[rad]	Rotation defined along the axis of the structural element

The horizontal displacement is based on rotation of the cross-section using the small angle approximation (Hartsuijker & Welleman, 2007). This allows to obtain the parabolic relationship shown in Fig. 5.3. However, the temperature strain also contributes to the horizontal displacement. This direction is unrestrained, allowing the material to expand relative to the NC without causing additional internal forces as indicated by Fig. 5.4:

$$u_{x_{tot}} = u_{x_\kappa} + u_{x_T} \tag{5.8}$$

with

$$\left.\begin{matrix} \varphi = \kappa y = -\dfrac{du_x}{dy} \\ u_x|_{y=\frac{H}{2}} = 0 \end{matrix}\right\} \rightarrow u_{x_\kappa} = \frac{1}{2}\kappa\left(\left(\frac{H}{2}\right)^2 - y^2\right) \qquad u_{x_T} = \int_{x_{rel}} \varepsilon_T dx_{rel}$$

where

$u_{x_{tot}}$	[mm]	Total horizontal displacement across the structural element
u_{x_κ}, u_{x_T}	[mm]	Horizontal displacement due to curvature, temperature strain

The vertical displacement is first dependent on the constant extensional strain which leads to a linear variation in height direction. The constant curvature contributes a second part, linear in both height and width directions. The latter is defined by the internal distance, governed by the cross-section and through the uniform thermal exposure constant along the height. Integration of the derivative in vertical direction while considering the symmetry results in:

$$\left.\begin{matrix} \varepsilon = (\varepsilon_0 + \kappa x_{rel}) = \dfrac{du_y}{dy} \\ u_y|_{y=0} = 0 \end{matrix}\right\} \rightarrow u_y = \varepsilon y = (\varepsilon_0 + \kappa x_{rel}) y \tag{5.9}$$

where

u_y	[mm]	Vertical displacement across the structural element

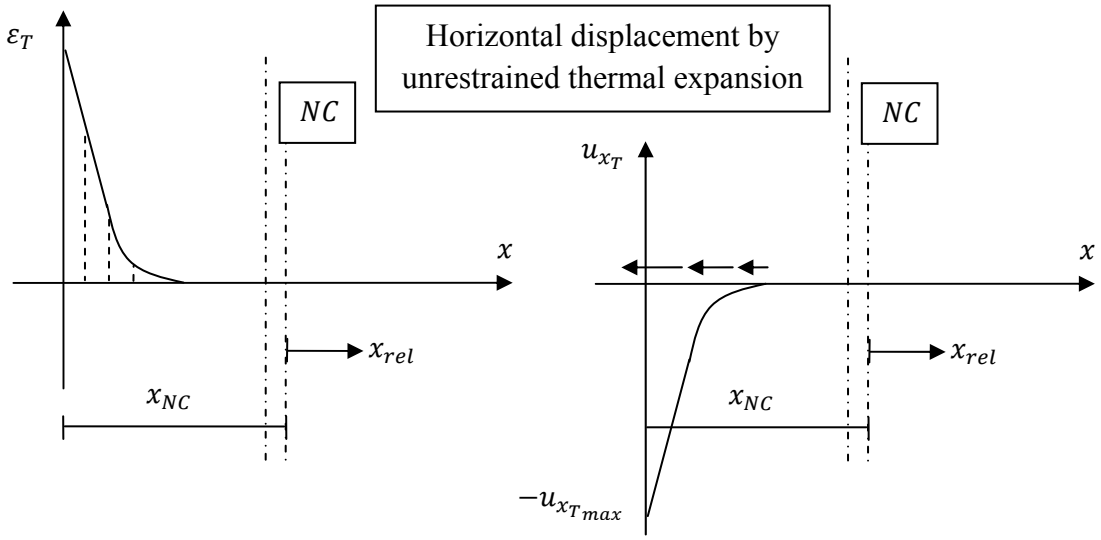

Fig. 5.4 *Temperature-induced strains extending the horizontal structural displacement without causing additional forces in the cross-section. This displacement component is constant across the height of the element.*

Support conditions

The structural boundary conditions are governed by the total vertical force and the total moment imposed at each support in accordance with the positive axes shown in Fig. 5.1. The partial restraints, by translational and rotational springs, have negative contributions based on the displacements (Bouma, 2000) stated in Eq. (5.7) and Eq. (5.9). Furthermore, the change of the NC in the cross-section introduces additional forces based on the development of the internal distance to the support. The vertical spring force is affected by the curvature and an additional moment is introduced based on the total vertical force and the internal distance:

$$F_{y_{S_{tot}}} = F_{y_S} - K_{y_S} u_{y_{max}} = F_{y_S} - K_{y_S}\left(\varepsilon_0 + \kappa\left(\frac{W}{2} - x_{NC}\right)\right)\frac{H}{2}$$

$$\begin{aligned} F_{\varphi_{S_{tot}}} &= F_{\varphi_S} - K_{\varphi_S}\varphi_{max} + F_{y_{S_{tot}}}\left(\frac{W}{2} - x_{NC}\right) \\ &= F_{\varphi_S} - K_{\varphi_S}\kappa\frac{H}{2} + \left(F_{y_S} - K_{y_S}\left(\varepsilon_0 + \kappa\left(\frac{W}{2} - x_{NC}\right)\right)\frac{H}{2}\right)\left(\frac{W}{2} - x_{NC}\right) \end{aligned} \tag{5.10}$$

where

$F_{y_{S_{tot}}}$	[N]	Total vertical force at the support
$F_{\varphi_{S_{tot}}}$	[Nmm]	Total moment at the support
F_{y_S}	[N]	External load through imposed axial force at the support
F_{φ_S}	[Nmm]	External load through imposed moment at the support
K_{y_S}	[N/mm]	Translational spring stiffness at the support
K_{φ_S}	[Nmm/rad]	Rotational spring stiffness at the support
$u_{y_{max}}$	[mm]	Maximum vertical displacement at the support
φ_{max}	[rad]	Maximum rotation at the support

The out-of-plane direction

Until now the element is discussed through consideration of the in-plane cross-sectional forces and deformations. However, the temperature gradient, for instance, acts as a uniform temperature strain also across the thickness. By only considering the in-plane behaviour, the out-of-plane direction is assumed not to introduce any form of restraint (Timoshenko & Goodier, 1970). This assumption becomes less valid in case the dimension in depth direction increases. The element can be thought as supported by adjacent elements exhibiting a similar behaviour, causing restraint in the out-of-plane deformation. This introduces additional forces that enhances the in-plane stress state as well as cause stresses to develop based on restraint in depth direction (Timoshenko & Goodier, 1970). A more elaborate discussion regarding this topic is left for later in this chapter in the section dealing with continuum mechanics.

5.1.4 Equilibrium between structural and cross-sectional forces

The balance of vertical and rotational equilibrium allows to relate the structural forces at the boundary to the internal cross-sectional forces (Hartsuijker & Welleman, 2007; Lagace, 2001). The vertical equilibrium equation is based on Eq. (5.6) and Eq. (5.10):

$$\begin{gathered}\sum V = 0 \rightarrow -N + F_{y_{S_{tot}}} = 0 \\ -\int_A E(\varepsilon_0 - \varepsilon_T)dA + F_{y_S} - K_{y_S}\left(\varepsilon_0 + \kappa\left(\frac{W}{2} - x_{NC}\right)\right)\frac{H}{2} = 0\end{gathered} \tag{5.11}$$

Similar considerations obtain rotational equilibrium which after rearranging reads:

$$\begin{gathered}\sum M = 0 \rightarrow -M + F_{\varphi_{S_{tot}}} = 0 \\ -\int_A E(\kappa x_{rel} - \varepsilon_T)x_{rel}dA + F_{\varphi_S} + F_{y_S}\left(\frac{W}{2} - x_{NC}\right) - K_{\varphi_S}\kappa\frac{H}{2} \\ - K_{y_S}\left(\varepsilon_0 + \kappa\left(\frac{W}{2} - x_{NC}\right)\right)\frac{H}{2}\left(\frac{W}{2} - x_{NC}\right) = 0\end{gathered} \tag{5.12}$$

Eq. (5.11) and Eq. (5.12) are expressed in the extensional strain and curvature respectively. The change of the NC causes both deformation parameters to become coupled:

$$\begin{gathered}\varepsilon_0 = \frac{\int_A E\varepsilon_T dA + F_{y_S} - \kappa K_{y_S}\left(\frac{W}{2} - x_{NC}\right)\frac{H}{2}}{\int_A EdA + K_{y_S}\frac{H}{2}} \\ \kappa = \frac{\int_A E\varepsilon_T x_{rel}dA + F_{\varphi_S} + F_{y_S}\left(\frac{W}{2} - x_{NC}\right) - \varepsilon_0 K_{y_S}\left(\frac{W}{2} - x_{NC}\right)\frac{H}{2}}{\int_A Ex_{rel}^2 dA + K_{\varphi_S}\frac{H}{2} + K_{y_S}\left(\frac{W}{2} - x_{NC}\right)^2\frac{H}{2}}\end{gathered} \tag{5.13}$$

The internal loading by the imposed temperature strain gradient as well as the extensional and bending stiffnesses are introduced to remove the integrals and simplify these relationships.

The extensional strain is mainly determined by the vertical loading and the corresponding stiffness. The imposed moment and bending stiffness govern, for the most part, the curvature:

$$\varepsilon_0 = \frac{N_T + F_{y_S} - \kappa K_{y_S}\left(\frac{W}{2} - x_{NC}\right)\frac{H}{2}}{EA + K_{y_S}\frac{H}{2}}$$
$$\kappa = \frac{M_T + F_{\varphi_S} - \left(\varepsilon_0 K_{y_S}\frac{H}{2} - F_{y_S}\right)\left(\frac{W}{2} - x_{NC}\right)}{EI + K_{\varphi_S}\frac{H}{2} + K_{y_S}\left(\frac{W}{2} - x_{NC}\right)^2\frac{H}{2}} \tag{5.14}$$

with

$$EA = \int_A E dA \qquad N_T = \int_A E\varepsilon_T dA$$

$$EI = \int_A E x_{rel}^2 dA \qquad M_T = \int_A E\varepsilon_T x_{rel} dA$$

where

I	[mm^4]	Moment of inertia of the cross-section of the structural element
EA	[N]	Extensional stiffness of the cross-section of the structural element
EI	[Nmm^2]	Bending stiffness of the cross-section of the structural element
N_T	[N]	Total thermal normal force acting on the cross-section
M_T	[Nmm]	Total thermal moment acting on the cross-section

5.1.5 Limit states in the structural behaviour

The deformation and resulting stress development have several limit states reflecting the type of loading as well as the type of restraint. Three limit states are defined, based on Eq. (5.14), to indicate the difference between structural and fire loading. A fourth limit state, representing the academic case of no stresses, obtained by Eq. (5.5), is also presented.

1st limit state - structural element without fire exposure

This limit state corresponds to an element partially restrained by spring support conditions and loaded by external forces. However, the element is not exposed to a fire resulting in the commonly used mechanical relationships for extension and curvature including the restraint (Hartsuijker & Welleman, 2007):

$$\varepsilon_0 = \frac{\overbrace{N_T}^{=0} + F_{y_S} - \kappa K_{y_S}\overbrace{\left(\frac{W}{2} - x_{NC}\right)}^{=0}\frac{H}{2}}{EA + K_{y_S}\frac{H}{2}} = \frac{F_{y_S}}{EA + K_{y_S}\frac{H}{2}}$$
$$\kappa = \frac{\overbrace{M_T}^{=0} + F_{\varphi_S} - \left(\varepsilon_0 K_{y_S}\frac{H}{2} - F_{y_S}\right)\overbrace{\left(\frac{W}{2} - x_{NC}\right)}^{=0}}{EI + K_{\varphi_S}\frac{H}{2} + K_{y_S}\underbrace{\left(\frac{W}{2} - x_{NC}\right)^2}_{=0}\frac{H}{2}} = \frac{F_{\varphi_S}}{EI + K_{\varphi_S}\frac{H}{2}} \tag{5.15}$$

2nd limit state - element with fire exposure

This opposite limit state corresponds to an unrestrained element exposed to a fire. The thermal normal force and moment are resisted by the cross-section. The thermal degradation of Young's modulus directly influences the stiffness and deformation:

$$\varepsilon_0 = \frac{N_T + \overbrace{F_{y_S}}^{=0} - \kappa \overbrace{K_{y_S}}^{=0}\left(\frac{W}{2} - x_{NC}\right)\frac{H}{2}}{EA + \underbrace{K_{y_S}}_{=0}\frac{H}{2}} = \frac{N_T}{EA}$$

$$\kappa = \frac{M_T + \overbrace{F_{\varphi_S}}^{=0} - \left(\varepsilon_0 \overbrace{K_{y_S}}^{=0}\frac{H}{2} - \overbrace{F_{y_S}}^{=0}\right)\left(\frac{W}{2} - x_{NC}\right)}{EI + \underbrace{K_{\varphi_S}}_{=0}\frac{H}{2} + \underbrace{K_{y_S}}_{=0}\left(\frac{W}{2} - x_{NC}\right)^2\frac{H}{2}} = \frac{M_T}{EI} \tag{5.16}$$

3rd limit state - full restraint

Another possibility is that the element is completely restrained during fire exposure. The thermal normal force and moment are counteracted by a compressive axial force and counteracting moment. Spring action is omitted since no deformations can occur, leading to the following relationship for the axial force:

$$\varepsilon_0 = \frac{N_T + F_{y_S} - \overbrace{\kappa}^{=0} K_{y_S}\left(\frac{W}{2} - x_{NC}\right)\frac{H}{2}}{EA + K_{y_S}\frac{H}{2}} = 0 \tag{5.17}$$

$$N_T + F_{y_S} = 0 \rightarrow F_{y_S} = -N_T$$

The counteracting moment is defined by the thermal moment decreased by an additional moment, based on the coinciding thermal normal force:

$$\kappa = \frac{M_T + F_{\varphi_S} - \left(\overbrace{\varepsilon_0}^{=0} K_{y_S}\frac{H}{2} - F_{y_S}\right)\left(\frac{W}{2} - x_{NC}\right)}{EI + K_{\varphi_S}\frac{H}{2} + K_{y_S}\left(\frac{W}{2} - x_{NC}\right)^2\frac{H}{2}} = 0$$

$$M_T + F_{\varphi_S} + F_{y_S}\left(\frac{W}{2} - x_{NC}\right) = 0 \tag{5.18}$$

$$\rightarrow F_{\varphi_S} = -M_T - F_{y_S}\left(\frac{W}{2} - x_{NC}\right) = -M_T + N_T\left(\frac{W}{2} - x_{NC}\right)$$

4th limit state - element with no stress development

The final limit state reflects the possibility for thermal deformation without stresses. The imposed strain is thus equal to the total strain (van Breugel, et al., 1998). In case Young's modulus is unaffected can the temperature strain only be constant or linear varying:

$$\sigma = E(\varepsilon_0 + \kappa x_{rel} - \varepsilon_T) = 0$$

$$\varepsilon_0 + \kappa x_{rel} - \varepsilon_T = 0 \rightarrow \varepsilon_T = \varepsilon_0 + \kappa x_{rel} = \varepsilon \tag{5.19}$$

5.1.6 Numerical approximation of the deformation and stress relationships

The integrals in Eq. (5.14) can numerically be approximated using the cross-sectional element discretisation from the previous chapter. The relationships commonly used in mechanics are introduced with the moment of inertia based on Steiner's rule (Hartsuijker & Welleman, 2007). This allows to define the integrals by summation across the element distribution:

$$EA = \int_A E dA \approx \sum_{i=1}^{n_{tot}} E_i A = \sum_{i=1}^{n_{tot}} E_i (D\Delta x)$$

$$ES = \int_A E x dA \approx \sum_{i=1}^{n_{tot}} E_i A x_i = \sum_{i=1}^{n_{tot}} E_i (D\Delta x) x_i \tag{5.20}$$

$$EI = \int_A E x_{rel}^2 dA \approx \sum_{i=1}^{n_{tot}} E_i I_i = \sum_{i=1}^{n_{tot}} E_i \left(\frac{D(\Delta x)^3}{12} + D\Delta x \left(x_{rel_i} \right)^2 \right)$$

where

$\cdots_i$		Indication for the node number, located at the centre of the element
D	[mm]	Unit thickness in depth direction of the structural element
Δx	[mm]	Constant element size distributed across the width
n_{tot}	[-]	Total number of nodes

The thermal normal force and moment are based on similar relationships reflecting the local expansion force and resulting moment contributions respectively:

$$N_T = \int_A E \varepsilon_T dA \approx \sum_{i=1}^{n_{tot}} E_i A \varepsilon_{T_i} = \sum_{i=1}^{n_{tot}} E_i (D\Delta x) \varepsilon_{T_i}$$

$$M_T = \int_A E \varepsilon_T x_{rel} dA \approx \sum_{i=1}^{n_{tot}} E_i A \varepsilon_{T_i} x_{rel_i} = \sum_{i=1}^{n_{tot}} E_i (D\Delta x) \varepsilon_{T_i} x_{rel_i} \tag{5.21}$$

The removal of the static moment contributions in the vertical and rotational equilibrium conditions requires that the origin of the axes is positioned at the NC (Hartsuijker & Welleman, 2007). So, Eq. (5.3) is approximated by using similar summations as previously established:

$$x_{NC} \approx \frac{\sum_{i=1}^{n_{tot}} E_i A x_i}{\sum_{i=1}^{n_{tot}} E_i A} \tag{5.22}$$

The numerical approximation of the integrals in the vertical equilibrium condition, defined in Eq. (5.14), reflects the imposed normal force and the extensional stiffness:

$$\varepsilon_0 \approx \frac{\sum_{i=1}^{n_{tot}} \left(E_i A \varepsilon_{T_i} \right) + F_{y_S} - \kappa K_{y_S} \left(\frac{W}{2} - x_{NC} \right) \frac{H}{2}}{\sum_{i=1}^{n_{tot}} (E_i A) + K_{y_S} \frac{H}{2}} \tag{5.23}$$

The rotational equilibrium condition is approximated by the introduction of the imposed moment and the bending stiffness:

$$\kappa \approx \frac{\sum_{i=1}^{n_{tot}}\left(E_i A \varepsilon_{T_i} x_{rel_i}\right) + F_{\varphi_S} - \left(\varepsilon_0 K_{y_S} \frac{H}{2} - F_{y_S}\right)\left(\frac{W}{2} - x_{NC}\right)}{\sum_{i=1}^{n_{tot}}(E_i I_i) + K_{\varphi_S} \frac{H}{2} + K_{y_S}\left(\frac{W}{2} - x_{NC}\right)^2 \frac{H}{2}} \tag{5.24}$$

The resulting stress state is based on Eq. (5.5) and is governed by the constant extensional strain and curvature defined by Eq. (5.23) and Eq. (5.24) respectively. However, both deformation properties are coupled, requiring a first solution before implementation into:

$$\sigma_i = E_i\left(\varepsilon_0 + \kappa x_{rel_i} - \varepsilon_{T_i}\right) \tag{5.25}$$

Finally, the reaction forces at the support are deduced from Eq. (5.10) based on the applied loading and the translational and rotational springs. Vertical displacement and rotation at the support are defined as follows:

$$\begin{aligned} R_{y_{S_{tot}}} &= F_{y_S} - K_{y_S} u_{y_{max}} \\ R_{\varphi_{S_{tot}}} &= F_{\varphi_S} - K_{\varphi_S} \varphi_{max} \end{aligned} \tag{5.26}$$

with

$$u_{y_{max}} = \left(\varepsilon_0 + \kappa\left(\frac{W}{2} - x_{NC}\right)\right)\frac{H}{2}$$

$$\varphi_{max} = \kappa \frac{H}{2}$$

where

$R_{y_{S_{tot}}}$	[N]	Total vertical reaction force at the support
$R_{\varphi_{S_{tot}}}$	[Nmm]	Total moment reaction at the support

5.1.7 Deformation and resulting stresses due to various scenarios

The deformation and stress state are determined for a part of a structural element with a width of 250 mm discretised by elements of 2.5 mm. This approach is similar to the cross-sectional schematisation used in the previous chapter. The height of the element is defined as 1000 mm whereas a unit thickness of 1.0 mm in depth direction is used. Deformation and stresses acting in the cross-section are determined for several loading scenarios. Under these circumstances the temperature distribution is defined to be constant or linear as well as based on the gradient caused by fire exposure. In this latter case is the temperature distribution obtained by FDM directly prescribed as internal loading to the cross-section.

The material is assumed to be homogeneous and characterised by the temperature-dependent properties shown in Fig. 5.5. Young's modulus is based on a linear decay using (van Breugel, et al., 1998) since (Eurocode 2, 2011b) does not provide a direct relationship. The imposed temperature strain is mainly determined by the aggregate type from which the concrete is made, characterised as RG or LS (Eurocode 2, 2011b).

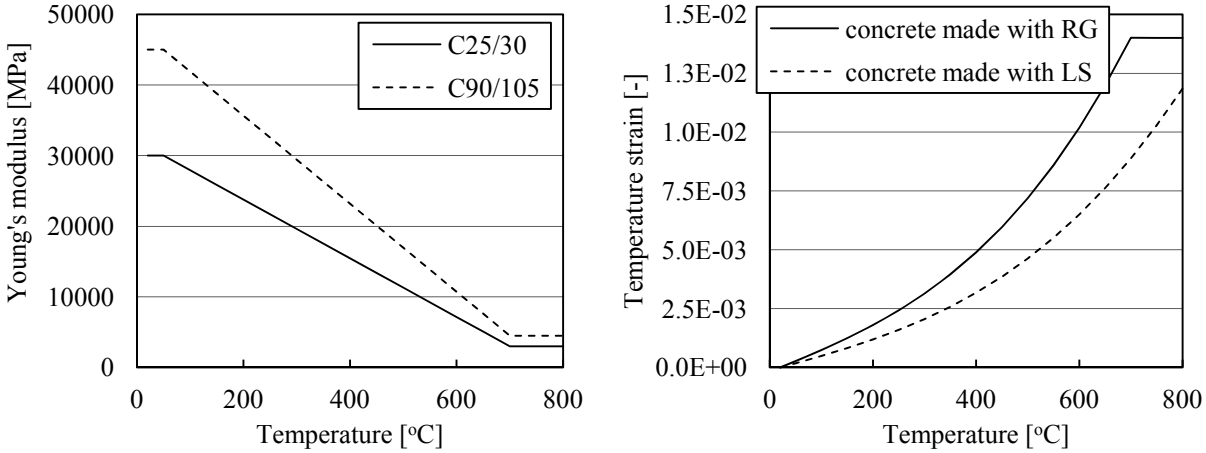

Fig. 5.5 *Development of Young's modulus reflecting a steady reduction with temperature (left)* (van Breugel, et al., 1998). *Temperature strains are independent of the strength class and determined by the aggregate type (right)* (Eurocode 2, 2011b).

It is important to consider that these numerically approximated deformations and stresses are based on linear elasticity and can surpass the tensile strength of the concrete. However, in this simplified cross-sectional model cracking is not included by assuming an infinite strength.

Constant temperature in the cross-section

The cross-section is characterised by the material properties and boundary conditions stated in Table 5.1. The mechanical response, at reference conditions, is governed by the linear stress distribution based on (Hartsuijker & Welleman, 2007):

$$\sigma_{max} = \frac{F_{y_S}}{A} \pm \frac{F_{\varphi_S} x_{max}}{I} = \frac{F_{y_S}}{DW} \pm \frac{F_{\varphi_S} x_{max}}{\frac{1}{12} DW^3} = -8.0 \text{ MPa} \pm -4.8 \text{ MPa} \tag{5.27}$$

where

σ_{max}	[MPa]	Stress at the cross-section at the exterior edge
x_{max}	[mm]	Distance from the cross-sectional centre to an exterior edge

Constant temperature scenarios				
Calculation	**5.1A**	**5.1B**	**5.1C**	**5.1D**
Reference temperature	**20 °C**	**20 °C**	**400 °C**	**400 °C**
Material (homogeneous)				
Strength class	C25/30	C25/30	C25/30	C25/30
Aggregate type	independent	independent	RG	RG
Boundary conditions				
Axial force	-2.0 kN	-2.0 kN	-2.0 kN	-2.0 kN
Moment	-0.05 kNm	-0.05 kNm	-0.05 kNm	-0.05 kNm
Axial spring stiffness		**4 kN/mm**		**4 kN/mm**
Rotational spring stiffness		**20 kNm/rad**		**20 kNm/rad**

Table 5.1 *Influence of a constant temperature on the stress state determined for several scenarios, reflecting external load with the possible addition of partial restraint.*

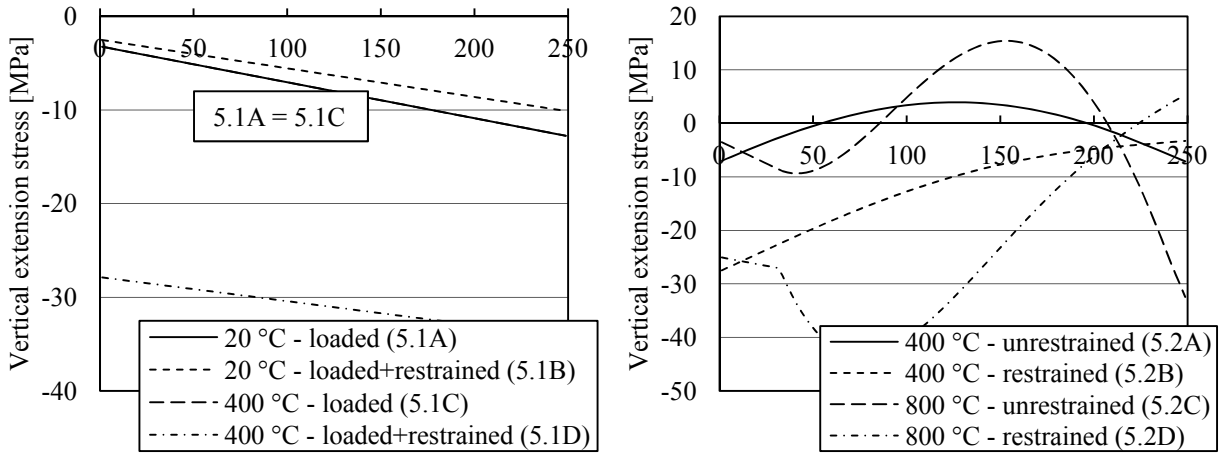

Fig. 5.6 *Stress level in the cross-section, characterised by a uniform temperature, only changing in case of external loading (left). Variation of the stiffness based on a linear temperature distribution leading to non-linear stresses (right).*

By increasing the constant temperature to 400 °C the stiffness in the cross-section reduces, but remains uniform. This is reflected by the left graph in Fig. 5.6 in which the stresses are linear and only influenced by the external partial restraint and loading. Without external partial restraint the stresses remain the same, but the deformation of the cross-section increases.

Linear temperature distribution in the cross-section

The stiffness in the cross-section changes considerably in the case that a linear temperature distribution is imposed defined by the maximum value at the left edge. The stresses become non-linearly extended by the addition of external restraint as indicated in Table 5.2. The stresses in the cross-section of the unrestrained element are, at a maximum temperature of 400 °C, relatively small compared with the other loading scenarios. However, as can be seen in the right graph of Fig. 5.6, the stresses increase substantially for the maximum temperature reaching 800 °C. Especially the element restrained by springs allows the compressive stresses to increase beyond the strength of C25/30. This is attributed to the steep gradient in the imposed temperature strain causing a substantial loading. The stiffness distribution also influences the location of the NC. Increasing the temperature from 400 °C to 800 °C causes the NC to be situated at around 15 mm and 42 mm to the right of the centroidal axis.

Linear temperature scenarios				
Calculation	**5.2A**	**5.2B**	**5.2C**	**5.2D**
Maximum temperature (left edge)	**400 °C**	**400 °C**	**800 °C**	**800 °C**
Material (homogeneous)				
Strength class	C25/30	C25/30	C25/30	C25/30
Aggregate type	RG	RG	RG	RG
Boundary conditions				
Axial spring stiffness		**4 kN/mm**		**4 kN/mm**
Rotational spring stiffness		**20 kNm/rad**		**20 kNm/rad**

Table 5.2 *Two linear temperature gradients, in combination with the possibility for external loading and restraint, are used to determine the stresses in the cross-section.*

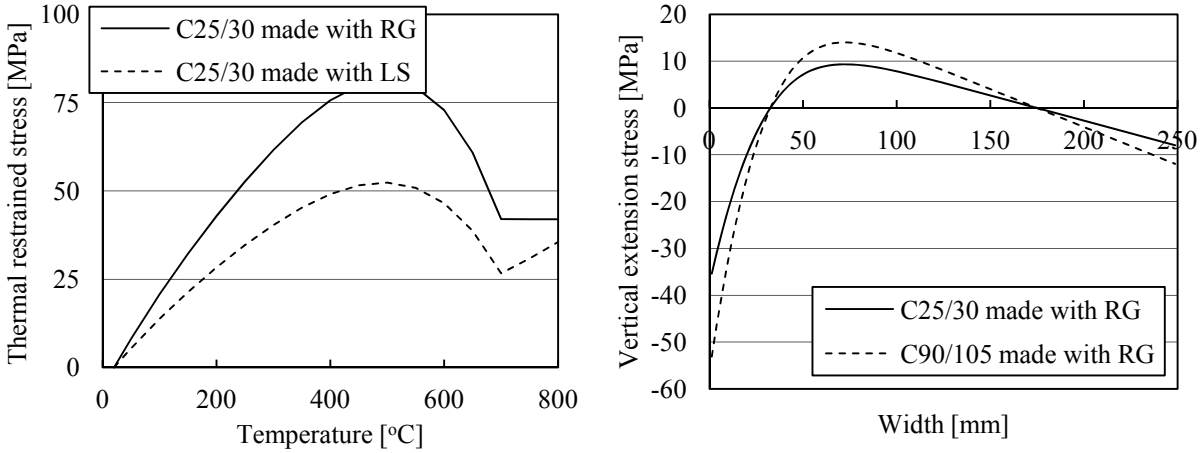

Fig. 5.7 *The product of Young's modulus and the temperature strain as a measure for the imposed thermal load (left)* (Dmitriyev, et al., 1969/1972)*. The increased stiffness of C90/105 affecting the unrestrained stresses caused by the temperature distribution obtained after 900 seconds of fire exposure based on ISO 834 (right).*

At these high temperatures also a reduction in the compressive stresses is observed. The reason for this becomes clear by considering the imposed thermal load by the material due to the temperature increase (Dmitriyev, et al., 1969/1972). This can be expressed through the product of Young's modulus and the temperature strain. These stresses develop in the case that a uniform temperature increase is restrained (Dmitriyev, et al., 1969/1972):

$$\sigma_T = E\varepsilon_T \tag{5.28}$$

where

σ_T	[MPa]	Thermal stress in the case of restrained expansion based on a uniform temperature increase

This relationships is graphically represented by the left graph of Fig. 5.7 based on (Eurocode 2, 2011b). The imposed thermal load increases for both concrete types until about 500 °C after which the degradation of the stiffness causes mitigation. The material is no longer capable of maintaining the thermal load development, governing the observed softening. In the surface layer the compressive stresses relax. The deformation continues, but the zone loading the cross-section reduces in width.

Temperature gradient caused by fire exposure

In the previous chapter the development of the temperature gradient in the cross-section due to fire exposure was determined by means of FDM. These steep temperature distributions are individually imposed as an instantaneous thermal loading of the cross-section. This simplification allows to determine the linear elastic stresses that develop. Recalling from the previous chapter, it was found that exposure according to the ISO 834 leads to a more moderate temperature development compared to the HC fire scenario. The resultant stresses are determined for an unrestrained cross-section loaded by the temperature gradient obtained after 900 seconds of exposure according to ISO 834. Both C25/30 and C90/105 are considered as indicated in Table 5.3.

Fire scenarios (I)		
Calculation	**5.3A**	**5.3B**
Incremental time step size	2.5 sec	2.5 sec
Temperature distribution after	300 / 600 / 900 / 1800 sec	
Material (homogeneous)		
Strength class	**C25/30**	**C90/105**
Aggregate type	RG	RG
Boundary conditions		
Fire scenario	ISO 834	ISO 834
Convective heat transfer coeff.	25 W/m^{2}K	25 W/m^{2}K
Axial force / moment		
Axial / rotational spring stiffness		

Table 5.3 *The influence of fire exposure on the cross-section is investigated based on time-dependent temperature gradients and the concrete strength class.*

The imposed temperature is sufficient to develop a distinctive stress state shown in the right graph of Fig. 5.7 (van Breugel, et al., 1998; Lottman, 2007). The expansion of the heated surface layer is partially restrained, causing the development of compressive stresses. The unheated centre of the cross-section is loaded in tension, forced by the deformation of the cross-section. At the unexposed right edge a small layer of compressive stresses develops. It is also observed that the higher Young's modulus of C90/105 increases the stresses.

In time, this stress state develops reflected by progress of the compression zone into the cross-section as seen in Fig. 5.8. The level of compressive loading increase and is sufficient to form cracks parallel to the heated surface. In the centre of the cross-section the width of the tensile zone reduces, but the load level increases far beyond the tensile strength. This will results in the formation of cracks perpendicular to the surface.

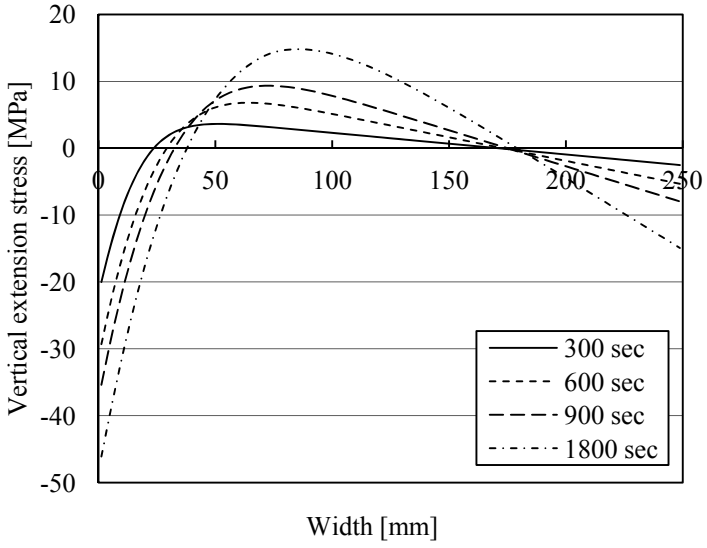

Fig. 5.8 *Exposure of C25/30 made with RG to the ISO 834 fire scenario causing a distinctive stress state. The thermal expansion of the heated surface layer is partially restrained whereas the centre of the cross-section is loaded in tension.*

Fire scenarios (II)				
Calculation	**5.4A**	**5.4B**	**5.4C**	**5.4D**
Incremental time step size	2.5 sec	2.5 sec	2.5 sec	2.5 sec
Temperature distribution after	900 / 1800 sec			
Material (homogeneous)				
Strength class	C25/30	C25/30	C25/30	C25/30
Aggregate type	**RG**	**LS**	**RG**	**RG**
Boundary conditions				
Fire scenario	HC	HC	HC	HC
Convective heat transfer coeff.	50 W/m^{2}K	50 W/m^{2}K	50 W/m^{2}K	50 W/m^{2}K
Axial force			**-2.0 kN**	**VAR.**
Moment			**-0.05 kNm**	**VAR.**
Axial spring stiffness			**4 kN/mm**	
Rotational spring stiffness			**20 kNm/rad**	

Table 5.4 *Thermal-induced stress state caused by fire exposure defined by the adopted scenario as influenced by several material and boundary conditions.*

Increasing the thermal exposure by a HC type of fire extends the loading. Various material and loading conditions, seen in Table 5.4, are examined in combination with the temperature gradient obtained after 900 seconds. From Fig. 5.9 the following observations are made:

- The temperature gradient governs for the most part the stress development. Compared to the ISO 834 fire scenario the unrestrained stresses increase by a factor two.

- The reduced thermal expansion of limestone aggregate moderately affects the stresses. This seems logical by considering the reduction in the imposed thermal load by changing the aggregate type as shown by the left graph of Fig. 5.7.

- Compared to the initial load, presented in Fig. 5.6, the stresses increase considerably. The linear elasticity assumption of superposition of stresses (Hartsuijker & Welleman, 2007) is still applicable as reflected by the externally loaded element.

- The addition of structural restraint increases the compressive stress level in the heated surface layer. The tensile loading acting on the centre of the cross-section is reduced.

- Full restraint of the cross-section results only in compressive stresses. The axial compression force and counteracting moment are variable in time, dependent on the imposed temperature distribution.

- By increasing the width of the cross-section or using a higher strength concrete both the extensional and bending stiffness's increase, affecting the deformation and stresses.

- The level of the stresses and the rate of development indicate a considerable loading of the cross-section. This will result in the rapid formation of cracks, extending on the initial pattern possibly present due to the external loading.

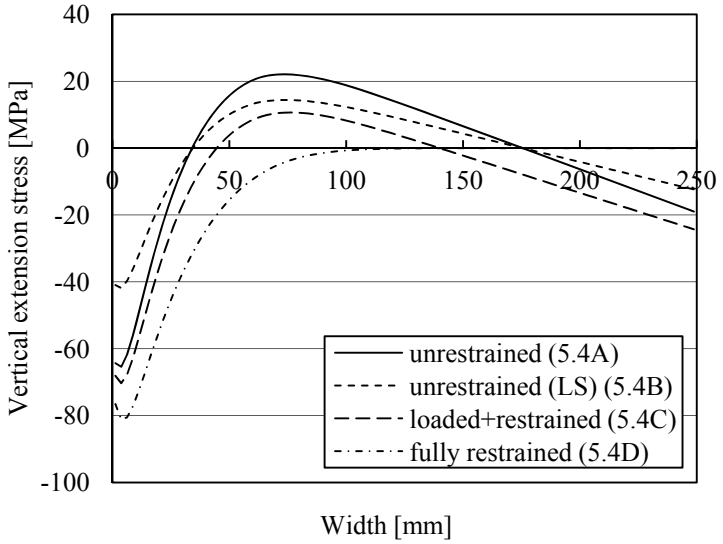

Fig. 5.9 *Loading of the C25/30 cross-section by the temperature gradient, obtained after 900 seconds of exposure based on the HC fire curve, as characterised by several stress states based on the following conditions: unrestrained (A), aggregates with reduced thermal expansion (B), loaded and restrained (C) or fully restrained (D).*

Continued loading is examined by imposing the temperature distribution obtained after 1800 seconds of fire exposure according to the HC curve. The same conditions as displayed in Table 5.4 are used. The resultant stress states shown in Fig. 5.10 indicate the general behaviour as previously mentioned. However, the temperatures in the heated surface layer exceed 500 ^{o}C which causes softening of the material. The imposed thermal load is no longer sustained and stresses reduce. A maximum compressive stress, varying from around 40 MPa to 80 MPa dependent on the loading conditions and the aggregate type, develops. The tensile stresses still indicate development since the temperature increase in the centre is limited.

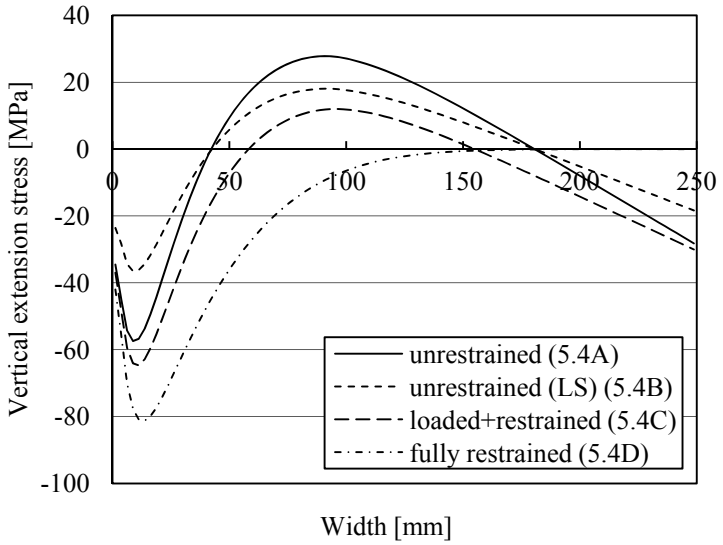

Fig. 5.10 *Temperature distribution after 1800 seconds of fire exposure corresponding to the HC curve indicating softening of the material. The stresses in the C25/30 cross-section are based on unrestrained (A), aggregates with reduced thermal expansion (B), loaded and restrained (C) or fully restrained (D).*

5.1.8 Conclusions with respect to the cross-sectional deformation and stresses

With respect to the deformation and stresses in the cross-section the following conclusions are drawn and remarks are made:

- The stresses in the cross-section are based on the total strain definition reflecting the imposed temperature strain and the linear strain according to Bernoulli's hypothesis (Hartsuijker & Welleman, 2007). This kinematic relationship governs the extensional and curvature deformation, whereas the mechanical strains cause the stresses.

- A constant temperature in the cross-section does not change the location of the NC and leads to a uniform or linear stress (Hartsuijker & Welleman, 2007). A temperature distribution causes a varying stiffness in the cross-section. The NC shifts from the centroidal axis towards the unheated side and the stress disitrbution is no longer linear.

- The equilibrium conditions are defined by the cross-sectional and structural forces, taking the symmetry of the statically indeterminate element into account (Hartsuijker & Welleman, 2007). The shift of the NC causes an eccentricity to develop at the support governing a moment contribution based on the axial force.

- The thermal stress state that develops in a heated cross-section is independent of the load and self-equilibrating (van Breugel, et al., 1998). Extension and curvature is caused by internal loading through a constant normal force and moment.

- Exposure of the element to a fire leads to a temperature gradient loading the cross-section. A distinctive stress state develops, characterised by compression of the heated surface layer. The unheated centre is loaded in tension by the deformed cross-section.

- The schematised C25/30 cross-section reflects that during a HC type of fire the compressive stresses can ultimately reach values between 60 and 80 MPa, dependent on the structural conditions. Both the ISO 834 and especially the HC fire scenario are sufficient to already cause cracking within minutes.

- The product of Young's modulus and the temperature strain can be used to assess the imposed thermal load (Dmitriyev, et al., 1969/1972). Temperatures exceeding 500 ^{o}C cause softening based on the stiffness reduction (Dmitriyev, et al., 1969/1972).

- Aggregates with a reduced thermal expansion limit the internal loading. However, the steep temperature gradient still governs the stress state which is only partially reduced.

- Structural restraint is governed by axial compression and counteracting bending. External forces extend the stresses through the linear elastic principle of superposition.

- Besides the structural loading also the cross-sectional restraint, based on the stiffness and the width governing the extensional and bending stiffness, needs to be considered.

5.2 Definition of the mechanical continuum

The derivation of the cross-sectional deformation and stresses is only applicable for a structural element characterised as a beam. However, commonly also different geometries are possible, requiring a more general approach. This is addressed by the definition of the mechanical continuum (Felippa, 2004b; Wells, 2006) characterised as a homogeneous material based on linear elasticity (Timoshenko & Goodier, 1970). The deformation of the continuum is governed by extension and shear (Felippa, 2004b; Wells, 2006), taking the thermal elongation of the material into account (Timoshenko & Goodier, 1970). Furthermore, also equilibrium of forces across the continuum is defined based on consideration of the stresses (Felippa, 2004b; Wells, 2006). Finally, several simplifications are indicated which allows to state the mechanical relationships commonly used to represent a 2D element (Timoshenko & Goodier, 1970; Prezemieniecki, 1968/1985).

5.2.1 Basic assumptions governing the continuum

With respect to the mechanical continuum the following assumptions are made:

1. The continuum is assumed infinitely strong neglecting, for the moment, the possibility of crack formation. This implies that the continuum only deforms based on material properties characterised by small or infinitesimal strains (Spencer, 1980/2004).

2. The continuum is only loaded at the boundaries by imposed tension or traction (Felippa, 2004b; Wells, 2006). The possibility of a distributed load across the continuum, for instance caused by self-weight, is again neglected.

3. The material is characterised as linear elastic and at the moment assumed isotropic or independent of direction (Timoshenko & Goodier, 1970). The total strain definition is used to include the temperature strains as an initial elongation of the material (Timoshenko & Goodier, 1970).

4. The continuum is governed by extensional and shear loading, neglecting local curvature of the material (Felippa, 2004b; Wells, 2006). The strains are assumed small or infinitesimal while the stresses are approximated by a first order variation (Timoshenko & Goodier, 1970; Spencer, 1980/2004; Wells, 2006).

5. Simplification of the continuum to represent a 2D element is commonly based on either a state of plane stress or a state of plane strain (Timoshenko & Goodier, 1970). Both define the out-of-plane deformation as either unrestrained or restrained respectively with the latter causing additional stresses (Timoshenko & Goodier, 1970).

5.2.2 Schematisation of the mechanical continuum

The stresses loading and the strains deforming the continuum are defined in the 3D Euclidean space (Timoshenko & Goodier, 1970; van Kan, et al., 2008). The continuum is represented through the second order Cauchy stress tensor and consists of extensional stresses defined parallel to the main axes, acting perpendicular to the intersection planes (Timoshenko &

Goodier, 1970; Felippa, 2004b). The shear stresses are defined to be parallel to the intersection planes in accordance with the remaining axes as schematically represented in Fig. 5.11. The diagonal of the tensor reflects the extensional stresses extended by the shear components (Timoshenko & Goodier, 1970; Spencer, 1980/2004; Wells, 2006). The indices refer to the intersection plane and the positive direction respectively as indicated in the following stress tensor:

$$\underline{\boldsymbol{\sigma}} = \begin{bmatrix} \sigma_{xx} & \sigma_{xy} & \sigma_{xz} \\ \sigma_{yx} & \sigma_{yy} & \sigma_{yz} \\ \sigma_{zx} & \sigma_{zy} & \sigma_{zz} \end{bmatrix} \tag{5.29}$$

where

$\underline{\boldsymbol{\sigma}}$ [MPa] Stress tensor (second order)

Establishing equilibrium for the symmetrical continuum allows to reduce the number of unique stress components (Timoshenko & Goodier, 1970). The stress tensor is in fact symmetrical with respect to the diagonal. This is commonly used to simplify the mechanical relationships (Felippa, 2004a; Wells, 2006) as used later in this chapter. The stress tensor also governs the equilibrium relationship with a decomposed applied traction vector along the boundary of the continuum using the unit outward normal vector (Spencer, 1980/2004; Wells, 2006; Felippa, 2004b). The order of the tensor thereby refers to the relationship between two vectors (Dullemond & Peeters, 1991-2010):

$$\underline{\boldsymbol{\sigma}}\boldsymbol{n}\big|_{\Gamma} = \boldsymbol{t} \tag{5.30}$$

where

$\boldsymbol{t}$ [MPa] Traction or tension vector applied along the boundary edge

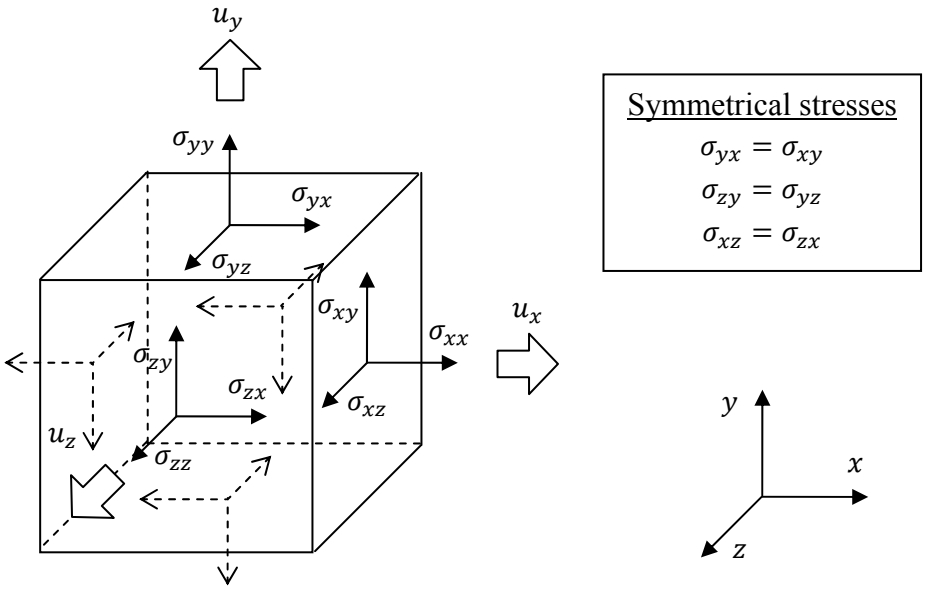

Fig. 5.11 *Schematic representation of a symmetrical continuum in* $\mathbb{R}^3$. *The stress components* (σ) *are based on the reference planes and the positive directions. The deformation is governed by the displacements* (u) *defined along the main axes* (Timoshenko & Goodier, 1970).

Equilibrium of stresses across the continuum

The stress components acting on the continuum are used to define translational and rotational equilibrium. The first, translational equilibrium, is defined by the balance of linear momentum (Wells, 2006). The body force, acting across the continuum, and the applied traction, present along the boundary edge, define equilibrium through (Spencer, 1980/2004; Wells, 2006):

$$\int_{\Omega} \boldsymbol{f} d\Omega + \int_{\Gamma} \boldsymbol{t} d\Gamma = 0 \tag{5.31}$$

with

$$\boldsymbol{f} = \begin{bmatrix} f_x \\ f_y \\ f_z \end{bmatrix} \qquad \boldsymbol{t} = \begin{bmatrix} t_x \\ t_y \\ t_z \end{bmatrix}$$

where

$\boldsymbol{f}$ [MPa] Body force vector defined across the continuum

The Gauss theorem, already used in chapter 4 (van Kan, et al., 2008), redefines the traction as the integral across the domain also inserting the second order stress tensor obtained from Eq. (5.30) (Spencer, 1980/2004; Wells, 2006):

$$\begin{aligned} &\int_{\Omega} \boldsymbol{f} d\Omega + \int_{\Gamma} \underline{\boldsymbol{\sigma}} \boldsymbol{n} d\Gamma = 0 \\ &\int_{\Omega} \boldsymbol{\nabla} \cdot \underline{\boldsymbol{\sigma}} + \boldsymbol{f} d\Omega = 0 \end{aligned} \tag{5.32}$$

Eq. (5.32) must also hold true for all sub-domains which allows the removal of the integral and obtains the balance of linear momentum (Spencer, 1980/2004; Wells, 2006). Again the body forces are omitted. This PDE is extended by Dirichlet essential boundary conditions or Neumann natural boundary conditions (van Kan, et al., 2008):

$$\boldsymbol{\nabla} \cdot \underline{\boldsymbol{\sigma}} + \overset{=0}{\tilde{\tilde{\boldsymbol{f}}}} = 0 \rightarrow \boldsymbol{\nabla} \cdot \underline{\boldsymbol{\sigma}} = 0 \tag{5.33}$$

For a 2D continuum, this relationship represents horizontal and vertical equilibrium as shown in Fig. 5.12 (Timoshenko & Goodier, 1970). The stress resultants acting on the continuum while using symmetry are related through:

$$\begin{aligned} &\sum H = 0 \rightarrow \frac{\partial \sigma_{xx}}{\partial x} + \frac{\partial \sigma_{xy}}{\partial y} + \overset{=0}{\tilde{\tilde{f}}_x} = 0 \\ &\sum V = 0 \rightarrow \frac{\partial \sigma_{xy}}{\partial x} + \frac{\partial \sigma_{yy}}{\partial y} + \overset{=0}{\tilde{\tilde{f}}_y} = 0 \end{aligned} \tag{5.34}$$

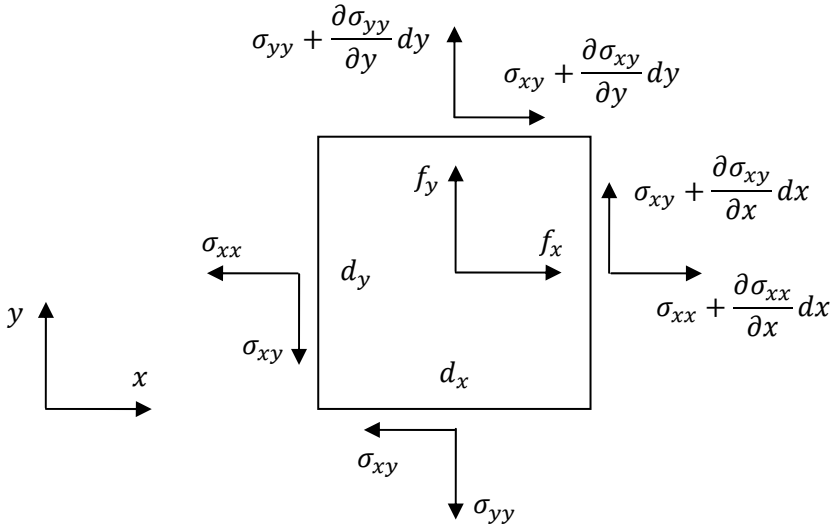

Fig. 5.12 *Schematic representation of the stresses in the mechanical continuum in* $\mathbb{R}^2$. *Stating horizontal and vertical equilibrium defines the stress resultant acting on the continuum* (Blaauwendraad, 2003).

Additionally, also rotational equilibrium or the balance of angular momentum could be stated across the continuum. However, the symmetric stress tensor implies that moment equilibrium is directly fulfilled (Spencer, 1980/2004; Wells, 2006). This also holds true for the 2D continuum since the stresses only cause higher order terms (Timoshenko & Goodier, 1970).

Kinematic relationship governed by the total strain definition

The deformation of the continuum is defined by the second order symmetric strain tensor using the same component definition (Timoshenko & Goodier, 1970; Felippa, 2004b). The deformation and thus the strains are relatively small, commonly referred to as infinitesimal (Timoshenko & Goodier, 1970; Spencer, 1980/2004; Wells, 2006):

$$\underline{\boldsymbol{\varepsilon}} = \begin{bmatrix} \varepsilon_{xx} & \varepsilon_{xy} & \varepsilon_{xz} \\ \varepsilon_{yx} & \varepsilon_{yy} & \varepsilon_{yz} \\ \varepsilon_{zx} & \varepsilon_{zy} & \varepsilon_{zz} \end{bmatrix} \tag{5.35}$$

where

$\underline{\boldsymbol{\varepsilon}}$ [-] Strain tensor (second order)

The strains, deforming the continuum, are defined by the symmetrical gradient (Timoshenko & Goodier, 1970; Wells, 2006). This kinematic relationship characterises each extensional strain by the derivative of the elongation displacement with respect to the same axis as shown in Fig. 5.11 (Timoshenko & Goodier, 1970; Blaauwendraad, 2003). Strains are not developed for rigid body motions, translating or rotating the continuum (Blaauwendraad, 2003). The shear strains are based on the reduction of the original right angle between adjacent planes (Timoshenko & Goodier, 1970; Blaauwendraad, 2003). This angular distortion is, through the symmetrical gradient, defined as half of the shearing strain:

$$\underline{\boldsymbol{\varepsilon}} = \boldsymbol{\nabla}^{\boldsymbol{s}}\boldsymbol{u} = \frac{1}{2}\left(\boldsymbol{\nabla u} + (\boldsymbol{\nabla u})^{\boldsymbol{T}}\right) \tag{5.36}$$

where

$\boldsymbol{u}$	[mm]	Displacement vector

The shearing strain is commonly used to define the shear deformation for a 2D continuum as shown in Fig. 5.13 (Timoshenko & Goodier, 1970; Wells, 2006). Both angles are governed by the derivative of the displacement with respect to the perpendicular axis which in combination leads to the coupled description (Blaauwendraad, 2003).

Material characterisation based on linear elasticity

The continuum is based on the assumption that at the local scale the material is homogeneous and characterised as elastic defined by Young's modulus (Timoshenko & Goodier, 1970). The material is also assumed isotropic (Timoshenko & Goodier, 1970), implying that no direction-dependent stiffness is present. This elastic relationship between the stresses and strains is governed by lateral contractions that develop in the directions perpendicular to the applied extension (Timoshenko & Goodier, 1970). This is defined by Poisson's ratio and couples the three extensional strains and stresses (Timoshenko & Goodier, 1970). The continuum is also loaded in shear which is characterised by the modulus of rigidity defined by Young's modulus and Poisson's ratio (Timoshenko & Goodier, 1970). The resultant fourth order elasticity tensor characterises the continuum similar to Eq. (5.1) (Spencer, 1980/2004; Felippa, 2004b; Wells, 2006):

$$\underline{\boldsymbol{\sigma}} = \boldsymbol{C} : \underline{\boldsymbol{\varepsilon}} \tag{5.37}$$

where

$\boldsymbol{C}$	[MPa]	Elasticity tensor (fourth order)

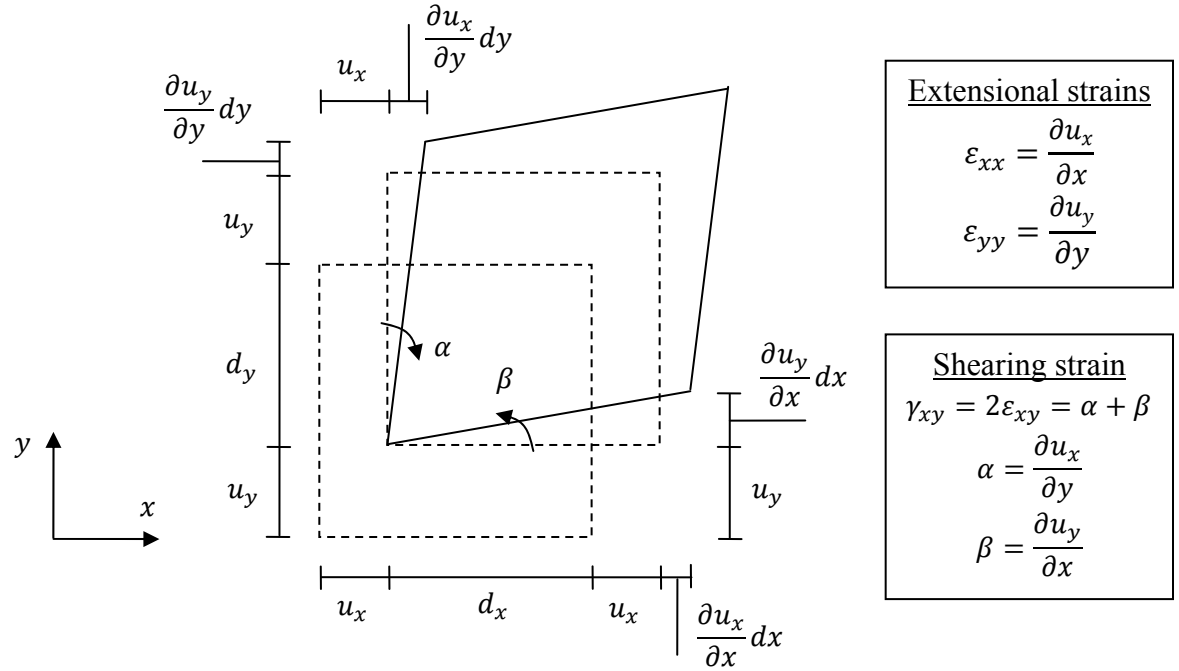

Fig. 5.13 *Schematic representation of the extension and shear deformation of the mechanical continuum in $\mathbb{R}^2$. The horizontal and vertical displacement are assumed linear across the continuum* (Blaauwendraad, 2003).

The strain definition, similar to Eq. (5.4), is extended by the temperature-induced strain tensor which only includes extensional components (Timoshenko & Goodier, 1970). No shear terms are present since free thermal deformation does not involve angular distortion (Timoshenko & Goodier, 1970; Prezemieniecki, 1968/1985). Deformation of the continuum is defined through the total strain tensor using Eq. (5.36) (Timoshenko & Goodier, 1970). The resultant mechanical strain tensor defines the stresses (Timoshenko & Goodier, 1970):

$$\underline{\boldsymbol{\varepsilon}} = \underline{\boldsymbol{\varepsilon_m}} + \underline{\boldsymbol{\varepsilon_T}} \rightarrow \underline{\boldsymbol{\varepsilon_m}} = \underline{\boldsymbol{\varepsilon}} - \underline{\boldsymbol{\varepsilon_T}} = \boldsymbol{\nabla^s u} - \underline{\boldsymbol{\varepsilon_T}} \tag{5.38}$$

where

$\underline{\boldsymbol{\varepsilon}}$	[-]	Total strain tensor (second order)
$\underline{\boldsymbol{\varepsilon_m}}$	[-]	Mechanical strain tensor inducing stresses (second order)
$\underline{\boldsymbol{\varepsilon_T}}$	[-]	Temperature-induced strain tensor (second order)

Inserting into Eq. (5.37) states the stress-strain relationship (Timoshenko & Goodier, 1970):

$$\underline{\boldsymbol{\sigma}} = \boldsymbol{C} : \left(\underline{\boldsymbol{\varepsilon}} - \underline{\boldsymbol{\varepsilon_T}}\right) = \boldsymbol{C} : \left(\boldsymbol{\nabla^s u} - \underline{\boldsymbol{\varepsilon_T}}\right) \tag{5.39}$$

The resultant PDE governing the isotropic mechanical continuum is obtained through inserting Eq. (5.39) into Eq. (5.33) (Spencer, 1980/2004; Wells, 2006):

$$\boldsymbol{\nabla} \cdot \left(\boldsymbol{C} : \left(\boldsymbol{\nabla^s u} - \underline{\boldsymbol{\varepsilon_T}}\right)\right) = 0 \tag{5.40}$$

Simplifications for a 2D continuum

The elasticity relationship stated in Eq. (5.39) is commonly expressed by using engineering notations which defines stresses and strains as vectors considering symmetry of the continuum (Wells, 2006; Prezemieniecki, 1968/1985). Also the shearing strain is introduced instead of half of the angular distortion (Prezemieniecki, 1968/1985; Wells, 2006):

$$\boldsymbol{\sigma} = \boldsymbol{D}(\boldsymbol{\varepsilon} - \boldsymbol{\varepsilon_T}) \tag{5.41}$$

with

$$\boldsymbol{\sigma} = \begin{bmatrix} \sigma_{xx} \\ \sigma_{yy} \\ \sigma_{zz} \\ \sigma_{xy} \\ \sigma_{yz} \\ \sigma_{zx} \end{bmatrix} \qquad \boldsymbol{\varepsilon} = \begin{bmatrix} \varepsilon_{xx} \\ \varepsilon_{yy} \\ \varepsilon_{zz} \\ 2\varepsilon_{xy} \\ 2\varepsilon_{yz} \\ 2\varepsilon_{zx} \end{bmatrix} = \begin{bmatrix} \varepsilon_{xx} \\ \varepsilon_{yy} \\ \varepsilon_{zz} \\ \gamma_{xy} \\ \gamma_{yz} \\ \gamma_{zx} \end{bmatrix} \qquad \boldsymbol{\varepsilon_T} = \begin{bmatrix} \varepsilon_T \\ \varepsilon_T \\ \varepsilon_T \\ 0 \\ 0 \\ 0 \end{bmatrix}$$

$$\varepsilon_{xx} = \frac{\partial u_x}{\partial x}$$

$$\varepsilon_{yy} = \frac{\partial u_y}{\partial y}$$

$$\varepsilon_{zz} = \frac{\partial u_z}{\partial z}$$

$$\boldsymbol{D} = \frac{1}{E} \begin{bmatrix} 1 & -\nu & -\nu & & & \\ -\nu & 1 & -\nu & & 0 & \\ -\nu & -\nu & 1 & & & \\ & & & 2(1+\nu) & 0 & 0 \\ & 0 & & 0 & 2(1+\nu) & 0 \\ & & & 0 & 0 & 2(1+\nu) \end{bmatrix}$$

$$\gamma_{xy} = \frac{\partial u_x}{\partial y} + \frac{\partial u_y}{\partial x}$$

$$\gamma_{yz} = \frac{\partial u_y}{\partial z} + \frac{\partial u_z}{\partial y}$$

$$\gamma_{zx} = \frac{\partial u_z}{\partial x} + \frac{\partial u_x}{\partial z}$$

where

ν	[-]	Poisson's ratio governing the lateral contraction of the material
$\boldsymbol{\sigma}$	[MPa]	Stress vector
$\boldsymbol{\varepsilon}, \boldsymbol{\varepsilon_T}$	[-]	Total strain, temperature-induced strain vector
$\boldsymbol{D}$	[MPa]	Elasticity tensor using engineering notation (fourth order)

A further simplification obtains the elasticity relationship for a 2D continuum based on schematisation of the deformation in the out-of-plane direction. Commonly, the following considerations are used (Timoshenko & Goodier, 1970; Prezemieniecki, 1968/1985):

- For a thin continuum, only in-plane stresses develop assumed continuous across the thickness or depth. This plane stress state governs the extensional strain in depth direction as defined by:

$$\begin{bmatrix}\sigma_{xx}\\ \sigma_{yy}\\ \sigma_{xy}\end{bmatrix} = \frac{E}{1-\nu^2}\begin{bmatrix}1 & \nu & 0\\ \nu & 1 & 0\\ 0 & 0 & \frac{1-\nu}{2}\end{bmatrix}\left(\begin{bmatrix}\varepsilon_{xx}\\ \varepsilon_{yy}\\ \gamma_{xy}\end{bmatrix} - \begin{bmatrix}\varepsilon_T\\ \varepsilon_T\\ 0\end{bmatrix}\right) \tag{5.42}$$

with

$\sigma_{zz} = 0$ $\qquad$ $\sigma_{zx} = \sigma_{yz} = 0$

$\varepsilon_{zz} = -\frac{\nu}{E}(\sigma_{xx} + \sigma_{yy}) + \varepsilon_T = -\frac{\nu}{1-\nu}(\varepsilon_{xx} + \varepsilon_{yy}) + \frac{1+\nu}{1-\nu}\varepsilon_T$ $\qquad$ $\gamma_{yz} = \gamma_{zx} = 0$

- For a uniformly loaded continuum with a relatively large thickness or depth, the out-of-plane strains are assumed restrained. The extensional stress in depth direction is defined by this plane strain state which is expressed by:

$$\begin{bmatrix}\sigma_{xx}\\ \sigma_{yy}\\ \sigma_{xy}\end{bmatrix} = \frac{E}{(1+\nu)(1-2\nu)}\begin{bmatrix}1-\nu & \nu & 0\\ \nu & 1-\nu & 0\\ 0 & 0 & \frac{1-2\nu}{2}\end{bmatrix}\left(\begin{bmatrix}\varepsilon_{xx}\\ \varepsilon_{yy}\\ \gamma_{xy}\end{bmatrix} - \begin{bmatrix}(1+\nu)\varepsilon_T\\ (1+\nu)\varepsilon_T\\ 0\end{bmatrix}\right) \tag{5.43}$$

with

$\varepsilon_{zz} = 0$ $\qquad$ $\gamma_{zx} = \gamma_{yz} = 0$

$\sigma_{zz} = \nu(\sigma_{xx} + \sigma_{yy}) - E\varepsilon_T = \frac{E\nu}{(1+\nu)(1-2\nu)}(\varepsilon_{xx} + \varepsilon_{yy}) - \frac{E}{1-2\nu}\varepsilon_T$ $\qquad$ $\sigma_{yz} = \sigma_{zx} = 0$

5.3 Continuum-based transformations

The material description of the 2D continuum is characterised by the direction-dependent decomposition of displacements, strains and stresses. The respective components are aligned with the axes of the global rectangular coordinate system as for instance indicated by Fig. 5.12 and Fig. 5.13. However, it will prove beneficial to define the displacements, strains and stresses in any set of perpendicular directions (Timoshenko & Goodier, 1970). This requires the definition of a local coordinate system based on rotation of the global coordinate system (Timoshenko & Goodier, 1970; Wells, 2006; Blom, 2009). The various components are related through definition of the rotation-based transformation tensors.

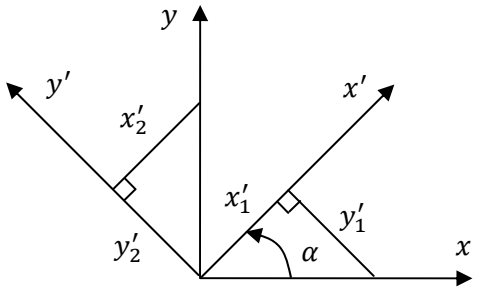

Coordinate relationships

$$x' = x'_1 + x'_2 = \cos\alpha x + \sin\alpha y$$
$$y' = -y'_1 + y'_2 = -\sin\alpha x + \cos\alpha y$$

Fig. 5.14 *Local coordinate system based on rotation of the global coordinate system, both in $\mathbb{R}^2$. Coordinate relationships define the transformation based on the angle of rotation.*

Transformation of coordinate systems

The local coordinate system is rotated in the, positively defined, counter-clockwise direction around the origin as schematically shown in Fig. 5.14. The horizontal and vertical axes are directly decomposed to form local components reflecting also a negative contribution (Wells, 2006; Blom, 2009). The coordinate relationships are defined using vectors through the second order coordinate transformation tensor (Wells, 2006; Blom, 2009). This transformation tensor has an orthogonal basis since both systems have perpendicular coordinate axes:

$$\boldsymbol{x'} = \boldsymbol{T_\alpha x} \tag{5.44}$$

with

$$\boldsymbol{T_\alpha}^{-1} = \boldsymbol{T_\alpha}^{T}$$

$$\boldsymbol{x} = \begin{bmatrix} x \\ y \end{bmatrix} \qquad \boldsymbol{x'} = \begin{bmatrix} x' \\ y' \end{bmatrix} \qquad \boldsymbol{T_\alpha} = \begin{bmatrix} \cos\alpha & \sin\alpha \\ -\sin\alpha & \cos\alpha \end{bmatrix}$$

where

$\boldsymbol{x}, \boldsymbol{x'}$	[mm]	Global, local coordinate system vector
$\boldsymbol{T_\alpha}$	[-]	Transformation tensor based on rotation of the coordinate system (second order)

Transformation of displacements and forces

This relationship is directly applicable to the displacements since these are defined as vector using the respective coordinate systems as a basis (Wells, 2006; Blom, 2009):

$$\boldsymbol{u'} = \boldsymbol{T_\alpha u} \tag{5.45}$$

with

$$\boldsymbol{u} = \begin{bmatrix} u_x \\ u_y \end{bmatrix} \qquad \boldsymbol{u'} = \begin{bmatrix} u_x{}' \\ u_y{}' \end{bmatrix}$$

where

$\boldsymbol{u}, \boldsymbol{u'}$	[mm]	Global, local displacement vector

Force vectors are decomposed using the same coordinate transformation tensor and thus the following holds (Wells, 2006; Blom, 2009):

$$\boldsymbol{F'} = \boldsymbol{T_\alpha F} \tag{5.46}$$

with

$$\boldsymbol{F} = \begin{bmatrix} F_x \\ F_y \end{bmatrix} \qquad \boldsymbol{F'} = \begin{bmatrix} F_x{}' \\ F_y{}' \end{bmatrix}$$

where

$\boldsymbol{F}, \boldsymbol{F'}$	[N]	Global, local force vector

Transformation of stresses

The principle of decomposition is also applicable to stresses. Recalling the relationship between the stress tensor and the applied traction using the unit outward vector (Spencer, 1980/2004). Both vectors are expressed in the local system using the coordinate transformation tensor while exploiting the orthogonal basis (Spencer, 1980/2004):

$$\begin{gathered} \underline{\boldsymbol{\sigma}}\boldsymbol{n} = \boldsymbol{t} \\ \underline{\boldsymbol{\sigma}}\boldsymbol{T_\alpha}^T\boldsymbol{n'} = \boldsymbol{T_\alpha}^T\boldsymbol{t'} \rightarrow \boldsymbol{T_\alpha}\underline{\boldsymbol{\sigma}}\boldsymbol{T_\alpha}^T\boldsymbol{n'} = \boldsymbol{t'} \\ \rightarrow \underline{\boldsymbol{\sigma'}} = \boldsymbol{T_\alpha}\underline{\boldsymbol{\sigma}}\boldsymbol{T_\alpha}^T \end{gathered} \tag{5.47}$$

where

$\underline{\boldsymbol{\sigma}}, \underline{\boldsymbol{\sigma'}}$	[MPa]	Global, local stress tensor (second order)

This general expression is, in this case, focused on the 2D stress state and independent of the plane stress or plane strain assumption (Timoshenko & Goodier, 1970). However, it is more convenient to redefine this relationship using engineering notation and combination of both second order transformation tensors leading to (Timoshenko & Goodier, 1970):

$$\boldsymbol{\sigma'} = \boldsymbol{T_\sigma}\boldsymbol{\sigma} \tag{5.48}$$

with

$$\boldsymbol{\sigma} = \begin{bmatrix} \sigma_{xx} \\ \sigma_{yy} \\ \sigma_{xy} \end{bmatrix} \qquad \boldsymbol{\sigma'} = \begin{bmatrix} \sigma_{xx}{}' \\ \sigma_{yy}{}' \\ \sigma_{xy}{}' \end{bmatrix} \qquad \boldsymbol{T_\sigma} = \begin{bmatrix} \cos^2\alpha & \sin^2\alpha & 2\sin\alpha\cos\alpha \\ \sin^2\alpha & \cos^2\alpha & -2\sin\alpha\cos\alpha \\ -\sin\alpha\cos\alpha & \sin\alpha\cos\alpha & \cos^2\alpha - \sin^2\alpha \end{bmatrix}$$

where

$\boldsymbol{\sigma}, \boldsymbol{\sigma'}$	[MPa]	Global, local stress vector
$\boldsymbol{T_\sigma}$	[-]	Stress transformation tensor (fourth order)

A plane across the continuum with a local coordinate system as seen in Fig. 5.15 is used to elaborate this transformation tensor (Timoshenko & Goodier, 1970). The stresses acting on the plane, aligned with the local coordinate system, must fulfil equilibrium (Timoshenko & Goodier, 1970). This is established by decomposition of the forces. In the same way, for a plane perpendicular to the current coordinate system, the remaining local extensional stress is obtained. Alternatively, also rotation of the previously obtained stress state can be used.

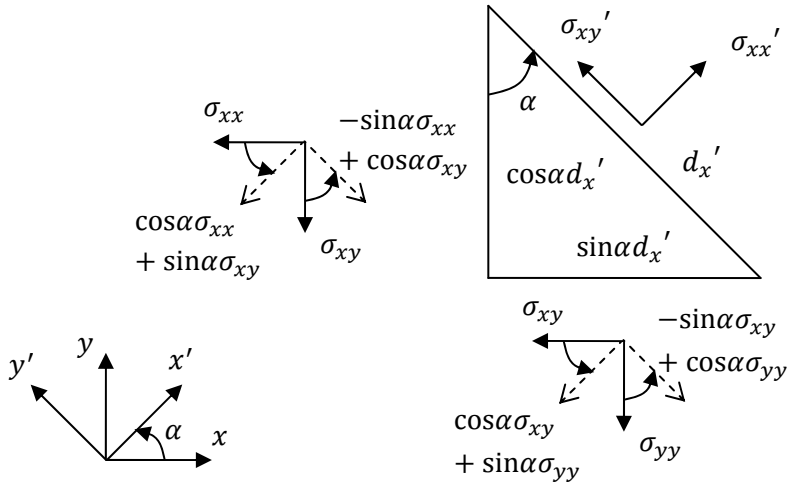

Equilibrium relationships

$$\sum H' = 0 \rightarrow \sigma_{xx}'d_x' - \cos\alpha(\sigma_{xx}\cos\alpha d_x') - \sin\alpha(\sigma_{yy}\sin\alpha d_x') - \sin\alpha(\sigma_{xy}\cos\alpha d_x') - \cos\alpha(\sigma_{xy}\sin\alpha d_x') = 0$$

$$\sigma_{xx}' = \sigma_{xx}\cos^2\alpha + \sigma_{yy}\sin^2\alpha + 2\sigma_{xy}\sin\alpha\cos\alpha$$

$$\sum V' = 0 \rightarrow \sigma_{xy}'d_x' + \sin\alpha(\sigma_{xx}\cos\alpha d_x') - \cos\alpha(\sigma_{yy}\sin\alpha d_x') - \cos\alpha(\sigma_{xy}\cos\alpha d_x') + \sin\alpha(\sigma_{xy}\sin\alpha d_x') = 0$$

$$\sigma_{xy}' = \sigma_{xy}(\cos^2\alpha - \sin^2\alpha) + (\sigma_{yy} - \sigma_{xx})\sin\alpha\cos\alpha$$

Fig. 5.15 *Schematic representation of the decomposition of forces in the mechanical continuum in* $\mathbb{R}^2$. *Horizontal and vertical equilibrium is defined in the local coordinate system* (Timoshenko & Goodier, 1970).

Transformation of strains

The second order coordinate transformation relationships relating the stress tensors also hold true for the strain tensors (Roylance, 2001):

$$\underline{\boldsymbol{\varepsilon}'} = \boldsymbol{T_\alpha}\underline{\boldsymbol{\varepsilon}}\boldsymbol{T_\alpha}^{\boldsymbol{T}} \tag{5.49}$$

where

$\underline{\boldsymbol{\varepsilon}}, \underline{\boldsymbol{\varepsilon}'}$ [-] Global, local strain tensor (second order)

However, it is important to remember that the shear strain, through the continuum definition as seen in Fig. 5.13, is defined as half of the shearing strain (Timoshenko & Goodier, 1970; Blaauwendraad, 2003). This is addressed by using engineering notation while introducing an additional transformation matrix to redefine both strain vectors (Roylance, 2001):

$$\boldsymbol{\varepsilon} = \boldsymbol{T_\gamma}\boldsymbol{\varepsilon}^* \tag{5.50}$$

with

$$\boldsymbol{\varepsilon} = \begin{bmatrix}\varepsilon_{xx}\\ \varepsilon_{yy}\\ \gamma_{xy}\end{bmatrix} \qquad \boldsymbol{\varepsilon}^* = \begin{bmatrix}\varepsilon_{xx}\\ \varepsilon_{yy}\\ \frac{1}{2}\gamma_{xy}\end{bmatrix} \qquad \boldsymbol{T_\gamma} = \begin{bmatrix}1 & 0 & 0\\ 0 & 1 & 0\\ 0 & 0 & 2\end{bmatrix}$$

where

$\boldsymbol{\varepsilon}, \boldsymbol{\varepsilon}^*$	[-]	Global strain vector expressed in (half of) the shearing strain
$\boldsymbol{T}_{\boldsymbol{\gamma}}$	[-]	Transformation matrix to define the shearing strain

The strains are transformed using the inverse of this diagonal matrix applied to the transformation tensor defined by Eq. (5.48) (Roylance, 2001). A new transformation tensor is defined which incorporates directly the shearing strain (Timoshenko & Goodier, 1970):

$$\begin{gathered} \boldsymbol{\varepsilon'}^* = \boldsymbol{T}_{\boldsymbol{\sigma}} \boldsymbol{\varepsilon}^* \\ \boldsymbol{T}_{\boldsymbol{\gamma}}{}^{-1} \boldsymbol{\varepsilon'} = \boldsymbol{T}_{\boldsymbol{\sigma}} \boldsymbol{T}_{\boldsymbol{\gamma}}{}^{-1} \boldsymbol{\varepsilon} \\ \rightarrow \boldsymbol{\varepsilon'} = \boldsymbol{T}_{\boldsymbol{\gamma}} \boldsymbol{T}_{\boldsymbol{\sigma}} \boldsymbol{T}_{\boldsymbol{\gamma}}{}^{-1} \boldsymbol{\varepsilon} = \boldsymbol{T}_{\boldsymbol{\varepsilon}} \boldsymbol{\varepsilon} \end{gathered} \tag{5.51}$$

with

$$\boldsymbol{\varepsilon} = \begin{bmatrix} \varepsilon_{xx} \\ \varepsilon_{yy} \\ \gamma_{xy} \end{bmatrix} \qquad \boldsymbol{\varepsilon'} = \begin{bmatrix} \varepsilon_{xx}{}' \\ \varepsilon_{yy}{}' \\ \gamma_{xy}{}' \end{bmatrix} \qquad \boldsymbol{T}_{\boldsymbol{\varepsilon}} = \begin{bmatrix} \cos^2\alpha & \sin^2\alpha & \sin\alpha\cos\alpha \\ \sin^2\alpha & \cos^2\alpha & -\sin\alpha\cos\alpha \\ -2\sin\alpha\cos\alpha & 2\sin\alpha\cos\alpha & \cos^2\alpha - \sin^2\alpha \end{bmatrix}$$

where

$\boldsymbol{\varepsilon}, \boldsymbol{\varepsilon'}$	[-]	Global, local strain vector expressed in the shearing strain
$\boldsymbol{T}_{\boldsymbol{\varepsilon}}$	[-]	Strain transformation tensor (fourth order)

5.4 Conclusions with respect to the continuum

The balance of linear momentum governing the continuum is based on:

- The PDE reflecting translational equilibrium between the body forces, acting across the continuum, and the tractions, imposed along the boundary edges, stated in Eq. (5.33) (Spencer, 1980/2004; Wells, 2006).

Regarding the definition of the continuum the following conclusions and remarks are made:

- Deformation of the continuum is defined by the symmetrical gradient of the displacements (Timoshenko & Goodier, 1970; Wells, 2006). The extension and shear strains are assumed infinitesimal in which the latter is defined as half of the shearing strain (Timoshenko & Goodier, 1970; Spencer, 1980/2004; Wells, 2006).

- The total strain definition is obtained by the introduction of the temperature-induced strain tensor reflecting only extensional components (Timoshenko & Goodier, 1970).

- The stresses and strains acting on the continuum are governed by second order symmetrical tensors (Timoshenko & Goodier, 1970). Both are related through the fourth order linear elastic tensor assuming isotropic conditions (Timoshenko & Goodier, 1970; Spencer, 1980/2004; Wells, 2006).

- Simplification of the continuum is commonly defined by stress and strain vectors related through the plane stress or plane strain elasticity tensor stated in Eq. (5.42) and Eq. (5.43) respectively (Timoshenko & Goodier, 1970; Prezemieniecki, 1968/1985).

Directional dependence in the definition of the displacements, strains and stresses across the continuum lead to the following:

- Displacements are decomposed by using the coordinate system transformation defined in Eq. (5.44) by the second order tensor (Wells, 2006; Blom, 2009).

- The tensor basis of the stresses and strains implies that decomposition involves a fourth order transformation which originates from rotation of the coordinate system (Spencer, 1980/2004). Using engineering notation allows to define the basic stress transformation relationship shown in Eq. (5.48) (Timoshenko & Goodier, 1970).

5.5 Stresses induced by pore pressure development

The continuum description will form the basis for the derivation of the FEM fracture mechanics model presented in chapter 8. However, this elastic material description can already be used to obtain insight into the mechanical consequences of pore pressures. Most important is to relate the pressure development to stresses in the surrounding material and possible fracture (Felicetti, et al., 2012). Limited information on this subject is, at present, available in literature. Mostly an effective stress-based approach is used in which the pressure is imposed on the surrounding material (Zienkiewicz, et al., 2005) taking sometimes also the level of saturation into account (Gray & Schrefler, 2001). In this paragraph the elastic stresses in a plate surrounding a pressure-loaded pore are determined. For this purpose, the PDE governing compatibility in rectangular coordinates is stated (Timoshenko & Goodier, 1970). Transformation to polar coordinates and solution allows to define the elastic stress state.

5.5.1 Basic assumptions governing the elastic stress state

The pressure-induced stresses are mainly based on the assumptions defining the 2D elastic and isotropic continuum. However some additional considerations are given:

1. The horizontal and vertical displacements of the continuum define both extensional strains and the shearing strain (Timoshenko & Goodier, 1970). This inequality is solved by definition of the compatibility condition (Timoshenko & Goodier, 1970).

2. Body forces and initial temperature strains are neglected. The compatibility equation is thus independent of the elastic material properties as well as the plane stress or plane strain assumption (Timoshenko & Goodier, 1970).

3. Transformation from rectangular to polar coordinates redefines the basis used in the Euclidean space (van Kan, et al., 2008). The Cartesian coordinates are express using the radius and the angle with respect to the origin (Timoshenko & Goodier, 1970).

5.5.2 Elasticity in rectangular coordinates

The stress state present in the 2D elastic and isotropic continuum is defined by the horizontal and vertical equilibrium equations stated in Eq. (5.34) (Timoshenko & Goodier, 1970). This description is statically indeterminate since three stresses are defined, requiring consideration of the elastic deformations (Timoshenko & Goodier, 1970).

Compatibility equation

The extensional strains are used to define the shearing strain by differentiation of the expressions provided in Fig. 5.13 (Timoshenko & Goodier, 1970). The resultant compatibility condition expresses the relationship between the strains ensuring continuously varying displacements across the continuum (Timoshenko & Goodier, 1970):

$$\frac{\partial^2 \gamma_{xy}}{\partial x \partial y} = \frac{\partial^2 \varepsilon_{xx}}{\partial y^2} + \frac{\partial^2 \varepsilon_{yy}}{\partial x^2} \tag{5.52}$$

Moreover, differentiation and addition of both equilibrium equations allows to define the shear stress based on both extensional stresses (Timoshenko & Goodier, 1970):

$$2\frac{\partial^2 \sigma_{xy}}{\partial x \partial y} = -\left(\frac{\partial^2 \sigma_{xx}}{\partial x^2} + \frac{\partial^2 \sigma_{yy}}{\partial y^2}\right) \tag{5.53}$$

By introducing the constitutive relationships governing linear elasticity in Eq. (5.52), differentiation while assuming a constant Poisson's ratio and inserting Eq. (5.53), the PDE for compatibility is obtained (Timoshenko & Goodier, 1970). The Laplacian operator of the extensional stresses is, by omitting the temperature strains, independent of the elastic material properties and assumptions (Timoshenko & Goodier, 1970):

$$\begin{aligned} \frac{\partial^2 \sigma_{xx}}{\partial x^2} + \frac{\partial^2 \sigma_{xx}}{\partial y^2} + \frac{\partial^2 \sigma_{yy}}{\partial x^2} + \frac{\partial^2 \sigma_{yy}}{\partial y^2} &= -\frac{\partial^2}{\partial x^2}(E\varepsilon_T) - \frac{\partial^2}{\partial y^2}(E\varepsilon_T) \\ \left(\frac{\partial^2}{\partial x^2} + \frac{\partial^2}{\partial y^2}\right)(\sigma_{xx} + \sigma_{yy}) &= \boldsymbol{\Delta}(\sigma_{xx} + \sigma_{yy}) = 0 \end{aligned} \tag{5.54}$$

5.5.3 Elasticity in polar coordinates

The Cartesian rectangular coordinates are expressed using the direction or angle and the length or radius with respect to the origin as seen in Fig. 5.16 (Timoshenko & Goodier, 1970). This defines the partial derivatives as follows (Timoshenko & Goodier, 1970):

$$\begin{aligned} \frac{\partial}{\partial x} &= \frac{\partial}{\partial r}\frac{\partial r}{\partial x} + \frac{\partial}{\partial \theta}\frac{\partial \theta}{\partial x} = \cos\theta \frac{\partial}{\partial r} - \frac{\sin\theta}{r}\frac{\partial}{\partial \theta} \\ \frac{\partial}{\partial y} &= \frac{\partial}{\partial r}\frac{\partial r}{\partial y} + \frac{\partial}{\partial \theta}\frac{\partial \theta}{\partial y} = \sin\theta \frac{\partial}{\partial r} + \frac{\cos\theta}{r}\frac{\partial}{\partial \theta} \end{aligned} \tag{5.55}$$

Hence, the first and especially the second order derivates are (Timoshenko & Goodier, 1970):

$$\begin{aligned} \frac{\partial^2}{\partial x^2} &= \cos^2\theta \frac{\partial^2}{\partial r^2} + \sin^2\theta \left(\frac{1}{r}\frac{\partial}{\partial r} + \frac{1}{r^2}\frac{\partial^2}{\partial \theta^2}\right) + \sin 2\theta \left(\frac{1}{r^2}\frac{\partial}{\partial \theta} - \frac{1}{r}\frac{\partial^2}{\partial r \partial \theta}\right) \\ \frac{\partial^2}{\partial y^2} &= \sin^2\theta \frac{\partial^2}{\partial r^2} + \cos^2\theta \left(\frac{1}{r}\frac{\partial}{\partial r} + \frac{1}{r^2}\frac{\partial^2}{\partial \theta^2}\right) - \sin 2\theta \left(\frac{1}{r^2}\frac{\partial}{\partial \theta} - \frac{1}{r}\frac{\partial^2}{\partial r \partial \theta}\right) \\ \frac{\partial^2}{\partial x \partial y} &= -\sin\theta\cos\theta \left(-\frac{\partial^2}{\partial r^2} + \frac{1}{r}\frac{\partial}{\partial r} + \frac{1}{r^2}\frac{\partial^2}{\partial \theta^2}\right) - \cos 2\theta \left(\frac{1}{r^2}\frac{\partial}{\partial \theta} - \frac{1}{r}\frac{\partial^2}{\partial r \partial \theta}\right) \end{aligned} \tag{5.56}$$

Compatibility equation

The transformation of Eq. (5.54) into polar coordinates requires two steps. First, the second order derivatives of the Laplacian operator are redefined using Eq. (5.56) (Timoshenko & Goodier, 1970):

$$\frac{\partial^2}{\partial x^2}+\frac{\partial^2}{\partial y^2}=\frac{\partial^2}{\partial r^2}+\frac{1}{r}\frac{\partial}{\partial r}+\frac{1}{r^2}\frac{\partial^2}{\partial \theta^2} \tag{5.57}$$

The second term reflects both extensional stresses. These are transformed using the first two components of the stress transformation tensor defined in Eq. (5.48). Addition of both stress transformations leads to (Timoshenko & Goodier, 1970):

$$\sigma_{xx}+\sigma_{yy}=\sigma_{rr}+\sigma_{\theta\theta} \tag{5.58}$$

Thus, the PDE for compatibility, expressed in polar coordinates, reflects the Laplacian with respect to the radial and tangential extensional stresses (Timoshenko & Goodier, 1970):

$$\left(\frac{\partial^2}{\partial r^2}+\frac{1}{r}\frac{\partial}{\partial r}+\frac{1}{r^2}\frac{\partial^2}{\partial \theta^2}\right)(\sigma_{rr}+\sigma_{\theta\theta})=\boldsymbol{\Delta}(\sigma_{rr}+\sigma_{\theta\theta})=0 \tag{5.59}$$

Airy's stress function

The commonly adopted solution approach is to use the principal of Airy's stress function (Timoshenko & Goodier, 1970). Through stress transformation the components full filling the equilibrium conditions as shown in Fig. 5.16 are stated (Timoshenko & Goodier, 1970):

$$\sigma_{rr}=\frac{1}{r}\frac{\partial\phi}{\partial r}+\frac{1}{r^2}\frac{\partial^2\phi}{\partial\theta^2} \qquad \sigma_{\theta\theta}=\frac{\partial^2\phi}{\partial r^2} \qquad \sigma_{r\theta}=\frac{1}{r^2}\frac{\partial\phi}{\partial\theta}-\frac{1}{r}\frac{\partial^2\phi}{\partial r\partial\theta} \tag{5.60}$$

where

ϕ [var.] Airy's stress function as solution for a 2D elastic continuum

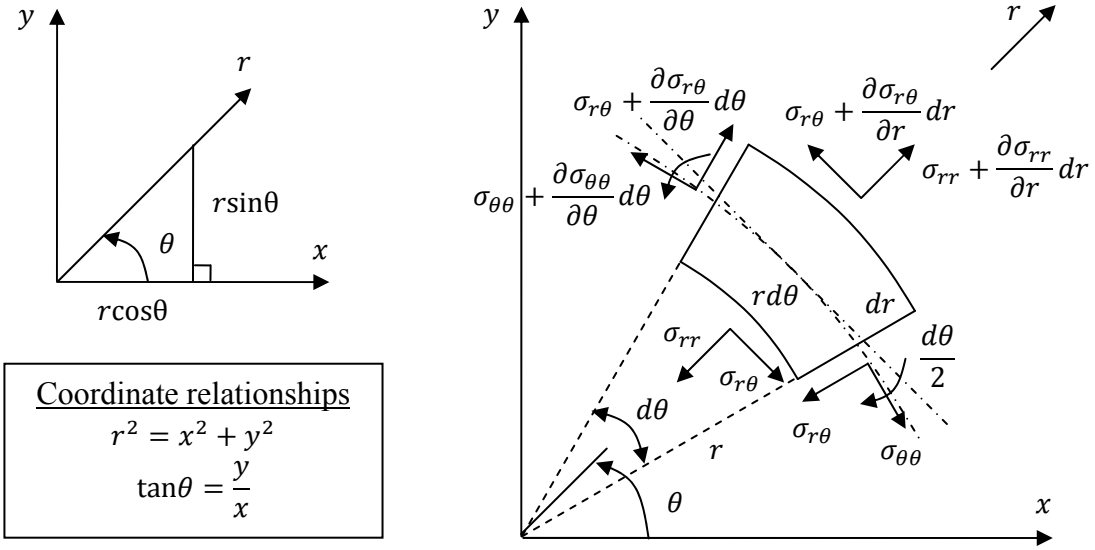

Fig. 5.16 *The polar coordinate system in $\mathbb{R}^2$ expressing the rectangular Cartesian coordinates in the radius and the angle (left). Equilibrium in radial and tangential direction defines the stress components (right)* (Timoshenko & Goodier, 1970).

Substitution of these relationships into the compatibility equation, stated by Eq. (5.59), leads to the following PDE omitting angular dependence (Timoshenko & Goodier, 1970):

$$\frac{\partial^4 \phi}{\partial r^4} + \frac{2}{r}\frac{\partial^3 \phi}{\partial r^3} - \frac{1}{r^2}\frac{\partial^2 \phi}{\partial r^2} + \frac{1}{r^3}\frac{\partial \phi}{\partial r} = 0 \tag{5.61}$$

The solution of Eq. (5.61) is obtained by substitution of Airy's stress function which for polar coordinates takes the following form (Timoshenko & Goodier, 1970):

$$\phi = A\ln r + Br^2 \ln r + Cr^2 + D \tag{5.62}$$

Substitution and differentiation leads to the stresses using Eq. (5.60). The omitted angular dependence is reflected by the absence of shear stresses (Timoshenko & Goodier, 1970):

$$\begin{aligned} \sigma_{rr} &= \frac{1}{r}\frac{\partial \phi}{\partial r} = \frac{A}{r^2} + B(2\ln r + 1) + 2C \\ \sigma_{\theta\theta} &= \frac{\partial^2 \phi}{\partial r^2} = -\frac{A}{r^2} + B(2\ln r + 3) + 2C \end{aligned} \tag{5.63}$$

Both relationships are reduced by consideration of the deformations shown in Fig. 5.16. The radial strain is only dependent on the displacement in the same direction as well as being defined through Hook's law based on both extensional stresses (Timoshenko & Goodier, 1970). Substitution and integration of the stresses defined in Eq. (5.63) results in an expression for the radial displacement (Timoshenko & Goodier, 1970). Furthermore, the curvature implies that the tangential strain is defined by both the radial and the circumferential displacements (Timoshenko & Goodier, 1970). Following the same procedure and substituting the previously found expression yields the tangential displacement defined by the second constant (Timoshenko & Goodier, 1970). However, this constant has to be neglected since the tangential displacement in a continuous circle should not reflect angular dependence (Timoshenko & Goodier, 1970).

5.5.4 Stresses due to pore pressures

The stresses are obtained through statement of the boundary conditions governing a pressure loaded pore as schematically shown in Fig. 5.17. The influence of the concave meniscus between the water phases is neglected, resulting in a uniform pressure defined relative to atmospheric conditions (Timoshenko & Goodier, 1970):

$$\begin{aligned} \sigma_{rr}|_{\Gamma_{r=r_i}} &= -P_{sat} \\ \sigma_{rr}|_{\Gamma_{r=r_o}} &= 0 \end{aligned} \tag{5.64}$$

where

r_i, r_o	[mm]	Inner, outer radius of the surrounding material

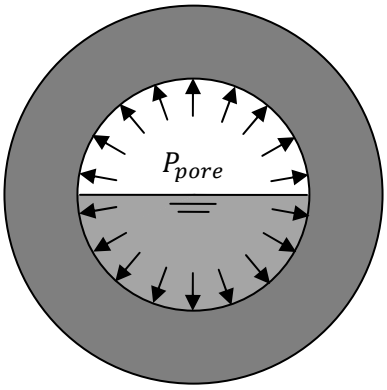

Pore pressure

$$P_{pore} = P_g - P_{atm}$$
$$= (P_{ga} + P_{gw}) - P_{atm}$$
$$\approx (P_{atm} + P_{sat}) - P_{atm} = P_{sat}$$

Fig. 5.17 *A schematic illustration of a uniformly pressure loaded pore characterised by assuming a flat surface between the gas and liquid phases.*

Stress state surrounding a pressure loaded pore

The stress state is obtained by neglecting the second term in Eq. (5.63) and using the boundary conditions represented by Eq. (5.64) (Timoshenko & Goodier, 1970):

$$\sigma_{rr} = \frac{r_i^2 P_g}{r_o^2 - r_i^2}\left(1 - \frac{r_o^2}{r}\right)$$
$$\sigma_{\theta\theta} = \frac{r_i^2 P_g}{r_o^2 - r_i^2}\left(1 + \frac{r_o^2}{r}\right) \tag{5.65}$$

The pore pressure is equilibrated at the edge of the pore by compressive radial stresses, diminishing with increasing radius (Timoshenko & Goodier, 1970). In tangential direction tensile stresses develop, being highest at the pore edge (Timoshenko & Goodier, 1970). It is important to observe that by increasing the radius of the surrounding material, the tangential stress state at the pore edge converges to the pore pressure values as shown in Fig. 5.18 (Timoshenko & Goodier, 1970). Tangential stresses reduce with increasing radius, dependent on the thickness of the surrounding material as indicated by Fig. 5.19. For high ratios of outer and inner radii the stress level approaches the imposed saturation pressure.

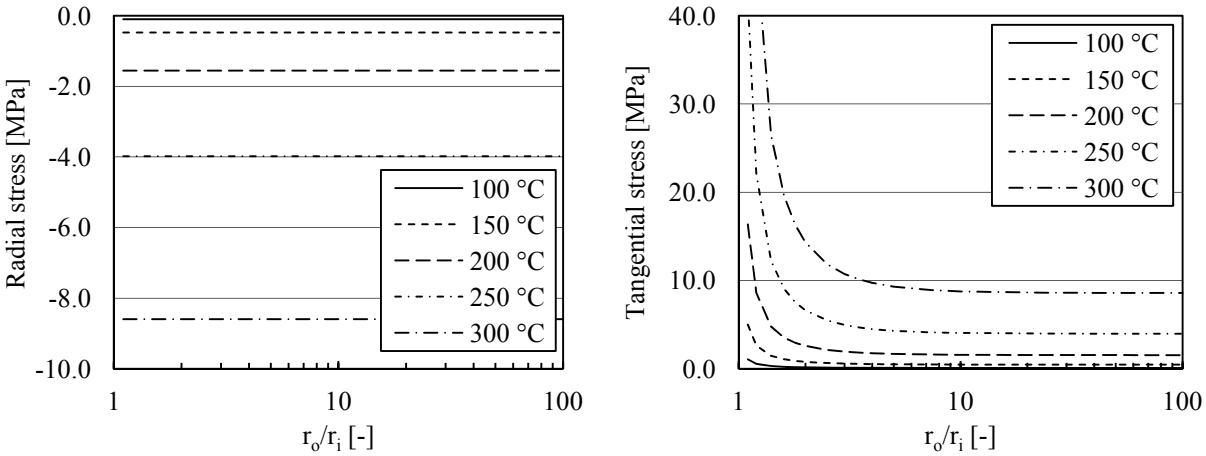

Fig. 5.18 *Radial (left) and tangential (right) pressure-induced stresses are largest at the pore edge and depend only on inner and outer radii of the material. Convergence occurs in case the outer radius becomes sufficiently large.*

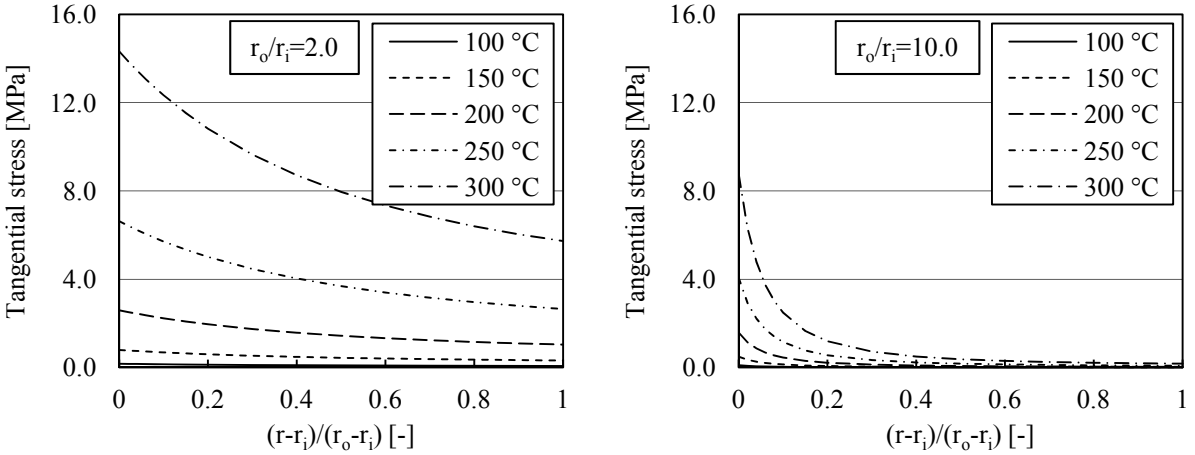

Fig. 5.19 *For small ratio's of outer and inner radii the tangential tensile stress at the pore edge becomes larger than the pressure (left). The reduction of the tangential stress through the radius increases for higher ratio's (right).*

From consideration of this infinitely strong elastic material it seems feasible that the tangential stresses at the pore edge can act as crack initiator. However, the influence on the development of the crack pattern is not clear since during crack opening the pressure rapidly reduces as estimated in chapter 4. Therefore, a more general approach is required using the pressure-induced stresses as additional internal loading.

Pressure-induced stresses as initial loading

Commonly an effective stress approach is adopted which indicates a direct analogy with the presented results (Gray & Schrefler, 2001; Zienkiewicz, et al., 2005). The localised constant pressure in the microstructure is assumed to cause uniformly distributed tensile stresses. Contrary to the initial temperature strain these stresses will also develop in unrestrained conditions. These imposed stresses are independent of the plane stress or plane strain assumption and included in the elasticity definition assuming a uniform pressure without shear (Gray & Schrefler, 2001; Zienkiewicz, et al., 2005):

$$\boldsymbol{\sigma} = \boldsymbol{D}(\boldsymbol{\varepsilon} - \boldsymbol{\varepsilon_T}) + \boldsymbol{\sigma_P} \tag{5.66}$$

with

$$\boldsymbol{\sigma_P} = \begin{bmatrix} \sigma_{P\,xx} \\ \sigma_{P\,yy} \\ \sigma_{P\,xy} \end{bmatrix} = \begin{bmatrix} P_{pore} - P_{atm} \\ P_{pore} - P_{atm} \\ 0 \end{bmatrix} = \begin{bmatrix} P_{sat} \\ P_{sat} \\ 0 \end{bmatrix}$$

where

P_{pore}	[MPa]	Pore pressure assumed governed by the uniform gas pressure
$\boldsymbol{\sigma_p}$	[MPa]	Pressure-induced stress vector

6 Isotropic FEM model for temperature and pore pressure

The derived FEM model extends on chapter 4 and describes the forced drying of a porous material, assumed to be homogeneous and isotropic. First, the conceptual idea is discussed after which the second part characterises the process of evaporation through the thermodynamic equilibrium between the water phases. The resultant pore or gas pressure is only based on the partially saturated vapour phase, neglecting the influence of dry air. The resultant coupled system of PDE's governs the time-dependent development of the temperature and the gas pressure. Neumann and periodical boundary conditions are defined to act on the cross-section of the structural element. In the third part, the system of PDE's is approximated by minimisation of the energy functional to define the weak form. Subsequently, Galerkin's method is used to obtain the FEM definition, approximated by linear 2D triangular elements. Time integration is included through an implicit Euler backward scheme using an incremental definition for the nodal variables. The solution procedure and analyses of the results are also elaborated. The final part of this chapter focuses on numerical validation by comparing the FEM to the FDM. Thereafter various results for fire exposed concrete are discussed. The influence of the concrete strength class, the type of fire exposure and the environmental conditions are examined. Pore pressure development based on the progress of the drying front is elaborated as well as the possibility to develop a moisture peak.

6.1 Conceptual idea, layout and material description

The presented FEM model focuses on the physical description of the fire exposed concrete element presented in chapter 3. The rapid propagation of heat and thus thermal energy across the concrete components drives the pore pressure to develop based on the evaporation of liquid water. This forced drying process is characterised using an averaged porous material, similar to chapter 4 (Hassanizadeh & Gray, 1979a; Bachmat & Bear, 1986). However, for the FEM model the focus is on the coupled description of temperature and pore pressure development. The pore pressure is assumed governed only by the vapour pressure based on thermodynamic equilibrium between the water phases (Genuchten, 1980; Pel & Huinink, 2007). The material description also includes heat and mass fluxes (Bear, 1972/1988).

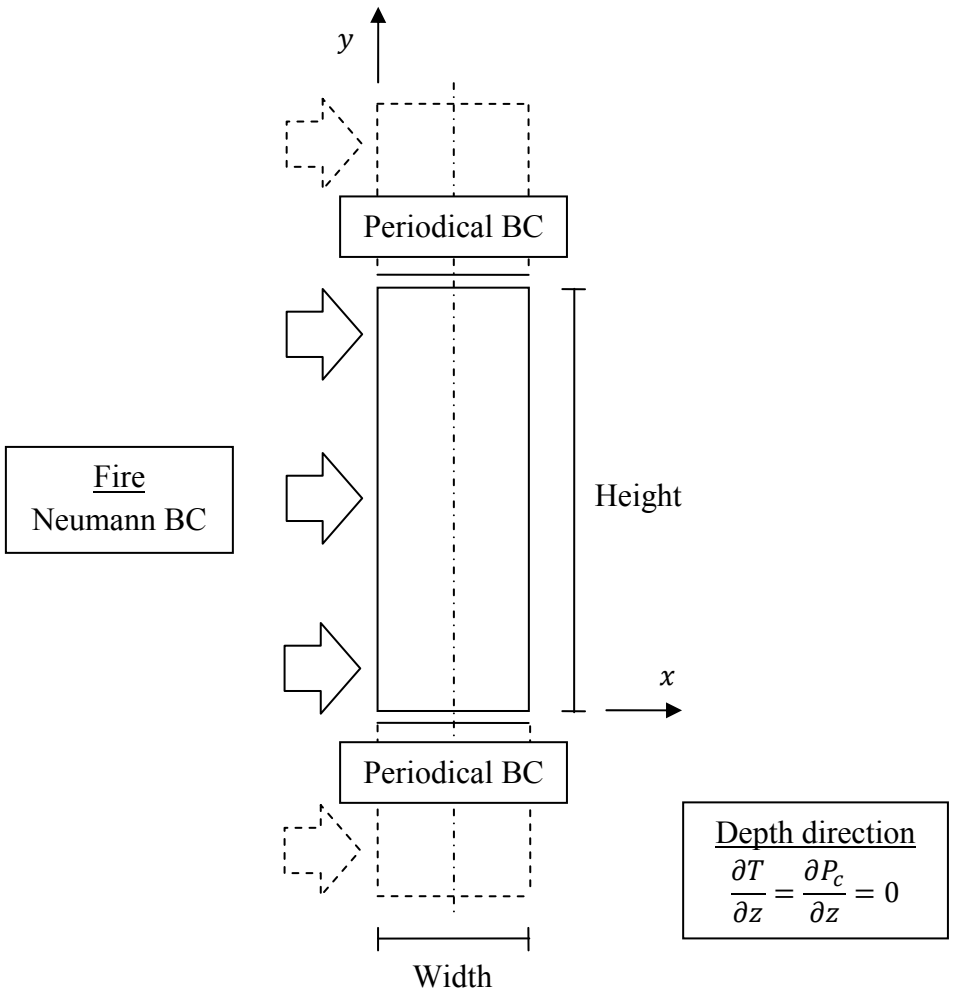

Fig. 6.1 *Schematic overview of the 2D concrete element exposed to a single sided fire represented by boundary conditions (BC). The in-plane material schematisation is characterised as homogeneous and isotropic.*

The resultant coupled system of PDE's is, in this chapter, stated for an isotropic continuum (Tenchev, et al., 2001; Gawin, et al., 2003). This simplifies the behaviour and assumes a homogeneous material without directional dependence. Aspects such as heterogeneity, based on the concrete components, as well as the definition of an anisotropic continuum, reflecting local cracking, are elaborated in the next chapter. The cross-section of the element is schematised as 2D, as shown in Fig. 6.1, while assuming a constant fire exposure in depth direction represented by a unit thickness. It is furthermore assumed that adjacent cross-sections tend to exhibit similar behaviour, allowing to characterise the out-of-plane direction by a constant temperature and pressure development. This implies that under isotropic conditions no fluxes pass between these cross-sections and the behaviour may be assumed independent from each other.

The resultant in-plane fluxes and gradients all describe a 2D distribution, requiring a similar local material description. This is provided by using 2D triangular elements to approximate the continuum. The usage of a 1D material description is not desirable since this implies that, at the local scale, the in-plane fluxes and gradients are uncoupled. This seems valid for

approximation of 1D flow perpendicular to the heated surface. However, each flux is forced to follow the orientation of the local material schematisation and cannot pass directly across the domain. This affectively includes an additional internal length scale which mitigates the flux and becomes more pronounced in case the gradients represent a 2D variation.

The cross-section is exposed at the left edge to a fire governed by Neumann boundary conditions (Tenchev, et al., 2001; Gawin, et al., 2003). The reference exterior conditions, defined at the right edge, are maintained using the same conservation equations. At the top and bottom edges periodical boundary conditions are enforced (Segal, 2008). These conditions affectively connect both edges, allowing heat and mass fluxes to pass in order to simulate a continuous material. The resultant drying process, characterised by the temperature and pore pressure, is predominately 1D perpendicular to the heated surface.

6.2 Theoretical framework governing the FEM definition

The derivation of the FEM model extends on the temperature progress and forced drying characterisation presented in chapter 4. Both processes are governed by conservation equations based on a continuum definition (Bear, 1972/1988). In this paragraph, the material description is extended and coupled leading to a system of PDE's extended by definition of the boundary conditions (Tenchev, et al., 2001; Gawin, et al., 2003). Also the possibility to reduce the system of PDE's in order to obtain the basic differential equation governing thermal conductivity is indicated.

6.2.1 Basic assumptions used to describe the behaviour of fire exposed concrete

Conservation of thermal energy

With respect to conservation of thermal energy and temperature development the following assumptions are made:

1. The heat flux is based on thermal conductivity and the temperature gradient described by Fourier's law (Bear, 1972/1988). The contribution by convection is neglected (Bear, 1972/1988) based on the relatively low permeability and resulting low velocity of the water phases. Furthermore, fire exposure is assumed constant in depth direction, allowing to neglect the out-of-plane temperature gradient.

2. A state of thermodynamic equilibrium is reached by assuming a local constant temperature across the material components (Hassanizadeh & Gray, 1979b; Bear & Bachmat, 1986).

3. The consumption or gain of energy by evaporation or condensation respectively is included to reflect the forced drying process. Energy consumption by the dehydration processes is neglected due to it's gradual development with temperature.

The exchange with the surrounding environment is based on:

4. The conservation of thermal energy as assumed only to be governed by convective heat transfer through a Neumann boundary condition (Kordina, et al., 1975).

Conservation of mass governing the water phases

Mass conservation of the water phases is defined by the following assumptions:

5. Liquid water is assumed incompressible whereas water vapour is defined as a perfect, compressible gas (Moran & Shapiro, 2004). Above the critical temperature liquid water no longer exists as a distinctive phase (Whitten, et al., 2010). The physical properties at these high temperatures are closely related to the numerical stability of the fractured porous material. This topic is therefore treated in the next chapter, dealing with the anisotropic continuum definition.

6. The influence of dry air is neglected since no exchange process or source is present. The pore pressure is defined only by the partially saturated water vapour phase, assuming thermodynamic equilibrium is reached (Hassanizadeh & Gray, 1979b; Bear & Bachmat, 1986).

7. The evaporation process is assumed instantaneous, according to the equilibrium relationship between the liquid and vapour phases of water. A desorption isotherm is used to characterise this process (Genuchten, 1980; Pel & Huinink, 2007).

8. Capillary water present at ambient conditions, defined by the RH, is assumed to be the main water source. Additional sources in the microstructure, such as gel water and adsorbed water, are neglected due to the irrelatively limited volume. Dehydration as a source of liquid water is also neglected due to the gradual release with temperature.

9. Mass fluxes govern the water phases and are based on pressure gradients assuming laminar, viscous flow according to Darcy's law (Bear, 1972/1988). The contribution by diffusion (Bear, 1972/1988) is neglected based on the more gradual time-dependent nature compared to the gas pressure build-up. Furthermore, the assumed constant fire exposure in depth direction allows to neglect the out-of-plane pressure gradients.

Drainage to the surrounding environment is governed by:

10. Mass conservation of the water phases, assuming only convective transfer governed by a Neumann boundary condition (Tenchev, et al., 2001; Gawin, et al., 2003).

6.2.2 Description of the continuum defining the porous material

The characterisation of the forced drying process is based on the conservation of thermal energy and mass of the water phases defined for an averaged porous material (Tenchev, et al., 2001; Gawin, et al., 2003). These continuum definitions, established for a REV (Hassanizadeh & Gray, 1979a; Bachmat & Bear, 1986) are described in chapter 4 and form the starting point for the definition of the FEM model. Both conservation equations are briefly restated and subsequently coupled to obtain the system of PDE's governing the FEM temperature and pore pressure model.

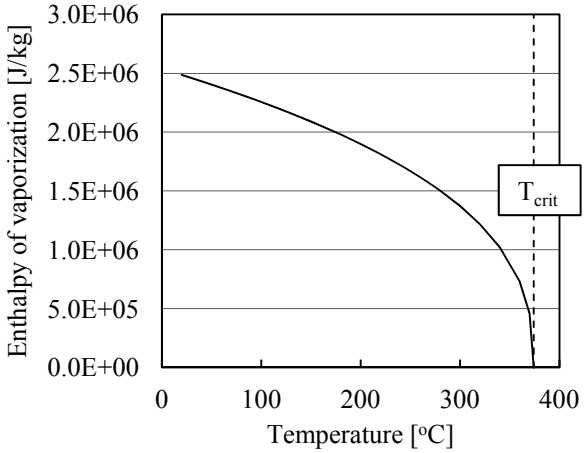

Fig. 6.2 *Energy consumption as defined by the enthalpy of vaporization, indicating a steady decline until the critical temperature* (Gawin, et al., 1999).

Conservation of thermal energy

The temperature progress across the material is governed by the PDE describing the conservation of energy (Bear, 1972/1988). The time derivative and the Fourier-based heat flux are extended by consumption of energy. The development of the evaporation process is characterised by the enthalpy which is related to internal energy and work performed at constant pressure (Moran & Shapiro, 2004). Commonly, the contribution by pressure related work is neglected, allowing the enthalpy of vaporization as shown in Fig. 6.2 to characterise the drying process (Tenchev, et al., 2001; Gawin, et al., 2003):

$$H_{vap} = U_{vap} + \overbrace{W_{vap}}^{\approx 0} \tag{6.1}$$

with

$$W_{vap} = \int P dV$$

where

H_{vap}	[J/kg]	Enthalpy of vaporization per unit of mass
U_{vap}	[J/kg]	Internal energy related to the vaporization process
W_{vap}	[J/kg]	Work produced at constant pressure to change the volume

The partial derivatives of both material properties with respect to temperature are neglected based on their gradual development. Using the thermal energy conservation equation from chapter 4 and introducing the consumption by evaporation as a subtraction leads to:

$$\frac{\partial(\rho C T)}{\partial t} + \boldsymbol{\nabla} \cdot \boldsymbol{q_T} = -H_{vap} \frac{\partial \overline{\rho_{vap}}}{\partial t} \tag{6.2}$$

with

$$\frac{\partial(\rho C T)}{\partial t} = \frac{\partial(\rho C T)}{\partial T} \frac{\partial T}{\partial t} \approx \rho C \frac{\partial T}{\partial t}$$

$$\boldsymbol{q_T} = -k \boldsymbol{\nabla} T$$

Conservation of water vapour

The gas phase is assumed only governed by the partially saturated water vapour pressure, defined by the RH based on Kelvin's equation (Bear, 1972/1988; Pel & Huinink, 2007):

$$P_g = \overset{\approx 0}{\widetilde{P_{ga}}} + P_{gw} = RHP_{sat} \tag{6.3}$$

The conservation of mass governing the water vapour phase is defined by the time derivative, the mass flux and the addition or source based on evaporation (Tenchev, et al., 2001; Gawin, et al., 2003). The time derivatives are determined with respect to the main variables, the temperature and the capillary pressure. Temperature-dependent partial derivatives are expressed only in the RH and the saturated water vapour pressure. The gradual temperature-dependent development of the porosity is neglected. As elaborated in chapter 4 the development of the liquid water saturation level is only dependent on the capillary pressure. The isotropic water vapour flux is characterised by Darcy's law including also the relative permeability and the dynamic viscosity (Couture, et al., 1996). The conservation equation of the water vapour phase becomes:

$$\frac{\partial\left(n(1-S_w)\frac{RHP_{sat}M_w}{RT}\right)}{\partial T}\frac{\partial T}{\partial t} + \frac{\partial\left(n(1-S_w)\frac{RHP_{sat}M_w}{RT}\right)}{\partial P_c}\frac{\partial P_c}{\partial t} + \boldsymbol{\nabla}\cdot\boldsymbol{q_{gw}} = \frac{\partial\overline{\rho_{vap}}}{\partial t} \tag{6.4}$$

with

$$\frac{\partial RH}{\partial T} = \left(\frac{P_c M_w}{{\rho_w}^2 RT}\frac{\partial \rho_w}{\partial T} + \frac{P_c M_w}{\rho_w RT^2}\right) e^{\frac{-P_c M_w}{\rho_w RT}}$$

$$\frac{\partial\left(n(1-S_w)\frac{RHP_{sat}M_w}{RT}\right)}{\partial T}\frac{\partial T}{\partial t} = \left(P_{sat}\frac{\partial RH}{\partial T} + RH\frac{\partial P_{sat}}{\partial T} - \frac{RHP_{sat}}{T}\right)\frac{n(1-S_w)M_w}{RT}\frac{\partial T}{\partial t}$$

$$\frac{\partial\left(n(1-S_w)\frac{RHP_{sat}M_w}{RT}\right)}{\partial P_c}\frac{\partial P_c}{\partial t} = -\left(RH\frac{\partial S_w}{\partial P_c} - (1-S_w)\frac{\partial RH}{\partial P_c}\right)\frac{nP_{sat}M_w}{RT}\frac{\partial P_c}{\partial t}$$

$$\boldsymbol{q_{gw}} = \overline{\rho_{gw}}\boldsymbol{v_{gw}} = -n(1-S_w)\frac{RHP_{sat}M_w}{RT}\left(\frac{K_{rel_g}K}{\mu_g}\boldsymbol{\nabla}P_{gw}\right)$$

The coupled description also affects the definition of the water vapour pressure gradient which becomes expressed in the temperature and the capillary pressure:

$$\boldsymbol{\nabla}P_g = \boldsymbol{\nabla}P_{gw} = \left(\frac{\partial RH}{\partial T}P_{sat} + RH\frac{\partial P_{sat}}{\partial T}\right)\boldsymbol{\nabla}T + \frac{\partial RH}{\partial P_c}P_{sat}\boldsymbol{\nabla}P_c \tag{6.5}$$

Conservation of liquid water

The pressure difference across the concave meniscus between both immiscible phases, water vapour and liquid water, is governed by the capillary pressure (Bear, 1972/1988; Pel & Huinink, 2007). During drying the coinciding relatively high capillary pressure mainly defines the water pressure (Bear, 1972/1988):

$$P_c = P_{gw} - P_w \rightarrow P_w = P_{gw} - P_c \tag{6.6}$$

The liquid water phase is based on the conservation relationship stated in chapter 4 in which the evaporation is reflected as a subtraction or sink (Tenchev, et al., 2001; Gawin, et al., 2003). Again the partial derivatives with respect to the temperature and the capillary pressure are introduced, reflecting a derivative of the liquid water density. The assumed laminar and viscous liquid water mass flux is governed by the velocity defined through Darcy's law (Bear, 1972/1988):

$$\frac{\partial(nS_w\rho_w)}{\partial T}\frac{\partial T}{\partial t}+\frac{\partial(nS_w\rho_w)}{\partial P_c}\frac{\partial P_c}{\partial t}+\boldsymbol{\nabla}\cdot\boldsymbol{q_w}=-\frac{\partial\overline{\rho_{vap}}}{\partial t} \tag{6.7}$$

with

$$\frac{\partial(nS_w\rho_w)}{\partial T}\frac{\partial T}{\partial t}=nS_w\frac{\partial\rho_w}{\partial T}\frac{\partial T}{\partial t}$$

$$\frac{\partial(nS_w\rho_w)}{\partial P_c}\frac{\partial P_c}{\partial t}=n\rho_w\frac{\partial S_w}{\partial P_c}\frac{\partial P_c}{\partial t}$$

$$\boldsymbol{q_w}=\overline{\rho_w}\boldsymbol{v_w}=-nS_w\rho_w\left(\frac{K_{rel_w}K}{\mu_w}\boldsymbol{\nabla}P_w\right)$$

The liquid water pressure gradient is, by using Eq. (6.6), expressed in both main variables. Compared to the water vapour pressure gradient, the capillary pressure term is extended:

$$\boldsymbol{\nabla}P_w=\left(\frac{\partial RH}{\partial T}P_{sat}+RH\frac{\partial P_{sat}}{\partial T}\right)\boldsymbol{\nabla}T+\left(\frac{\partial RH}{\partial P_c}P_{sat}-1\right)\boldsymbol{\nabla}P_c \tag{6.8}$$

Coupled system of PDE's

The process of evaporation is, similar as in chapter 4, assumed governed by an instantaneous development according to the thermodynamic equilibrium between both water phases (Genuchten, 1980; Pel & Huinink, 2007). The coupled thermal energy conservation equation is obtained by inserting Eq. (6.4) into Eq. (6.2) (Tenchev, et al., 2001; Gawin, et al., 2003). This includes energy consumption or gain based on the development of the water vapour phase reflecting contributions by the time derivatives and the mass flux (Lottman, et al., 2011; Lottman, et al., 2013):

$$\begin{gathered}\frac{\partial\overline{\rho_T}}{\partial t}+\boldsymbol{\nabla}\cdot\boldsymbol{q_T}=-H_{vap}\left(\frac{\partial\overline{\rho_{gw}}}{\partial t}+\boldsymbol{\nabla}\cdot\boldsymbol{q_{gw}}\right)\\ \frac{\partial(\rho CT)}{\partial t}+H_{vap}\frac{\partial\left(n(1-S_w)\frac{RHP_{sat}M_w}{RT}\right)}{\partial t}\\ -\boldsymbol{\nabla}\cdot(k\boldsymbol{\nabla}T)-H_{vap}\boldsymbol{\nabla}\cdot\left(n(1-S_w)\frac{RHP_{sat}M_w}{RT}\left(\frac{K_{rel_g}K}{\mu_g}\boldsymbol{\nabla}P_{gw}\right)\right)=0\end{gathered} \tag{6.9}$$

Inserting Eq. (6.4) into Eq. (6.7) allows to obtain the coupled conservation equation for the water phases (Tenchev, et al., 2001; Gawin, et al., 2003). This relationship defines thermodynamic equilibrium between the water phases and is, compared to chapter 4, extended by temperature dependence (Lottman, et al., 2011; Lottman, et al., 2013):

$$\frac{\partial \overline{\rho_w}}{\partial t} + \boldsymbol{\nabla} \cdot \boldsymbol{q_w} = -\left(\frac{\partial \overline{\rho_{gw}}}{\partial t} + \boldsymbol{\nabla} \cdot \boldsymbol{q_{gw}}\right)$$

$$\frac{\partial (n S_w \rho_w)}{\partial t} + \frac{\partial \left(n(1-S_w)\frac{RHP_{sat}M_w}{RT}\right)}{\partial t} \tag{6.10}$$

$$-\boldsymbol{\nabla} \cdot \left(n S_w \rho_w \left(\frac{K_{rel_w} K}{\mu_w} \boldsymbol{\nabla} P_w\right)\right) - \boldsymbol{\nabla} \cdot \left(n(1-S_w)\frac{RHP_{sat}M_w}{RT}\left(\frac{K_{rel_g} K}{\mu_g} \boldsymbol{\nabla} P_{gw}\right)\right) = 0$$

Both conservation equation's are rearranged and the vapour and liquid water pressure gradients, defined by Eq. (6.5) and Eq. (6.8) respectively, are inserted. So, the resultant coupled system of PDE's is stated as:

$$\left(C_{TT_1}\frac{\partial T}{\partial t}\right) + H_{vap}\left(C_{TT_2}\frac{\partial T}{\partial t} + C_{TP}\frac{\partial P_c}{\partial t}\right) - \boldsymbol{\nabla} \cdot \left(K_{TT_1}\boldsymbol{\nabla} T\right) - H_{vap}\boldsymbol{\nabla} \cdot \left(K_{TT_2}\boldsymbol{\nabla} T + K_{TP}\boldsymbol{\nabla} P_c\right) = 0$$

$$\left(C_{PT}\frac{\partial T}{\partial t} + C_{PP}\frac{\partial P_c}{\partial t}\right) - \boldsymbol{\nabla} \cdot \left(K_{PT}\boldsymbol{\nabla} T + K_{PP}\boldsymbol{\nabla} P_c\right) = 0 \tag{6.11}$$

with

$$C_{TT_1} = \frac{\partial \overline{\rho_T}}{\partial T} = \rho C$$

$$C_{TT_2} = \frac{\partial \overline{\rho_{gw}}}{\partial T} = \left(P_{sat}\frac{\partial RH}{\partial T} + RH\frac{\partial P_{sat}}{\partial T} - \frac{RHP_{sat}}{T}\right)\frac{n(1-S_w)M_w}{RT}$$

$$C_{TP} = \frac{\partial \overline{\rho_{gw}}}{\partial P_c} = -\left(RH\frac{\partial S_w}{\partial P_c} - (1-S_w)\frac{\partial RH}{\partial P_c}\right)\frac{nP_{sat}M_w}{RT}$$

$$C_{PT} = \frac{\partial \overline{\rho_w}}{\partial T} + \frac{\partial \overline{\rho_{gw}}}{\partial T} = nS_w\frac{\partial \rho_w}{\partial T} + \left(P_{sat}\frac{\partial RH}{\partial T} + RH\frac{\partial P_{sat}}{\partial T} - \frac{RHP_{sat}}{T}\right)\frac{n(1-S_w)M_w}{RT}$$

$$C_{PP} = \frac{\partial \overline{\rho_w}}{\partial P_c} + \frac{\partial \overline{\rho_{gw}}}{\partial P_c} = n\rho_w\frac{\partial S_w}{\partial P_c} - \left(RH\frac{\partial S_w}{\partial P_c} - (1-S_w)\frac{\partial RH}{\partial P_c}\right)\frac{nP_{sat}M_w}{RT}$$

$$K_{TT_1} = k$$

$$K_{TT_2} = n(1-S_w)\frac{RHP_{sat}M_w}{RT}\left(\frac{K_{rel_g}K}{\mu_g}\right)\left(\frac{\partial RH}{\partial T}P_{sat} + RH\frac{\partial P_{sat}}{\partial T}\right)$$

$$K_{TP} = n(1-S_w)\frac{RHP_{sat}M_w}{RT}\left(\frac{K_{rel_g}K}{\mu_g}\right)\frac{\partial RH}{\partial P_c}P_{sat}$$

$$K_{PT} = nS_w\rho_w\left(\frac{K_{rel_w}K}{\mu_w}\right)\left(\frac{\partial RH}{\partial T}P_{sat} + RH\frac{\partial P_{sat}}{\partial T}\right) + n(1-S_w)\frac{RHP_{sat}M_w}{RT}\left(\frac{K_{rel_g}K}{\mu_g}\right)\left(\frac{\partial RH}{\partial T}P_{sat} + RH\frac{\partial P_{sat}}{\partial T}\right)$$

$$K_{PP} = nS_w\rho_w\left(\frac{K_{rel_w}K}{\mu_w}\right)\left(\frac{\partial RH}{\partial P_c}P_{sat} - 1\right) + n(1-S_w)\frac{RHP_{sat}M_w}{RT}\left(\frac{K_{rel_g}K}{\mu_g}\right)\frac{\partial RH}{\partial P_c}P_{sat}$$

Various contributions are present which are considered in the following way:

- The first terms on the left hand side represent the mass of the system, consisting of the partial derivatives with respect the main variables (van Kan, et al., 2008). These mass constants are multiplied with the time derivatives of the variables.

- The remaining terms, commonly referred to as the stiffness of the system, are governed by the heat and mass fluxes across the isotropic continuum (van Kan, et al., 2008). These stiffness constants are multiplied with the gradient of the variables.

- The mass and stiffness constants related to energy consumption by evaporation are separately defined. This is reflected in the first conservation equation.

The final expression for the coupled system of PDE's is obtained by grouping the mass and stiffness coefficients. Important is to notice that the resultant matrices, governing the coupled behaviour, are not symmetrical:

$$\left(\boldsymbol{M_I} + H_{vap}\boldsymbol{M_{II}}\right)\frac{\partial \boldsymbol{c}}{\partial t} - \boldsymbol{\nabla}\cdot(\boldsymbol{S_I}\boldsymbol{\nabla c}) - H_{vap}\boldsymbol{\nabla}\cdot(\boldsymbol{S_{II}}\boldsymbol{\nabla c}) = 0 \tag{6.12}$$

with

$$\frac{\partial \boldsymbol{c}}{\partial t} = \begin{bmatrix} \dfrac{\partial T}{\partial t} \\ \dfrac{\partial P_c}{\partial t} \end{bmatrix} \qquad \boldsymbol{\nabla c} = \begin{bmatrix} \boldsymbol{\nabla} T \\ \boldsymbol{\nabla} P_c \end{bmatrix}$$

$$\boldsymbol{M_I} = \begin{bmatrix} C_{TT_1} & 0 \\ C_{PT} & C_{PP} \end{bmatrix} \qquad \boldsymbol{M_{II}} = \begin{bmatrix} C_{TT_2} & C_{TP} \\ 0 & 0 \end{bmatrix}$$

$$\boldsymbol{S_I} = \begin{bmatrix} K_{TT_1} & 0 \\ K_{PT} & K_{PP} \end{bmatrix} \qquad \boldsymbol{S_{II}} = \begin{bmatrix} K_{TT_2} & K_{TP} \\ 0 & 0 \end{bmatrix}$$

where

$\boldsymbol{c}$	[var.]	Temperature and capillary pressure vector
$\boldsymbol{M_I}$	[var.]	Mass matrix of partial derivatives with respect to variables
$\boldsymbol{M_{II}}$	[var.]	Mass matrix reflecting the influence of the water vapour partial derivatives on the conservation of thermal energy
$\boldsymbol{S_I}$	[var.]	Stiffness matrix based on the isotropic fluxes
$\boldsymbol{S_{II}}$	[var.]	Stiffness matrix reflecting the influence of the water vapour mass flux on the conservation of thermal energy

Reduction of the system of PDE's

Important is to notice that by neglecting the constants related to the second conservation equation, the mass and stiffness matrices reflect the basic Fourier differential equation. The system of PDE's becomes uncoupled, reflecting only the temperature as a variable. This concept is used throughout this thesis in case only the progress of temperature is to be determined by the FEM model. Furthermore, it will also form the basis for definition of the aggregates, as discussed in the next chapter.

6.2.3 Neumann and periodical boundary conditions

The definition of the system of PDE's is extended by boundary conditions taking a similar form as discussed in chapter 4. In the schematic overview presented in Fig. 6.1 two different types are indicated:

- Neumann boundary conditions (van Kan, et al., 2008) are imposed at the left and right edges of the cross-section. These govern the interaction with the surrounding environment based on the conservation of thermal energy and mass of the water phases (Tenchev, et al., 2001; Gawin, et al., 2003).

- At the top and bottom edges periodical boundary conditions are prescribed (Segal, 2008). The top and bottom edges are connected to simulate a continuous behaviour.

Neumann boundary condition - conservation of thermal energy

Both energy fluxes at the boundary, based on heat and mass flow, are equilibrated by the external heat transfer based on the time-dependent temperature development (Tenchev, et al., 2001; Gawin, et al., 2003). The conservation of energy is expressed in the stiffness coefficients and the outwards orientated gradient of the variables. The latter neglects flow parallel to the cross-section which does not contribute to the system (van Kan, et al., 2008):

$$\begin{aligned}
&\left(\boldsymbol{q_T} + H_{vap}\boldsymbol{q_{gw}}\right)\cdot\boldsymbol{n}\big|_{\Gamma_A} = \alpha_A(T - T_\infty)\\
&-\left(\left(K_{TT_1}\boldsymbol{\nabla}T\right)\cdot\boldsymbol{n} + H_{vap}\left(K_{TT_2}\boldsymbol{\nabla}T + K_{TP}\boldsymbol{\nabla}P_c\right)\cdot\boldsymbol{n}\right)\Big|_{\Gamma_A} = \alpha_A(T - T_\infty)\\
&-\left(K_{TT_1}\frac{\partial T}{\partial n} + H_{vap}\left(K_{TT_2}\frac{\partial T}{\partial n} + K_{TP}\frac{\partial P_c}{\partial n}\right)\right)\Big|_{\Gamma_A} = \alpha_A(T - T_\infty)
\end{aligned} \tag{6.13}$$

Neumann boundary condition - mass conservation of the water phases

Conservation of mass at the boundary states equilibrium between the liquid and vapour fluxes as well as the external transfer defined by the water vapour pressure (Tenchev, et al., 2001; Gawin, et al., 2003). Again the stiffness coefficients are introduced. It is important to consider that the water vapour pressure is not a main variable and requires some additional considerations as will be discussed during definition of the incremental time discretisation:

$$\begin{aligned}
&\left(\boldsymbol{q_w} + \boldsymbol{q_{gw}}\right)\cdot\boldsymbol{n}\big|_{\Gamma_A} = \beta_A\left(\rho_{gw} - \rho_{gw_\infty}\right)\\
&-\left(K_{PT}\boldsymbol{\nabla}T + K_{PP}\boldsymbol{\nabla}P_c\right)\cdot\boldsymbol{n}\big|_{\Gamma_A} = \beta_A\left(\rho_{gw} - \rho_{gw_\infty}\right)\\
&-\left(K_{PT}\frac{\partial T}{\partial n} + K_{PP}\frac{\partial P_c}{\partial n}\right)\Big|_{\Gamma_A} = \beta_A\left(\rho_{gw} - \rho_{gw_\infty}\right)
\end{aligned} \tag{6.14}$$

Periodical boundary conditions

The cross-section is in height direction assumed to be continuous. This allows the heat and mass fluxes to pass across the top and bottom edges into adjacent cross-sections and vice versa. Since each cross-section is assumed to be representative, this affectively implies that

the top edge is connected to the bottom edge. This is referred to as a periodical boundary condition based on the reoccurrence of the relationships in height direction (Segal, 2008):

$$\left.\begin{matrix} T(x,H,t) = T(x,0,t) \\ P_c(x,H,t) = P_c(x,0,t) \end{matrix}\right\} \rightarrow \boldsymbol{c}(x,H,t) = \boldsymbol{c}(x,0,t) \tag{6.15}$$

6.3 Solution approach to define the FEM schematisation

The system of coupled PDE's, stated in Eq. (6.12), and the boundary conditions, defined by Eq. (6.13) and Eq. (6.14), are numerically approximated using the FEM. First, the weak form of the system of PDE's is stated taking the boundary conditions into account (van Kan, et al., 2008). Thereafter, Galerkin's method is used to define the FEM discretisation, based on 2D triangular elements (van Kan, et al., 2008). Time integration is implemented through an Euler backwards scheme using an incremental definition of the variables (van Kan, et al., 2008).

6.3.1 Minimisation of energy in order to obtain the weak form

The coupled system of PDE's is also known as the strong form (van Kan, et al., 2008). The second order derivatives require a quadratic variation of the variables across the domain (Zienkiewicz, et al., 2005). However, in derivation of the finite element approximation the PDE's are commonly stated in their weak formulation (van Kan, et al., 2008). This will prove beneficial since less stringent conditions are imposed on the smoothness of the solution (van Kan, et al., 2008).

For this purpose, a time-dependent functional is defined based on the dot product of the variables with the coupled system of PDE's (van Kan, et al., 2008; Zienkiewicz, et al., 2005). The term functional refers to the vector basis of the function, expressed into a scalar quantity (Vermolen, 2005). The following relationship states this functional based on contributions from both PDE's (Zienkiewicz, et al., 2005):

$$\frac{\partial (J_T + J_P)}{\partial t} = \int_{\Omega} \boldsymbol{c} \cdot \left(\left(\boldsymbol{M_I} + H_{vap} \boldsymbol{M_{II}} \right) \frac{\partial \boldsymbol{c}}{\partial t} \right) d\Omega - \int_{\Omega} \frac{1}{2} \boldsymbol{c} \cdot \left(\boldsymbol{\nabla} \cdot (\boldsymbol{S_I} \boldsymbol{\nabla c}) + H_{vap} \boldsymbol{\nabla} \cdot (\boldsymbol{S_{II}} \boldsymbol{\nabla c}) \right) d\Omega \tag{6.16}$$

where

J_T	[KJ/m^3]	Functional contribution based on the conservation of thermal energy
J_P	[kgJ/m^3]	Functional contribution based on mass conservation of the water phases

Relationship between functional minimisation and the coupled system of PDE's

The relationship with the system of PDE's is based on the variational principle according to which small changes to the solution do not constitute a change to the functional (Zienkiewicz, et al., 2005). In other words, the solution of the system of PDE's defines the functional to be stationary (Zienkiewicz, et al., 2005). This is expressed through minimisation of the functional with respect to the variables, obtaining the system of PDE's (van Kan, et al., 2008; Zienkiewicz, et al., 2005). Solving the minimisation thus becomes equal to solving the system of PDE's (van Kan, et al., 2008; Zienkiewicz, et al., 2005).

Establishing this relationship requires minimization of the function with respect to the variables. First, the mass integral in Eq. (6.16) is considered which through rearranging based on the dyadic product defines two matrix contributions. The first results in the identity matrix multiplied by the basic mass integral. The second is omitted based on the constant, non-symmetrical, mass matrix:

$$\begin{aligned}\int_{\Omega} \frac{\partial}{\partial \boldsymbol{c}}\left(\boldsymbol{c}\cdot\left(\boldsymbol{M}\frac{\partial \boldsymbol{c}}{\partial t}\right)\right)d\Omega &= \int_{\Omega} \frac{\partial}{\partial \boldsymbol{c}}\otimes\boldsymbol{c}\left(\boldsymbol{M}\frac{\partial \boldsymbol{c}}{\partial t}\right)+\frac{\partial}{\partial \boldsymbol{c}}\otimes\left(\boldsymbol{M}\frac{\partial \boldsymbol{c}}{\partial t}\right)\boldsymbol{c}d\Omega \\ &= \int_{\Omega} \boldsymbol{I}\left(\boldsymbol{M}\frac{\partial \boldsymbol{c}}{\partial t}\right)+\overbrace{\left(\frac{\partial}{\partial t}\otimes\frac{\partial \boldsymbol{c}}{\partial t}\boldsymbol{M}^{\boldsymbol{T}}\right)}^{=0}\boldsymbol{c}d\Omega = \int_{\Omega} \boldsymbol{M}\frac{\partial \boldsymbol{c}}{\partial t}d\Omega\end{aligned} \tag{6.17}$$

The stiffness integral is mainly governed by the Laplacian operator as already indicated in chapter 4 (van Kan, et al., 2008). Rearranging according to the dyadic product again defines two contributions with the second requiring additional consideration. Examination of the term between brackets defines a matrix with the rows based on the partial derivatives with respect to each of the variables. Multiplication by the variables vector allows to omit the off diagonal terms and produces the stiffness integral:

$$\begin{aligned}\int_{\Omega} \frac{1}{2}\frac{\partial}{\partial \boldsymbol{c}}\Big(\boldsymbol{c}\cdot\big(\boldsymbol{\nabla}\cdot(\boldsymbol{S}\boldsymbol{\nabla}\boldsymbol{c})\big)\Big)d\Omega &= \int_{\Omega} \frac{1}{2}\Big(\frac{\partial}{\partial \boldsymbol{c}}\otimes\boldsymbol{c}\big(\boldsymbol{\nabla}\cdot(\boldsymbol{S}\boldsymbol{\nabla}\boldsymbol{c})\big)+\frac{\partial}{\partial \boldsymbol{c}}\otimes\big(\boldsymbol{\nabla}\cdot(\boldsymbol{S}\boldsymbol{\nabla}\boldsymbol{c})\big)\boldsymbol{c}\Big)d\Omega \\ &= \int_{\Omega} \frac{1}{2}\left(\boldsymbol{I}\big(\boldsymbol{\nabla}\cdot(\boldsymbol{S}\boldsymbol{\nabla}\boldsymbol{c})\big)+\left(\big(\boldsymbol{\nabla}\cdot(\boldsymbol{S}\boldsymbol{\nabla}\boldsymbol{c})\big)\otimes\frac{\partial}{\partial \boldsymbol{c}}\right)^{\boldsymbol{T}}\boldsymbol{c}\right)d\Omega \\ &= \int_{\Omega} \frac{1}{2}\big(\boldsymbol{\nabla}\cdot(\boldsymbol{S}\boldsymbol{\nabla}\boldsymbol{c})+\boldsymbol{\nabla}\cdot(\boldsymbol{S}\boldsymbol{\nabla}\boldsymbol{c})\big)d\Omega = \int_{\Omega} \boldsymbol{\nabla}\cdot(\boldsymbol{S}\boldsymbol{\nabla}\boldsymbol{c})d\Omega\end{aligned} \tag{6.18}$$

Both derivatives define the minimisation of the functional, stated in Eq. (6.16), with respect to the variables. Consideration that this must also hold for all sub-domains indeed confirms the relationship with the coupled system of PDE's:

$$\begin{aligned}\frac{\partial}{\partial \boldsymbol{c}}\frac{\partial(J_T+J_P)}{\partial t} &= \int_{\Omega}\big(\boldsymbol{M_I}+H_{vap}\boldsymbol{M_{II}}\big)\frac{\partial \boldsymbol{c}}{\partial t}d\Omega-\int_{\Omega}\Big(\boldsymbol{\nabla}\cdot(\boldsymbol{S_I}\boldsymbol{\nabla}\boldsymbol{c})+H_{vap}\boldsymbol{\nabla}\cdot(\boldsymbol{S_{II}}\boldsymbol{\nabla}\boldsymbol{c})\Big)d\Omega=0 \\ &\rightarrow \big(\boldsymbol{M_I}+H_{vap}\boldsymbol{M_{II}}\big)\frac{\partial \boldsymbol{c}}{\partial t}-\boldsymbol{\nabla}\cdot(\boldsymbol{S_I}\boldsymbol{\nabla}\boldsymbol{c})-H_{vap}\boldsymbol{\nabla}\cdot(\boldsymbol{S_{II}}\boldsymbol{\nabla}\boldsymbol{c})=0\end{aligned} \tag{6.19}$$

Equilibrium between energy across the domain and energy sources along the boundary

Returning to the definition of the functional in Eq. (6.16) forms the starting point for the derivation of the weak form. The second order derivatives of the stiffness terms are reduced using integration by parts applied to Gauss' divergence theorem (van Kan, et al., 2008; Segal, 2008). The boundary integrals are expressed in the outward gradient of the variables:

$$\int_{\Omega} \boldsymbol{\nabla} \cdot (\boldsymbol{S}\boldsymbol{\nabla}\boldsymbol{c}\boldsymbol{c}) d\Omega = \int_{\Gamma} (\boldsymbol{S}\boldsymbol{\nabla}\boldsymbol{c}\boldsymbol{c}) \cdot \boldsymbol{n} d\Gamma$$

$$\int_{\Omega} \boldsymbol{\nabla} \cdot (\boldsymbol{S}\boldsymbol{\nabla}\boldsymbol{c}) \cdot \boldsymbol{c} + (\boldsymbol{S}\boldsymbol{\nabla}\boldsymbol{c}) : \boldsymbol{\nabla}\boldsymbol{c} d\Omega = \int_{\Gamma} \left(\boldsymbol{S}\frac{\partial \boldsymbol{c}}{\partial n}\right) \cdot \boldsymbol{c} d\Gamma \tag{6.20}$$

$$\int_{\Omega} \boldsymbol{c} \cdot \boldsymbol{\nabla} \cdot (\boldsymbol{S}\boldsymbol{\nabla}\boldsymbol{c}) d\Omega = -\int_{\Omega} \boldsymbol{\nabla}\boldsymbol{c} : \boldsymbol{S}\boldsymbol{\nabla}\boldsymbol{c} d\Omega + \int_{\Gamma} \boldsymbol{c} \cdot \boldsymbol{S}\frac{\partial \boldsymbol{c}}{\partial n} d\Gamma$$

The left hand side reflects the stiffness terms present in Eq. (6.16) which after inserting, rearranging and omitting brackets if possible yields the functional governed only by first order derivatives. Both the mass and stiffness integrals across the domain reflect symmetry with respect to the solution (van Kan, et al., 2008; Zienkiewicz, et al., 2005):

$$\frac{\partial (J_T + J_P)}{\partial t} = \int_{\Omega} \boldsymbol{c} \cdot \left(\boldsymbol{M_I} + H_{vap}\boldsymbol{M_{II}}\right)\frac{\partial \boldsymbol{c}}{\partial t} d\Omega$$

$$+ \int_{\Omega} \frac{1}{2}\boldsymbol{\nabla}\boldsymbol{c} : \boldsymbol{S_I}\boldsymbol{\nabla}\boldsymbol{c} d\Omega + \int_{\Omega} \frac{1}{2} H_{vap}\boldsymbol{\nabla}\boldsymbol{c} : \boldsymbol{S_{II}}\boldsymbol{\nabla}\boldsymbol{c} d\Omega \tag{6.21}$$

$$- \int_{\Gamma_A} \frac{1}{2}\boldsymbol{c} \cdot \boldsymbol{S_I}\frac{\partial \boldsymbol{c}}{\partial n} d\Gamma_A - \int_{\Gamma_A} \frac{1}{2} H_{vap}\boldsymbol{c} \cdot \boldsymbol{S_{II}}\frac{\partial \boldsymbol{c}}{\partial n} d\Gamma_A$$

Each conservation equation is represented by definition of thermodynamic equilibrium between the internal and kinetic energies across the domain and the energy sources along the boundary. Using the thermal energy and mass densities as well as the heat and mass fluxes allows to represent the functional as conservation of energy:

$$\frac{\partial (J_T + J_P)}{\partial t} = \int_{\Omega} T\left(\frac{\partial \overline{\rho_T}}{\partial t} + H_{vap}\frac{\partial \overline{\rho_{gw}}}{\partial t}\right) d\Omega + \int_{\Omega} P_c\left(\frac{\partial \overline{\rho_w}}{\partial t} + \frac{\partial \overline{\rho_{gw}}}{\partial t}\right) d\Omega$$

$$+ \int_{\Omega} \frac{1}{2}\boldsymbol{\nabla} T \cdot \left(\boldsymbol{q_T} + H_{vap}\boldsymbol{q_{gw}}\right) d\Omega + \int_{\Omega} \frac{1}{2}\boldsymbol{\nabla} P_c \cdot \left(\boldsymbol{q_w} + \boldsymbol{q_{gw}}\right) d\Omega \tag{6.22}$$

$$- \int_{\Gamma_A} \frac{1}{2} T\left(\boldsymbol{q_T} + H_{vap}\boldsymbol{q_{gw}}\right) \cdot \boldsymbol{n} d\Gamma_A - \int_{\Gamma_A} \frac{1}{2} P_c\left(\boldsymbol{q_w} + \boldsymbol{q_{gw}}\right) \cdot \boldsymbol{n} d\Gamma_A$$

$$\rightarrow \frac{\partial (J_T + J_P)}{\partial t} = \left(\frac{\partial U_T}{\partial t} + \frac{\partial U_P}{\partial t}\right) + \left(\frac{\partial E_{kin_T}}{\partial t} + \frac{\partial E_{kin_P}}{\partial t}\right) - \left(\frac{\partial Q_{A_T}}{\partial t} + \frac{\partial Q_{A_P}}{\partial t}\right)$$

where

U_T	[KJ]	Internal energy across the domain associated with energy change
E_{kin_T}	[KJ]	Kinetic energy across the domain associated with the heat flux
U_P	[kgJ/m^3]	Internal energy across the domain associated with mass change
E_{kin_P}	[kgJ/m^3]	Kinetic energy across the domain associated with the mass fluxes
Q_{A_T}	[KJ]	Source of thermal energy along the boundary
Q_{A_P}	[kgJ/m^3]	Source of energy related to mass exchange along the boundary

Minimisation of the energy functional

The solution of this energy functional and thus the system of PDE's is defined by the approximate solution and a complimentary variation also referred to as the test function (Vermolen, 2005; van Kan, et al., 2008). This variation or test function is not known and governed by an arbitrary scalar parameter (Vermolen, 2005; van Kan, et al., 2008):

$$\boldsymbol{c}(\boldsymbol{x},t) = \hat{\boldsymbol{c}}(\boldsymbol{x},t) + \epsilon_C \boldsymbol{\eta_C}(\boldsymbol{x}) \tag{6.23}$$

where

ϵ_C	[-]	Arbitrary parameter governing the contribution of the variation
$\hat{\boldsymbol{c}}$	[var.]	Approximate solution vector, temperature and capillary pressure
$\boldsymbol{\eta_C}$	[var.]	Variation or test function vector, temperature and capillary pressure

Eq. (6.23) is inserted into Eq. (6.21) while also grouping the stiffness terms. The partial derivatives and the gradients are also expressed in the approximate solution and the variation:

$$\begin{aligned}\frac{\partial(J_T + J_P)}{\partial t} &= \int_{\Omega} (\hat{\boldsymbol{c}} + \epsilon_C \boldsymbol{\eta_C}) \cdot \left(\boldsymbol{M_I} + H_{vap}\boldsymbol{M_{II}}\right) \frac{\partial(\hat{\boldsymbol{c}} + \epsilon_C \boldsymbol{\eta_C})}{\partial t} d\Omega \\ &+ \int_{\Omega} \frac{1}{2} \boldsymbol{\nabla}(\hat{\boldsymbol{c}} + \epsilon_C \boldsymbol{\eta_C}) : \left(\boldsymbol{S_I} + H_{vap}\boldsymbol{S_{II}}\right) \boldsymbol{\nabla}(\hat{\boldsymbol{c}} + \epsilon_C \boldsymbol{\eta_C}) d\Omega \\ &- \int_{\Gamma_A} \frac{1}{2} (\hat{\boldsymbol{c}} + \epsilon_C \boldsymbol{\eta_C}) \cdot \left(\boldsymbol{S_I} + H_{vap}\boldsymbol{S_{II}}\right) \frac{\partial(\hat{\boldsymbol{c}} + \epsilon_C \boldsymbol{\eta_C})}{\partial n} d\Gamma_A\end{aligned} \tag{6.24}$$

A sufficiently accurate approximate solution is obtained in case the influence of the variation is minimal. This inflection point is defined by minimisation of the energy functional with respect to the parameter which being a scalar quantity leads to the following relation (Vermolen, 2005; van Kan, et al., 2008):

$$\begin{aligned}\frac{d}{d\epsilon_C}\frac{\partial(J_T + J_P)}{\partial t} &= \int_{\Omega} \boldsymbol{\eta_C} \cdot \left(\boldsymbol{M_I} + H_{vap}\boldsymbol{M_{II}}\right) \frac{\partial(\hat{\boldsymbol{c}} + \epsilon_C \boldsymbol{\eta_C})}{\partial t} d\Omega + \int_{\Omega} \boldsymbol{\nabla}\boldsymbol{\eta_C} : \left(\boldsymbol{S_I} + H_{vap}\boldsymbol{S_{II}}\right) \boldsymbol{\nabla}\hat{\boldsymbol{c}} d\Omega \\ &+ \int_{\Omega} \epsilon_C \boldsymbol{\nabla}\boldsymbol{\eta_C} : \left(\boldsymbol{S_I} + H_{vap}\boldsymbol{S_{II}}\right) \boldsymbol{\nabla}\boldsymbol{\eta_C} d\Omega - \int_{\Gamma_A} \frac{1}{2} \boldsymbol{\eta_C} \cdot \left(\boldsymbol{S_I} + H_{vap}\boldsymbol{S_{II}}\right) \frac{\partial(\hat{\boldsymbol{c}} + \epsilon_C \boldsymbol{\eta_C})}{\partial n} d\Gamma_A = 0\end{aligned} \tag{6.25}$$

The weak form is obtained through omitting the influence of the variation by stating the governing parameter as zero (Vermolen, 2005; van Kan, et al., 2008). The variation is thus removed from the first partial derivative, neglecting time dependence. The boundary integral is only governed by the approximate solution and the weak form thus becomes:

$$\left.\frac{d}{d\epsilon_C}\frac{\partial(J_T+J_P)}{\partial t}\right|_{\epsilon_C=0} = \int_\Omega \boldsymbol{\eta_C}\cdot\left(\boldsymbol{M_I}+H_{vap}\boldsymbol{M_{II}}\right)\frac{\partial\hat{\boldsymbol{c}}}{\partial t}d\Omega$$

$$+\int_\Omega \boldsymbol{\nabla\eta_C}:\left(\boldsymbol{S_I}+H_{vap}\boldsymbol{S_{II}}\right)\boldsymbol{\nabla}\hat{\boldsymbol{c}}d\Omega-\int_{\Gamma_A}\boldsymbol{\eta_C}\cdot\left(\boldsymbol{S_I}+H_{vap}\boldsymbol{S_{II}}\right)\frac{\partial\hat{\boldsymbol{c}}}{\partial n}d\Gamma_A=0 \tag{6.26}$$

The obtained result indicates that the weak form is directly available by multiplying the system of PDE's with the variation or test function and integrating across the domain as commonly adopted (van Kan, et al., 2008; Segal, 2008). From consideration of the variation it also becomes clear that it can be interpreted as virtual temperature or capillary pressure development that disturbs thermodynamic equilibrium (Zienkiewicz, et al., 2005). This incremental functional development is expressed omitting the indicative sign for the approximate solution as commonly adopted (van Kan, et al., 2008):

$$\frac{\delta(J_T+J_P)}{\partial t} = \int_\Omega \boldsymbol{\delta c}\cdot\left(\boldsymbol{M_I}+H_{vap}\boldsymbol{M_{II}}\right)\frac{\partial\boldsymbol{c}}{\partial t}d\Omega$$

$$+\int_\Omega \boldsymbol{\nabla\delta c}:\left(\boldsymbol{S_I}+H_{vap}\boldsymbol{S_{II}}\right)\boldsymbol{\nabla c}d\Omega-\int_{\Gamma_A}\boldsymbol{\delta c}\cdot\left(\boldsymbol{S_I}+H_{vap}\boldsymbol{S_{II}}\right)\frac{\partial\boldsymbol{c}}{\partial n}d\Gamma_A=0 \tag{6.27}$$

Weak form governing the transport continuum

The final expression for the weak form is obtained through inserting the Neumann boundary conditions, defined by Eq. (6.13) and Eq. (6.14) (van Kan, et al., 2008). Two contributions are obtained with the left hand side expressed in the temperature and the density of the water vapour phase. Force contributions are governed by the imposed behaviour at a distance from the surface:

$$\int_\Omega \boldsymbol{\eta_C}\cdot\left(\boldsymbol{M_I}+H_{vap}\boldsymbol{M_{II}}\right)\frac{\partial\boldsymbol{c}}{\partial t}d\Omega+\int_\Omega \boldsymbol{\nabla\eta_C}:\left(\boldsymbol{S_I}+H_{vap}\boldsymbol{S_{II}}\right)\boldsymbol{\nabla c}d\Omega$$

$$+\int_{\Gamma_A}\boldsymbol{\eta_C}\cdot\begin{bmatrix}\alpha_A T\\ \beta_A\rho_{gw}\end{bmatrix}d\Gamma_A=\int_{\Gamma_A}\boldsymbol{\eta_C}\cdot\begin{bmatrix}\alpha_A T_\infty\\ \beta_A\rho_{gw_\infty}\end{bmatrix}d\Gamma_A \tag{6.28}$$

The weak form is governed by first order derivatives which allow the approximation of the solution to vary linearly across the domain, commonly referred to as C^0 continuity (van Kan, et al., 2008). Finding a solution which fulfils the weak form thus proves more convenient compared to the higher order strong form as previously stated.

6.3.2 FEM definition by means of Galerkin's method

The solution of the weak form, stated in Eq. (6.28), is obtained through numerical approximation. The point-based approach of the FDM as presented in chapter 4 is less suitable, especially considering the implementation for a 2D cross-section (Zienkiewicz, et al., 2005). Moreover, the symmetric mass and stiffness integrals with respect to the variation and the solution, as present in the weak form, allow for a different approximation technique based on Galerkin's method (van Kan, et al., 2008; Zienkiewicz, et al., 2005). As such, the weak form is approximated by a linear combination of basis functions and nodal variables (van Kan, et al., 2008; Segal, 2008). Applying Galerkin's method will naturally lead to a FEM discretisation (van Kan, et al., 2008).

Galerkin's method

The first order weak form requires that the basis functions have C^0 continuity (van Kan, et al., 2008). These functions are linearly continuous in the domain and have piecewise continuous derivatives (van Kan, et al., 2008). Across the domain also nodal variables are defined which include edges at which Neumann boundary conditions are imposed (van Kan, et al., 2008):

$$\boldsymbol{c}(\boldsymbol{x},t) \approx \sum_{j=1}^{n_{tot}} \boldsymbol{N_{C_j}}(\boldsymbol{x})\boldsymbol{c_j}(t) \tag{6.29}$$

where

$\cdots_j$		Indication for the node number
n_{tot}	[-]	Total number of nodes across the domain
$\boldsymbol{c_j}$	[var.]	Nodal variables vector, temperature and capillary pressure
$\boldsymbol{N_{C_j}}$	[m]	Nodal basis function matrix, temperature and capillary pressure

The variation or test function must also be C^0 continuous and is commonly defined from the same domain as the approximate solution, omitting time dependence (van Kan, et al., 2008; Segal, 2008):

$$\boldsymbol{\eta_C}(\boldsymbol{x}) \approx \sum_{i=1}^{n_{tot}} \boldsymbol{N_{C_i}}(\boldsymbol{x})\boldsymbol{\eta_{C_i}} \tag{6.30}$$

where

$\cdots_i$		Indication for the node number
$\boldsymbol{\eta_{C_i}}$	[var.]	Nodal variation or test vector, temperature and capillary pressure
$\boldsymbol{N_{C_i}}$	[m]	Nodal basis function matrix, temperature and capillary pressure

Inserting Eq. (6.29) and Eq. (6.30) into the weak form, defined by Eq. (6.28), leads to Galerkin's approximation expressed in the nodal variables (van Kan, et al., 2008). The gradient of the variables and the variation are approximated by the gradient of the shape functions and the nodal values. Furthermore, the dot products are defined by the transpose of the nodal variation vector taken outside the integrals (Wells, 2006). The boundary integrals are, for the moment, not approximated since the water vapour density is not a variable:

$$\sum_{i=1}^{n_{tot}} \boldsymbol{\eta_{C_i}}^{T} \sum_{j=1}^{n_{tot}} \left(\int_{\Omega} \boldsymbol{N_{C_i}}^{T} (\boldsymbol{M_I} + H_{vap}\boldsymbol{M_{II}}) \boldsymbol{N_{C_j}} d\Omega \frac{\partial \boldsymbol{c_j}}{\partial t} + \int_{\Omega} (\boldsymbol{\nabla N_{C_i}})^{T} (\boldsymbol{S_I} + H_{vap}\boldsymbol{S_{II}}) \boldsymbol{\nabla N_{C_j}} d\Omega \, \boldsymbol{c_j} \right)$$
$$+ \sum_{i=1}^{n_{tot}} \boldsymbol{\eta_{C_i}}^{T} \int_{\Gamma_A} \boldsymbol{N_{C_i}}^{T} \begin{bmatrix} \alpha_A T \\ \beta_A \rho_{gw} \end{bmatrix} d\Gamma_A = \sum_{i=1}^{n_{tot}} \boldsymbol{\eta_{C_i}}^{T} \int_{\Gamma_A} \boldsymbol{N_{C_i}}^{T} \begin{bmatrix} \alpha_A T_{\infty} \\ \beta_A \rho_{gw_{\infty}} \end{bmatrix} d\Gamma_A \tag{6.31}$$

However, the approximate solution must hold true for all possible variations. This makes the choice arbitrary and the following applies (van Kan, et al., 2008; Segal, 2008):

$$\sum_{j=1}^{n_{tot}} \left(\int_{\Omega} \boldsymbol{N_{C_i}}^{T} (\boldsymbol{M_I} + H_{vap}\boldsymbol{M_{II}}) \boldsymbol{N_{C_j}} d\Omega \frac{\partial \boldsymbol{c_j}}{\partial t} + \int_{\Omega} (\boldsymbol{\nabla N_{C_i}})^{T} (\boldsymbol{S_I} + H_{vap}\boldsymbol{S_{II}}) \boldsymbol{\nabla N_{C_j}} d\Omega \, \boldsymbol{c_j} \right)$$
$$+ \int_{\Gamma_A} \boldsymbol{N_{C_i}}^{T} \begin{bmatrix} \alpha_A T \\ \beta_A \rho_{gw} \end{bmatrix} d\Gamma_A = \int_{\Gamma_A} \boldsymbol{N_{C_i}}^{T} \begin{bmatrix} \alpha_A T_{\infty} \\ \beta_A \rho_{gw_{\infty}} \end{bmatrix} d\Gamma_A \qquad (i = 1, \cdots, n_{tot}) \tag{6.32}$$

FEM discretisation of the domain

The FEM definition is obtained by discretisation of the domain using a finite number of elements (van Kan, et al., 2008). Each element is described by its nodal variables and the corresponding basis functions (van Kan, et al., 2008). The latter are in the FEM commonly referred to as shape functions to indicate the approximation, in this case linear, across each element (Segal, 2008). The gradient of the variables are expressed through the constant gradient matrix as commonly adopted (Wells, 2006; Felippa, 2004a; Blom, 2009):

$$\boldsymbol{c}(\boldsymbol{x}, t) \approx \sum_{e=1}^{e_{tot}} \boldsymbol{N_C}^{\boldsymbol{e}}(\boldsymbol{x}) \boldsymbol{c}^{\boldsymbol{e}}(t)$$
$$\boldsymbol{\nabla c}(\boldsymbol{x}, t) \approx \sum_{e=1}^{e_{tot}} \boldsymbol{\nabla_C N_C}^{\boldsymbol{e}}(\boldsymbol{x}) \boldsymbol{c}^{\boldsymbol{e}}(t) = \sum_{e=1}^{e_{tot}} \boldsymbol{B_C}^{\boldsymbol{e}} \boldsymbol{c}^{\boldsymbol{e}}(t) \tag{6.33}$$

where

$\ldots^{e}$		Indication for the element number
e_{tot}	[-]	Total number of elements distributed across the domain
$\boldsymbol{c^e}$	[var.]	Element nodal temperature and capillary pressure vector
$\boldsymbol{N_C}^{\boldsymbol{e}}$	[m]	Element matrix of the shape functions
$\boldsymbol{B_C}^{\boldsymbol{e}}$	[1/m]	Element gradient matrix of the shape functions

Using these relationships, Eq. (6.32) is restated based on the FEM approach expressed in the nodal variables (van Kan, et al., 2008). The FEM definition is characterised by summation across the domain of the element mass and stiffness matrices. The boundary integrals are only based on elements along the outer edges expressed in the temperature and the water vapour density. For both boundary contributions, the FEM discretisation is included after the water vapour pressure is redefined in the nodal variables as addressed in the next section:

$$\sum_{e=1}^{e_{tot}}\left(\int_{\Omega^e}\boldsymbol{N_C}^{e\boldsymbol{T}}\left(\boldsymbol{M_I}^{e}+\left(H_{vap}\boldsymbol{M_{II}}\right)^{\boldsymbol{e}}\right)\boldsymbol{N_C}^{\boldsymbol{e}}d\Omega^e\frac{\partial \boldsymbol{c^e}}{\partial t}+\int_{\Omega^e}\boldsymbol{B_C}^{e\boldsymbol{T}}\left(\boldsymbol{S_I}^{e}+\left(H_{vap}\boldsymbol{S_{II}}\right)^{\boldsymbol{e}}\right)\boldsymbol{B_C}^{\boldsymbol{e}}d\Omega^e\,\boldsymbol{c^e}\right)$$
$$+\sum_{e=1}^{e_{tot}}\left(\int_{\Gamma_A{}^e}\boldsymbol{N_C}^{e\boldsymbol{T}}\begin{bmatrix}\alpha_A T\\ \beta_A\rho_{gw}\end{bmatrix}d\Gamma_A{}^e\right)=\sum_{e=1}^{e_{tot}}\left(\int_{\Gamma_A{}^e}\boldsymbol{N_C}^{e\boldsymbol{T}}\begin{bmatrix}\alpha_A T_\infty\\ \beta_A\rho_{gw_\infty}\end{bmatrix}d\Gamma_A{}^e\right) \tag{6.34}$$

6.3.3 Time integration using an incremental Euler backward scheme

The FEM definition is characterised by non-linear relationships such as the desorption isotherm as well as the saturated vapour pressure and the density of liquid water. The solution also defines the mass and the stiffness of the system which, especially at increasing temperatures, complicates the behaviour. Explicit time integration, such as the Euler forward scheme used in chapter 4, defines the system based on the current time step (Vermolen, 2005). This approach is relatively straightforward and directly defines the FEM definition. However, this approach also reduces accuracy of the approximated solution and could eventually become numerically unstable. Under these circumstances, the approximate solution increasingly deviates from the actual solution. This is especially problematic since the solution has to remain within physical limits defined by the desorption isotherm.

Incremental definition of the variables

Numerical approximation is best obtained by using an Euler backward time integration scheme (van Kan, et al., 2008; Segal, 2008). This states the system based on the solution defined at the next time step, ensuring that deviations in the approximation are damped or reduced (van Kan, et al., 2008; Segal, 2008). No limitations on the size of the time step is thus required for this implicit approach (van Kan, et al., 2008; Segal, 2008). The time step is only restricted based on accuracy requirements (Segal, 2008). However, the solution is a priori not known which is addressed through an incremental definition of the variables at the next time step (Davie, et al., 2006):

$$\boldsymbol{c_{k+1}^{t+1}}=\boldsymbol{c_k^{t+1}}+\Delta\boldsymbol{c_k^{t+1}} \tag{6.35}$$

where

$\ldots^t$ Indication for the incremental time step

$\cdots_k$ Indication for the incremental step

Starting point for obtaining the solution defined at the next time step could be the solution at the current time step. However, convergence is improved by using a first order approximation of the solution based on the current and the previous time steps (van Kan, et al., 2008; Segal, 2008). Since throughout the calculation a constant size of the time step is used, the following approximation applies:

$$\boldsymbol{c_1^{t+1}}=\boldsymbol{c^t}+\Delta t\left[\frac{\partial \boldsymbol{c}}{\partial t}\right]^t\approx\boldsymbol{c^t}+\Delta t\left(\frac{\boldsymbol{c^t}-\boldsymbol{c^{t-1}}}{\Delta t}\right)=2\boldsymbol{c^t}-\boldsymbol{c^{t-1}} \tag{6.36}$$

The time derivative of the variables in Eq. (6.34) is approximated (Vermolen, 2005), while also introducing Eq. (6.35), by:

$$\frac{\partial \boldsymbol{c}}{\partial t} \approx \frac{\boldsymbol{c^{t+1}} - \boldsymbol{c^{t}}}{\Delta t} = \frac{\left(\boldsymbol{c_k^{t+1}} + \Delta \boldsymbol{c_k^{t+1}}\right) - \boldsymbol{c^{t}}}{\Delta t} \tag{6.37}$$

In addition, the incremental definition affects the gradient of the variables as approximated by the constant element gradient matrices:

$$\begin{aligned} \boldsymbol{\nabla c} &\approx \boldsymbol{\nabla c^{t+1}} = \boldsymbol{\nabla}\left(\boldsymbol{c_k^{t+1}} + \Delta \boldsymbol{c_k^{t+1}}\right) = \boldsymbol{\nabla c_k^{t+1}} + \boldsymbol{\nabla}\left(\Delta \boldsymbol{c_k^{t+1}}\right) \\ &\approx \boldsymbol{B_C}^{\boldsymbol{e}} \boldsymbol{c^e_k^{t+1}} + \boldsymbol{B_C}^{\boldsymbol{e}} \Delta \boldsymbol{c^e_k^{t+1}} = \boldsymbol{B_C}^{\boldsymbol{e}}\left(\boldsymbol{c^e_k^{t+1}} + \Delta \boldsymbol{c^e_k^{t+1}}\right) \end{aligned} \tag{6.38}$$

Boundary conditions

The incremental definition of the variables is also used to define the Neumann boundary conditions. The first condition, defined by Eq. (6.13), poses no problem since the temperature is a variable:

$$T_{k+1}^{t+1} = T_k^{t+1} + \Delta T_k^{t+1} \tag{6.39}$$

The second condition, expressed in the density of the water vapour phase as stated in Eq. (6.14), is redefined based on a first order approximation. This defines the incremental density based on the partial derivatives and the incremental variables:

$$\rho_{gw}{}_{k+1}^{t+1} = \rho_{gw}{}_{k}^{t+1} + \Delta \rho_{gw}{}_{k}^{t+1} \tag{6.40}$$

with

$$\rho_{gw}{}_{k}^{t+1} = \frac{RH_k^{t+1} P_{sat}{}_k^{t+1} M_w}{R T_k^{t+1}}$$

$$\begin{aligned} \Delta \rho_{gw}{}_{k}^{t+1} &\approx \Delta t \left[\frac{\partial \rho_{gw}}{\partial t}\right]_k^{t+1} = \Delta t \left[\frac{\partial \rho_{gw}}{\partial T}\frac{\partial T}{\partial t} + \frac{\partial \rho_{gw}}{\partial P_c}\frac{\partial P_c}{\partial t}\right]_k^{t+1} \approx \left[\frac{\partial \rho_{gw}}{\partial T}\right]_k^{t+1} \Delta T_k^{t+1} + \left[\frac{\partial \rho_{gw}}{\partial P_c}\right]_k^{t+1} \Delta P_c{}_k^{t+1} \\ &= \left(\left(P_{sat}{}_k^{t+1}\left[\frac{\partial RH}{\partial T}\right]_k^{t+1} + RH_k^{t+1}\left[\frac{\partial P_{sat}}{\partial T}\right]_k^{t+1} - \frac{RH_k^{t+1} P_{sat}{}_k^{t+1}}{T_k^{t+1}}\right)\frac{M_w}{R T_k^{t+1}}\right)\Delta T_k^{t+1} \\ &\quad + \left(P_{sat}{}_k^{t+1}\left[\frac{\partial RH}{\partial P_c}\right]_k^{t+1}\frac{M_w}{R T_k^{t+1}}\right)\Delta P_c{}_k^{t+1} \end{aligned}$$

FEM definition based on Euler backward time integration

The previous relationships are inserted into the FEM definition represented by Eq. (6.34) which becomes expressed in the incremental nodal variables. The element mass and stiffness matrices are defined at the current incremental solution of the next time step (Vermolen, 2005). Neumann boundary conditions are defined by two contributions, with at the left hand side the matrix reflecting the partial derivatives of Eq. (6.40). Also introduced, the element shape functions governing the incremental nodal variables. The right hand side represents the imposed behaviour at a distance from the surface, defined constant at the next time step:

$$\sum_{e=1}^{e_{tot}}\left(\int_{\Omega^e}\boldsymbol{N_C}^{eT}\left(\boldsymbol{M_I}^{e\,t+1}_{k}+\left(H_{vap}\boldsymbol{M_{II}}\right)^{e\,t+1}_{k}\right)\boldsymbol{N_C}^{e}d\Omega^e\left(\frac{\left(\boldsymbol{c}^{e\,t+1}_{k}+\Delta\boldsymbol{c}^{e\,t+1}_{k}\right)-\boldsymbol{c}^{e\,t}}{\Delta t}\right)\right)$$
$$+\sum_{e=1}^{e_{tot}}\left(\int_{\Omega^e}\boldsymbol{B_C}^{eT}\left(\boldsymbol{S_I}^{e\,t+1}_{k}+\left(H_{vap}\boldsymbol{S_{II}}\right)^{e\,t+1}_{k}\right)\boldsymbol{B_C}^{e}d\Omega^e\left(\boldsymbol{c}^{e\,t+1}_{k}+\Delta\boldsymbol{c}^{e\,t+1}_{k}\right)\right) \tag{6.41}$$

$$+\sum_{e=1}^{e_{tot}}\left(\int_{\Gamma_A^e}\boldsymbol{N_C}^{eT}\left(\begin{bmatrix}\alpha_A T^{e\,t+1}_{k}\\ \beta_A\rho_{gw}{}^{e\,t+1}_{k}\end{bmatrix}+\begin{bmatrix}\alpha_A & 0\\ \beta_{A_T}{}^{t+1}_{k} & \beta_{A_P}{}^{t+1}_{k}\end{bmatrix}\boldsymbol{N_C}^{e}\Delta\boldsymbol{c}^{e\,t+1}_{k}\right)d\Gamma_A{}^{e}\right)=\sum_{e=1}^{e_{tot}}\left(\int_{\Gamma_A^e}\boldsymbol{N_C}^{eT}\begin{bmatrix}\alpha_A T_\infty{}^{t+1}\\ \beta_A\rho_{gw_\infty}{}^{t+1}\end{bmatrix}d\Gamma_A{}^{e}\right)$$

with

$$\beta_{A_T}{}^{t+1}_{k}=\beta_A\left[\frac{\partial\rho_{gw}}{\partial T}\right]^{t+1}_{k}=\beta_A\left(\left(P_{sat}{}^{t+1}_{k}\left[\frac{\partial RH}{\partial T}\right]^{t+1}_{k}+RH^{t+1}_{k}\left[\frac{\partial P_{sat}}{\partial T}\right]^{t+1}_{k}-\frac{RH^{t+1}_{k}P_{sat}{}^{t+1}_{k}}{T^{t+1}_{k}}\right)\frac{M_w}{RT^{t+1}_{k}}\right)$$

$$\beta_{A_P}{}^{t+1}_{k}=\beta_A\left[\frac{\partial\rho_{gw}}{\partial P_c}\right]^{t+1}_{k}=\beta_A\left(P_{sat}{}^{t+1}_{k}\left[\frac{\partial RH}{\partial P_c}\right]^{t+1}_{k}\frac{M_w}{RT^{t+1}_{k}}\right)$$

where

$\beta_{A_T}{}^{t+1}_{k},\beta_{A_P}{}^{t+1}_{k}$ [var.] Convective mass transfer coefficients including partial derivatives of the water vapour density with respect to the temperature, capillary pressure

6.4 Incremental FEM definition

6.4.1 Discretisation based on homogeneous and isotropic 2D triangular elements

The FEM definition, stated in Eq. (6.41), is expressed in the incremental nodal variables. After rearranging the following is obtained reflecting the homogeneous and isotropic element discretisation:

$$\sum_{e=1}^{e_{tot}}\left(\boldsymbol{M_{sys}}^{e\,t+1}_{k}+\Delta t\boldsymbol{S_{sys}}^{e\,t+1}_{k}\right)\sum_{e=1}^{e_{tot}}\Delta\boldsymbol{c_{sys}}^{e\,t+1}_{k}+\Delta t\sum_{e=1}^{e_{tot}}\boldsymbol{S_{bc}}^{e\,t+1}_{k}\sum_{e=1}^{e_{tot}}\Delta\boldsymbol{c_{sys}}^{e\,t+1}_{k}$$
$$=-\left(\sum_{e=1}^{e_{tot}}\left(\boldsymbol{M_{sys}}^{e\,t+1}_{k}\left(\boldsymbol{c_{sys}}^{e\,t+1}_{k}-\boldsymbol{c_{sys}}^{e\,t}\right)+\Delta t\boldsymbol{S_{sys}}^{e\,t+1}_{k}\boldsymbol{c_{sys}}^{e\,t+1}_{k}\right)\right)-\Delta t\sum_{e=1}^{e_{tot}}\boldsymbol{Q_{bc}}^{e\,t+1}_{k} \tag{6.42}$$

with

$$\boldsymbol{c_{sys}}^{e\,t+1}_{k}=\boldsymbol{c}^{e\,t+1}_{k}$$

$$\boldsymbol{M_{sys}}^{e\,t+1}_{k}=\int_{\Omega^e}\boldsymbol{N_C}^{eT}\left(\boldsymbol{M_I}^{e\,t+1}_{k}+\left(H_{vap}\boldsymbol{M_{II}}\right)^{e\,t+1}_{k}\right)\boldsymbol{N_C}^{e}d\Omega^e$$

$$\boldsymbol{S_{sys}}^{e\,t+1}_{\;k} = \int_{\Omega^e} \boldsymbol{B_C}^{eT} \left(\boldsymbol{S_I}^{e\,t+1}_{\;k} + \left(H_{vap} \boldsymbol{S_{II}} \right)^{e\,t+1}_{\;k} \right) \boldsymbol{B_C}^{e} d\Omega^e$$

$$\boldsymbol{S_{bc}}^{e\,t+1}_{\;k} = \int_{\Gamma_A{}^e} \boldsymbol{N_C}^{eT} \begin{bmatrix} \alpha_A & 0 \\ \beta_{A_T}{}^{t+1}_{\;k} & \beta_{A_P}{}^{t+1}_{\;k} \end{bmatrix} \boldsymbol{N_C}^{e} d\Gamma_A{}^e$$

$$\boldsymbol{Q_{bc}}^{e\,t+1}_{\;k} = \int_{\Gamma_A{}^e} \boldsymbol{N_C}^{eT} \begin{bmatrix} \alpha_A \left(T^{e\,t+1}_{\;k} - T_\infty{}^{t+1} \right) \\ \beta_A \left(\rho_{gw}{}^{e\,t+1}_{\;k} - \rho_{gw_\infty}{}^{t+1} \right) \end{bmatrix} d\Gamma_A{}^e = \int_{\Gamma_A{}^e} \boldsymbol{N_C}^{eT} \begin{bmatrix} \alpha_A \left(T^{e\,t+1}_{\;k} - T_\infty{}^{t+1} \right) \\ \beta_A \dfrac{M_w}{R} \left(\dfrac{P_{gw}{}^{e\,t+1}_{\;k}}{T^{e\,t+1}_{\;k}} - \dfrac{P_{gw_\infty}{}^{t+1}}{T_\infty{}^{t+1}} \right) \end{bmatrix} d\Gamma_A{}^e$$

where

$\boldsymbol{c_{sys}}^{e\,t}$	[var.]	Element nodal variables vector at the current time step
$\boldsymbol{c_{sys}}^{e\,t+1}_{\;k}$	[var.]	Element nodal variables vector at the current incremental time step
$\boldsymbol{M_{sys}}^{e\,t+1}_{\;k}$	[var.]	Element system mass matrix at the current incremental time step
$\boldsymbol{S_{sys}}^{e\,t+1}_{\;k}$	[var.]	Element system stiffness matrix at the current incremental time step
$\boldsymbol{S_{bc}}^{e\,t+1}_{\;k}$	[var.]	Element stiffness matrix reflecting the contributions by the Neumann boundary conditions at the current incremental time step
$\boldsymbol{Q_{bc}}^{e\,t+1}_{\;k}$	[var.]	Element nodal vector reflecting the contributions by the Neumann boundary conditions at the current incremental time step

Several contributions are present which together characterise the system based on:

- The left hand side of the system is defined by summation across the domain of the element mass and stiffness matrices at the current time step increment. This system matrix is multiplied by the system vector based on the incremental nodal variables.

- The right hand side represents the system force vector defined by the element matrices multiplied with the nodal variables vector defined at the current and the next time step.

- Neumann boundary conditions are governed by the time step and contribute to the left hand side additional stiffness based on the transfer coefficients. The right hand side expresses the change in temperature and water vapour pressure at the surface.

- Periodical boundary conditions are enforced by coupling the nodal variables at the outer edges (Segal, 2008) also referred to as master-slave relationships (Hartmann & Katz, 2007). Elements connected to nodes situated at the top edge are in fact connected to the opposite nodes along the bottom edge.

- As mentioned, the basic Fourier differential equation for thermal conductivity is obtained through neglecting the constants related to the second conservation equation. This reduces the mass and stiffness contributions as well as the system and only the temperature development is determined.

6.4.2 Spatial integration based on linear triangular shape functions

The element-based integrals are numerically approximated by using 2D triangular elements as presented in Fig. 6.3 (van Kan, et al., 2008). Each element is based on connecting three nodes that are positioned counter clockwise (van Kan, et al., 2008; Felippa, 2004a). Nodes are defined randomly in horizontal and vertical direction of the global coordinate system. Care should be taken not to connect nodes that cause elements to overlap or cross. This is ensured by using a rectangular grid-based node distribution with local random positioning (Schlangen, 1993; Vervuurt, 1997). The chosen numbering also leads to a positive area based on the nodal coordinate differences (Felippa, 2004a):

$$A^e = \frac{x_{21}y_{31} - y_{12}x_{13}}{2} \tag{6.43}$$

with

$x_{ij} = x_i - x_j$ $\qquad$ $y_{ij} = y_i - y_j$

where

A^e	[m^2]	Area of the 2D triangular element
x_i, y_i	[m]	Cartesian coordinate defined by the x-axis, y-axis of node 'i'

Natural coordinate systems

The basis of the FEM discretisation is formed by definition of element-based coordinate systems. Perpendicular to each edge natural coordinate axes are introduced that define the global coordinates based on nodal values (van Kan, et al., 2008; Felippa, 2004a). An additional relationship is introduced, stated as first in Fig. 6.3, to normalise the natural coordinate systems (van Kan, et al., 2008; Felippa, 2004a). These three conditions define, at the most, linear interpolation functions governing the element expressed by the natural coordinates systems (van Kan, et al., 2008; Felippa, 2004a):

$$\begin{bmatrix}\xi_1\\ \xi_2\\ \xi_3\end{bmatrix} = \frac{1}{2A^e}\begin{bmatrix}x_2y_3 - x_3y_2 & y_{23} & x_{32}\\ x_3y_1 - x_1y_3 & y_{31} & x_{13}\\ x_1y_2 - x_2y_1 & y_{12} & x_{21}\end{bmatrix}\begin{bmatrix}1\\ x\\ y\end{bmatrix} \tag{6.44}$$

where

ξ_1, ξ_2, ξ_3	[m]	Natural coordinate systems defined perpendicular to each edge of the triangular element

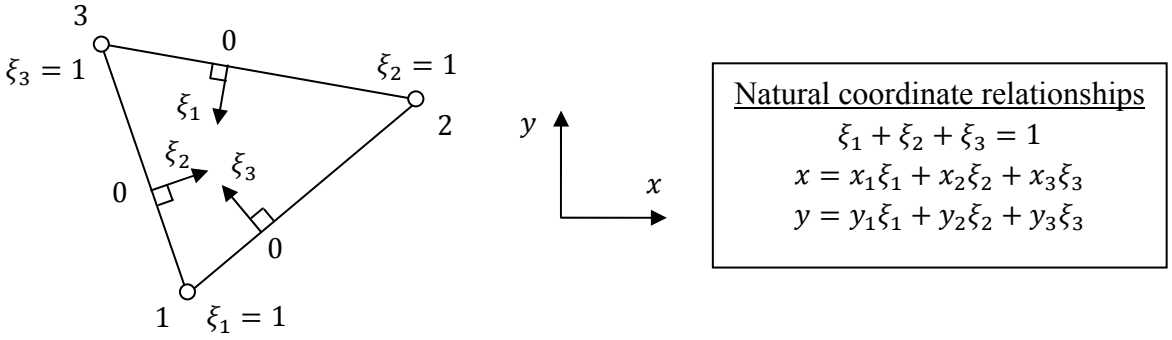

Fig. 6.3 *Schematic representation of the triangular element in* $\mathbb{R}^2$. *Global coordinates are expressed by natural coordinate systems, defined perpendicular to each edge. The sum of the natural coordinates is unity* (van Kan, et al., 2008; Felippa, 2004a).

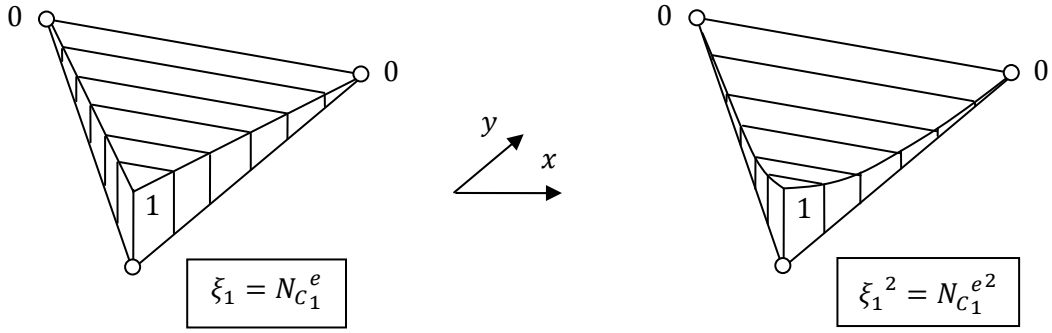

Fig. 6.4 *Schematic representation of the triangular linear shape function (left) governing the first node in* $\mathbb{R}^2$ (Felippa, 2004a; Zienkiewicz, et al., 2005)*. The quadratic form of this shape function (right) is used for the consistent mass matrix.*

Element discretisation

The natural coordinates systems are used to define the nodal shape functions governing the distribution of the variables since the linear basis fulfils C^0 continuity (van Kan, et al., 2008; Felippa, 2004a). Moreover, the normalisation provides for continuous approximation of the variables across the domain by ensuring compatibility between elements (van Kan, et al., 2008; Felippa, 2004a). The shape functions thus vary linearly across the element governed by the definition of unity at the corresponding node and zero at the remaining nodes as seen in Fig. 6.4 (Felippa, 2004a; Zienkiewicz, et al., 2005). Using the FEM discretisation in Eq. (6.33) while also taking the incremental approach into account defines the contribution for each element (Felippa, 2004a; Zienkiewicz, et al., 2005):

$$\boldsymbol{c^e}(\boldsymbol{x^e}, t, k) \approx \boldsymbol{N_C}^{\boldsymbol{e}}(\boldsymbol{x^e})\boldsymbol{c_k^{e\,t+1}} \tag{6.45}$$

with

$$\boldsymbol{c^e}(\boldsymbol{x^e}, t, k) = \begin{bmatrix} T^e(\boldsymbol{x^e}, t, k) \\ P_c{}^e(\boldsymbol{x^e}, t, k) \end{bmatrix}$$

$$\boldsymbol{N_C}^{\boldsymbol{e}}(\boldsymbol{x^e}) = \begin{bmatrix} \xi_1 & 0 & \xi_2 & 0 & \xi_3 & 0 \\ 0 & \xi_1 & 0 & \xi_2 & 0 & \xi_3 \end{bmatrix} = \begin{bmatrix} N_{C_1}^{\ e} & 0 & N_{C_2}^{\ e} & 0 & N_{C_3}^{\ e} & 0 \\ 0 & N_{C_1}^{\ e} & 0 & N_{C_2}^{\ e} & 0 & N_{C_3}^{\ e} \end{bmatrix}$$

$$\boldsymbol{c_k^{e\,t+1}} = \begin{bmatrix} T_{1\,k}^{e\,t+1} \\ P_{c_{1_k}}^{e\,t+1} \\ T_{2\,k}^{e\,t+1} \\ P_{c_{2_k}}^{e\,t+1} \\ T_{3\,k}^{e\,t+1} \\ P_{c_{3_k}}^{e\,t+1} \end{bmatrix}$$

The gradient of the variables is approximated as constant across each element based on the partial derivatives of the linear nodal shape functions (Felippa, 2004a; Zienkiewicz, et al., 2005). With regard to this the derivatives of the variables are grouped in each direction which will prove beneficial in definition of the flux across the element:

$$\boldsymbol{\nabla c^e}(t, k) \approx \boldsymbol{B_C}^{\boldsymbol{e}}\boldsymbol{c_k^{e\,t+1}} \tag{6.46}$$

with

$$\boldsymbol{\nabla c^e}(t,k) = \begin{bmatrix} \dfrac{\partial \boldsymbol{c^e}(t,k)}{\partial x} \\ \dfrac{\partial \boldsymbol{c^e}(t,k)}{\partial y} \end{bmatrix} = \begin{bmatrix} \dfrac{\partial T^e(t,k)}{\partial x} \\ \dfrac{\partial {P_c}^e(t,k)}{\partial x} \\ \dfrac{\partial T^e(t,k)}{\partial y} \\ \dfrac{\partial {P_c}^e(t,k)}{\partial y} \end{bmatrix} \qquad \begin{bmatrix} \dfrac{\partial T^e(t,k)}{\partial N_{C_1}^e} \\ \dfrac{\partial {P_c}^e(t,k)}{\partial N_{C_1}^e} \\ \dfrac{\partial T^e(t,k)}{\partial N_{C_2}^e} \\ \dfrac{\partial {P_c}^e(t,k)}{\partial N_{C_2}^e} \\ \dfrac{\partial T^e(t,k)}{\partial N_{C_3}^e} \\ \dfrac{\partial {P_c}^e(t,k)}{\partial N_{C_3}^e} \end{bmatrix} = \begin{bmatrix} {T_1}_k^{e\,t+1} \\ {P_{c_1}}_k^{e\,t+1} \\ {T_2}_k^{e\,t+1} \\ {P_{c_2}}_k^{e\,t+1} \\ {T_3}_k^{e\,t+1} \\ {P_{c_3}}_k^{e\,t+1} \end{bmatrix} = \boldsymbol{c_k^{e\,t+1}}$$

$$\boldsymbol{B_C}^{\boldsymbol{e}} = \begin{bmatrix} \dfrac{\partial N_{C_1}^e}{\partial x} & 0 & \dfrac{\partial N_{C_2}^e}{\partial x} & 0 & \dfrac{\partial N_{C_3}^e}{\partial x} & 0 \\ 0 & \dfrac{\partial N_{C_1}^e}{\partial x} & 0 & \dfrac{\partial N_{C_2}^e}{\partial x} & 0 & \dfrac{\partial N_{C_3}^e}{\partial x} \\ \dfrac{\partial N_{C_1}^e}{\partial y} & 0 & \dfrac{\partial N_{C_2}^e}{\partial y} & 0 & \dfrac{\partial N_{C_3}^e}{\partial y} & 0 \\ 0 & \dfrac{\partial N_{C_1}^e}{\partial y} & 0 & \dfrac{\partial N_{C_2}^e}{\partial y} & 0 & \dfrac{\partial N_{C_3}^e}{\partial y} \end{bmatrix} = \frac{1}{2A^e} \begin{bmatrix} y_{23} & 0 & y_{31} & 0 & y_{12} & 0 \\ 0 & y_{23} & 0 & y_{31} & 0 & y_{12} \\ x_{32} & 0 & x_{13} & 0 & x_{21} & 0 \\ 0 & x_{32} & 0 & x_{13} & 0 & x_{21} \end{bmatrix}$$

Both relationships are used to evaluate the integrals in the FEM definition of Eq. (6.42). The element mass and stiffness matrices are determined and the contributions governed by the Neumann boundary conditions are stated. The latter are defined only for elements with an edge located at the left and right outer edges.

Element mass matrix

The contribution of each element to the mass of the continuum is determined by the first integral. Integration involves nodal shape functions that vary linearly across each element. These could be evaluated numerically using Gauss integration (Felippa, 2004a; Zienkiewicz, et al., 2005). However, consideration of the shape functions, shown for example in Fig. 6.4, makes solving these integrals relatively straightforward. The resultant consistent mass matrix is expressed in the nodal-based sub-matrices, stated in Eq. (6.12), reflecting row dependence of the variables. Diagonal contributions are defined by the quadratic of the shape functions (Felippa, 2004a; Zienkiewicz, et al., 2005):

$$\boldsymbol{M_{sys}}_{\boldsymbol{k}}^{\boldsymbol{e\,t+1}} = \frac{DA^e}{12} \begin{bmatrix} 2\boldsymbol{M_{sys}}_{\boldsymbol{1_k}}^{\boldsymbol{e\,t+1}} & \boldsymbol{M_{sys}}_{\boldsymbol{1_k}}^{\boldsymbol{e\,t+1}} & \boldsymbol{M_{sys}}_{\boldsymbol{1_k}}^{\boldsymbol{e\,t+1}} \\ \boldsymbol{M_{sys}}_{\boldsymbol{2_k}}^{\boldsymbol{e\,t+1}} & 2\boldsymbol{M_{sys}}_{\boldsymbol{2_k}}^{\boldsymbol{e\,t+1}} & \boldsymbol{M_{sys}}_{\boldsymbol{2_k}}^{\boldsymbol{e\,t+1}} \\ \boldsymbol{M_{sys}}_{\boldsymbol{3_k}}^{\boldsymbol{e\,t+1}} & \boldsymbol{M_{sys}}_{\boldsymbol{3_k}}^{\boldsymbol{e\,t+1}} & 2\boldsymbol{M_{sys}}_{\boldsymbol{3_k}}^{\boldsymbol{e\,t+1}} \end{bmatrix} \tag{6.47}$$

with

$$\boldsymbol{M_{sys}}_{\boldsymbol{i\,k}}^{\boldsymbol{e\,t+1}} = \boldsymbol{M_{I}}_{\boldsymbol{i\,k}}^{\boldsymbol{e\,t+1}} + \left(H_{vap}\boldsymbol{M_{II}}\right)_{\boldsymbol{i\,k}}^{\boldsymbol{e\,t+1}}$$

where

$\boldsymbol{M_{sys}}_{i\,k}^{e\,t+1}$ [var.] Element system mass matrix defined at node 'i' at the current incremental time step

As an alternative, based on the diagonal dominance, the mass integral is approximated using the Newton-Cotes rule (van Kan, et al., 2008; Segal, 2008). Summation across the contributions only involves the shape functions corresponding to the node, resulting in the formation of the diagonal or lumped mass matrix (van Kan, et al., 2008; Zienkiewicz, et al., 2005). Each node thus represents a third of the thermal energy and mass densities. The same matrix is obtained by addition across each row in Eq. (6.47) (Zienkiewicz, et al., 2005):

$$\boldsymbol{M_{sys}}_{k}^{e\,t+1} \approx D\frac{2A^e}{6}\left(\sum_{j=1}^{3}\left(\boldsymbol{N_C}_i^{e\,T}\left(\boldsymbol{M_I}_{i\,k}^{e\,t+1}+\left(H_{vap}\boldsymbol{M_{II}}\right)_{i\,k}^{e\,t+1}\right)\boldsymbol{N_C}_j^{e}\right)\right) \qquad (i=1,\cdots,3)$$

$$=\frac{DA^e}{3}\begin{bmatrix}\boldsymbol{M_{sys}}_{1_k}^{e\,t+1} & 0 & 0\\ 0 & \boldsymbol{M_{sys}}_{2_k}^{e\,t+1} & 0\\ 0 & 0 & \boldsymbol{M_{sys}}_{3_k}^{e\,t+1}\end{bmatrix} \qquad (6.48)$$

Lumping is beneficial since this simplifies the system, especially in case of explicit time integration (Segal, 2008). Implicit solution schemes become mainly governed by the Laplacian operator defining the constant element fluxes (van Kan, et al., 2008).

Element stiffness matrix

The heat and mass fluxes across each element are described by the stiffness of the continuum, defined through the second integral in Eq. (6.42). Direct integration determines the element stiffness matrix based on the constant gradient matrix and the averaged nodal sub-matrices defined by Eq. (6.12). The heat and mass fluxes are thus constant across the element. The partial derivatives of the variables are grouped with respect to each global direction, allowing for a straightforward definition. Under isotropic conditions the stiffness matrix thus reflects only diagonal contributions through the identity matrix:

$$\boldsymbol{S_{sys}}_{k}^{e\,t+1} = DA^e\boldsymbol{B_C}^{e\,T}\left(\boldsymbol{S_I}_{k}^{e\,t+1}+\left(H_{vap}\boldsymbol{S_{II}}\right)_{k}^{e\,t+1}\right)\boldsymbol{IB_C}^{e} \qquad (6.49)$$

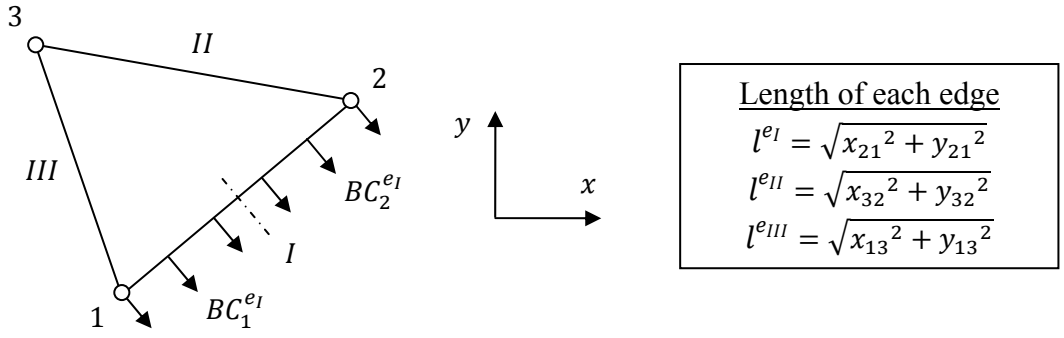

Fig. 6.5 *Boundary conditions are imposed along the edges of 2D triangular element in* $\mathbb{R}^2$ *as indicated. The length of these edges are determined by Pythagorean's theorem.*

Neumann boundary conditions

The remaining integral at the left hand side is only determined for elements with an edge situated at the boundary. Such an edge is shown in Fig. 6.5 and indicates the outward orientated gradient of the variables as described by the Neumann boundary conditions. Commonly, Newton-Cotes integration is used to approximate the boundary integral, omitting interaction between the stiffness components (van Kan, et al., 2008; Segal, 2008). This additional matrix is defined by the linear shape functions along the edge and reflects equal contributions to both nodes which in this case obtains (van Kan, et al., 2008; Segal, 2008):

$$\boldsymbol{S_{bc}}^{\boldsymbol{e\,t+1}}_{\boldsymbol{k}} \approx D \sum_{d=I}^{III} \frac{l^{e_d}}{2} \sum_{j_d=1}^{2} \left(\boldsymbol{N_{C_{i_d}}^{e\ T}} \begin{bmatrix} \alpha_A & 0 \\ \beta_{A_T}{}^{e\ t+1}_{i_{d_k}} & \beta_{A_P}{}^{e\ t+1}_{i_{d_k}} \end{bmatrix} \boldsymbol{N_{C_{j_d}}^{e}} \right) \qquad (i_d = 1, \cdots, 2)$$

$$\rightarrow D \frac{l^{e_I}}{2} \begin{bmatrix} \alpha_A & 0 & & \\ \beta_{A_T}{}^{e\,t+1}_{1_k} & \beta_{A_P}{}^{e\,t+1}_{1_k} & 0 & \\ & & \alpha_A & 0 \\ 0 & & \beta_{A_T}{}^{e\,t+1}_{2_k} & \beta_{A_P}{}^{e\,t+1}_{2_k} \end{bmatrix} \tag{6.50}$$

where

$\ldots^{e_d}$		Indication for the edge of the triangular element
$\cdots_{i_d}, \cdots_{j_d}$		Indications for the node number at edge 'd' of the triangular element
l^{e_d}	[m]	Length of edge 'd' of the triangular element

As an alternative, the sub-matrices governing the Neumann boundary conditions are directly imposed on the system at the incremental nodal variables. This procedure is more convenient, since the element mass and stiffness matrices are first assembled after which each nodal boundary condition is included once.

The corresponding integral at the right hand side represent the difference between the temperature and water vapour pressure at the surface, defined at the current incremental step and the corresponding values situated at a distance. Using Newton-Cotes integration leads to the following force vector corresponding to the first edge (van Kan, et al., 2008; Segal, 2008):

$$\boldsymbol{Q_{bc}}^{\boldsymbol{e\,t+1}}_{\boldsymbol{k}} \approx D \sum_{d=I}^{III} \frac{l^{e_d}}{2} \left(\boldsymbol{N_{C_{i_d}}^{e\ T}} \begin{bmatrix} \alpha_A \left(T_{i_{d_k}}^{e\ t+1} - T_\infty{}^{t+1} \right) \\ \beta_A \dfrac{M_w}{R} \left(\dfrac{P_{gw}{}^{e\ t+1}_{i_{d_k}}}{T_{i_{d_k}}^{e\ t+1}} - \dfrac{P_{gw_\infty}{}^{t+1}}{T_\infty{}^{t+1}} \right) \end{bmatrix} \right) \qquad (i_d = 1, \cdots, 2)$$

$$\rightarrow D \frac{l^{e_I}}{2} \begin{bmatrix} \alpha_A \left(T_{1\,k}^{e\,t+1} - T_\infty{}^{t+1} \right) \\ \beta_A \dfrac{M_w}{R} \left(\dfrac{P_{gw}{}^{e\,t+1}_{1_k}}{T_{1\,k}^{e\,t+1}} - \dfrac{P_{gw_\infty}{}^{t+1}}{T_\infty{}^{t+1}} \right) \\ \alpha_A \left(T_{2\,k}^{e\,t+1} - T_\infty{}^{t+1} \right) \\ \beta_A \dfrac{M_w}{R} \left(\dfrac{P_{gw}{}^{e\,t+1}_{2_k}}{T_{2\,k}^{e\,t+1}} - \dfrac{P_{gw_\infty}{}^{t+1}}{T_\infty{}^{t+1}} \right) \end{bmatrix} \tag{6.51}$$

These nodal force contributions are also imposed once at the incremental variables along the boundary. Each node is characterised by contributions defining the temperature and the water vapour pressure development respectively. Important is to consider that the imposed values, characterising the boundary conditions, are assumed constant along each outer edge.

6.5 Obtaining the solution and results analyses

The solution is based on solving the FEM definition in Eq. (6.42). The size of the system matrix, governed by the number of nodal variables in the FEM discretisation, requires an iterative solution technique to be of practical use (van Kan, et al., 2008). The type is chosen based on the coupled system of PDE's being characterised by non-symmetrical element mass and stiffness matrices defined in Eq. (6.47) or Eq. (6.48) and Eq. (6.49) respectively. The resultant linear system in simplified form reads (van Kan, et al., 2008; Barrett, et al., 1994):

$$\boldsymbol{Ax} = \boldsymbol{b} \tag{6.52}$$

where

$\boldsymbol{x}$	[var.]	Solution vector
$\boldsymbol{b}$	[var.]	Force vector
$\boldsymbol{A}$	[var.]	System matrix

A BiConjugate Gradient Stabilized Solver with Preconditioning is used (van Kan, et al., 2008; Barrett, et al., 1994). This solver is based on variation of the conjugate gradient (CG) method, suitable for unsymmetrical matrices (van Kan, et al., 2008). The CG method approximates the solution of Eq. (6.52) by minimisation of the following system (van Kan, et al., 2008):

$$\frac{1}{2}\boldsymbol{x^T Ax} - \boldsymbol{b^T x} \tag{6.53}$$

The rate of convergence is improved by using a classical Jacobi preconditioning based on the diagonal of the system matrix (van Kan, et al., 2008; Barrett, et al., 1994). Through preconditioning Eq. (6.52) is modified by left multiplication leading to:

$$\boldsymbol{P^{-1}Ax} = \boldsymbol{P^{-1}b} \tag{6.54}$$

where

$\boldsymbol{P}$	Jacobi matrix to precondition the system

Incremental development and convergence of variables

The solution at the next time step is first approximated based on the previous time steps using Eq. (6.36). After this predictor step, the solver starts the corrector step with an initial incremental solution for the nodal variables of zero. The obtained solution increment is used to update the current approximation using Eq. (6.35). Additional incremental steps, checked through convergence requirements (Tenchev, et al., 2001), are found not to be required. The adopted solution approach, of a predictor and subsequent a corrector step, commonly provides sufficient accuracy.

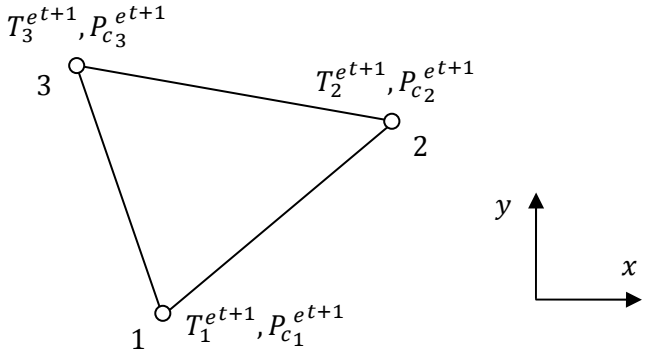

Variables and parameters averaging (element)

$$T_{avg}{}^{e\,t+1} = \frac{\sum_{i=1}^{3} T_i^{e\,t+1}}{3}$$

$$P_{c_{avg}}{}^{e\,t+1} = \frac{\sum_{i=1}^{3} P_{c_i}{}^{e\,t+1}}{3}$$

$$P_{gw_{avg}}{}^{e\,t+1} = \frac{\sum_{i=1}^{3} P_{gw_i}{}^{e\,t+1}}{3}$$

$$S_{w_{avg}}{}^{e\,t+1} = \frac{\sum_{i=1}^{3} S_{w_i}{}^{e\,t+1}}{3}$$

Fig. 6.6 *The linear approximation of the temperature and capillary pressure across the 2D triangular element in $\mathbb{R}^2$ allows for averaging based on the nodal values.*

Averaged element nodal parameters

The temperature and the capillary pressure are linearly approximated by the nodal shape functions across the 2D triangular element as reflected by Fig. 6.6. This approximation allows to determine the averaged variables based on the nodal values. Derivative parameters, such as the water vapour pressure and the liquid water saturation level, are averaged similarly. These are governed by the Kelvin equation and the saturated water vapour pressure (Pel & Huinink, 2007) or the desorption isotherm (Genuchten, 1980; Baroghel-Bouny, 1994a) respectively.

Cross-sectional distributions

The element-based parameters are subsequently also averaged across the domain using a cross-sectional subdivision into zones in width direction. This allows to obtain similar distributions as presented in chapter 4. From these cross-sectional distributions the behaviour located at several depths from the heated surface is also obtainable.

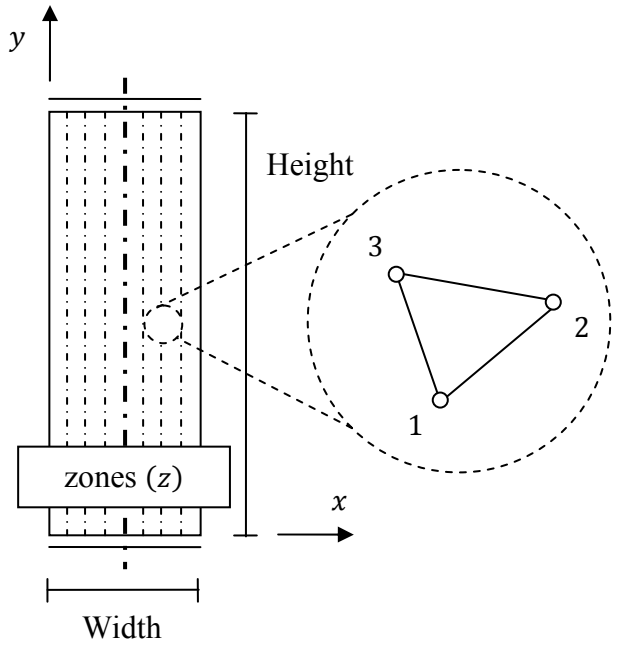

Variables and parameters averaging (per zone)

$$T_{avg_z}{}^{t+1} = \frac{\sum_{e=1}^{e_{tot_z}} \left(T_{avg}{}^{e\,t+1} A^e\right)}{\sum_{e=1}^{e_{tot_z}} A^e}$$

$$P_{c_{avg_z}}{}^{t+1} = \frac{\sum_{e=1}^{e_{tot_z}} \left(P_{c_{avg}}{}^{e\,t+1} A^e\right)}{\sum_{e=1}^{e_{tot_z}} A^e}$$

$$P_{gw_{avg_z}}{}^{t+1} = \frac{\sum_{e=1}^{e_{tot_z}} \left(P_{gw_{avg}}{}^{e\,t+1} A^e\right)}{\sum_{e=1}^{e_{tot_z}} A^e}$$

$$S_{w_{avg_z}}{}^{t+1} = \frac{\sum_{e=1}^{e_{tot_z}} \left(S_{w_{avg}}{}^{e\,t+1} A^e\right)}{\sum_{e=1}^{e_{tot_z}} A^e}$$

Fig. 6.7 *Cross-sectional distributions are obtained through averaging the element-based parameters across zones in width direction as indicated in $\mathbb{R}^2$.*

6.6 Conclusions with respect to the FEM definition

With respect to the theoretical framework the following conclusions are drawn and remarks are made:

- The concrete element is schematised as a 2D cross-section characterised by a homogeneous and isotropic material description. The out-of-plane fluxes are neglected, assuming a continuous temperature and pressure in depth direction.

- Forced drying of a porous material is characterised by the coupled conservation of thermal energy and mass of the water phases (Bear, 1972/1988; Pel & Huinink, 2007). The resultant system of PDE's is defined by Eq. (6.12) (Tenchev, et al., 2001; Gawin, et al., 2003). This continuum description can be reduced to reflect the basic Fourier differential equation for thermal conductivity.

- Neumann boundary conditions at the left and right edges are based on conservation of thermal energy and mass of the water phases, stated in Eq. (6.13) and Eq. (6.14) respectively (Tenchev, et al., 2001; Gawin, et al., 2003). Periodical boundary conditions, stated in Eq. (6.15), schematise continuity along the top and bottom edges (Segal, 2008).

The solution, based on a FEM approximation, is governed by the following:

- The coupled system of PDE's is multiplied by the variables to define a functional as stated in Eq. (6.16) (van Kan, et al., 2008; Zienkiewicz, et al., 2005). Minimisation of this functional with respect to the solution obtains the system of PDE's (van Kan, et al., 2008; Zienkiewicz, et al., 2005). Solution of this minimisation therefore equals solution of the system of PDE's (van Kan, et al., 2008; Zienkiewicz, et al., 2005).

- Integration by parts applied to Gauss' divergence theorem defines the functional as conservation of energy, stated in Eq. (6.21) or alternatively Eq. (6.22) (van Kan, et al., 2008; Zienkiewicz, et al., 2005). The approximated solution is complemented by a variation or test function (van Kan, et al., 2008). Minimisation of the functional with respect to this test function defines the variational or weak form as in Eq. (6.28) (van Kan, et al., 2008; Zienkiewicz, et al., 2005).

- The solution is approximated by Galerkin's method based on a linear combination of basis or shape functions and nodal variables (van Kan, et al., 2008; Segal, 2008). The FEM discretisation, stated in Eq. (6.34), is obtained through approximation of the solution governed by elements distributed across the domain (van Kan, et al., 2008).

- Time integration is defined by an implicit Euler backward scheme expressed in the next time step (van Kan, et al., 2008; Vermolen, 2005). The incremental definition of the nodal variables (Davie, et al., 2006), in Eq. (6.35), affecting also the Neumann boundary conditions, is initially predicted by a first order approximation.

- The FEM definition in Eq. (6.42) is based on linear 2D triangular elements defined by Eq. (6.45) and Eq. (6.46) (van Kan, et al., 2008; Felippa, 2004a; Zienkiewicz, et al., 2005). The element mass matrix is stated in consistent form by Eq. (6.47) or as lumped approximation in Eq. (6.48). The isotropic element stiffness matrix is stated in Eq. (6.49). Neumann boundary conditions govern the stiffness matrix in Eq. (6.50) and the force vector in Eq. (6.51).

About the iterative solution technique and the results analyses the following is mentioned:

- The unsymmetrical FEM definition is Jacobi preconditioned and solved by a BiConjugate Gradient Stabilized Solver (van Kan, et al., 2008; Barrett, et al., 1994).

- Approximation through linear nodal shape functions allows to average the temperature and capillary pressure across each element. Cross-sectional distributions are obtained by averaging the element values across zones in width direction.

6.7 FEM approximation based on homogeneous and isotropic concrete

The FEM definition is used to approximate the temperature and pore pressure development for a representative cross-section. In this paragraph first the homogeneous discretisation based on 2D triangular elements is presented. The boundaries, governed by Neumann or periodical conditions, are also indicated. Thereafter, comparison to FDM results from chapter 4 is used to check for a correct implementation and a sufficiently accurate approximation.

6.7.1 Homogeneous discretisation of the cross-section

The cross-section used is shown in Fig. 6.8 and is relatively small compared to the structural element discussed in chapter 3. However, it is assumed that only local material behaviour governs the progress of thermal energy and mass in the cross-section. Structural interaction is not present with the behaviour assumed constant in height direction imposed through the periodical boundary conditions. The rectangular cross-section has a width and height of 150 mm, as stated in Table 6.1, with the former allowing for comparison to previous results.

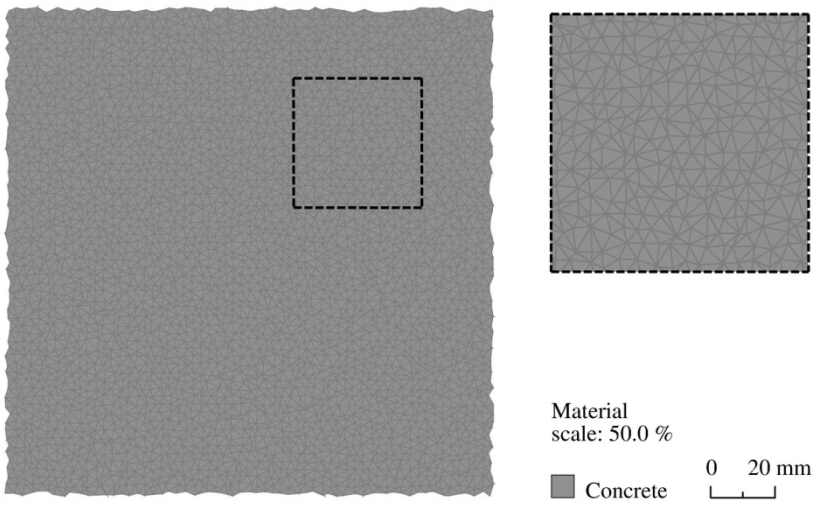

Fig. 6.8 *Discretisation by 2D triangular elements used to numerically approximate the homogeneous and isotropic concrete cross-section.*

Geometry of the mesh	
Width	150 mm
Height	150 mm
Unit thickness	1 mm
FEM discretisation	
Total number of nodes	3721
Total number of triangles	7200

Table 6.1 *Dimensions and element discretisation representing the mesh used to approximate the rectangular concrete cross-section.*

Neumann boundary conditions are defined constant along the left and right edges in which the former characterises fire exposure or a dried state, dependent on the chosen scenario. The opposite edge is maintained at reference conditions. Discretisation is based on triangular elements, randomly distributed with an internal length scale of 2.5 mm. This relatively dense mesh is chosen in anticipation of the aggregate distribution as presented in the next chapter.

6.7.2 Validation based on comparison to FDM results

Several results, reflecting the fire and drying scenarios discussed in chapter 4, are used to validate the FEM definition. Both approximate solution techniques should yield a similar solution. However, the coupled FEM model requires some additional considerations in order to compare the results to the simplified and uncoupled FDM relationships.

Temperature development based on various fire scenarios

Validation of the progress of thermal energy is only based on approximation of Fourier's PDE for thermal conductivity. Several possibilities exist to affectively uncouple the FEM model, with at the beginning of this chapter the indicated solution approach of element mass and stiffness reduction. The constants governing the conservation of mass are removed and only the temperature is defined as variable. Maintaining the vapour pressure at reference conditions is not sufficient to omit forced drying since temperature development will also affect thermodynamic equilibrium between the water phases. The former approach is adopted and will also be used to schematise the aggregate particles in the cross-section.

Fire scenarios (I)		
Calculation	**6.1A**	**6.1B**
Reference temperature	20 ^{o}C	20 ^{o}C
Duration	1800 sec	1800 sec
Incremental time step size	2.5 sec	2.5 sec
Material (homogeneous)		
Strength class	independent	independent
Boundary conditions		
Fire curve	**ISO 834**	**HC**
Convective heat transfer coeff.	**25 W/m^{2}K**	**50 W/ m^{2}K**

Table 6.2 *Fire scenarios used to validate the FEM definition with respect to temperature development in the cross-section.*

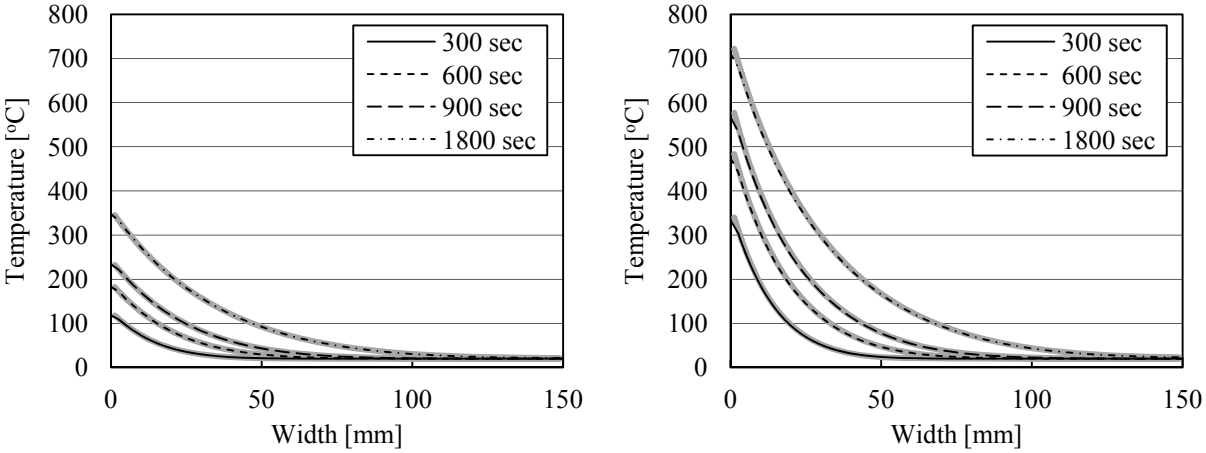

Fig. 6.9 *The temperature distributions caused by fire exposure according to ISO 834 (left) and HC (right) showing identical results for FEM and FDM.*

Several fire scenarios, displayed in Table 6.2, are compared to assess the numerical approximation by the FEM. These temperature distributions are obtained by averaging across zones in width direction, as schematically elaborated in Fig. 6.7. Comparison to FDM results, restated from chapter 4 and shown in Fig. 6.9, indicates for both types of fire exposure a similar progress of temperature. Furthermore, differences between a consistent or a lumped mass matrix are limited, attributed to the small temperature variation across each element.

Temperature-dependent drying of the cross-section

Drying of the cross-section is validated by using the coupled FEM definition. However, it is important to consider that the uniform temperature in the cross-section is approximated as constant. To ensure that no temperature variations can occur, the coupling between both PDE's temporarily is removed by omitting the enthalpy. The second boundary condition imposes a linear reduction of the initial gas pressure. Unconditional stability of the Euler backward scheme allows to use larger time step sizes as shown in Table 6.3.

Drying scenarios		
Calculation	**6.2A**	**6.2B**
Reference temperature	250 °C	250 °C
Reference RH	80 %	80 %
Duration	**1.5 hrs**	**0.5 hrs**
Incremental time step size	**0.2 sec**	**0.3 sec**
Material (homogeneous)		
Strength class	**C25/30**	**C90/105**
Initial saturation level	**46 %**	**75 %**
Boundary conditions		
Exterior vapour pressure (dry)	1000 Pa	1000 Pa
Exterior vapour pressure (ref)	3.2E+6 Pa	3.2E+6 Pa
Convective mass transfer coeff.	0.03 m/s	0.03 m/s

Table 6.3 *Drying scenarios used to validate the FEM definition with respect to capillary pressure development in the cross-section.*

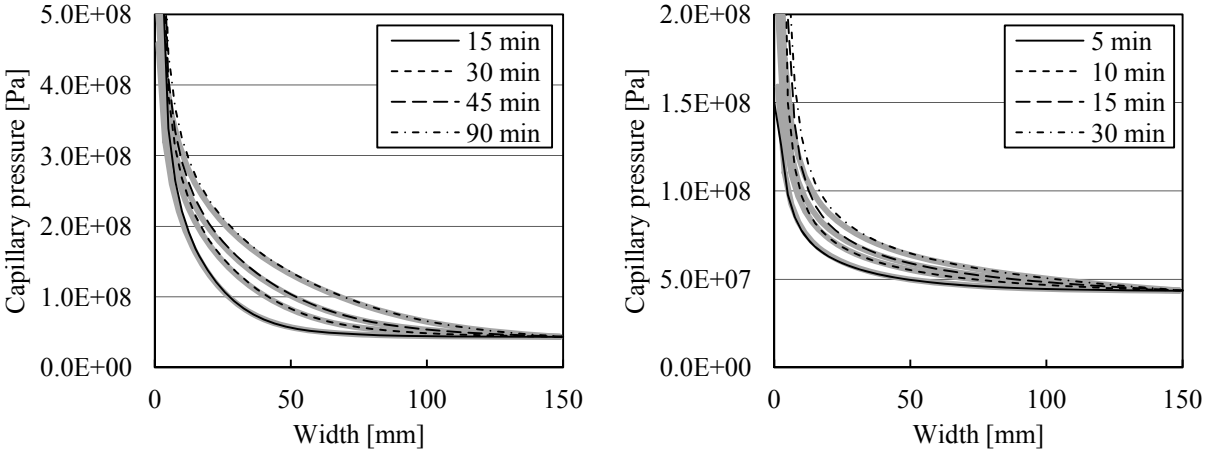

Fig. 6.10 *Comparison of capillary pressure distributions due to drying of the C25/30 (left) or the C90/105 (right) cross-section for FEM and FDM calculations.*

Comparing the FEM approximations for both drying scenarios with the FDM results taken from chapter 4 shows good agreement for the capillary pressure distributions obtained. At the dried left edge the pressure gradient approximated by the FEM reaches slightly higher values than calculated by FDM. This is attributed to the FDM using a second order central difference scheme whereas the FEM is based on a first order approximation using Gauss' divergence theorem. Similar differences also govern the Neumann boundary condition which is expressed as gradient across the edge or at the edge respectively. For steep gradients this could explain the small differences which, from a certain distance into the cross-section, become negligible.

Conclusions with respect to the FEM implementation

From the discussed numerical results the following conclusions can be drawn:

- The FEM definition and element discretisation are sufficiently accurate to approximate the temperature and capillary pressure in the cross-section.

- Differences in the solution between a consistent or a lumped element mass matrix are limited. However, the diagonal system mass matrix improves the rate of convergence and is therefore used in the remainder of this thesis.

6.8 Coupled temperature and pore pressure development due to fire exposure

During exposure to a fire, both the progress of thermal energy and the process of forced drying develops. This requires the coupled basis of the FEM definition with the Neumann boundary conditions defined at the left edge reflecting both the temperature and vapour pressure development. The design fire curve governs the time-dependent development of the air temperature whereas the initial exterior vapour pressure is maintained at a dried state. With respect to the latter no numerical instability can occur, since the initial vapour pressure in the cross-section at reference temperature is of similar order. In this paragraph several numerical results are discussed in order to indicate the influence of the concrete strength class, the type of fire exposure and the environmental conditions. The respective properties for the water phases as well as the material are taken from chapter 4. It is recalled that deformation or fracture due to the pressure development is not considered in this model.

Fire scenarios (II)		
Calculation	**6.3A**	**6.3B**
Reference temperature	20 °C	20 °C
Reference RH	80 %	80 %
Duration	1800 sec	1800 sec
Incremental time step size	**0.2 sec**	**0.3 sec**
Material (homogeneous)		
Strength class	**C25/30**	**C90/105**
Initial saturation level	**58 %**	**85 %**
Boundary conditions		
Fire curve	ISO 834	ISO 834
Convective heat transfer coeff.	25 W/m^{2}K	25 W/ m^{2}K
Exterior vapour pressure (dry)	1000 Pa	1000 Pa
Convective mass transfer coeff.	0.03 m/s	0.03 m/s

Table 6.4 *Gas pressure development as investigated by variation of the concrete strength class based on exposure to a standard fire scenario.*

6.8.1 Influence of the concrete strength class

Gas pressure development in a fire exposed cross-section is for the most part influenced by the strength. The denser pore structure of C90/105 compared to C25/30 allows for higher pressures to be attained. This is numerically examined by comparing both concrete types during fire exposure according to the ISO 834 curve. Initial conditions for the environment are similar with the RH causing a higher saturation level in the C90/105 cross-section. An overview of the remaining characterisation is provided in Table 6.4.

From the resultant gas pressure distributions the influence of the concrete strength directly becomes clear. The maximum pressures attained are approximated to increase almost twofold in the denser microstructure of C90/105 as observed in Fig. 6.11. Furthermore, the combination of reduced permeability and higher initial saturation level also mitigates the progress of the drying front into the cross-section. The coinciding pressures are located closer to the fire exposed left edge.

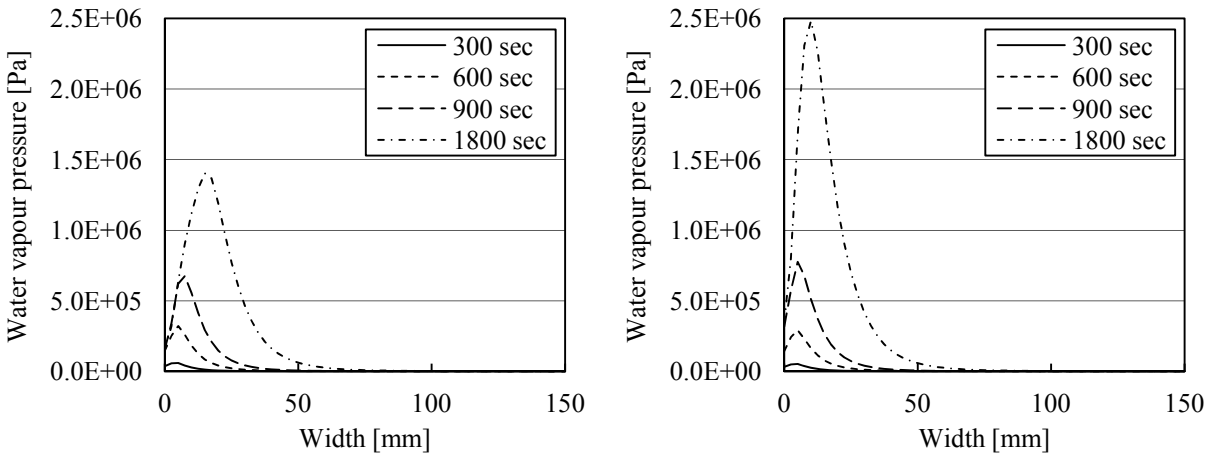

Fig. 6.11 *Distributions indicating that C25/30 (left) dries at a higher rate and develops lower pressures compared to C90/105 (right), both fire exposed to ISO 834.*

Fire scenarios (III)		
Calculation	**6.4A**	**6.4B**
Reference temperature	20 °C	20 °C
Reference RH	80 %	80 %
Duration	1800 sec	1800 sec
Incremental time step size	**0.2 sec**	**0.3 sec**
Material (homogeneous)		
Strength class	**C25/30**	**C90/105**
Initial saturation level	**58 %**	**85 %**
Boundary conditions		
Fire curve	HC	HC
Convective heat transfer coeff.	50 W/m^{2}K	50 W/ m^{2}K
Exterior vapour pressure (dry)	1000 Pa	1000 Pa
Convective mass transfer coeff.	0.03 m/s	0.03 m/s

Table 6.5 *Influence of the imposed thermal energy on the gas pressure development as determined for both concrete types.*

6.8.2 Influence of the type of fire exposure

The second main influencing parameter is the type of thermal exposure, characterised by the heating rate and the temperatures attained. This is investigated by exposing both concrete types to a HC type of fire as indicated in Table 6.5. The surface temperature will develop faster, influencing the progress of thermal energy into the cross-section.

Comparing the gas pressure distributions obtained, shown in Fig. 6.12 and Fig. 6.13, indicates that indeed gas pressures are approximated to increase. Interestingly, the maximum values determined for the C90/105 cross-section are again roughly doubled compared to C25/30. For both concrete types a steep moisture gradient is determined at which the maximum gas pressures can be seen to develop. However, drying is a relatively slow process since after 30 min of fire exposure two-thirds of the cross-section is still unaffected. This indicates that the drying front is closely related to the progress of thermal energy. In time the progress of the temperature gradient as well as the gas pressure peak mitigates.

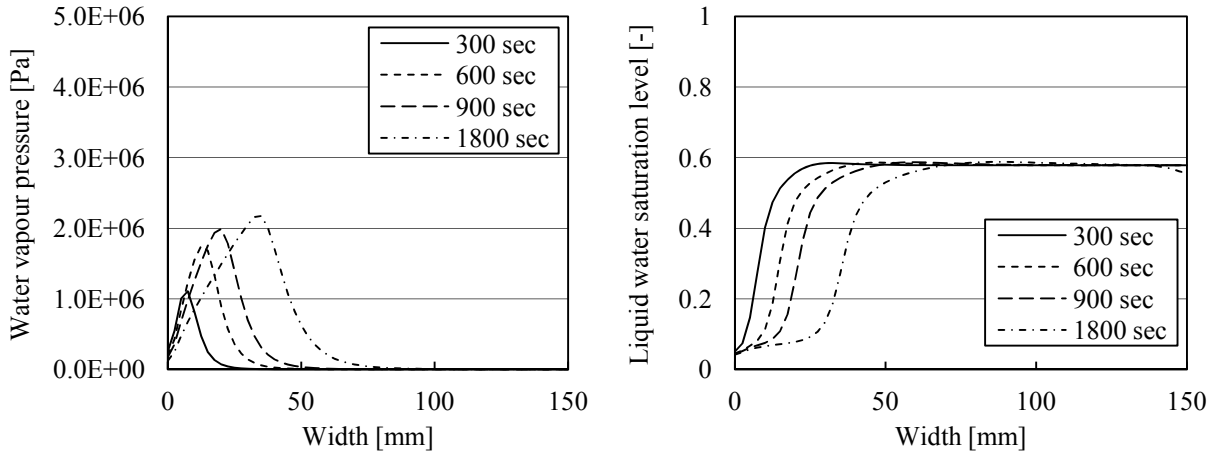

Fig. 6.12 *Exposure to a fire according to the HC curve causing gas pressures to develop more rapidly (left) at a steep drying front (right) as determined for C25/30.*

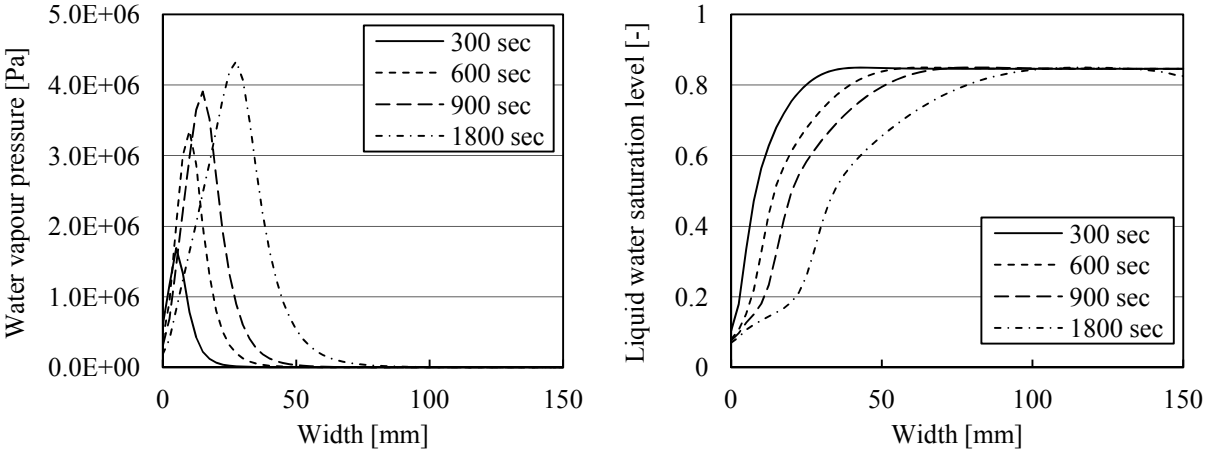

Fig. 6.13 *The reduced permeability and higher initial saturation of C90/105 causes the gas pressures to attain higher values as determined for a HC type of fire.*

6.8.3 Influence of the environmental conditions

The consequences of fire exposure are not only determined by the development of the air temperature. Also the RH of the surrounding environment is of importance. By increasing the initial saturation level, more moisture is available to develop the gas pressure. The extent of this influence is numerically approximated by exposing a C25/30 cross-section, equilibrated to three different RH's, to an ISO type of fire. A RH of 50 % or 80 % corresponds to an internal or external climate respectively (Khoury, 2008a; Edvardsen, 2004). The lowest RH of 20 %, stated in Table 6.6, can be seen as partially dried.

In the previous results the cross-section is conditioned at a RH of 80 %. By reducing the initial RH to 50 % or even 20 % the maximum gas pressures reduce to around 1.0E+6 Pa or lower respectively. However, for both these lower environmental conditionings an increase in moisture level is found as seen in Fig. 6.14.

Fire scenarios (IV)			
Calculation	**6.5A**	**6.5B**	**6.5C**
Reference temperature	20 ^{o}C	20 ^{o}C	20 ^{o}C
Reference RH	**20 %**	**50 %**	**80 %**
Duration	3600 sec	3600 sec	3600 sec
Incremental time step size	0.2 sec	0.2 sec	0.2 sec
Material (homogeneous)			
Strength class	C25/30	C25/30	C25/30
Initial saturation level	**14 %**	**27 %**	**58 %**
Boundary conditions			
Fire curve	ISO 834	ISO 834	ISO 834
Convective heat transfer coeff.	25 W/m^{2}K	25 W/m^{2}K	25 W/m^{2}K
Exterior vapour pressure (dry)	1000 Pa	1000 Pa	1000 Pa
Convective mass transfer coeff.	0.03 m/s	0.03 m/s	0.03 m/s

Table 6.6 *Examination of the effect of the environmental conditions for the C25/30 cross-section in a relatively dry, internal and external climate.*

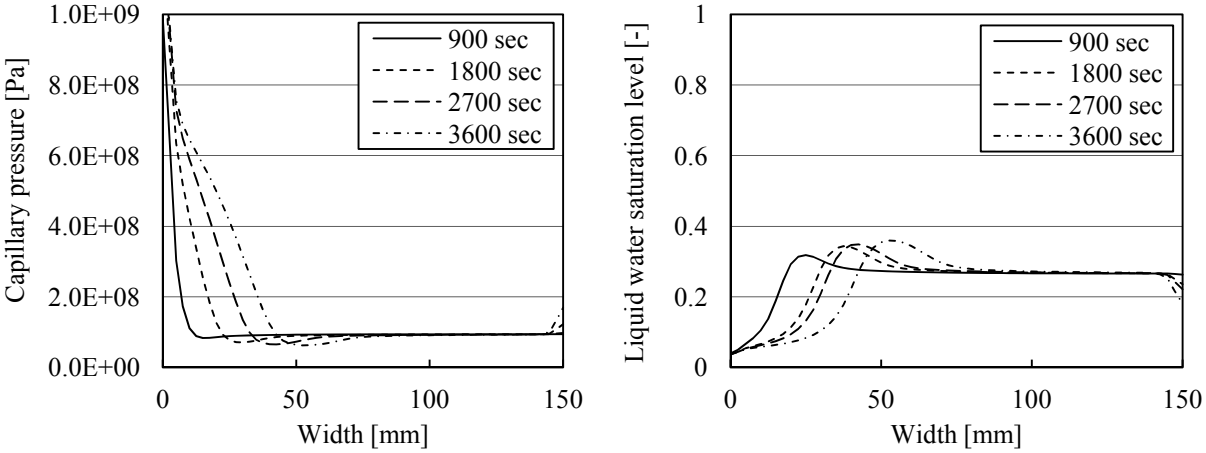

Fig. 6.14 *Forced drying of C25/30, conditioned at a RH of 50 %, indicating a reduction in capillary pressure (left) due to partial wetting of the cross-section (right).*

Especially subjected to a RH of 50 %, representative for an internal climate (Khoury, 2008a), indicates partial wetting of the cross-section. This increase in the saturation level is situated in front of the pressure peak and is still limited, not causing a saturated state. This difference in drying characterisation is attributed to the lower saturation level initially present in the cross-section impeding the flow of liquid water. The condensation of vapour levelled-off at the drying front thus mainly extends the moisture level. At higher RH's and corresponding moisture levels, part of the condensed vapour is driven to the heated surface by the capillary pressure gradient.

The relationship between the gas pressure and the saturation level is expressed by the development in time at various depths relative to the left edge. In Fig. 6.15 the pressure is seen to increase during evaporation of liquid water, with the maximum values obtained for almost dry conditions. With increasing depth the maximum pressures as well as the saturation levels increase with the latter reflecting partial wetting of the material. A different perspective is provided by Fig. 6.16 in which the distributions of the main parameters after 1800 seconds of fire exposure across the discretised cross-section are shown.

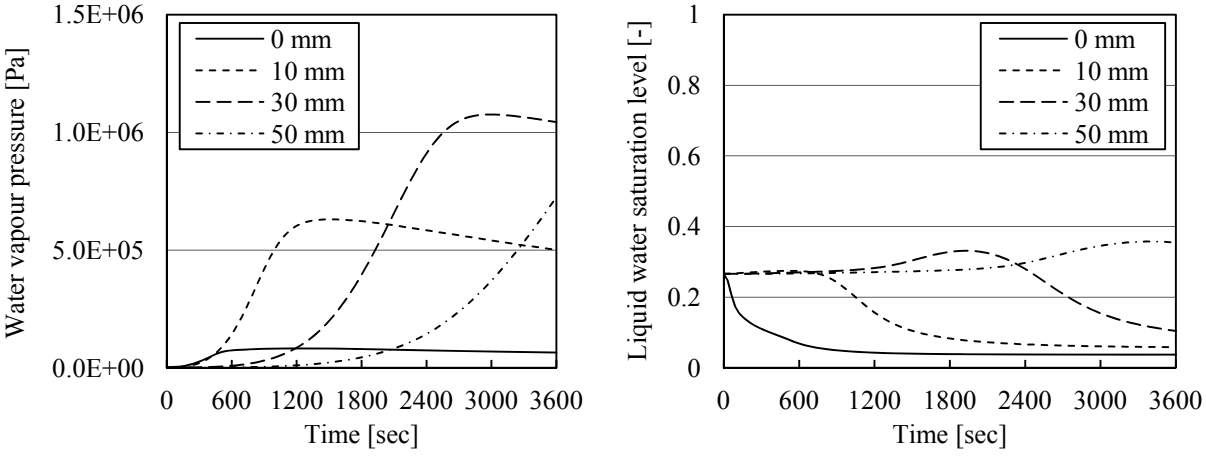

Fig. 6.15 *Continued fire exposure of the C25/30 cross-section, initially equilibrated at a RH of 50 %, reflects progressive drying (right) during which gas pressures ultimately alleviate (left). The depths are defined relative to the fire exposed left edge.*

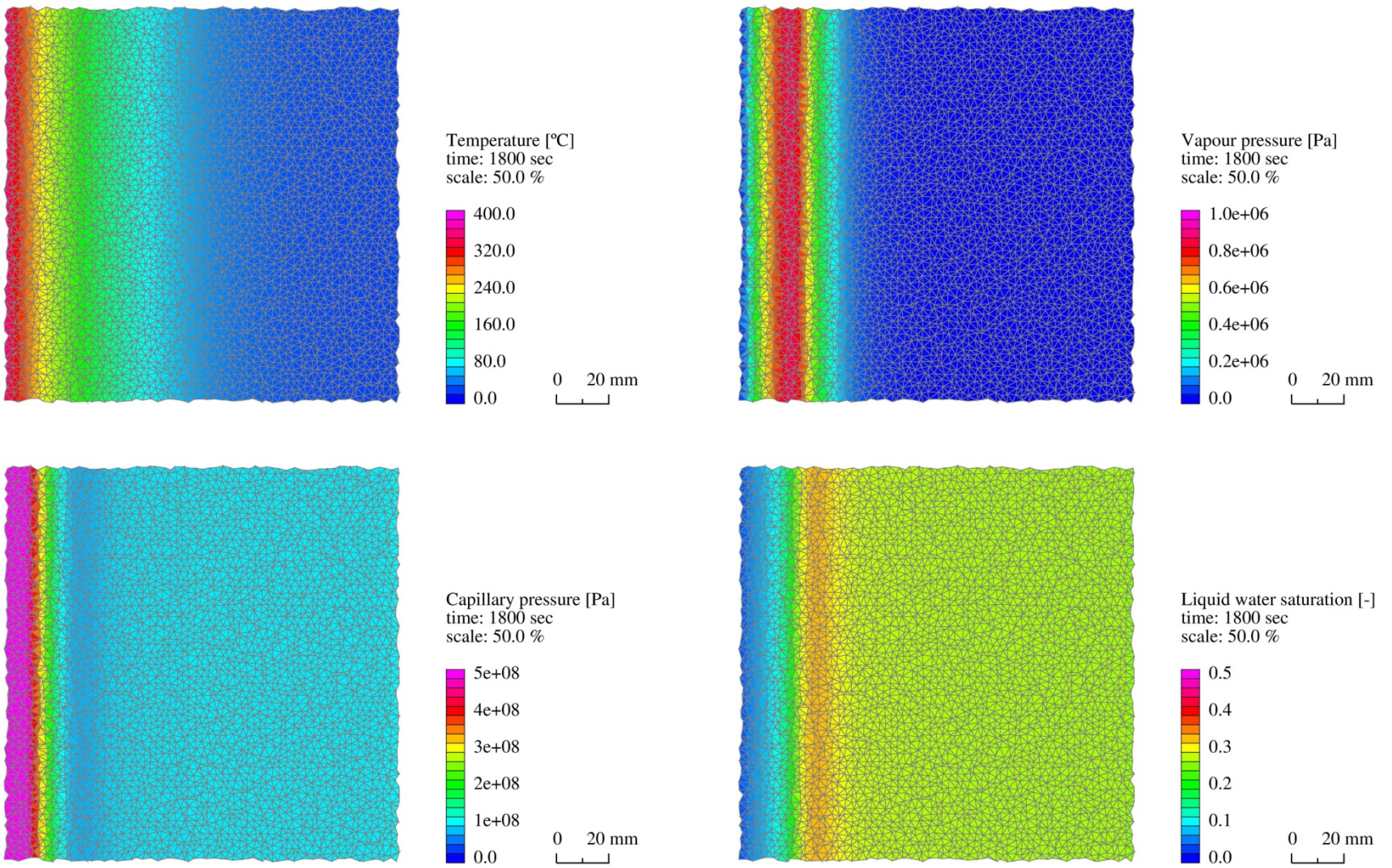

Fig. 6.16 *Distributions of temperature, gas and capillary pressure as well as liquid water saturation level in C25/30 during fire exposure based on ISO 834. The cross-section, initially at a RH of 50 %, indicates a moisture increase in front of the pressure peak.*

Fire scenarios (V)			
Calculation	**6.6A**	**6.6B**	**6.6C**
Reference temperature	20 °C	20 °C	20 °C
Reference RH	**50 %**	**80 %**	**95 %**
Duration	3600 sec	3600 sec	3600 sec
Incremental time step size	0.3 sec	0.3 sec	0.3 sec
Material (homogeneous)			
Strength class	C90/105	C90/105	C90/105
Initial saturation level	**48 %**	**85 %**	**99 %**
Boundary conditions			
Fire curve	HC	HC	HC
Convective heat transfer coeff.	50 W/m^{2}K	50 W/m^{2}K	50 W/m^{2}K
Exterior vapour pressure (dry)	1000 Pa	1000 Pa	1000 Pa
Convective mass transfer coeff.	0.03 m/s	0.03 m/s	0.03 m/s

Table 6.7 *Environmental conditions governing an internal, external and an almost saturated C90/105 cross-section during fire exposure.*

The influence of the environment is also numerically approximated for a C90/105 cross-section, initially subjected to a RH of 50 %, 80 % and 95% respectively. This increases the initial moisture level from partial to almost full saturation, as indicated in Table 6.7, before exposure to a fire according to the HC curve. The peak gas pressure is of course directly related to the initial moisture content. However, the depth of these pressure peaks is roughly similar, indicating again the close relationship with the progress of thermal energy.

Increasing the ambient RH not only changes the initial moisture level, but also the characterisation of the drying process. At an initial RH corresponding to internal conditions still a limited increase in the saturation level in front of the pressure peak is observed. However, from Fig. 6.17 it also seen that in case of almost saturation only drying is observed. This also develops at the opposite unheated edge, based on the gradual progress of thermal energy. The progress of drying is also shown in Fig. 6.18 providing for an initial ambient RH of 80 %.

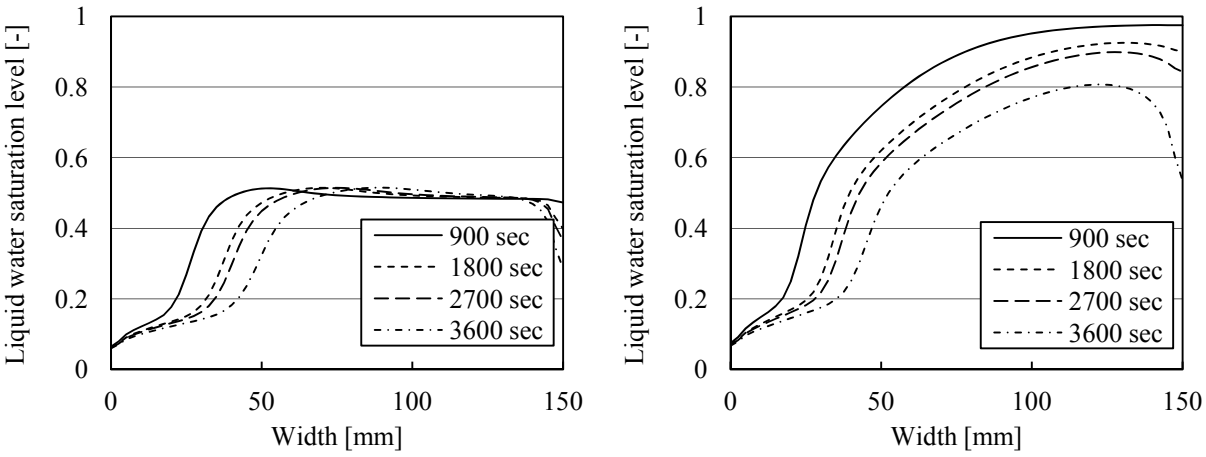

Fig. 6.17 *Environmental conditions determining the drying process which is different for a C90/105 at an initial RH of 50 % (left) compared to a RH of 95 % (right).*

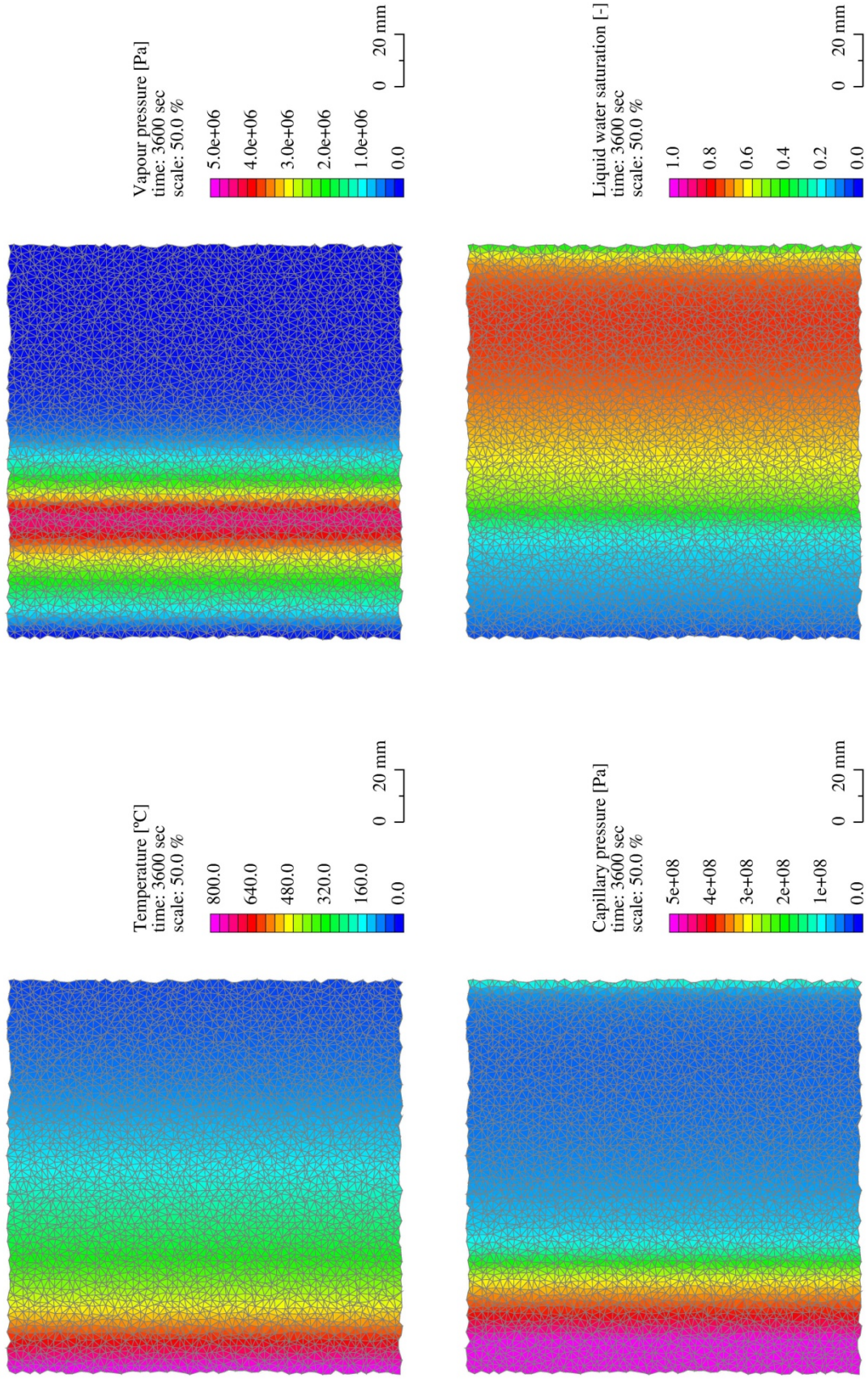

Fig. 6.18 *Progress of the drying front in a C90/105 cross-section, initially at a RH of 80 %, during fire exposure according to the HC curve. The thermal energy has progressed to the opposite edge whereas the pressure peak is situated at a third of the width.*

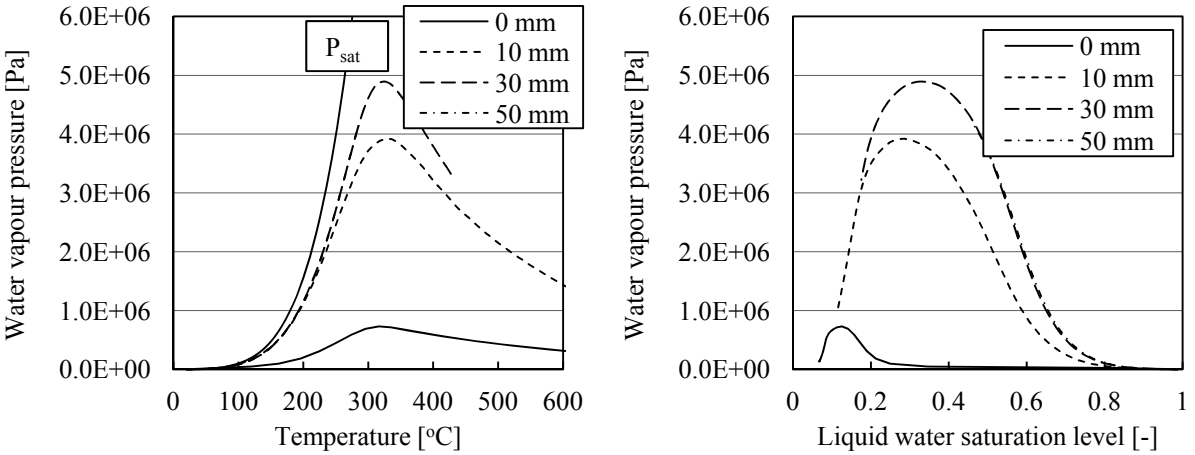

Fig. 6.19 *Comparison of the gas pressures at various depths with the saturated pressure for C90/105 at an initial ambient RH of 95 % (left). Maximum pressures are reached in case the equilibrium RH above the moisture level becomes insufficient (right).*

At the drying front the highest gas pressures are attained for relatively low saturation levels as seen in the Fig. 6.19. Below a saturation level of 0.2 to 0.4 the remaining moisture is insufficient to maintain the pressure development. This characterises the drying process for which a reduction in saturation level also corresponds to a reduction in RH. Under these circumstance the vapour pressure is also estimated to progressively deviate from the saturated state.

6.9 Conclusions with respect to fire exposed concrete

Regarding fire exposed concrete the following conclusions can be drawn based on the numerical results discussed:

- Gas pressure development is closely related to the progress of thermal energy. Through increasing the heating rate and the air temperatures attained, the cross-section dries faster and develops higher pressures. These gas pressure surpass the tensile strength of the concrete and could cause fracture. However, this is not considered for this purely physical model.

- In time the progress of thermal energy reduces which influences the drying process and consequently the gas pressure development. However, the temperatures reached can still be sufficient to maintain the pressures.

- The denser pore structure of C90/105 causes gas pressures to roughly double compared to C25/30, governed mainly by the reduced permeability. During a HC type of fire exposure the pore pressures in a C90/105 cross-section equilibrated at exterior conditions were estimated to surpass 4.0 MPa.

- Gas pressures develop at a steep drying front with the maximum values attained for relatively low saturation levels of 0.2 to 0.4. Under these circumstances the equilibrium RH of the vapour phase above the remaining moisture level is insufficient to maintain the pressure increase.

- An increase in the saturation level in front of the pressure peak is only approximated for C25/30 and to a lesser extent C90/105 conditioned at a RH of 50 %. This is attributed to the lower saturation levels which mitigate the flow of liquid water that levels the condensed vapour off.

- Initial environmental conditions causing almost full saturation did only indicate drying of C90/105 while causing the highest gas pressures. With respect to this result, it needs to be considered that the non-linear drying characterisation assumes a partial level of saturation at all times.

- An almost dried state of the cross-section is only reached for low RH's that do not correspond to real life circumstances. However, in reducing the amount of moisture present in the cross-section, obviously the increase of the gas pressure becomes limited.

- In case of sufficient penetration by the thermal energy partial drying can also occur at the unexposed opposite edge of the cross-section. The gradual temperature increase disturbs thermodynamic equilibrium initially established between both water phases.

7 Anisotropic FEM model for temperature and pore pressure

The derived FEM model approximates the temperature and pressure development, assuming the porous material to be homogeneous and isotropic. In this chapter the material description is extended to reflect heterogeneity as well as anisotropic behaviour. First, the system of PDE's, valid for a porous material, is restated. Aggregates are characterised as solid material and are assumed impermeable with respect to flow of the water phases. Thereafter thermal conductivity and permeability tensors are introduced, assumed to initially govern isotropic fluxes. Local material directions are defined aligned with the edges of the 2D triangular element. These reflect the incremental coupling with the fracture mechanics model presented in chapter 9 and define the orientation and opening of the cracks. The largest crack width characterises the anisotropic permeability tensor based on conservation of energy between the local and global mass fluxes. The next part addresses the numerical stability which involves the material characterisation around the critical temperature. Also the considerable change associated with the anisotropic permeability is discussed, addressed by adaptive time stepping and an incremental development. In the remainder of this chapter first the influence of the aggregates on the pore pressure development is examined. Thereafter an initial crack pattern is used to assess the mitigating effect on the pressure development.

7.1 Conceptual idea behind the heterogeneous and anisotropic material description

Concrete is commonly characterised as a homogeneous material with isotropic properties (Tenchev, et al., 2001; Gawin, et al., 2003). This simplifies the behaviour and allows to approximate the temperature and the pore pressure development as indicated in the previous chapter. However, at a lower scale concrete is a heterogeneous material consisting of aggregate particles connected to the surrounding mortar through interfacial zones as shown in Fig. 7.1. The latter are characterised as porous material across which temperatures and pressures develop. The aggregates tend to exhibit behaviour as solid material that only allows for thermal conductivity. By assuming a negligible porosity impermeable obstacles are formed to the flow of the water phases. In line with this material description also cracking develops based on imposed structural or internal mechanical loading.

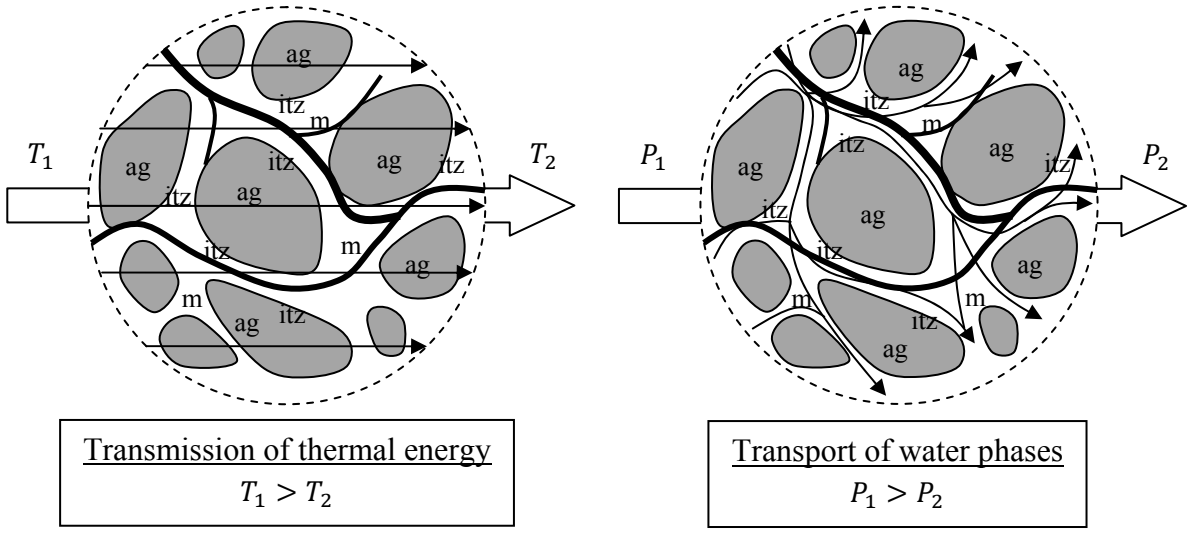

Fig. 7.1 *Overview of the material schematisation with transmission of thermal energy across all concrete components. Transport of the water phases is assumed through the mortar and interfacial zones, considerably influenced by cracks.*

The coupled system of PDE's, based on the conservation of thermal energy and mass of the water phases, is only valid for a homogeneous porous material. The aggregates, distributed in the cross-section of the concrete element, introduce a localised solid material description. This characterisation of only allowing for transmission of thermal energy is directly available through reduction of the local material description. The continuum definition, under these circumstances, is only governed by Fourier's differential equation for thermal conductivity with the temperature as the main variable. Material discontinuities are thus included in the cross-section across which the water phases and the mass fluxes are assumed not present.

The description is further enhanced by introducing material tensors in the heat and mass flux definitions (Bear, 1972/1988; Zienkiewicz, et al., 2005). Both the thermal conductivity and the permeability tensors are initially assumed isotropic or direction-independent (Bear, 1972/1988; Zienkiewicz, et al., 2005). The heterogeneity in the 2D material description is also reflected by restriction to in-plane fluxes only. The distribution of the concrete components and the crack pattern are assumed to be constant in depth direction. This allows to uncouple the heat and mass fluxes in the out-of-plane direction and again assume constant temperatures and pressures.

This continuum description is extended by material directions aligned with the edges of the 2D triangular element. These govern the incremental coupling with the fracture mechanics model presented in chapter 9. The distribution, orientation and opening of the cracks is schematised by brittle fracture of 1D bars (Schlangen, 1993; Vervuurt, 1997). However, since in-plane fluxes are defined by perpendicular directions, only a single contribution reflecting the largest crack width is considered. This local influence is defined through permeability increase based on crack opening parallel to the crack edges (Bear, 1972/1988). Conservation of energy based on coordinate transformation relates the local and global mass fluxes governing the water phases (Zienkiewicz, et al., 2005). The heat flux across the crack remains isotropic and defined by the material, neglecting possible thermal conductivity changes.

The resultant directional permeability causes both global mass fluxes to become anisotropic and thus are no longer assumed to align with the pressure gradients (Bear, 1972/1988; Zienkiewicz, et al., 2005). Flow of the water phases becomes dependent on orientation and opening of the crack pattern. Moreover, the cracks tend to form passages in the cross-section with a considerable increase in flow capability compared to the surrounding material. These discontinuities in the material description require additional considerations in order to maintain numerical stability. This applies to both the mass flux definition and the approximation of the time-dependent solution.

7.2 Theoretical considerations and anisotropic FEM definition

Derivation of the heterogeneity is based on the coupled system of PDE's representing the forced drying of the porous material as stated in chapter 6. This continuum description is in case of aggregates reduced to reflect a solid material. In this paragraph both material descriptions are given and the reduction is elaborated. Additional consideration is given to the consequences of including material variations reflected at the aggregate edges. Subsequently, both heat and mass fluxes are extended by in-plane thermal conductivity and permeability tensors, assumed initially isotropic (Bear, 1972/1988; Zienkiewicz, et al., 2005). Also local material directions are defined, aligned with the edges of the 2D triangular element. Thereafter, anisotropy is introduced through the local permeability tensor based on the largest crack width present across the material directions. Conservation of kinetic energy based on the local and global mass fluxes yields the element permeability tensor.

7.2.1 Basic assumptions governing the material description

Heterogeneous material description

With respect to the solid and porous material characterisations the following assumptions are made:

1. The aggregate particles represent solid material which is assumed impermeable and no liquid and vapour phases of water are present. The possibility for liquid water, as present in some aggregate types, is neglected (fib WP-4.3-1, 2007).

2. The mortar and interfacial zones are characterised as porous material based on the assumptions presented in chapter 6. Special consideration is given to the critical temperature at which liquid water is no longer a distinct phase (Whitten, et al., 2010). In this respect, continuity in the material description is maintained by characterisation of the liquid phase based on the imposed capillary pressure development.

3. Across both material descriptions a state of thermodynamic equilibrium is assumed (Hassanizadeh & Gray, 1979b; Bear & Bachmat, 1986).

Interaction with the surrounding environment is influenced by the material description:

4. Exchange of thermal energy (Kordina, et al., 1975) applies to both materials whereas drainage is only present in case of a porous material (Tenchev, et al., 2001; Gawin, et al., 2003).

Anisotropic continuum definition

Regarding the anisotropic continuum definition the following assumptions are made:

5. The anisotropic continuum is governed by the conservation of thermal energy and mass of the water phases. Both mass densities are unaffected by the directional dependence. The heat and mass fluxes are characterised by assuming in-plane isotropic thermal conductivity and permeability tensors respectively (Bear, 1972/1988; Zienkiewicz, et al., 2005).

6. The edges of the 2D triangular element represent local material directions which govern the crack influence based on incremental coupling with the facture mechanics model. However, since a flux is defined in both in-plane perpendicular directions only the largest crack width is assumed to govern the anisotropic permeability.

7. Conservation of kinetic energy relates the local and global mass flux definitions. The local permeability tensor is through coordinate transformations expressed in the global coordinate system (Bear, 1972/1988; Zienkiewicz, et al., 2005).

Crack initiation and subsequent opening

Initiation and especially opening of the crack is based on the following assumptions:

8. The sudden increase in volume available for the water phases is not included in the definition of the continuum. This geometrically non-linear behaviour would require the mass of the water phases to be redistributed, causing instant changes in the temperatures and pressures which is not desirable for numerical stability.

9. The local and global mass fluxes governing the water phases are assumed isotropic until fracture occurs. Thereafter, the local anisotropic permeability is defined parallel to the crack edges (Bear, 1972/1988). Directional dependence is reflected by the global mass fluxes being no longer assumed to align with the gradient of the variables.

10. Both mass fluxes are defined parallel to assumed impervious and straight crack edges, separated by the crack width (Bear, 1972/1988). Under these circumstances is the flow still assumed to be laminar with the veloctiy characterised by Poiseuille's law, neglecting possible friction effects (Bear, 1972/1988).

7.2.2 Description of the heterogeneous continuum

The homogeneous material description is extended by including the distribution of the concrete components in the cross-section. The mortar and interfacial zones are characterised as porous material and governed by the coupled system of PDE's as stated in chapter 6. Both the thermal energy and the mass densities of the water phases are conserved according to:

$$\left(\boldsymbol{M_I} + H_{vap}\boldsymbol{M_{II}}\right)\frac{\partial \boldsymbol{c}}{\partial t} - \boldsymbol{\nabla}\cdot(\boldsymbol{S_I}\boldsymbol{\nabla c}) - H_{vap}\boldsymbol{\nabla}\cdot(\boldsymbol{S_{II}}\boldsymbol{\nabla c}) = 0 \tag{7.1}$$

The aggregate particles are assumed to represent solid material governed only by the basic Fourier differential equation for thermal conductivity. Furthermore, the particles are also

assumed to form impermeable obstacles in the continuum to the flow of the water phases. Both can be included by local reduction of the system of PDE's stated in Eq. (7.1). The contribution by the second conservation equation governing the water phases is omitted leading to:

$$\left(\boldsymbol{M_I} + \overbrace{H_{vap}\boldsymbol{M_{II}}}^{=0}\right)\frac{\partial \boldsymbol{c}}{\partial t} - \boldsymbol{\nabla}\cdot(\boldsymbol{S_I}\boldsymbol{\nabla c}) - \overbrace{H_{vap}\boldsymbol{\nabla}\cdot(\boldsymbol{S_{II}}\boldsymbol{\nabla c})}^{=0} = 0$$
$$\rightarrow \boldsymbol{M_I}\frac{\partial \boldsymbol{c}}{\partial t} - \boldsymbol{\nabla}\cdot(\boldsymbol{S_I}\boldsymbol{\nabla c}) = 0 \tag{7.2}$$

with

$$\boldsymbol{M_I} = \begin{bmatrix} C_{TT_1} & 0 \\ \underbrace{C_{PT}}_{=0} & \underbrace{C_{PP}}_{=0} \end{bmatrix} = \begin{bmatrix} C_{TT_1} & 0 \\ 0 & 0 \end{bmatrix} \qquad \boldsymbol{S_I} = \begin{bmatrix} K_{TT_1} & 0 \\ \underbrace{K_{PT}}_{=0} & \underbrace{K_{PP}}_{=0} \end{bmatrix} = \begin{bmatrix} K_{TT_1} & 0 \\ 0 & 0 \end{bmatrix}$$

Interface between solid and porous material

The interface between both material descriptions, as present at the edges of the aggregates, is defined as discontinuous. Where the heat flux is able to pass across the domain, the mass fluxes of the water phases are restricted to the porous material description. In this respect, the cross-section can be thought of as disrupted by material discontinuities. This affectively implies that in the cross-section boundary conditions are imposed at the aggregate edges representing this flow restriction. Regarding the conservation of thermal energy the expression for the Neumann boundary condition from the previous chapter is restated. However, only the second contribution, based on water vapour mass flux, is included since thermal conductivity is not affected by the material interface:

$$\left(H_{vap}\boldsymbol{q_{gw}}\right)\cdot\boldsymbol{n}\big|_{\Gamma_{ag}} = 0$$
$$-H_{vap}\left(K_{TT_2}\frac{\partial T}{\partial n} + K_{TP}\frac{\partial P_c}{\partial n}\right)\Big|_{\Gamma_{ag}} = 0 \tag{7.3}$$

In addition, the Neumann boundary condition at the solid-porous material interface reflecting the conservation of mass governing the water phases becomes:

$$\left(\boldsymbol{q_w} + \boldsymbol{q_{gw}}\right)\cdot\boldsymbol{n}\big|_{\Gamma_{ag}} = 0$$
$$-\left(K_{PT}\frac{\partial T}{\partial n} + K_{PP}\frac{\partial P_c}{\partial n}\right)\Big|_{\Gamma_{ag}} = 0 \tag{7.4}$$

These localised boundary conditions are implicitly imposed by changing the PDE governing the material description. No additional contributions are associated with the solid and porous material interface. As a result, the mass fluxes are forced to pass around the solid material which enforces the condition of impermeable aggregate particles.

Local solid material transformation

In case of aggregates, the local continuum is no longer characterised by the capillary pressure which requires a corresponding reduction in the mass and stiffness matrices. This is obtained by the following transformation, removing the rows and columns containing zero's:

$$\boldsymbol{M_I}^* = \boldsymbol{T_{ag}}^T \boldsymbol{M_I} \boldsymbol{T_{ag}}$$
$$\boldsymbol{S_I}^* = \boldsymbol{T_{ag}}^T \boldsymbol{S_I} \boldsymbol{T_{ag}} \tag{7.5}$$

with

$$\boldsymbol{T_{ag}} = \begin{bmatrix} 1 \\ 0 \end{bmatrix}$$

where

$\boldsymbol{T_{ag}}$	[-]	Transformation matrix used to reduce the local system definition
$\boldsymbol{M_I}^*$	[J/m^{3}K]	Reduced mass matrix based on the solid material description
$\boldsymbol{S_I}^*$	[W/mK]	Reduced stiffness matrix based on the solid material description

In addition, it is useful to also define these relationships based on the identity matrix in order maintain the material description:

$$\boldsymbol{M_I} = \boldsymbol{T_{ag}}^T \boldsymbol{M_I} \boldsymbol{T_{ag}}$$
$$\boldsymbol{S_I} = \boldsymbol{T_{ag}}^T \boldsymbol{S_I} \boldsymbol{T_{ag}} \tag{7.6}$$

with

$$\boldsymbol{T_{ag}} = \begin{bmatrix} 1 & 0 \\ 0 & 1 \end{bmatrix}$$

Implementation of the afore mentioned local material reduction in the FEM definition is relatively straightforward. For this purpose the constants in the element mass and stiffness matrices are defined according to the material description. The nodes are defined depending on the location, which inside an aggregate particle means reduction according to Eq. (7.5). The remaining nodes are unchanged based on Eq. (7.6). The combination of all three types of nodes generates the element material transformation matrix which ensures that all nodal variables are defined across the domain:

$$\boldsymbol{c}^e = \boldsymbol{T_{ag}}^e \boldsymbol{c_{sys}}^e \tag{7.7}$$

with

$$\boldsymbol{c}^e = \begin{bmatrix} \boldsymbol{c}_1^e \\ \boldsymbol{c}_2^e \\ \boldsymbol{c}_3^e \end{bmatrix} \qquad \boldsymbol{c_{sys}}^e = \begin{bmatrix} \boldsymbol{c_{sys}}_1^e \\ \boldsymbol{c_{sys}}_2^e \\ \boldsymbol{c_{sys}}_3^e \end{bmatrix} \qquad \boldsymbol{T_{ag}}^e = \begin{bmatrix} \boldsymbol{T_{ag}}_1^e & 0 & 0 \\ 0 & \boldsymbol{T_{ag}}_2^e & 0 \\ 0 & 0 & \boldsymbol{T_{ag}}_3^e \end{bmatrix}$$

where

$\boldsymbol{T_{ag}}^e$	[-]	Element transformation matrix for reduction of the nodal variables

The element mass is transformed based on the nodal variables using the approach from Eq. (7.5) and Eq. (7.6) which after integration obtains the consistent or lumped matrix:

$$\boldsymbol{M_{sys}}_{\boldsymbol{k}}^{\boldsymbol{e}\,\boldsymbol{t+1}} = \int_{\Omega^e} \boldsymbol{T_{ag}}^{\boldsymbol{eT}} \boldsymbol{N_C}^{\boldsymbol{eT}} \left(\boldsymbol{M_I}_{\boldsymbol{k}}^{\boldsymbol{e}\,\boldsymbol{t+1}} + \left(H_{vap} \boldsymbol{M_{II}} \right)_{\boldsymbol{k}}^{\boldsymbol{e}\,\boldsymbol{t+1}} \right) \boldsymbol{N_C}^{\boldsymbol{e}} \boldsymbol{T_{ag}}^{\boldsymbol{e}} d\Omega^e \tag{7.8}$$

The same transformation is applied to the element stiffness matrix, approximating the heat and mass fluxes as constant across each element:

$$\boldsymbol{S_{sys}}_{\boldsymbol{k}}^{\boldsymbol{e}\,\boldsymbol{t+1}} = \int_{\Omega^e} \boldsymbol{T_{ag}}^{\boldsymbol{eT}} \boldsymbol{B_C}^{\boldsymbol{eT}} \left(\boldsymbol{S_I}_{\boldsymbol{k}}^{\boldsymbol{e}\,\boldsymbol{t+1}} + \left(H_{vap} \boldsymbol{S_{II}} \right)_{\boldsymbol{k}}^{\boldsymbol{e}\,\boldsymbol{t+1}} \right) \boldsymbol{B_C}^{\boldsymbol{e}} \boldsymbol{T_{ag}}^{\boldsymbol{e}} d\Omega^e \tag{7.9}$$

Neumann and periodical boundary conditions

Transformation of the matrix and vector contributions imposed by Neumann's boundary conditions could be obtained through similar relationships. However, aggregates situated at the left and right outer edges only conduct thermal energy. Thus it is realistic to make the following distinction in the imposed boundary conditions:

- Exchange of thermal energy with the surrounding environment is independent of the material and applied to all surface nodes.
- Drainage of mass, governing the water phases, is only imposed at surface nodes being part of the porous material. This extends the concept of impermeable aggregate particles to the boundary of the domain.

Periodical boundary conditions are enforced by ensuring that in the definition of the nodal variables governing the master nodes, along the bottom edge, the slave nodes at the opposite edge are considered. Sudden changes in the material description are avoided by a symmetrical schematisation with respect to the horizontal axis. This ensures that the same material description is present at both edges in order to maintain the periodical conditions between the nodal variables and ensure a smooth transition of the heat and mass fluxes.

7.2.3 Anisotropic continuum description

The material description, defined by the system of PDE's stated in Eq. (7.1), is valid for an isotropic continuum. This implies that the material is not direction-dependent (Bear, 1972/1988; Zienkiewicz, et al., 2005). However, materials can exhibit directional dependence especially in case cracks are present (Bear, 1972/1988). This mainly influences the permeability whereas the thermal conductivity is assumed to remain isotropic. The latter neglects the possible influence a crack could have on the thermal conductivity of the material. A local crack considerably influences the permeability dependent on orientation and opening (England & Khoylou, 1995; Neuzil & Tracy, 1981). Under these circumstances the mass fluxes of the water phases become anisotropic, governed by the directional permeability expressed in the axes of the coordinate system (Bear, 1972/1988; Zienkiewicz, et al., 2005).

Anisotropic heat and mass fluxes

The heat flux across the continuum is extended by the introduction of the 3D second order thermal conductivity tensor (Bear, 1972/1988; Zienkiewicz, et al., 2005). However, through consideration of the constant temperature across the material description in depth direction

only in-plane contributions remain (Zienkiewicz, et al., 2005). Furthermore, this tensor is also symmetric since both the flux and the temperature gradient can be decomposed through coordinate transformation, as will be proven later in this chapter (Bear, 1972/1988; Zienkiewicz, et al., 2005):

$$\boldsymbol{q_T} = -\boldsymbol{k}\boldsymbol{\nabla}T \tag{7.10}$$

with

$$\frac{\partial T}{\partial z} = 0$$

$$\boldsymbol{k} = \begin{bmatrix} k_{xx} & k_{xy} & 0 \\ k_{yx} & k_{yy} & 0 \\ 0 & 0 & k_{zz} \end{bmatrix} \approx \begin{bmatrix} k_{xx} & k_{xy} \\ k_{yx} & k_{yy} \end{bmatrix}$$

where

$\boldsymbol{k}$	[W/mK]	Thermal conductivity tensor (second order)

The mass fluxes governing the vapour and liquid phases of water are based on Darcy's law in which the second order permeability tensor is introduced (Bear, 1972/1988; Zienkiewicz, et al., 2005). Again only in-plane contributions are considered which allows to omit the directional component defined in depth direction. Hence, both mass fluxes are characterised by the symmetrical 2D permeability tensor (Bear, 1972/1988; Zienkiewicz, et al., 2005):

$$\begin{aligned} \boldsymbol{q_{gw}} &= -n(1-S_w)\rho_{gw}\left(\frac{K_{rel_g}}{\mu_g}\right)\boldsymbol{K}\boldsymbol{\nabla}P_{gw} \\ \boldsymbol{q_w} &= -nS_w\rho_w\left(\frac{K_{rel_w}}{\mu_w}\right)\boldsymbol{K}\boldsymbol{\nabla}P_w \end{aligned} \tag{7.11}$$

with

$$\frac{\partial T}{\partial z} = \frac{\partial P_c}{\partial z} = 0$$

$$\boldsymbol{K} = \begin{bmatrix} K_{xx} & K_{xy} & 0 \\ K_{yx} & K_{yy} & 0 \\ 0 & 0 & K_{zz} \end{bmatrix} \approx \begin{bmatrix} K_{xx} & K_{xy} \\ K_{yx} & K_{yy} \end{bmatrix}$$

where

$\boldsymbol{K}$	[m^2]	Permeability tensor (second order)

Anisotropic system of coupled PDE's

The coupled system of PDE's, stated in Eq. (7.1), is extended to reflect the anisotropic continuum description. Compared to chapter 6 the mass sub-matrices are unaffected since no spatial derivatives are present. The time-dependent distribution of the averaged thermal energy and water phase mass densities across the domain thus remains the same. However, the stiffness of the system is redefined with the heat flux according to Eq. (7.10) and the mass fluxes as stated by Eq. (7.11) (Bear, 1972/1988; Zienkiewicz, et al., 2005). The coupled system of PDE's is characterised by the same stiffness constants as in chapter 6, stating the

anisotropic material tensors separately. For convenience only the porous material description is presented since the aggregates are deduced through reduction of the terms:

$$\left(\boldsymbol{M_I} + H_{vap}\boldsymbol{M_{II}}\right)\frac{\partial \boldsymbol{c}}{\partial t} - \boldsymbol{\nabla}\cdot(\boldsymbol{S_I}\boldsymbol{\nabla c}) - H_{vap}\boldsymbol{\nabla}\cdot(\boldsymbol{S_{II}}\boldsymbol{\nabla c}) = 0 \tag{7.12}$$

with

$$K_{TT_1} = \boldsymbol{k}$$

$$K_{TT_2} = n(1-S_w)\frac{RHP_{sat}M_w}{RT}\left(\frac{K_{rel_g}}{\mu_g}\right)\boldsymbol{K}\left(\frac{\partial RH}{\partial T}P_{sat} + RH\frac{\partial P_{sat}}{\partial T}\right)$$

$$K_{TP} = n(1-S_w)\frac{RHP_{sat}M_w}{RT}\left(\frac{K_{rel_g}}{\mu_g}\right)\boldsymbol{K}\frac{\partial RH}{\partial P_c}P_{sat}$$

$$K_{PT} = nS_w\rho_w\left(\frac{K_{rel_w}}{\mu_w}\right)\boldsymbol{K}\left(\frac{\partial RH}{\partial T}P_{sat} + RH\frac{\partial P_{sat}}{\partial T}\right) + n(1-S_w)\frac{RHP_{sat}M_w}{RT}\left(\frac{K_{rel_g}}{\mu_g}\right)\boldsymbol{K}\left(\frac{\partial RH}{\partial T}P_{sat} + RH\frac{\partial P_{sat}}{\partial T}\right)$$

$$K_{PP} = nS_w\rho_w\left(\frac{K_{rel_w}}{\mu_w}\right)\boldsymbol{K}\left(\frac{\partial RH}{\partial P_c}P_{sat} - 1\right) + n(1-S_w)\frac{RHP_{sat}M_w}{RT}\left(\frac{K_{rel_g}}{\mu_g}\right)\boldsymbol{K}\frac{\partial RH}{\partial P_c}P_{sat}$$

$$\boldsymbol{S_I} = \begin{bmatrix} K_{TT_1} & 0 \\ K_{PT} & K_{PP} \end{bmatrix} \qquad \boldsymbol{S_{II}} = \begin{bmatrix} K_{TT_2} & K_{TP} \\ 0 & 0 \end{bmatrix}$$

Isotropic flux definitions before fracture

The solid and porous material descriptions are initially assumed isotropic which requires simplification of the element thermal conductivity and permeability tensors defined in Eq. (7.10) and Eq. (7.11) respectively. First, diagonal stiffness tensors are formed in case the principal directions of the material are aligned with the global coordinate system (Bear, 1972/1988; Zienkiewicz, et al., 2005). This type of anisotropy defines the flux components as independent in the global directions. The second simplification assumes isotropic conditions through using the identity matrix (Bear, 1972/1988; Zienkiewicz, et al., 2005). In doing so, the flux definition as stated later in Eq. (7.33) becomes comparable to the isotropic element stiffness matrix as elaborated in the previous chapter:

$$\begin{aligned} \boldsymbol{k^e} &= \begin{bmatrix} {k_{xx}}^e & 0 \\ 0 & {k_{yy}}^e \end{bmatrix} = \begin{bmatrix} k^e & 0 \\ 0 & k^e \end{bmatrix} = k^e\boldsymbol{I} \\ \boldsymbol{K^e} &= \begin{bmatrix} {K_{xx}}^e & 0 \\ 0 & {K_{yy}}^e \end{bmatrix} = \begin{bmatrix} K^e & 0 \\ 0 & K^e \end{bmatrix} = K^e\boldsymbol{I} \end{aligned} \tag{7.13}$$

7.2.4 Crack opening and directional permeability

The initial isotropic permeability becomes direction-dependent after fracture (Bear, 1972/1988). The orientation of the crack and the subsequent opening during localisation of deformations characterises the influence. Flow of liquid water and especially water vapour

along the crack is assumed to still be characterised as laminar and viscous, allowing the use of Darcy's law (Bear, 1972/1988). The resultant permeability is based on the simplified flow between parallel plates, expressed by the crack width and governed by the relationship derived in chapter 4 (Bear, 1972/1988). It is important to consider that the obtained local increase of the permeability, even in case of a relatively small crack width, is substantial compared to the surrounding material, as defined by:

$$K_{cr}{}' = \frac{w'^2}{12} \tag{7.14}$$

where

$K_{cr}{}'$	[m^2]	Local permeability defined parallel to the crack edges by opening
w'	[m]	Local crack width defined perpendicular to the crack edges

Anisotropic local permeability tensor governing the crack

Directional dependence is governed by the local permeability development according to Eq. (7.14) (Bear, 1972/1988). Both the vapour and liquid water mass fluxes are assumed to align with the crack, with the orientation fixed and the opening varies dependent on the mechanical loading. The corresponding local permeability tensor of the fractured material defines the flow of both phases parallel to the crack edges. This is schematically indicated in Fig. 7.2 using the adopted FEM approximation by 2D triangular elements. The local mass flux is perpendicular to the crack width and causes anisotropy in the permeability of the element:

$$\boldsymbol{K'^e} = \begin{bmatrix} K_{xx}{}'^e & 0 \\ 0 & K_{yy}{}'^e \end{bmatrix} = \begin{bmatrix} 0 & 0 \\ 0 & K_{cr}{}'^e \end{bmatrix} \tag{7.15}$$

Triangular orientation of three possible in-plane mass flux definitions

The anisotropic mass flux definitions are based on the 2D triangular element with each of three edges representing a material direction as schematically shown in Fig. 7.3. These material directions coincide with the 1D bars, defining the fracture mechanics behaviour as presented in chapter 9 (Schlangen, 1993; Vervuurt, 1997). Each material direction is governed by a rotated local coordinate system which defines both the axial and the perpendicular direction, forming a complete description of the in-plane fluxes (Zienkiewicz, et al., 2005).

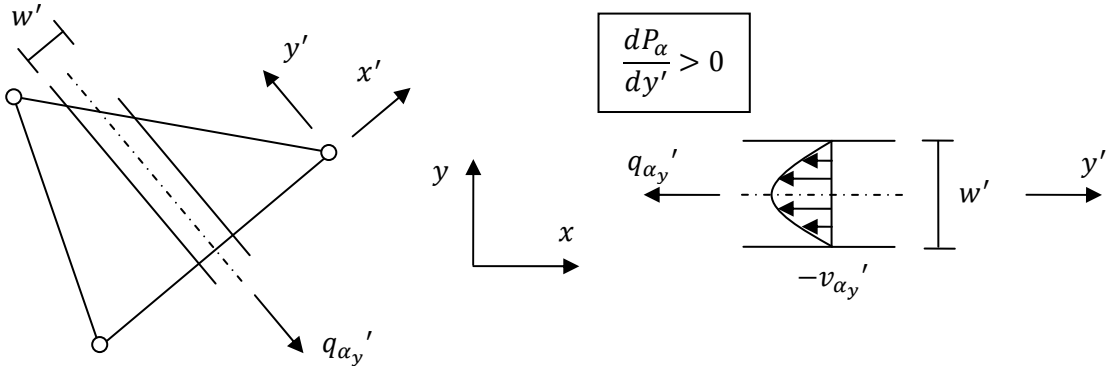

Fig. 7.2 *Crack opening govering both the vapour and liquid water mass fluxes in* $\mathbb{R}^2$. *The main flux contribution acts perpendicular to the crack width while assuming a laminar flow according to Darcy's law* (Bear, 1972/1988).

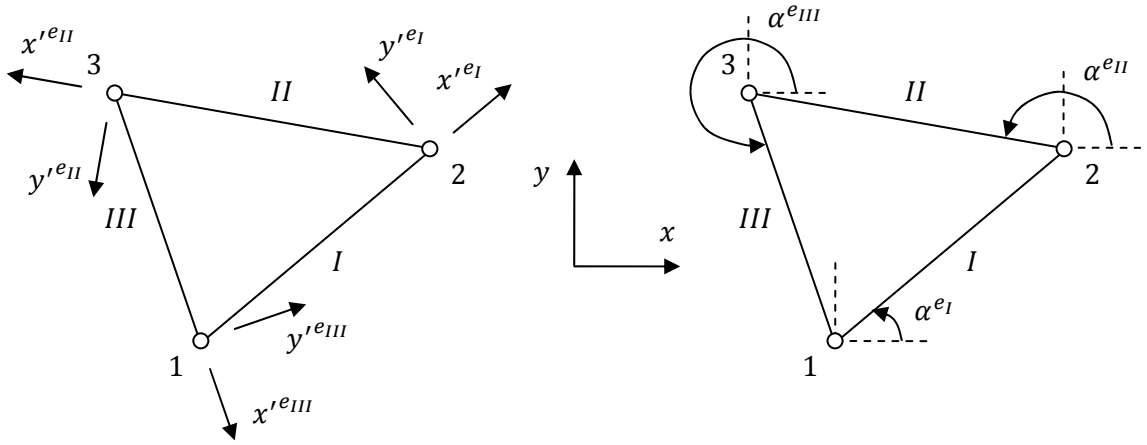

Fig. 7.3 *Schematic representation of the triangular element in $\mathbb{R}^2$. The anisotropic mass fluxes can be defined along each edge in accordance with the local coordinate system (left). Each direction is governed by coordinate transformation (right).*

Both perpendicular axes are required since the mass fluxes are characterised by pressure gradients which define 2D spatial derivatives across the element. In other words, a set of three local 1D derivatives is not sufficient to approximate the global 2D gradient as already mentioned in the previous chapter.

This difference between approximation by three 1D bars or by a 2D triangular element poses a problem in coupling both FEM models. In order to still obtain a global mass flux definition the crack width is used as a criterion. The material direction with the largest crack width defines the local permeability tensor. The remaining possibly fractured material directions are thus discarded. Alternatively, an averaging approach could be used, but the large variation in permeability on crack opening, as shown in chapter 4, makes this approach less suitable.

Coordinate transformation based on a material direction

Each local coordinate system is related to the global coordinate system through the transformation tensor defined in chapter 5 (Spencer, 1980/2004; Wells, 2006; Blom, 2009). It is important to consider that the local coordinate system can represent each of three material directions separately, dependent on the largest crack width present:

$$\boldsymbol{x'^{e_d}} = \boldsymbol{T_\alpha}^{e_d}\boldsymbol{x^e} \tag{7.16}$$

with

$$\boldsymbol{x^e} = \begin{bmatrix} x^e \\ y^e \end{bmatrix} \qquad \boldsymbol{x'^{e_d}} = \begin{bmatrix} x'^{e_d} \\ y'^{e_d} \end{bmatrix} \qquad \boldsymbol{T_\alpha}^{e_d} = \begin{bmatrix} \cos\alpha^{e_d} & \sin\alpha^{e_d} \\ -\sin\alpha^{e_d} & \cos\alpha^{e_d} \end{bmatrix}$$

where

$\ldots^{e_d}$		Indication for the edge of the triangular element
α^{e_d}	[rad]	Angle of edge 'd' of the triangular element
$\boldsymbol{x^e}, \boldsymbol{x'^{e_d}}$	[m]	Global, local element coordinate system vectors with the latter based on direction 'd' having the largest crack width
$\boldsymbol{T_\alpha}^{e_d}$	[-]	Element coordinate transformation tensor (second order)

In addition, this coordinate transformation relationship is also used to relate the local and global gradients. The partial derivatives of the global coordinate system are obtained through inserting Eq. (7.16) using orthogonality (Dullemond & Peeters, 1991-2010). After rearranging, the derivatives reduce to the identity matrix and only the constant transformation matrix remains (Dullemond & Peeters, 1991-2010; Zienkiewicz, et al., 2005). So, gradients also transform according to coordinate relationships as defined through:

$$\begin{aligned}\boldsymbol{\nabla}(\cdots)'^{e_d} &= \frac{\partial}{\partial \boldsymbol{x}'^{e_d}}\boldsymbol{x}^{e\boldsymbol{T}}\boldsymbol{\nabla}(\cdots)^{e} = \frac{\partial}{\partial \boldsymbol{x}'^{e_d}}\left(\boldsymbol{T_\alpha}^{e_d\boldsymbol{T}}\boldsymbol{x}'^{e_d}\right)^{\boldsymbol{T}}\boldsymbol{\nabla}(\cdots)^{e} = \frac{\partial}{\partial \boldsymbol{x}'^{e_d}}\boldsymbol{x}'^{e_d\boldsymbol{T}}\boldsymbol{T_\alpha}^{e_d}\boldsymbol{\nabla}(\cdots)^{e} \\ &= \boldsymbol{I}\boldsymbol{T_\alpha}^{e_d}\boldsymbol{\nabla}(\cdots)^{e} = \boldsymbol{T_\alpha}^{e_d}\boldsymbol{\nabla}(\cdots)^{e}\end{aligned} \tag{7.17}$$

Conservation of kinetic energy and anisotropic global permeability tensor

In case of one or several fractured material directions local mass fluxes are introduced which are to be related to the global directions. This is obtained through conservation of the kinetic energy across the triangular element and thus across the domain. Recalling from the previous chapter the stiffness contribution to the mass conservation of the water phases, expressed in both coordinate systems. The global mass fluxes are defined by Eq. (7.11) whereas the local mass fluxes are based on the anisotropic permeability tensor stated in Eq. (7.15):

$$\begin{aligned}\frac{\partial {E_{kin_P}}^{e}}{\partial t} &= \frac{\partial {E_{kin_P}}^{'e_d}}{\partial t} \\ \int_{\Omega^e}\frac{1}{2}(\boldsymbol{\nabla}{P_c}^{e})^{\boldsymbol{T}}\left(\boldsymbol{q_w}^{e}+\boldsymbol{q_{gw}}^{e}\right)d\Omega^{e} &= \int_{\Omega'^{e_d}}\frac{1}{2}\left(\boldsymbol{\nabla}{P_c}'^{e_d}\right)^{\boldsymbol{T}}\left(\boldsymbol{q_w}'^{e_d}+\boldsymbol{q_{gw}}'^{e_d}\right)d\Omega'^{e_d}\end{aligned} \tag{7.18}$$

This kinetic energy relationship is first simplified by omitting the integrals due to the constant element fluxes and gradients as discussed in the previous chapter. Consideration of the mass flux definitions in Eq. (7.11) indicates that only the permeability tensor is the affected property and it is appropriate to state for instance:

$$(\boldsymbol{\nabla}{P_c}^{e})^{\boldsymbol{T}}\boldsymbol{K}^{\boldsymbol{e}}\boldsymbol{\nabla}{P_c}^{e} = \left(\boldsymbol{\nabla}{P_c}'^{e_d}\right)^{\boldsymbol{T}}\boldsymbol{K}'^{e_d}\boldsymbol{\nabla}{P_c}'^{e_d} \tag{7.19}$$

The local gradient of the capillary pressure is expressed through coordinate transformation based on Eq. (7.17). As a result, the global element permeability tensor is obtained (Dullemond & Peeters, 1991-2010; Zienkiewicz, et al., 2005):

$$\begin{aligned}(\boldsymbol{\nabla}{P_c}^{e})^{\boldsymbol{T}}\boldsymbol{K}^{\boldsymbol{e}}\boldsymbol{\nabla}{P_c}^{e} &= (\boldsymbol{T_\alpha}^{e_d}\boldsymbol{\nabla}{P_c}^{e})^{\boldsymbol{T}}\boldsymbol{K}'^{e_d}\boldsymbol{T_\alpha}^{e_d}\boldsymbol{\nabla}{P_c}^{e} = (\boldsymbol{\nabla}{P_c}^{e})^{\boldsymbol{T}}\boldsymbol{T_\alpha}^{e_d\boldsymbol{T}}\boldsymbol{K}'^{e_d}\boldsymbol{T_\alpha}^{e_d}\boldsymbol{\nabla}{P_c}^{e} \\ &\rightarrow \boldsymbol{K}^{\boldsymbol{e}} = \boldsymbol{T_\alpha}^{e_d\boldsymbol{T}}\boldsymbol{K}'^{e_d}\boldsymbol{T_\alpha}^{e_d}\end{aligned} \tag{7.20}$$

Evaluation of this relationship confirms that the global element tensor is indeed independent of the coordinate system for an isotropic material and symmetric for an anisotropic material as was previously assumed (Bear, 1972/1988; Zienkiewicz, et al., 2005). The following is obtained in case the first edge of the triangular element has the largest crack width:

$$\boldsymbol{K}^{\boldsymbol{e}} = \boldsymbol{T_\alpha}^{e_I\boldsymbol{T}}\boldsymbol{K}'^{e_I}\boldsymbol{T_\alpha}^{e_I} \tag{7.21}$$

Anisotropic permeability influence

By introducing directional dependence in the local permeability tensor the components of the mass fluxes are still aligned with the corresponding contributions to the local gradients (Bear, 1972/1988; Zienkiewicz, et al., 2005). However, through coordinate transformations, defined in Eq. (7.20) applied to the element permeability tensor stated in Eq. (7.15), anisotropy in the global flux definition is introduced (Bear, 1972/1988; Zienkiewicz, et al., 2005). As a results, the global permeability tensor is no longer diagonal. Both the vapour and liquid mass fluxes rotate, depending on the orientation of the crack, and are not assumed to align with the pressure gradients.

The influence of a crack is thus determined by the considerable increase of the permeability as well as the orientation with respect to the pressure distribution. Cracks tend to represent sudden changes in the assumed continuous material description. These discontinuities in the FEM definition characterise the development of the incremental variables. In this respect several numerical instability issues can arise as discussed hereafter.

7.3 Numerical stability

The applicability and usability of the FEM model is determined by the numerical stability during the incremental calculations. In the previous chapter several considerations are discussed in order to improve convergence. An implicit Euler backward time integration is used extended through a first order estimation of the incremental variables (van Kan, et al., 2008; Segal, 2008). A further stabilisation is obtained by neglecting the dry air phase since no constitutive relationship, such as the desorption isotherm, exists to maintain the physical limits. Relative permeability's are included which stabilize the material description through limitation of a mass flux at a relatively low phase density (van Kan, et al., 2008). However, three additional aspects are considered which are especially of importance for the cracks.

7.3.1 Critical temperature

At temperatures higher than 300 ^{o}C, the non-linearity of the saturated water vapour pressure and the density of liquid water become increasingly apparent. This is illustrated in Fig. 7.4 by the imposed capillary pressure through the Neumann boundary conditions governing fire exposure. Partial wetting of the cross-section is indicated through the capillary pressure reduction based on the inverse of Kelvin's equation as restated from chapter 4:

$$P_{c_{\infty fire}} = -\ln\left(\frac{P_{gw_{\infty fire}}}{P_{sat}}\right)\frac{\rho_w R T_{\infty fire}}{M_w} \tag{7.22}$$

where

$P_{c_{\infty fire}}$	[Pa]	Capillary pressure at distance from the fire exposed surface
$T_{\infty fire}$	[K]	Temperature at distance from the exposed surface according to the time-dependent prescribed fire curve
$P_{gw_{\infty fire}}$	[Pa]	Pressure of the water vapour phase at distance from the fire exposed surface maintained at 1000 Pa

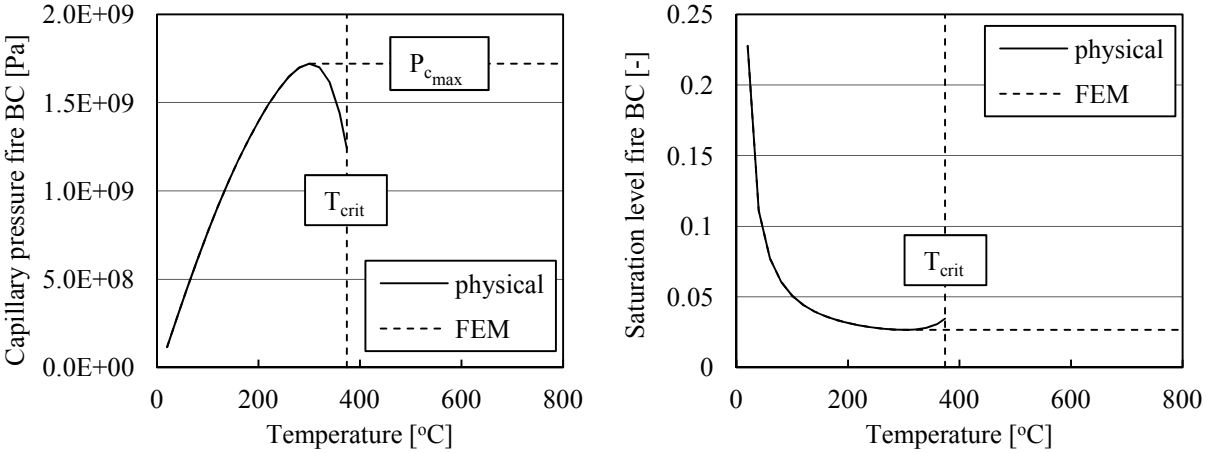

Fig. 7.4 *Imposed capillary pressure development (left) at the fire exposed surface indicating partial wetting near the critical point (right). This is overcome by assuming a constant capillary pressure at temperatures higher than 300 °C.*

A further complication is that at temperatures exceeding the critical point of liquid water, the partially saturated material description is effectively no longer valid as already mentioned in chapter 4. However, during fire exposure the temperature rapidly exceeds this point requiring the material description to account for this. A possibility is to maintain the water properties at the values obtained at the critical temperature. However, this would allow the capillary pressure to continuously increase, dependent only on the temperature according to Eq. (7.22). This could lead to numerical stability issues especially in the cracks, causing exceedingly low saturation levels with corresponding vapour pressures.

The adopted solution is to maintain the imposed capillary pressure at the maximum value as shown in the left graph of Fig. 7.4. This cannot directly be imposed since the boundary conditions are only governed by the temperature and the water vapour density. This behaviour is included by definition of the water properties at these high temperatures. The saturated water vapour pressure is maintained at the critical temperature value using a smooth transition curve as illustrated in the left graph of Fig. 7.5. The density of liquid water is defined in order to maintain the capillary pressure development. Using Eq. (7.22) and stating the maximum capillary pressure attained around a temperature of 300 °C results in:

$$T \geq 575K\ (301.85℃) \rightarrow \rho_w = -\frac{P_{c_{max}} M_w}{\ln\left(\frac{P_{gw_{\infty fire}}}{P_{sat}}\right) RT} \tag{7.23}$$

where

$P_{c_{max}}$ [Pa] Maximum capillary pressure defined at 1.72E9 Pa

The temperature-dependent transition from the physical to the imposed density of liquid water, according to Eq. (7.23), is seen in the right graph of Fig. 7.5. This smooth curve ensures that the imposed capillary pressure at the dried surface reaches a maximum. However, in the cross-section the RH and thus vapour pressure can still vary dependent on the saturation level, allowing for the drying process to continue at temperatures exceeding the critical point.

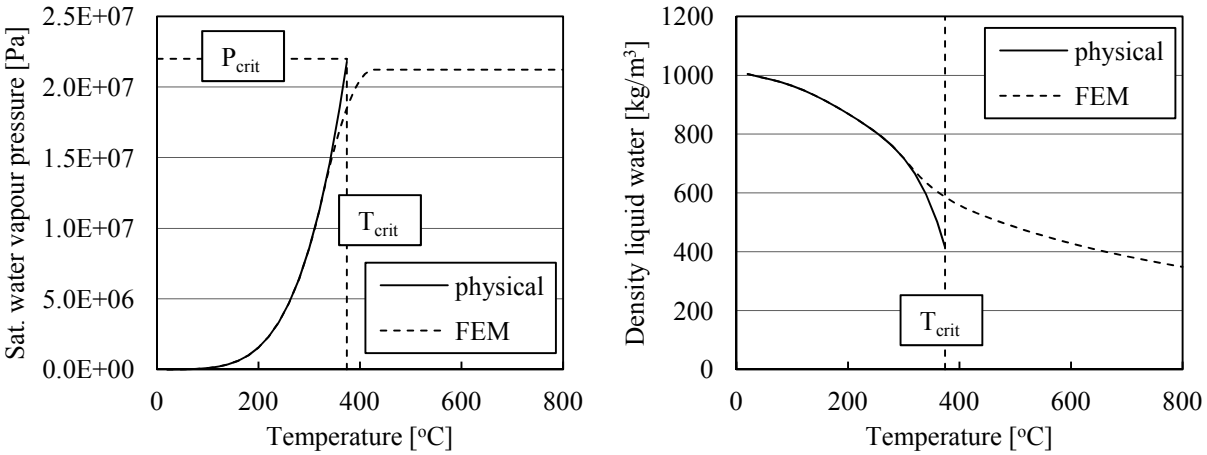

Fig. 7.5 *Above the critical temperature the saturated water vapour pressure is maintained to avoid extreme values (left). The development of the liquid water density ensures a constant maximum capillary pressure at the dried surface (right).*

At these high temperatures the RH is only dependent on the capillary pressure as obtained by inserting the liquid water density from Eq. (7.23) into the inverse of the Kelvin equation. Increasing temperatures at constant capillary pressure thus define the RH according to:

$$T \geq 575K\ (301.85°C) \rightarrow RH = \left(\frac{P_{gw_{\infty_{fire}}}}{P_{sat}}\right)^{\frac{P_c}{P_{cmax}}} \tag{7.24}$$

In addition, the liquid water saturation level also remains constant with capillary pressure since no temperature dependence is included as indicated in the left graph of Fig. 7.6. Some authors overcome this be definition of rapid drying of the material around the critical temperature using the desorption isotherm (Dal Pont, 2004; Zeiml, et al., 2008b). However, this relatively sudden change in behaviour is numerically not desirable especially in the vicinity of cracks. Furthermore, at these high temperatures the material is mostly already in a dried state, mediating the need to include these modifications. The rapidly reducing enthalpy of vaporization near the critical temperature is subsequently ommited, uncoupling both PDE's.

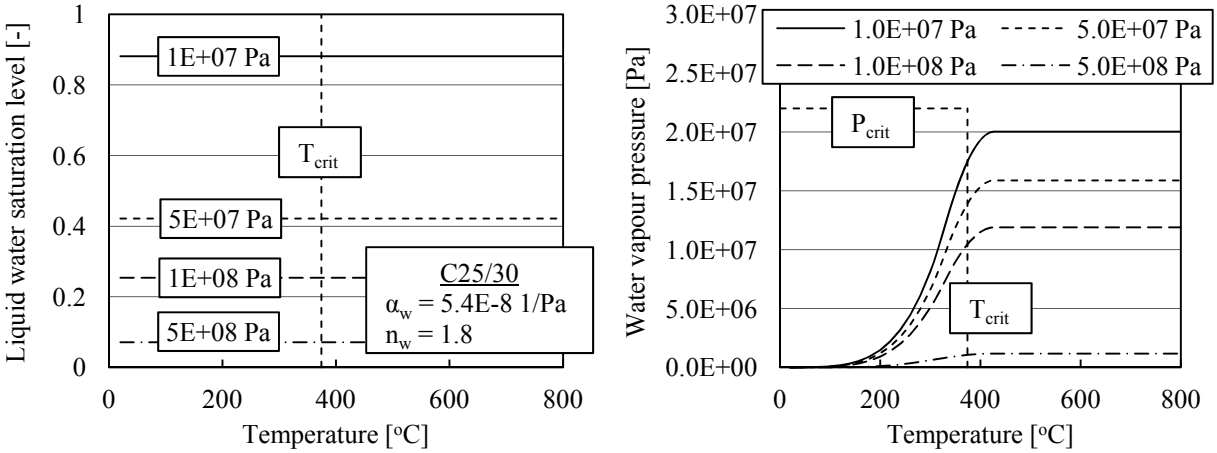

Fig. 7.6 *Above the critical temperature the capillary pressure still defines the saturation level (left). The water vapour pressure is governed by the assumed constant RH and saturation pressure affected only by changing capillary pressures (right).*

7.3.2 Incremental time step size variation

In the previous chapter the Euler backward time integration is defined based on a constant incremental step size throughout the calculation. This proved to be sufficient in case the non-linear behaviour develops gradually. However, by introducing discontinuities through cracks the level of non-linearity increases and it may no longer be sufficient to use a constant time step. Several possibilities to implement adaptive time stepping can thus be considered, based mainly on a convergence requirement (Söderlind & Wang, 2006). This could be defined with respect to the incremental development of the variables as obtained by the second, corrector, step. However, it was found that using the number of iterations required to solve the FEM system results in a better estimation of the development. Furthermore, to avoid sudden time step changes a limiter function is adopted (van Kan, et al., 2008). The resultant time step size variation is expressed by the following relationships which is graphically shown in Fig. 7.7:

$$\frac{\Delta t^{t+1}}{\Delta t^{t}} = 0.5 + \frac{r + |r|}{2(1 + |r|)} \tag{7.25}$$

with

$$r = \frac{conv.}{k_{max}}$$

where

r	[-]	Ratio of convergence
$conv.$	[-]	Convergence criterion
k_{max}	[-]	Maximum number of iterations by the solver

The first order prediction is through variation of the time step size expressed by:

$$\boldsymbol{c_1^{t+1}} = \boldsymbol{c^t} + \Delta t^{t+1}\left[\frac{\partial \boldsymbol{c}}{\partial t}\right]^t \approx \boldsymbol{c^t} + \frac{\Delta t^{t+1}}{\Delta t^{t}}\left(\boldsymbol{c^t} - \boldsymbol{c^{t-1}}\right) \tag{7.26}$$

Changing the time step size also affects the FEM definition, stated in Eq. (7.31), by the stiffness terms governing the heat and mass fluxes. Also the terms defining the Neumann boundary conditions are modified since these are stated at the next time increment.

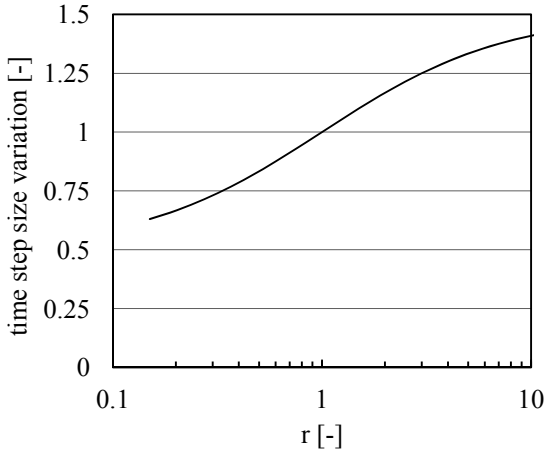

Fig. 7.7 *Variation of the incremental time step size based on the maximum number of iterations by the solver using a limiter function.*

7.3.3 Crack opening and development of the anisotropic permeability

The coupling with the fracture mechanics model poses additional numerical stability issues based on the sudden and localised opening of the crack. Whereas an initial crack pattern directly influences the temperature and pressure development, this is not the case during incremental coupling. Cracks develop in a porous material which is until fracture assumed to be isotropic and continuous. Both aspects are modified in case the crack is formed. The substantial increase of permeability disturbs the continuous material schematisation whereas the anisotropy could force the mass fluxes to no longer align with the pressure gradients.

Numerical instabilities could develop caused by the non-linear behaviour of the nodal masses and the development of the variables. The first aspect is governed by the definition of the forced drying process based on the desorption isotherm (Pel & Huinink, 2007; Bear, 1972/1988). The capillary pressure development governs the physical state of the mass which especially at high liquid water saturation levels quickly reduces. Furthermore, the forced drying process is also influenced by the mass fluxes through the assumed instantaneous development of thermodynamic equilibrium between the water phases (Tenchev, et al., 2001; Gawin, et al., 2003). The permeability of the crack increases the velocities of the mass fluxes, imposing higher constraints on the development of the drying process.

Maximum crack opening

Stability is initially improved by defining a maximum crack opening. This measure is straightforward and improves the convergence by mitigating the imposed permeability:

$$K_{cr}{}'^{e} \leq K_{cr_{max}}{}' \tag{7.27}$$

where

$K_{cr_{max}}{}'$ [m^2] Maximum permeability of the crack

Approximation of the anisotropic flux definition

The second modification aims to impose less stringent conditions on the characterisation of the crack. The assumed simplified crack only defines the mass fluxes parallel to the edges. The level of anisotropy is mitigated by including also a limited permeability increase in the perpendicular direction. This flux factor is introduced in the element permeability tensor on the diagonal as follows:

$$\boldsymbol{K}'^{\boldsymbol{e}} = \begin{bmatrix} K_{xx}{}'^{e} & 0 \\ 0 & K_{yy}{}'^{e} \end{bmatrix} = \begin{bmatrix} 0 & 0 \\ 0 & K_{cr}{}'^{e} \end{bmatrix} \approx \begin{bmatrix} \beta_{cr} K_{cr}{}'^{e} & 0 \\ 0 & K_{cr}{}'^{e} \end{bmatrix} \tag{7.28}$$

where

β_{cr} [-] Flux factor governing the permeability perpendicular to the crack

The flow of the water phases between the crack edges is governed by pressure variations in this direction. A pressure gradient perpendicular to the crack could for instance develop by an aggregate particle. Flow perpendicular to the crack is also of importance in case the direction of the crack path is not sufficiently aligned with the pressure gradient. By reducing the level of anisotropy the mass flow is allowed to partially deviate from the crack path.

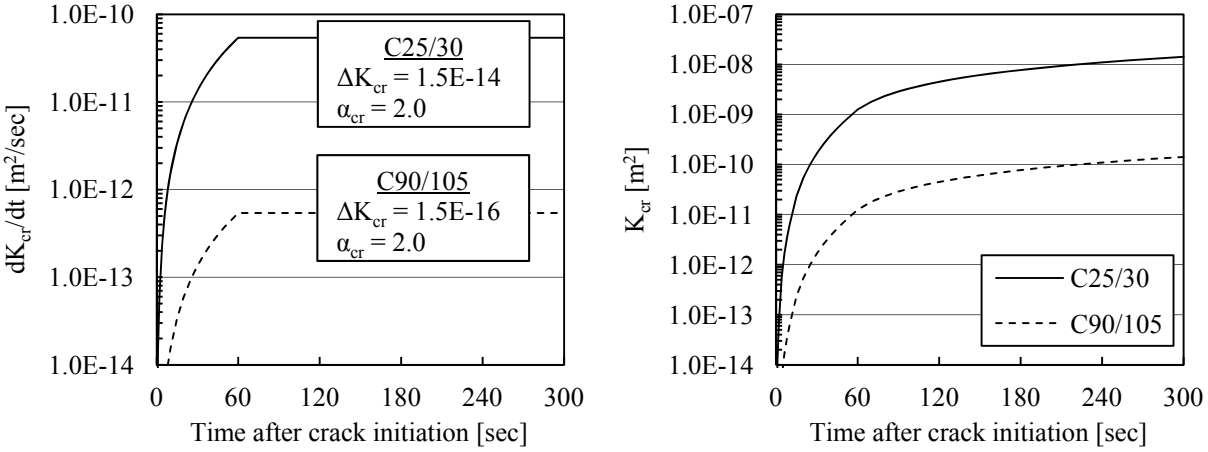

Fig. 7.8 *Incremental development of the crack permeability based on the concrete strength class and the time relative to initiation.*

Incremental development of the permeability governing the crack

The third stabilisation measure is focussed on the sudden permeability increase of the crack at initiation. This causes fluctuations in the solution of the variables governing the masses of the surrounding material. These instabilities are addressed through an incremental development of the crack permeability. With time the permeability increases gradually, allowing the mass of the surrounding material to adhere to the localised discontinuity. The definition of the crack permeability is based on the current state of the material and the incremental development from the time of initiation:

$$K_{cr}{}'^{e\,t+1}_{k+1} = K_{cr}{}'^{e\,t+1}_{k} + \Delta t \left[\frac{dK_{cr}{}'^{e}}{d(t - t_{cr}{}^{e})}\right]^{t+1}_{k} \tag{7.29}$$

with

$$K_{cr}{}'^{e\,t_{cr}{}^{e}+1}_{k} = K'^{e\,t} = K^{e\,t} \qquad K_{cr}{}'^{e\,t+1}_{k} = K_{cr}{}'^{e\,t}$$

where

$t_{cr}{}^{e}$	[s]	Element-based time of fracture
$K_{cr}{}'^{e\,t+1}_{k}, K_{cr}{}'^{e\,t+1}_{k+1}$	[m²]	Element crack permeability at the current, next incremental time step
$K_{cr}{}'^{e\,t_{cr}{}^{e}+1}_{k}$	[m²]	Element permeability at the first step after crack initiation

For the incremental development of the crack a quadratic relationship is used based on the time increment after initiation, expressed using the Euler backward integration scheme. A maximum rate of crack opening is also defined using the time increment in order to avoid numerical instabilities. The following relationship is graphically represented in Fig. 7.8 with the differentiation between the concrete strength classes elaborated in chapter 9:

$$\left[\frac{dK_{cr}{}'^{e}}{d(t - t_{cr}{}^{e})}\right]^{t+1}_{k} = \Delta K_{cr}\left((t + \Delta t) - t_{cr}{}^{e}\right)^{\alpha_{cr}} \tag{7.30}$$

with

$$\left((t+\Delta t)-{t_{cr}}^{e}\right) \leq \Delta t_{cr_{max}}$$

where

$\Delta t_{cr_{max}}$	[s]	Maximum time increment during which the crack opens at increasing rate
$\Delta K_{cr}, \alpha_{cr}$	$[m^2/s^{\alpha_{cr}+1}]$, [-]	Parameters governing the crack permeability development

7.4 Incremental FEM definition

7.4.1 Discretisation based on heterogeneous and anisotropic 2D triangular elements

The isotropic FEM definition from the previous chapter is restated, based on the heterogeneous continuum and the anisotropic fluxes. The coupled system of PDE's becomes:

$$\begin{aligned}&\sum_{e=1}^{e_{tot}}\left(\boldsymbol{M_{sys}}_{\boldsymbol{k}}^{\boldsymbol{e\,t+1}}+\Delta t\boldsymbol{S_{sys}}_{\boldsymbol{k}}^{\boldsymbol{e\,t+1}}\right)\sum_{e=1}^{e_{tot}}\Delta\boldsymbol{c_{sys}}_{\boldsymbol{k}}^{\boldsymbol{e\,t+1}}+\Delta t\sum_{e=1}^{e_{tot}}\boldsymbol{S_{bc}}_{\boldsymbol{k}}^{\boldsymbol{e\,t+1}}\sum_{e=1}^{e_{tot}}\Delta\boldsymbol{c_{sys}}_{\boldsymbol{k}}^{\boldsymbol{e\,t+1}}\\&=-\left(\sum_{e=1}^{e_{tot}}\left(\boldsymbol{M_{sys}}_{\boldsymbol{k}}^{\boldsymbol{e\,t+1}}\left(\boldsymbol{c_{sys}}_{\boldsymbol{k}}^{\boldsymbol{e\,t+1}}-\boldsymbol{c_{sys}}^{\boldsymbol{e\,t}}\right)+\Delta t\boldsymbol{S_{sys}}_{\boldsymbol{k}}^{\boldsymbol{e\,t+1}}\boldsymbol{c_{sys}}_{\boldsymbol{k}}^{\boldsymbol{e\,t+1}}\right)\right)-\Delta t\sum_{e=1}^{e_{tot}}\boldsymbol{Q_{bc}}_{\boldsymbol{k}}^{\boldsymbol{e\,t+1}}\end{aligned} \tag{7.31}$$

with

$$\boldsymbol{M_{sys}}_{\boldsymbol{k}}^{\boldsymbol{e\,t+1}}=\int_{\Omega^e}\boldsymbol{T_{ag}}^{\boldsymbol{eT}}\boldsymbol{N_C}^{\boldsymbol{eT}}\left(\boldsymbol{M_I}_{\boldsymbol{k}}^{\boldsymbol{e\,t+1}}+\left(H_{vap}\boldsymbol{M_{II}}\right)_{\boldsymbol{k}}^{\boldsymbol{e\,t+1}}\right)\boldsymbol{N_C}^{\boldsymbol{e}}\boldsymbol{T_{ag}}^{\boldsymbol{e}}d\Omega^e$$

$$\boldsymbol{S_{sys}}_{\boldsymbol{k}}^{\boldsymbol{e\,t+1}}=\int_{\Omega^e}\boldsymbol{T_{ag}}^{\boldsymbol{eT}}\boldsymbol{B_C}^{\boldsymbol{eT}}\left(\boldsymbol{S_I}_{\boldsymbol{k}}^{\boldsymbol{e\,t+1}}+\left(H_{vap}\boldsymbol{S_{II}}\right)_{\boldsymbol{k}}^{\boldsymbol{e\,t+1}}\right)\boldsymbol{B_C}^{\boldsymbol{e}}\boldsymbol{T_{ag}}^{\boldsymbol{e}}d\Omega^e$$

$$\boldsymbol{S_{bc}}_{\boldsymbol{k}}^{\boldsymbol{e\,t+1}}=\int_{\Gamma_A{}^e}\boldsymbol{T_{ag}}^{\boldsymbol{eT}}\boldsymbol{N_C}^{\boldsymbol{eT}}\begin{bmatrix}\alpha_A & 0\\ \beta_{A_T}{}_k^{t+1} & \beta_{A_P}{}_k^{t+1}\end{bmatrix}\boldsymbol{N_C}^{\boldsymbol{e}}\boldsymbol{T_{ag}}^{\boldsymbol{e}}d\Gamma_A{}^e$$

$$\boldsymbol{Q_{bc}}_{\boldsymbol{k}}^{\boldsymbol{e\,t+1}}=\int_{\Gamma_A{}^e}\boldsymbol{T_{ag}}^{\boldsymbol{eT}}\boldsymbol{N_C}^{\boldsymbol{eT}}\begin{bmatrix}\alpha_A\left(T^e{}_k^{t+1}-T_\infty{}^{t+1}\right)\\ \beta_A\dfrac{M_w}{R}\left(\dfrac{P_{gw}{}_k^{e\,t+1}}{T^e{}_k^{t+1}}-\dfrac{P_{gw_\infty}{}^{t+1}}{T_\infty{}^{t+1}}\right)\end{bmatrix}d\Gamma_A{}^e$$

In order to obtain an anisotropic FEM definition the following needs to be considered:

- The heterogeneous continuum definition effects both the element mass and stiffness matrices as reflected by the transformation matrix. The nodal variables are initially all assumed as porous material and only reduced if situated inside an aggregate particle.

- At aggregate edges material discontinuities are introduced through the solid element matrices reflecting undefined rows and columns for the second conservation equation. No contributions to the mass or stiffness of the porous nodal variables are imposed.

- The element heat and mass fluxes are assumed isotropic until a crack develops. The latter is governed by incremental coupling based on brittle fracture of the 1D bars. Under these circumstances the mass fluxes become anisotropic characterised by the global element permeability tensor based on the material direction with the largest crack width.

- Neumann boundary conditions are reflected by contributions to the left and right hand side. Both are transformed according to the nodal variables along the boundary and directly assigned accordingly.

7.4.2 Spatial integration applied to the anisotropic flux definition

The element stiffness matrix, governing the anisotropic heat and mass fluxes, is numerically approximated by the same 2D triangular elements as used in the previous chapter (van Kan, et al., 2008). For the isotropic continuum, the vector reflecting the gradient of the variables was chosen to obtain a diagonal element stiffness matrix. However, the introduction of the material tensors affects the lay-out of this variables gradient vector. The gradients are no longer grouped per axis, but rather per variable as indicated. To account for this an additional transformation is defined, which interchanges the second and third row and column:

$$\boldsymbol{\nabla c^{*}}^{\boldsymbol{e}}_{\boldsymbol{k}}{}^{\boldsymbol{t+1}} = \boldsymbol{T_{\nabla}} \boldsymbol{\nabla c}^{\boldsymbol{e}}_{\boldsymbol{k}}{}^{\boldsymbol{t+1}} \tag{7.32}$$

with

$$\boldsymbol{\nabla c}^{\boldsymbol{e}}_{\boldsymbol{k}}{}^{\boldsymbol{t+1}} = \begin{bmatrix} \frac{\partial T^{e}_{k}{}^{t+1}}{\partial x} \\ \frac{\partial P_{c}{}^{e}_{k}{}^{t+1}}{\partial x} \\ \frac{\partial T^{e}_{k}{}^{t+1}}{\partial y} \\ \frac{\partial P_{c}{}^{e}_{k}{}^{t+1}}{\partial y} \end{bmatrix} \qquad \boldsymbol{\nabla c^{*}}^{\boldsymbol{e}}_{\boldsymbol{k}}{}^{\boldsymbol{t+1}} = \begin{bmatrix} \frac{\partial T^{e}_{k}{}^{t+1}}{\partial x} \\ \frac{\partial T^{e}_{k}{}^{t+1}}{\partial y} \\ \frac{\partial P_{c}{}^{e}_{k}{}^{t+1}}{\partial x} \\ \frac{\partial P_{c}{}^{e}_{k}{}^{t+1}}{\partial y} \end{bmatrix} \qquad \boldsymbol{T_{\nabla}}^{\boldsymbol{e}} = \begin{bmatrix} 1 & 0 & 0 & 0 \\ 0 & 0 & 1 & 0 \\ 0 & 1 & 0 & 0 \\ 0 & 0 & 0 & 1 \end{bmatrix}$$

where

$\boldsymbol{T_{\nabla}}^{\boldsymbol{e}}$ [-] Element transformation matrix for modification of the gradient

Inserting of this relationship into Eq. (7.9), representing the element stiffness matrix, adds an additional transformation:

$$\boldsymbol{S_{sys}}^{\boldsymbol{e}}_{\boldsymbol{k}}{}^{\boldsymbol{t+1}} = \int_{\Omega^e} \boldsymbol{T_{ag}}^{\boldsymbol{eT}} \boldsymbol{B_C}^{\boldsymbol{eT}} \boldsymbol{T_{\nabla}}^{\boldsymbol{eT}} \left(\boldsymbol{S_I}^{\boldsymbol{e}}_{\boldsymbol{k}}{}^{\boldsymbol{t+1}} + \left(H_{vap} \boldsymbol{S_{II}} \right)^{\boldsymbol{e}}_{\boldsymbol{k}}{}^{\boldsymbol{t+1}} \right) \boldsymbol{T_{\nabla}}^{\boldsymbol{e}} \boldsymbol{B_C}^{\boldsymbol{e}} \boldsymbol{T_{ag}}^{\boldsymbol{e}} d\Omega^e \tag{7.33}$$

For FEM implementation it is convenient to separate this stiffness term in a coefficient matrix and a material tensor. The former takes the form described in chapter 6, omitting the material characterisation for the stiffness coefficients defined in Eq. (7.12). The element material tensor is through the identity matrix restated while transformation based on Eq. (7.32) defines the second contribution. Using both matrices the following relations are defined:

$$\boldsymbol{S_{sys_T}}_{\boldsymbol{k}}^{\boldsymbol{et+1}} = DA^{e}\boldsymbol{T_{ag}}^{\boldsymbol{eT}}\boldsymbol{B_C}^{\boldsymbol{eT}}\left(\boldsymbol{S_{I_T}}^{**}{}_{\boldsymbol{k}}^{\boldsymbol{et+1}}\boldsymbol{I}\left(\boldsymbol{T_\nabla}^{\boldsymbol{eT}}\boldsymbol{k}_{\boldsymbol{k}}^{\boldsymbol{et+1}}\boldsymbol{IT_\nabla}^{\boldsymbol{e}}\right)\right)\boldsymbol{B_C}^{\boldsymbol{e}}\boldsymbol{T_{ag}}^{\boldsymbol{e}}$$

$$\boldsymbol{S_{sys_P}}_{\boldsymbol{k}}^{\boldsymbol{et+1}} = DA^{e}\boldsymbol{T_{ag}}^{\boldsymbol{eT}}\boldsymbol{B_C}^{\boldsymbol{eT}}\left(\left(\boldsymbol{S_{I_P}}^{**}{}_{\boldsymbol{k}}^{\boldsymbol{et+1}} + \left(H_{vap}\boldsymbol{S_{II}}^{**}\right)_{\boldsymbol{k}}^{\boldsymbol{et+1}}\right)\boldsymbol{I}\left(\boldsymbol{T_\nabla}^{\boldsymbol{eT}}\boldsymbol{K}_{\boldsymbol{k}}^{\boldsymbol{et+1}}\boldsymbol{IT_\nabla}^{\boldsymbol{e}}\right)\right)\boldsymbol{B_C}^{\boldsymbol{e}}\boldsymbol{T_{ag}}^{\boldsymbol{e}} \tag{7.34}$$

with

$$\boldsymbol{S_{I_T}}^{**} = \begin{bmatrix} K_{TT_1}{}^{**} & 0 \\ 0 & 0 \end{bmatrix} \qquad \boldsymbol{S_{I_P}}^{**} = \begin{bmatrix} 0 & 0 \\ K_{PT}{}^{**} & K_{PP}{}^{**} \end{bmatrix} \qquad \boldsymbol{S_{II}}^{**} = \begin{bmatrix} K_{TT_2}{}^{**} & K_{TP}{}^{**} \\ 0 & 0 \end{bmatrix}$$

where

$\boldsymbol{S_{I_T}}^{**}, \boldsymbol{S_{I_P}}^{**}, \boldsymbol{S_{II}}^{**}$	[var.]	Stiffness coefficient matrices without material characterisation
$\boldsymbol{S_{sys_T}}_{\boldsymbol{k}}^{\boldsymbol{et+1}}$	[var.]	Element system stiffness matrix based on the isotropic heat flux
$\boldsymbol{S_{sys_P}}_{\boldsymbol{k}}^{\boldsymbol{et+1}}$	[var.]	Element system stiffness matrix based on the anisotropic vapour and liquid water mass fluxes

7.5 Conclusions with respect to the FEM definition

With respect to the heterogeneous continuum definition the following conclusions and remarks are stated:

- The mortar and interfacial zones are characterised as porous material governed by the coupled system of PDE's based on forced drying as stated in Eq. (7.1). Aggregate particles are assumed impermeable and are only defined by Fourier's differential equation for thermal conductivity using Eq. (7.2).

- Material discontinuities are introduced through definition of solid and porous descriptions. The heat flux passes across the domain dependent on the material. However, the mass fluxes are only defined for the porous mortar and interfacial zones.

- Heterogeneity is implemented by local reduction of the porous material description using the element transformation matrix based on the nodal variables. This reduces both element matrices, according to Eq. (7.8) and Eq. (7.9) respectively.

Regarding the anisotropic flux definitions across the material the following is defined:

- Heat and mass fluxes are characterised by second order thermal conductivity and permeability tensors as stated in Eq. (7.10) and Eq. (7.11) respectively (Bear, 1972/1988; Zienkiewicz, et al., 2005). Only in-plane contributions under isotropic conditions are considered until fracture (Bear, 1972/1988; Zienkiewicz, et al., 2005).

- Along the three edges of the 2D triangular element material directions are defined, each represented by a rotated coordinate system. These govern the incremental coupling with the fracture mechanics model based on brittle fracture of 1D bars (Schlangen, 1993; Vervuurt, 1997).

- Through consideration of the 2D gradient basis of the mass flux definitions only the largest crack width present is used to define the anisotropic permeability stated in Eq. (7.15). The mass fluxes of the water phases are assumed mainly perpendicular to the crack width and characterised by opening through Eq. (7.14) (Bear, 1972/1988).

- Conservation of kinetic energy, stated in Eq. (7.18), is used to relate the local and global mass fluxes. The resultant global element permeability tensor is stated in Eq. (7.20) (Bear, 1972/1988; Zienkiewicz, et al., 2005).

About the numerical stability the following is mentioned:

- The critical temperature is addressed to avoid partial wetting of the material imposed by the capillary pressure at the boundary. The density of liquid water reflects transition from a physical basis to characterisation based on numerical considerations.

- Numerical stability is also enhanced by considering the sudden and localised crack opening. The element permeability tensor is characterised by a maximum crack width and mitigation of the level of anisotropy by a flux factor governing the perpendicular flow. Gradual time dependence is assumed in case of fracture mechanics coupling.

The FEM approximated solution is based on:

- The FEM definition stated in Eq. (7.31) in which the element stiffness is initially based on isotropic heat and mass fluxes. However, after fracture both mass fluxes become anisotropic, characterising the direction-dependent permeability of the crack.

- In order to include the thermal conductivity and especially the permeability tensor the spatial integration of the element stiffness matrix is modified. In Eq. (7.34) separate matrices are defined to represent the nodal-based stiffness coefficients and the material flux characterisations.

7.6 FEM approximation based on heterogeneous and isotropic concrete

The influence of the combined solid and porous material description is evaluated for the same cross-section as presented in the previous chapter. The heterogeneous element discretisation is elaborated based on introducing several aggregate particles across the material (Schlangen, 1993; Vervuurt, 1997). These aggregates are surrounded by interfacial zones with the remaining material schematised as mortar (Schlangen, 1993; Vervuurt, 1997). Subsequently, the properties governing the concrete components with respect to the conservation of thermal energy and mass of the water phases are presented. The interfacial zones are characterised as mortar with key material properties modified through factors to reflect the more porous microstructure as is the case for normal strength concrete (Müller & Rubner, 1994). The aggregates are assumed impermeable, only described by properties governing the progress of thermal energy. Neumann and periodical boundary conditions, similar to the previous chapters, are implemented. However, the material schematisation is in height direction modified to enable the periodical conditions for this random heterogeneous mesh.

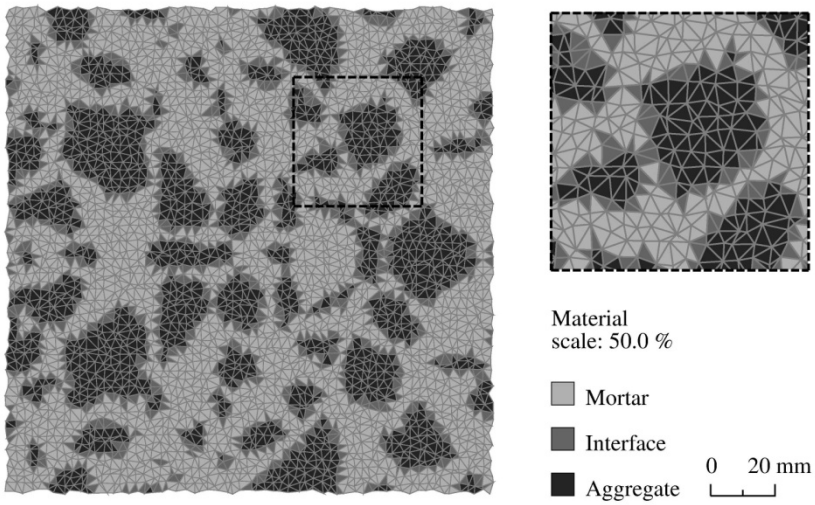

Fig. 7.9 *Discretisation by 2D triangular elements used to numerically approximate the heterogeneous and isotropic concrete cross-section.*

7.6.1 Heterogeneous discretisation of the cross-section

Distribution of the aggregates particles is based on overlaying the mesh with a scanned image of an actual concrete cross-section (Schlangen, 1993; Vervuurt, 1997). For each edge of the triangular element a solid or porous material is determined based on the location relative to the scanned image. Edges located in both solid and porous material are characterised as interfacial zone. Thereafter, the material definition of the triangular element is determined by evaluating the various materials assigned to each of the edges. In case all edges are characterised as aggregate, the element is defined as solid material. A schematisation as mortar is used for all edges identified as a porous material. The remaining elements are interfacial zones which, as seen in Fig. 7.9, surround the particles. The largest aggregates present in the cross-section have a width of around 25 mm with also several smaller sizes filling the space in between. The material is also symmetrical with respect to the horizontal central axis while considering the random nature of the mesh. This behaviour is included to extend the periodical boundaries and allow for a continuous description of the material.

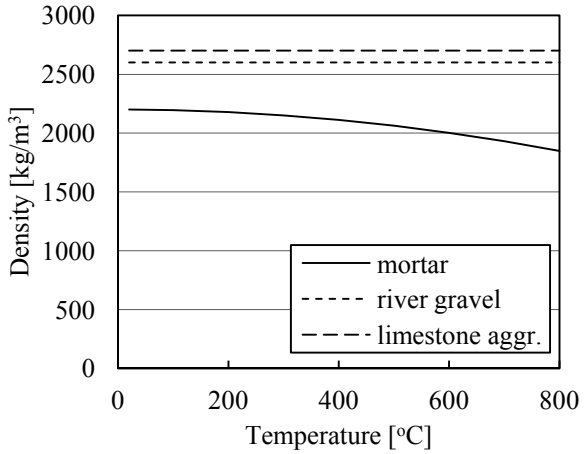

Fig. 7.10 *Development with temperature of the mortar density based on consideration of mass loss measurements by* (Černý, et al., 2003)*. The densities of river gravel and limestone aggregate are assumed constant* (Giaccio & Zerbino, 1998; Zhu, 2012).

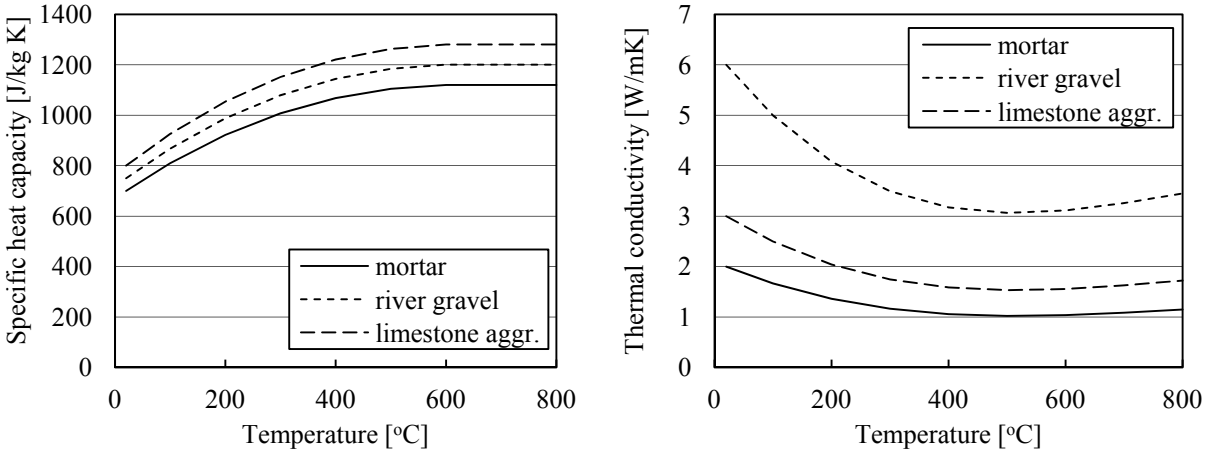

Fig. 7.11 *Temperature-dependent development of specific heat capacity* (Poděbradská, et al., 2003) *and thermal conductivity* (Černý, et al., 2003) *of mortar. Corresponding properties for the aggregate types are obtained from* (Robertson, 1988)*.*

7.6.2 Material properties of the concrete components

Obtaining the temperature-dependent properties that determine the conservation of thermal energy and mass of the water phases is already challenging for concrete as a homogeneous material. The heterogeneous basis of the FEM model requires these properties to be separately defined based on the concrete components. Characterisation is made more difficult still by the high temperatures that develop. In this thesis a simplified approach is adopted in order to define relationships based on various literature references. The aim is to capture the general behaviour rather than focus on temperature intervals with corresponding chemical processes.

Conservation of thermal energy

The progress of thermal energy is characterised by the density, the specific heat capacity and the thermal conductivity which are all defined independently of the mortar strength class as shown in Fig. 7.10 and Fig. 7.11. Compared to the material schematisation presented in chapter 6 the density and the specific heat capacity are both defined temperature-dependent with the latter indicating a gradual increase (Poděbradská, et al., 2003). The development with temperature of the thermal conductivity is comparable to concrete (Černý, et al., 2003). Furthermore, two aggregate types are considered which are of sedimentary origin as found in rivers, commonly used in the Netherlands, or formed through consolidation of calcite. Especially the thermal conductivity of river gravel (Robertson, 1988) is found to be relatively high compared to the mortar (Černý, et al., 2003). Finally, the properties of the interfacial zone are defined similar to the mortar. With respect to the progress of thermal energy the porous material is assumed homogeneous as indicated by the ratios shown in Table 7.1.

Ratio of properties interfacial zone to mortar	
Strength class	independent
ρ_{itz}'/ρ_m'	1.0
C_{itz}'/C_m'	1.0
k_{itz}'/k_m'	1.0

Table 7.1 *Ratios of the properties governing the conservation of thermal energy between the interfacial zone and the mortar, independent of the strength class.*

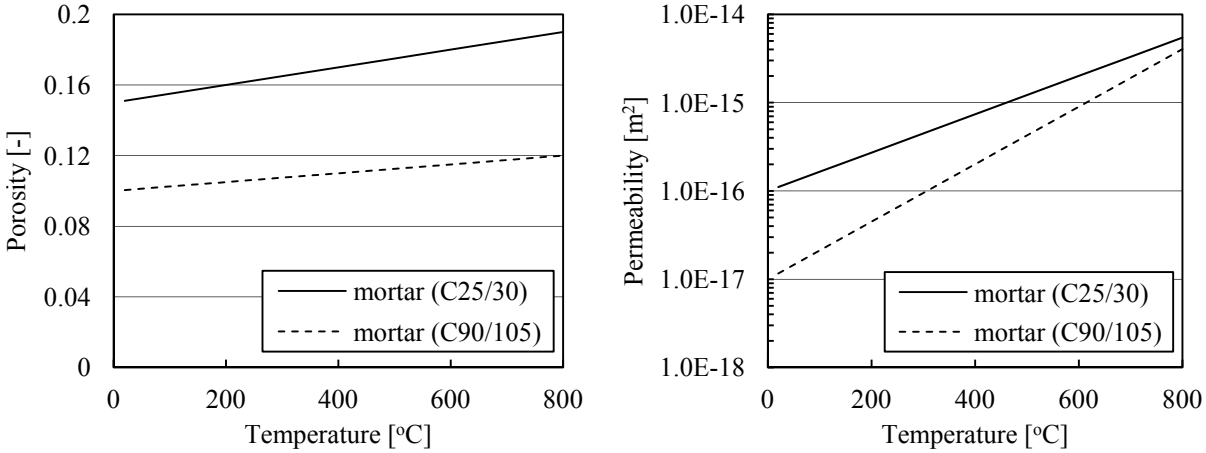

Fig. 7.12 *Influence of temperature development on the porosity (left) and the permeability (right) of normal and high strength mortar as defined by considering concrete measurements reported in* (IREX, 2005).

Conservation of mass of the water phases

The heterogeneous discretisation consists of solid and porous materials with the former assumed impermeable. These aggregate particles affectively form obstacles to the flow of the water phases and are excluded from the discretisation governing this conservation equation. The porosity and permeability of the surrounding mortar is defined dependent on the temperature. However, also the concrete strength has a significant influence with the density increasing for higher strength classes (IREX, 2005). This is reflected by the porosity and especially permeability development as seen in Fig. 7.12. These simplified relationships are restated from chapter 4 since experimental measurements of these properties for mortar are not readably available in literature. The same also applies for the desorption isotherms (Baroghel-Bouny, 1994a) and the relative permeability relationships (Dal Pont, 2004), taken from the same chapter.

The properties of the interfacial zone are assumed to be determined by the strength of the mortar. Both the porosity and especially the permeability are assumed higher in the weaker and less well developed interfacial zones surrounding the aggregates as present in C25/30 (Müller & Rubner, 1994). For C90/105 only a small increase compared to the mortar values is considered. The relationships governing the desorption isotherm and the relative permeability's are assumed only based on the mortar strength class. An overview of the corresponding ratios is provided in Table 7.2.

Ratio of properties interfacial zone to mortar		
Strength class	C25/30	C90/105
$n_{itz}{}'/n_m{}'$	**1.4**	**1.1**
$K_{itz}{}'/K_m{}'$	**2.0**	**1.2**
$S_{w_{itz}}{}'/S_{w_m}{}'$	1.0	1.0
$K_{rel_{itz}}{}'/K_{rel_m}{}'$	1.0	1.0

Table 7.2 *Ratios of the properties governing the conservation of mass of the water phases between the interfacial zone and the mortar.*

7.7 Aggregate influence on the temperature and pore pressure development

The heterogeneous and isotropic concrete cross-section is exposed to several fire scenarios to numerically investigate the influence of the aggregate particles. These scenarios are similar to the previous chapter and focus on the concrete, characterised by the strength class of the mortar and the aggregate type. Both standard and hydrocarbon types of fires as well as different initial environmental conditions are used. The numerical results presented are used to discuss the influence of the aggregate particles, both at the global and the local level. Two aspects are mainly considered with the former being the higher thermal conductivity of especially the river gravel particles. The second aspect focuses on the assumed impermeable character of the particles, impeding the flow of the water phases. Of interest is the influence on the forced drying process and the coinciding gas pressures.

7.7.1 Global influence of the aggregate particles

The differences between a homogeneous or a heterogeneous material description is first examined at the global level by exposure of the cross-section to a standard type of fire. Both the strength class of the mortar as well as the type of aggregate are used to characterise the material which is initially equilibrated at a RH of 80 %. Boundary conditions and incremental time step sizes are comparable to the previous chapter as seen in Table 7.3.

For the C25/30 cross-section the influence of the aggregates on the overall gas pressure development is indicated in Fig. 7.13 to be limited. Only a small pressure change is indicated in the heterogeneous distributions by comparison to the corresponding homogeneous results restated from chapter 6. The maximum values are also situated approximately at the same depth. Similar observations also hold true for the development of the temperature and the progress of the drying front. However, it is noted that the temperature is averaged across all materials. Gas pressures and other drying parameters are averaged across the porous material.

Fire scenarios (I)			
Calculation	**7.1A**	**7.1B**	**7.1C**
Reference temperature	20 °C	20 °C	20 °C
Reference RH	80 %	80 %	80 %
Duration	1800 sec	1800 sec	1800 sec
Incremental time step size	**0.2 sec**	**0.3 sec**	**0.3 sec**
Material (heterogeneous)			
Strength class	**C25/30**	**C90/105**	**C90/105**
Aggregate type	**RG**	**RG**	**LS**
Initial saturation level	**58 %**	**85 %**	**85 %**
Boundary conditions			
Fire curve	ISO 834	ISO 834	ISO 834
Convective heat transfer coeff.	25 W/m^{2}K	25 W/ m^{2}K	25 W/m^{2}K
Exterior vapour pressure (dry)	1000 Pa	1000 Pa	1000 Pa
Convective mass transfer coeff.	0.03 m/s	0.03 m/s	0.03 m/s

Table 7.3 *Influence of the heterogeneous material description on the overall gas pressure development as investigated by exposure to a standard fire scenario.*

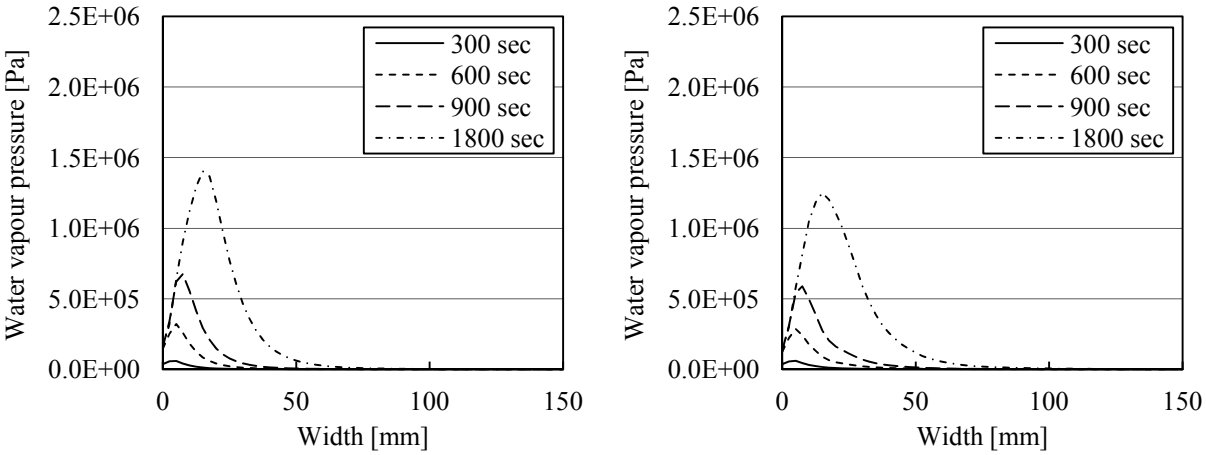

Fig. 7.13 *Including solid particles causes similar averaged global gas pressures in the C25/30 cross-section by comparing distributions based on a homogeneous (left) or a heterogeneous (right) material description.*

The effect of changing the material characterisation of the particles is examined by comparing the influence of river gravel or limestone aggregates. The gas pressures that develop in the heterogeneous C90/105 cross-section, shown in Fig. 7.14, are almost the same. This behaviour is also caused by the reduced progress of the gas pressure peak which in the denser microstructure is situated closer to the fire exposed edge. This further mitigates the influence of the solid material due to the close proximity of the surrounding environment.

7.7.2 Local influence of the aggregate particles

The previous results indicate that from a global perspective a homogeneous material description is sufficient to determine the behaviour. However, local influences by the aggregates do exist and become more established in case the drying process is allowed to progress deeper into the cross-section. This is investigated by increasing the imposed thermal energy while also extending the duration as indicated in Table 7.4. Initial environmental conditions are chosen based on observations from the previous chapter. For the C25/30 the focus is on the influence of the particles on the development of a partially saturated layer. The possibility to develop a saturated state with corresponding pressures is examined for C90/105.

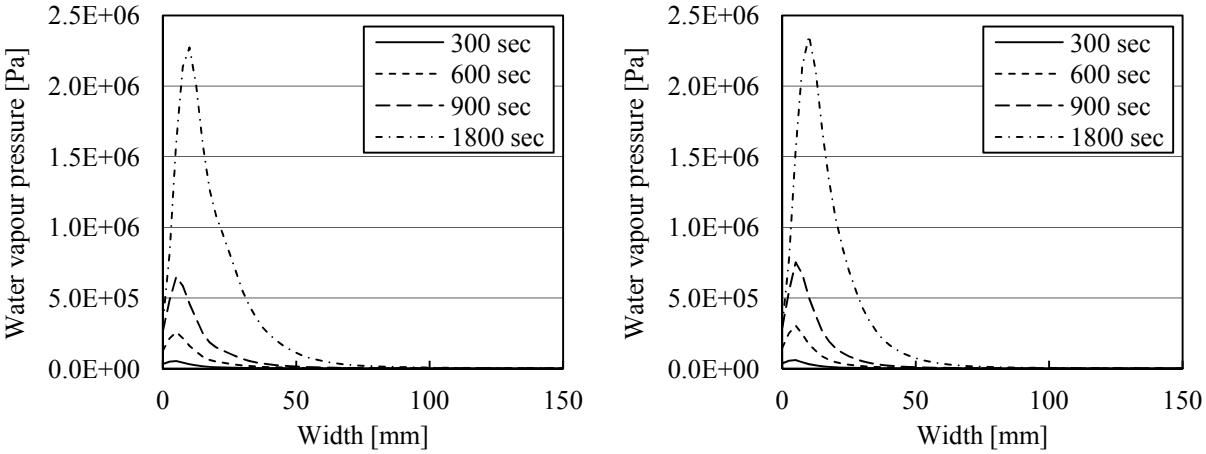

Fig. 7.14 *Pressure distributions obtained for C90/105 made with RG (left) and LS (right), exposed to a standard fire, indicating only limited influence of the aggregate type.*

Fire scenarios (II)			
Calculation	**7.2A**	**7.2B**	**7.2C**
Reference temperature	20 °C	20 °C	20 °C
Reference RH	**50 %**	**50 %**	**95 %**
Duration	3600 sec	3600 sec	3600 sec
Incremental time step size	**0.2 sec**	**0.2 sec**	**0.3 sec**
Material (heterogeneous)			
Strength class	**C25/30**	**C25/30**	**C90/105**
Aggregate type	**RG**	**RG**	**RG**
Initial saturation level	**27 %**	**27 %**	**99 %**
Boundary conditions			
Fire curve	**ISO 834**	**HC**	**HC**
Convective heat transfer coeff.	**25 W/m^{2}K**	**50 W/ m^{2}K**	**50 W/m^{2}K**
Exterior vapour pressure (dry)	1000 Pa	1000 Pa	1000 Pa
Convective mass transfer coeff.	0.03 m/s	0.03 m/s	0.03 m/s

Table 7.4 *Variation of the type of fire exposure and the environmental conditions to examine the local influence of the aggregates.*

Influence of the type of fire exposure

By increasing the imposed thermal energy the drying front progresses faster into the cross-section and attains higher gas pressure. This is illustrated in Fig. 7.15 by comparing the gas pressures that develop in the C25/30 cross-section due to both types of fire exposure. The influence of the aggregates becomes clear by examination of the cross-sectional distributions. The solid particles form obstacles in the material and mitigate the possibility to level off the formed vapour and to a lesser extent the liquid water. This is observed in Fig. 7.16 to cause higher pressures in the vicinity of the largest aggregates, promoting the vapour to flow around the particles. The progress of the drying front also indicates an influence of the aggregates. Reduction of the saturation level takes longer in front of the solid material since the vapour flux driven into the cross-section is blocked. These effects also develop in narrow spaces between aggregates. The increased porosity and especially permeability of the interfacial zones are also seen to alleviate the saturation level surrounding some of the aggregates.

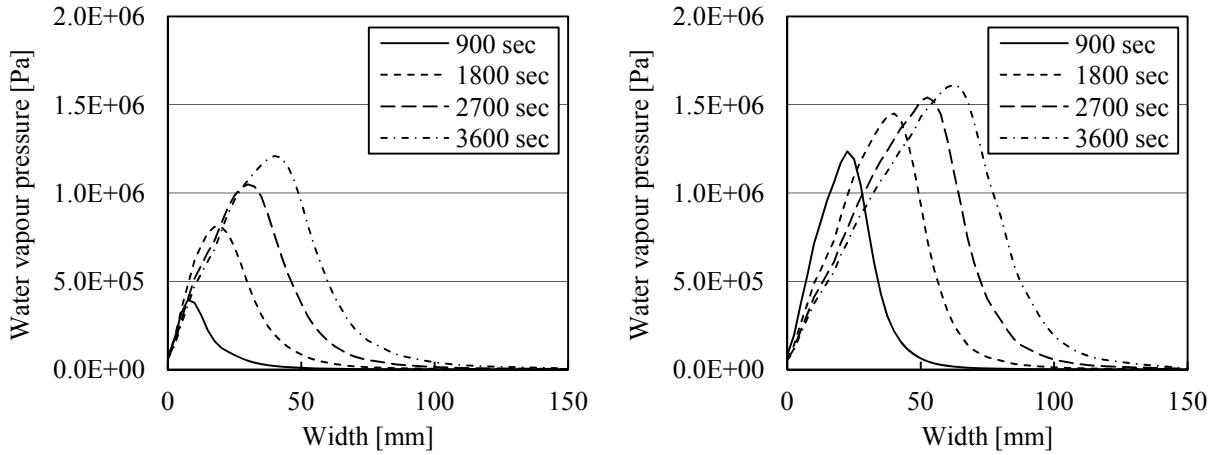

Fig. 7.15 *Increasing the intensity of fire exposure from an ISO (left) to a HC (right) scenario governs the gas pressure development in the C25/30 cross-section.*

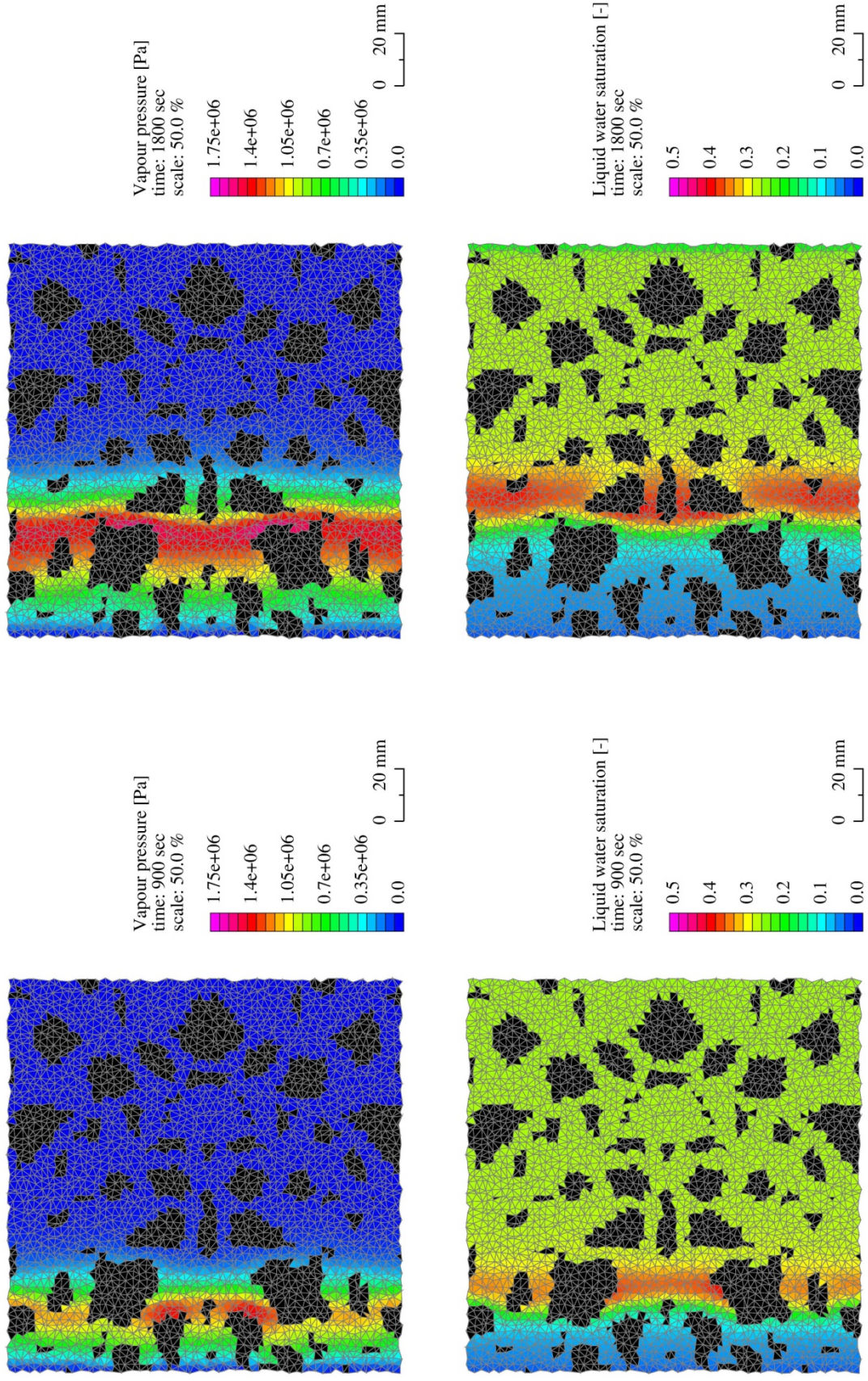

Fig. 7.16 *The RG particles in the C25/30 cross-section, exposed to a HC type of fire, locally impede the ability of the gas pressure to level off the formed vapour. The saturation level, based on an initial RH of 50%, is affected by the more porous interfacial zones.*

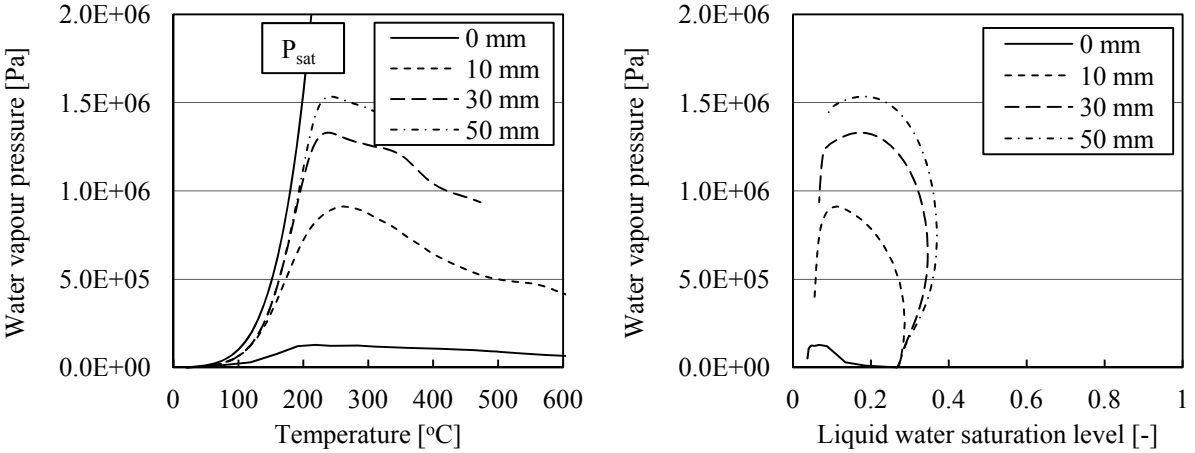

Fig. 7.17 *The highest gas pressures in C25/30 made with RG, initially at internal conditions and exposed to a HC type of fire, are attained for a still partially saturated state.*

Further insight is provided by assessing the relationships between gas pressure development and the temperature or saturation level. In Fig. 7.17 the relationship with the saturated pressure is again established. Similar graphs are also presented in chapter 6 for a homogeneous C90/105. However, for this C25/30 initial partial wetting is observed after which the maximum pressure is reached during drying at a saturation level of around 20 %.

Influence of the concrete strength class

The influence of the RG aggregates on the mass fluxes across the material is also numerically determined for a C90/105 cross-section. Overall gas pressure distributions, provided in Fig. 7.18, indicate substantial values due to the almost saturated initial conditions. Near the aggregates again an increase in the gas pressure as well as the saturation level is observed in Fig. 7.19. However, the higher density of the microstructure in C90/105 causes the pressure increase to be more profound. The pressure gradient in transverse direction is required to be larger compared to C25/30 in order for the water phases to pass around the particles. This process is not mitigated by the interfacial zones which are assumed similar in properties to the surrounding mortar. Furthermore, some temperature variations are indicated based on the higher thermal conductivity of river gravel compared to the surrounding mortar.

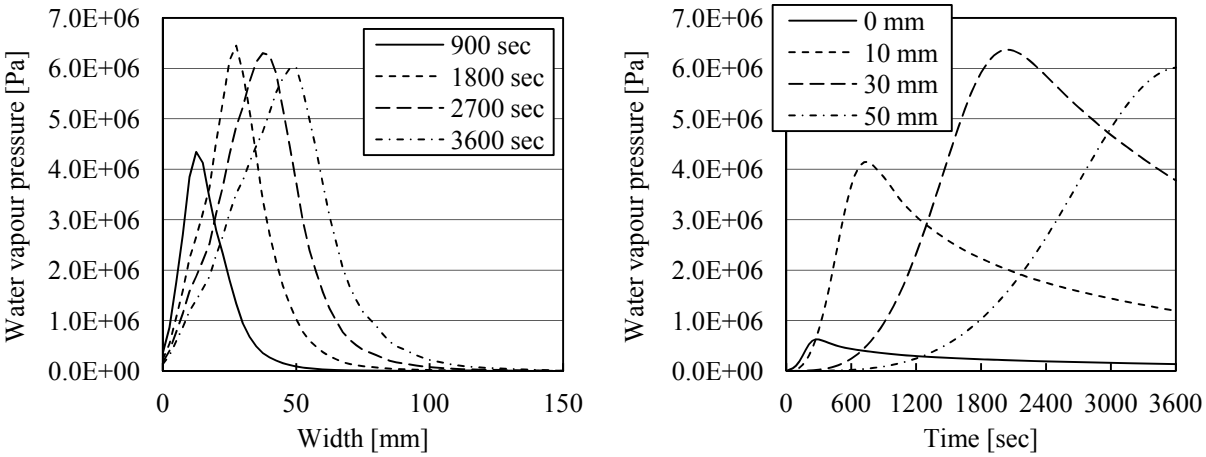

Fig. 7.18 *The highest gas pressures are found for an almost saturated C90/105 exposed to a HC-based fire, expressed in the cross-section (left) and at various depths (right).*

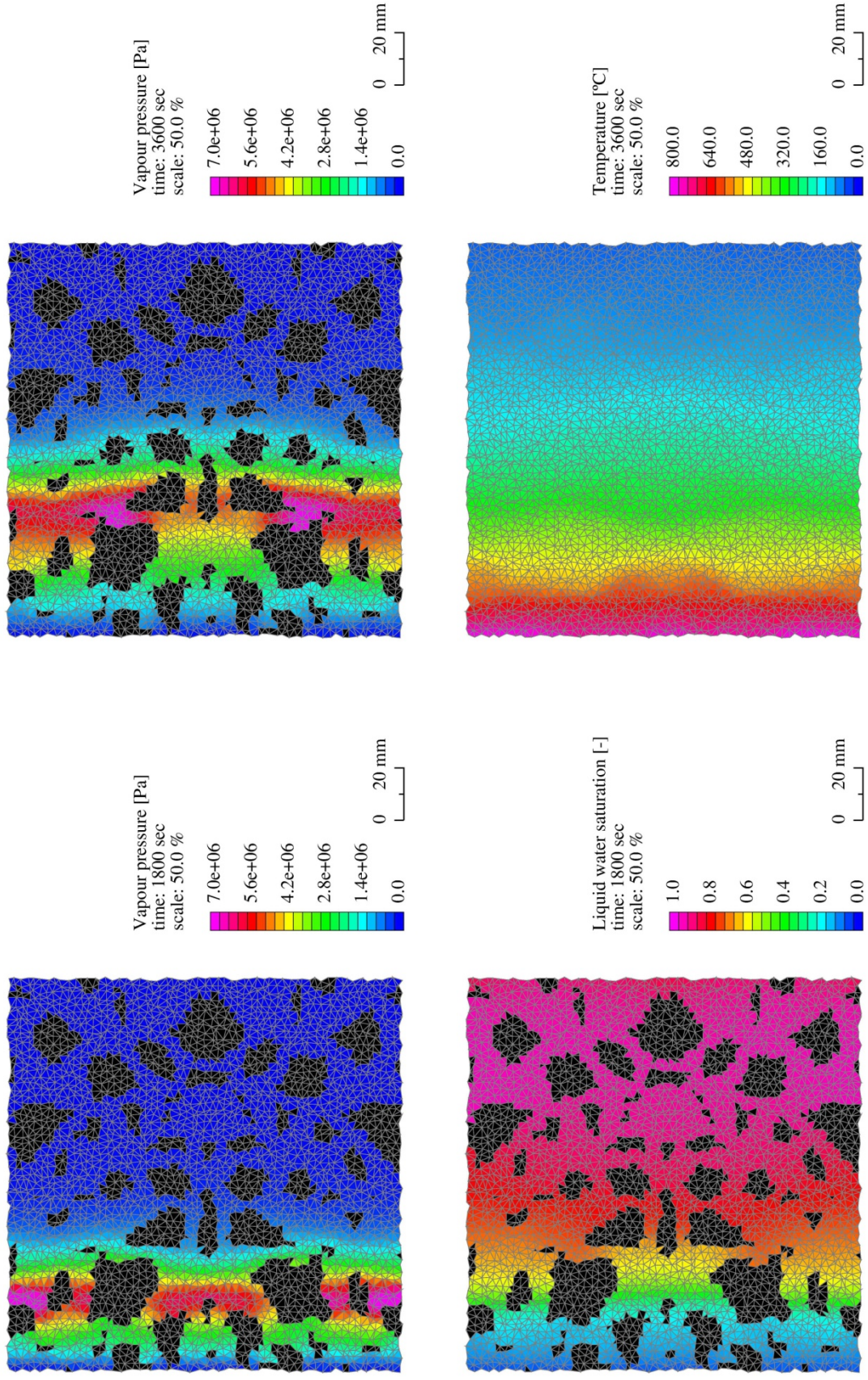

Fig. 7.19 *Higher gas pressures are attained near the aggregates in the dense microstructure of C90/105, subjected to a RH of 95 % before exposure to a fire corresponding to the HC curve. Temperature variations arise due to the higher conductivity of the particles.*

7.8 FEM approximation based on heterogeneous and anisotropic concrete

The final extension of the FEM temperature and pore pressure model is the introduction of anisotropy through cracks. Several cracks are defined in order to investigate the local influence on the forced drying process. First, the orientation and procedure to define an individual crack path is briefly elaborated, Subsequently, the porous material description is revisited in order to focus on the direction-dependent flow conditions along the crack. Under these circumstances the permeability of the material is no longer characterised by the strength class of the mortar, but defined by opening of the crack. The mass flux definitions are modified to reflect the anisotropic conditions. In this not only the substantial permeability increase based on the crack width, but also the level of directional dependence needs to be considered. The simplified crack pattern allows to quantify the local permeability tensor and examine the influence on the global directional dependence.

Initial horizontal crack pattern in the cross-section

Three horizontal cracks with different lengths and assumed constant opening are initially present in the cross-section (Lottman, et al., 2011). However, since no mechanical coupling is used to determine these cracks a different approach is adopted. For this purpose, it needs to be considered that the element permeability tensor governing the crack is assumed defined by the material direction with the largest crack width. With respect to this definition only the vertices of the triangular elements along the crack paths are considered to be fractured that are part of the porous material as well as orientated in vertical direction. The resultant cracks have predominantly a horizontal orientation, evenly distributed across the height.

By transformation of the local element permeability, defined by the fractured material direction in Eq. (7.28), the global directional dependence is determined. For a simplified crack, assuming only mass fluxes parallel to the crack edges, the global behaviour is reflected mainly by the horizontal permeability as shown in Fig. 7.20. The vertical permeability as well as the interaction between both principal directions is negligible. The figure also indicates the localised discontinuous permeability of the crack with respect to the surrounding material.

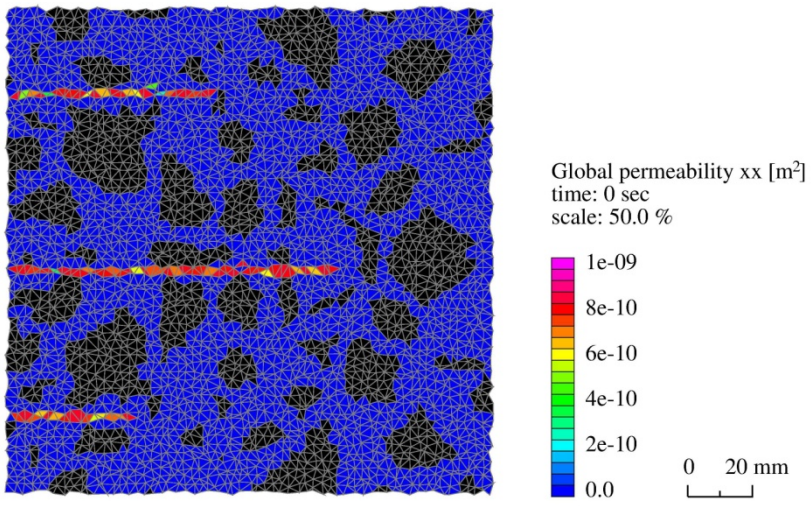

Fig. 7.20 *Cracks in the heterogeneous cross-section with a constant opening of 0.1 mm as characterised by an assumed perfect anisotropic local permeability.*

Ratio of permeability of crack to mortar		
Crack width	0.1 mm	0.5 mm
$K_m{}'$	1.0E-16 m^2	1.0E-16 m^2
$K_{cr}{}'$	8.3E-10 m^2	2.1E-8 m^2
$K_{cr}{}'/K_m{}'$	8.3E+6	2.1E+8

Table 7.5 *Influence of local fracture on the numerical stability expressed by the permeability ratio of the crack to the surrounding mortar.*

7.9 Temperature and pore pressure development influenced by cracks

The influence of the initial crack pattern is investigated by exposure of the cross-section to the same fire scenarios as used in the previous paragraph. The aim is not only to focus on the local influence of the anisotropic permeability increase, but to also asses the numerical stability. Two sets of cracks are therefore used in this paragraph, which only differ in opening as shown in Table 7.5. In chapter 4 it was already indicated that even these relatively small cracks cause a substantial local permeability increase. The local anisotropic mass flux further enhances the non-linearity and discontinuity in the FEM definition.

In this paragraph first the numerical stability is checked by comparing results for the same cracked cross-section with only the level of anisotropy varied. This is governed by including a local permeability increase perpendicular to the crack. Various possibility's are considered which vary from a perfect anisotropic to an isotropic crack. In the remainder of this section the focus is on the influence of the crack pattern on the forced drying process. Of interest is especially the ability to level off the formed water vapour in order to mitigate gas pressures. Additional aspects to be considered are the possibility for temperature effects as well as variation in the levels of drying along the crack. Both are considered through variation of the crack opening, the strength class, the fire scenario and the environmental conditioning, allowing for direct comparison with previous results.

7.9.1 Influence of the level of anisotropy in the mass flux definition

The mass flux definition of the water phases along the crack are characterised by the local increase of permeability based on opening (Bear, 1972/1988). In the perpendicular direction the theoretical formulation assumes no flow, as indicated in the local element matrix in Eq. (7.15). However, this introduces a localised perfect anisotropic crack with the surrounding material assumed to remain isotropic. The fluxes are forced to follow the crack path with no ability for redistribution of mass between the crack edges. Since this assumption has the largest consequences for the numerical stability, first the influence of the direction-dependent flow is examined. The cracks in the C25/30 cross-section have a constant opening of 0.1 mm. Each numerical simulation assumes a different characterisation of the crack. The reference behaviour is based on perfect anisotropy with no flow perpendicular to the crack. Thereafter, variation of the perpendicular factor introduces an additional local permeability increase between the crack edges, referred to as partial anisotropy. The final results reflect an isotropic crack with in both principal local directions the same permeability increase. For the material characterisations, boundary conditions and other parameters Table 7.6 is provided.

Fire scenarios (III)				
Calculation	**7.3A**	**7.3B**	**7.3C**	**7.3D**
Reference temperature	20 °C	20 °C	20 °C	20 °C
Reference RH	80 %	80 %	80 %	80 %
Duration	1800 sec	1800 sec	1800 sec	1800 sec
Incremental initial time step size	0.2 sec	0.2 sec	0.2 sec	0.2 sec
Material (heterogeneous)				
Strength class	C25/30	C25/30	C25/30	C25/30
Aggregate type	RG	RG	RG	RG
Initial saturation level	58 %	58 %	58 %	58 %
Boundary conditions				
Fire curve	HC	HC	HC	HC
Convective heat transfer coeff.	50 W/ m^{2}K	50 W/ m^{2}K	50 W/ m^{2}K	50 W/ m^{2}K
Exterior vapour pressure (dry)	1000 Pa	1000 Pa	1000 Pa	1000 Pa
Convective mass transfer coeff.	0.03 m/s	0.03 m/s	0.03 m/s	0.03 m/s
Characterisation of the cracks				
Constant crack width	0.1 mm	0.1 mm	0.1 mm	0.1 mm
Flux factor	**0.0**	**0.2**	**0.6**	**1.0**

Table 7.6 *Variation of the anisotropic factors governing the directional dependence in order to examine the numerical stability.*

The influence of directional dependence in the flow conditions along the cracks is best illustrated by the development of the time step size. In Fig. 7.21 the anisotropic mass flux definition is indicated to reduce the initial time step size within 300 seconds, marking the progress of the drying front into the cross-section and especially the cracks. This behaviour is also observed for the isotropic cracks, but time step size reduction occurs later. The minimum time step size reached under those circumstances is 3 times larger than in the anisotropic case. However, compared to the initial time step size still a reduction by 75 percent occurs. Similar time step size development, as observed for the isotropic case, also governs both partial levels of anisotropy.

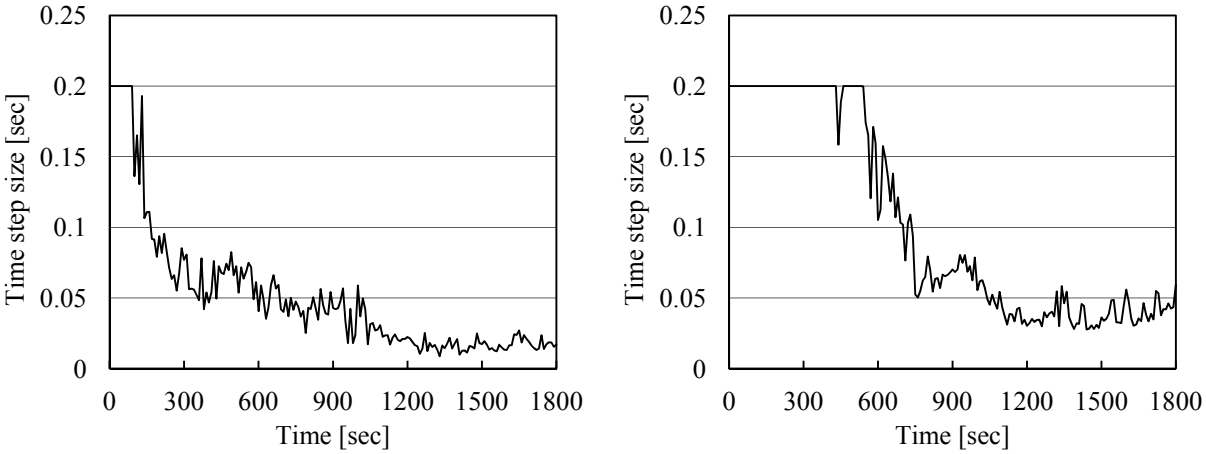

Fig. 7.21 *Numerical stability as reflected by the development of the time step size, assuming perfect anisotropy (left) or isotropy (right) in the mass flux definition.*

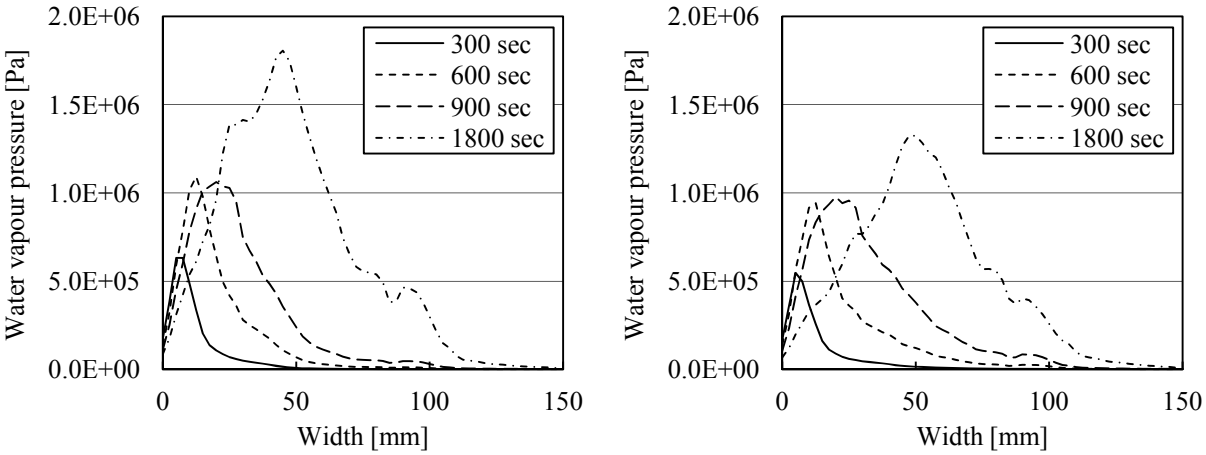

Fig. 7.22 *Averaged gas pressure distributions in the C25/30 cross-section, reflecting perfect anisotropic (left) or isotropic (right) conditions along the cracks.*

From these results it can be deduced that including cracks in the cross-section is firstly affected by the permeability increase and secondly by the anisotropic definition. The dominating aspect governing the numerical stability is the strong discontinuous behaviour of the crack compared to the surrounding material. Furthermore, examination of Fig. 7.22 indicates that higher gas pressures are determined in case of perfect anisotropic conditions along the crack. By only allowing the fluxes to develop parallel to the crack edges, no ability for mass redistribution of the water phases is present. Sudden gas pressure changes can develop due to misalignment between the crack path and the pressure gradients. Local mass fluxes become insufficiently sustained, affecting numerical stability. However, consideration of a partial anisotropy of 20 percent already improves stability. The ability to redistribute the water phases across the crack causes a more continuous gas pressure reduction along the crack. The remaining simulations also reveal that a further mitigation of the level of anisotropy does no cause significant changes in for instance the gas pressure distribution.

Conclusions regarding the crack development

Considering this discussion and the numerical results are the following conclusions made:

- The flux factor, governing the level of anisotropy included in the permeability of the crack, influences the ability to redistribute both water phases. This obtains a numerically more stable development of the variables along the crack edges.

- By considering 20 % of the crack permeability to also characterise the perpendicular direction numerical stability improves and the flow is still predominately anisotropic. In the remainder of this thesis the flux factor is assumed constant and defined as 0.2.

7.9.2 Drying of the cross-section characterised by an initial crack pattern

The influence of the crack pattern is further examined for the C25/30 cross-section made with RG, exposed to a standard fire, based on the flux factor defined as 0.2 with the remaining parameters according to Table 7.6. Averaged temperature and gas pressure distributions could be used to assess the impact of the cracks. However, the discontinuous behaviour is best illustrated by the actual variable distributions.

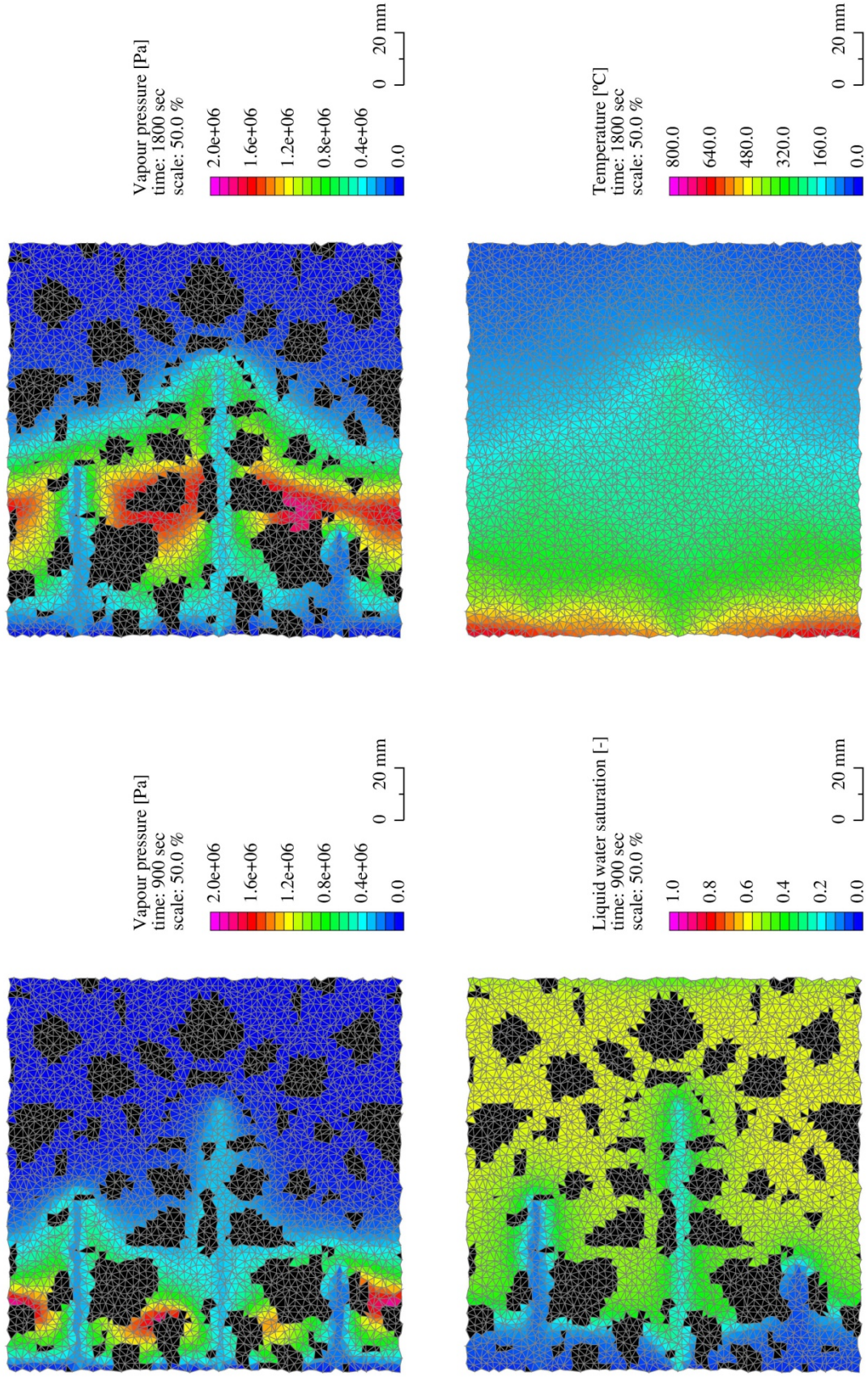

Fig. 7.23 *Cracks with a constant opening of 0.1 mm have a significant influence on the forced drying process as indicated for C25/30. The material surrounding the crack dries faster while mitigating gas pressures and disturbing the progress of thermal energy.*

Compared to the distributions shown for the non-cracked cross-sections several additional aspects are observed which have a strong localised character. Thermal exposure still drives the drying front into the cross-section. However, the gas pressure is no longer continuous, but is largely mitigated in the material surrounding the cracks as shown in Fig. 7.23. Steep pressure gradients develop along the crack paths, marking the sudden and substantial difference in permeability. The extent of these discontinuities also depends on the permeability of the surrounding material as well as the presence of aggregates. At some distance from the crack the gas pressure is indicated to still increase. The vicinity and accessibility to a crack edge governs the ability to drain the water phases to the exterior.

The drying front extends further into the cross-section along the entire length of the cracks. This behaviour is attributed to the crack permeability, allowing the formed water vapour to escape to the surface. However, condensation of levelled-off vapour deeper in the cross-section is not estimated to maintain or increase the saturation. The capillary pressure development imposed at the heated boundary combined with the high permeability of the cracks allows liquid water to escape. Along the cracks the saturation level reduces, affecting thermodynamic equilibrium. At the heated surface the continued mass fluxes of vapour and liquid water through the cracks cause a cooling effect. Part of the thermal energy is consumed by the sustained process of evaporation. Deeper inside the cross-section the vapour and liquid mass fluxes are orientated in opposite directions which forces condensation at increasing temperatures. As a consequence gas pressures rise, causing the distribution to increasingly deviate from the initial uniform peak, promoting drying of material surrounding the crack.

These thermodynamic processes are reflected in the development of a gradual temperature gradient along each crack. Heat fluxes towards the surrounding material develop, allowing thermal energy to gradually propagate in the directions perpendicular to the cracks. The heated part of the cross-section increases, characterised by localised reduced temperature gradients. The coupled FEM definition will thus reflect discontinuous behaviour in both the conservation of thermal energy and in particular the mass of the water phases.

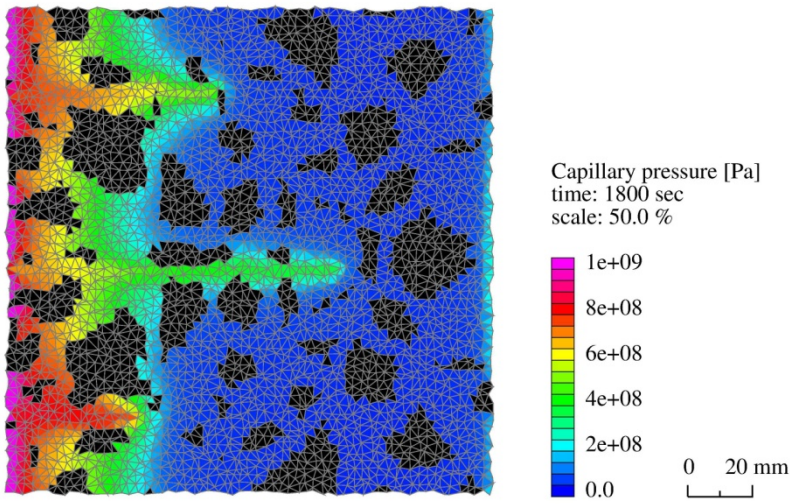

Fig. 7.24 *Numerical stability as affected by the development of the capillary pressure which through the cracks extends into the cross-section.*

The process of forced drying along the crack continues until similar minimum saturation levels have been reached as in the heated surface layer. The corresponding capillary pressure gradient extends towards the heated surface and governs the developing equilibrium state as seen in Fig. 7.24. This figure also illustrates the reason for including the transition from a physical to a numerical definition of the density of liquid water. Around the critical temperature the capillary pressure development indicates a sudden non-linear change from drying to wetting. This behaviour proved to cause numerical stability issues since it involves partial wetting of already dried cracks. By imposing an assumed constant capillary pressure beyond the critical point the cracks remain dry, enhancing numerical stability.

7.9.3 Influence of the concrete strength class

The previous results indicate that the level of gas pressure mitigation is affected by the permeability of the material surrounding the cracks. This is further explored by variation of the strength class, reflecting a C25/30 and a C90/105 cross-section, as stated by the scenarios in Table 7.7. The cracks are also assumed larger, having a constant opening of 0.5 mm.

The higher transport capability of the cracks extends the possibility for drainage to the surrounding environment. However, only a limited increase in the progress of the drying front into the C25/30 cross-section is observed by comparison of Fig. 7.25 to Fig. 7.23. Coinciding gas pressures are similar and observed to increase as the distance to a crack edge increases. These perhaps surprising results are caused by the permeability of the surrounding material and its ability to level-off the water phases in a crack. Additional crack opening and corresponding increase of permeability is only more effective in the case that sufficient mass is able to reach the crack edge. In this respect a dense pattern of relatively small cracks is thus more effective than several larger more isolated cracks.

Fire scenarios (IV)		
Calculation	**7.4A**	**7.4B**
Reference temperature	20 ^{o}C	20 ^{o}C
Reference RH	80 %	80 %
Duration	1800 sec	1800 sec
Incremental initial time step size	0.2 sec	0.2 sec
Material (heterogeneous)		
Strength class	**C25/30**	**C90/105**
Aggregate type	RG	RG
Initial saturation level	**58 %**	**85 %**
Boundary conditions		
Fire curve	HC	HC
Convective heat transfer coeff.	50 W/ m^{2}K	50 W/ m^{2}K
Exterior vapour pressure (dry)	1000 Pa	1000 Pa
Convective mass transfer coeff.	0.03 m/s	0.03 m/s
Characterisation of the cracks		
Constant crack width	0.5 mm	0.5 mm

Table 7.7 *Investigation of pressure mitigation by cracks based on strength class variation.*

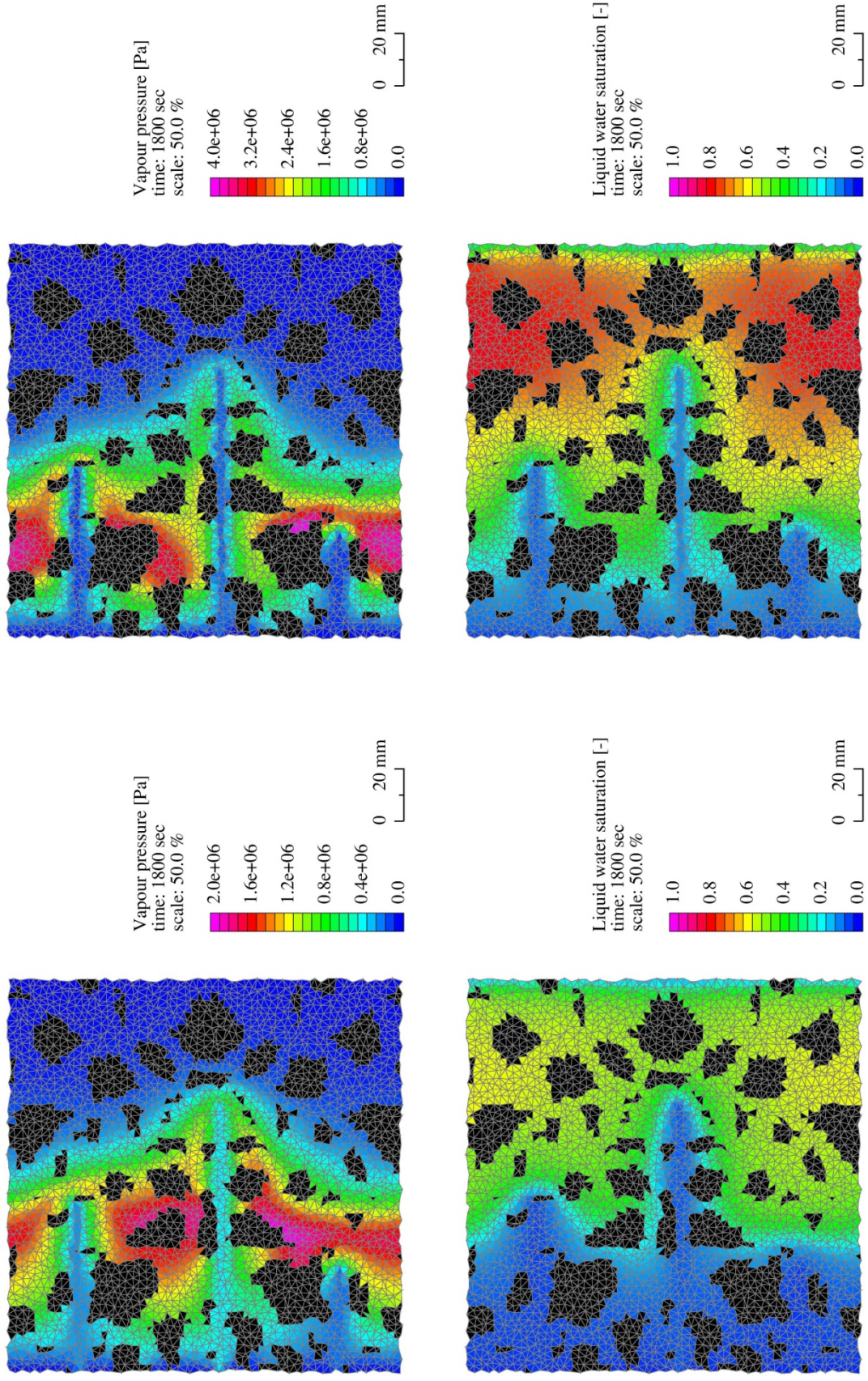

Fig. 7.25 *Comparison between a C25/30 (left) and a C90/105 (right) cross-section indicating that the permeability of the material governs the effectiveness of the cracks in mitigating the gas pressure. The larger crack opening (0.5 mm) has a limited influence.*

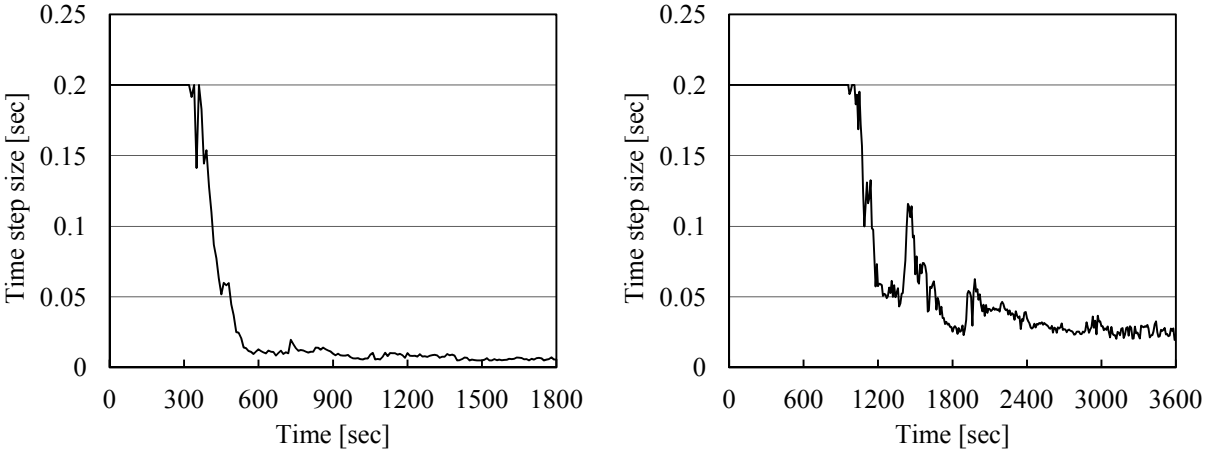

Fig. 7.26 *Time step size development for the cracked C25/30 cross-section exposed to a HC (left) or an ISO (right) type of fire, indicating improved numerical stability.*

This behaviour is also observed for C90/105 for which the reduced permeability of the porous material causes more pronounced gas pressure gradients along the crack edges. The cracks tend to be more isolated from the surrounding material while they still cause drying deeper in the cross-section based on the higher initial saturation level. Furthermore, for both fire scenarios a temperature plateau developed along the cracks. However, compared to previous results the temperature is more uniform while only limited influence by the strength class is observed. This again reflects the localised nature of the cracks and their interaction with the exterior environment. Finally, especially the first simulation indicates that the higher level of discontinuity makes the numerical stability more challenging. Convergence requires additional time and the step size reduces further as seen in the left graph of Fig. 7.26.

Fire scenarios (V)		
Calculation	**7.5A**	**7.5B**
Reference temperature	20 ^{o}C	20 ^{o}C
Reference RH	**80 %**	**95 %**
Duration	3600 sec	3600 sec
Incremental initial time step size	0.2 sec	0.2 sec
Material (heterogeneous)		
Strength class	**C25/30**	**C90/105**
Aggregate type	RG	RG
Initial saturation level	**58 %**	**99 %**
Boundary conditions		
Fire curve	ISO 834	ISO 834
Convective heat transfer coeff.	25 W/ m^{2}K	25 W/ m^{2}K
Exterior vapour pressure (dry)	1000 Pa	1000 Pa
Convective mass transfer coeff.	0.03 m/s	0.03 m/s
Characterisation of the cracks		
Constant crack width	0.5 mm	0.5 mm

Table 7.8 *Two fire scenarios representing a lower thermal exposure, used to estimate the temperature dependence on the drying process along the cracks.*

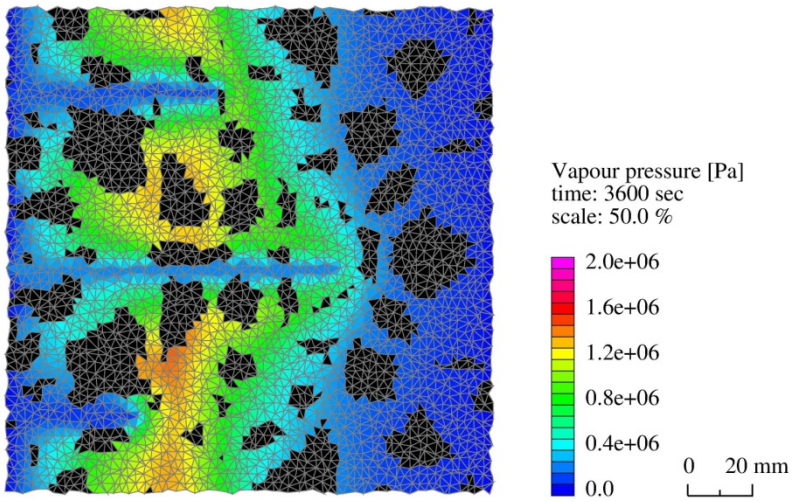

Fig. 7.27 *An ISO type of fire mitigating the thermal exposure and allowing a gradual and numerically more stable drying process in the cracked C25/30 cross-section.*

7.9.4 Influence of the type of fire exposure and the environmental conditions

The final set of simulations is aimed at determinating the possibility for the imposed thermal energy and the initial saturation level to influence the crack behaviour. Both the C25/30 and C90/105 cross-sections are exposed to a standard type of fire with the latter also equilibrated at a RH of 95%. The remaining parameters and properties can be found in Table 7.8.

The C25/30 cross-section is estimated to dry more gradually with limited gas pressure development as illustrated by Fig. 7.27. The reduced thermal exposure combined with the localised cracks as well as the longer duration is sufficient to level-off most of the formed vapour. The highest gas pressures are observed in regions situated furthest away from a crack. In the C90/105 cross-section still pressures develop. However, these are always lower than in non-fractured conditions, considering also the effect of the higher initial RH. The reduced thermal exposure is also observed from the temperature plateau along the crack which is estimated to attain lower values. In both simulations the numerical stability improved, as for instance reflected by the time step size development in the right graph of Fig. 7.26.

7.10 Conclusions with respect to fire exposed concrete

Based on the previously discussed numerical results the following conclusions are drawn with respect to the aggregate particles:

- The global influence is limited and depends on the distribution of the aggregates. Concrete is therefore commonly characterised as homogeneous, based on an averaged material behaviour.

- The local influence depends on the size of the aggregate, impeding the flow of the water phases. In case of sufficient size an increase of the gas pressure opposite the fire exposed surface develops, forcing the mass fluxes to pass around the particle.

- The influence of the assumed impermeable solid material is higher in C90/105, based on the interfacial zones being characterised by only a limited addition in the transport capabilities compared to the surrounding mortar.

- Additional local effects are caused by the higher thermal conductivity of the solid material. This promotes the progress of thermal energy which causes local disturbances in the temperature distribution.

From the results based on including an initial crack pattern the following is deduced with respect to the numerical stability:

- The substantial increase of permeability extended by the level of anisotropy represents a strong discontinuity in the FEM definition. Both govern the numerical stability as reflected by the time-dependent incremental step size.

- Numerical stability is enhanced by reducing the imposed thermal energy from a HC to an ISO type of fire. Only limited influence by the concrete strength class is observed, reflecting the localised behaviour of the cracks and their interaction with the exterior environment.

The numerical results governed by an initial crack pattern also allow to conclude and remark the following:

- Mitigation of the gas pressure by the initial crack pattern does not only depend on the crack width, but is also affected by the permeability of the surrounding material. Both govern the ability to drain the formed vapour towards the exterior environment.

- The results of especially C90/105 suggest that reducing the crack spacing enables more liquid and vapour to escape to the exterior environment. Thus the effectiveness of the crack pattern in mitigation of the gas pressure is increased.

- The higher transport capabilities of each crack allows the forced drying process to infiltrate deeper into the cross-section. Liquid water is levelled- off towards the heated surface based on the capillary pressure gradient extending into the cracks.

- Along each crack a temperature plateau develops, characterised at the heated surface by a cooling effect. More energy is consumed by evaporation of liquid water flowing towards the surface. At the opposite end of the crack, a temperature increase is observed. Condensation of levelled-off vapour causes gas pressures to develop, partially mitigated by the opposite flow direction of liquid water.

- A reduction of the thermal exposure permits the crack pattern more time to level-off the water phases. Gradually developing gas pressures are further alleviated. The lower temperatures and gas pressures both have a beneficial effect on the numerical stability.

8 Isotropic FEM model for mechanics

The derived FEM model focuses on the displacements and resulting stresses due to the combined action of internal loading and structural forces. The first paragraph discusses the conceptual idea, reflecting on the structural considerations for the concrete element. In the second part the assumed homogeneous and isotropic material is characterised by extensional and shear deformation, based on the mechanical continuum described in chapter 5. Internal loading by extensional temperature strains are obtained through incremental coupling with the FEM model presented in chapter 6. The PDE is subsequently extended through definition of the rigid body coupling conditions along the outer edges of the structural element. Central supports are governed by combined Dirichlet and Neumann boundary conditions. Thereafter the PDE is numerically approximated by stating the weak form. Again the concept of minimisation of the energy functional is used. Galerkin's method obtains the FEM definition based on discretisation by linear 2D triangular elements. Incremental time dependence is introduced to characterise the boundary conditions. As a result nodal displacements as well as element strains and stresses are stated in an incremental form. The fourth part elaborates on the solution procedure and the analysis of the results. The final part of this chapter again focuses on numerical validation through comparison with previously presented results. Several key aspects are elaborated such as the in-plane mechanical schematisation and the possibility for stress disturbances due to the imposed boundary conditions.

8.1 Conceptual idea, layout and material schematisation

The presented FEM model focuses on the mechanical description of a part of the fire exposed concrete structural element presented in chapter 3. The steep temperature gradient that develops in the cross-section governs the thermal expansion of the concrete components (Hartsuijker & Welleman, 2007). Resulting stresses are based on extension and shear deformation, affected by the imposed initial elongation strains as elaborated in chapter 5 (Timoshenko & Goodier, 1970; Prezemieniecki, 1968/1985). The stresses that arise from the imposed water vapour pressure distribution are considered in the next chapter, dealing with the FEM definition based on an anisotropic continuum (Timoshenko & Goodier, 1970).

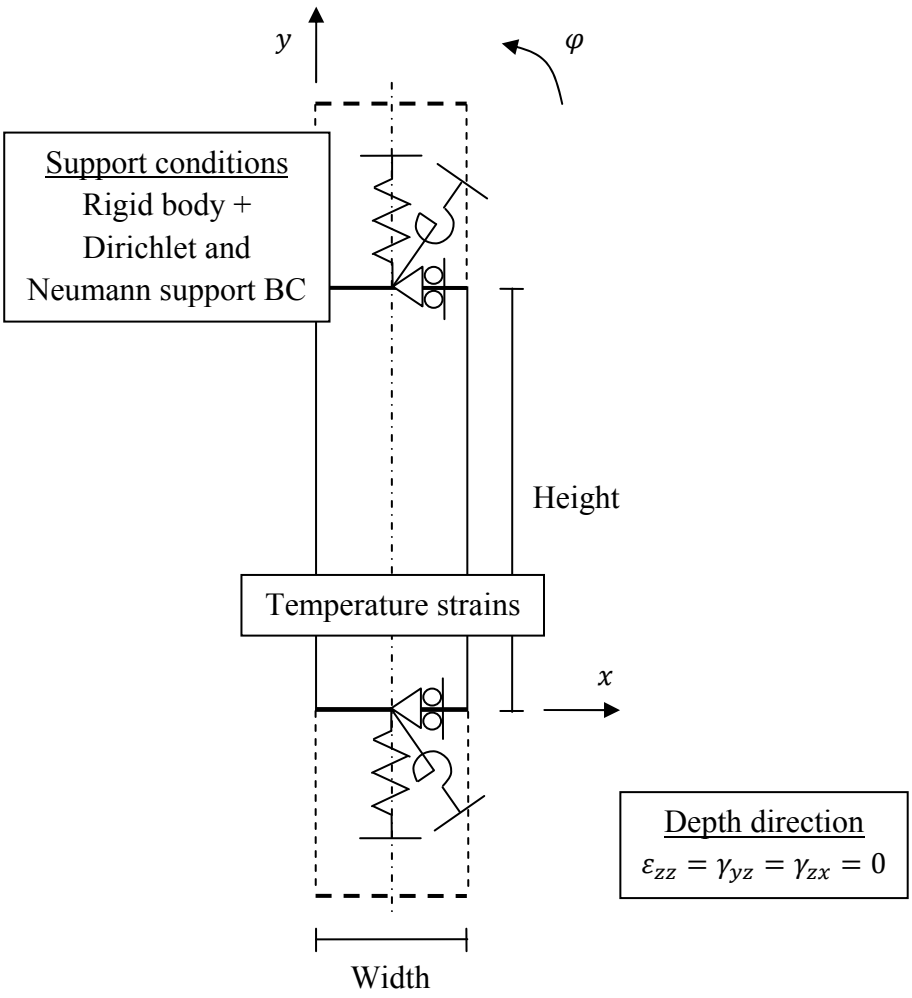

Fig. 8.1 *Schematic overview of the 2D concrete structural element with support and rigid body boundary conditions. The in-plane material schematisation is characterised as homogeneous and isotropic, loaded by initial temperature strains.*

The resultant PDE is, in this chapter, stated for an isotropic continuum (Timoshenko & Goodier, 1970; Wells, 2006; Felippa, 2004a). This assumes a homogeneous material, without directional dependence, taking only the lateral contraction or Poisson's effect into account (Timoshenko & Goodier, 1970). Heterogeneity as well as anisotropy based on crack development are presented in the next chapter. Incremental coupling with the FEM isotropic model, stated in chapter 6, defines the time-dependent temperature distributions. These determine the material characterisation by Young's modulus and the temperature strain.

The cross-section of the element, shown in Fig. 8.1, is schematised as 2D through assuming a constant behaviour in depth direction represented by a unit thickness. It is assumed that adjacent cross-sections tend to exhibit similar behaviour and that the out-of-plane displacement is thus impeded. Restraint of the extensional and shearing strains govern the cross-sectional deformation, commonly referred to as a plane strain approach (Timoshenko & Goodier, 1970). Additional in-plane stresses also arise based on the lateral contraction (Timoshenko & Goodier, 1970). FEM discretisation of this cross-section is obtained by 2D triangular elements, with a similar linear form as in the previous chapters.

The cross-section is schematised to deform based on the linear strain definition according to Bernoulli's hypothesis (Hartsuijker & Welleman, 2007). This is imposed by characterisation of each outer edge as a rigid body, defined by vertical elongation and rotation (Hartmann & Katz, 2007). Coupling conditions are required to define the displacement along these outer edges (Hartmann & Katz, 2007). Both central supports are governed by a Dirichlet boundary condition representing the fixed horizontal direction. The axial translation and rotation are defined through a Neumann boundary condition, allowing to impose spring stiffnesses and external forces (Bouma, 2000).

8.2 Theoretical framework governing the FEM definition

The derivation of the FEM model extends on the mechanical-based displacement and stress considerations presented in chapter 5. For FEM definition the continuum description is used which in this paragraph is first restated (Timoshenko & Goodier, 1970). Support boundary conditions govern the structural interaction and reflect a combined Dirichlet and Neumann formulation. Rigid body boundary conditions are discussed in the next paragraph.

8.2.1 Basic assumptions used to describe the behaviour of fire exposed concrete

Material behaviour

With respect to the material description the following assumptions are made:

1. The material is assumed homogeneous and isotropic as well as linear elastic, based on Hooke's law (Timoshenko & Goodier, 1970). The assumption of small strains defines the deformation (Hartsuijker & Welleman, 2007).

2. Unrestrained or free temperature strain development of the material is included as an initial elongation to impose the main thermal deformations (Timoshenko & Goodier, 1970). Initial stresses due to pore pressures are neglected in the isotropic FEM model.

3. Additional deformations, characterised by for instance transient thermal strain (Anderberg & Thelandersson, 1976) or load-induced thermal strain (Khoury, 2006a), are not explicitly included in the strain definition. Non-linear deformations are assumed to be mainly attributed to initiation, opening and propagation of the crack pattern as is the topic of the next chapter. However, the current model is assumed infinitely strong with no cracking included.

4. Time-dependent behaviour is included only through incremental development of the temperature distribution. Additional time-dependent aspects, such as creep or relaxation (RILEM TC-HTC, 2004), are neglected since the focus is on the onset of fire exposure and the possible occurrence of spalling. This implies that the sudden thermal impact only causes instantaneous and reversible linear elastic strains without considering the possibility of the material to relax under sustained load (Kelly, 2008).

Structural behaviour

The following assumptions are related to the structural behaviour:

5. The schematisation of the cross-section is based on a 2D plane strain assumption (Timoshenko & Goodier, 1970). The out-of-plane deformation is assumed to be restrained in the depth direction, assuming an infinite length.

6. Deformation of the cross-section is characterised by Bernoulli's hypothesis (Hartsuijker & Welleman, 2007) imposed by definition of rigid bodies (Hartmann & Katz, 2007). Along the top and the bottom edges coupling conditions are defined that govern elongation and rotation relationships relative to the central supports. These relationships are deformation-dependent and require an incremental definition.

7. Both central supports reflect interaction with the surrounding structure through constant translational and rotational springs as well as constant axial forces and moments (Bouma, 2000). The horizontal displacement of each support is restrained to obtain a fixed point for the rigid body.

8. The influence of self-weight on the deformation behaviour is neglected and assumed relatively small in these accidental load scenarios.

8.2.2 Description of the mechanical continuum

The characterisation of the stresses, strains and displacements is based on the balance of linear momentum, assuming linear elasticity (Timoshenko & Goodier, 1970; Spencer, 1980/2004). This continuum definition is described in chapter 5 and is directly applicable for the definition of the FEM model. For the sake of completeness a short overview is provided.

Balance of linear momentum

The continuum is characterised by the second order stress tensor reflecting extension and shear components (Timoshenko & Goodier, 1970). This stress tensor is symmetric since the continuum is in equilibrium (Timoshenko & Goodier, 1970). Furthermore, the continuum is also not in motion and only static contributions are thus considered in the balance of linear momentum (Spencer, 1980/2004; Felippa, 2004b). The resultant PDE is restated from chapter 5 and the influence of the distributed body forces, for instance self-weight, is again neglected (Spencer, 1980/2004; Wells, 2006):

$$\boldsymbol{\nabla} \cdot \underline{\boldsymbol{\sigma}} = 0 \tag{8.1}$$

Deformation assuming linear elasticity

The stresses are induced by strains defined as a symmetric second order tensor (Timoshenko & Goodier, 1970). The extension and shear strain components are assumed to be relatively small or infinitesimal (Spencer, 1980/2004). This assumption is governed by the symmetric gradient of the displacements which reads (Timoshenko & Goodier, 1970; Spencer, 1980/2004):

$$\underline{\boldsymbol{\varepsilon}} = \boldsymbol{\nabla}^{s}\boldsymbol{u} \tag{8.2}$$

The relationship between stresses and strains is characterised by linear elasticity assuming, as a first approximation, an isotropic material (Timoshenko & Goodier, 1970). Deformation of the continuum is based on extensional strains causing lateral contraction in the perpendicular directions defined by Poisson's ratio (Timoshenko & Goodier, 1970). Shear strains are governed by the modulus of rigidity and defined as half the angular distortion (Timoshenko & Goodier, 1970):

$$\underline{\boldsymbol{\sigma}} = \boldsymbol{C} : \underline{\boldsymbol{\varepsilon}} \tag{8.3}$$

The temperature strains are included by definition of the mechanical strain tensor governed by the deformation of the continuum using Eq. (8.2) (Timoshenko & Goodier, 1970):

$$\underline{\boldsymbol{\varepsilon_m}} = \underline{\boldsymbol{\varepsilon}} - \underline{\boldsymbol{\varepsilon_T}} = \boldsymbol{\nabla^s u} - \underline{\boldsymbol{\varepsilon_T}} \tag{8.4}$$

Combination of Eq. (8.3) and Eq. (8.4) and inserting them into Eq. (8.1) leads to the PDE that characterises the isotropic mechanical continuum (Spencer, 1980/2004; Wells, 2006):

$$\boldsymbol{\nabla} \cdot \underline{\boldsymbol{\sigma}} = \boldsymbol{\nabla} \cdot \left(\boldsymbol{C} : \left(\boldsymbol{\nabla^s u} - \underline{\boldsymbol{\varepsilon_T}} \right) \right) = 0 \tag{8.5}$$

2D continuum assuming plane strain behaviour

The simplification of the stresses governed by Eq. (8.5) for a 2D cross-section involves the definition of the mechanical behaviour in the out-of-plane direction. For the concrete structural element a state of plane strain is chosen, assuming that the displacement in depth direction is restrained (Timoshenko & Goodier, 1970; Prezemieniecki, 1968/1985). Using engineering notation (Wells, 2006), the shearing strain is defined as the reduction of the original right angle between adjacent planes (Timoshenko & Goodier, 1970; Blaauwendraad, 2003). This defines the shearing strain as governed by partial derivatives with respect to the horizontal and vertical displacements (Timoshenko & Goodier, 1970; Felippa, 2004a). Both extensional strains are uncoupled and influenced by the uniform thermal elongation in the in-plane directions (Timoshenko & Goodier, 1970). Initial stresses due to pore pressure development are, for the moment, neglected. The resultant stress-strain relationship becomes (Timoshenko & Goodier, 1970; Prezemieniecki, 1968/1985):

$$\boldsymbol{\sigma} = \boldsymbol{D}(\boldsymbol{\varepsilon} - \boldsymbol{\varepsilon_T}) \tag{8.6}$$

with

$$\boldsymbol{\sigma} = \begin{bmatrix} \sigma_{xx} \\ \sigma_{yy} \\ \sigma_{xy} \end{bmatrix} \qquad \boldsymbol{\varepsilon} = \begin{bmatrix} \varepsilon_{xx} \\ \varepsilon_{yy} \\ \gamma_{xy} \end{bmatrix} = \begin{bmatrix} \varepsilon_{xx} \\ \varepsilon_{yy} \\ 2\varepsilon_{xy} \end{bmatrix} = \begin{bmatrix} \dfrac{\partial u_x}{\partial x} \\ \dfrac{\partial u_y}{\partial y} \\ \dfrac{\partial u_x}{\partial y} + \dfrac{\partial u_y}{\partial x} \end{bmatrix} \qquad \boldsymbol{\varepsilon_T} = (1+\nu) \begin{bmatrix} \varepsilon_T \\ \varepsilon_T \\ 0 \end{bmatrix}$$

$$\boldsymbol{D} = \frac{E}{(1+\nu)(1-2\nu)} \begin{bmatrix} 1-\nu & \nu & 0 \\ \nu & 1-\nu & 0 \\ 0 & 0 & \dfrac{1-2\nu}{2} \end{bmatrix} \qquad \varepsilon_{zz} = \gamma_{yz} = \gamma_{zx} = 0$$

$$\sigma_{zz} = \nu\left(\sigma_{xx} + \sigma_{yy}\right) - E\varepsilon_T$$

8.2.3 Support conditions

The PDE, stated in Eq. (8.5), is extended by definition of boundary conditions. These are indicated in the schematic overview of Fig. 8.1 and are the FEM equivalent for the behaviour discussed in chapter 5:

- Along the top and bottom edges of the cross-section rigid bodies are defined relative to the central supports (Hartmann & Katz, 2007). These require coupling conditions based on incremental displacements as discussed in the next paragraph.

- The central supports are governed by combined Dirichlet and Neumann boundary conditions (van Kan, et al., 2008). The former expresses the restraint of the horizontal displacement. Interaction with the surrounding structure is defined by the latter support condition based on the balance of linear momentum (Wells, 2006).

- Along the left and right outer edges no external displacements or forces are imposed since fire exposure is represented as an internal material-based load.

Combined Dirichlet and Neumann boundary conditions

The rigid bodies are each governed by deformation of a central support, characterised by both Dirichlet and Neumann conditions. However, each of these conditions can only be imposed separately at the variables (van Kan, et al., 2008). The Dirichlet boundary condition prescribes the horizontal displacement as restraint in order to provide a fixed point for each rigid body:

$$u_x|_{\Gamma_{S_D}} = 0 \tag{8.7}$$

Interaction with the surrounding structure is governed by a Neumann boundary condition, imposed at the remaining variables defined at the supports. The balance of linear momentum, at the support, is expressed using the stress tensor and the unit outward normal vector (Spencer, 1980/2004; Wells, 2006). This is equilibrated by concentrated forces rather than a distributed traction as stated in chapter 5. Partial restraint in axial and rotational direction (Bouma, 2000) are reflected by the negative contribution. External forces are defined positive in tension (Bouma, 2000). Both contributions are stated after definition of the rigid body boundary conditions, since these govern the variables at the supports, and read:

$$\begin{aligned} \underline{\boldsymbol{\sigma}}\boldsymbol{n}\big|_{\Gamma_{S_N}} &= -\boldsymbol{K_S u} + \boldsymbol{F_S} \\ \Big(\boldsymbol{C}\colon\big(\boldsymbol{\nabla^s u} - \underline{\boldsymbol{\varepsilon_T}}\big)\Big)\boldsymbol{n}\Big|_{\Gamma_{S_N}} &= -\boldsymbol{K_S u} + \boldsymbol{F_S} \end{aligned} \tag{8.8}$$

where

$\boldsymbol{F_S}$	[var.]	External load defined as force vector at the support
$\boldsymbol{K_S}$	[var.]	Spring stiffness matrix governing the structural interaction

The remaining outer edges, exposed to the surrounding environment, are considered not loaded by external forces. This affectively defines an additional Neumann boundary condition, stating the free edges of the cross-section according to:

$$\underline{\boldsymbol{\sigma}}\boldsymbol{n}\big|_{\Gamma_A} = 0 \tag{8.9}$$

8.3 Solution approach to define the FEM schematisation

Derivation of the FEM schematisation is based on the initial PDE, stated in Eq. (8.5), and the boundary conditions, defined by Eq. (8.7), Eq. (8.8) and Eq (8.9). For numerical approximation the same procedure as presented in chapter 6 is used. The PDE or strong form is reduced in order to obtain the weak form which through Galerkin's method leads to a FEM descretisation (van Kan, et al., 2008). This is implemented for the plane strain cross-section using engineering notation (Felippa, 2004a; van Kan, et al., 2008). Discretisation in time is discussed reflecting on the coupling with the FEM transport and pore pressure model as well as the rigid body boundary conditions. An incremental definition is introduced based on the elastic strain energy while extending the boundary conditions to include rigid body motions.

8.3.1 Minimisation of energy in order to obtain the weak form

Derivation of the finite element approximation is again based on the weak form of the PDE through consideration of the mechanical functional (van Kan, et al., 2008; Zienkiewicz, et al., 2005). The dot product of the displacements and the system of PDE omits the temperature elongations since no internal energy development is associated with this contribution:

$$J_\sigma = \int_\Omega \frac{1}{2}(\boldsymbol{u}-\boldsymbol{u_T})\cdot(\boldsymbol{\nabla}\cdot\underline{\boldsymbol{\sigma}})d\Omega = \int_\Omega \frac{1}{2}(\boldsymbol{u}-\boldsymbol{u_T})\cdot\left(\boldsymbol{\nabla}\cdot\left(\boldsymbol{C}\colon\left(\boldsymbol{\nabla^s u}-\underline{\boldsymbol{\varepsilon_T}}\right)\right)\right)d\Omega \tag{8.10}$$

where

J_σ	[J]	Functional based on the balance of linear momentum
$\boldsymbol{u_T}$	[mm]	Displacement vector based on the imposed temperature strain

Relationship between functional minimisation and the PDE

In chapter 6 it was elaborated that minimisation of the functional with respect to the variables obtains the coupled system of PDE's (van Kan, et al., 2008; Zienkiewicz, et al., 2005). The same approach is used with the variables defined by the imposed displacements, neglecting temperature-induced elongations. The stiffness integral, represented by Eq. (8.10), is differentiated, obtaining two contributions based on the dyadic product. The first produces the basic stiffness integral expressed in the stress resultant. The second contribution is rearranged and through consideration of the partial derivatives multiplied by the imposed displacements also the basic stiffness integral is obtained:

$$\frac{\partial}{\partial(\boldsymbol{u}-\boldsymbol{u_T})}J_\sigma = \int_\Omega \frac{1}{2}\left(\frac{\partial}{\partial(\boldsymbol{u}-\boldsymbol{u_T})}\otimes(\boldsymbol{u}-\boldsymbol{u_T})(\boldsymbol{\nabla}\cdot\underline{\boldsymbol{\sigma}}) + \frac{\partial}{\partial(\boldsymbol{u}-\boldsymbol{u_T})}\otimes(\boldsymbol{\nabla}\cdot\underline{\boldsymbol{\sigma}})(\boldsymbol{u}-\boldsymbol{u_T})\right)d\Omega$$

$$= \int_\Omega \frac{1}{2}\left(\boldsymbol{I}(\boldsymbol{\nabla}\cdot\underline{\boldsymbol{\sigma}}) + \left((\boldsymbol{\nabla}\cdot\underline{\boldsymbol{\sigma}})\otimes\frac{\partial}{\partial(\boldsymbol{u}-\boldsymbol{u_T})}\right)^{\boldsymbol{T}}(\boldsymbol{u}-\boldsymbol{u_T})\right)d\Omega \tag{8.11}$$

$$= \int_\Omega \frac{1}{2}(\boldsymbol{\nabla}\cdot\underline{\boldsymbol{\sigma}} + \boldsymbol{\nabla}\cdot\underline{\boldsymbol{\sigma}})d\Omega = \int_\Omega \boldsymbol{\nabla}\cdot\underline{\boldsymbol{\sigma}}d\Omega$$

Using Eq. (8.11) to define the minimisation of the functional stated in Eq. (8.10) confirms the relationship with the PDE, assuming that this also holds true for all sub-domains:

$$\frac{\partial}{\partial(\boldsymbol{u}-\boldsymbol{u_T})}J_\sigma = \int_\Omega \boldsymbol{\nabla}\cdot\underline{\boldsymbol{\sigma}}d\Omega = 0$$
$$\rightarrow \boldsymbol{\nabla}\cdot\underline{\boldsymbol{\sigma}} = 0 \tag{8.12}$$

Equilibrium between energy across the domain and work along the boundary

The weak form is obtained by first using integration by parts applied to Gauss' divergence theorem (van Kan, et al., 2008; Segal, 2008). In the second term, the symmetric gradient of the displacements is used based on consideration of the symmetric stress tensor (Wells, 2006). In the following definition the Neumann boundary condition governing the free left and right outer edges, stated by Eq. (8.9), is directly omitted:

$$\int_\Omega \boldsymbol{\nabla}\cdot\left(\underline{\boldsymbol{\sigma}}(\boldsymbol{u}-\boldsymbol{u_T})\right)d\Omega = \int_{\Gamma_S}\left(\underline{\boldsymbol{\sigma}}(\boldsymbol{u}-\boldsymbol{u_T})\right)\cdot\boldsymbol{n}d\Gamma_S$$
$$\int_\Omega (\boldsymbol{u}-\boldsymbol{u_T})\cdot\boldsymbol{\nabla}\cdot\underline{\boldsymbol{\sigma}} + \boldsymbol{\nabla^s}(\boldsymbol{u}-\boldsymbol{u_T}):\underline{\boldsymbol{\sigma}}d\Omega = \int_{\Gamma_S}(\boldsymbol{u}-\boldsymbol{u_T})\cdot\underline{\boldsymbol{\sigma}}\boldsymbol{n}d\Gamma_S \tag{8.13}$$

with

$$\boldsymbol{\nabla u}:\underline{\boldsymbol{\sigma}} = \boldsymbol{\nabla^s u}:\underline{\boldsymbol{\sigma}}$$

The first term at the left hand side represents the integral present in Eq. (8.10). After inserting, rearranging and introducing the temperature strain tensor only first order derivatives govern the functional (van Kan, et al., 2008). The stiffness integral across the domain is characterised by symmetry with respect to the gradient of the displacements and the temperature strain tensor. Furthermore, the boundary integral reflects the stresses concentrated at both supports:

$$J_\sigma = -\int_\Omega \frac{1}{2}\left(\boldsymbol{\nabla^s u}-\underline{\boldsymbol{\varepsilon_T}}\right):\boldsymbol{C}:\left(\boldsymbol{\nabla^s u}-\underline{\boldsymbol{\varepsilon_T}}\right)d\Omega + \int_{\Gamma_S}\frac{1}{2}(\boldsymbol{u}-\boldsymbol{u_T})\cdot\boldsymbol{C}:\left(\boldsymbol{\nabla^s u}-\underline{\boldsymbol{\varepsilon_T}}\right)\boldsymbol{n}d\Gamma_S \tag{8.14}$$

The concept of energy conservation is reflected by expressing the functional in the elastic strain energy that develops across the domain and the produced work along the boundary (Timoshenko & Goodier, 1970):

$$J_\sigma = -\int_\Omega \frac{1}{2}\underline{\boldsymbol{\varepsilon_m}}:\underline{\boldsymbol{\sigma}}d\Omega + \int_{\Gamma_S}\frac{1}{2}(\boldsymbol{u}-\boldsymbol{u_T})\cdot\underline{\boldsymbol{\sigma}}\boldsymbol{n}d\Gamma_S$$
$$\rightarrow J_\sigma = -U_\varepsilon + W_S \tag{8.15}$$

where

U_ε	[J]	Elastic strain energy across the domain
W_S	[J]	Work produced at the supports by imposed stress concentrations

Minimisation of the energy functional

The solution of this energy functional and thus the PDE is defined through the approximate displacements and a complimentary variation or test function (Vermolen, 2005; van Kan, et al., 2008). However, the variation or test function is defined to be zero at Dirichlet boundary conditions since these displacements are known (van Kan, et al., 2008):

$$\boldsymbol{u}(\boldsymbol{x}) = \hat{\boldsymbol{u}}(\boldsymbol{x}) + \epsilon_U \boldsymbol{\eta_U}(\boldsymbol{x}) \tag{8.16}$$

where

ϵ_U	[-]	Arbitrary parameter governing the contribution of the variation
$\hat{\boldsymbol{u}}$	[mm]	Approximate displacement vector
$\boldsymbol{\eta_U}$	[mm]	Variation or test function vector for the displacements

Eq. (8.16) is inserted into Eq. (8.14) while the boundary integral is divided into two contributions, reflecting the Dirichlet and the Neumann conditions at the supports:

$$\begin{aligned} J_\sigma = &- \int_\Omega \frac{1}{2}\left(\boldsymbol{\nabla^s}(\hat{\boldsymbol{u}} + \epsilon_U \boldsymbol{\eta_U}) - \underline{\boldsymbol{\varepsilon_T}}\right) : \boldsymbol{C} : \left(\boldsymbol{\nabla^s}(\hat{\boldsymbol{u}} + \epsilon_U \boldsymbol{\eta_U}) - \underline{\boldsymbol{\varepsilon_T}}\right) d\Omega \\ &+ \int_{\Gamma_{S_D}} \frac{1}{2}(\boldsymbol{u} - \boldsymbol{u_T}) \cdot \boldsymbol{C} : \left(\boldsymbol{\nabla^s u} - \underline{\boldsymbol{\varepsilon_T}}\right) \boldsymbol{n} d\Gamma_{S_D} \\ &+ \int_{\Gamma_{S_N}} \frac{1}{2}\left((\hat{\boldsymbol{u}} + \epsilon_U \boldsymbol{\eta_U}) - \boldsymbol{u_T}\right) \cdot \boldsymbol{C} : \left(\boldsymbol{\nabla^s}(\hat{\boldsymbol{u}} + \epsilon_U \boldsymbol{\eta_U}) - \underline{\boldsymbol{\varepsilon_T}}\right) \boldsymbol{n} d\Gamma_{S_N} \end{aligned} \tag{8.17}$$

Functional minimisation with respect to the variation is obtained through the arbitrary scalar parameter (Vermolen, 2005; van Kan, et al., 2008). The contribution by the Dirichlet boundary integral vanishes since this part of the solution is a priori known:

$$\begin{aligned} \frac{\partial}{\partial \epsilon_U} J_\sigma = &- \left(\int_\Omega \boldsymbol{\nabla^s \eta_U} : \boldsymbol{C} : \boldsymbol{\nabla^s} \hat{\boldsymbol{u}} d\Omega + \int_\Omega \epsilon_U \boldsymbol{\nabla^s \eta_U} : \boldsymbol{C} : \boldsymbol{\nabla^s \eta_U} d\Omega - \int_\Omega \boldsymbol{\nabla^s \eta_U} : \boldsymbol{C} : \underline{\boldsymbol{\varepsilon_T}} d\Omega \right) \\ &+ \int_{\Gamma_{S_N}} \frac{1}{2} \boldsymbol{\eta_U} \cdot \boldsymbol{C} : \left(\boldsymbol{\nabla^s}(\hat{\boldsymbol{u}} + \epsilon_U \boldsymbol{\eta_U}) - \underline{\boldsymbol{\varepsilon_T}}\right) \boldsymbol{n} d\Gamma_{S_N} = 0 \end{aligned} \tag{8.18}$$

Definition of the parameter as zero removes the influence of the variation from the minimisation and obtains the weak form (Vermolen, 2005; van Kan, et al., 2008). The boundary integral is expressed by the approximate solution only and a single contribution remains as reflected by the second term:

$$\left.\frac{\partial}{\partial \epsilon_U} J_\sigma\right|_{\epsilon_U = 0} = - \int_\Omega \boldsymbol{\nabla^s \eta_U} : \boldsymbol{C} : \left(\boldsymbol{\nabla^s} \hat{\boldsymbol{u}} - \underline{\boldsymbol{\varepsilon_T}}\right) d\Omega + \int_{\Gamma_{S_N}} \boldsymbol{\eta_U} \cdot \boldsymbol{C} : \left(\boldsymbol{\nabla^s} \hat{\boldsymbol{u}} - \underline{\boldsymbol{\varepsilon_T}}\right) \boldsymbol{n} d\Gamma_{S_N} = 0 \tag{8.19}$$

Again it is observed that the weak form is directly available by multiplying the PDE with the variation or test function and integrating across the domain as commonly adopted (van Kan, et al., 2008; Segal, 2008). Furthermore, the variation can be thought of as a virtual displacement that disturbs the static equilibrium equation (Wells, 2006; Zienkiewicz, et al., 2005). In that respect, the incremental development of the functional expressed by the solution reads:

$$\delta J_\sigma = -\int_\Omega \boldsymbol{\nabla^s \delta u} : \boldsymbol{C} : \left(\boldsymbol{\nabla^s u} - \underline{\boldsymbol{\varepsilon_T}}\right) d\Omega + \int_{\Gamma_{S_N}} \boldsymbol{\delta u} \cdot \boldsymbol{C} : \left(\boldsymbol{\nabla^s u} - \underline{\boldsymbol{\varepsilon_T}}\right) \boldsymbol{n} d\Gamma_{S_N} = 0 \tag{8.20}$$

Weak form governing the mechanical continuum

Consideration of the various terms obtains the final expression for the weak form. The first term is separated into the stiffness and the imposed strain across the domain, represented at the left and right hand side respectively. The Neumann boundary condition is fulfilled by inserting Eq. (8.8) into the boundary integral (van Kan, et al., 2008). Two contributions are obtained with the spring action or the external forces defined at the left or right hand side respectively:

$$\int_\Omega \boldsymbol{\nabla^s \eta_U} : \boldsymbol{C} : \boldsymbol{\nabla^s u} d\Omega + \int_{\Gamma_{S_N}} \boldsymbol{\eta_U} \cdot \boldsymbol{K_S u} d\Gamma_{S_N} = \int_\Omega \boldsymbol{\nabla^s \eta_U} : \boldsymbol{C} : \underline{\boldsymbol{\varepsilon_T}} d\Omega + \int_{\Gamma_{S_N}} \boldsymbol{\eta_U} \cdot \boldsymbol{F_S} d\Gamma_{S_N} \tag{8.21}$$

8.3.2 FEM definition by means of Galerkin's method

The stiffness terms governing the weak form, reflected by the first and second integrals in Eq. (8.21), are symmetric with respect to the displacement and the variation. Galerkin's method is thus used to numerically approximate the weak form and obtain the FEM discretisation (van Kan, et al., 2008).

Galerkin's method

The first order weak form requires the solution and the variation to fulfil C^0 continuity, similar to the approximation used in chapter 6 (van Kan, et al., 2008). Both are governed by linear combinations of basis functions and nodal displacements (van Kan, et al., 2008; Segal, 2008). The Dirichlet boundary condition, representing the horizontal restraint at the supports, is included in the approximate solution (van Kan, et al., 2008):

$$\boldsymbol{u}(\boldsymbol{x}) \approx \sum_{j=1}^{n_{tot}-n_S} \boldsymbol{N_{U_j}}(\boldsymbol{x}) \boldsymbol{u_j} + \sum_{j=(n_{tot}-n_S)+1}^{n_{tot}} \boldsymbol{N_{U_j}}(\boldsymbol{x}) \boldsymbol{u_{S_j}} \tag{8.22}$$

where

$\cdots_j$		Indication for the node number
n_{tot}	[-]	Total number of nodes across the domain
n_S	[-]	Number of nodes at which Dirichlet conditions are imposed
$\boldsymbol{u_{S_j}}$	[mm]	Imposed displacement vector at the supports
$\boldsymbol{u_j}$	[mm]	Nodal displacement vector
$\boldsymbol{N_{U_j}}$	[mm]	Nodal basis function matrix for the displacements

Approximation of the variation or test function is only implemented across a part of the domain associated with the unknown solution. The variation is, as already used in establishing the weak form, defined zero at Dirichlet boundary conditions (van Kan, et al., 2008):

$$\boldsymbol{\eta_U}(\boldsymbol{x}) \approx \sum_{i=1}^{n_{tot}-n_S} \boldsymbol{N_{U_i}}(\boldsymbol{x})\boldsymbol{\eta_{U_i}} \tag{8.23}$$

where

$\cdots_i$		Indication for the node number
$\boldsymbol{\eta_{U_i}}$	[mm]	Nodal variation or test function vector for the displacements
$\boldsymbol{N_{U_i}}$	[mm]	Nodal basis function matrix for the displacements

Inserting Eq. (8.22) and Eq. (8.23) in the weak form, defined by Eq. (8.21), leads to Galerkin's approximation expressed in the nodal displacements (van Kan, et al., 2008). The gradients of the displacements and the variation are approximated through the gradient of the shape functions and the nodal displacements with the latter expressed as vector. This introduces engineering notation and allows to include the plane strain elasticity tensor and temperature strain vector defined in Eq. (8.6). The Dirichlet boundary condition defines an additional force representing the imposed horizontal displacement at the supports. In this respect the term related to the spring stiffness is directly omitted, since these originate from the Neumann boundary condition:

$$\begin{aligned}
&\sum_{i=1}^{n_{tot}-n_S} \boldsymbol{\eta_{U_i}}^{\boldsymbol{T}} \sum_{j=1}^{n_{tot}-n_S} \left(\int_{\Omega} \left(\boldsymbol{\nabla N_{U_i}}\right)^{\boldsymbol{T}} \boldsymbol{D} \boldsymbol{\nabla N_{U_j}} d\Omega \, \boldsymbol{u_j} + \int_{\Gamma_{S_N}} \boldsymbol{N_{U_i}}^{\boldsymbol{T}} \boldsymbol{K_S} \boldsymbol{N_{U_j}} d\Gamma_{S_N} \, \boldsymbol{u_j} \right) \\
&\quad = \sum_{i=1}^{n_{tot}-n_s} \boldsymbol{\eta_{U_i}}^{\boldsymbol{T}} \left(\int_{\Omega} \left(\boldsymbol{\nabla N_{U_i}}\right)^{\boldsymbol{T}} \boldsymbol{D} \boldsymbol{\varepsilon_T} d\Omega + \int_{\Gamma_{S_N}} \boldsymbol{N_{U_i}}^{\boldsymbol{T}} \boldsymbol{F_S} d\Gamma_{S_N} \right) \\
&- \sum_{i=1}^{n_{tot}-n_S} \boldsymbol{\eta_{U_i}}^{\boldsymbol{T}} \sum_{j=(n_{tot}-n_S)+1}^{n_{tot}} \left(\int_{\Omega} \left(\boldsymbol{\nabla N_{U_i}}\right)^{\boldsymbol{T}} \boldsymbol{D} \boldsymbol{\nabla N_{U_j}} d\Omega \begin{bmatrix} \overbrace{\tilde{u}_{S_x}}^{=0} \\ 0 \end{bmatrix} + \underbrace{\int_{\Gamma_{S_N}} \boldsymbol{N_{U_i}}^{\boldsymbol{T}} \boldsymbol{K_S} \boldsymbol{N_{U_j}} d\Gamma_{S_N} \begin{bmatrix} \overbrace{\tilde{u}_{S_x}}^{=0} \\ 0 \end{bmatrix}}_{=0} \right)
\end{aligned} \tag{8.24}$$

This relationship must apply to all possible variations which by neglecting the last two terms associated with the imposed restraint leads to:

$$\begin{aligned}
&\sum_{j=1}^{n_{tot}-n_S} \left(\int_{\Omega} \left(\boldsymbol{\nabla N_{U_i}}\right)^{\boldsymbol{T}} \boldsymbol{D} \boldsymbol{\nabla N_{U_j}} d\Omega \, \boldsymbol{u_j} \right) + \sum_{j=1}^{n_{tot}-n_S} \left(\int_{\Gamma_{S_N}} \boldsymbol{N_{U_i}}^{\boldsymbol{T}} \boldsymbol{K_S} \boldsymbol{N_{U_j}} d\Gamma_{S_N} \, \boldsymbol{u_j} \right) \\
&= \sum_{j=1}^{n_{tot}-n_S} \left(\int_{\Omega} \left(\boldsymbol{\nabla N_{U_i}}\right)^{\boldsymbol{T}} \boldsymbol{D} \boldsymbol{\varepsilon_T} d\Omega \right) + \sum_{j=1}^{n_{tot}-n_S} \left(\int_{\Gamma_{S_N}} \boldsymbol{N_{U_i}}^{\boldsymbol{T}} \boldsymbol{F_S} d\Gamma_{S_N} \right) \qquad (i = 1, \cdots, n_{tot} - n_S)
\end{aligned} \tag{8.25}$$

FEM discretisation of the domain

Discretisation of the domain results in the FEM definition based on stating the element shape functions and corresponding nodal displacements (van Kan, et al., 2008). The element shape function matrix is based on a similar 2D triangular approximation as used in chapter 6. However, the constant gradient matrix is in this case dependent on the approximation of the global strains. Finally, the horizontal restraint at both supports is excluded from the solution:

$$\begin{aligned} \boldsymbol{u}(\boldsymbol{x}) &\approx \sum_{e=1}^{e_{tot}} \boldsymbol{N_U}^{\boldsymbol{e}}(\boldsymbol{x})\boldsymbol{u}^{\boldsymbol{e}} + \boldsymbol{N_U}^{\boldsymbol{e}}(\boldsymbol{x}) \overset{=\mathbf{0}}{\widetilde{\boldsymbol{u_S}}} = \sum_{e=1}^{e_{tot}} \boldsymbol{N_U}^{\boldsymbol{e}}(\boldsymbol{x})\boldsymbol{u}^{\boldsymbol{e}} \\ \boldsymbol{\nabla u}(\boldsymbol{x}) = \boldsymbol{\varepsilon}(\boldsymbol{x}) &\approx \sum_{e=1}^{e_{tot}} \boldsymbol{\nabla_U N_U}^{\boldsymbol{e}}(\boldsymbol{x})\boldsymbol{u}^{\boldsymbol{e}} = \sum_{e=1}^{e_{tot}} \boldsymbol{B_U}^{\boldsymbol{e}}\boldsymbol{u}^{\boldsymbol{e}} \end{aligned} \tag{8.26}$$

where

$\ldots^e$		Indication for the element number
e_{tot}	[-]	Total number of elements across the domain
$\boldsymbol{u}^{\boldsymbol{e}}$	[mm]	Element nodal displacement vector
$\boldsymbol{N_U}^{\boldsymbol{e}}$	[mm]	Element matrix of the shape functions
$\boldsymbol{B_U}^{\boldsymbol{e}}$	[1/mm]	Element gradient matrix of the shape functions

The FEM definition is characterised by the summation of the element stiffness matrices across the domain using the nodal displacements as variables. The boundary integrals only represent elements along the outer edges at which the Neumann boundary condition is applied. The contribution by the Dirichlet boundary condition is no longer present based on the imposed restraint. The corresponding nodal variables are omitted from the FEM definition as is addressed through including the rigid body coupling conditions:

$$\begin{aligned} &\sum_{e=1}^{e_{tot}} \left(\int_{\Omega^e} \boldsymbol{B_U}^{\boldsymbol{eT}} \boldsymbol{D^e B_U}^{\boldsymbol{e}} d\Omega^e \, \boldsymbol{u^e} \right) + \sum_{e=1}^{e_{tot}} \left(\int_{\Gamma_{S_N}{}^e} \boldsymbol{N_U}^{\boldsymbol{eT}} \boldsymbol{K_S N_U}^{\boldsymbol{e}} d\Gamma_{S_N}{}^e \, \boldsymbol{u^e} \right) \\ &= \sum_{e=1}^{e_{tot}} \left(\int_{\Omega^e} \boldsymbol{B_U}^{\boldsymbol{eT}} \boldsymbol{D^e \varepsilon_T}^{\boldsymbol{e}} d\Omega^e \right) + \sum_{e=1}^{e_{tot}} \left(\int_{\Gamma_{S_N}{}^e} \boldsymbol{N_U}^{\boldsymbol{eT}} \boldsymbol{F_S} d\Gamma_{S_N}{}^e \right) \end{aligned} \tag{8.27}$$

8.3.3 Time dependence through incremental stresses and displacements

The FEM definition, presented in Eq. (8.27), reflects loading by external forces as well as internal temperature strains. The latter requires an incremental coupling with the FEM temperature and pore pressure model, presented in chapter 6. For this purpose the static definition, extended by a time approximation, is based on the development of the imposed temperature distribution. This governs the non-linear development of Young's modulus and the temperature strain which the FEM definition is able to represent based on static equilibrium as for instance used in chapter 5. Alternatively, also an incremental approach can be used based on superposition of time-dependent equilibrium stress states (Zienkiewicz, et al., 2005).

An incremental approach is however required for the rigid body boundary conditions along the top and bottom edges. Deformation of the cross-section develops by translational and especially rotational motions of these edges (Hartmann & Katz, 2007). These motions are characterised by coupling conditions through linear relationships dependent on the deformed state (Hartmann & Katz, 2007). The current FEM definition is thus restated in incremental form to accommodate this geometrical non-linear behaviour (Zienkiewicz, et al., 2005).

Incremental definition of displacements, stresses and strains

The deformation-dependent non-linear rigid body motions are addressed through incremental definition of the displacements across the domain (Zienkiewicz, et al., 2005; Biot, 1965):

$$\boldsymbol{u^{t+1}} = \boldsymbol{u^{t}} + \Delta\boldsymbol{u^{t}} \tag{8.28}$$

The stresses, mechanical and temperature strains take a similar form (Zienkiewicz, et al., 2005; Biot, 1965):

$$\begin{aligned} \boldsymbol{\sigma^{t+1}} &= \boldsymbol{\sigma^{t}} + \Delta\boldsymbol{\sigma^{t}} \\ \boldsymbol{\varepsilon_m}^{\boldsymbol{t+1}} &= \boldsymbol{\varepsilon_m}^{\boldsymbol{t}} + \Delta\boldsymbol{\varepsilon_m}^{\boldsymbol{t}} \\ \boldsymbol{\varepsilon_T}^{\boldsymbol{t+1}} &= \boldsymbol{\varepsilon_T}^{\boldsymbol{t}} + \Delta\boldsymbol{\varepsilon_T}^{\boldsymbol{t}} \end{aligned} \tag{8.29}$$

Furthermore, it will be proven that the temperature-dependent development of the elasticity tensor also requires an incremental definition:

$$\boldsymbol{D^{t+1}} = \boldsymbol{D^{t}} + \Delta\boldsymbol{D^{t}} \tag{8.30}$$

Incremental elastic strain energy

The FEM definition is extended by stating the development of the elastic strain energy for each element, reflecting a first order approximation:

$$U_\varepsilon{}^{et+1} = U_\varepsilon{}^{et} + \Delta t \left[\frac{\partial U_\varepsilon{}^{e}}{\partial t}\right]^{t} \tag{8.31}$$

The first term at the right hand side reflects the current state of the elastic strain energy present in each element defined through Eq. (8.15). Using plane stress or plane strain yields the commonly used expression (Timoshenko & Goodier, 1970; Prezemieniecki, 1968/1985):

$$U_\varepsilon{}^{et} = \int_{\Omega^e} \frac{1}{2} \boldsymbol{\varepsilon_m}^{\boldsymbol{et^T}} \boldsymbol{\sigma^{et}} d\Omega^e = \int_{\Omega^e} \frac{1}{2} \boldsymbol{\varepsilon_m}^{\boldsymbol{et^T}} \boldsymbol{D^{et}} \boldsymbol{\varepsilon_m}^{\boldsymbol{et}} d\Omega^e \tag{8.32}$$

Development of the elastic strain energy is governed by the derivative with respect to time. Consideration of this scalar quantity, leads to two contributions. The first contribution represents the influence of the incremental mechanical strains which are neglected based on the small or infinitesimal strain assumption (Timoshenko & Goodier, 1970; Spencer, 1980/2004). The second term represents the incremental stresses based on development of the elasticity tensor and the mechanical strains:

$$\left[\frac{\partial {U_\varepsilon}^e}{\partial t}\right]^t = \int_{\Omega^e} \frac{1}{2}\left(\frac{\partial}{\partial t}{\boldsymbol{\varepsilon_m}}^{\boldsymbol{et}^{\boldsymbol{T}}}\boldsymbol{\sigma}^{\boldsymbol{et}} + {\boldsymbol{\varepsilon_m}}^{\boldsymbol{et}^{\boldsymbol{T}}}\frac{\partial}{\partial t}\boldsymbol{\sigma}^{\boldsymbol{et}}\right) d\Omega^e$$
$$= \int_{\Omega^e} \frac{1}{2}\left(\underbrace{\frac{\partial}{\partial t}{\boldsymbol{\varepsilon_m}}^{\boldsymbol{et}^{\boldsymbol{T}}}}_{\approx 0}\left(\boldsymbol{D}^{\boldsymbol{et}}{\boldsymbol{\varepsilon_m}}^{\boldsymbol{et}}\right) + {\boldsymbol{\varepsilon_m}}^{\boldsymbol{et}^{\boldsymbol{T}}}\frac{\partial}{\partial t}\left(\boldsymbol{D}^{\boldsymbol{et}}{\boldsymbol{\varepsilon_m}}^{\boldsymbol{et}}\right)\right) d\Omega^e \tag{8.33}$$

The incremental elastic strain energy is determined by approximation of the time derivative in Eq. (8.31) using Eq. (8.33). The term between brackets represents the incremental stresses that develop across each element (Zienkiewicz, et al., 2005):

$$\Delta {U_\varepsilon}^{et} = \Delta t\left[\frac{\partial {U_\varepsilon}^e}{\partial t}\right]^t \approx \Delta t\frac{\Delta {U_\varepsilon}^{et}}{\Delta t} = \int_{\Omega^e} \frac{1}{2}{\boldsymbol{\varepsilon_m}}^{\boldsymbol{et}^{\boldsymbol{T}}}\Delta\boldsymbol{\sigma}^{\boldsymbol{et}} d\Omega^e$$
$$= \int_{\Omega^e} \frac{1}{2}{\boldsymbol{\varepsilon_m}}^{\boldsymbol{et}^{\boldsymbol{T}}}\left(\Delta\boldsymbol{D}^{\boldsymbol{et}}{\boldsymbol{\varepsilon_m}}^{\boldsymbol{et}} + \boldsymbol{D}^{\boldsymbol{et}}\Delta{\boldsymbol{\varepsilon_m}}^{\boldsymbol{et}}\right) d\Omega^e \tag{8.34}$$

The following contributions define the incremental stress development:

- The first term governs the stress reduction due to a stiffness variation. By including this term, the elastic strain energy or alternatively the mechanical load is preserved throughout the cross-section.

- The change in elastic strain energy through imposed temperature strains is governed by the second term. This ensures that additional thermal loading can develop throughout the cross-section.

Incremental global forces

The incremental forces acting across the domain are obtained by the incremental elastic strain energy defined per element using Eq. (8.32) while taking the imposed displacements into account (Timoshenko & Goodier, 1970). The gradient matrix can be thought of to distribute the stresses acting across the element to equivalent nodal forces (Prezemieniecki, 1968/1985; Zienkiewicz, et al., 2005). The resultant expression defines the work by these nodal forces as:

$$\Delta {U_\varepsilon}^{et} = \Delta {W_F}^{et} = \int_{\Omega^e} \frac{1}{2}{\boldsymbol{\varepsilon_m}}^{\boldsymbol{et}^{\boldsymbol{T}}}\Delta\boldsymbol{\sigma}^{\boldsymbol{et}} d\Omega^e = \int_{\Omega^e} \frac{1}{2}\left({\boldsymbol{B_U}}^{\boldsymbol{e}}\left(\boldsymbol{u}^{\boldsymbol{et}} - {\boldsymbol{u_T}}^{\boldsymbol{et}}\right)\right)^{\boldsymbol{T}}\Delta\boldsymbol{\sigma}^{\boldsymbol{et}} d\Omega^e$$
$$= \int_{\Omega^e} \frac{1}{2}\left(\boldsymbol{u}^{\boldsymbol{et}} - {\boldsymbol{u_T}}^{\boldsymbol{et}}\right)^{\boldsymbol{T}}{\boldsymbol{B_U}}^{\boldsymbol{eT}}\Delta\boldsymbol{\sigma}^{\boldsymbol{et}} d\Omega^e = \frac{1}{2}\left(\boldsymbol{u}^{\boldsymbol{et}} - {\boldsymbol{u_T}}^{\boldsymbol{et}}\right)^{\boldsymbol{T}}\Delta\boldsymbol{F}^{\boldsymbol{et}} \tag{8.35}$$

where

$\Delta {W_F}^{et}$	[J]	Incremental work produced by the element forces at the current time step
$\Delta\boldsymbol{F}^{\boldsymbol{et}}$	[N]	Incremental element nodal force vector defined at the current time step

The incremental global forces based on the temperature-induced stresses are defined by inserting Eq. (8.34) into the force increment stated in Eq. (8.35) (Zienkiewicz, et al., 2005):

$$\Delta \boldsymbol{F_T}^{\boldsymbol{et}} = \int_{\Omega^e} \boldsymbol{B_U}^{\boldsymbol{eT}} \Delta \boldsymbol{\sigma}^{\boldsymbol{et}} d\Omega^e$$

$$= \int_{\Omega^e} \boldsymbol{B_U}^{\boldsymbol{eT}} \left(\boldsymbol{D}^{\boldsymbol{et+1}} - \boldsymbol{D}^{\boldsymbol{et}}\right)\left(\boldsymbol{B_U}^{\boldsymbol{e}} \boldsymbol{u}^{\boldsymbol{et}} - \boldsymbol{\varepsilon_T}^{\boldsymbol{et}}\right) d\Omega^e \tag{8.36}$$

$$+ \int_{\Omega^e} \boldsymbol{B_U}^{\boldsymbol{eT}} \boldsymbol{D}^{\boldsymbol{et}} \left(\boldsymbol{B_U}^{\boldsymbol{e}} \Delta \boldsymbol{u}^{\boldsymbol{et}} - \left(\boldsymbol{\varepsilon_T}^{\boldsymbol{et+1}} - \boldsymbol{\varepsilon_T}^{\boldsymbol{et}}\right)\right) d\Omega^e$$

where

$\Delta \boldsymbol{F_T}^{\boldsymbol{et}}$	[N]	Incremental element nodal force vector representing the temperature-induced stresses

The first term expresses the change in stiffness with respect to the displacements and temperature strains defined at the current time step. The variation in temperature strain is defined by the second term, using the elastic stiffness at the current time step.

8.3.4 Rigid body boundary conditions

The incremental displacements are also used to define the rigid body boundary conditions. These impose the linear strain, according to Bernoulli's hypothesis (Hartsuijker & Welleman, 2007), through axial translation and rotation of the outer edges as schematically represented in Fig. 8.2 (Hartmann & Katz, 2007). The displacement along these edges is dependent or coupled to the deformation of the central supports, each defined by (Hartmann & Katz, 2007):

$$\begin{aligned} {u_{y_S}}^{t+1} &= {u_{y_S}}^{t} + \Delta {u_{y_S}}^{t} \\ {\varphi_S}^{t+1} &= {\varphi_S}^{t} + \Delta {\varphi_S}^{t} \end{aligned} \tag{8.37}$$

where

$\cdots_S$		Indication for the support number
${u_{y_S}}^{t}, {u_{y_S}}^{t+1}$	[mm]	Vertical displacement of the support at the current, next time step
$\Delta {u_{y_S}}^{t}$	[mm]	Incremental vertical displacement of the support at the current step
${\varphi_S}^{t}, {\varphi_S}^{t+1}$	[rad]	Rotation of the support at the current, next time step
$\Delta {\varphi_S}^{t}$	[rad]	Incremental rotation of the support at the current step

Rigid bodies are formed through stating coupling conditions which define the deformational relationships along these outer edges (Hartmann & Katz, 2007). These conditions define the geometrical non-linearity, expressed in a local coordinate system aligned with the deformed boundary edge. The incremental displacements of nodes situated along each edge is also defined by the distance relative to the support, initially based on the horizontal global nodal coordinates (Hartmann & Katz, 2007). Time-dependent development is included through the incremental horizontal displacements defined in the local coordinate system:

$$d_{rel_{i_{rb}}}{}^{t+1} = d_{rel_{i_{rb}}}{}^{t} + \Delta d_{rel_{i_{rb}}}{}^{t} \tag{8.38}$$

with

$$\Delta d_{rel_{i_{rb}}}{}^{t} = \Delta u_{x}{}'_{i_{rb}}{}^{t} = \cos\varphi_S{}^{t}\Delta u_{x_{i_{rb}}}{}^{t} + \sin\varphi_S{}^{t}\Delta u_{y_{i_{rb}}}{}^{t}$$

where

$\cdots_{i_{rb}}$		Indication for the node number situated along the rigid body
$\Delta u_{x}{}'_{i_{rb}}{}^{t}, \Delta u_{y}{}'_{i_{rb}}{}^{t}$	[mm]	Incremental local horizontal, vertical nodal displacement at the current time step at rigid body node 'i'
$d_{rel_{i_{rb}}}{}^{t}, d_{rel_{i_{rb}}}{}^{t+1}$	[mm]	Relative distance rigid body node 'i' at the current, next step
$\Delta d_{rel_{i_{rb}}}{}^{t}$	[mm]	Incremental relative distance rigid body node 'i' at the step

Rigid body motions through incremental coupling conditions

The rotation of the support and the relative distance along the edge to the support are both defined at the current time step. Using Fig. 8.2 allows to obtain the following incremental nodal contributions (Hartmann & Katz, 2007):

- The incremental vertical global displacement of the support is decomposed based on the rotation of the rigid body. Two contributions are obtained, representing the constant incremental horizontal and vertical local displacements along the edge.

- An additional vertical local displacement is determined by the assumed relatively small incremental rotation of the edge and the distance relative to the support. This approximates the circumferential and tangential displacements as equal.

- The final contribution represents the incremental temperature elongation along the edge relative to the support. Only prescribed displacements in the local horizontal direction are included and assumed to develop unrestrained.

The coupling conditions, shown schematically in Fig. 8.2, define the second order transformation tensor governing the incremental displacement relationships (Hartmann & Katz, 2007). It is observed that this transformation tensor is not orthogonal which will be addressed later (Wells, 2006; Spencer, 1980/2004). The temperature elongation extends the rigid body induced mechanical deformation to form the combined incremental displacements:

$$\Delta \boldsymbol{u}'_{\boldsymbol{i_{rb}}}{}^{\boldsymbol{t}} = \boldsymbol{T_{rb}}'_{\boldsymbol{i_{rb}}}{}^{\boldsymbol{t}} \Delta \boldsymbol{u_S}{}^{\boldsymbol{t}} + \Delta \boldsymbol{u_T}'_{\boldsymbol{i_{rb}}}{}^{\boldsymbol{t}} \tag{8.39}$$

with

$$\Delta \boldsymbol{u_S}{}^{\boldsymbol{t}} = \begin{bmatrix} \Delta u_{y_S}{}^{t} \\ \Delta \varphi_S{}^{t} \end{bmatrix} \qquad \Delta \boldsymbol{u}'_{\boldsymbol{i_{rb}}}{}^{\boldsymbol{t}} = \begin{bmatrix} \Delta u_{x}{}'_{i_{rb}}{}^{t} \\ \Delta u_{y}{}'_{i_{rb}}{}^{t} \end{bmatrix} \qquad \Delta \boldsymbol{u_T}'_{\boldsymbol{i_{rb}}}{}^{\boldsymbol{t}} = \begin{bmatrix} \Delta d_{rel_{T\,i_{rb}}}{}^{t} \\ 0 \end{bmatrix}$$

$$\boldsymbol{T_{rb}}'_{\boldsymbol{i_{rb}}}{}^{\boldsymbol{t}} = \begin{bmatrix} \sin\varphi_S{}^{t} & 0 \\ \cos\varphi_S{}^{t} & d_{rel_{i_{rb}}}{}^{t} \end{bmatrix}$$

where

$\Delta d_{rel_{T\,i_{rb}}}{}^{t}$	[mm]	Incremental temperature elongation at rigid body node 'i' defined relative to the support
$\Delta \boldsymbol{u_S}^{\boldsymbol{t}}$	[var.]	Incremental displacement vector at the support
$\Delta \boldsymbol{u'}_{\boldsymbol{i_{rb}}}{}^{\boldsymbol{t}}$	[mm]	Incremental displacement vector at rigid body node 'i'
$\Delta \boldsymbol{u_T}'_{\boldsymbol{i_{rb}}}{}^{\boldsymbol{t}}$	[mm]	Incremental prescribed elongation vector at rigid body node 'i'
$\boldsymbol{T_{rb}}'_{\boldsymbol{i_{rb}}}{}^{\boldsymbol{t}}$	[var.]	Nodal transformation tensor based on coupling conditions expressed in the rotated coordinate system (second order)

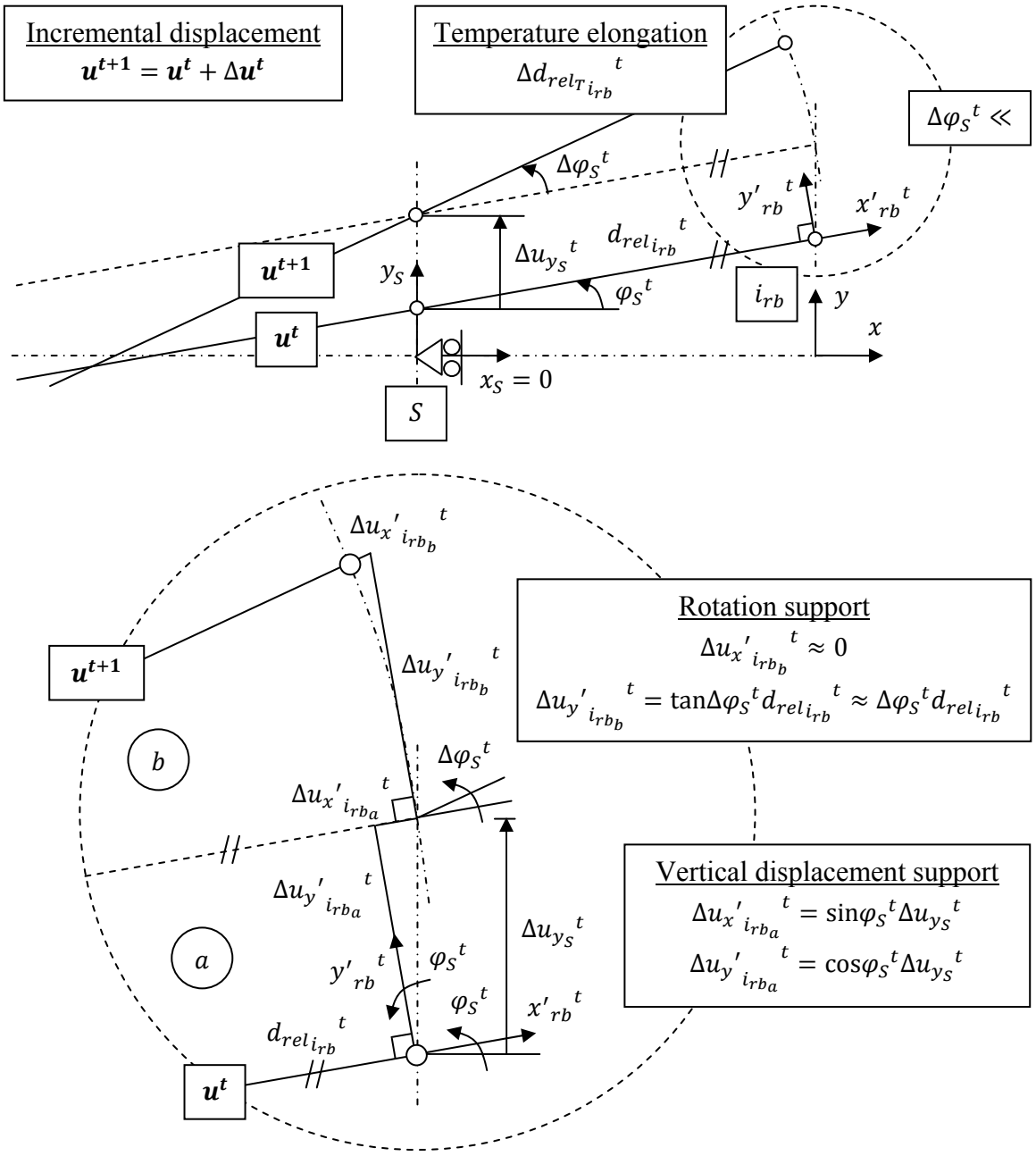

Fig. 8.2 *The rigid body motion in $\mathbb{R}^2$ is characterised by vertical translation and rotation relative to the central support. The incremental local displacements along the edge are expressed in a rotated coordinate system based on the deformed state. Additional temperature elongations along the edge are defined separately.*

Rigid body transformations in the global coordinate system

The previous relationship expresses the local displacements based on the displacements defined at the support expressed in the global coordinate system. An additional nodal variable is introduced at both supports representing incremental rotations. However, for FEM implementation this relationship is redefined by expressing also the coupled nodal variables in the global coordinate system. This requires the coordinate transformation tensor and exploiting its orthogonal basis. In the following the prescribed local temperature elongations are also expressed in the global coordinate system:

$$\begin{aligned} \Delta \boldsymbol{u}'_{i_{rb}}{}^{t} &= \boldsymbol{T}_{\varphi_S}{}^{t} \Delta \boldsymbol{u}_{i_{rb}}{}^{t} = \boldsymbol{T}_{rb}{}'_{i_{rb}}{}^{t} \Delta \boldsymbol{u}_{S}{}^{t} + \Delta \boldsymbol{u}_{T}{}'_{i_{rb}}{}^{t} \\ \Delta \boldsymbol{u}_{i_{rb}}{}^{t} &= \boldsymbol{T}_{\varphi_S}{}^{t^T} \left(\boldsymbol{T}_{rb}{}'_{i_{rb}}{}^{t} \Delta \boldsymbol{u}_{S}{}^{t} + \Delta \boldsymbol{u}_{T}{}'_{i_{rb}}{}^{t} \right) = \boldsymbol{T}_{rb_{i_{rb}}}{}^{t} \Delta \boldsymbol{u}_{S}{}^{t} + \Delta \boldsymbol{u}_{T_{i_{rb}}}{}^{t} \end{aligned} \tag{8.40}$$

with

$$\Delta \boldsymbol{u}_{i_{rb}}{}^{t} = \begin{bmatrix} \Delta u_{x_{i_{rb}}}{}^{t} \\ \Delta u_{y_{i_{rb}}}{}^{t} \end{bmatrix} \qquad \Delta \boldsymbol{u}_{T_{i_{rb}}}{}^{t} = \begin{bmatrix} \cos\varphi_S{}^{t} \Delta d_{rel_{T}{}_{i_{rb}}}{}^{t} \\ \sin\varphi_S{}^{t} \Delta d_{rel_{T}{}_{i_{rb}}}{}^{t} \end{bmatrix}$$

$$\boldsymbol{T}_{\varphi_S}{}^{t} = \begin{bmatrix} \cos\varphi_S{}^{t} & \sin\varphi_S{}^{t} \\ -\sin\varphi_S{}^{t} & \cos\varphi_S{}^{t} \end{bmatrix} \qquad \boldsymbol{T}_{rb_{i_{rb}}}{}^{t} = \begin{bmatrix} 0 & -\sin\varphi_S{}^{t} d_{rel_{i_{rb}}}{}^{t} \\ 1 & \cos\varphi_S{}^{t} d_{rel_{i_{rb}}}{}^{t} \end{bmatrix}$$

where

$\Delta \boldsymbol{u}_{i_{rb}}{}^{t}, \Delta \boldsymbol{u}_{T_{i_{rb}}}{}^{t}$	[mm]	Incremental displacement, temperature elongation vector defined in the global coordinate system
$\boldsymbol{T}_{rb_{i_{rb}}}{}^{t}$	[var.]	Nodal transformation tensor based on coupling conditions defined in the global coordinate system (second order)

Through definition of Eq. (8.40) the previously discussed requirement for including the incremental elastic strain energy becomes apparent. Moreover, this transformation tensor is also used to impose the restraint in horizontal direction as well as introduce the additional nodal variables at the supports. By definition the relative distance and the thermal elongation at the supports are zero which reduces Eq. (8.40) to only state dependence on the vertical incremental displacement. The rotational variable is thus only defined by stiffness connected to the support characterised by the relative distance.

It is also useful to introduce the identity matrix for the remaining nodes not situated along the edges. Under these circumstances the transformation relationship takes the form:

$$\Delta \boldsymbol{u}_{i}{}^{t} = \boldsymbol{T}_{rb_{i_{rb}}}{}^{t} \Delta \boldsymbol{u}_{i}{}^{t} \tag{8.41}$$

with

$$\boldsymbol{T}_{rb_{i_{rb}}}{}^{t} = \begin{bmatrix} 1 & 0 \\ 0 & 1 \end{bmatrix}$$

The element-based rigid body transformation tensor and prescribed temperature elongation vector are constructed by using Eq. (8.40) and Eq. (8.41) dependent on the location of the nodes as for instance shown in Fig. 8.3:

$$\Delta \boldsymbol{u}^{et} = \boldsymbol{T_{rb}}^{et} \Delta \boldsymbol{u_{sys}}^{et} + \Delta \boldsymbol{u_T}^{et} \tag{8.42}$$

with

$$\Delta \boldsymbol{u_{sys}}^{et} = \begin{bmatrix} \Delta \boldsymbol{u_{sys}}_1^{et} \\ \Delta \boldsymbol{u_{sys}}_2^{et} \\ \Delta \boldsymbol{u_{sys}}_3^{et} \end{bmatrix} \qquad \Delta \boldsymbol{u}^{et} = \begin{bmatrix} \Delta \boldsymbol{u}_1^{et} \\ \Delta \boldsymbol{u}_2^{et} \\ \Delta \boldsymbol{u}_3^{et} \end{bmatrix} \qquad \Delta \boldsymbol{u_T}^{et} = \begin{bmatrix} \Delta \boldsymbol{u_T}_1^{et} \\ \Delta \boldsymbol{u_T}_2^{et} \\ \Delta \boldsymbol{u_T}_3^{et} \end{bmatrix}$$

$$\boldsymbol{T_{rb}}^{et} = \begin{bmatrix} \boldsymbol{T_{rb}}_1^{et} & 0 & 0 \\ 0 & \boldsymbol{T_{rb}}_2^{et} & 0 \\ 0 & 0 & \boldsymbol{T_{rb}}_3^{et} \end{bmatrix}$$

where

$\Delta \boldsymbol{u_{sys}}^{et}$	[var.]	Incremental element nodal displacement vector based on consideration of the rigid body coupling conditions
$\Delta \boldsymbol{u}^{et}, \Delta \boldsymbol{u_T}^{et}$	[mm]	Incremental element nodal displacement, elongation vector
$\boldsymbol{T_{rb}}^{et}$	[var.]	Element rigid body transformation tensor reflecting the nodal coupling conditions (second order)

Incremental global forces including rigid body transformations

The same approach also holds for the incremental forces which for coupled nodes are defined at the support representing the imposed vertical force and moment contributions. However, temperature effects are neglected since these are only characterised as prescribed elongations. So, using Eq. (8.40) in inverse form while remembering that the rigid body transformation tensor is not orthogonal results in the incremental global nodal forces:

$$\Delta \boldsymbol{F_S}^{t} = \boldsymbol{T_{rb_{i_{rb}}}}^{t^{-1}} \Delta \boldsymbol{F_{i_{rb}}}^{t} \tag{8.43}$$

where

$\Delta \boldsymbol{F_S}^{t}$	[var.]	Incremental force vector at the support at the current time step
$\Delta \boldsymbol{F_{i_{rb}}}^{t}$	[N]	Incremental force vector at rigid body node 'i' at the current step

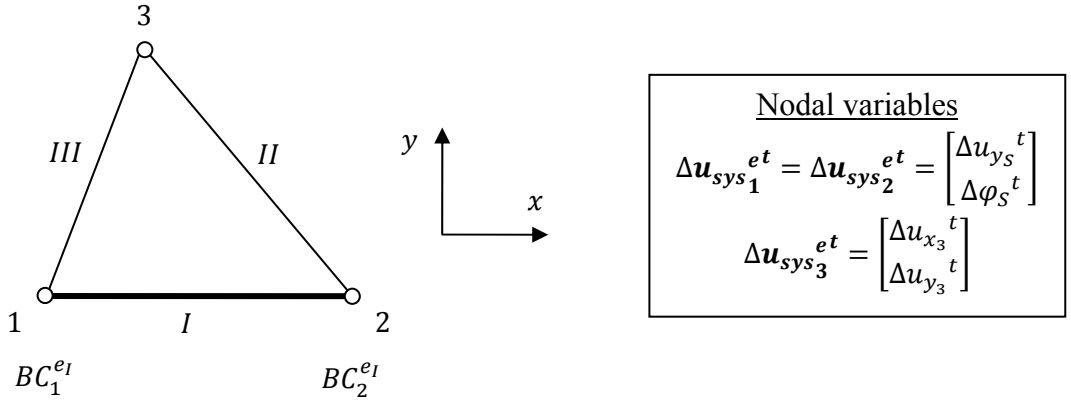

Fig. 8.3 *Boundary conditions are imposed along the first edge of the 2D triangular element in $\mathbb{R}^2$. Both coupled nodes are characterised by translation and rotation of the rigid body, considering their relative distances to the governing support.*

However, to preserve the symmetry in the mechanical stiffness formulation orthogonality is assumed (Hartmann & Katz, 2007; Blaauwendraad, 2004). This approximation is correct since the following can be stated:

$$\begin{aligned} \boldsymbol{T_{rb_{i_{rb}}}}^{t^T}\boldsymbol{T_{rb_{i_{rb}}}}^{t}\Delta\boldsymbol{F_S}^{t} &= \boldsymbol{T_{rb_{i_{rb}}}}^{t^T}\boldsymbol{T_{rb_{i_{rb}}}}^{t}\boldsymbol{T_{rb_{i_{rb}}}}^{t^{-1}}\Delta\boldsymbol{F_{i_{rb}}}^{t} \\ \Delta\boldsymbol{F_S}^{t} &= \left(\boldsymbol{T_{rb_{i_{rb}}}}^{t^T}\boldsymbol{T_{rb_{i_{rb}}}}^{t}\right)^{-1}\boldsymbol{T_{rb_{i_{rb}}}}^{t^T}\Delta\boldsymbol{F_{i_{rb}}}^{t} \end{aligned} \tag{8.44}$$

with

$$\left(\boldsymbol{T_{rb_{i_{rb}}}}^{t^T}\boldsymbol{T_{rb_{i_{rb}}}}^{t}\right)^{-1} = \begin{bmatrix}1 & 0\\ 0 & 1\end{bmatrix} + \begin{bmatrix} \frac{1}{\sin^2{\varphi_S}^t} - 1 & -\frac{cos{\varphi_S}^t}{\sin^2{\varphi_S}^t {d_{rel}}_{i_{rb}}^{\,t}} \\ -\frac{cos{\varphi_S}^t}{\sin^2{\varphi_S}^t {d_{rel}}_{i_{rb}}^{\,t}} & \frac{1}{\sin^2{\varphi_S}^t {d_{rel}}_{i_{rb}}^{\,t^2}} - 1 \end{bmatrix}$$

The matrix multiplication between brackets at the right hand side is divided into two contributions with the first represented by the identity matrix. The second matrix represents the non-orthogonal condition and reflects terms that approach infinity for limited total edge rotations. Assuming orthogonality ensures fulfilment of vertical force and moment equilibrium along the edge. The axial incremental support force consist of vertical force contributions. The incremental moment at the support is based on both horizontal and vertical forces taking the relative distance into account. So, the incremental global supports are approximated as follows:

$$\Delta\boldsymbol{F_S}^{t} \approx \boldsymbol{T_{rb_{i_{rb}}}}^{t^T}\Delta\boldsymbol{F_{i_{rb}}}^{t} \tag{8.45}$$

Moreover, the element-based transposed rigid body transformation tensor defines the incremental global nodal forces at the support according to:

$$\Delta\boldsymbol{F_{sys}}^{et} \approx \boldsymbol{T_{rb}}^{et^T}\Delta\boldsymbol{F}^{et} \tag{8.46}$$

where

$\Delta\boldsymbol{F_{sys}}^{et}$	[var.]	Incremental element nodal force vector based on consideration of the rigid body coupling conditions
$\Delta\boldsymbol{F}^{et}$	[N]	Incremental element nodal force vector

The incremental forces, presented in Eq. (8.36), are through Eq. (8.42) and Eq. (8.46) defined to act across the domain as well as at the supports:

$$\begin{aligned} \Delta\boldsymbol{F_{T_{sys}}}^{et} = \boldsymbol{T_{rb}}^{et^T}\Delta\boldsymbol{F_T}^{et} &= \int_{\Omega^e} \boldsymbol{T_{rb}}^{et^T}\boldsymbol{B_U}^{eT}\left(\boldsymbol{D}^{et+1} - \boldsymbol{D}^{et}\right)\left(\boldsymbol{B_U}^{e}\boldsymbol{u}^{et} - \boldsymbol{\varepsilon_T}^{et}\right)d\Omega^e \\ &+ \int_{\Omega^e} \boldsymbol{T_{rb}}^{et^T}\boldsymbol{B_U}^{eT}\boldsymbol{D}^{et}\left(\boldsymbol{B_U}^{e}\left(\boldsymbol{T_{rb}}^{et}\Delta\boldsymbol{u_{sys}}^{et} + \Delta\boldsymbol{u_T}^{et}\right) - \left(\boldsymbol{\varepsilon_T}^{et+1} - \boldsymbol{\varepsilon_T}^{et}\right)\right)d\Omega^e \end{aligned} \tag{8.47}$$

The force contributions based on the incremental stresses are affected differently:

- The first term, defining the influence of a stiffness variation, is a priori known and governed by the deformed state of the element. The rigid body transformation tensor thus only influences the resultant incremental nodal forces.

- The second term, governing the additional imposed temperature strain, includes the incremental displacements which are also affected by the rigid body transformation as well as the prescribed temperature elongation.

8.3.5 Support conditions

The Neumann boundary condition, defined at both supports, is already reflected in the FEM definition of Eq. (8.27). The incremental spring forces become dependent on the incremental displacements, reflecting a single contribution due to the assumed constant stiffness. The external forces are also constant and imposed before fire exposure. The spring stiffness matrix and the external force vector are expressed in the nodal variables at the support, omitting thus the need to include the rigid body transformation tensor. Furthermore, each support is represented as a node at which stiffness and force contributions are concentrated. Hence, the integrals of the nodal shape functions are omitted and the following is directly obtained:

$$\Delta \boldsymbol{F_{S_{sys}}}^{\boldsymbol{t}} = -\int_{\Gamma_{S_N}{}^{e}} \boldsymbol{N_U}^{eT} \boldsymbol{K_S} \boldsymbol{N_U}^{e} d\Gamma_{S_N}{}^{e}\, \Delta \boldsymbol{u_S}^{\boldsymbol{t}} + \int_{\Gamma_{S_N}{}^{e}} \boldsymbol{N_U}^{eT} \boldsymbol{F_S}^{\boldsymbol{t_0}} d\Gamma_{S_N}{}^{e} = -(\boldsymbol{K_S} \Delta \boldsymbol{u_S}^{\boldsymbol{t}}) + \boldsymbol{F_S}^{\boldsymbol{t_0}} \tag{8.48}$$

with

$$\boldsymbol{F_S} = \begin{bmatrix} F_{y_S} \\ F_{\varphi_S} \end{bmatrix} \qquad \boldsymbol{K_S} = \begin{bmatrix} K_{y_S} & 0 \\ 0 & K_{\varphi_S} \end{bmatrix}$$

where

t_0	[s]	Initial or start time before fire exposure develops
$\Delta \boldsymbol{F_{S_{sys}}}^{\boldsymbol{t}}$	[var.]	Incremental force vector defined at the support expressed in the rigid body nodal variables

8.4 Incremental FEM definition

8.4.1 Discretisation based on homogeneous and isotropic 2D triangular elements

Static equilibrium is considered between the internal temperature-induced forces, defined by Eq. (8.47), and the external imposed structural loading, as reflected in Eq. (8.48). The resultant time-dependent incremental FEM definition is obtained after rearranging:

$$\begin{aligned} &\sum_{e=1}^{e_{tot}} \boldsymbol{K_{sys}}^{\boldsymbol{et}} \sum_{e=1}^{e_{tot}} \Delta \boldsymbol{u_{sys}}^{\boldsymbol{et}} + \sum_{S=1}^{2} \boldsymbol{K_S} \sum_{S=1}^{2} \Delta \boldsymbol{u_S}^{\boldsymbol{t}} \\ &= \sum_{S=1}^{2} \boldsymbol{F_S}^{\boldsymbol{t_0}} - \sum_{e=1}^{e_{tot}} \Delta \boldsymbol{F_{T_{sys_a}}}^{\boldsymbol{et}} + \sum_{e=1}^{e_{tot}} \Delta \boldsymbol{F_{T_{sys_b}}}^{\boldsymbol{et}} - \sum_{e=1}^{e_{tot}} \Delta \boldsymbol{F_{T_{bc}}}^{\boldsymbol{et}} \end{aligned} \tag{8.49}$$

with

$$\boldsymbol{K_{sys}}^{\boldsymbol{et}} = \int_{\Omega^e} \boldsymbol{T_{rb}}^{\boldsymbol{et^T}} \boldsymbol{B_U}^{\boldsymbol{eT}} \boldsymbol{D^{et}} \boldsymbol{B_U}^{\boldsymbol{e}} \boldsymbol{T_{rb}}^{\boldsymbol{et}} d\Omega^e$$

$$\Delta \boldsymbol{F_{T_{sys_a}}}^{\boldsymbol{et}} = \int_{\Omega^e} \boldsymbol{T_{rb}}^{\boldsymbol{et^T}} \boldsymbol{B_U}^{\boldsymbol{eT}} \left(\boldsymbol{D^{et+1}} - \boldsymbol{D^{et}}\right)\left(\boldsymbol{B_U}^{\boldsymbol{e}} \boldsymbol{u^{et}} - \boldsymbol{\varepsilon_T}^{\boldsymbol{et}}\right) d\Omega^e$$

$$\Delta \boldsymbol{F_{T_{sys_b}}}^{\boldsymbol{et}} = \int_{\Omega^e} \boldsymbol{T_{rb}}^{\boldsymbol{et^T}} \boldsymbol{B_U}^{\boldsymbol{eT}} \boldsymbol{D^{et}} \left(\boldsymbol{\varepsilon_T}^{\boldsymbol{et+1}} - \boldsymbol{\varepsilon_T}^{\boldsymbol{et}}\right) d\Omega^e$$

$$\Delta \boldsymbol{F_{T_{bc}}}^{\boldsymbol{et}} = \int_{\Omega^e} \boldsymbol{T_{rb}}^{\boldsymbol{et^T}} \boldsymbol{B_U}^{\boldsymbol{eT}} \boldsymbol{D^{et}} \boldsymbol{B_U}^{\boldsymbol{e}} \Delta \boldsymbol{u_T}^{\boldsymbol{et}} d\Omega^e$$

where

$\boldsymbol{K_{sys}}^{\boldsymbol{et}}$	[var.]	Element system matrix at the current time step
$\Delta \boldsymbol{F_{T_{sys_a}}}^{\boldsymbol{et}}$	[var.]	Element nodal force vector governing the stiffness variation dependent on the current and next time step
$\Delta \boldsymbol{F_{T_{sys_b}}}^{\boldsymbol{et}}$	[var.]	Element nodal force vector governing the additional temperature strain dependent on the current and next time step
$\Delta \boldsymbol{F_{T_{bc}}}^{\boldsymbol{et}}$	[var.]	Element nodal force vector governing the prescribed elongation dependent on the temperature strain development along the edge

The following contributions are present which characterise the system based on:

- The left hand side of the system is defined by summation across the domain of the element stiffness matrices. The system matrix is multiplied by the system vector based on the incremental nodal displacements across the domain and at the supports.

- The right hand side represents the system force vector with the second and third terms governing the temperature-induced stresses. These represent stiffness variations and additional temperature strains based on the current and the next time step.

- The final contribution to the right hand side reflects the temperature-induced elongation forces acting along the top and bottom edges. These are defined relative to the central supports and based on the unrestrained temperature strain development.

- The system definition is influenced by the rigid body transformation tensor, imposing master-slave relationships along the outer edges (Hartmann & Katz, 2007). Nodes situated along these edges are coupled to the central supports.

- Structural interaction at these supports is characterised by the Neumann boundary condition. This is represented by the spring stiffness matrices at the left hand side. The external force vectors are included at the right hand side only before fire exposure.

8.4.2 Spatial integration based on linear triangular shape functions

The element-based integrals are numerically approximated by using 2D triangular elements (van Kan, et al., 2008). These elements, similar to the ones used in chapter 6, full fill C^0 continuity through linear varying shape functions (van Kan, et al., 2008; Felippa, 2004a). Across each element the nodal displacements are linearly approximated while ensuring compatibility between elements (van Kan, et al., 2008; Felippa, 2004a). For each element, the incremental displacements are defined according to Eq. (8.26) which obtains:

$$\Delta \boldsymbol{u}^{\boldsymbol{e}}(\boldsymbol{x}^{\boldsymbol{e}}, t) \approx \boldsymbol{N_U}^{\boldsymbol{e}}(\boldsymbol{x}^{\boldsymbol{e}}) \Delta \boldsymbol{u}^{\boldsymbol{et}} \tag{8.50}$$

with

$$\Delta \boldsymbol{u}(\boldsymbol{x}^{\boldsymbol{e}}, t) = \begin{bmatrix} \Delta {u_x}^e(\boldsymbol{x}^{\boldsymbol{e}}, t) \\ \Delta {u_y}^e(\boldsymbol{x}^{\boldsymbol{e}}, t) \end{bmatrix}$$

$$\boldsymbol{N_U}^{\boldsymbol{e}}(\boldsymbol{x}^{\boldsymbol{e}}) = \begin{bmatrix} \xi_1 & 0 & \xi_2 & 0 & \xi_3 & 0 \\ 0 & \xi_1 & 0 & \xi_2 & 0 & \xi_3 \end{bmatrix} = \begin{bmatrix} N_{U_1}^e & 0 & N_{U_2}^e & 0 & N_{U_3}^e & 0 \\ 0 & N_{U_1}^e & 0 & N_{U_2}^e & 0 & N_{U_3}^e \end{bmatrix} \qquad \Delta \boldsymbol{u}^{\boldsymbol{et}} = \begin{bmatrix} \Delta {u_{x_1}}^{et} \\ \Delta {u_{y_1}}^{et} \\ \Delta {u_{x_2}}^{et} \\ \Delta {u_{y_2}}^{et} \\ \Delta {u_{x_3}}^{et} \\ \Delta {u_{y_3}}^{et} \end{bmatrix}$$

The incremental strains are constant across each element through consideration of the partial derivatives of the linear nodal shape functions (Felippa, 2004a; Zienkiewicz, et al., 2005). These elements are therefore commonly referred to as constant strain triangles (Felippa, 2004a; Blom, 2009). It is important to realise that the third row in this gradient matrix represents the coupled derivatives governing the shearing strain (Felippa, 2004a):

$$\Delta \boldsymbol{\varepsilon}^{\boldsymbol{e}}(t) \approx \boldsymbol{B_U}^{\boldsymbol{e}} \Delta \boldsymbol{u}^{\boldsymbol{et}} \tag{8.51}$$

with

$$\Delta \boldsymbol{\varepsilon}^{\boldsymbol{e}}(t) = \begin{bmatrix} \Delta {\varepsilon_{xx}}^e(t) \\ \Delta {\varepsilon_{yy}}^e(t) \\ \Delta {\gamma_{xy}}^e(t) \end{bmatrix} = \begin{bmatrix} \dfrac{\partial \Delta {u_x}^e(t)}{\partial x} \\ \dfrac{\partial \Delta {u_y}^e(t)}{\partial y} \\ \dfrac{\partial \Delta {u_x}^e(t)}{\partial y} + \dfrac{\partial \Delta {u_y}^e(t)}{\partial x} \end{bmatrix} \begin{bmatrix} \dfrac{\partial \Delta {u_x}^e(t)}{\partial N_{U_1}^e} \\ \dfrac{\partial \Delta {u_y}^e(t)}{\partial N_{U_1}^e} \\ \dfrac{\partial \Delta {u_x}^e(t)}{\partial N_{U_2}^e} \\ \dfrac{\partial \Delta {u_y}^e(t)}{\partial N_{U_2}^e} \\ \dfrac{\partial \Delta {u_x}^e(t)}{\partial N_{U_3}^e} \\ \dfrac{\partial \Delta {u_y}^e(t)}{\partial N_{U_3}^e} \end{bmatrix} = \begin{bmatrix} \Delta {u_{x_1}}^{et} \\ \Delta {u_{y_1}}^{et} \\ \Delta {u_{x_2}}^{et} \\ \Delta {u_{y_2}}^{et} \\ \Delta {u_{x_3}}^{et} \\ \Delta {u_{y_3}}^{et} \end{bmatrix} = \Delta \boldsymbol{u}^{\boldsymbol{et}}$$

$$\boldsymbol{B_U}^{\boldsymbol{e}} = \begin{bmatrix} \dfrac{\partial N_{U_1}^e}{\partial x} & 0 & \dfrac{\partial N_{U_2}^e}{\partial x} & 0 & \dfrac{\partial N_{U_3}^e}{\partial x} & 0 \\ 0 & \dfrac{\partial N_{U_1}^e}{\partial y} & 0 & \dfrac{\partial N_{U_2}^e}{\partial y} & 0 & \dfrac{\partial N_{U_3}^e}{\partial y} \\ \dfrac{\partial N_{U_1}^e}{\partial y} & \dfrac{\partial N_{U_1}^e}{\partial x} & \dfrac{\partial N_{U_2}^e}{\partial y} & \dfrac{\partial N_{U_2}^e}{\partial x} & \dfrac{\partial N_{U_3}^e}{\partial y} & \dfrac{\partial N_{U_3}^e}{\partial x} \end{bmatrix} = \frac{1}{2A^e} \begin{bmatrix} y_{23} & 0 & y_{31} & 0 & y_{12} & 0 \\ 0 & x_{32} & 0 & x_{13} & 0 & x_{21} \\ x_{32} & y_{23} & x_{13} & y_{31} & x_{21} & y_{12} \end{bmatrix}$$

Inserting these relationships into the FEM definition, stated in Eq. (8.49), and evaluation of the integrals obtains the element stiffness matrix and the nodal force vectors. The Neumann boundary condition is already established by consideration of the stiffness and force concentrations at the supports.

Element stiffness matrix

The contribution of each element to the stiffness of the continuum is determined by the integral at the left hand side. The elasticity tensor, the rigid body transformation tensor and the gradient matrix, stated in Eq. (8.6), Eq. (8.42) and Eq. (8.51) respectively, are all defined constant across the element. So, direct integration obtains the element stiffness matrix:

$$\boldsymbol{K_{sys}}^{\boldsymbol{et}} = DA^{e}\boldsymbol{T_{rb}}^{\boldsymbol{et^T}}\boldsymbol{B_U}^{e^T}\boldsymbol{D}^{\boldsymbol{et}}\boldsymbol{B_U}^{e}\boldsymbol{T_{rb}}^{\boldsymbol{et}} \tag{8.52}$$

Temperature-induced nodal forces

The thermal forces are governed by two contributions which are defined by the first and second integrals at the right hand side of Eq. (8.49). Direct integration yields the following relations:

$$\begin{aligned}\Delta\boldsymbol{F_{T_{sys_a}}}^{\boldsymbol{et}} &= DA^{e}\boldsymbol{T_{rb}}^{\boldsymbol{et^T}}\boldsymbol{B_U}^{e^T}\left(\boldsymbol{D}^{\boldsymbol{et+1}} - \boldsymbol{D}^{\boldsymbol{et}}\right)\left(\boldsymbol{B_U}^{e}\boldsymbol{u}^{\boldsymbol{et}} - \boldsymbol{\varepsilon_T}^{\boldsymbol{et}}\right)\\ \Delta\boldsymbol{F_{T_{sys_b}}}^{\boldsymbol{et}} &= DA^{e}\boldsymbol{T_{rb}}^{\boldsymbol{et^T}}\boldsymbol{B_U}^{e^T}\boldsymbol{D}^{\boldsymbol{et}}\left(\boldsymbol{\varepsilon_T}^{\boldsymbol{et+1}} - \boldsymbol{\varepsilon_T}^{\boldsymbol{et}}\right)\end{aligned} \tag{8.53}$$

Along the top and bottom edges additional thermal forces are imposed based on prescribed temperature elongations. These are assumed to develop unrestrained and relative to the central support. Summation of the element contributions outwards defines the total incremental displacement assumed to develop along the rotated edge. So, the thermal elongation forces along the boundary, defined by the third integral, are approximated as:

$$\Delta\boldsymbol{F_{T_{bc}}}^{\boldsymbol{et}} = DA^{e}\boldsymbol{T_{rb}}^{\boldsymbol{et^T}}\boldsymbol{B_U}^{e^T}\boldsymbol{D}^{\boldsymbol{et}}\boldsymbol{B_U}^{e}\Delta\boldsymbol{u_T}^{\boldsymbol{et}} \tag{8.54}$$

8.5 Obtaining the solution and results analyses

The FEM definition in Eq. (8.49) approximates the isotropic and linear elastic continuum, defined by Eq. (8.5), considering the plane strain stress increment expressed by Eq. (8.6) (Timoshenko & Goodier, 1970). Solution is obtained through a more common Conjugate Gradient Solver with Jacobi Preconditioning based on consideration of the symmetrical FEM discretisation (van Kan, et al., 2008; Barrett, et al., 1994).

Incremental nodal displacements

The solver starts with an initial incremental solution for the nodal displacements of zero. The obtained incremental solution is used to update the current global displacements according to Eq. (8.28). For nodes across the domain this is relatively straightforward. However, for nodes situated along the outer edges, the rigid body transformation tensor, defined by Eq. (8.40), needs to be considered. Prescribed temperature elongations are directly added to the global displacements.

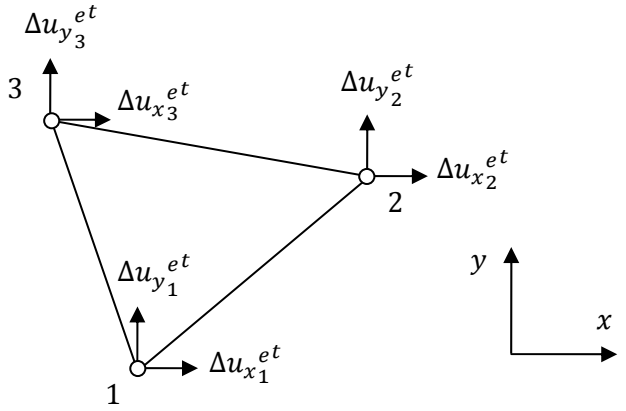

Incremental stresses and strains (element)

$$\Delta\boldsymbol{\sigma}^{\boldsymbol{et}} = \begin{bmatrix} \Delta\sigma_{xx}{}^{et} \\ \Delta\sigma_{yy}{}^{et} \\ \Delta\sigma_{xy}{}^{et} \end{bmatrix}$$

$$\Delta\boldsymbol{\varepsilon}^{\boldsymbol{et}} = \begin{bmatrix} \Delta\varepsilon_{xx}{}^{et} \\ \Delta\varepsilon_{yy}{}^{et} \\ \Delta\gamma_{xy}{}^{et} \end{bmatrix}$$

Fig. 8.4 *Linear approximation of the incremental displacements across the 2D triangular element in $\mathbb{R}^2$ defining the stress and strain increments to be constant.*

Incremental element strains, stresses and the total elastic strain energy

For the isotropic FEM discretisation only the global mechanical strains and especially stresses are of interest, defined in incremental form through Eq. (8.29) (Zienkiewicz, et al., 2005). The incremental global displacements across each element are approximated through linear shape functions and the nodal values as shown in Fig. 8.4 (Felippa, 2004a). This defines the incremental global strains to be constant based on Eq. (8.51), omitting the imposed temperature strain increment:

$$\Delta\boldsymbol{\varepsilon_m}^{\boldsymbol{et}} = \boldsymbol{B_U}^{\boldsymbol{e}}\Delta\boldsymbol{u}^{\boldsymbol{et}} - \left(\boldsymbol{\varepsilon_T}^{\boldsymbol{et+1}} - \boldsymbol{\varepsilon_T}^{\boldsymbol{et}}\right) \tag{8.55}$$

The incremental global stresses are first defined by the stiffness variation of the element which is preliminary known and based on the mechanical strains using the current deformed state. The second contribution is determined by the incremental global nodal displacements and reflects the structural response to the incremental forces. This latter contribution is thus governed by the mechanical strain increment. So, restating both contributions from Eq. (8.36):

$$\Delta\boldsymbol{\sigma}^{\boldsymbol{et}} = \left(\boldsymbol{D}^{\boldsymbol{et+1}} - \boldsymbol{D}^{\boldsymbol{et}}\right)\left(\boldsymbol{B_U}^{\boldsymbol{e}}\boldsymbol{u}^{\boldsymbol{et}} - \boldsymbol{\varepsilon_T}^{\boldsymbol{et}}\right) + \boldsymbol{D}^{\boldsymbol{et}}\left(\boldsymbol{B_U}^{\boldsymbol{e}}\Delta\boldsymbol{u}^{\boldsymbol{et}} - \left(\boldsymbol{\varepsilon_T}^{\boldsymbol{et+1}} - \boldsymbol{\varepsilon_T}^{\boldsymbol{et}}\right)\right) \tag{8.56}$$

The total mechanical strains and stresses present in each element are used to determine the elastic strain energy defined at the next time step. Using Eq. (8.32) and applying direct integration yields the following:

$$U_{\varepsilon}{}^{et+1} = \int_{\Omega^e} \frac{1}{2}\boldsymbol{\varepsilon_m}^{\boldsymbol{et+1}^{\boldsymbol{T}}}\boldsymbol{\sigma}^{\boldsymbol{et+1}}d\Omega^e = \frac{DA^e}{2}\boldsymbol{\varepsilon_m}^{\boldsymbol{et+1}^{\boldsymbol{T}}}\boldsymbol{\sigma}^{\boldsymbol{et+1}} \tag{8.57}$$

Incremental support reactions

The support reactions are governed by the incremental global displacements through Eq. (8.48). The initially imposed external forces are partially restrained by the incremental spring forces which for each support are defined by:

$$\Delta\boldsymbol{F}_{\boldsymbol{S_{sys}}}{}^{\boldsymbol{t}} = \boldsymbol{F_S}^{\boldsymbol{t_0}} - \boldsymbol{K_S}\Delta\boldsymbol{u_S}^{\boldsymbol{t}} \tag{8.58}$$

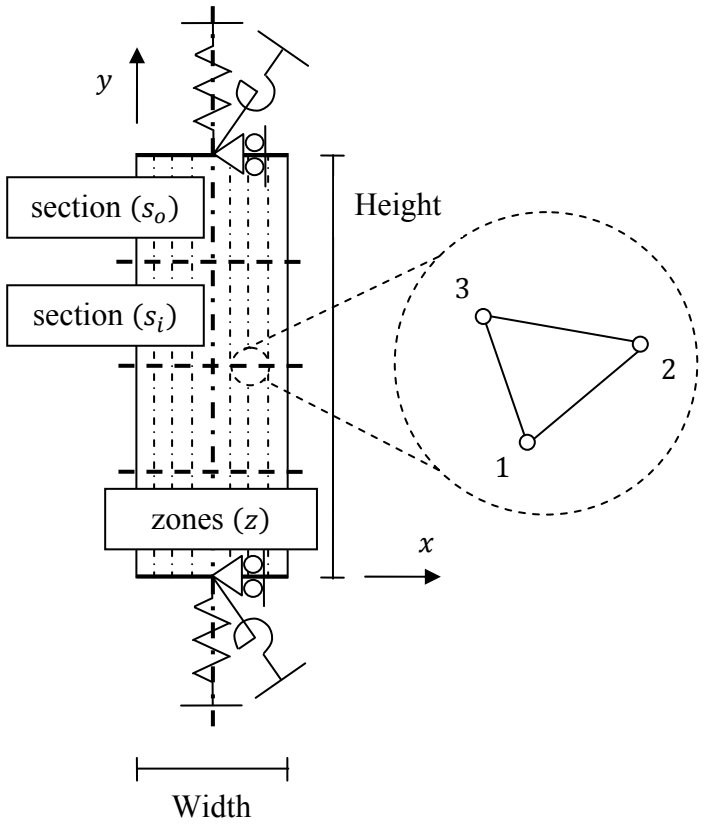

Stress averaging
(per section, per zone)

$$\sigma_{xx}{}_{avg}{}_{z}^{s\,t+1} = \frac{\sum_{e=1}^{e_{tot_z}^s}\left(\sigma_{xx}{}^{e\,t+1} A^e\right)}{\sum_{e=1}^{e_{tot_z}^s} A^e}$$

$$\sigma_{yy}{}_{avg}{}_{z}^{s\,t+1} = \frac{\sum_{e=1}^{e_{tot_z}^s}\left(\sigma_{yy}{}^{e\,t+1} A^e\right)}{\sum_{e=1}^{e_{tot_z}^s} A^e}$$

$$\sigma_{xy}{}_{avg}{}_{z}^{s\,t+1} = \frac{\sum_{e=1}^{e_{tot_z}^s}\left(\sigma_{xy}{}^{e\,t+1} A^e\right)}{\sum_{e=1}^{e_{tot_z}^s} A^e}$$

Fig. 8.5 *Cross-sectional distributions are obtained through averaging the element-based constant stresses across zones in width direction. The subdivision in height direction distinguishes between outer and inner sections as indicated in* $\mathbb{R}^2$.

Cross-sectional distributions

Similar to chapter 6 the constant element stresses are averaged by using the cross-sectional subdivision in width direction. However, in height direction also 4 sections are distinguished, reflecting the symmetrical conditions. Across both top sections, schematically shown in Fig. 8.5, stresses are averaged in order to assess the influence of the rigid bodies. The cross-sectional stress distributions obtained are comparable to the numerical results from chapter 5.

8.6 Conclusions with respect to the FEM definition

Regarding the theoretical framework the following conclusions and remarks are made:

- Schematisation of the concrete element reflects a 2D cross-section characterised by a homogeneous and isotropic material description. The out-of-plane displacements are restrained governed by a plane strain assumption (Timoshenko & Goodier, 1970).

- The balance of linear momentum defines static equilibrium across the continuum as stated in Eq. (8.1) (Spencer, 1980/2004; Felippa, 2004b). The symmetrical stress and strain tensors are related through the linear elastic material description according to Hooke's law (Timoshenko & Goodier, 1970). The resultant PDE is stated in Eq. (8.5) (Spencer, 1980/2004; Wells, 2006) or through engineering notation defined by the stresses in Eq. (8.6) (Prezemieniecki, 1968/1985; Wells, 2006).

- Structural interaction is imposed through combined Dirichlet and Neumann boundary conditions (van Kan, et al., 2008) as stated in Eq. (8.7) and Eq. (8.8) respectively. Imposing the linear strain according to Bernoulli's hypothesis (Hartsuijker & Welleman, 2007) involves definition of rigid bodies along the outer edges, characterised by incremental coupling conditions (Hartmann & Katz, 2007).

The FEM approximation of the incremental displacements is based on:

- Definition of the energy functional involving the dot product between the variables and the PDE as stated in Eq. (8.10) (van Kan, et al., 2008; Zienkiewicz, et al., 2005). Minimisation of this functional with respect to the displacements, neglecting imposed temperature elongations, defines the PDE.

- Conservation of energy is obtained through integration by parts applied to Gauss' divergence theorem stated for the functional in Eq. (8.14) (van Kan, et al., 2008; Zienkiewicz, et al., 2005). The internal elastic strain energy and the produced work by forces at the supports are expressed by Eq. (8.15). The weak form in Eq. (8.21) is obtained by minimisation of the functional with respect to the parameter governing the variation (van Kan, et al., 2008; Zienkiewicz, et al., 2005).

- The solution is approximated by Galerkin's method based on a linear combination of basis or shape functions and nodal variables (van Kan, et al., 2008; Segal, 2008). FEM discretisation by elements distributed across the domain is formulated by Eq. (8.27) (van Kan, et al., 2008).

- The FEM definition is restated in incremental form obtained through consideration of the element-based elastic strain energy, leading to the incremental stresses stated in Eq. (8.34) (Zienkiewicz, et al., 2005).

- Rigid bodies defined at both outer edges are based on incremental vertical translational and rotational motions (Hartmann & Katz, 2007). The transformation tensor relates the incremental nodal displacements along the edge to deformation of the central support, expressed in the global coordinate system through Eq. (8.40). Temperature elongations are prescribed along the edge relative to the central support.

- The incremental FEM definition in Eq. (8.49) is obtained by consideration of static equilibrium between the internal temperature-induced forces, Eq. (8.47), and the imposed structural loading, Eq. (8.48). Linear triangular elements defined by Eq. (8.50) and Eq. (8.51) govern the FEM approximation (van Kan, et al., 2008; Felippa, 2004a; Zienkiewicz, et al., 2005). The element stiffness matrix is stated in Eq. (8.52) whereas the temperature-induced nodal force vectors are presented in Eq. (8.53). From Eq. (8.48) the Neumann boundary condition is directly obtained.

The solution approach and results analyses are addressed by consideration of:

- The symmetrical FEM definition is solved by a Jacobi preconditioned Conjugate Gradient Solver (van Kan, et al., 2008; Barrett, et al., 1994). The incremental solution is used through Eq. (8.28) to develop the displacements while considering the rigid body transformations and temperature elongations. Incremental stresses reflect stiffness variations and imposed temperature strains as stated by Eq. (8.56).

- Cross-sectional distributions are obtained by averaging the element stresses across zones in width direction. Furthermore, an additional subdivision in inner and outer sections is provided to assess the structural boundary conditions.

8.7 FEM approximation based on homogeneous and isotropic concrete

Validation of the FEM definition with respect to the incremental displacements and stresses is implemented for the concrete structural element. After briefly presenting the homogeneous discretisation by 2D triangular elements, the support and rigid body boundary conditions are discussed. Subsequently, several loading scenarios with and without internal temperature strain development are examined. Comparison with results from chapter 5 allows to check for a correct implementation as well as determine if static equilibrium is approximated with sufficient accuracy.

8.7.1 Homogeneous discretisation of the cross-section

The cross-section used is shown in Fig. 8.6 and represents part of the structural element as discussed in chapter 3. The height is chosen four times larger than the width of 250 mm in order to mitigate possible edge effects caused by imposing the rigid body boundary conditions. Contrary to the material mesh used in the previous chapters are the top and bottom edges straight in order to impose the coupling conditions. Both central supports are governed by the Neumann boundary condition, representing structural interaction in the axial and rotational directions. Displacement in the horizontal direction is restrained by fixed supports. Internal loading of the cross-section is characterised only by imposed strains, dependent on the temperature distribution assumed constant in height direction. The material is discretised by the same randomly orientated triangular elements as used in chapter 6. The resulting dense mesh is adopted by consideration of the required detail in the crack pattern at the material level as is the focus of the next chapter. An overview of the characterisation of the mesh is provided in Table 8.1.

Geometry of the mesh	
Width	250 mm
Height	1000 mm
Unit thickness	1 mm
FEM discretisation	
Total number of nodes	40501
Total number of triangles	80000

Table 8.1 *Dimensions and element discretisation of the mesh used to approximate the concrete structural element.*

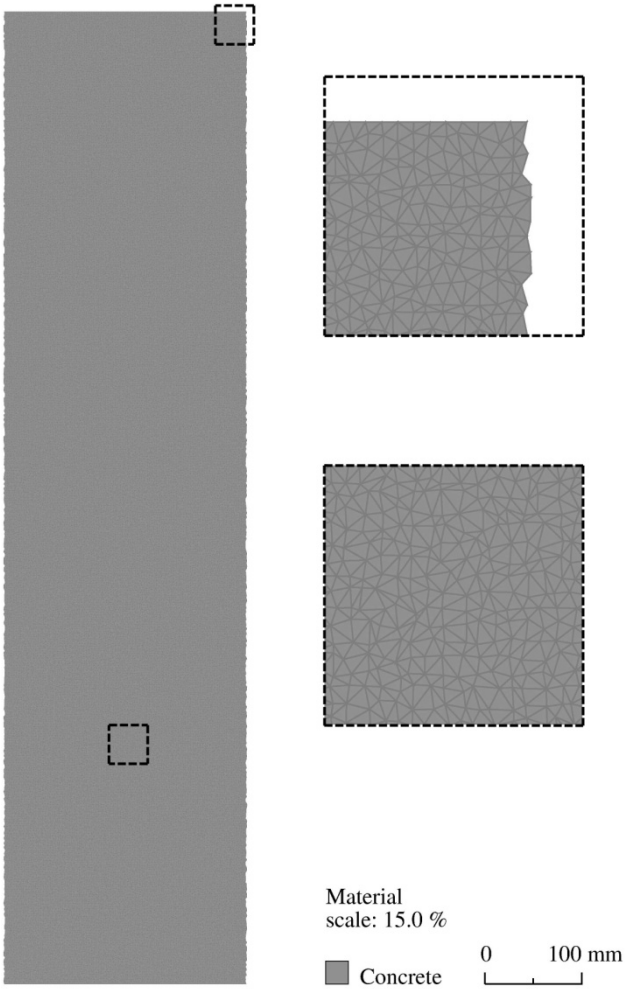

Fig. 8.6 *Discretisation by 2D triangular elements used to numerically approximate the behaviour of the homogeneous and isotropic concrete structural element*

8.7.2 Validation of static equilibrium by comparison of displacements and stresses

The FEM definition is validated by comparison of results obtained for several loading scenarios as presented in chapter 5. Both numerical approximations are defined to fulfil the static equilibrium conditions and should thus yield the same results. This is checked through the displacements and forces at the top support as well as averaging of the global element stresses in order to obtain the cross-sectional distributions as indicated in Fig. 8.5. The assumed homogeneous material is characterised by the properties indicated in chapter 5. However, the FEM definition is based on the 2D simplification of the mechanical continuum using a plane strain assumption while considering the lateral contractions (Timoshenko & Goodier, 1970). For plane concrete, Poisson's ratio is at reference conditions commonly assumed constant as stated in Table 8.2 (Eurocode 2, 2011a).

Material (homogeneous)	
Strength class	independent
Poisson's ratio	0.2

Table 8.2 *Constant material property required to characterise homogeneous concrete, independent of the strength class* (Eurocode 2, 2011a).

Constant temperature scenarios		
Calculation	**8.1A**	**8.1B**
Reference temperature	**20 °C**	**400 °C**
Material (homogeneous)		
Strength class	C25/30	C25/30
Aggregate type	independent	RG
Boundary conditions		
Axial force	-2.0 kN	-2.0 kN
Moment	-0.05 kNm	-0.05 kNm
Axial spring stiffness	4 kN/mm	4 kN/mm
Rotational spring stiffness	20 kNm/rad	20 kNm/rad

Table 8.3 *Two scenarios used to validate the FEM definition with respect to a uniform temperature distribution in the cross-section.*

The relationship between perpendicular strains during thermally-induced deformations is hardly investigated (RILEM TC-HTC, 2004). In this thesis, Poisson's ratio is therefore assumed constant which implies that only variation of Young's modulus governs the temperature dependence in the stiffness characterisation of the material. Finally, recalling from chapter 5, this elasticity tensor can also reflect a plane stress assumption. In validation of the FEM definition both material schematisations are interchanged for comparison with the cross-sectional relationships.

Constant temperature in the cross-section

Two uniform temperatures, shown in Table 8.3, are used to validate the numerical approximation of static equilibrium. At reference conditions only the strength class governs the structural response to the externally imposed forces. At elevated temperatures also internal loading is introduced through imposed strains, largely affected by the aggregate type (Eurocode 2, 2011b). Comparison with results taken from chapter 5 indicates that the FEM definition yields the same cross-sectional stresses at reference conditions with only limited influence of the chosen structural simplification. However, it is also observed from Fig. 8.7 that at a constant temperature of 400 °C the stresses increase by around 20 percent.

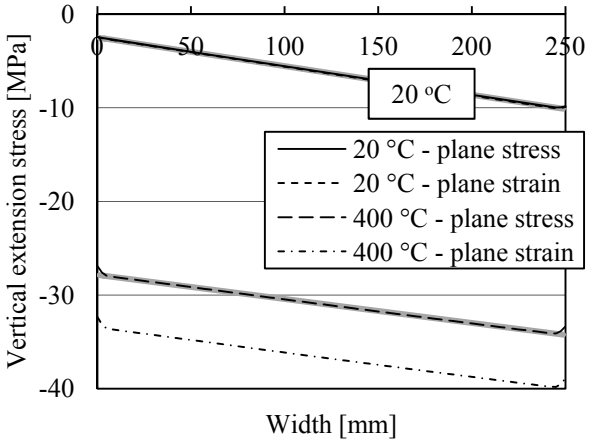

Fig. 8.7 *Comparison of the vertical normal stress distributions at uniform temperatures in the C25/30 cross-section for both numerical approximations.*

Linear temperature scenarios (I)		
Calculation	**8.2A**	**8.2B**
Maximum temperature (left edge)	**400 °C**	**800 °C**
Material (homogeneous)		
Strength class	C25/30	C25/30
Aggregate type	RG	RG
Boundary conditions		
Axial spring stiffness	4 kN/mm	4 kN/mm
Rotational spring stiffness	20 kNm/rad	20 kNm/rad

Table 8.4 *Temperature gradients used to validate the non-linear stress distribution in the cross-section based on partial restraint.*

These results indicate that the cross-sectional relationships, derived in chapter 5 by consideration of only in-plane static equilibrium, actually represent a plane stress assumption. The influence of this inherent assumption increases with development of the displacement in depth direction. At high temperatures the restraint of the uniform out-of-plane thermal expansion increases the in-plane mechanical strains as governed by Poisson's ratio (Timoshenko & Goodier, 1970; Prezemieniecki, 1968/1985). This is reflected in the definition of the elasticity tensor as well as the imposed temperature strain vector.

Linear temperature in the cross-section

The ability for the FEM definition to determine non-linear stress distributions is validated by assuming linear temperature gradients in the cross-section as indicated in Table 8.4. The resultant cross-sectional stress distributions shown in Fig. 8.8 indicate a good agreement for the plane stress state in comparison with results restated from chapter 5. Moreover, assuming a plane strain schematisation, again causes a 20 percent increase of the vertical stresses. It is important to notice as well that the FEM model captures softening of the compressive stresses at the left edge caused by the thermal loading exceeding a temperature of 500 °C. This is reflected for both material schematisations, indicating also a sudden change due to the constant temperature strain at temperatures higher than 700 °C (Eurocode 2, 2011b).

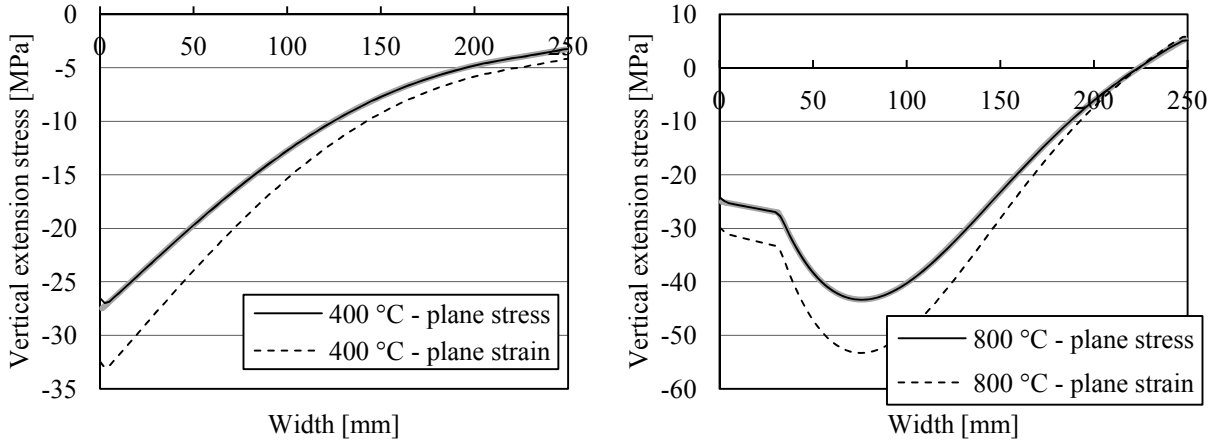

Fig. 8.8 *Stress distributions in the C25/30 cross-section imposed by a linear temperature gradient indicating a sufficient approximation by the FEM definition.*

Deformation at top support			
Calculation	Reference	Plane stress	Plane strain
Maximum temperature = 400 ^{o}C			
Vertical displacement	7.5E-1 mm	7.5E-1 mm	9.1E-1 mm
Rotation	-6.4E-3 rad	-6.4E-3 rad	-7.8E-3 rad
Maximum temperature = 800 ^{o}C			
Vertical displacement	1.5E0 mm	1.5E0 mm	1.8E0 mm
Rotation	-1.1E-2 rad	-1.1E-2 rad	-1.4E-2 rad

Table 8.5 *Overview of the deformation variables at the top support assuming linear temperature variations in combination with cross-sectional schematisations.*

A final check is provided in Table 8.5 through the vertical displacement and rotation at the top support. The results indicate the same general trend in comparison to the reference values obtained from chapter 5. The plane stress schematisation estimates the same deformations whereas the restraint in the out-of-plane direction increases both support variables. Similar results can also be determined for the axial force and moment at the support.

Temperature gradient caused by fire exposure

The final check is provided through imposing the temperature distributions after 900 and 1800 seconds of exposure according to a HC fire curve, obtained using the FEM model stated in chapter 6. Both scenarios, restated from chapter 5 in Table 8.6, represent instant thermal loading of the material. From the resultant cross-sectional stresses in Fig. 8.9 it is observed that the plane stress assumption yields the same results in comparison to the reference state. The plane strain schematisation increases the thermal loading. Compressive stresses in the heated surface layer are around 20 percent higher. In the centre of the cross-section the same increase is indicated for the tensile stress state. Furthermore, softening of the compressive stresses indicates the same peak as already observed in chapter 5. This aspect in the thermal stress distribution is present for both in-plane schematisations and with sufficiently accuracy captured by the FEM approximation.

Fire scenarios (I)		
Calculation	**8.3A**	**8.3B**
Incremental time step size	2.5 sec	2.5 sec
Temperature distribution after	900 / 1800 sec	
Material (homogeneous)		
Strength class	C25/30	C25/30
Aggregate type	RG	RG
Boundary conditions		
Fire scenario	HC	HC
Convective heat transfer coeff.	50 W/m^{2}K	50 W/m^{2}K
Axial spring stiffness	4 kN/mm	4 kN/mm
Rotational spring stiffness	20 kNm/rad	20 kNm/rad

Table 8.6 *Validation of thermal stresses based on two temperature distributions characterised by material and boundary conditions.*

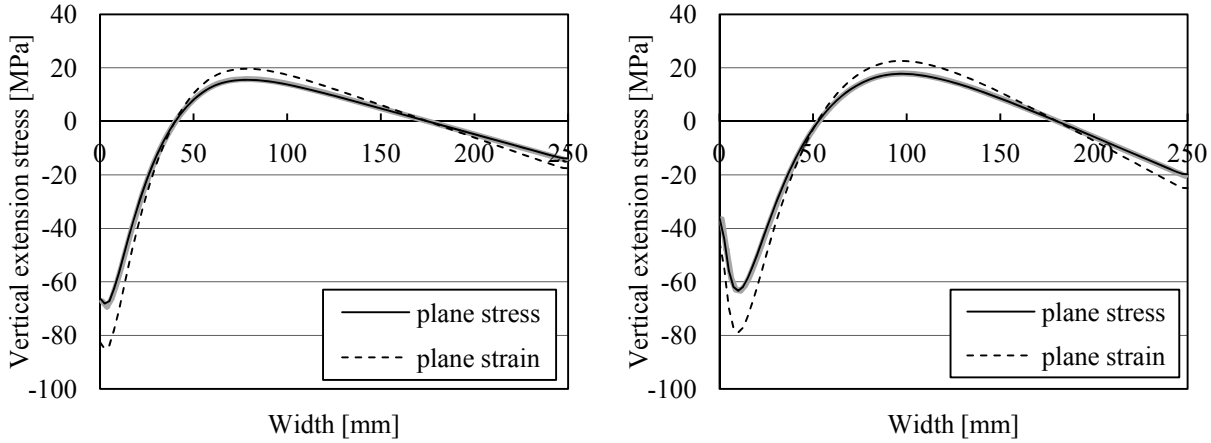

Fig. 8.9 *Instant loading of C25/30 after 900 seconds (left) and 1800 seconds (right) of fire exposure reflecting the influence of the adopted mechanical schematisation.*

Validation of the vertical displacement and rotation at the top support confirms this as reflected in Table 8.7. It is also remarked that compared with the imposed linear temperature distributions the differences with respect to the reference state are marginally larger. This is attributed to the non-linear Young's modulus and imposed temperature strain distributions in the cross-section.

Incremental development of displacements and stresses

In the preceding calculations time-dependent development of the temperature-induced displacements and stresses is not included. In order to validate the adopted incremental FEM approach, the highest linear temperature scenario is considered. The maximum temperature of 800 ^{o}C is, through a number of load increments, imposed at the left edge of the structural element. The plane stress elasticity tensor of each triangular element is under these circumstances defined at the previous load step, characterised by the temperature-dependent Young's modulus. Internal loading consist of incremental temperature strains extended by the forces required to redistribute the stresses caused by variation of the element-based stiffness. Structural boundary conditions are assumed to be constant. Addition of the displacement and stress increments is characterised by the linear elastic assumption of superposition governing the mechanical response. Finally, the number of load steps is also varied to reflect on possible non-linear effects as indicated in Table 8.8.

Deformation at top support			
Calculation	Reference	Plane stress	Plane strain
Temperature distribution after 900 sec			
Vertical displacement	1.6E-1 mm	1.6E-1 mm	2.0E-1 mm
Rotation	-3.3E-3 rad	-3.2E-3 rad	-3.9E-3 rad
Temperature distribution after 1800 sec			
Vertical displacement	2.8E-1 mm	2.8E-1 mm	3.4E-1 mm
Rotation	-5.0E-3 rad	-5.0E-3 rad	-6.0E-3 rad

Table 8.7 *Influence of the adopted schematisation in comparison with the reference deformation at the top support imposed by fire-based temperature distributions.*

Linear temperature scenario (II)		
Calculation	**8.4A**	**8.4B**
Reference temperature	20 °C	20 °C
Maximum temperature (left edge)	800 °C	800 °C
Number of incremental load steps	1 X	8 X, 16 X, 32 X, 64 X, 128 X
Material (homogeneous)		
Strength class	C25/30	C25/30
Aggregate type	RG	RG
Boundary conditions		
Axial spring stiffness	4 kN/mm	4 kN/mm
Rotational spring stiffness	20 kNm/rad	20 kNm/rad

Table 8.8 *Validation of the incremental displacements and stresses for a linear temperature scenario based on the number of load steps.*

Incremental development of the cross-sectional stresses is validated by comparison with the plane stress solution stated in chapter 5. Whereas the instant results, shown in the right graph of Fig. 8.8, are almost identical, the incremental solutions are characterised by a converging behaviour. The vertical stresses shown in Fig. 8.10 are estimated to approach the static solution by increasing the number of load steps. Reduction of the temperature increment allows the force contributions to become sufficiently small. This behaviour is especially pronounced at the left edge where softening of the material occurs.

It is also observed that comparing the converged results to the instant static stress distributions indicates no significant changes. The FEM definition is based on characterisation of the material through element-based strains relative to the reference state. Geometric non-linearity is only considered for the rigid body boundary conditions. Under these circumstances the influence of the incremental approach is limited and reflects mainly superposition.

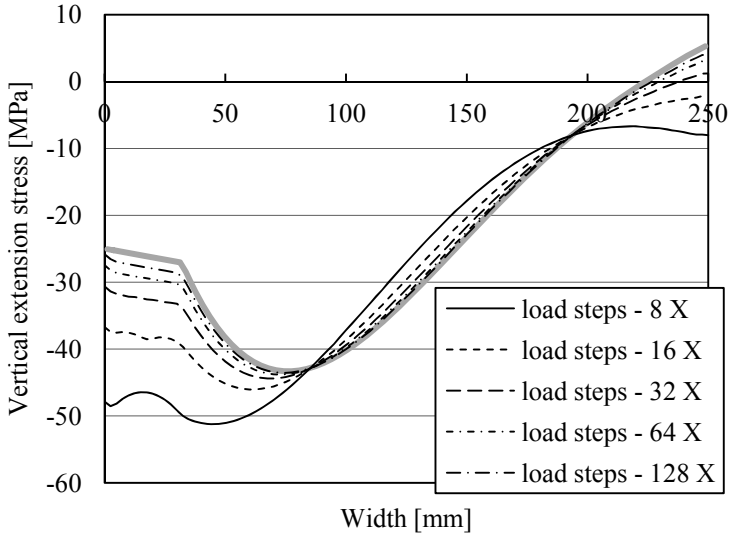

Fig. 8.10 *Incremental development of the main stresses in the C25/30 cross-section, reflecting the non-linear influence of temperature-induced material softening.*

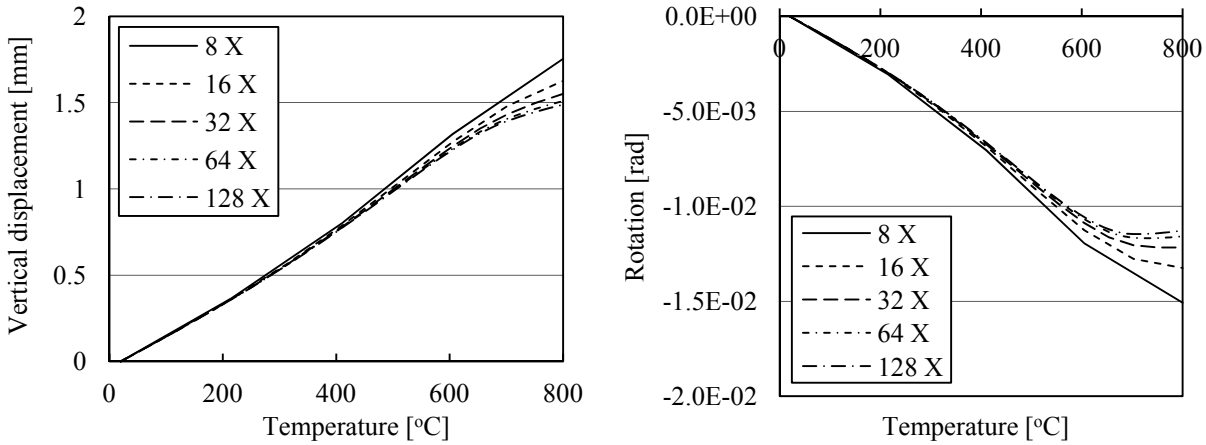

Fig. 8.11 *Vertical displacement (left) and rotation (right) development at the top support indicating dependence on the number of load steps.*

This is also illustrated in Fig. 8.11 by the incremental dependence of the vertical displacement and rotation at the top support. At temperatures lower than 500 °C only a small influence of the load increment is observed. However, softening of the material causes both deformation variables to relax, requiring a reduction of the step size to avoid overestimation.

Conclusions regarding the FEM definition

Based on the presented numerical validations the following can be deduced:

- The FEM definition and element discretisation are sufficiently accurate to approximate in-plane static equilibrium in the cross-section.

- The cross-sectional distributions determined in chapter 5 are based on consideration of in-plane static equilibrium. This inherent simplification assumes a plane stress schematisation and neglects the out-of-plane direction.

- Structural schematisation through a plane strain assumption increases deformations and stresses by around 20 percent. This is attributed to restraint of the out-of-plane strains, governed by assumed constant Poisson's ratio.

- Accuracy of the incremental displacements, strains and stresses are based on the possibility of non-linear structural behaviour caused by softening of the material.

8.8 Displacements and stresses due to fire exposure

Actual fire scenarios are characterised by coupling with the FEM temperature model presented in chapter 6. Subsequent incremental loading of the structural element defines the mechanical response, for which a larger time step size is used to reduce calculation times. The linear elastic increments are governed by the temperature-dependent material properties and the type of fire exposure. Furthermore, assumed constant structural boundary conditions are extended by an initial load step in case of external forces. It is important to mention that from here on only structural schematisation by a plane strain assumption is considered. The material is still assumed infinitely strong, neglecting the possibility for crack development.

Fire scenarios (II)				
Calculation	**8.5A**	**8.5B**	**8.5C**	**8.5D**
Reference temperature	20 °C	20 °C	20 °C	20 °C
Duration	1800 sec	1800 sec	1800 sec	1800 sec
Incremental time step size	2.5 sec	2.5 sec	2.5 sec	2.5 sec
Incremental load step size	60 sec	60 sec	60 sec	60 sec
Material (homogeneous)				
Strength class	**C25/30**	**C90/105**	**C25/30**	**C90/105**
Aggregate type	**RG**	**RG**	**RG**	**LS**
Boundary conditions				
Fire scenario	**ISO 834**	**ISO 834**	**HC**	**HC**
Convective heat transfer coeff.	**25 W/m^{2}K**	**25 W/m^{2}K**	**50 W/m^{2}K**	**50 W/m^{2}K**
Axial spring stiffness				
Rotational spring stiffness				

Table 8.9 *Examination of the unrestrained incremental displacements and stresses through consideration of the strength, aggregate type and type of fire exposure.*

8.8.1 Influence of the strength class, aggregate type and the type of fire exposure

Investigation of the influence of incremental thermal loading is carried out for various fire scenarios as indicated in Table 8.9. In each of the numerical approximations the cross-section is unrestrained, allowing only for the influence of the material and the fire curve. Comparison between the vertical stresses in the cross-section made of C25/30 or C90/105 with river gravel aggregates is made in Fig. 8.12. The only differences are the attained maximum stresses. It is also observed that in case of unrestrained expansion the deformations are the same. This is attributed to Young's modulus, governing both the stiffness and the imposed thermal load.

Another interesting point is that through the usage of the aggregates with a lower thermal expansion, such as limestone, the thermal loading can be mitigated. This behaviour was already reported in chapter 5 and is further examined in Fig. 8.13. Fire exposure of C25/30 made with RG and C90/105 made with LS is indicated to cause similar stresses in the cross-section. However, the deformation variables at the top support are for the latter lower.

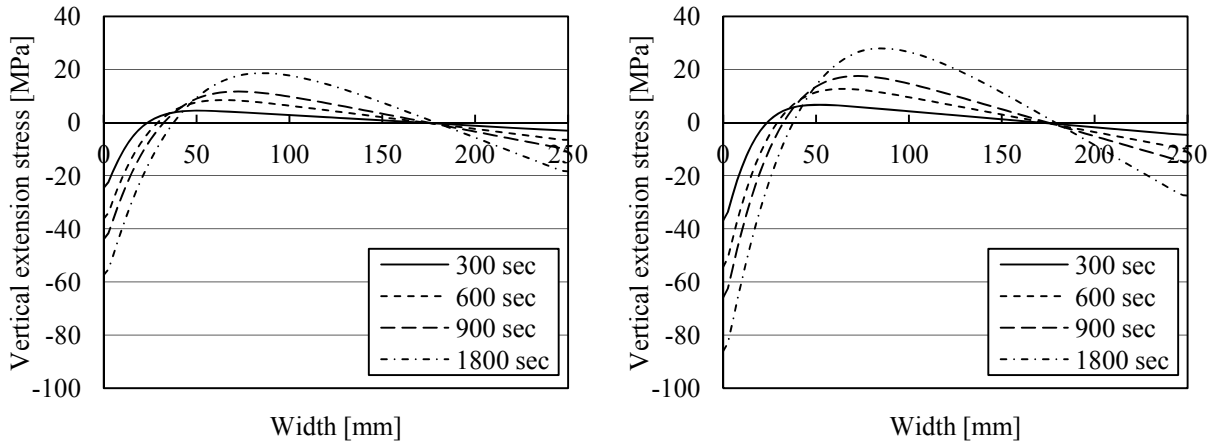

Fig. 8.12 *The higher Young's modulus of C90/105 (right) compared to C25/30 (left) governs the stresses in the unrestrained cross-section during exposure to an ISO fire.*

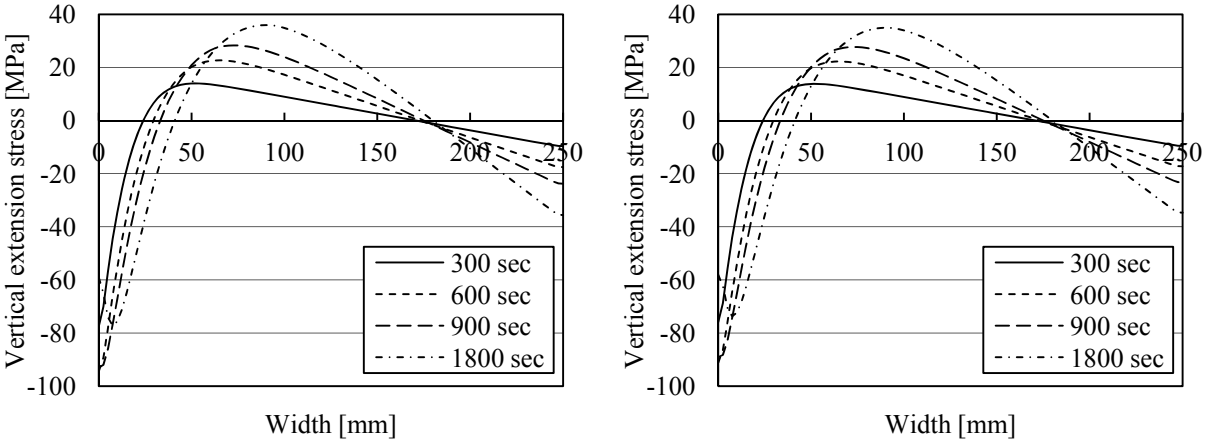

Fig. 8.13 *By increasing the thermal load to represent a HC type of fire, the unrestrained stress distributions of C25/30 made with RG (left) and C90/105 made with LS (right) are almost identical.*

8.8.2 Influence of the structural boundary conditions

Until this point only limited attention is given to the rigid body boundary conditions. Only the theoretical derivation is provided. It is therefore useful to determine the deformation characterisation of the structural cross-section with respect to various loading scenarios. In Table 8.10 the reference state is represented by the unrestrained thermal deformation caused by exposure to a HC type of fire. Subsequently, partial restraint and also external forces are imposed. To assess the structural influence of the boundary condition and the possibility for edge effects it is recalled that the stresses are averaged for both inner and outer sections.

Fire scenarios (III)			
Calculation	**8.6A**	**8.6B**	**8.6C**
Reference temperature	20 ^{o}C	20 ^{o}C	20 ^{o}C
Duration	3600 sec	3600 sec	3600 sec
Incremental time step size	2.5 sec	2.5 sec	2.5 sec
Incremental load step size	60 sec	60 sec	60 sec
Material (homogeneous)			
Strength class	C25/30	C25/30	C25/30
Aggregate type	RG	RG	RG
Boundary conditions			
Fire scenario	HC	HC	HC
Convective heat transfer coeff.	50 W/m^{2}K	50 W/m^{2}K	50 W/m^{2}K
Axial force			**-2.0 kN**
Moment			**-0.05 kNm**
Axial spring stiffness		**4 kN/mm**	**4 kN/mm**
Rotational spring stiffness		**20 kNm/rad**	**20 kNm/rad**

Table 8.10 *The schematisation of the boundary is investigated by assessing the influence of partial restraint and external loading.*

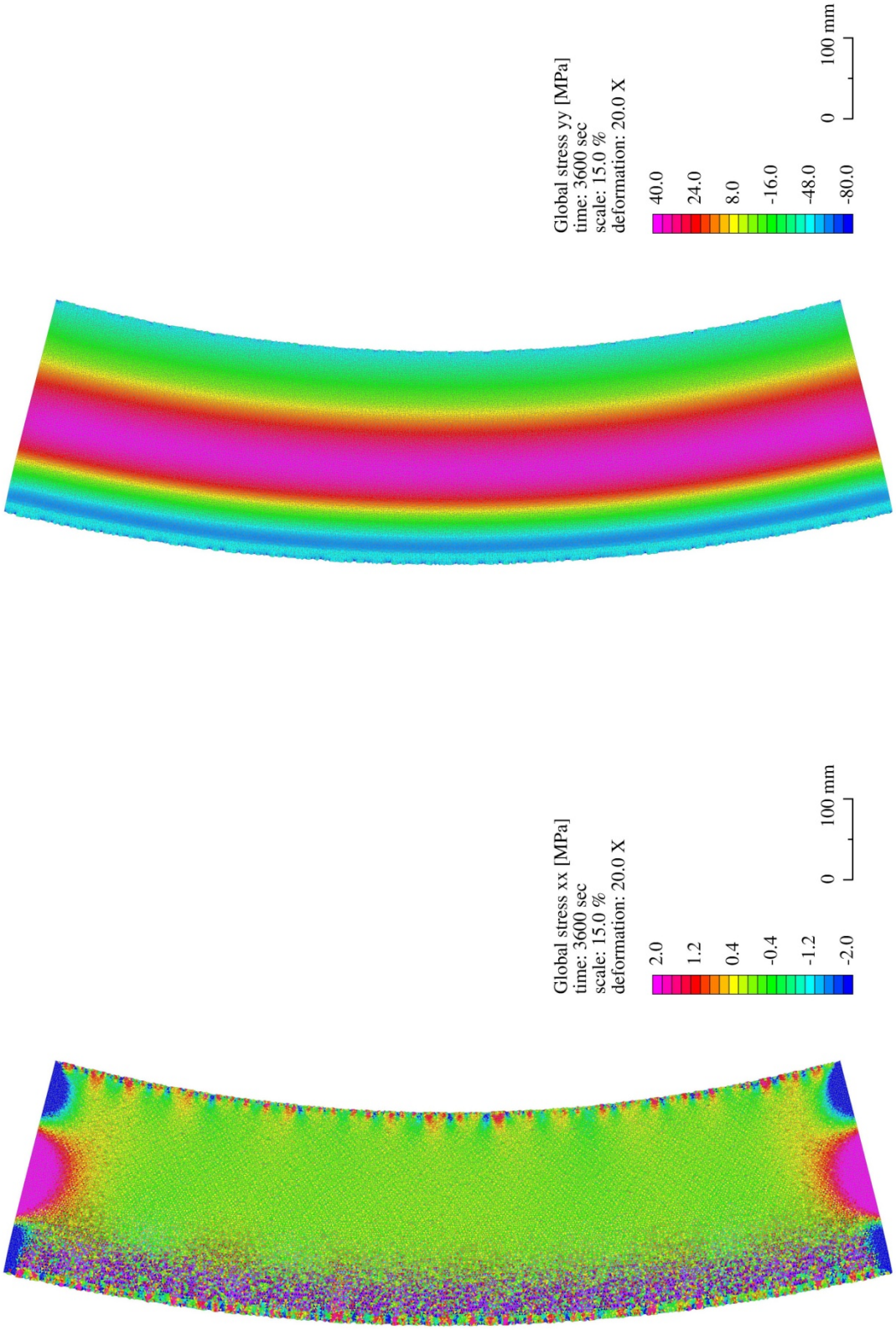

Fig. 8.14 *Distributions of horizontal and vertical stresses in the unrestrained C25/30 cross-section after 3600 seconds of fire exposure according to the HC fire curve. Limited disturbances in the stresses are indicated in the surface layer and along the rigid bodies.*

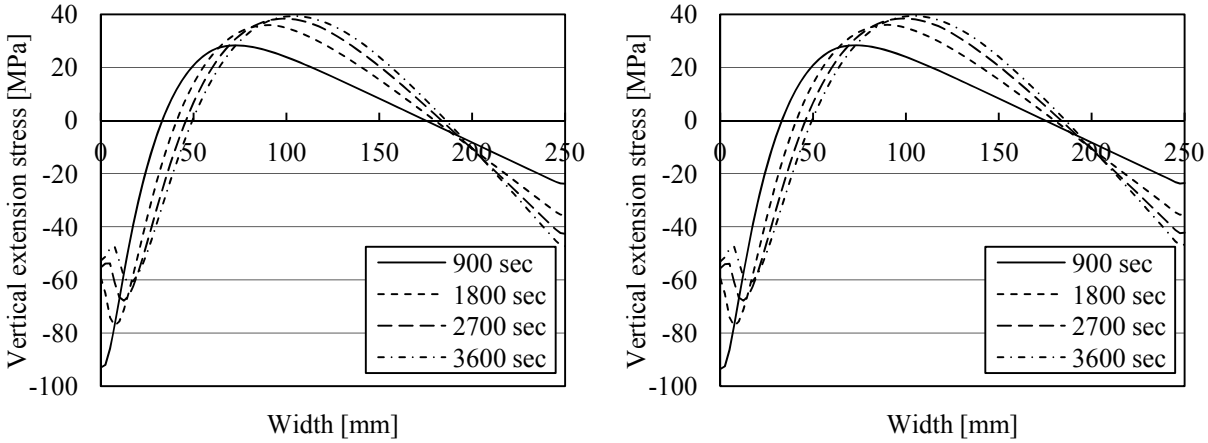

Fig. 8.15 *Unrestrained vertical stresses averaged over the inner (left) and outer (right) sections of the C25/30 cross-section are indicated to be similar.*

The first main goal of the boundary conditions is to ensure that the in-plane stresses are constant along the height, as illustrated in Fig. 8.14. These results are characterised by the coupling conditions, extended by prescribed displacements along the outer edges. These unrestrained thermal deformations in horizontal direction are needed to ensure a sufficiently accurate approximation, further mitigating possible edge effects. Comparison of the unrestrained vertical stress distributions, presented in Fig. 8.15, confirms that in the outer and inner sections the same principal stresses act.

In chapter 5 it was elaborated that a constant moment in height direction implies that no shear forces develop (Hartsuijker & Welleman, 2007). Therefore, a second important requirement is that only limited horizontal stresses develop. The in-plane distribution seen in Fig. 8.14 indicates relatively small horizontal stresses especially in the heated surface layer, probably due to the imposed strain. At the top and bottom edges larger localisations are found. However, the location and values indicate that these stresses are attributed to the imposed rigid bodies. Similar observations are also made from the determined averaged horizontal stresses in the outer section as presented in the left graph of Fig. 8.16. Finally, a check of the shear stresses indicates a similar, but more moderate influence.

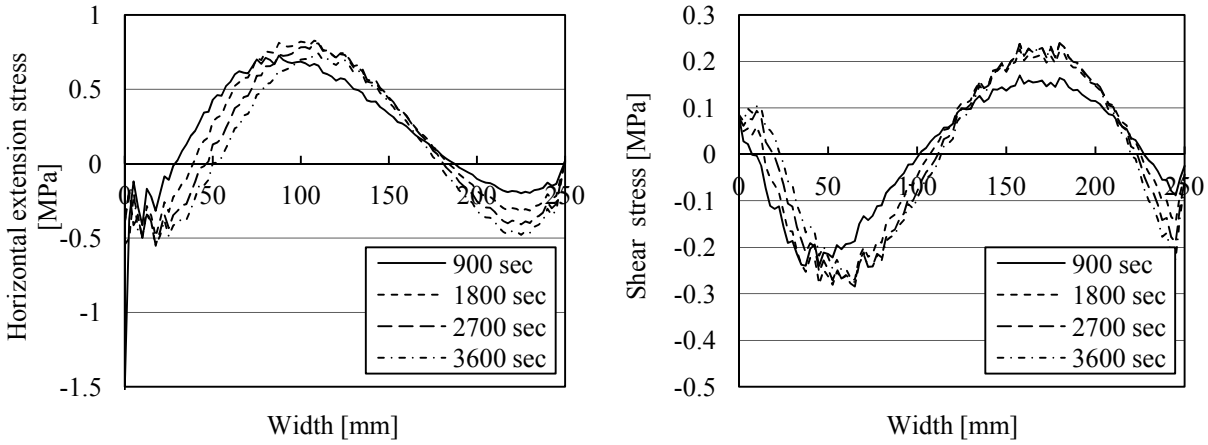

Fig. 8.16 *Distributions of the averaged horizontal (left) and shear (right) stresses in the outer section, indicating the influence of the unrestrained boundary.*

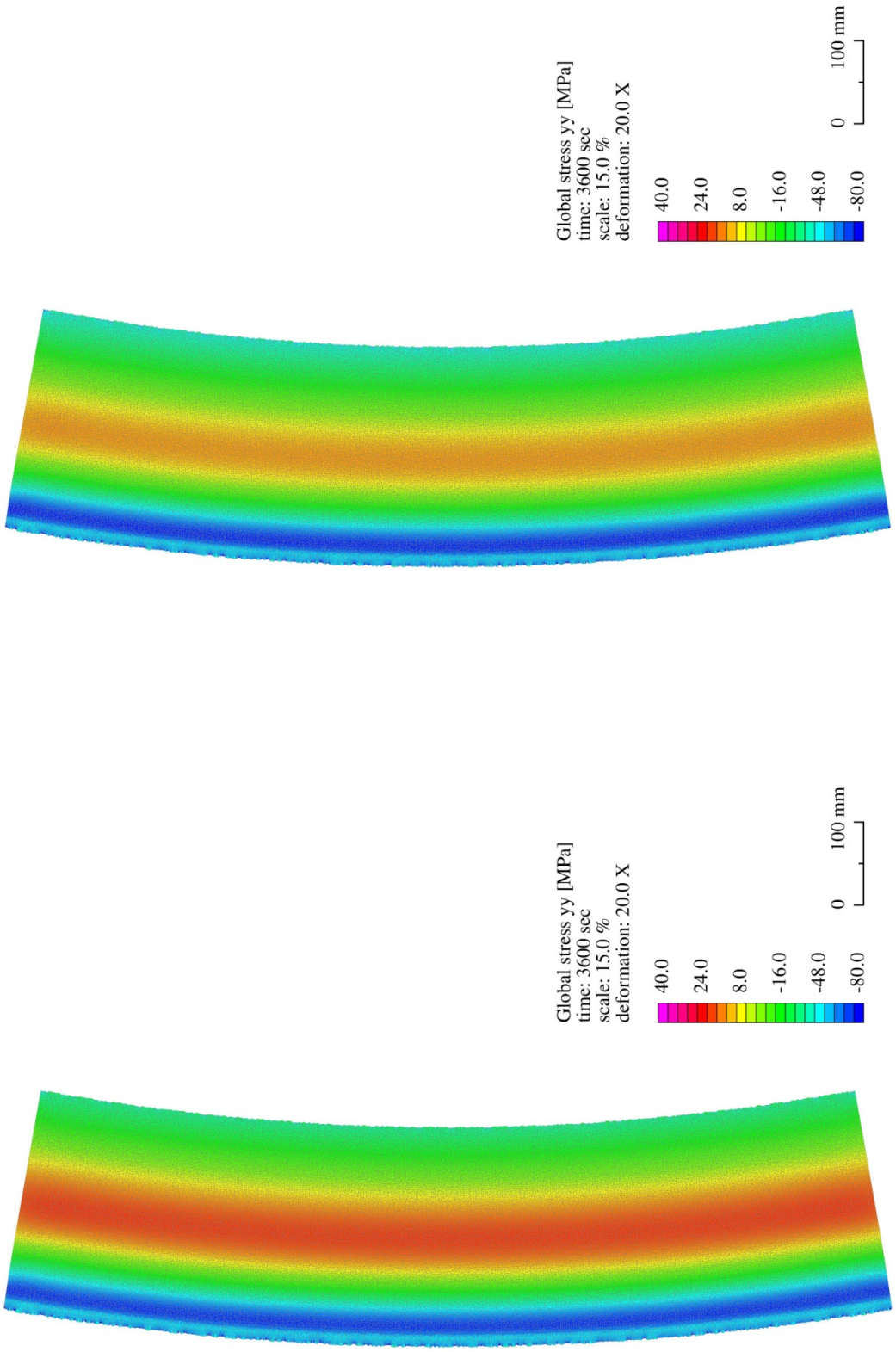

Fig. 8.17 *Partial restraint without load reduces deformations and increases the compressive stresses, indicating also softening (left). Addition of external forces disturbs the initial state and extends the load on the cross-section (right).*

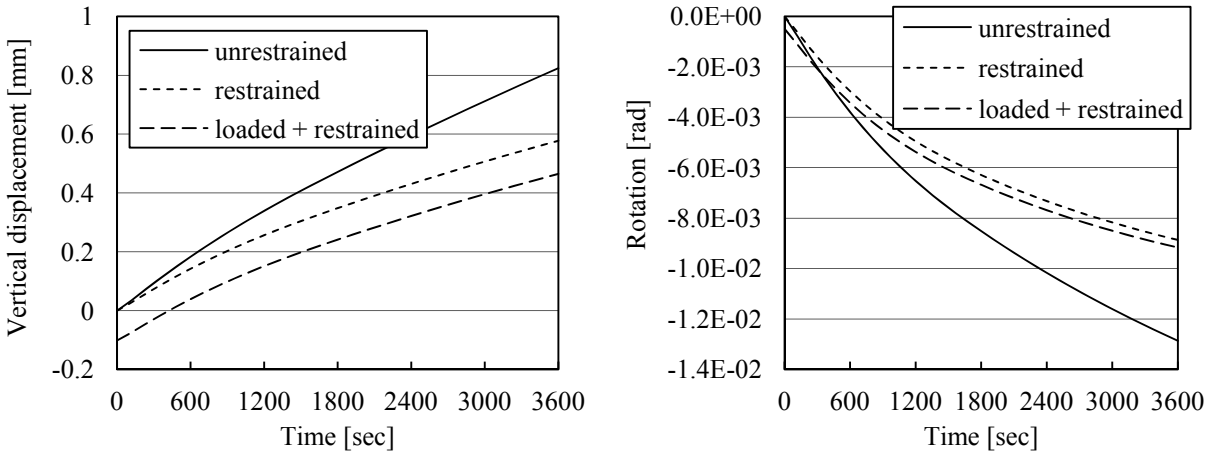

Fig. 8.18 *Time-dependent development of the vertical displacement (left) and rotation (right) at the top support, reflecting restraint as well as initial deformation.*

By addition of axial and rotational restraint the deformations reduce. This is illustrated by the vertical in-plane stress distributions for these loading scenarios shown in Fig. 8.17. In both cases the thermal displacements are observed to reduce. The initial contraction of the loaded cross-section is neutralised within 600 seconds of fire exposure, reflecting on the substantial thermal exposure. As a final characterisation the incremental linear relationship between the spring stiffness and the vertical displacement or rotation at the top support is indicated in Fig. 8.18. With time the deformation and thus the level of restraint increases. Moreover, introducing also external forces and moments affects the initial state of the cross-section. Before thermal exposure an initial vertical contraction as well as rotation are imposed. These remain present during fire exposure and affectively translate both deformation distributions. Similar graphs are also possible for the axial force and moment, excluding the unrestrained case.

8.9 Conclusions with respect to fire exposed concrete

In addition to chapter 5 and based on the numerical results discussed the following conclusions can be drawn with respect to fire exposed concrete:

- Unrestrained deformation of cross-sections with varying concrete strength classes, having the same temperature dependence of Young's modulus as well as the imposed strain, will have the same displacements. However, in-plane stresses vary in dependence of the stiffness of the material.

- A lower imposed strain reduces the internal thermal loading of the material. A limestone-based C90/105 can exhibit similar stresses as a C25/30 made of river gravel. This is also reflected by the thermal deformations which in the latter case are higher.

With respect to the FEM definition the following has also to be considered:

- Ensuring a sufficiently accurate approximation of the boundary conditions includes checking whether the main vertical stresses are continuous across the height of the cross-section. Furthermore, horizontal extension and shear stresses should be limited by considering the symmetrical cross-section and the absence of shear forces.

- Including the unrestrained temperature-induced displacements along the top and bottom edges is required in order to mitigate disturbances in the various stress fields. However, imposing the coupling conditions will still cause some limited effects.

- Increasing the width of the structural element causes a higher level of cross-sectional restraint. However, increasing the height only affects the solution in case of partially restrained support conditions since the cross-sectional properties remain unaffected.

9 Anisotropic FEM model for fracture mechanics

The derived FEM model approximates the displacements and stresses, assuming a homogeneous and isotropic material. The material definition is in this chapter redefined to include anisotropy as well as heterogeneity. The starting point is again the PDE while taking the plane strain assumption into account. Subsequent is the mechanical continuum based on approximation of the global strains using a direction-dependent stiffness. This is represented by sets of three triangular orientated 1D bars loaded by initial temperature strains and pressure-induced stresses. The schematisation is elaborated by conservation of elastic strain energy through strain-based transformation. Heterogeneity is characterised by the various concrete components. In this continuum description crack initiation is simplified as brittle fracture of extensional bars. However, it was found that numerical instabilitties can arise for the hinged bars due to insufficient redistribution of the fracture forces. Bernoulli-Euler beams are added to define the local rotations, obtaining a traditional lattice. The final parts first compare numerical results to chapters 5 and 8, reflecting on the influence of local bending. The remainder of this chapter presents simulations of fire exposed concrete, indicating the differences between temperature and pore pressure loading. The development of thermal instabilities in the heated surface layer indicates a possible spalling mechanism.

9.1 Conceptual idea behind the heterogeneous and anisotropic material description

The homogeneous and isotropic material description of concrete is commonly used to determine the mechanical behaviour (Timoshenko & Goodier, 1970; Zienkiewicz, et al., 2005). Through consideration of a plane strain assumption the displacements, strains and stresses are approximated for a 2D cross-section (Prezemieniecki, 1968/1985; Zienkiewicz, et al., 2005). However, as discussed in chapter 7, concrete is at a local scale characterised by several components as illustrated in Fig. 9.1. Especially in NSC, the aggregate particles tend to have a higher stiffness and tensile strength compared to the surrounding mortar and especially the interfacial zones (van Mier, 1997). Across this material description temperature strains develop extended by pressure-induced stresses between the aggregates. Combined with the structural loading these determine the displacements, stresses and level of cracking.

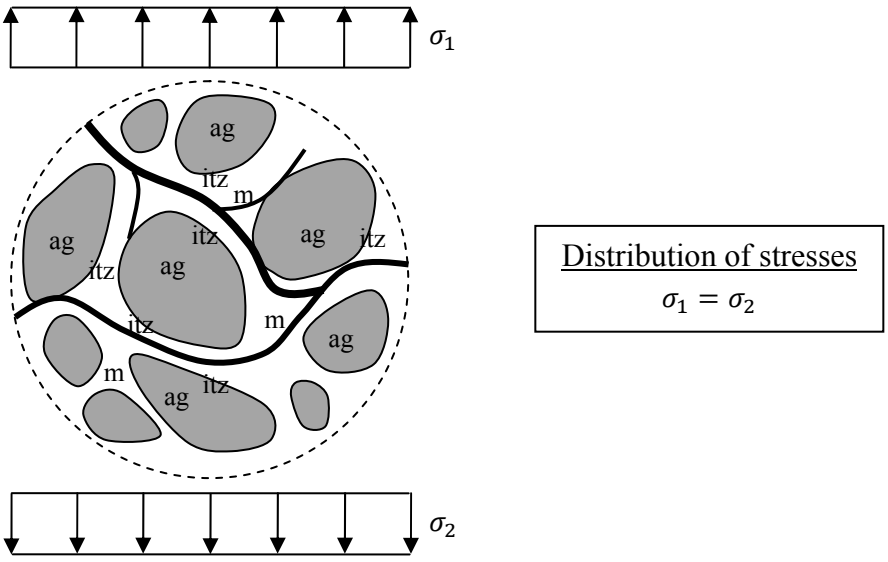

Fig. 9.1 *Overview of the material schematisation of concrete based on distribution of stresses across the concrete components affected by local cracking.*

The resultant PDE, based on the balance of linear momentum with consideration of linear elasticity, is only valid for a homogeneous and isotropic material (Timoshenko & Goodier, 1970; Felippa, 2004a). This material description is redefined by definition of an anisotropic continuum based on approximation of the extension and shearing strains (Prezemieniecki, 1968/1985; Blaauwendraad, 2004). Local elongation strains are defined, schematised by 1D bars forming together a triangular network (Prezemieniecki, 1968/1985; Blaauwendraad, 2004; Felippa, 2004a). Conservation of elastic strain energy based on strain transformation of sets of three triangular orientated bars defines the global stresses and stiffness (Timoshenko & Goodier, 1970; Felippa, 2004a). This schematisation omits the need for shear panels as is required for a square network of bars (Prezemieniecki, 1968/1985; Blaauwendraad, 2004).

Heterogeneity is reflected by the distribution of the concrete components used to characterise the extensional stiffness and temperature elongation strain of each bar. The influence of gas pressures is directly imposed on the mortar and interfacial zones through the induced stresses (Timoshenko & Goodier, 1970; Zienkiewicz, et al., 2005). Both these types of internal loading are governed by incremental coupling with the FEM temperature and pore pressure model in chapter 7. The distribution of the concrete components and the crack pattern are thereby assumed constant in depth direction to maintain the plane strain assumption. As a result an anisotropic definition of the global material stiffness is obtained.

Crack initiation is in this anisotropic continuum characterised by brittle extensional fracture and subsequent removal of bars from the system (Schlangen, 1993; Vervuurt, 1997). This incremental process assumes the crack as a material discontinuity characterised by genuine separation with no stiffness contribution (Schlangen, 1993; Vervuurt, 1997). Subsequent opening of the crack localises deformations, causing the stresses in the surrounding material to redistribute (van Mier, 1997). A local mechanism is formed based on the hinged bars while considering the possible coinciding relatively large deformations through a geometrical non-linear extension of the equilibrium conditions (Bathe, 1986; Gavin, 2014; Felippa, 2014).

In the traditional lattice also local bending is included by using 1D Bernoulli-Euler beams (Schlangen, 1993; Vervuurt, 1997). This bending deformation is believed to extend the 1D schematisation to reflect a higher order Cosserat continuum (Herrmann & Roux, 1990; Dos Reis & Ganghoffer, 2011). In this particular continuum additional curvature-based couple stresses originate from also considering rotational equilibrium (de Borst & Sluys, 1991; Dos Reis & Ganghoffer, 2011). Stresses across the continuum vary with symmetry of both shear strains no longer assumed based on introduction of local material rotations (de Borst & Sluys, 1991; de Borst, 1991). Approximation of this continuum by varying the bending properties in a rectangular network of beams can for instance be found in (Dos Reis & Ganghoffer, 2011). For a regular triangular lattice the properties of the 1D beams and the fracture behaviour is discussed in detail by (Schlangen & Garboczi, 1997).

In this thesis the main force transfer is based on schematisation of each element by three triangularly orientated 1D bars. The 1D Bernoulli-Euler beams are introduced in order to improve the redistribution of the fracture forces, obtaining a traditional lattice (Schlangen, 1993; Vervuurt, 1997). By considering restraint of the nodal rotations the hinged mechanism is partially counteracted in order to obtain a numerically more stable response governing the localisation and propagation of the crack.

9.2 Theoretical considerations and anisotropic FEM definition

Derivation of this anisotropic and heterogeneous continuum is based on the stresses governing the PDE, restated according to a plane strain assumption as defined in chapter 8 (Timoshenko & Goodier, 1970). In this paragraph the global strains are approximated through definition of three 1D bars forming a triangular basis (Prezemieniecki, 1968/1985; Blaauwendraad, 2004; Felippa, 2004a). The local axial strains are transformed to express the relationship with the global strains (Felippa, 2004a). Subsequently, conservation of elastic strain energy indicates the global stresses as well as the global stiffness (Felippa, 2004a). The FEM definition is obtained by including the initial temperature strains and possible initial pressure stresses acting on each bar (Timoshenko & Goodier, 1970). Thereafter heterogeneity is introduced by varying the material properties based on the disitrbution of the concrete components. The possibility for relatively large deformations is addressed through a geometrical non-linear description of the deformed bars (Gavin, 2014; Felippa, 2014). The anisotropic influence is also extended by local cracking, included through brittle fracture of the 1D bars (Schlangen, 1993; Vervuurt, 1997). The addition of the 1D Bernoulli-Euler beams (Schlangen, 1993; Vervuurt, 1997) is elaborated in the next paragraph dealing with the numerical stability.

9.2.1 Basic assumptions governing the material description

Anisotropic continuum definition

Regarding the anisotropic continuum the following assumptions are stated:

1. The global extension and shearing strains are approximated by three 1D bars, arranged according to a triangular grid (Prezemieniecki, 1968/1985; Blaauwendraad, 2004). Together these axial elongations characterise the local anisotropic continuum definition (Felippa, 2004a).

2. The bars are characterised as linear elastic 1D elements based on Hooke's law until fracture with the deformations initially assumed infinitesimally small (Timoshenko & Goodier, 1970). A plane strain assumption is again imposed through consideration of restraint in the out-of-plane direction (Timoshenko & Goodier, 1970).

3. Conservation of elastic strain energy combined with transformation of the axial strains defines the global stresses acting across the triangular area (Felippa, 2004a). A similar reasoning also defines the global anisotropic stiffness tensor (Felippa, 2004a).

4. In order to conserve the elastic strain energy, the anisotropic axial strains are each defined across the area of the continuum. The cross-section of each bar thus reflects the average internal height of the triangular area perpendicular to the edge or the 1D element axis (Prezemieniecki, 1968/1985; Blaauwendraad, 2004; Felippa, 2004a).

Heterogeneous material description

5. Aggregates and the surrounding mortar and interfacial zones are all assumed defined by Hooke's law until fracture (Schlangen, 1993; Vervuurt, 1997). The various concrete components characterise the extensional stiffness and the temperature strains (Schlangen, 1993; Vervuurt, 1997). Time-dependent creep and relaxation are not considered and all strains are reversible. This neglects viscoelastic effects such as rate or load dependence and permanent deformations (Kelly, 2008; Spencer, 1980/2004).

6. Pressure-induced stresses are also considered as internal loading acting between the aggregates (Timoshenko & Goodier, 1970). These initial stresses are based on an assumed uniform water vapour pressure neglecting the influence of the concave meniscus (Gray & Schrefler, 2001; Zienkiewicz, et al., 2005).

Crack initiation and subsequent opening

The initiation and opening of cracks are described using the following assumptions:

7. The initiation of a crack is based on brittle extensional fracture of bars (Schlangen, 1993; Vervuurt, 1997). Redistribution of stresses is taken into account through incremental crack development while conserving the elastic strain energy.

8. Opening of the crack is based on the removal of the axial stiffness associated with the fractured bars (Schlangen, 1993; Vervuurt, 1997). The stiffness reduction ensures localisation of deformations extended by the hinged connection of the bars.

9. Genuine separation of the material causes the development of localised relatively large displacements and rotations. These are addressed through a geometric non-linear definition of the bars, reflecting deformation increments (Gavin, 2014; Felippa, 2014).

10. Redistribution of incremental fracture forces is improved through including local bending based on 1D Bernoulli-Euler beams (Schlangen, 1993; Vervuurt, 1997). Elongation and especially rotation of the hinged bars is partially counteracted to stabilise the solution and ensure that loads are spread along the crack edges.

9.2.2 Anisotropic continuum description

Deformation of a plane strain continuum is governed by two extensional strains, each defined by the derivative of the axial displacement with respect to the same coordinate axis (Timoshenko & Goodier, 1970). The shearing strain reflects a coupled description expressed in both in-plane axial displacements with respect to the perpendicular axes (Timoshenko & Goodier, 1970). The resultant stress-strain relationship, as restated from chapter 8, reads (Timoshenko & Goodier, 1970; Prezemieniecki, 1968/1985):

$$\boldsymbol{\sigma} = \boldsymbol{D}(\boldsymbol{\varepsilon} - \boldsymbol{\varepsilon_T}) \tag{9.1}$$

with

$$\boldsymbol{\sigma} = \begin{bmatrix}\sigma_{xx}\\ \sigma_{yy}\\ \sigma_{xy}\end{bmatrix} \qquad \boldsymbol{\varepsilon} = \begin{bmatrix}\varepsilon_{xx}\\ \varepsilon_{yy}\\ \gamma_{xy}\end{bmatrix} = \begin{bmatrix}\varepsilon_{xx}\\ \varepsilon_{yy}\\ 2\varepsilon_{xy}\end{bmatrix} = \begin{bmatrix}\dfrac{\partial u_x}{\partial x}\\ \dfrac{\partial u_y}{\partial y}\\ \dfrac{\partial u_x}{\partial y} + \dfrac{\partial u_y}{\partial x}\end{bmatrix} \qquad \boldsymbol{\varepsilon_T} = (1+\nu)\begin{bmatrix}\varepsilon_T\\ \varepsilon_T\\ 0\end{bmatrix}$$

$$\boldsymbol{D} = \frac{E}{(1+\nu)(1-2\nu)}\begin{bmatrix}1-\nu & \nu & 0\\ \nu & 1-\nu & 0\\ 0 & 0 & \dfrac{1-2\nu}{2}\end{bmatrix} \qquad \varepsilon_{zz} = \gamma_{yz} = \gamma_{zx} = 0$$

$$\sigma_{zz} = \nu(\sigma_{xx} + \sigma_{yy}) - E\varepsilon_T$$

As an alternative, three extensional strains are defined which, as will be shown, together approximate the global strains (Prezemieniecki, 1968/1985; Blaauwendraad, 2004; Felippa, 2004a). These local strains are based on a triangular orientation of 1D bars as shown in Fig. 9.2 (Prezemieniecki, 1968/1985; Blaauwendraad, 2004).

Triangular orientation of three 1D bars

Each bar is characterised by the local extensional strain which through Hook's law defines the axial stress (Timoshenko & Goodier, 1970). Additional stresses, for instance in the local perpendicular direction, are omitted since only the axial strain is considered. This assumes that in-plane no stresses or forces can be transmitted in other directions than along the locally defined axes. Furthermore, the out-of-plane extensional stress is based on the plane strain assumption as stated in Eq. (9.1) (Timoshenko & Goodier, 1970). Rearranging while assuming constant Poisson's ratio defines the following:

$$\begin{aligned}\varepsilon_{xx}{}' &= \frac{1}{E'}\left(\sigma_{xx}{}' - \nu\left(\sigma_{yy}{}' + \sigma_{zz}{}'\right)\right) + \varepsilon_{T'}\\ &= \frac{1}{E'}\left((1-\nu^2)\sigma_{xx}{}' - (\nu+\nu^2)\overbrace{\sigma_{yy}{}'}^{=0}\right) + (1+\nu)\varepsilon_{T'}\end{aligned} \tag{9.2}$$

$$\rightarrow \varepsilon_{xx}{}' = \frac{1-\nu^2}{E'}\sigma_{xx}{}' + (1+\nu)\varepsilon_{T'}$$

with

$$\sigma_{zz}{}' = \nu\left(\sigma_{xx}{}' + \sigma_{yy}{}'\right) - E'\varepsilon_{T'}$$

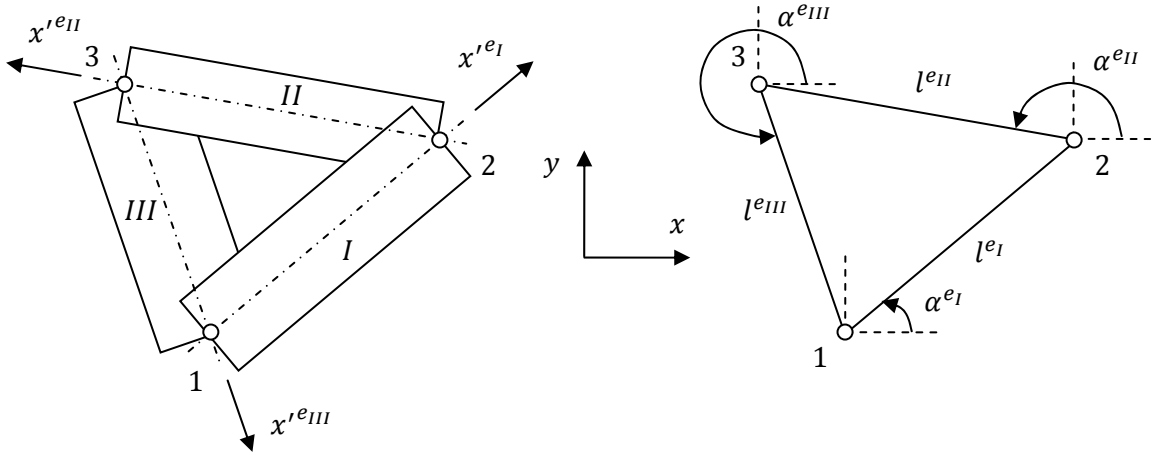

Fig. 9.2 *Schematic representation of three triangular orientated 1D bars in $\mathbb{R}^2$. These characterise the extensional strains based on the local coordinate systems (left). Each bar is defined by its length and angle in the global coordinate system (right).*

Hence, the local extensional stress is defined by inversion expressed in the total and the temperature strains:

$$\sigma_{xx}{}' = \frac{E'}{1-\nu^2}(\varepsilon_{xx}{}' - (1+\nu)\varepsilon_{T'}) \tag{9.3}$$

The FEM discretisation for a triangular area across the continuum consists of three bars, each dependent on a local coordinate axis as shown in Fig. 9.2. This anisotropic definition characterises the local axial strains and stresses by an uncoupled diagonal elasticity tensor:

$$\boldsymbol{\sigma}'^{\boldsymbol{e}} = \boldsymbol{D}'^{\boldsymbol{e}}\left(\boldsymbol{\varepsilon}'^{\boldsymbol{e}} - \boldsymbol{\varepsilon_T}'^{\boldsymbol{e}}\right) \tag{9.4}$$

with

$$\boldsymbol{\sigma}'^{\boldsymbol{e}} = \begin{bmatrix} \sigma'^{e_I} \\ \sigma'^{e_{II}} \\ \sigma'^{e_{III}} \end{bmatrix} \qquad \boldsymbol{\varepsilon}'^{\boldsymbol{e}} = \begin{bmatrix} \varepsilon'^{e_I} \\ \varepsilon'^{e_{II}} \\ \varepsilon'^{e_{III}} \end{bmatrix} \qquad \boldsymbol{\varepsilon_T}'^{\boldsymbol{e}} = (1+\nu)\begin{bmatrix} \varepsilon_T{}'^{e_I} \\ \varepsilon_T{}'^{e_{II}} \\ \varepsilon_T{}'^{e_{III}} \end{bmatrix}$$

$$\boldsymbol{D}'^{\boldsymbol{e}} = \frac{1}{1-\nu^2}\begin{bmatrix} E'^{e_I} & 0 & 0 \\ 0 & E'^{e_{II}} & 0 \\ 0 & 0 & E'^{e_{III}} \end{bmatrix}$$

where

σ'^{e_d}	[MPa]	Local axial stress of the bar aligned with edge 'd'
$\varepsilon'^{e_d}, \varepsilon_T{}'^{e_d}$	[-]	Local extension, temperature strain of the bar aligned with edge 'd'
E'^{e_d}	[MPa]	Local Young's modulus of the bar aligned with edge 'd'
$\boldsymbol{\sigma}'^{\boldsymbol{e}}$	[MPa]	Local axial stress vector governing the bars
$\boldsymbol{\varepsilon}'^{\boldsymbol{e}}, \boldsymbol{\varepsilon_T}'^{\boldsymbol{e}}$	[-]	Local extensional, temperature strain vector governing the bars
$\boldsymbol{D}'^{\boldsymbol{e}}$	[MPa]	Local elasticity tensor reflecting the stiffness (fourth order)

Gas pressure loading through imposed stresses

Until now the internal loading of the cross-section consists only of temperature strains. However, as discussed in chapter 5, pore pressures also cause stresses in the surrounding

material. It was estimated by using linear elasticity that the tangential tensile stresses at the edge of a single pore can be considered equal to the imposed pressure (Timoshenko & Goodier, 1970). This relatively simple relationship is included by imposing initial stresses, commonly referred to as an effective stress approach (Gray & Schrefler, 2001; Zienkiewicz, et al., 2005). In the definition of the bars, represented by Eq. (9.4), the pore pressure is included through initial local stresses, defined relative to atmospheric conditions:

$$\boldsymbol{\sigma'^{e}} = \boldsymbol{D'^{e}}\left(\boldsymbol{\varepsilon'^{e}} - \boldsymbol{\varepsilon_T}'^{e}\right) + \boldsymbol{\sigma_P}'^{e} \tag{9.5}$$

with

$$\boldsymbol{\sigma_P}'^{e} = \left(\boldsymbol{P_{gw}}'^{e} - \boldsymbol{P_{atm}}\right)$$

$$\boldsymbol{\sigma_P}'^{e} = \begin{bmatrix} {\sigma_P}'^{e_I} \\ {\sigma_P}'^{e_{II}} \\ {\sigma_P}'^{e_{III}} \end{bmatrix} \qquad \boldsymbol{P_{gw}}'^{e} = \begin{bmatrix} {P_{gw}}^{e_I} \\ {P_{gw}}^{e_{II}} \\ {P_{gw}}^{e_{III}} \end{bmatrix} \qquad \boldsymbol{P_{atm}} = \begin{bmatrix} P_{atm} \\ P_{atm} \\ P_{atm} \end{bmatrix}$$

where

${\sigma_P}'^{e_d}$	[MPa]	Local imposed stress on the bar aligned with edge 'd'
${P_{gw}}'^{e_d}$	[MPa]	Local vapour pressure acting in the bar aligned with edge 'd'
$\boldsymbol{\sigma_P}'^{e}$	[MPa]	Local imposed stress vector governing the bars
$\boldsymbol{P_{gw}}'^{e}, \boldsymbol{P_{atm}}$	[MPa]	Local water vapour, atmospheric pressure vector

Coordinate transformation based on three material directions

Each set of local coordinate axes is related to the global coordinate system through the transformation tensor stated in chapter 5 (Wells, 2006; Blom, 2009). However, the local perpendicular coordinate axis is neglected since a 1D bar only deforms through axial displacement. The resultant transformation tensor or rather transposed vector remains orthogonal (Spencer, 1980/2004) and defines the local material direction. Furthermore, it will prove convenient to group together the nodal relationships defined in each material direction to obtain the element coordinate transformation tensor:

$$\boldsymbol{x_M}'^{e} = \boldsymbol{T_{\alpha_M}}'^{e}\boldsymbol{x^e} \tag{9.6}$$

with

$$\boldsymbol{x^e} = \begin{bmatrix} x_1^e \\ y_1^e \\ x_2^e \\ y_2^e \\ x_3^e \\ y_3^e \end{bmatrix} \qquad \boldsymbol{x_M}'^{e} = \begin{bmatrix} {x'}_1^{e_I} \\ {x'}_2^{e_I} \\ {x'}_2^{e_{II}} \\ {x'}_3^{e_{II}} \\ {x'}_3^{e_{III}} \\ {x'}_1^{e_{III}} \end{bmatrix} \qquad \boldsymbol{T_{\alpha_M}}'^{e} = \begin{bmatrix} \cos\alpha^{e_I} & \sin\alpha^{e_I} & 0 & 0 & 0 & 0 \\ 0 & 0 & \cos\alpha^{e_I} & \sin\alpha^{e_I} & & \\ & 0 & \cos\alpha^{e_{II}} & \sin\alpha^{e_{II}} & 0 & 0 \\ & & 0 & 0 & \cos\alpha^{e_{II}} & \sin\alpha^{e_{II}} \\ 0 & 0 & & 0 & \cos\alpha^{e_{III}} & \sin\alpha^{e_{III}} \\ \cos\alpha^{e_{III}} & \sin\alpha^{e_{III}} & & & 0 & 0 \end{bmatrix}$$

where

$\alpha^{e_I}, \alpha^{e_{II}}, \alpha^{e_{III}}$	[rad]	Angle of the edges of the triangular element
$\boldsymbol{x_M}'^{e}$	[mm]	Local element coordinate system vector based on the triangular material directions
$\boldsymbol{T_{\alpha_M}}'^{e}$	[-]	Element coordinate transformation tensor based on the triangular material directions (second order)

Strain transformation based on three 1D bars

The extensional strains governing the three bars define together the global strains through a second order transformation tensor (Felippa, 2004a; Zienkiewicz, et al., 2005). The basis for this tensor is the extensional strain transformation stated in chapter 5 (Timoshenko & Goodier, 1970; Roylance, 2001). However, in each material direction the extensional strain is defined through the angle with respect to the global coordinate system (Felippa, 2004a; Zienkiewicz, et al., 2005). This results in the following transformation relationship in which both the local and the global strains are defined constant across the element. In literature, this tensor is sometimes referred to as the strain rosette, referring to the transformation in a specific point (Timoshenko & Goodier, 1970; Felippa, 2004a):

$$\boldsymbol{\varepsilon}'^{\boldsymbol{e}} = \boldsymbol{T}_{\boldsymbol{\varepsilon_M}}{}'^{\boldsymbol{e}}\boldsymbol{\varepsilon}^{\boldsymbol{e}} \tag{9.7}$$

with

$$\boldsymbol{\varepsilon}^{\boldsymbol{e}} = \begin{bmatrix} \varepsilon_{xx}{}^{e} \\ \varepsilon_{yy}{}^{e} \\ \gamma_{xy}{}^{e} \end{bmatrix} \qquad \boldsymbol{T}_{\boldsymbol{\varepsilon_M}}{}'^{\boldsymbol{e}} = \begin{bmatrix} \cos^2\alpha^{e_I} & \sin^2\alpha^{e_I} & \sin\alpha^{e_I}\cos\alpha^{e_I} \\ \cos^2\alpha^{e_{II}} & \sin^2\alpha^{e_{II}} & \sin\alpha^{e_{II}}\cos\alpha^{e_{II}} \\ \cos^2\alpha^{e_{III}} & \sin^2\alpha^{e_{III}} & \sin\alpha^{e_{III}}\cos\alpha^{e_{III}} \end{bmatrix}$$

where

$\boldsymbol{T}_{\boldsymbol{\varepsilon_M}}{}'^{\boldsymbol{e}}$ [-] Element strain transformation tensor based on the extensional strains in each local material direction (fourth order)

From this strain transformation tensor it becomes apparent that the proposed FEM discretisation is sufficient to represent the global strains (Prezemieniecki, 1968/1985; Blaauwendraad, 2004; Felippa, 2004a). No additional contributions need to be considered in order to obtain static equilibrium.

A final remark is that this extensional strain transformation tensor is non-orthogonal, implying that the inverse is not equal to its transpose (Spencer, 1980/2004). Inversion of Eq. (9.7) requires definition of the following transformation tensor using the global nodal coordinate differences (Felippa, 2004a):

$$\boldsymbol{\varepsilon}^{\boldsymbol{e}} = \boldsymbol{T}_{\boldsymbol{\varepsilon_M}}{}'^{\boldsymbol{e-1}}\boldsymbol{\varepsilon}'^{\boldsymbol{e}} \tag{9.8}$$

with

$$\boldsymbol{T}_{\boldsymbol{\varepsilon_M}}{}'^{\boldsymbol{e-1}} = \frac{1}{4A^{e2}} \begin{bmatrix} y_{23}y_{13}l^{e_I 2} & y_{31}y_{21}l^{e_{II} 2} & y_{12}y_{32}l^{e_{III} 2} \\ x_{23}x_{13}l^{e_I 2} & x_{31}x_{21}l^{e_{II} 2} & x_{12}x_{32}l^{e_{III} 2} \\ (y_{32}x_{13}+x_{32}y_{13})l^{e_I 2} & (y_{13}x_{21}+x_{13}y_{21})l^{e_{II} 2} & (y_{21}x_{32}+x_{21}y_{32})l^{e_{III} 2} \end{bmatrix}$$

where

$\boldsymbol{T}_{\boldsymbol{\varepsilon_M}}{}'^{\boldsymbol{e-1}}$ [-] Inverse of the element strain transformation tensor based on the extensional strains in each local material direction (fourth order)

Conservation of elastic strain energy and global stresses

The global stresses are determined through preservation of element-based elastic strain energy defined in the global and local directions as restated from the previous chapter (Felippa, 2004a; Zienkiewicz, et al., 2005):

$$U_{\varepsilon}{}^{e} = U_{\varepsilon}{}'^{e}$$

$$\int_{\Omega^e} \frac{1}{2} \boldsymbol{\varepsilon_m}^{eT} \boldsymbol{\sigma}^e d\Omega^e = \int_{\Omega'^e} \frac{1}{2} \boldsymbol{\varepsilon_m}'^{eT} \boldsymbol{\sigma}'^e d\Omega'^e \tag{9.9}$$

This relationship is simplified since for each element the stresses and strains are assumed constant and thus the integrals are omitted. Furthermore, no elastic strain energy is associated with the temperature strain (Felippa, 2004a; Zienkiewicz, et al., 2005). Hence, global stresses are directly obtained through (Felippa, 2004a):

$$\begin{gathered} \boldsymbol{\varepsilon}^{eT} \boldsymbol{\sigma}^e = \boldsymbol{\varepsilon}'^{eT} \boldsymbol{\sigma}'^e = \left(\boldsymbol{T}_{\boldsymbol{\varepsilon_M}}{}'^{e} \boldsymbol{\varepsilon}^e\right)^T \boldsymbol{\sigma}'^e = \boldsymbol{\varepsilon}^{eT} \boldsymbol{T}_{\boldsymbol{\varepsilon_M}}{}'^{eT} \boldsymbol{\sigma}'^e \\ \rightarrow \boldsymbol{\sigma}^e = \boldsymbol{T}_{\boldsymbol{\varepsilon_M}}{}'^{eT} \boldsymbol{\sigma}'^e \end{gathered} \tag{9.10}$$

Conservation of elastic strain energy and the anisotropic stiffness tensor

Following a similar reasoning also the global anisotropic stiffness tensor can be determined (Felippa, 2004a; Zienkiewicz, et al., 2005). For this purpose the conservation of the element-based elastic strain energy is restated from Eq. (9.9) (Felippa, 2004a; Zienkiewicz, et al., 2005). The local elasticity tensor is defined in Eq. (9.4) and represents the uncoupled direction-dependent extensional stiffness (Felippa, 2004a; Zienkiewicz, et al., 2005):

$$U_{\varepsilon}{}^{e} = U_{\varepsilon}{}'^{e}$$

$$\int_{\Omega^e} \frac{1}{2} \boldsymbol{\varepsilon_m}^{eT} \boldsymbol{\sigma}^e d\Omega^e = \int_{\Omega'^e} \frac{1}{2} \boldsymbol{\varepsilon_m}'^{eT} \boldsymbol{\sigma}'^e d\Omega'^e \tag{9.11}$$

$$\int_{\Omega^e} \frac{1}{2} \boldsymbol{\varepsilon_m}^{eT} \boldsymbol{D}^e \boldsymbol{\varepsilon_m}^e d\Omega^e = \int_{\Omega'^e} \frac{1}{2} \boldsymbol{\varepsilon_m}'^{eT} \boldsymbol{D}'^e \boldsymbol{\varepsilon_m}'^e d\Omega'^e$$

Insertion of the local strain transformation tensor stated in Eq. (9.7) and rearranging defines the global elasticity tensor (Felippa, 2004a; Zienkiewicz, et al., 2005):

$$\boldsymbol{\varepsilon}^{eT} \boldsymbol{D}^e \boldsymbol{\varepsilon}^e = \boldsymbol{\varepsilon}'^{eT} \boldsymbol{D}'^e \boldsymbol{\varepsilon}'^e$$

$$\begin{gathered} \boldsymbol{\varepsilon}^{eT} \boldsymbol{D}^e \boldsymbol{\varepsilon}^e = \left(\boldsymbol{T}_{\boldsymbol{\varepsilon_M}}{}'^{e} \boldsymbol{\varepsilon}^e\right)^T \boldsymbol{D}'^e \boldsymbol{T}_{\boldsymbol{\varepsilon_M}}{}'^{e} \boldsymbol{\varepsilon}^e = \boldsymbol{\varepsilon}^{eT} \boldsymbol{T}_{\boldsymbol{\varepsilon_M}}{}'^{eT} \boldsymbol{D}'^e \boldsymbol{T}_{\boldsymbol{\varepsilon_M}}{}'^{e} \boldsymbol{\varepsilon}^e \\ \rightarrow \boldsymbol{D}^e = \boldsymbol{T}_{\boldsymbol{\varepsilon_M}}{}'^{eT} \boldsymbol{D}'^e \boldsymbol{T}_{\boldsymbol{\varepsilon_M}}{}'^{e} \end{gathered} \tag{9.12}$$

9.2.3 Geometric non-linear deformations

The anisotropic definition of three triangularly orientated bars is sufficient to approximate the basic time-dependent linear elastic deformations. Physical non-linear behaviour is included through coupling with the temperature and pore pressure model presented in chapter 7 (Zienkiewicz, et al., 2005). This defines the elasticity tensor as well as the temperature strain and pressure-induced stress vectors. Similar considerations as discussed in chapter 6 define the incremental approach in order to include the rigid body boundary conditions at the top and bottom edges. As a result, the mechanical continuum becomes geometrically non-linear as expressed through the coupling conditions (Hartmann & Katz, 2007).

The bars themselves are connected through hinges which only allow for axial force transmission. During deformation each triangular set of bars maintains horizontal and vertical equilibrium (Hartsuijker & Welleman, 2006). However, the assumed incremental brittle fracture mechanics approach removes bars to simulate cracking (Schlangen, 1993; Vervuurt, 1997). This promotes the localisation of deformations and forms a fracture mechanism. Under these circumstances the small strain assumption, used to define the axial strain of the bars, could become less warranted (Felippa, 2004a; Wells, 2006). An incremental definition of the deformed bars is necessary to capture these geometric non-linear effects (Bathe, 1986; Gavin, 2014; Felippa, 2014).

Incremental displacements, stresses and strains

Similar as in the previous chapter the global displacements are stated in incremental form (Zienkiewicz, et al., 2005; Biot, 1965). However, besides time dependence also the incremental crack development process is reflected in the following definition. Local displacements are not defined incrementally since the geometrical non-linear approach will align the local coordinate systems with the deformed state of the bars:

$$\boldsymbol{u}_{k+1}^{t+1} = \boldsymbol{u}_{k}^{t+1} + \Delta\boldsymbol{u}_{k}^{t+1} \tag{9.13}$$

with

$$\boldsymbol{u}_{1}^{t+1} = \boldsymbol{u}^{t}$$

where

$\cdots_k$ Indication for the incremental crack step

Stresses and strains are for the anisotropic continuum defined in local incremental form according to (Zienkiewicz, et al., 2005; Biot, 1965):

$$\begin{aligned}
\boldsymbol{\sigma'}_{k+1}^{t+1} &= \boldsymbol{\sigma'}_{k}^{t+1} + \Delta\boldsymbol{\sigma'}_{k}^{t+1} \\
\boldsymbol{\sigma_P'}_{k+1}^{t+1} &= \boldsymbol{\sigma_P'}_{k}^{t+1} + \Delta\boldsymbol{\sigma_P'}_{k}^{t+1} \\
\boldsymbol{\varepsilon_m'}_{k+1}^{t+1} &= \boldsymbol{\varepsilon_m'}_{k}^{t+1} + \Delta\boldsymbol{\varepsilon_m'}_{k}^{t+1} \\
\boldsymbol{\varepsilon_T'}_{k+1}^{t+1} &= \boldsymbol{\varepsilon_T'}_{k}^{t+1} + \Delta\boldsymbol{\varepsilon_T'}_{k}^{t+1}
\end{aligned} \tag{9.14}$$

with

$$\boldsymbol{\sigma'}_{\mathbf{1}}^{\boldsymbol{t+1}} = \boldsymbol{\sigma'}^{\boldsymbol{t}} \qquad \boldsymbol{\sigma_P'}_{\mathbf{1}}^{\boldsymbol{t+1}} = \boldsymbol{\sigma_P'}^{\boldsymbol{t}}$$

$$\boldsymbol{\varepsilon_m'}_{\mathbf{1}}^{\boldsymbol{t+1}} = \boldsymbol{\varepsilon_m'}^{\boldsymbol{t}} \qquad \boldsymbol{\varepsilon_T'}_{\mathbf{1}}^{\boldsymbol{t+1}} = \boldsymbol{\varepsilon_T'}^{\boldsymbol{t}}$$

And finally, temperature and crack dependence of the local elasticity tensor is reflected by:

$$\boldsymbol{D'}_{\boldsymbol{k+1}}^{\boldsymbol{t+1}} = \boldsymbol{D'}_{\boldsymbol{k}}^{\boldsymbol{t+1}} + \Delta \boldsymbol{D'}_{\boldsymbol{k}}^{\boldsymbol{t+1}} \tag{9.15}$$

with

$$\boldsymbol{D'}_{\mathbf{1}}^{\boldsymbol{t+1}} = \boldsymbol{D'}^{\boldsymbol{t}}$$

Definition of the incremental elongation and rotation deformation

In engineering mechanics (Hartsuijker & Welleman, 2007) and basic FEM (Felippa, 2004a; Wells, 2006) elongation is commonly assumed to develop only along the bar axis. The bar remains defined in the reference state, not affected by the incremental deformations. This material-based approximation is valid for most structural applications, but may no longer be sufficient in case of relatively large local deformations such as occurring during cracking. This second order effect takes into account that for large deformations the axial forces are no longer positioned and orientated based on the reference state. Under these circumstances the local equilibrium conditions are influenced by the translation and rotation of the normal force present in each bar (Bathe, 1986; Gavin, 2014; Felippa, 2014).

This geometric non-linear behaviour requires a Lagrangian approach in order to include the influence of large strains and rotations (Bathe, 1986; Felippa, 2014). The reference state of the anisotropic FEM definition is characterised by the deformed state of the bars at the current time and crack step. Subsequent description of the incremental displacements allows to state the stiffness relationships (Bathe, 1986; Gavin, 2014; Felippa, 2014). This will involve material as well as geometrical contributions based on the elastic strain energy increment.

The following aspects are considered:

- Elongation of the bar is governed by the incremental axial strain assumed to develop parallel to the local horizontal axis (Bathe, 1986; Gavin, 2014; Felippa, 2014). This material contribution assumes that the strain increment is relatively small.

- Changing the position and orientation of the normal force present in the bar goes along two geometrical contributions (Bathe, 1986; Gavin, 2014; Felippa, 2014). The local horizontal component of the decomposed axial force is translated based on the incremental strain. Additionally, also a perpendicular force contribution is defined based on the local vertical displacement governing the incremental rotation.

The material- and geometry-based contributions follow from local displacements as schematically represented in Fig. 9.3 for a typical bar. The initial length is defined by Pythagoras' theory based on the nodal coordinates. These global coordinates also define the angle of the bar based on the orientation in the radial circle.

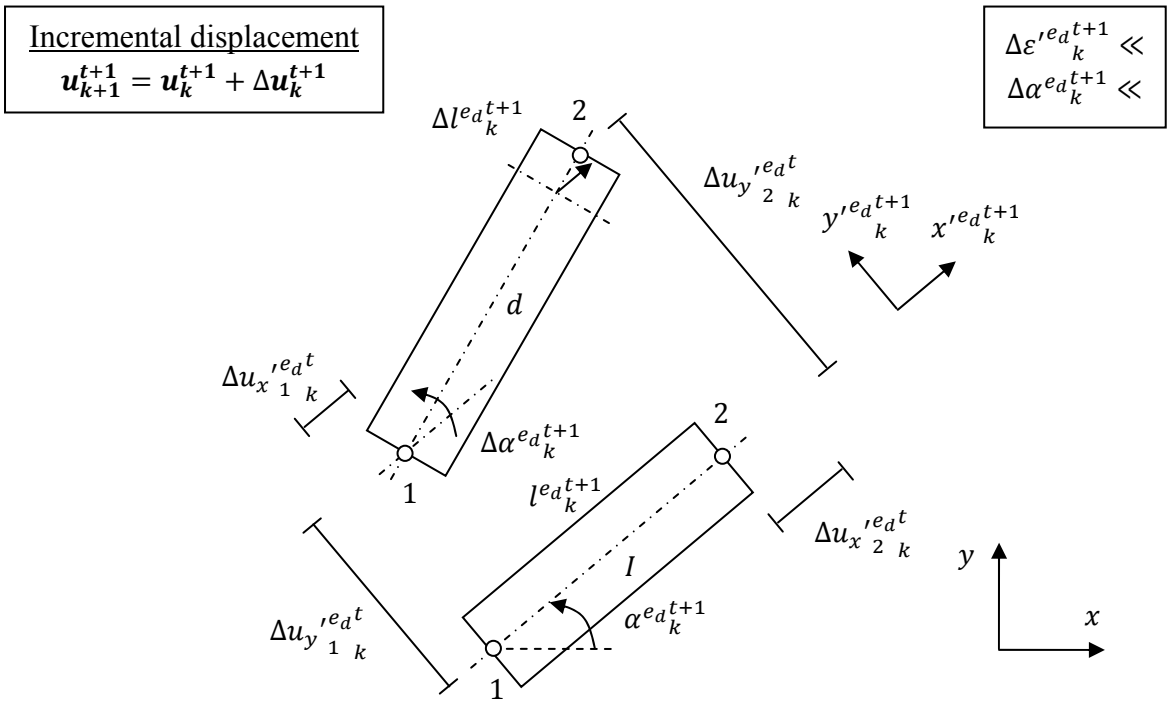

Fig. 9.3 *Schematic representation of the geometric non-linear displacements of the 1D bar in $\mathbb{R}^2$. The incremental elongation and rotation, expressed in the local coordinate system, are both assumed relatively small* (Bathe, 1986; Gavin, 2014).

For a small elongation the geometrical non-linearity is characterised by the incremental strain based on the local horizontal nodal displacements (Bathe, 1986; Gavin, 2014):

$$l^{e_d}{}_{k+1}^{t+1} = l^{e_d}{}_k^{t+1} + \Delta l^{e_d}{}_k^{t+1} \tag{9.16}$$

with

$$\Delta l^{e_d}{}_k^{t+1} = \Delta u_x{}'^{e_d}{}_{2\ k}^{t+1} - \Delta u_x{}'^{e_d}{}_{1\ k}^{t+1} = \Delta\varepsilon'^{e_d}{}_k^{t+1} l^{e_d}{}_k^{t+1} \rightarrow \Delta\varepsilon'^{e_d}{}_k^{t+1} = \frac{\Delta u_x{}'^{e_d}{}_{2\ k}^{t+1} - \Delta u_x{}'^{e_d}{}_{1\ k}^{t+1}}{l^{e_d}{}_k^{t+1}}$$

where

$\Delta u_x{}'^{e_d}{}_{i_d\ k}^{t+1}$	[mm]	Incremental local horizontal displacement of node 'i' along edge 'd'
$\Delta\varepsilon'^{e_d}{}_k^{t+1}$	[-]	Incremental local extensional strain of bar 'd' at the current step
$l^{e_d}{}_k^{t+1}, l^{e_d}{}_{k+1}^{t+1}$	[mm]	Length of bar 'd' at the current, next step
$\Delta l^{e_d}{}_k^{t+1}$	[mm]	Incremental length of bar 'd' at the current step

Incremental rotation is approximated through consideration of the local vertical nodal displacements and the bar length at the current incremental step (Bathe, 1986; Gavin, 2014):

$$\alpha^{e_d}{}_{k+1}^{t+1} = \alpha^{e_d}{}_k^{t+1} + \Delta\alpha^{e_d}{}_k^{t+1} \tag{9.17}$$

with

$$\tan\Delta\alpha^{e_d}{}_k^{t+1} = \frac{\Delta u_y{}'^{e_d}{}_{2\ k}^{t+1} - \Delta u_y{}'^{e_d}{}_{1\ k}^{t+1}}{l^{e_d}{}_k^{t+1}} \approx \Delta\alpha^{e_d}{}_k^{t+1}$$

where

$\Delta u_y{}'^{e_d\,t+1}_{i_d\;k}$	[mm]	Incremental local vertical displacement of node 'i' along edge 'd'
$\alpha^{e_d\,t+1}_{k}, \alpha^{e_d\,t+1}_{k+1}$	[rad]	Angle of bar 'd' at the current, next step
$\Delta\alpha^{e_d\,t+1}_{k}$	[rad]	Incremental angle of bar 'd' at the current step

Incremental elastic strain energy for each individual bar

The geometrical non-linear extension of the FEM definition is best explained by examination of this single bar. Compared to the previous chapter are the deformations assumed to influence the equilibrium conditions. This influence is characterised as elongation and rotation of the bar expressed in the local coordinate system aligned with the deformed axis as shown in Fig. 9.3 (Bathe, 1986; Gavin, 2014). Only linear variation along the bar axis of the local displacements are assumed to contribute based on omitting rigid body motions. Using the mechanical strain integral along the bar axis defines these displacements as follows:

$$\frac{\partial}{\partial t}\left(\boldsymbol{u}'^{\boldsymbol{e_d\,t+1}}_{\boldsymbol{k}} - \boldsymbol{u_T}'^{\boldsymbol{e_d\,t+1}}_{\boldsymbol{k}}\right) = \frac{\partial}{\partial t}\left(\begin{bmatrix} u_x{}'^{e_d\,t+1}_{k} \\ u_y{}'^{e_d\,t+1}_{k} \end{bmatrix} - \begin{bmatrix} u_T{}'^{e_d\,t+1}_{k} \\ 0 \end{bmatrix}\right)$$

$$= \int_{l^{e_d}} \frac{\partial}{\partial t}\left(\begin{bmatrix} \left[\frac{\partial u_x}{\partial x}\right]'^{e_d\,t+1}_{k} \\ \left[\frac{\partial u_y}{\partial x}\right]'^{e_d\,t+1}_{k} \end{bmatrix} - \begin{bmatrix} \varepsilon_T{}'^{e_d\,t+1}_{k} \\ 0 \end{bmatrix}\right) dl^{e_d} = \int_{l^{e_d}} \frac{\partial}{\partial t}\begin{bmatrix} \varepsilon_m{}'^{e_d\,t+1}_{k} \\ \alpha^{e_d\,t+1}_{k} \end{bmatrix} dl^{e_d} \tag{9.18}$$

where

$\boldsymbol{u}'^{\boldsymbol{e_d\,t+1}}_{\boldsymbol{k}}$	[mm]	Displacement vector governing bar 'd' at the current step
$\boldsymbol{u_T}'^{\boldsymbol{e_d\,t+1}}_{\boldsymbol{k}}$	[mm]	Displacement vector governing the thermal elongation of bar 'd'

The corresponding local forces are obtained through decomposition of the normal force present in the bar using the incremental rotation (Bathe, 1986; Gavin, 2014). Similar terms as previously established are defined, reflecting the mechanical strain and rotation increment:

$$\boldsymbol{N}'^{\boldsymbol{e_d\,t+1}}_{\boldsymbol{k}} = \begin{bmatrix} N_x{}'^{e_d\,t+1}_{k} \\ N_y{}'^{e_d\,t+1}_{k} \end{bmatrix} = \int_{A^{e_d}} \begin{bmatrix} \sigma'^{e_d\,t+1}_{k} & 0 \\ 0 & \sigma'^{e_d\,t+1}_{k} \end{bmatrix} \begin{bmatrix} \cos\Delta\alpha^{e_d\,t+1}_{k} \\ \sin\Delta\alpha^{e_d\,t+1}_{k} \end{bmatrix} dA^{e_d}$$

$$\approx \int_{A^{e_d}} \begin{bmatrix} \sigma'^{e_d\,t+1}_{k} \\ 0 \end{bmatrix} dA^{e_d} + \int_{A^{e_d}} \begin{bmatrix} \sigma'^{e_d\,t+1}_{k} & 0 \\ 0 & \sigma'^{e_d\,t+1}_{k} \end{bmatrix} \begin{bmatrix} \Delta\varepsilon_m{}'^{e_d\,t+1}_{k} \\ \Delta\alpha^{e_d\,t+1}_{k} \end{bmatrix} dA^{e_d} \tag{9.19}$$

with

$$\cos\Delta\alpha^{e_d\,t+1}_{k} = \frac{l^{e_d\,t+1}_{k} + \left(\Delta u_x{}'^{e_d\,t+1}_{2\;k} - \Delta u_x{}'^{e_d\,t+1}_{1\;k}\right) - \Delta l_T{}^{e_d\,t+1}_{k}}{l^{e_d\,t+1}_{k}} \approx 1 + \Delta\varepsilon_m{}'^{e_d\,t+1}_{k}$$

$$\sin\Delta\alpha^{e_d\,t+1}_{k} = \frac{\Delta u_y{}'^{e_d\,t+1}_{2\;k} - \Delta u_y{}'^{e_d\,t+1}_{1\;k}}{l^{e_d\,t+1}_{k}} \approx \Delta\alpha^{e_d\,t+1}_{k}$$

where

$\boldsymbol{N'^{e_d}_k{}^{t+1}}$ [N] Normal force vector acting at the cross-section of bar 'd' defined in the local coordinate system at the current step

Combination of the previous relationships defines the geometrical elastic strain energy contribution based on the work produced by the displacement of the local normal forces. Only the second term in Eq. (9.19) is considered since incremental forces based on the current state are required. The approximation of the total elastic strain energy increment also considers the material-based incremental stresses, governing the additional straining similar to chapter 8:

$$\Delta t\left[\frac{\partial U_\varepsilon{}'^{e_d}}{\partial t}\right]_k^{t+1} \approx \Delta U_\varepsilon{}'^{e_d}{}_k^{t+1} = \int_{\Omega'^{e_d}} \frac{1}{2}\varepsilon_m{}'^{e_d}{}_k^{t+1}\Delta\sigma'^{e_d}{}_k^{t+1} d\Omega'^{e_d}$$
$$+ \int_{\Omega'^{e_d}} \frac{1}{2}\begin{bmatrix}\Delta\varepsilon_m{}'^{e_d}{}_k^{t+1}\\ \Delta\alpha^{e_d}{}_k^{t+1}\end{bmatrix}^T \begin{bmatrix}\sigma'^{e_d}{}_k^{t+1} & 0\\ 0 & \sigma'^{e_d}{}_k^{t+1}\end{bmatrix}\begin{bmatrix}\Delta\varepsilon_m{}'^{e_d}{}_k^{t+1}\\ \Delta\alpha^{e_d}{}_k^{t+1}\end{bmatrix} d\Omega'^{e_d} \tag{9.20}$$

Incremental elastic strain energy across the element

For each of the three bars the incremental elastic strain energy is defined according to Eq. (9.20), obtaining an expression in the three axial directions (Bathe, 1986; Gavin, 2014):

$$\Delta U_\varepsilon{}'^{e}{}_k^{t+1} = \int_{\Omega'^{e}} \frac{1}{2}\left(\boldsymbol{\varepsilon_m}{}'^{\boldsymbol{e}}{}_{\boldsymbol{k}}^{\boldsymbol{t+1}{}^T}\Delta\boldsymbol{\sigma}'^{\boldsymbol{e}}{}_{\boldsymbol{k}}^{\boldsymbol{t+1}} + \begin{bmatrix}\Delta\boldsymbol{\varepsilon_m}{}'^{\boldsymbol{e}}{}_{\boldsymbol{k}}^{\boldsymbol{t+1}}\\ \Delta\boldsymbol{\alpha}^{\boldsymbol{e}}{}_{\boldsymbol{k}}^{\boldsymbol{t+1}}\end{bmatrix}^{\boldsymbol{T}}\boldsymbol{\sigma}'^{\boldsymbol{e}}{}_{\boldsymbol{k}}^{\boldsymbol{t+1}}\boldsymbol{I}\begin{bmatrix}\Delta\boldsymbol{\varepsilon_m}{}'^{\boldsymbol{e}}{}_{\boldsymbol{k}}^{\boldsymbol{t+1}}\\ \Delta\boldsymbol{\alpha}^{\boldsymbol{e}}{}_{\boldsymbol{k}}^{\boldsymbol{t+1}}\end{bmatrix}\right) d\Omega'^{e} \tag{9.21}$$

The following contributions define the incremental elastic strain energy for the anisotropic FEM definition:

- Additional elongation of the bars is characterised by the first term based on the incremental stresses. These material contributions are governed by the incremental strains assumed to develop in the local horizontal directions of the deformed bars.

- The second term represents the translation and rotation of the normal force present in each of the deformed bars. Both incremental strains and rotations are used to define the local horizontal and vertical geometrical relationships.

The material and geometric deformations are approximated using two different element gradient matrices (Bathe, 1986; Gavin, 2014). Both these matrices are dependent on the current deformed state of the bars and restates the previous relationship:

$$\Delta U_\varepsilon{}'^{e}{}_k^{t+1} = \int_{\Omega'^{e}} \frac{1}{2}\left(\boldsymbol{u'^{e}_k{}^{t+1}} - \boldsymbol{u_T}{}'^{\boldsymbol{e}}{}_{\boldsymbol{k}}^{\boldsymbol{t+1}}\right)^{\boldsymbol{T}}\boldsymbol{B_{U_M}}{}'^{\boldsymbol{e}}{}_{\boldsymbol{k}}^{\boldsymbol{t+1}{}^T}\Delta\boldsymbol{\sigma}'^{\boldsymbol{e}}{}_{\boldsymbol{k}}^{\boldsymbol{t+1}} d\Omega'^{e} \tag{9.22}$$

$$+ \int_{\Omega'^{e}} \frac{1}{2}\left(\Delta\boldsymbol{u'^{e}_k{}^{t+1}} - \Delta\boldsymbol{u_T}{}'^{\boldsymbol{e}}{}_{\boldsymbol{k}}^{\boldsymbol{t+1}}\right)^{\boldsymbol{T}}\boldsymbol{B_{U_G}}{}'^{\boldsymbol{e}}{}_{\boldsymbol{k}}^{\boldsymbol{t+1}{}^T}\boldsymbol{\sigma}'^{\boldsymbol{e}}{}_{\boldsymbol{k}}^{\boldsymbol{t+1}}\boldsymbol{I}\left(\boldsymbol{B_{U_G}}{}'^{\boldsymbol{e}}{}_{\boldsymbol{k}}^{\boldsymbol{t+1}}\Delta\boldsymbol{u'^{e}_k{}^{t+1}} - \left(\boldsymbol{\varepsilon_T}{}'^{\boldsymbol{e}}{}_{\boldsymbol{k+1}}^{\boldsymbol{t+1}} - \boldsymbol{\varepsilon_T}{}'^{\boldsymbol{e}}{}_{\boldsymbol{k}}^{\boldsymbol{t+1}}\right)\right) d\Omega'^{e}$$

where

$\boldsymbol{B_{U_M}}'^{e\,t+1}_{\;k}$	[1/mm]	Element gradient matrix of the material-based shape functions
$\boldsymbol{B_{U_G}}'^{e\,t+1}_{\;k}$	[1/mm]	Element gradient matrix of the geometrical-based shape functions

The final extension towards a FEM definition involves the nodal forces. These are obtained using the gradient matrices to distribute the normal forces present in the bars. Two contributions are defined with the former governing the material-based incremental stresses acting on the deformed bars. The latter term ensures through decomposition that the current normal forces remain aligned with the bars during incremental deformations. In this respect these geometrical forces are of an incremental nature. The additional stiffness contributed by these forces is also independent of the adopted coordinate system (Bathe, 1986). Hence, the strain energy or work increment reflecting both contributions reads:

$$\begin{aligned}\Delta U_{\varepsilon}{}'^{e\,t+1}_{\;k} &= \Delta W_F{}'^{e\,t+1}_{\;k} \\ &= \frac{1}{2}\left(\left(\boldsymbol{u}'^{e\,t+1}_{k} - \boldsymbol{u_T}'^{e\,t+1}_{k}\right)^{T} \Delta \boldsymbol{F_M}'^{e\,t+1}_{k} + \left(\Delta\boldsymbol{u}'^{e\,t+1}_{k} - \Delta\boldsymbol{u_T}'^{e\,t+1}_{k}\right)^{T} \Delta \boldsymbol{F_G}'^{e\,t+1}_{k}\right)\end{aligned} \tag{9.23}$$

where

$\Delta\boldsymbol{F_M}'^{e\,t+1}_{\;k}$	[N]	Incremental element nodal force vector representing the material-based contributions
$\Delta\boldsymbol{F_G}'^{e\,t+1}_{\;k}$	[N]	Incremental element nodal force vector representing the geometrical-based contributions

Coordinate transformation based on three geometrical directions

Local coordinate systems consisting of both local principal directions are first defined for each of the three bars. The coordinate transformation tensor stated in Eq. (9.6) is extended by including the vertical direction as stated in chapter 5 (Wells, 2006; Blom, 2009):

$$\boldsymbol{x_G}'^{e} = \boldsymbol{T_{\alpha_G}}'^{e}\boldsymbol{x^e} \tag{9.24}$$

with

$$\boldsymbol{x_G}'^{e} = \begin{bmatrix} x'^{e_I}_{1} \\ y'^{e_I}_{1} \\ x'^{e_I}_{2} \\ y'^{e_I}_{2} \\ x'^{e_{II}}_{2} \\ y'^{e_{II}}_{2} \\ x'^{e_{II}}_{3} \\ y'^{e_{II}}_{3} \\ x'^{e_{III}}_{3} \\ y'^{e_{III}}_{3} \\ x'^{e_{III}}_{1} \\ y'^{e_{III}}_{1} \end{bmatrix} \qquad \boldsymbol{T_{\alpha_G}}'^{e} = \begin{bmatrix} \cos\alpha^{e_I} & \sin\alpha^{e_I} & 0 & 0 & & \\ -\sin\alpha^{e_I} & \cos\alpha^{e_I} & 0 & 0 & & \\ 0 & 0 & \cos\alpha^{e_I} & \sin\alpha^{e_I} & & \\ 0 & 0 & -\sin\alpha^{e_I} & \cos\alpha^{e_I} & & \\ & & \cos\alpha^{e_{II}} & \sin\alpha^{e_{II}} & 0 & 0 \\ & 0 & -\sin\alpha^{e_{II}} & \cos\alpha^{e_{II}} & 0 & 0 \\ & & 0 & 0 & \cos\alpha^{e_{II}} & \sin\alpha^{e_{II}} \\ & & 0 & 0 & -\sin\alpha^{e_{II}} & \cos\alpha^{e_{II}} \\ 0 & 0 & & & \cos\alpha^{e_{III}} & \sin\alpha^{e_{III}} \\ 0 & 0 & & & -\sin\alpha^{e_{III}} & \cos\alpha^{e_{III}} \\ \cos\alpha^{e_{III}} & \sin\alpha^{e_{III}} & 0 & & 0 & 0 \\ -\sin\alpha^{e_{III}} & \cos\alpha^{e_{III}} & & & 0 & 0 \end{bmatrix}$$

where

$\boldsymbol{x_G}'^{e}$	[mm]	Local element coordinate system vector based on the triangular geometrical directions
$\boldsymbol{T_{\alpha_G}}'^{e}$	[-]	Element coordinate transformation tensor based on the triangular geometrical directions (second order)

Incremental local and global material-based forces

The incremental local forces across the domain are obtained through consideration of the stresses defined by Eq. (9.5) substituted into the first term of Eq. (9.23). Two material-based contributions are included reflecting temperature and pressure dependence:

$$\begin{aligned}\Delta \boldsymbol{F_{T_M}}_{\boldsymbol{k}}^{\boldsymbol{et+1}} + \Delta \boldsymbol{F_{P_M}}_{\boldsymbol{k}}^{\boldsymbol{et+1}} &= \int_{\Omega'^{e}} \boldsymbol{T_{\alpha_M}}'^{\boldsymbol{et+1}^{\boldsymbol{T}}}_{\boldsymbol{k}} \left(\Delta \boldsymbol{F_{T_M}}'^{\boldsymbol{et+1}}_{\boldsymbol{k}} + \Delta \boldsymbol{F_{P_M}}'^{\boldsymbol{et+1}}_{\boldsymbol{k}}\right) d\Omega'^{e} \\ &= \int_{\Omega'^{e}} \boldsymbol{T_{\alpha_M}}'^{\boldsymbol{et+1}^{\boldsymbol{T}}}_{\boldsymbol{k}} \boldsymbol{B_{U_M}}'^{\boldsymbol{et+1}^{\boldsymbol{T}}}_{\boldsymbol{k}} \Delta \boldsymbol{\sigma}'^{\boldsymbol{et+1}}_{\boldsymbol{k}} d\Omega'^{e}\end{aligned} \tag{9.25}$$

where

$\Delta \boldsymbol{F_{T_M}}_{\boldsymbol{k}}^{\boldsymbol{et+1}}$	[N]	Incremental element nodal force vector representing the material-based temperature-induced stresses
$\Delta \boldsymbol{F_{P_M}}_{\boldsymbol{k}}^{\boldsymbol{et+1}}$	[N]	Incremental element nodal force vector representing the material-based pressure-induced stresses

Incremental temperature-induced stresses are based on stiffness variation as well as initial elongation strain development. However, the geometrical non-linear FEM definition implies that only the mechanical strain increment is defined by the element gradient matrix. So, compared to chapter 8 is the first integral expressed using the strains present in the current step as defined by Eq. (9.14). In the following also the transformation of the incremental global displacements, using Eq. (9.6), is included:

$$\begin{aligned}\Delta \boldsymbol{F_{T_M}}_{\boldsymbol{k}}^{\boldsymbol{et+1}} &= \int_{\Omega'^{e}} \boldsymbol{T_{\alpha_M}}'^{\boldsymbol{et+1}^{\boldsymbol{T}}}_{\boldsymbol{k}} \boldsymbol{B_{U_M}}'^{\boldsymbol{et+1}^{\boldsymbol{T}}}_{\boldsymbol{k}} \left(\boldsymbol{D}'^{\boldsymbol{et+1}}_{\boldsymbol{k+1}} - \boldsymbol{D}'^{\boldsymbol{et+1}}_{\boldsymbol{k}}\right)\left(\boldsymbol{\varepsilon}'^{\boldsymbol{et+1}}_{\boldsymbol{k}} - \boldsymbol{\varepsilon_T}'^{\boldsymbol{et+1}}_{\boldsymbol{k}}\right) d\Omega'^{e} \\ &+ \int_{\Omega'^{e}} \boldsymbol{T_{\alpha_M}}'^{\boldsymbol{et+1}^{\boldsymbol{T}}}_{\boldsymbol{k}} \boldsymbol{B_{U_M}}'^{\boldsymbol{et+1}^{\boldsymbol{T}}}_{\boldsymbol{k}} \boldsymbol{D}'^{\boldsymbol{et+1}}_{\boldsymbol{k}} \left(\boldsymbol{B_{U_M}}'^{\boldsymbol{et+1}}_{\boldsymbol{k}} \boldsymbol{T_{\alpha_M}}'^{\boldsymbol{et+1}}_{\boldsymbol{k}} \Delta \boldsymbol{u}^{\boldsymbol{et+1}}_{\boldsymbol{k}} - \left(\boldsymbol{\varepsilon_T}'^{\boldsymbol{et+1}}_{\boldsymbol{k+1}} - \boldsymbol{\varepsilon_T}'^{\boldsymbol{et+1}}_{\boldsymbol{k}}\right)\right) d\Omega'^{e}\end{aligned} \tag{9.26}$$

Additional equivalent global nodal forces are governed by the incremental pressure-induced stresses using the same approach:

$$\Delta \boldsymbol{F_{P_M}}_{\boldsymbol{k}}^{\boldsymbol{et+1}} = \int_{\Omega'^{e}} \boldsymbol{T_{\alpha_M}}'^{\boldsymbol{et+1}^{\boldsymbol{T}}}_{\boldsymbol{k}} \boldsymbol{B_{U_M}}'^{\boldsymbol{et+1}^{\boldsymbol{T}}}_{\boldsymbol{k}} \left(\boldsymbol{\sigma_P}'^{\boldsymbol{et+1}}_{\boldsymbol{k+1}} - \boldsymbol{\sigma_P}'^{\boldsymbol{et+1}}_{\boldsymbol{k}}\right) d\Omega'^{e} \tag{9.27}$$

Local and global geometrical-based forces

The incremental translation and rotation of the current axial stress state is governed by the second term in Eq. (9.23). These local incremental forces are characterised by the axial stress defined as diagonal matrix and the geometrical non-linear element gradient matrix. The strain and rotation increments are approximated by the local displacements using also coordinate transformations according to Eq. (9.24):

$$\Delta \boldsymbol{F}_{\boldsymbol{T}_G}{}_{\boldsymbol{k}}^{\boldsymbol{et+1}} = \int_{\Omega'^e} \boldsymbol{T}_{\boldsymbol{\alpha}_M}{}'_{\boldsymbol{k}}^{\boldsymbol{et+1}^{\boldsymbol{T}}} \Delta \boldsymbol{F}_{\boldsymbol{T}_G}{}'_{\boldsymbol{k}}^{\boldsymbol{et+1}} d\Omega'^e$$

$$= \int_{\Omega'^e} \boldsymbol{T}_{\boldsymbol{\alpha}_G}{}'_{\boldsymbol{k}}^{\boldsymbol{et+1}^{\boldsymbol{T}}} \boldsymbol{B}_{\boldsymbol{U}_G}{}'_{\boldsymbol{k}}^{\boldsymbol{et+1}^{\boldsymbol{T}}} \boldsymbol{\sigma}'_{\boldsymbol{k}}^{\boldsymbol{et+1}} \boldsymbol{I} \left(\boldsymbol{B}_{\boldsymbol{U}_G}{}'_{\boldsymbol{k}}^{\boldsymbol{et+1}} \boldsymbol{T}_{\boldsymbol{\alpha}_G}{}'_{\boldsymbol{k}}^{\boldsymbol{et+1}} \Delta \boldsymbol{u}_{\boldsymbol{k}}^{\boldsymbol{et+1}} - \left(\boldsymbol{\varepsilon}_{\boldsymbol{T}}{}'_{\boldsymbol{k+1}}^{\boldsymbol{et+1}} - \boldsymbol{\varepsilon}_{\boldsymbol{T}}{}'_{\boldsymbol{k}}^{\boldsymbol{et+1}} \right) \right) d\Omega'^e \quad (9.28)$$

where

$\Delta \boldsymbol{F}_{\boldsymbol{T}_G}{}_{\boldsymbol{k}}^{\boldsymbol{et+1}}$	[N]	Incremental element nodal force vector representing the geometrical alignment of the current stress state

Local heterogeneous material description

The distribution of the concrete components in the cross-section characterises the mechanical properties defined by the elasticity tensor and the temperature strain vector in Eq. (9.5). Both the solid and porous material are thus assumed to deform according to linear elasticity (Schlangen, 1993; Vervuurt, 1997). The level of anisotropy increases in case the three bars are characterised by different concrete components and especially at high temperatures. Furthermore, pressure-induced stresses only develop in the porous material based on assumed impermeably aggregates as discussed in chapter 7.

9.2.4 Crack initiation through brittle extensional fracture

The level of anisotropy in the local continuum changes considerably in case a crack develops. Crack initiation occurs by the tensile stresses exceeding the strength of the material (van Mier, 1997; Schlangen, 1993). This local weakening of the material is, especially at high temperatures, caused by the relatively low tensile strength of concrete (RILEM TC-HTC, 2004). Tensile fracture is therefore commonly used to approximate cracking, for instance through a discrete approach based on brittle fracture (Schlangen, 1993; Vervuurt, 1997) or a smeared concept including softening to describe crack opening (de Borst, 1986; Rots, 1988). Other fracture types based on shearing or tearing are also distinguished (Schlangen, 1993).

Incremental brittle fracture of bars

The local tension-based initiation forms the basis for the assumed brittle fracture mechanics approach used to simulate cracking (Schlangen, 1993; Vervuurt, 1997). This process starts at the bar with the highest load level when the axial tensile stress exceeds the strength of the concrete (Schlangen, 1993; Vervuurt, 1997). After fracture, the material in this direction is assumed to have no stiffness contribution (Schlangen, 1993; Vervuurt, 1997):

$$\frac{\sigma'}{f_t'} > 1 \rightarrow E' = E_{cr}' = 0 \tag{9.29}$$

where

f_t'	[MPa]	Axial tensile strength of the local material direction
E'	[MPa]	Young's modulus of the local material direction
E_{cr}'	[MPa]	Young's modulus of the cracked local material direction

In this simplified approach it is assumed that the stiffness perpendicular to crack is negligible, avoiding the usage of local softening. The local elasticity tensor in the anisotropic FEM definition is modified to reflect the fractured bar as shown in Fig. 9.4. This affectively removes the fractured bar from the domain and the corresponding nodes are no longer connected (Schlangen, 1993; Vervuurt, 1997). The material is genuinely separated and any force transfer across the crack is supposed to be impossible.

Crack development is based on continuation through an incremental approach, allowing to determine the deformations and redistributed stresses surrounding the crack (Schlangen, 1993; Vervuurt, 1997). Additional linear elastic steps define more bars to be fractured, using the peak tensile stresses to drive the crack propagation (van Mier, 1997). This incremental crack development process continues until equilibrium is reached between the tensile stresses and the material strength. Under these circumstances, no bars fulfil the fracture criterion stated by Eq. (9.29) (Schlangen, 1993; Vervuurt, 1997).

Boundary condition at the edge of the crack

The removal of stiffness in a material direction changes the discretisation of the cross-section on which the incremental approach is based. Fracturing of a bar is therefore only possible in case the elastic strain energy across the domain is maintained. From Eq. (9.21) only the first material contribution needs to be considered since after fracture no stress is assumed to be transmitted across the crack. The fracture process involves the instantaneous and complete reduction of the local axial stiffness to ensure sufficient localisation occurs.

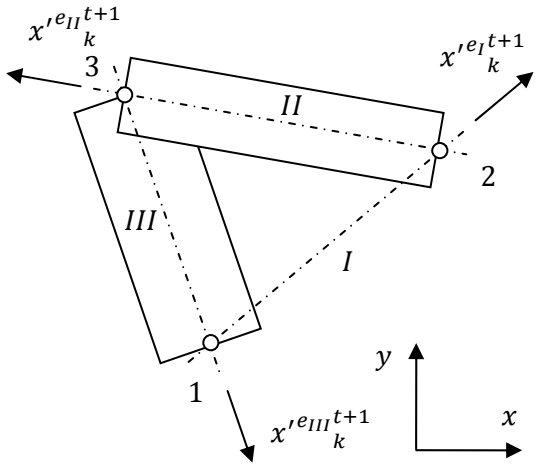

Modified local elasticity tensor

$$\boldsymbol{D'^{e\,t+1}_{k+1}} = \frac{1}{1-\nu^2}\begin{bmatrix} 0 & 0 & 0 \\ 0 & E'^{e_{II}}{}_{k+1}^{t+1} & 0 \\ 0 & 0 & E'^{e_{III}}{}_{k+1}^{t+1} \end{bmatrix}$$

Modified local stress vector

$$\boldsymbol{\sigma'^{e\,t+1}_{k+1}} = \begin{bmatrix} 0 \\ \sigma'^{e_{II}}{}_{k+1}^{t+1} \\ \sigma'^{e_{III}}{}_{k+1}^{t+1} \end{bmatrix}$$

Fig. 9.4 *Schematic representation of the cracked triangularly orientated set of 1D bars in $\mathbb{R}^2$. After fracture of the first bar the local elasticity tensor is modified and the stress is redistributed to the surrounding bars.*

Nodes previously connected by the bar form a new crack edge at which the normal force or alternatively the stress contribution is redistributed into the system. It is important to consider that the temperature strain imposed by the bar is no longer present. However, the removal of stiffness is, through consideration of the local stress in Eq. (9.5), assumed not to influence the imposed pressure. So, at the crack edge the following local-based boundary condition holds:

$$\Delta\boldsymbol{\sigma}'^{\boldsymbol{e}\boldsymbol{t+1}}_{\boldsymbol{k}} \cdot \boldsymbol{n}'\Big|_{\Gamma_{cr}{}'^{e}} = \Delta\sigma_{cr}{}'^{e\,t+1}_{k} = \sigma'^{e\,t+1}_{k} \tag{9.30}$$

where

$\Delta\sigma_{cr}{}'^{e\,t+1}_{k}$	[MPa]	Local incremental axial stress governing the redistribution of the normal force present in the fractured bar
$\boldsymbol{n}'$	[-]	Unit outward normal vector defined by the local coordinate systems

The remaining incremental steps reflect the additional gas pressure development at this edge:

$$\Delta\boldsymbol{\sigma}'^{\boldsymbol{e}\boldsymbol{t+1}}_{\boldsymbol{k}} \cdot \boldsymbol{n}'\Big|_{\Gamma_{cr}{}'^{e}} = \sigma_{P}{}'^{e\,t+1}_{k+1} - \sigma_{P}{}'^{e\,t+1}_{k} \tag{9.31}$$

Incremental local and global fracture forces

The redistribution of the stress at fracture is based on a similar force relationship as the temperature-induced stiffness variation stated in Eq. (9.26). However, in this case the stiffness is completely removed dependent on the incremental time and crack step. The stresses are redistributed to the surrounding material based on the following nodal forces:

$$\Delta\boldsymbol{F}_{\boldsymbol{cr_M}}{}^{\boldsymbol{e}\boldsymbol{t+1}}_{\boldsymbol{k}} = \int_{\Omega'^{e}} \boldsymbol{T}_{\boldsymbol{\alpha_M}}{}'^{\boldsymbol{e}\boldsymbol{t+1}^{\boldsymbol{T}}}_{\boldsymbol{k}} \Delta\boldsymbol{F}_{\boldsymbol{cr_M}}{}'^{\boldsymbol{e}\boldsymbol{t+1}}_{\boldsymbol{k}} d\Omega'^{e} = \int_{\Omega'^{e}} \boldsymbol{T}_{\boldsymbol{\alpha_M}}{}'^{\boldsymbol{e}\boldsymbol{t+1}^{\boldsymbol{T}}}_{\boldsymbol{k}} \boldsymbol{B}_{\boldsymbol{U_M}}{}'^{\boldsymbol{e}\boldsymbol{t+1}^{\boldsymbol{T}}}_{\boldsymbol{k}} \boldsymbol{\sigma}'^{\boldsymbol{e}\boldsymbol{t+1}}_{\boldsymbol{k}} d\Omega'^{e} \tag{9.32}$$

where

$\Delta\boldsymbol{F}_{\boldsymbol{cr_M}}{}^{\boldsymbol{e}\boldsymbol{t+1}}_{\boldsymbol{k}}$	[N]	Incremental element nodal force vector governing the material-based redistribution of stresses at fracture

Estimation of the crack width

An estimation for the crack opening or crack width is obtained through using the local displacement increments. The deformed state of the bar at fracture is used as reference length, including mechanical as well as thermal effects. The incremental crack width is thus directly available from the local horizontal displacements as indicated for a typical bar:

$$w'^{e_d\,t+1}_{k+1} = w'^{e_d\,t+1}_{k} + \Delta w'^{e_d\,t+1}_{k} \tag{9.33}$$

with

$$\Delta w'^{e_d\,t+1}_{k} = \Delta u_x{}'^{e_d\,t+1}_{2\quad k} - \Delta u_x{}'^{e_d\,t+1}_{1\quad k}$$

where

$w'^{e_d\,t+1}_{k}, w'^{e_d\,t+1}_{k+1}$	[mm]	Crack width along the axis of fractured bar 'd' at the current, next step
$\Delta w'^{e_d\,t+1}_{k}$	[mm]	Incremental crack width at the current step

Anisotropic stiffness influence

The sudden reduction in material stiffness characterises the crack which becomes directionally fixed (Schlangen, 1993; Vervuurt, 1997), considering only geometrical non-linear effects. Two aspects govern the material response. First, the removal of stiffness forces the crack to open under sustained loading. This localises deformations causing relaxation of the stresses in the surrounding material (van Mier, 1997). Local strains, stresses and stiffness are affected by the direction-dependent removal of each bar (Felippa, 2004a; Zienkiewicz, et al., 2005). The fourth order transformations, defined by Eq. (9.7), Eq. (9.10) and Eq. (9.12) respectively, govern the anisotropic global strains, stresses and stiffness.

The cracks also tend to form strong discontinuities in the material, affecting the local and global force transfer in the cross-section. This second aspect is governed by the schematisation of the crack edges as stress free, considering that only pressures are imposed. No normal forces are transmitted across the crack which forces the load to be transferred through the 1D bars situated at both edges. Changing the local transfer of forces is reflected in rotation of the stresses in the surrounding material. Along the crack shear stresses develop based on the directional change of the principal stresses. Moreover, additional global stresses could also arise based on the orientation as well as opening along the crack path. With distance to the crack edges the influence of the newly imposed boundary condition reduces.

9.3 Numerical stability

The anisotropic FEM definition by sets of three 1D bars is sufficient to represent the global strains, considering also the adopted in-plane schematisation. Axial forces are transmitted between the hinged bars which through the triangular orientation provide local as well as global static equilibrium. During the incremental fracture process bars are removed, creating crack edges at which the corresponding stresses are imposed as a Neumann boundary condition. This redistribution by localised forces governs the crack opening and the subsequent relaxation of the surrounding material. However, the assumed hinged nodes could allow for the deformations to become too localised, causing an overly weak response and the possibility for numerical instability. In this paragraph additional stiffness is defined through first considering the nature of these instabilities. Thereafter the Bernoulli-Euler beam element is stated using unit displacements at the nodes in order to reflect the local stiffness definition.

9.3.1 Stabilised redistribution of incremental fracture forces

The local definition of three constant strains implies that only axial forces are considered to represent the mechanical response of the material. Each node is thereby assumed to act as a hinge, stabilised by the local equilibrium of static forces. The schematisation of each element as three bars is also considered stable through the same equilibrium considerations. However, by removing one or several bars this element definition can become unstable. Under these circumstances equilibration of imposed forces can cause the remaining bars to exhibit relatively large elongations and especially rotations. These relatively large deformations develop in case insufficient confinement is provided by the surrounding material. This was found to especially occur at the heated surface or in highly cracked parts of the cross-section.

These displacements are firstly caused by the absence of a local force definition perpendicular to the bar axis. Only through local decomposition of the axial force equilibrium is attained. In this respect the interaction between the bars in the triangular orientation is required to stabilise the mechanical response. By weakening the triangular element definition, the local system insufficiently resembles a truss. A local mechanism is formed, caused by the schematisation. The assumed hinged nodes are the second cause, allowing the remaining bars to freely rotate. This localised weakening is surrounded by material which dependent on the level of cracking tends to be stiffer. Under these circumstance deformations could become localised in only some of the surrounding bars. A weakened material response develops which insufficiently redistributes the fracture forces, causing cracks to not localise and propagate correctly.

Improving the fracture behaviour requires that the element has a second load transfer mechanism which defines a perpendicular force-stiffness relationship along each bar. Introduction of additional shear deformation is insufficient since this does not stabilise the free rotation at the hinges. However, by including bending the local displacement perpendicular to the bar axis is defined, reflecting shear force as well as moment contributions. The latter governs the rotational restraint at the nodes which, based on a Bernoulli-Euler hypothesis, goes back to the traditional lattice approach used in this thesis (Schlangen, 1993; Vervuurt, 1997). This particular beam considers cross-sectional rotations only by bending, neglecting possible shear force contributions (Wells, 2006; Felippa, 2004a).

The benefit of defining local bending is the possibility for imposed forces to curve the material directions. Local elongations and especially rotations of bars surrounding a crack are limited by the bending stiffness of the added beams. Furthermore, by definition of the nodal rotational restraint the overall deformations will reflect non-linear contributions. Imposing the localised incremental fracture forces results in a distributed displacement across the surrounding nodes along the crack edge. This spreads the load and limits the possibilities for a overly weak and too localised behaviour, obtaining a smoother displacement.

By extending the element definition to include local curvature the strains are no longer constant in any of the material directions. Extensional stresses are extended by moment contributions which vary linearly along each beam axis (Schlangen, 1993; Vervuurt, 1997). Also parabolic shear stresses develop in the assumed rectangular cross-section (Hartsuijker & Welleman, 2007). In this respect it needs to be considered that local bending is only considered for redistribution, extending the main local axial force transfer. In determination of the amount of bending it should therefore be ensured that only limited stiffening in the mechanical response is observed.

9.3.2 Derivation of three 1D Bernoulli-Euler beams

Derivation of a single Bernoulli-Euler beam from the fourth order differential equation is readily available in literature (Wells, 2006; Felippa, 2004a; Blom, 2009). However, in this section the various stiffness contributions are elaborated through unit nodal displacements (Prezemieniecki, 1968/1985). This allows to focus on the local vertical displacements as defined by the bending deformation. Incremental local forces are determined based on imposing unit displacements at both nodes of a typical beam.

Incremental nodal unit displacements to define the individual beam stiffness

Bending is characterised by the moment-curvature relationship, restated from chapter 5, while omitting the incremental steps. The vertical displacement and rotation are considered positive in accordance with the local coordinate system as seen in Fig. 9.5. Through consideration of rotational equilibrium expressed in the shear force and moment at the first node, also defined positive in the local directions, this becomes (Prezemieniecki, 1968/1985):

$$\Delta M'^{e_d} = E'^{e_d} I'^{e_d} \Delta\kappa'^{e_d} = E'^{e_d} I'^{e_d} \frac{d\Delta\varphi^{e_d}}{dx'^{e_d}} = E'^{e_d} I'^{e_d} \frac{d^2 \Delta u_y{}'^{e_d}}{dx'^{e_d 2}} = \Delta F_y{}'^{e_d}_1 x'^{e_d} - \Delta M_1^{e_d} \tag{9.34}$$

where

$\Delta\kappa'^{e_d}$	[1/mm]	Incremental local curvature along the axis of beam 'd'
$\Delta\varphi^{e_d}$	[rad]	Incremental rotation along the axis of beam 'd'
$\Delta F_y{}'^{e_d}_1$	[N]	Incremental vertical force defined at the first node of beam 'd'
$\Delta M_1^{e_d}$	[Nmm]	Incremental moment defined at the first node of beam 'd'

Integration with respect to the local axis defines the incremental rotation and the incremental local vertical displacement expressed in unknown constants (Prezemieniecki, 1968/1985):

$$\begin{aligned} \Delta\varphi^{e_d} &= \frac{d\Delta u_y{}'^{e_d}}{dx'^{e_d}} = \frac{\Delta F_y{}'^{e_d}_1}{2E'^{e_d} I'^{e_d}} x'^{e_d 2} - \frac{\Delta M_1^{e_d}}{E'^{e_d} I'^{e_d}} x'^{e_d} + C_1 \\ \Delta u_y{}'^{e_d} &= \frac{\Delta F_y{}'^{e_d}_1}{6E'^{e_d} I'^{e_d}} x'^{e_d 3} - \frac{\Delta M_1^{e_d}}{2E'^{e_d} I'^{e_d}} x'^{e_d 2} + C_1 x'^{e_d} + C_2 \end{aligned} \tag{9.35}$$

Both constants of integration are defined by the nodal boundary conditions, considering also the vertical displacement along the beam axis (Hartsuijker & Welleman, 2007). At the inflection point of this elastic curve the moment is zero, defining the equilibrium relationship with the shear force (Hartsuijker & Welleman, 2007; Prezemieniecki, 1968/1985).

The first elastic curve in Fig. 9.5 is used to define the nodal shear forces and moments required to cause a unit vertical displacement at node 1. After fulfilling two of the restrained boundary conditions while introducing the equilibrium relationship the local incremental vertical displacement is defined by (Prezemieniecki, 1968/1985):

$$\Delta u_y{}'^{e_d} = \frac{\Delta F_y{}'^{e_d}_1}{6E'^{e_d} I'^{e_d}} \left(x'^{e_d 3} + \frac{l^{e_d 3}}{2} \right) - \frac{\Delta M_1^{e_d}}{2E'^{e_d} I'^{e_d}} x'^{e_d 2} \tag{9.36}$$

Similar considerations also define the incremental vertical displacement based on the second elastic curve (Prezemieniecki, 1968/1985):

$$\Delta u_y{}'^{e_d} = \frac{\Delta F_y{}'^{e_d}_1}{6E'^{e_d} I'^{e_d}} \left(x'^{e_d 3} - l^{e_d 2} x'^{e_d} \right) - \frac{\Delta M_1^{e_d}}{2E'^{e_d} I'^{e_d}} \left(x'^{e_d 2} - l^{e_d} x'^{e_d} \right) \tag{9.37}$$

Both cubic vertical displacements reflect the higher order of the differential equation and define the curvature and the moment as linear along the beam axis. Shear forces are constant based on fulfilling vertical equilibrium (Hartsuijker & Welleman, 2007).

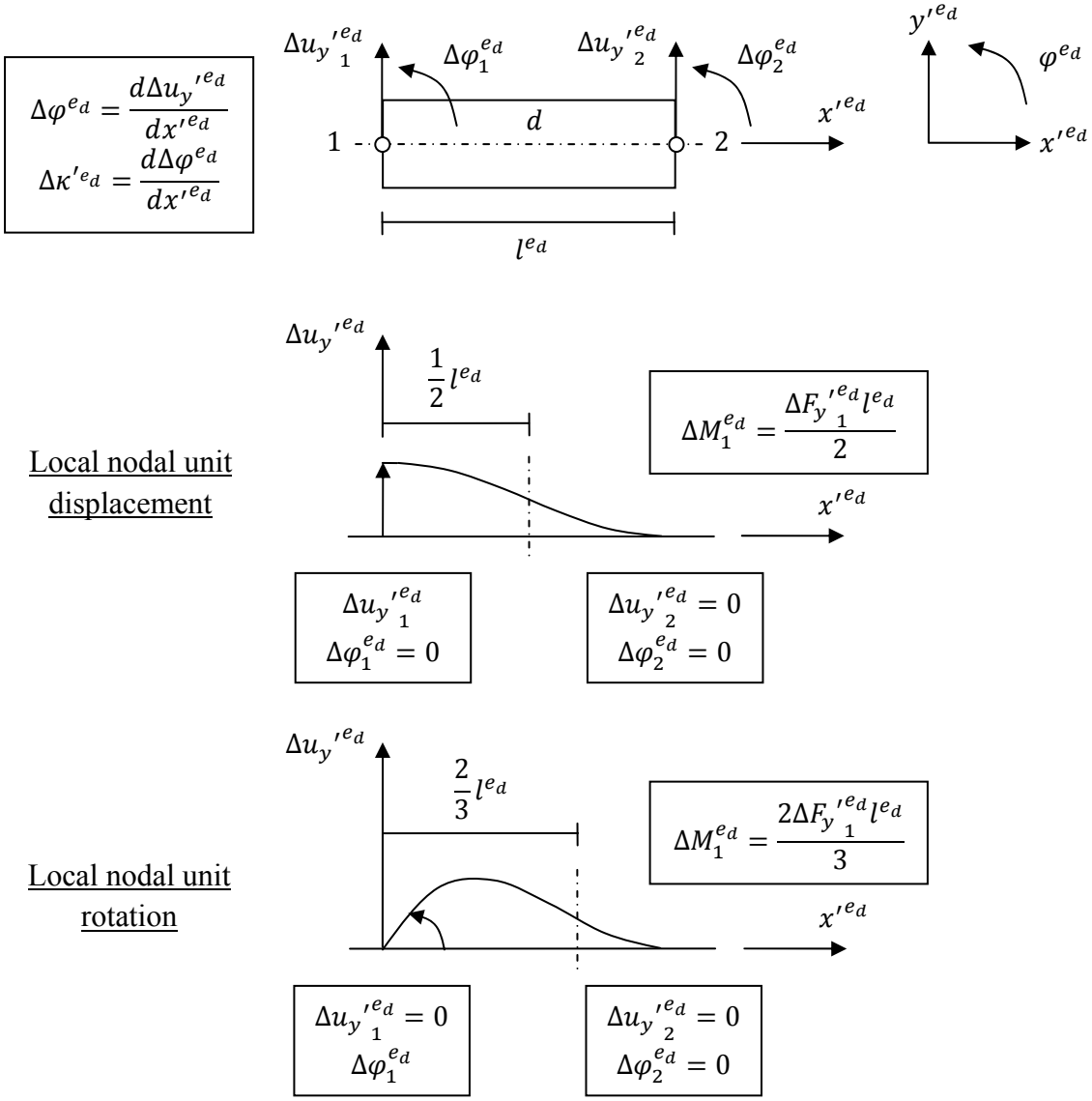

Fig. 9.5 *Schematic representation of the incremental local vertical displacement through unit displacements at the first node of the 1D beam in $\mathbb{R}^2$. In both elastic curves the point of inflection with the corresponding equilibrium relationship is indicated* (Prezemieniecki, 1968/1985).

The nodal shear forces and moments required to impose both unit displacements while restraining the remaining variables are derived by fulfilling the corresponding boundary condition (Prezemieniecki, 1968/1985). Through consideration of vertical and rotational equilibrium half of the Bernoulli-Euler beam stiffness matrix is obtained (Prezemieniecki, 1968/1985). Similar deliberations with respect to unit displacements defined at the second node can be used to obtain the remaining contributions (Prezemieniecki, 1968/1985).

Combination of the resultant four force-displacement relationships defines the Bernoulli-Euler beam (Prezemieniecki, 1968/1985). The constant shear force and the linear moment distribution along the beam axis directly define the beam stiffness relationship by:

$$\Delta \boldsymbol{F_B}'^{\boldsymbol{e_d}} = \boldsymbol{K_B}'^{\boldsymbol{e_d}} \Delta \boldsymbol{u_B}'^{\boldsymbol{e_d}} \tag{9.38}$$

with

$$\Delta \boldsymbol{F_B}'^{e_d} = \begin{bmatrix} \Delta {F_y}'^{e_d}_1 \\ \Delta {M'}^{e_d}_1 \\ \Delta {F_y}'^{e_d}_2 \\ \Delta {M'}^{e_d}_2 \end{bmatrix} \qquad \Delta \boldsymbol{u_B}'^{e_d} = \begin{bmatrix} \Delta {u_y}'^{e_d}_1 \\ \Delta {\varphi'}^{e_d}_1 \\ \Delta {u_y}'^{e_d}_2 \\ \Delta {\varphi'}^{e_d}_2 \end{bmatrix}$$

$$\boldsymbol{K_B}'^{e_d} = \begin{bmatrix} \frac{12E'^{e_d}I'^{e_d}}{{l^{e_d}}^3} & \frac{6E'^{e_d}I'^{e_d}}{{l^{e_d}}^2} & -\frac{12E'^{e_d}I'^{e_d}}{{l^{e_d}}^3} & \frac{6E'^{e_d}I'^{e_d}}{{l^{e_d}}^2} \\ \frac{6E'^{e_d}I'^{e_d}}{{l^{e_d}}^2} & \frac{4E'^{e_d}I'^{e_d}}{l^{e_d}} & -\frac{6E'^{e_d}I'^{e_d}}{{l^{e_d}}^2} & \frac{2E'^{e_d}I'^{e_d}}{l^{e_d}} \\ -\frac{12E'^{e_d}I'^{e_d}}{{l^{e_d}}^3} & -\frac{6E'^{e_d}I'^{e_d}}{{l^{e_d}}^2} & \frac{12E'^{e_d}I'^{e_d}}{{l^{e_d}}^3} & -\frac{6E'^{e_d}I'^{e_d}}{{l^{e_d}}^2} \\ \frac{6E'^{e_d}I'^{e_d}}{{l^{e_d}}^2} & \frac{2E'^{e_d}I'^{e_d}}{l^{e_d}} & -\frac{6E'^{e_d}I'^{e_d}}{{l^{e_d}}^2} & \frac{4E'^{e_d}I'^{e_d}}{l^{e_d}} \end{bmatrix}$$

where

$\Delta \boldsymbol{F_B}'^{e_d}$	[var.]	Incremental local force vector defined by beam 'd'
$\Delta \boldsymbol{u_B}'^{e_d}$	[var.]	Incremental local displacement vector defined by beam 'd'
$\boldsymbol{K_B}'^{e_d}$	[var.]	Local bending stiffness matrix defined by beam 'd'

As an alternative the above stated relationship can also be defined through using cubic shape functions, taking the same form as the elastic curves shown in Fig. 9.5 (Wells, 2006; Felippa, 2004a; Blom, 2009).

Local definition of the bending stiffness across the element

For each of the three beams the stiffness definition according to Eq. (9.38) is stated. Combination of these individual relationships defines the local diagonal element stiffness matrix governing the bending contributions:

$$\Delta \boldsymbol{F_B}'^{e} = \boldsymbol{K_B}'^{e} \Delta \boldsymbol{u_B}'^{e} \tag{9.39}$$

with

$$\Delta \boldsymbol{F_B}'^{e} = \begin{bmatrix} \Delta \boldsymbol{F_B}'^{e_I} \\ \Delta \boldsymbol{F_B}'^{e_{II}} \\ \Delta \boldsymbol{F_B}'^{e_{III}} \end{bmatrix} \qquad \Delta \boldsymbol{u_B}'^{e} = \begin{bmatrix} \Delta \boldsymbol{u_B}'^{e_I} \\ \Delta \boldsymbol{u_B}'^{e_{II}} \\ \Delta \boldsymbol{u_B}'^{e_{III}} \end{bmatrix}$$

$$\boldsymbol{K_B}'^{e} = \begin{bmatrix} \boldsymbol{K_B}'^{e_I} & 0 & 0 \\ 0 & \boldsymbol{K_B}'^{e_{II}} & 0 \\ 0 & 0 & \boldsymbol{K_B}'^{e_{III}} \end{bmatrix}$$

where

$\Delta \boldsymbol{F_B}'^{e}$	[var.]	Incremental local element force vector associated with bending
$\Delta \boldsymbol{u_B}'^{e}$	[var.]	Incremental local element displacement vector associated with bending
$\boldsymbol{K_B}'^{e}$	[var.]	Local element bending stiffness matrix

Definition of coordinate transformations and the rigid body boundary conditions

By definition of local bending an additional variable is introduced at each node. This nodal rotation is not present in the current global coordinate systems and requires definition of the following element transformation relationship:

$$\boldsymbol{x}^{\boldsymbol{e}} = \boldsymbol{T}_{\boldsymbol{\varphi}}{}^{\boldsymbol{e}}(\boldsymbol{x}^{\boldsymbol{e}} + \boldsymbol{\varphi}^{\boldsymbol{e}}) \tag{9.40}$$

with

$$\boldsymbol{x}^{\boldsymbol{e}} = \begin{bmatrix} x_1^e \\ y_1^e \\ x_2^e \\ y_2^e \\ x_3^e \\ y_3^e \end{bmatrix} \qquad \boldsymbol{x}^{\boldsymbol{e}} + \boldsymbol{\varphi}^{\boldsymbol{e}} = \begin{bmatrix} x_1^e \\ y_1^e \\ 0 \\ x_2^e \\ y_2^e \\ 0 \\ x_3^e \\ y_3^e \\ 0 \end{bmatrix} + \begin{bmatrix} 0 \\ 0 \\ \varphi_1^e \\ 0 \\ 0 \\ \varphi_2^e \\ 0 \\ 0 \\ \varphi_3^e \end{bmatrix} \qquad \boldsymbol{T}_{\boldsymbol{\varphi}}{}^{\boldsymbol{e}} = \begin{bmatrix} 1 & 0 & 0 & & 0 & & & 0 & \\ 0 & 1 & 0 & & & & & & \\ & 0 & & 1 & 0 & 0 & & 0 & \\ & & & 0 & 1 & 0 & & & \\ & 0 & & & 0 & & 1 & 0 & 0 \\ & & & & & & 0 & 1 & 0 \end{bmatrix}$$

where

$\boldsymbol{T}_{\boldsymbol{\varphi}}{}^{\boldsymbol{e}}$ [-] Element transformation matrix used to extent the nodal variables

Both the material and geometrical coordinate transformation tensors, defined in Eq. (9.6) and Eq. (9.24) respectively, are transformed using the previous relationship. This does not change these coordinate transformations, but only includes undefined rotational variables:

$$\boldsymbol{x_M}'^{\boldsymbol{e}} = \boldsymbol{T}_{\boldsymbol{\alpha_M}}{}'^{\boldsymbol{e}}\boldsymbol{T}_{\boldsymbol{\varphi}}{}^{\boldsymbol{e}}(\boldsymbol{x}^{\boldsymbol{e}} + \boldsymbol{\varphi}^{\boldsymbol{e}}) \qquad \boldsymbol{x_G}'^{\boldsymbol{e}} = \boldsymbol{T}_{\boldsymbol{\alpha_G}}{}'^{\boldsymbol{e}}\boldsymbol{T}_{\boldsymbol{\varphi}}{}^{\boldsymbol{e}}(\boldsymbol{x}^{\boldsymbol{e}} + \boldsymbol{\varphi}^{\boldsymbol{e}}) \tag{9.41}$$

The local coordinate systems used in case of bending consist of vertical directions as well as rotations. However, since rotations are unaffected by coordinate transformations, the following directly holds (Wells, 2006; Blom, 2009):

$$\boldsymbol{x_B}'^{\boldsymbol{e}} = \boldsymbol{T}_{\boldsymbol{\alpha_B}}{}'^{\boldsymbol{e}}(\boldsymbol{x}^{\boldsymbol{e}} + \boldsymbol{\varphi}^{\boldsymbol{e}}) \tag{9.42}$$

with

$$\boldsymbol{x_B}'^{\boldsymbol{e}} = \begin{bmatrix} y'^{e_I}_1 \\ \varphi'^{e_I}_1 \\ y'^{e_I}_2 \\ \varphi'^{e_I}_2 \\ y'^{e_{II}}_2 \\ \varphi'^{e_{II}}_2 \\ y'^{e_{II}}_3 \\ \varphi'^{e_{II}}_3 \\ y'^{e_{III}}_3 \\ \varphi'^{e_{III}}_3 \\ y'^{e_{III}}_1 \\ \varphi'^{e_{III}}_1 \end{bmatrix} \qquad \boldsymbol{T}_{\boldsymbol{\alpha_B}}{}'^{\boldsymbol{e}} = \begin{bmatrix} -\sin\alpha^{e_I} & \cos\alpha^{e_I} & 0 & 0 & 0 & 0 & & & \\ 0 & 0 & 1 & 0 & 0 & 0 & & & \\ 0 & 0 & 0 & -\sin\alpha^{e_I} & \cos\alpha^{e_I} & 0 & & 0 & \\ 0 & 0 & 0 & 0 & 0 & 1 & & & \\ & & & -\sin\alpha^{e_{II}} & \cos\alpha^{e_{II}} & 0 & 0 & 0 & 0 \\ & 0 & & 0 & 0 & 1 & 0 & 0 & 0 \\ & & & 0 & 0 & 0 & -\sin\alpha^{e_{II}} & \cos\alpha^{e_{II}} & 0 \\ & & & 0 & 0 & 0 & 0 & 0 & 1 \\ 0 & 0 & 0 & & & & -\sin\alpha^{e_{III}} & \cos\alpha^{e_{III}} & 0 \\ 0 & 0 & 0 & & 0 & & 0 & 0 & 1 \\ -\sin\alpha^{e_{III}} & \cos\alpha^{e_{III}} & 0 & & & & 0 & 0 & 0 \\ 0 & 0 & 1 & & & & 0 & 0 & 0 \end{bmatrix}$$

where

$\boldsymbol{x_B}'^{e}$	[var.]	Local element coordinate system vector based on the triangular bending directions
$\boldsymbol{T_{\alpha_B}}'^{e}$	[-]	Element coordinate transformation tensor based on the triangular bending directions (second order)

The next step towards FEM implementation is consideration of the rigid body boundary conditions. These are defined by coupling conditions, ensuring that the top and bottom edges remain straight during deformation (Hartmann & Katz, 2007). With respect to bending the cross-section of the beam is required to remain perpendicular to the outer edge during rotation. This is imposed through extending the nodal rigid body transformation matrix, restated from chapter 8, while still considering the prescribed thermal displacements. The element rigid body transformation tensor is changed according to:

$$\Delta \boldsymbol{u}_{\boldsymbol{i}_{\boldsymbol{k}}}^{\boldsymbol{t+1}} = \boldsymbol{T}_{\boldsymbol{rb}_{\boldsymbol{i}_{\boldsymbol{rb}\boldsymbol{k}}}}^{\boldsymbol{t+1}} \Delta \boldsymbol{u}_{\boldsymbol{S}_{\boldsymbol{k}}}^{\boldsymbol{t+1}} + \Delta \boldsymbol{u}_{\boldsymbol{T}_{\boldsymbol{i}_{\boldsymbol{rb}\boldsymbol{k}}}}^{\boldsymbol{t+1}} \tag{9.43}$$

with

$$\Delta \boldsymbol{u}_{\boldsymbol{i}_{\boldsymbol{rb}\boldsymbol{k}}}^{\boldsymbol{t+1}} = \begin{bmatrix} \Delta u_{x_{i_{rb}k}}^{t+1} \\ \Delta u_{y_{i_{rb}k}}^{t+1} \\ \Delta \varphi_{i_{rb}k}^{t+1} \end{bmatrix} \qquad \Delta \boldsymbol{u}_{\boldsymbol{T}_{\boldsymbol{i}_{\boldsymbol{rb}\boldsymbol{k}}}}^{\boldsymbol{t+1}} = \begin{bmatrix} \cos\varphi_{S_k}^{t+1} \Delta d_{rel_{T\,i_{rb}k}}^{t+1} \\ \sin\varphi_{S_k}^{t+1} \Delta d_{rel_{T\,i_{rb}k}}^{t+1} \\ 0 \end{bmatrix}$$

$$\boldsymbol{T}_{\boldsymbol{rb}_{\boldsymbol{i}_{\boldsymbol{rb}\boldsymbol{k}}}}^{\boldsymbol{t+1}} = \begin{bmatrix} 0 & -\sin\varphi_{S_k}^{t+1} d_{rel_{i_{rb}k}}^{t+1} \\ 1 & \cos\varphi_{S_k}^{t+1} d_{rel_{i_{rb}k}}^{t+1} \\ 0 & 1 \end{bmatrix}$$

Incremental elastic strain energy across the element

The definition of the incremental forces associated with local bending in Eq. (9.39) is directly applicable for FEM implementation in case no temperature effects are considered. However, Young's modulus is characterised by a gradual reduction with temperature which needs to be considered. For this purpose the incremental elastic strain energy is expressed in the local displacements and forces similar to Eq. (9.23), focussing on the bending contributions. Two aspects need to be considered, the first being that no curvature of the material is assumed to develop due to the constant temperature along each beam axis. Secondly, the geometrically non-linear term is not considered for the beams since the axial force transfer is assumed as the main load bearing system. So, only the first material-based term remains:

$$\Delta U_{\varepsilon}{}'^{e\,t+1}_{k} = \Delta W_{F}{}'^{e\,t+1}_{k} = \frac{1}{2}\left(\boldsymbol{u_B}'^{\boldsymbol{e}\boldsymbol{t+1}^{\boldsymbol{T}}}_{\boldsymbol{k}} \Delta \boldsymbol{F_B}'^{\boldsymbol{e}\boldsymbol{t+1}}_{\boldsymbol{k}} + \underbrace{\Delta \boldsymbol{u}'^{\boldsymbol{e}\boldsymbol{t+1}^{\boldsymbol{T}}}_{\boldsymbol{k}} \boldsymbol{F_B}'^{\boldsymbol{e}\boldsymbol{t+1}}_{\boldsymbol{k}}}_{\approx 0} \right) \tag{9.44}$$

Incremental local and global bending-based forces

The incremental local forces defined by the temperature dependence of the bending stiffness are through coordinate transformation, stated in Eq. (9.42), expressed in their global counterpart. Two contributions are obtained which firstly represent the redistribution of shear

forces and moments due to stiffness variation. The second term reflects the incremental global displacements caused by additional bending:

$$\Delta \boldsymbol{F}_{\boldsymbol{T}_B}{}_{\boldsymbol{k}}^{\boldsymbol{e}\boldsymbol{t}+\boldsymbol{1}} = \int_{\Omega'^e} \boldsymbol{T}_{\boldsymbol{\alpha}_B}{}'_{\boldsymbol{k}}{}^{\boldsymbol{e}\boldsymbol{t}+\boldsymbol{1}\boldsymbol{T}} \Delta \boldsymbol{F}_{\boldsymbol{T}_B}{}'_{\boldsymbol{k}}{}^{\boldsymbol{e}\boldsymbol{t}+\boldsymbol{1}} d\Omega'^e$$

$$= \int_{\Omega'^e} \boldsymbol{T}_{\boldsymbol{\alpha}_B}{}'_{\boldsymbol{k}}{}^{\boldsymbol{e}\boldsymbol{t}+\boldsymbol{1}\boldsymbol{T}} \left(\boldsymbol{K}_{\boldsymbol{B}}{}'_{\boldsymbol{k}+\boldsymbol{1}}{}^{\boldsymbol{e}\boldsymbol{t}+\boldsymbol{1}} - \boldsymbol{K}_{\boldsymbol{B}}{}'_{\boldsymbol{k}}{}^{\boldsymbol{e}\boldsymbol{t}+\boldsymbol{1}} \right) \boldsymbol{T}_{\boldsymbol{\alpha}_B}{}'_{\boldsymbol{k}}{}^{\boldsymbol{e}\boldsymbol{t}+\boldsymbol{1}} \boldsymbol{u}_{\boldsymbol{B}}{}_{\boldsymbol{k}}^{\boldsymbol{e}\boldsymbol{t}+\boldsymbol{1}} d\Omega'^e \tag{9.45}$$

$$+ \int_{\Omega'^e} \boldsymbol{T}_{\boldsymbol{\alpha}_B}{}'_{\boldsymbol{k}}{}^{\boldsymbol{e}\boldsymbol{t}+\boldsymbol{1}\boldsymbol{T}} \boldsymbol{K}_{\boldsymbol{B}}{}'_{\boldsymbol{k}}{}^{\boldsymbol{e}\boldsymbol{t}+\boldsymbol{1}} \boldsymbol{T}_{\boldsymbol{\alpha}_B}{}'_{\boldsymbol{k}}{}^{\boldsymbol{e}\boldsymbol{t}+\boldsymbol{1}} \Delta \boldsymbol{u}_{\boldsymbol{B}}{}_{\boldsymbol{k}}^{\boldsymbol{e}\boldsymbol{t}+\boldsymbol{1}} d\Omega'^e$$

where

$\Delta \boldsymbol{F}_{\boldsymbol{T}_B}{}_{\boldsymbol{k}}^{\boldsymbol{e}\boldsymbol{t}+\boldsymbol{1}}$ [var.] Incremental element nodal force vector representing the bending-based temperature contributions

Addition to the incremental local and global fracture forces

During the incremental fracture process bars are removed from the system. The same principal also holds for the corresponding beams (Schlangen, 1993; Vervuurt, 1997). Conservation of elastic strain energy involves redistribution of the nodal shear forces and moments. Combined with the also redistributed axial forces it is ensured that static equilibrium is preserved without introducing additional local disturbances. So, the following additional incremental global forces are imposed at both crack edges at fracture:

$$\Delta \boldsymbol{F}_{\boldsymbol{cr}_B}{}_{\boldsymbol{k}}^{\boldsymbol{e}\boldsymbol{t}+\boldsymbol{1}} = \int_{\Omega'^e} \boldsymbol{T}_{\boldsymbol{\alpha}_B}{}'_{\boldsymbol{k}}{}^{\boldsymbol{e}\boldsymbol{t}+\boldsymbol{1}\boldsymbol{T}} \Delta \boldsymbol{F}_{\boldsymbol{cr}_B}{}'_{\boldsymbol{k}}{}^{\boldsymbol{e}\boldsymbol{t}+\boldsymbol{1}} d\Omega'^e$$

$$= \int_{\Omega'^e} \boldsymbol{T}_{\boldsymbol{\alpha}_B}{}'_{\boldsymbol{k}}{}^{\boldsymbol{e}\boldsymbol{t}+\boldsymbol{1}\boldsymbol{T}} \boldsymbol{K}_{\boldsymbol{B}}{}'_{\boldsymbol{k}}{}^{\boldsymbol{e}\boldsymbol{t}+\boldsymbol{1}} \boldsymbol{T}_{\boldsymbol{\alpha}_B}{}'_{\boldsymbol{k}}{}^{\boldsymbol{e}\boldsymbol{t}+\boldsymbol{1}} \boldsymbol{u}_{\boldsymbol{B}}{}_{\boldsymbol{k}}^{\boldsymbol{e}\boldsymbol{t}+\boldsymbol{1}} d\Omega'^e \tag{9.46}$$

where

$\Delta \boldsymbol{F}_{\boldsymbol{cr}_B}{}_{\boldsymbol{k}}^{\boldsymbol{e}\boldsymbol{t}+\boldsymbol{1}}$ [var.] Incremental element nodal force vector representing the bending-based fracture forces

9.4 Incremental FEM definition

9.4.1 Discretisation based on heterogeneous and anisotropic 1D bars and beams

The isotropic FEM definition, stated in the previous chapter, is modified based on consideration of static equilibrium for the anisotropic continuum. After rearranging and including the rigid body coupling conditions while considering the additional rotational variable, the various incremental time- and crack-dependent force contributions are obtained. Each element is schematised by three 1D bars as well as 1D beams. Both 1D elements are

allowed to be combined since each separately describes the displacement in one of the local directions. The local stiffness definitions are thus uncoupled and can be superimposed:

$$\begin{aligned}\sum_{e=1}^{e_{tot}}\left(\boldsymbol{K_{M_{sys}}}_{\boldsymbol{k}}^{\boldsymbol{et+1}}+\boldsymbol{K_{G_{sys}}}_{\boldsymbol{k}}^{\boldsymbol{et+1}}+\boldsymbol{K_{B_{sys}}}_{\boldsymbol{k}}^{\boldsymbol{et+1}}\right)\sum_{e=1}^{e_{tot}}\Delta\boldsymbol{u_{sys}}_{\boldsymbol{k}}^{\boldsymbol{et+1}}+\sum_{S=1}^{2}\boldsymbol{K_S}\sum_{S=1}^{2}\Delta\boldsymbol{u_S}_{\boldsymbol{k}}^{\boldsymbol{t+1}}\\ =\sum_{S=1}^{2}\boldsymbol{F_S}^{\boldsymbol{t_0}}-\sum_{e=1}^{e_{tot}}\Delta\boldsymbol{F_{T_{M_{sys_a}}}}_{\boldsymbol{k}}^{\boldsymbol{et+1}}+\sum_{e=1}^{e_{tot}}\Delta\boldsymbol{F_{T_{M_{sys_b}}}}_{\boldsymbol{k}}^{\boldsymbol{et+1}}-\sum_{e=1}^{e_{tot}}\Delta\boldsymbol{F_{P_{M_{sys}}}}_{\boldsymbol{k}}^{\boldsymbol{et+1}}\\ +\sum_{e=1}^{e_{tot}}\Delta\boldsymbol{F_{T_{G_{sys}}}}_{\boldsymbol{k}}^{\boldsymbol{et+1}}-\sum_{e=1}^{e_{tot}}\Delta\boldsymbol{F_{T_{B_{sys}}}}_{\boldsymbol{k}}^{\boldsymbol{et+1}}\\ -\sum_{e=1}^{e_{tot}}\Delta\boldsymbol{F_{T_{M_{bc}}}}_{\boldsymbol{k}}^{\boldsymbol{et+1}}-\sum_{e=1}^{e_{tot}}\Delta\boldsymbol{F_{T_{G_{bc}}}}_{\boldsymbol{k}}^{\boldsymbol{et+1}}-\sum_{e=1}^{e_{tot}}\Delta\boldsymbol{F_{T_{B_{bc}}}}_{\boldsymbol{k}}^{\boldsymbol{et+1}}\\ +\sum_{e=1}^{e_{tot}}\Delta\boldsymbol{F_{cr_{M_{sys}}}}_{\boldsymbol{k}}^{\boldsymbol{et+1}}+\sum_{e=1}^{e_{tot}}\Delta\boldsymbol{F_{cr_{B_{sys}}}}_{\boldsymbol{k}}^{\boldsymbol{et+1}}\end{aligned}\tag{9.47}$$

with

$$\boldsymbol{K_{M_{sys}}}_{\boldsymbol{k}}^{\boldsymbol{et+1}}=\int_{\Omega'^{e}}\boldsymbol{T_{rb}}_{\boldsymbol{k}}^{\boldsymbol{et+1^T}}\boldsymbol{T_{\varphi}}^{\boldsymbol{eT}}\boldsymbol{T_{\alpha_M}}'^{\boldsymbol{et+1^T}}_{\boldsymbol{k}}\boldsymbol{B_{U_M}}'^{\boldsymbol{et+1^T}}_{\boldsymbol{k}}\boldsymbol{D'}^{\boldsymbol{et+1}}_{\boldsymbol{k}}\boldsymbol{B_{U_M}}'^{\boldsymbol{et+1}}_{\boldsymbol{k}}\boldsymbol{T_{\alpha_M}}'^{\boldsymbol{et+1}}_{\boldsymbol{k}}\boldsymbol{T_{\varphi}}^{\boldsymbol{e}}\boldsymbol{T_{rb}}_{\boldsymbol{k}}^{\boldsymbol{et+1}}d\Omega'^{e}$$

$$\boldsymbol{K_{G_{sys}}}_{\boldsymbol{k}}^{\boldsymbol{et+1}}=\int_{\Omega'^{e}}\boldsymbol{T_{rb}}_{\boldsymbol{k}}^{\boldsymbol{et+1^T}}\boldsymbol{T_{\varphi}}^{\boldsymbol{eT}}\boldsymbol{T_{\alpha_G}}'^{\boldsymbol{et+1^T}}_{\boldsymbol{k}}\boldsymbol{B_{U_G}}'^{\boldsymbol{et+1^T}}_{\boldsymbol{k}}\boldsymbol{\sigma'}^{\boldsymbol{et+1}}_{\boldsymbol{k}}\boldsymbol{I}\boldsymbol{B_{U_G}}'^{\boldsymbol{et+1}}_{\boldsymbol{k}}\boldsymbol{T_{\alpha_G}}'^{\boldsymbol{et+1}}_{\boldsymbol{k}}\boldsymbol{T_{\varphi}}^{\boldsymbol{e}}\boldsymbol{T_{rb}}_{\boldsymbol{k}}^{\boldsymbol{et+1}}d\Omega'^{e}$$

$$\boldsymbol{K_{B_{sys}}}_{\boldsymbol{k}}^{\boldsymbol{et+1}}=\boldsymbol{T_{rb}}_{\boldsymbol{k}}^{\boldsymbol{et+1^T}}\boldsymbol{T_{\alpha_B}}'^{\boldsymbol{et+1^T}}_{\boldsymbol{k}}\boldsymbol{K_B}'^{\boldsymbol{et+1}}_{\boldsymbol{k}}\boldsymbol{T_{\alpha_B}}'^{\boldsymbol{et+1}}_{\boldsymbol{k}}\boldsymbol{T_{rb}}_{\boldsymbol{k}}^{\boldsymbol{et+1}}$$

$$\Delta\boldsymbol{F_{T_{M_{sys_a}}}}_{\boldsymbol{k}}^{\boldsymbol{et+1}}=\int_{\Omega'^{e}}\boldsymbol{T_{rb}}_{\boldsymbol{k}}^{\boldsymbol{et+1^T}}\boldsymbol{T_{\varphi}}^{\boldsymbol{eT}}\boldsymbol{T_{\alpha_M}}'^{\boldsymbol{et+1^T}}_{\boldsymbol{k}}\boldsymbol{B_{U_M}}'^{\boldsymbol{et+1^T}}_{\boldsymbol{k}}\left(\boldsymbol{D'}^{\boldsymbol{et+1}}_{\boldsymbol{k+1}}-\boldsymbol{D'}^{\boldsymbol{et+1}}_{\boldsymbol{k}}\right)\left(\boldsymbol{\varepsilon'}^{\boldsymbol{et+1}}_{\boldsymbol{k}}-\boldsymbol{\varepsilon_T}'^{\boldsymbol{et+1}}_{\boldsymbol{k}}\right)d\Omega'^{e}$$

$$\Delta\boldsymbol{F_{T_{M_{sys_b}}}}_{\boldsymbol{k}}^{\boldsymbol{et+1}}=\int_{\Omega'^{e}}\boldsymbol{T_{rb}}_{\boldsymbol{k}}^{\boldsymbol{et+1^T}}\boldsymbol{T_{\varphi}}^{\boldsymbol{eT}}\boldsymbol{T_{\alpha_M}}'^{\boldsymbol{et+1^T}}_{\boldsymbol{k}}\boldsymbol{B_{U_M}}'^{\boldsymbol{et+1^T}}_{\boldsymbol{k}}\boldsymbol{D'}^{\boldsymbol{et+1}}_{\boldsymbol{k}}\left(\boldsymbol{\varepsilon_T}'^{\boldsymbol{et+1}}_{\boldsymbol{k+1}}-\boldsymbol{\varepsilon_T}'^{\boldsymbol{et+1}}_{\boldsymbol{k}}\right)d\Omega'^{e}$$

$$\Delta\boldsymbol{F_{P_{M_{sys}}}}_{\boldsymbol{k}}^{\boldsymbol{et+1}}=\int_{\Omega'^{e}}\boldsymbol{T_{rb}}_{\boldsymbol{k}}^{\boldsymbol{et+1^T}}\boldsymbol{T_{\varphi}}^{\boldsymbol{eT}}\boldsymbol{T_{\alpha_M}}'^{\boldsymbol{et+1^T}}_{\boldsymbol{k}}\boldsymbol{B_{U_M}}'^{\boldsymbol{et+1^T}}_{\boldsymbol{k}}\left(\boldsymbol{\sigma_P}'^{\boldsymbol{et+1}}_{\boldsymbol{k+1}}-\boldsymbol{\sigma_P}'^{\boldsymbol{et+1}}_{\boldsymbol{k}}\right)d\Omega'^{e}$$

$$\Delta\boldsymbol{F_{T_{G_{sys}}}}_{\boldsymbol{k}}^{\boldsymbol{et+1}}=\int_{\Omega'^{e}}\boldsymbol{T_{rb}}_{\boldsymbol{k}}^{\boldsymbol{et+1^T}}\boldsymbol{T_{\varphi}}^{\boldsymbol{eT}}\boldsymbol{T_{\alpha_G}}'^{\boldsymbol{et+1^T}}_{\boldsymbol{k}}\boldsymbol{B_{U_G}}'^{\boldsymbol{et+1^T}}_{\boldsymbol{k}}\boldsymbol{\sigma'}^{\boldsymbol{et+1}}_{\boldsymbol{k}}\boldsymbol{I}\left(\boldsymbol{\varepsilon_T}'^{\boldsymbol{et+1}}_{\boldsymbol{k+1}}-\boldsymbol{\varepsilon_T}'^{\boldsymbol{et+1}}_{\boldsymbol{k}}\right)d\Omega'^{e}$$

$$\Delta \boldsymbol{F}_{T_{B_{sys}}}{}_{\boldsymbol{k}}^{\boldsymbol{e}t+1} = \boldsymbol{T_{rb}}{}_{\boldsymbol{k}}^{\boldsymbol{e}t+1^{\boldsymbol{T}}} \boldsymbol{T_{\alpha_B}}{}_{\boldsymbol{k}}^{\prime \boldsymbol{e}t+1^{\boldsymbol{T}}} \left(\boldsymbol{K_B}{}_{\boldsymbol{k+1}}^{\prime \boldsymbol{e}t+1} - \boldsymbol{K_B}{}_{\boldsymbol{k}}^{\prime \boldsymbol{e}t+1} \right) \boldsymbol{T_{\alpha_B}}{}_{\boldsymbol{k}}^{\prime \boldsymbol{e}t+1} \boldsymbol{u}_{\boldsymbol{k}}^{\boldsymbol{e}t+1}$$

$$\Delta \boldsymbol{F}_{T_{M_{bc}}}{}_{\boldsymbol{k}}^{\boldsymbol{e}t+1} = \int_{\Omega'^{e}} \boldsymbol{T_{rb}}{}_{\boldsymbol{k}}^{\boldsymbol{e}t+1^{\boldsymbol{T}}} \boldsymbol{T_{\varphi}}^{\boldsymbol{e}\boldsymbol{T}} \boldsymbol{T_{\alpha_M}}{}_{\boldsymbol{k}}^{\prime \boldsymbol{e}t+1^{\boldsymbol{T}}} \boldsymbol{B_{U_M}}{}_{\boldsymbol{k}}^{\prime \boldsymbol{e}t+1^{\boldsymbol{T}}} \boldsymbol{D'}_{\boldsymbol{k}}^{\boldsymbol{e}t+1} \boldsymbol{B_{U_M}}{}_{\boldsymbol{k}}^{\prime \boldsymbol{e}t+1} \boldsymbol{T_{\alpha_M}}{}_{\boldsymbol{k}}^{\prime \boldsymbol{e}t+1} \boldsymbol{T_{\varphi}}^{\boldsymbol{e}} \Delta \boldsymbol{u_T}{}_{\boldsymbol{k}}^{\boldsymbol{e}t+1} d\Omega'^{e}$$

$$\Delta \boldsymbol{F}_{T_{G_{bc}}}{}_{\boldsymbol{k}}^{\boldsymbol{e}t+1} = \int_{\Omega'^{e}} \boldsymbol{T_{rb}}{}_{\boldsymbol{k}}^{\boldsymbol{e}t+1^{\boldsymbol{T}}} \boldsymbol{T_{\varphi}}^{\boldsymbol{e}\boldsymbol{T}} \boldsymbol{T_{\alpha_G}}{}_{\boldsymbol{k}}^{\prime \boldsymbol{e}t+1^{\boldsymbol{T}}} \boldsymbol{B_{U_G}}{}_{\boldsymbol{k}}^{\prime \boldsymbol{e}t+1^{\boldsymbol{T}}} \boldsymbol{\sigma'}_{\boldsymbol{k}}^{\boldsymbol{e}t+1} \boldsymbol{I} \boldsymbol{B_{U_G}}{}_{\boldsymbol{k}}^{\prime \boldsymbol{e}t+1} \boldsymbol{T_{\alpha_G}}{}_{\boldsymbol{k}}^{\prime \boldsymbol{e}t+1} \boldsymbol{T_{\varphi}}^{\boldsymbol{e}} \Delta \boldsymbol{u_T}{}_{\boldsymbol{k}}^{\boldsymbol{e}t+1} d\Omega'^{e}$$

$$\Delta \boldsymbol{F}_{T_{B_{bc}}}{}_{\boldsymbol{k}}^{\boldsymbol{e}t+1} = \boldsymbol{T_{rb}}{}_{\boldsymbol{k}}^{\boldsymbol{e}t+1^{\boldsymbol{T}}} \boldsymbol{T_{\alpha_B}}{}_{\boldsymbol{k}}^{\prime \boldsymbol{e}t+1^{\boldsymbol{T}}} \boldsymbol{K_B}{}_{\boldsymbol{k}}^{\prime \boldsymbol{e}t+1} \boldsymbol{T_{\alpha_B}}{}_{\boldsymbol{k}}^{\prime \boldsymbol{e}t+1} \Delta \boldsymbol{u_T}{}_{\boldsymbol{k}}^{\boldsymbol{e}t+1}$$

$$\Delta \boldsymbol{F}_{cr_{M_{sys}}}{}_{\boldsymbol{k}}^{\boldsymbol{e}t+1} = \int_{\Omega'^{e}} \boldsymbol{T_{rb}}{}_{\boldsymbol{k}}^{\boldsymbol{e}t+1^{\boldsymbol{T}}} \boldsymbol{T_{\alpha_M}}{}_{\boldsymbol{k}}^{\prime \boldsymbol{e}t+1^{\boldsymbol{T}}} \boldsymbol{B_{U_M}}{}_{\boldsymbol{k}}^{\prime \boldsymbol{e}t+1^{\boldsymbol{T}}} \boldsymbol{\sigma'}_{\boldsymbol{k}}^{\boldsymbol{e}t+1} d\Omega'^{e}$$

$$\Delta \boldsymbol{F}_{cr_{B_{sys}}}{}_{\boldsymbol{k}}^{\boldsymbol{e}t+1} = \boldsymbol{T_{rb}}{}_{\boldsymbol{k}}^{\boldsymbol{e}t+1^{\boldsymbol{T}}} \boldsymbol{T_{\alpha_B}}{}_{\boldsymbol{k}}^{\prime \boldsymbol{e}t+1^{\boldsymbol{T}}} \boldsymbol{K_B}{}_{\boldsymbol{k}}^{\prime \boldsymbol{e}t+1} \boldsymbol{T_{\alpha_B}}{}_{\boldsymbol{k}}^{\prime \boldsymbol{e}t+1} \boldsymbol{u}_{\boldsymbol{k}}^{\boldsymbol{e}t+1}$$

where

$\boldsymbol{K_{M_{sys}}}{}_{\boldsymbol{k}}^{\boldsymbol{e}t+1}$	[var.]	Element material system matrix at the current time, crack step
$\boldsymbol{K_{G_{sys}}}{}_{\boldsymbol{k}}^{\boldsymbol{e}t+1}$	[var.]	Element geometrical system matrix at the current time, crack step
$\boldsymbol{K_{B_{sys}}}{}_{\boldsymbol{k}}^{\boldsymbol{e}t+1}$	[var.]	Element bending system matrix at the current time, crack step
$\Delta \boldsymbol{F}_{T_{M_{sys_a}}}{}_{\boldsymbol{k}}^{\boldsymbol{e}t+1}$	[var.]	Element force vector governing material-based stiffness variation
$\Delta \boldsymbol{F}_{T_{M_{sys_b}}}{}_{\boldsymbol{k}}^{\boldsymbol{e}t+1}$	[var.]	Element force vector governing the temperature strain increment
$\Delta \boldsymbol{F}_{P_{M_{sys}}}{}_{\boldsymbol{k}}^{\boldsymbol{e}t+1}$	[var.]	Element force vector governing the pressure stress increment
$\Delta \boldsymbol{F}_{T_{G_{sys}}}{}_{\boldsymbol{k}}^{\boldsymbol{e}t+1}$	[var.]	Element force vector governing the geometrical-based change in stress orientation due to the temperature strain increment
$\Delta \boldsymbol{F}_{T_{B_{sys}}}{}_{\boldsymbol{k}}^{\boldsymbol{e}t+1}$	[var.]	Element force vector governing bending-based stiffness variation
$\Delta \boldsymbol{F}_{T_{M_{bc}}}{}_{\boldsymbol{k}}^{\boldsymbol{e}t+1}$	[var.]	Element force vector governing material-based thermal elongation
$\Delta \boldsymbol{F}_{T_{G_{bc}}}{}_{\boldsymbol{k}}^{\boldsymbol{e}t+1}$	[var.]	Element force vector governing geometrical-based thermal elongation
$\Delta \boldsymbol{F}_{T_{B_{bc}}}{}_{\boldsymbol{k}}^{\boldsymbol{e}t+1}$	[var.]	Element force vector governing bending-based thermal elongation
$\Delta \boldsymbol{F}_{cr_{M_{sys}}}{}_{\boldsymbol{k}}^{\boldsymbol{e}t+1}$	[var.]	Element force vector governing the material-based redistribution of stresses at fracture
$\Delta \boldsymbol{F}_{cr_{B_{sys}}}{}_{\boldsymbol{k}}^{\boldsymbol{e}t+1}$	[var.]	Element force vector governing the bending-based redistribution at fracture

In order to obtain this anisotropic definition the following needs to considered:

- The left hand side characterises the system by summation across the domain of the element stiffness matrices based on the combined influence of the three bars and beams. The first two contributions characterise the material and geometrical non-linear behaviour of the bars. Anisotropy of the local elasticity tensor is governed by the heterogeneity and especially the removal of stiffness for fractured bars. The third stiffness matrix includes the local bending contribution. The resultant system matrix is multiplied by the system vector based on the incrementally defined nodal variables, reflecting displacement in both global directions and rotation.

- The second and third terms on the right hand side represent the temperature-dependent nodal forces for the bars. The fourth term is based on the gas pressure and is only assumed present for bars representing mortar or interfacial zones. These forces define the material-based contributions to the system force vector and are only included at the incremental time step.

- Translation and rotation of the normal forces present in the bars is governed by the geometrical stiffness matrix. However, the influence of the incremental temperature strain development is omitted through definition of the fifth contribution to the system force vector. The sixth force contribution reflects the redistribution of bending-based forces due to stiffness variation.

- Temperature-induced elongation forces along the top and bottom edges reflect contributions based on the material, geometrical and bending stiffness matrices.

- The last two contributions to the system force vector govern the redistribution of stresses during incremental crack development and are only included at fracture. Both the forces carried by the bars as well as the beams are redistributed at the crack edge. In the remaining incremental steps pressure-induced stresses remain imposed since these are assumed not to be affected by the stiffness reduction.

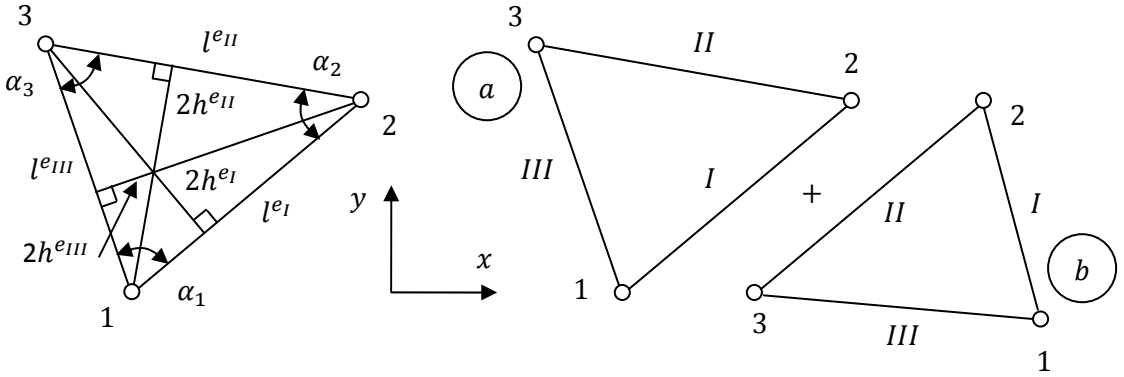

Fig. 9.6 *Schematic representation of the altitudes defining the cross-sectional height of each of the 1D bars in $\mathbb{R}^2$ (left). Definition of triangles leads to parallel bars, representing adjacent areas (right).*

9.4.2 Spatial integration applied to the anisotropic definition

Through conservation of elastic strain energy the global strains are expressed in the local extensional strains, each assumed constant across the triangular area. This implies that the cross-section of each bar is governed by half of the internal height and the out-of-plane thickness. The former are indicated in the left picture of Fig. 9.6 as the altitudes of the triangle defined perpendicular to each of the bar axis (Felippa, 2004a). Both the cross-sectional area and the length of the bars are grouped to form diagonal matrices in order to numerically approximate the integrals in the anisotropic FEM definition. Furthermore, only the bar lengths and angles are influenced by the incremental geometrical definition. The cross-sectional areas are assumed constant to avoid determination of corresponding force redistributions:

$$\boldsymbol{A'^{e}} = \begin{bmatrix} A^{e_I} & 0 & 0 \\ 0 & A^{e_{II}} & 0 \\ 0 & 0 & A^{e_{III}} \end{bmatrix} \qquad \boldsymbol{l'^{e}{}_{k}^{t+1}} = \begin{bmatrix} {l^{e_I}}_k^{t+1} & 0 & 0 \\ 0 & {l^{e_{II}}}_k^{t+1} & 0 \\ 0 & 0 & {l^{e_{III}}}_k^{t+1} \end{bmatrix} \tag{9.48}$$

with

$$h^{e_I} = \frac{\sin\alpha_1 l^{e_{II}}}{2} \qquad h^{e_{II}} = \frac{\sin\alpha_2 l^{e_I}}{2} \qquad h^{e_{III}} = \frac{\sin\alpha_3 l^{e_{II}}}{2}$$

$$A^{e_I} = h^{e_I} D \qquad A^{e_{II}} = h^{e_{II}} D \qquad A^{e_{III}} = h^{e_{III}} D$$

where

$\alpha_1, \alpha_2, \alpha_3$	[rad]	Angle at each node between adjacent edges of the triangle
$h^{e_I}, h^{e_{II}}, h^{e_{III}}$	[mm]	Internal height perpendicular to the axis, assumed constant
$A^{e_I}, A^{e_{II}}, A^{e_{III}}$	[mm^2]	Cross-sectional area of each bar, assumed constant
${l^{e_I}}_k^{t+1}, {l^{e_{II}}}_k^{t+1}, {l^{e_{III}}}_k^{t+1}$	[mm]	Length of each bar dependent on the current step
$\boldsymbol{A'^{e}}$	[mm^2]	Element matrix containing the constant cross-sectional areas
$\boldsymbol{l'^{e}{}_{k}^{t+1}}$	[mm]	Element matrix containing the bar lengths at the current step

Similar to the 2D isotropic approximation must the 1D bars full fill C^0 continuity (van Kan, et al., 2008) as is ensured through linear varying shape functions. However, the basis differs and is formed by the natural coordinate systems aligned with the bar axes as shown in Fig. 9.7 (van Kan, et al., 2008; Felippa, 2004a). Inversion of these local natural coordinate systems leads to the following uncoupled definition, reflecting the geometrical non-linear influence through the incremental dependence (Felippa, 2004a):

$$\begin{bmatrix} \xi_I \\ \xi_{II} \\ \xi_{III} \end{bmatrix} = \begin{bmatrix} \frac{1}{{l^{e_I}}_k^{t+1}} & 0 & 0 \\ 0 & \frac{1}{{l^{e_{II}}}_k^{t+1}} & 0 \\ 0 & 0 & \frac{1}{{l^{e_{III}}}_k^{t+1}} \end{bmatrix} \begin{bmatrix} {x'^{e_I}}_k^{t+1} \\ {x'^{e_{II}}}_k^{t+1} \\ {x'^{e_{III}}}_k^{t+1} \end{bmatrix} \tag{9.49}$$

where

$\xi_I, \xi_{II}, \xi_{III}$	[mm]	Natural coordinate systems defined parallel to the bar axes

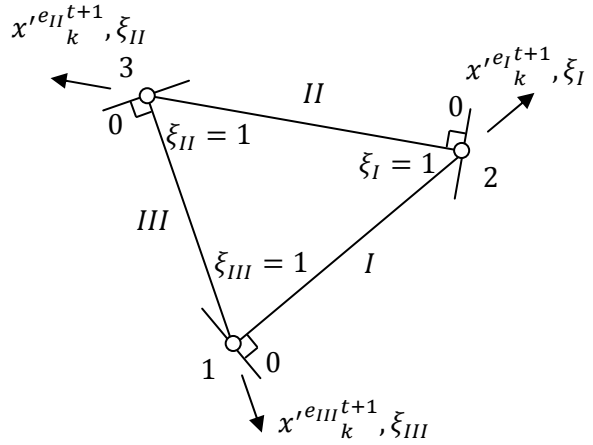

Natural coordinate relationships

$$x'^{e_I}{}_k^{t+1} = l^{e_I}{}_k^{t+1} \xi_I$$
$$x'^{e_{II}}{}_k^{t+1} = l^{e_{II}}{}_k^{t+1} \xi_{II}$$
$$x'^{e_{III}}{}_k^{t+1} = l^{e_{III}}{}_k^{t+1} \xi_{III}$$

Fig. 9.7 *A schematic representation of the three triangular orientated natural coordinate systems in* $\mathbb{R}^2$. *These align with the bar axes defined at the current step to characterise the local material directions* (van Kan, et al., 2008; Felippa, 2004a).

In using this 1D FEM discretisation the following needs to be considered:

- Each natural coordinate axis is only defined along the bar axis, assumed constant in the perpendicular direction. The uncoupled definition indicates that no additional relationship is imposed that relates the natural coordinate systems.

- Each triangular area across the domain is approximated by three bars. This leads to the definition of parallel bars, representing adjacent areas, across the domain as schematically indicated in the right picture of Fig. 9.6. The material stiffness, temperature strain and pressure-induced stress are the same for both bars.

- Parallel bars are characterised by the same length whereas the angles differ by half of the radial circle to reflect the orientation of both local axes. The geometrically non-linear definition governs the incremental development of both the length and the angle of the bars.

- In case of parallel aligned bars the axial strain is constant across both cross-sectional areas. This allows to add the stiffness and force contributions for both bars at the nodal variables.

- Parallel aligned bars are also loaded by the same stress, but not by the same normal force based on the varying cross-sectional areas. This implies that upon fracture both are removed to represent the total incremental fracture forces.

Approximation of the material-based incremental deformations

For each bar the nodal shape functions are based on the natural coordinate system which leads to a linear distribution of the axial displacement along its axis (van Kan, et al., 2008; Felippa, 2004a). These nodal shape functions are defined constant perpendicular to the bar axis as shown in Fig. 9.8.

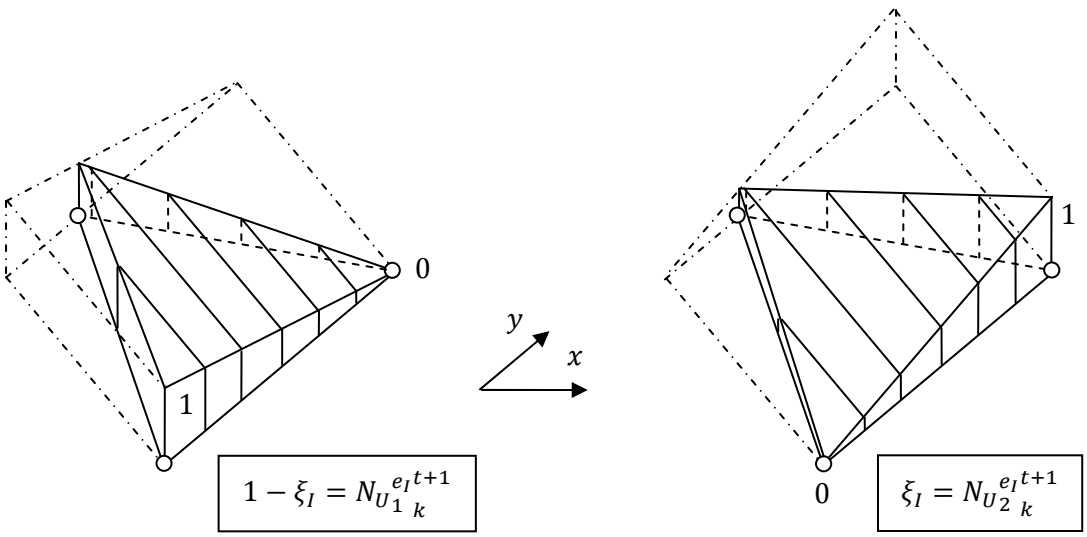

Fig. 9.8 *Schematic representation of the linear shape functions governing both nodes of the first bar in* $\mathbb{R}^2$ (Felippa, 2004a; Zienkiewicz, et al., 2005).

Combination of three bars leads to the local axial displacement approximation for each element (Felippa, 2004a):

$$\Delta \boldsymbol{u_x}'^{\boldsymbol{e}}(\boldsymbol{x_M}'^{\boldsymbol{e}}, t, k) \approx \boldsymbol{N_{U_M}}'^{\boldsymbol{e t+1}}_{\boldsymbol{k}}(\boldsymbol{x_M}'^{\boldsymbol{e}}) \Delta \boldsymbol{u_x}'^{\boldsymbol{e t+1}}_{\boldsymbol{k}} \tag{9.50}$$

with

$$\Delta \boldsymbol{u_x}'^{\boldsymbol{e}}(\boldsymbol{x_M}'^{\boldsymbol{e}}, t, k) = \begin{bmatrix} \Delta u_x{}'^{e_I}(x'^{e_I}, t, k) \\ \Delta u_x{}'^{e_{II}}(x'^{e_{II}}, t, k) \\ \Delta u_x{}'^{e_{III}}(x'^{e_{III}}, t, k) \end{bmatrix} \qquad \Delta \boldsymbol{u_x}'^{\boldsymbol{e t+1}}_{\boldsymbol{k}} = \begin{bmatrix} \Delta u_x{}'^{e_I t+1}_{1\ k} \\ \Delta u_x{}'^{e_I t+1}_{2\ k} \\ \Delta u_x{}'^{e_{II} t+1}_{2\ k} \\ \Delta u_x{}'^{e_{II} t+1}_{3\ k} \\ \Delta u_x{}'^{e_{III} t+1}_{3\ k} \\ \Delta u_x{}'^{e_{III} t+1}_{1\ k} \end{bmatrix}$$

$$\boldsymbol{N_{U_M}}'^{\boldsymbol{e t+1}}_{\boldsymbol{k}}(\boldsymbol{x_M}'^{\boldsymbol{e}}) = \begin{bmatrix} 1-\xi_I & \xi_I & 0 & 0 & 0 & 0 \\ 0 & 0 & 1-\xi_{II} & \xi_{II} & 0 & 0 \\ 0 & 0 & 0 & 0 & 1-\xi_{III} & \xi_{III} \end{bmatrix}$$
$$= \begin{bmatrix} N_{U_1}{}^{e_I t+1}_{\ k} & N_{U_2}{}^{e_I t+1}_{\ k} & 0 & 0 & 0 & 0 \\ 0 & 0 & N_{U_2}{}^{e_{II} t+1}_{\ k} & N_{U_3}{}^{e_{II} t+1}_{\ k} & 0 & 0 \\ 0 & 0 & 0 & 0 & N_{U_3}{}^{e_{III} t+1}_{\ k} & N_{U_1}{}^{e_{III} t+1}_{\ k} \end{bmatrix}$$

where

$\boldsymbol{N_{U_M}}'^{\boldsymbol{e t+1}}_{\boldsymbol{k}}$ [mm] Element matrix of the material-based shape functions

The material contributions to the elastic strain energy are based only on the incremental strains as defined by Eq. (9.21). Using the linear approximated axial displacement defines the strain increment as constant along each bar. The local element gradient matrix based on the three incremental strains also reflects the geometrical non-linear definition (Felippa, 2004a):

$$\Delta\boldsymbol{\varepsilon'}^{\boldsymbol{e}}(t,k) \approx \boldsymbol{B_{U_M}}'^{\boldsymbol{e}t+1}_{\boldsymbol{k}}\,\Delta\boldsymbol{u_x}'^{\boldsymbol{e}t+1}_{\boldsymbol{k}} \tag{9.51}$$

with

$$\Delta\boldsymbol{\varepsilon'}^{\boldsymbol{e}}(t,k) = \begin{bmatrix} \Delta\varepsilon'^{e_I}(t,k) \\ \Delta\varepsilon'^{e_{II}}(t,k) \\ \Delta\varepsilon'^{e_{III}}(t,k) \end{bmatrix} = \begin{bmatrix} \dfrac{\partial \Delta u_x'^{e_I}(t,k)}{\partial x'^{e_I}{}_k^{t+1}} \\ \dfrac{\partial \Delta u_x'^{e_{II}}(t,k)}{\partial x'^{e_{II}}{}_k^{t+1}} \\ \dfrac{\partial \Delta u_x'^{e_{III}}(t,k)}{\partial x'^{e_{III}}{}_k^{t+1}} \end{bmatrix} \begin{bmatrix} \dfrac{\partial \Delta u_x'^{e_I}(t,k)}{\partial N_{U_1}{}^{e_I t+1}_k} \\ \dfrac{\partial \Delta u_x'^{e_I}(t,k)}{\partial N_{U_2}{}^{e_I t+1}_k} \\ \dfrac{\partial \Delta u_x'^{e_{II}}(t,k)}{\partial N_{U_2}{}^{e_{II} t+1}_k} \\ \dfrac{\partial \Delta u_x'^{e_{II}}(t,k)}{\partial N_{U_3}{}^{e_{II} t+1}_k} \\ \dfrac{\partial \Delta u_x'^{e_{III}}(t,k)}{\partial N_{U_3}{}^{e_{III} t+1}_k} \\ \dfrac{\partial \Delta u_x'^{e_{III}}(t,k)}{\partial N_{U_1}{}^{e_{III} t+1}_k} \end{bmatrix} = \begin{bmatrix} \Delta u_x'^{e_I t+1}{}_{1\ k} \\ \Delta u_x'^{e_I t+1}{}_{2\ k} \\ \Delta u_x'^{e_{II} t+1}{}_{2\ k} \\ \Delta u_x'^{e_{II} t+1}{}_{3\ k} \\ \Delta u_x'^{e_{III} t+1}{}_{3\ k} \\ \Delta u_x'^{e_{III} t+1}{}_{1\ k} \end{bmatrix} = \Delta\boldsymbol{u_x}'^{\boldsymbol{e}t+1}_{\boldsymbol{k}}$$

$$\boldsymbol{B_{U_M}}'^{\boldsymbol{e}t+1}_{\boldsymbol{k}} = \begin{bmatrix} \dfrac{\partial N_{U_1}{}^{e_I t+1}_k}{\partial x'^{e_I}{}_k^{t+1}} & \dfrac{\partial N_{U_2}{}^{e_I t+1}_k}{\partial x'^{e_I}{}_k^{t+1}} & 0 & 0 & 0 & 0 \\ 0 & 0 & \dfrac{\partial N_{U_2}{}^{e_{II} t+1}_k}{\partial x'^{e_{II}}{}_k^{t+1}} & \dfrac{\partial N_{U_3}{}^{e_{II} t+1}_k}{\partial x'^{e_{II}}{}_k^{t+1}} & 0 & 0 \\ 0 & 0 & 0 & 0 & \dfrac{\partial N_{U_3}{}^{e_{III} t+1}_k}{\partial x'^{e_{III}}{}_k^{t+1}} & \dfrac{\partial N_{U_1}{}^{e_{III} t+1}_k}{\partial x'^{e_{III}}{}_k^{t+1}} \end{bmatrix}$$

$$= \begin{bmatrix} -\dfrac{1}{l^{e_I}{}_k^{t+1}} & \dfrac{1}{l^{e_I}{}_k^{t+1}} & 0 & 0 & 0 & 0 \\ 0 & 0 & -\dfrac{1}{l^{e_{II}}{}_k^{t+1}} & \dfrac{1}{l^{e_{II}}{}_k^{t+1}} & 0 & 0 \\ 0 & 0 & 0 & 0 & -\dfrac{1}{l^{e_{III}}{}_k^{t+1}} & \dfrac{1}{l^{e_{III}}{}_k^{t+1}} \end{bmatrix}$$

Approximation of the geometry-based incremental deformations

Geometrical deformations are based on the incremental strains and rotations as also indicated in Eq. (9.21) (Bathe, 1986; Gavin, 2014). Again linear displacements are assumed for both horizontal and vertical directions as shown in Fig. 9.3 (Bathe, 1986; Gavin, 2014). This approximation defines a similar element matrix of geometrical-based shape functions which through differentiation with respect to the axes of the bars defines both deformations. The constant strain increments are again approximated by the horizontal displacements, obtaining similar terms as previously established (Bathe, 1986; Gavin, 2014). The incremental rotations, defined by the vertical displacements, are as indicated in Eq. (9.17) constant for each bar (Bathe, 1986; Gavin, 2014). Moreover, the resultant local element gradient matrix indeed defines the incremental geometrical stiffness contributions independent of the adopted coordinate system (Bathe, 1986). This can be proven through coordinate transformation using parts of Eq. (9.47). In what follows the identity matrix is introduced to reduce the notation since for each set of local displacements the same derivative of the shape function is used:

$$\begin{bmatrix} \Delta\boldsymbol{\varepsilon'}^{\boldsymbol{e}}(t,k) \\ \Delta\boldsymbol{\alpha}^{\boldsymbol{e}}(t,k) \end{bmatrix} \approx \boldsymbol{B_{U_G}}'^{\boldsymbol{e}t+1}_{\boldsymbol{k}}\,\Delta\boldsymbol{u}'^{\boldsymbol{e}t+1}_{\boldsymbol{k}} \tag{9.52}$$

with

$$\begin{bmatrix}\Delta\boldsymbol{\varepsilon'^{e}}(t,k)\\ \Delta\boldsymbol{\alpha^{e}}(t,k)\end{bmatrix}=\begin{bmatrix}\Delta\varepsilon'^{e_I}(t,k)\\ \Delta\alpha^{e_I}(t,k)\\ \Delta\varepsilon'^{e_{II}}(t,k)\\ \Delta\alpha^{e_{II}}(t,k)\\ \Delta\varepsilon'^{e_{III}}(t,k)\\ \Delta\alpha^{e_{III}}(t,k)\end{bmatrix}=\begin{bmatrix}\frac{\partial\Delta {u_x}'^{e_I}(t,k)}{\partial {x'^{e_I}}_k^{t+1}}\\ \frac{\partial\Delta {u_y}'^{e_I}(t,k)}{\partial {x'^{e_I}}_k^{t+1}}\\ \frac{\partial\Delta {u_x}'^{e_{II}}(t,k)}{\partial {x'^{e_{II}}}_k^{t+1}}\\ \frac{\partial\Delta {u_y}'^{e_{II}}(t,k)}{\partial {x'^{e_{II}}}_k^{t+1}}\\ \frac{\partial\Delta {u_x}'^{e_{III}}(t,k)}{\partial {x'^{e_{III}}}_k^{t+1}}\\ \frac{\partial\Delta {u_y}'^{e_{III}}(t,k)}{\partial {x'^{e_{III}}}_k^{t+1}}\end{bmatrix}\begin{bmatrix}\frac{\partial\Delta\boldsymbol{u'^{e_I}}(t,k)}{\partial {N_{U_1}}^{e_I t+1}_k}\\ \frac{\partial\Delta\boldsymbol{u'^{e_I}}(t,k)}{\partial {N_{U_2}}^{e_I t+1}_k}\\ \frac{\partial\Delta\boldsymbol{u'^{e_{II}}}(t,k)}{\partial {N_{U_2}}^{e_{II} t+1}_k}\\ \frac{\partial\Delta\boldsymbol{u'^{e_{II}}}(t,k)}{\partial {N_{U_3}}^{e_{II} t+1}_k}\\ \frac{\partial\Delta\boldsymbol{u'^{e_{III}}}(t,k)}{\partial {N_{U_3}}^{e_{III} t+1}_k}\\ \frac{\partial\Delta\boldsymbol{u'^{e_{III}}}(t,k)}{\partial {N_{U_1}}^{e_{III} t+1}_k}\end{bmatrix}=\begin{bmatrix}\Delta {u_x}'^{e_I t+1}_{1\ k}\\ \Delta {u_y}'^{e_I t+1}_{1\ k}\\ \Delta {u_x}'^{e_I t+1}_{2\ k}\\ \Delta {u_y}'^{e_I t+1}_{2\ k}\\ \Delta {u_x}'^{e_{II} t+1}_{2\ k}\\ \Delta {u_y}'^{e_{II} t+1}_{2\ k}\\ \Delta {u_x}'^{e_{II} t+1}_{3\ k}\\ \Delta {u_y}'^{e_{II} t+1}_{3\ k}\\ \Delta {u_x}'^{e_{III} t+1}_{3\ k}\\ \Delta {u_y}'^{e_{III} t+1}_{3\ k}\\ \Delta {u_x}'^{e_{III} t+1}_{1\ k}\\ \Delta {u_y}'^{e_{III} t+1}_{1\ k}\end{bmatrix}=\Delta\boldsymbol{u'^{e\,t+1}_{k}}$$

$$\boldsymbol{B_{U_G}}'^{\boldsymbol{e\,t+1}}_{\boldsymbol{k}}=\begin{bmatrix}\frac{\partial {N_{U_1}}^{e_I t+1}_k}{\partial {x'^{e_I}}_k^{t+1}}\boldsymbol{I} & \frac{\partial {N_{U_2}}^{e_I t+1}_k}{\partial {x'^{e_I}}_k^{t+1}}\boldsymbol{I} & 0 & 0 & 0 & 0\\ 0 & 0 & \frac{\partial {N_{U_2}}^{e_{II} t+1}_k}{\partial {x'^{e_{II}}}_k^{t+1}}\boldsymbol{I} & \frac{\partial {N_{U_3}}^{e_{II} t+1}_k}{\partial {x'^{e_{II}}}_k^{t+1}}\boldsymbol{I} & 0 & 0\\ 0 & 0 & 0 & 0 & \frac{\partial {N_{U_3}}^{e_{III} t+1}_k}{\partial {x'^{e_{III}}}_k^{t+1}}\boldsymbol{I} & \frac{\partial {N_{U_1}}^{e_{III} t+1}_k}{\partial {x'^{e_{III}}}_k^{t+1}}\boldsymbol{I}\end{bmatrix}$$
$$=\begin{bmatrix}-\frac{1}{{l^{e_I}}_k^{t+1}}\boldsymbol{I} & \frac{1}{{l^{e_I}}_k^{t+1}}\boldsymbol{I} & 0 & 0 & 0 & 0\\ 0 & 0 & \frac{1}{{l^{e_{II}}}_k^{t+1}}\boldsymbol{I} & \frac{1}{{l^{e_{II}}}_k^{t+1}}\boldsymbol{I} & 0 & 0\\ 0 & 0 & 0 & 0 & -\frac{1}{{l^{e_{III}}}_k^{t+1}}\boldsymbol{I} & \frac{1}{{l^{e_{III}}}_k^{t+1}}\boldsymbol{I}\end{bmatrix}$$

Approximation of the bending-based incremental deformations

Local curvature for each element is defined by three beams characterised by the moment of inertia. Since the element stiffness matrix and the various force contributions directly define the nodal shear force and moment contributions a numerical solution of integrals is not required. The same holds true for the approximation of the vertical displacements which are, through consideration of elastic curves, included in the definition. Furthermore, both the length and the angle of the bars are also used to characterise the beams.

For implementation of the beams it also needs to be considered that the adopted approach in definition of parallel bars cannot be used. Contrary to the bars are the stresses in the beams not constant, but vary linearly in each cross-section as well as along their axes. The bending stiffness contributions are therefore based on single beams with the main property, the moment of inertia, defined by the altitudes of adjacent areas as schematically indicated in Fig. 9.9. The definition of this property for a rectangular cross-section is relatively straightforward and reflects the cubic dependence on the height (Hartsuijker & Welleman, 2007). In the following definition also a bending factor is introduced in order to vary the bending stiffness

through the moment of inertia. This will allow to examine the influence of the addition of local bending stiffness on the deformations and stresses in the cross-section:

$$I'^{e_d} = \frac{D(\gamma_B h^{e_d})^3}{12} \tag{9.53}$$

where

h^{e_d}	[mm]	Internal height perpendicular to the axis of beam 'd'
I'^{e_d}	[mm^4]	Moment of inertia of beam 'd', considering adjacent areas
γ_B	[-]	Bending factor governing the influence of the Bernoulli-Euler beam

Incremental development of the fracture process

The removal of fractured bars and beams is followed by a recalculation of the incremental displacements based on the modified system. This stepwise approach to determine the crack propagation is relatively time consuming. Calculation times are reduced in case more 1D elements are fractured in the same incremental step. However, this number is limited since crack development is driven by the redistribution of the fracture forces. In order to still be able to fracture several 1D elements the subdivision into sections, as elaborated in the previous chapter, is considered. In each section in every incremental step only a limited number of 1D elements is fractured. The height of these sections should be sufficiently large to avoid that adjacent cracks consume the same elastic strain energy during propagation.

The modified system also requires additional considerations. Especially in case several 1D elements are removed the possibility exists that nodes become disconnected. These disconnected nodes are characterised by the corresponding variables in the system matrix having no stiffness contributions. Solving a system with undefined variables is not possible and requires removal of the respective nodes. However, it is more convenient to maintain the system and add a 'one' on the diagonal of the matrix. Since at disconnected nodes also no forces are imposed, solution of the system will yield no additional displacements for the corresponding variables. Regarding the fracture process it has also to be considered that numerical instabilities can arise based on small pieces of the material becoming separated from the remaining cross-section. The subsequent large deformations destabilise the solution which is overcome by, on occasion, reinstating an individual 1D element.

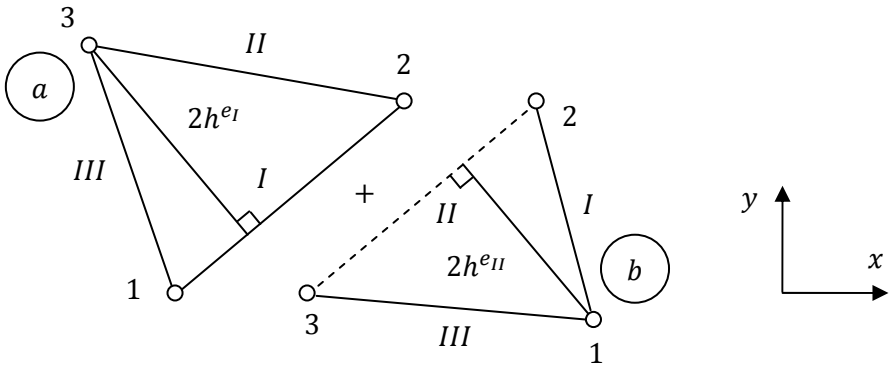

Fig. 9.9 *Schematic representation of two triangles reflecting the definition of the 1D beams in $\mathbb{R}^2$. For adjacent areas only a single beam is considered, characterised by the altitudes of both triangles.*

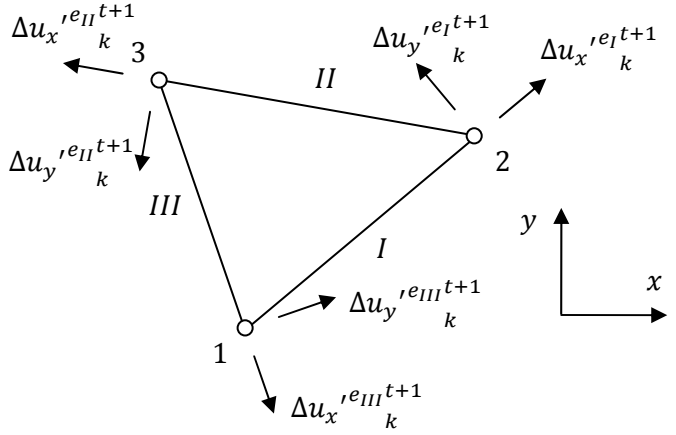

Incremental stresses and strains (element)

$$\Delta\boldsymbol{\sigma}'^{\boldsymbol{e}\,\boldsymbol{t+1}}_{\boldsymbol{k}} = \begin{bmatrix} \Delta\sigma'^{e_I\,t+1}_{k} \\ \Delta\sigma'^{e_{II}\,t+1}_{k} \\ \Delta\sigma'^{e_{III}\,t+1}_{k} \end{bmatrix}$$

$$\Delta\boldsymbol{\varepsilon}'^{\boldsymbol{e}\,\boldsymbol{t+1}}_{\boldsymbol{k}} = \begin{bmatrix} \Delta\varepsilon'^{e_I\,t+1}_{k} \\ \Delta\varepsilon'^{e_{II}\,t+1}_{k} \\ \Delta\varepsilon'^{e_{III}\,t+1}_{k} \end{bmatrix}$$

Fig. 9.10 *Linear approximation of the incremental displacements across the 1D bars in* $\mathbb{R}^2$ *defining the constant stress and strain increments.*

9.4.3 Obtaining the solution and results analyses

The anisotropic FEM definition approximates the incremental development of the global displacements based on Eq. (9.13). Through coordinate transformation using Eq. (9.24) the local incremental horizontal and vertical displacements are determined as shown in Fig. 9.10. Updating the length and angle of the bars is based on Eq. (9.16) and Eq. (9.17) respectively.

Incremental element strains, stresses and the total elastic strain energy

The local mechanical strains and especially the stresses characterise the material terms in the incremental elastic strain energy definition stated in Eq. (9.21). The geometrical terms do not constitute a strain or stress increment as these govern the influence of the current mechanical state on the deformations. Local bending-induced strains and stresses are neglected since the transfer of normal forces is assumed to be the main load transfer mechanism.

The linear approximation of the axial displacements defines the strain increment as constant across each not fractured bar. Using the material-based element gradient matrix in Eq. (9.51), while considering the temperature strain increment, the following is stated:

$$\Delta\boldsymbol{\varepsilon_m}'^{\boldsymbol{e}\,\boldsymbol{t+1}}_{\boldsymbol{k}} = \boldsymbol{B_{U_M}}'^{\boldsymbol{e}}\boldsymbol{T_{\alpha_M}}'^{\boldsymbol{e}\,\boldsymbol{t+1}}_{\boldsymbol{k}}\boldsymbol{T_{\varphi}}^{\boldsymbol{e}}\Delta\boldsymbol{u}^{\boldsymbol{e}\,\boldsymbol{t+1}}_{\boldsymbol{k}} - \left(\boldsymbol{\varepsilon_T}'^{\boldsymbol{e}\,\boldsymbol{t+1}}_{\boldsymbol{k+1}} - \boldsymbol{\varepsilon_T}'^{\boldsymbol{e}\,\boldsymbol{t+1}}_{\boldsymbol{k}}\right) \tag{9.54}$$

Three different contributions are considered to govern the incremental local stresses based on Eq. (9.25) to Eq. (9.27). The first and third term represent the stiffness variation and pressure-induced stresses respectively, which both are a priori known. The second term reflects the structural response of the not fractured bars based on the incremental strains:

$$\begin{aligned}\Delta\boldsymbol{\sigma}'^{\boldsymbol{e}\,\boldsymbol{t+1}}_{\boldsymbol{k}} &= \left(\boldsymbol{D}'^{\boldsymbol{e}\,\boldsymbol{t+1}}_{\boldsymbol{k+1}} - \boldsymbol{D}'^{\boldsymbol{e}\,\boldsymbol{t+1}}_{\boldsymbol{k}}\right)\left(\boldsymbol{\varepsilon}'^{\boldsymbol{e}\,\boldsymbol{t+1}}_{\boldsymbol{k}} - \boldsymbol{\varepsilon_T}'^{\boldsymbol{e}\,\boldsymbol{t+1}}_{\boldsymbol{k}}\right) \\ &+\boldsymbol{D}'^{\boldsymbol{e}\,\boldsymbol{t+1}}_{\boldsymbol{k}}\left(\boldsymbol{B_{U_M}}'^{\boldsymbol{e}}\boldsymbol{T_{\alpha_M}}'^{\boldsymbol{e}\,\boldsymbol{t+1}}_{\boldsymbol{k}}\boldsymbol{T_{\varphi}}^{\boldsymbol{e}}\Delta\boldsymbol{u}^{\boldsymbol{e}\,\boldsymbol{t+1}}_{\boldsymbol{k}} - \left(\boldsymbol{\varepsilon_T}'^{\boldsymbol{e}\,\boldsymbol{t+1}}_{\boldsymbol{k+1}} - \boldsymbol{\varepsilon_T}'^{\boldsymbol{e}\,\boldsymbol{t+1}}_{\boldsymbol{k}}\right)\right) + \left(\boldsymbol{\sigma_P}'^{\boldsymbol{e}\,\boldsymbol{t+1}}_{\boldsymbol{k+1}} - \boldsymbol{\sigma_P}'^{\boldsymbol{e}\,\boldsymbol{t+1}}_{\boldsymbol{k}}\right)\end{aligned} \tag{9.55}$$

Subsequent are the total local mechanical strains and stresses acting in the bars determined through Eq. (9.14). Direct integration leads to the total elastic strain energy present:

$$U_{\varepsilon}{}'^{e\,t+1}_{k+1} = \int_{\Omega'^e} \frac{1}{2} \boldsymbol{\varepsilon_m}'^{e\,t+1\,T}_{k+1} \boldsymbol{\sigma}'^{e\,t+1}_{k+1} d\Omega'^e = \frac{1}{2} \boldsymbol{A}'^e \boldsymbol{l}^{e\,t+1}_{k} \boldsymbol{\varepsilon_m}'^{e\,t+1\,T}_{k+1} \boldsymbol{\sigma}'^{e\,t+1}_{k+1} \tag{9.56}$$

Global structural response

The overall structural response is defined by transformation of the local mechanical strains and stresses in the current reference system using Eq. (9.8) and Eq. (9.10) respectively (Felippa, 2004a). The element-based total elastic strain energy is recalled from chapter 8 using the previous expressions:

$$U_{\varepsilon}{}^{e\,t+1}_{k+1} = \int_{\Omega^e} \frac{1}{2} \boldsymbol{\varepsilon_m}^{e\,t+1\,T}_{k+1} \boldsymbol{\sigma}^{e\,t+1}_{k+1} d\Omega^e = \frac{DA^e}{2} \boldsymbol{\varepsilon_m}^{e\,t+1\,T}_{k+1} \boldsymbol{\sigma}^{e\,t+1}_{k+1} \tag{9.57}$$

with

$$\boldsymbol{\varepsilon_m}^{e\,t+1}_{k+1} = \boldsymbol{T}_{\varepsilon_M}{}'^{e\,t+1\,-1}_{k} \boldsymbol{\varepsilon_m}'^{e\,t+1}_{k+1} \qquad \boldsymbol{\sigma}^{e\,t+1}_{k+1} = \boldsymbol{T}_{\varepsilon_M}{}'^{e\,t+1\,T}_{k} \boldsymbol{\sigma}'^{e\,t+1}_{k+1}$$

9.5 Conclusions with respect to the FEM definition

With respect to the 1D bars defined in the anisotropic continuum the following conclusions and remarks are stated:

- The plane strain mechanical continuum is schematised by three triangularly orientated bars, each characterising the local axial displacements (Prezemieniecki, 1968/1985; Blaauwendraad, 2004; Felippa, 2004a). Local extensional stresses are defined by the diagonal stiffness tensor in Eq. (9.4). The temperature strains and pressure-induced stresses in Eq. (9.5) are defined relative to atmospheric conditions.

- The global strains are, through the second order transformation tensor in Eq. (9.7), related to the local strains (Timoshenko & Goodier, 1970; Felippa, 2004a). Conservation of elastic strain energy in Eq. (9.10) and Eq. (9.12) defines the local and global stresses as well as the stiffnesses (Felippa, 2004a; Zienkiewicz, et al., 2005).

- Geometric non-linearity is implemented through incremental development of the global displacements in Eq. (9.13) as well as the local strains, stresses and stiffness using Eq. (9.14) and Eq. (9.15) respectively (Zienkiewicz, et al., 2005).

- The incremental displacements in the local directions govern the change in length and rotation for a single bar as stated in Eq. (9.16) and Eq. (9.17) respectively (Bathe, 1986; Gavin, 2014). Through the incremental elastic strain energy both the material and the geometrical contributions are determined which in Eq. (9.21) are based on the three bars (Bathe, 1986; Gavin, 2014).

- Additional straining of the material is governed by incremental temperature and pressure forces in Eq. (9.26) and Eq. (9.27). Incremental deformation of the normal forces acting in the bars is reflected by the geometrical forces stated in Eq. (9.28).

- Heterogeneity is reflected by the bars being characterised as aggregate, mortar or interfacial zone, each described according to Hooke's law of linear elasticity (Schlangen, 1993; Vervuurt, 1997). Temperature-dependent development of Young's modulus and the temperature strain governs the incremental normal force.

Regarding the incremental fracture process and the numerical stability the following conclusions are drawn:

- Crack initiation is based on brittle extensional fracture of bars, removing the stiffness and force contributions from the FEM system (Schlangen, 1993; Vervuurt, 1997). This material separation assumes that normal force transfer across the crack is not possible.

- In order to preserve the elastic strain energy the axial stresses acting in the fractured bars are redistributed at the crack edges based on the boundary condition in Eq. (9.30). The corresponding incremental fracture forces are derived according to Eq. (9.32) with gas pressures assumed to remain present.

- The coupling with the FEM temperature and pore pressure model is governed by estimation of the crack opening in Eq. (9.33) based on the local axial displacements.

- The hinged bars could allow for insufficient redistribution of fracture forces, causing too localised deformations. These numerical instabilities are addressed by including local bending based on 1D Bernoulli-Euler beams, creating a traditional lattice through Eq. (9.39) (Schlangen, 1993; Vervuurt, 1997; Prezemieniecki, 1968/1985).

- Additional incremental forces based on temperature-induced variation of the bending stiffness is stated in Eq. (9.45). Fracture of bars goes along with removal of the beams, requiring to redistribute the shear forces and moments as defined by Eq. (9.46).

The FEM approximation of the incremental displacements is based on:

- The anisotropic FEM definition in Eq. (9.47), reflecting the material-, geometrical- and bending-based contributions. Addition of local bending introduces nodal rotations, requiring to extend the local coordinate transformations and the rigid body conditions.

- Spatial integration of the material and geometrical contributions governing the bars is based on the constant element gradient matrices stated in Eq. (9.51) (Felippa, 2004a) and Eq. (9.52) respectively (Bathe, 1986; Gavin, 2014). Both the length and the angle are incrementally defined to reflect the geometric non-linearity.

- The cross-sectional area of the bars is governed by half of the internal height of the triangle. Across the domain parallel aligned bars are defined. Beams are separately defined with the moment of inertia governed by the internal height of adjacent areas.

- Incremental material-based local stresses are defined in Eq. (9.55) and are based on stiffness variation, pressure development and the incremental mechanical strains.

9.6 FEM approximation based on heterogeneous and anisotropic concrete

The derived anisotropic FEM schematisation is implemented for a part of a concrete structural element. First, the heterogeneous material distribution is presented, indicating the schematisation by 1D elements and the differences with the triangular mesh. The aggregate particles and the surrounding mortar are both assumed characterised as linear elastic (Schlangen, 1993; Vervuurt, 1997). Interfacial zones are, similar to chapter 7, based on modified mortar properties in order to reflect the reduced strength and stiffness of the microstructure in NSC (Müller & Rubner, 1994). Subsequently the mesh is presented, briefly reflecting on the dimensions and support conditions. In the second part of this paragraph the anisotropic FEM definition is validated through evaluation of static equilibrium. Both the schematisation by 1D bars as well as the addition of local bending is discussed through comparison of the displacements at the top support and the global stresses.

9.6.1 Heterogeneous discretisation of the cross-section

In order to implemented heterogeneity the same procedure is used as described in chapter 7. However, since the 1D bars each define a single edge of the triangular element, the determination of the corresponding material characterisation is straightforward (Schlangen, 1993; Vervuurt, 1997). Element edges are characterised based on their relative location in the scanned image. Bars situated in an aggregate particle or in the surrounding mortar are assigned with the properties accordingly. Interfacial properties are prescribed to edges located in both materials. The resultant mesh is shown in Fig. 9.11 which compared to chapter 8 has a height of 600 mm in order to reduce the calculation time for the incremental facture process.

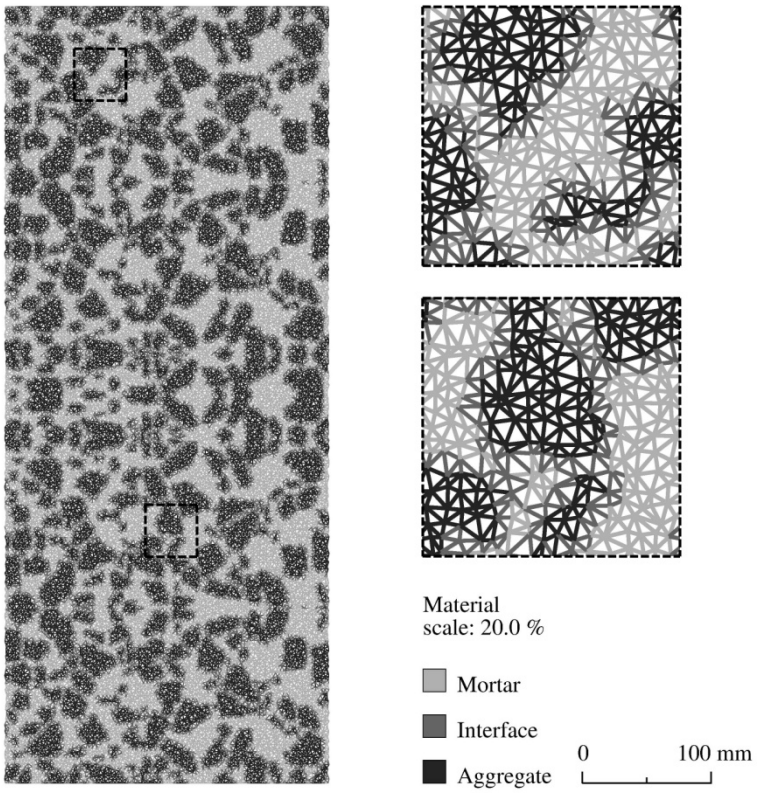

Fig. 9.11 *Discretisation by triangularly orientated 1D elements used to numerically approximate the heterogeneous and anisotropic concrete cross-section.*

Geometry of the mesh	
Width	250 mm
Height	600 mm
Unit thickness	1 mm
FEM discretisation	
Total number of nodes	24341
Total number of triangles	48000

Table 9.1 *Dimensions and triangular element discretisation of the mesh used to approximate the concrete structural element.*

This is reflected in Table 9.1 by the nodal reduction governing the dimensions of the system matrix. Furthermore, symmetry of the material components with respect to the horizontal central axis is required in order to couple them with the FEM transport and pore pressure model. Finally, along the top and bottom edges the support conditions are imposed.

9.6.2 Material properties of the concrete components

Characterisation of the main material properties is based on similar considerations as stated in chapter 7. A simplified approach is adopted since the temperature-dependent development of Young's modulus and the tensile strength based on the strength class of the mortar is at the moment not directly available in literature. Both are based on reference values at ambient conditions and the development with temperature of the corresponding properties of concrete.

In Fig. 9.12 Young's modulus of both mortar types are indicated to reduce with temperature. However, based on consideration of NSC (Castillo & Durrani, 1990) and HSC (Pimienta, 2001) measurements the mortar of C90/105 is more affected by the dehydration processes. Similar temperature dependence is also assumed to govern the development of the tensile strength, based on concrete results by (Thelandersson, 1971; Felicetti & Gambarova, 1998). Both properties are assumed constant at temperatures higher than 600 °C with only 20 % and 10 % of the initial values remaining for C25/30 and C90/105 respectively.

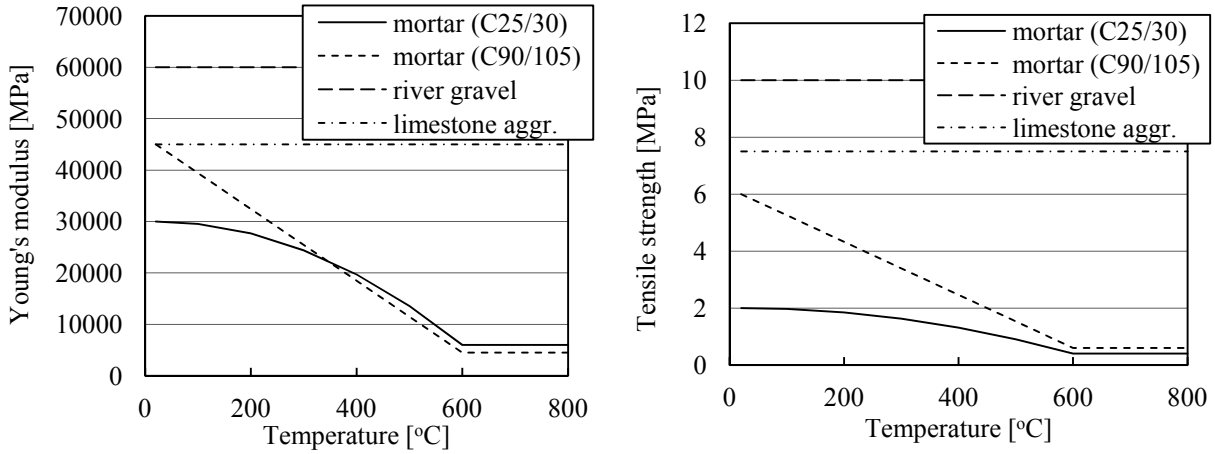

Fig. 9.12 *Development of Young's modulus and the tensile strength based for mortar on considering concrete measurements by* (Castillo & Durrani, 1990; Pimienta, 2001) *and* (Thelandersson, 1971; Felicetti & Gambarova, 1998). *Aggregate properties are taken from* (Dmitriyev, et al., 1969/1972) *and* (Zhu, 2012).

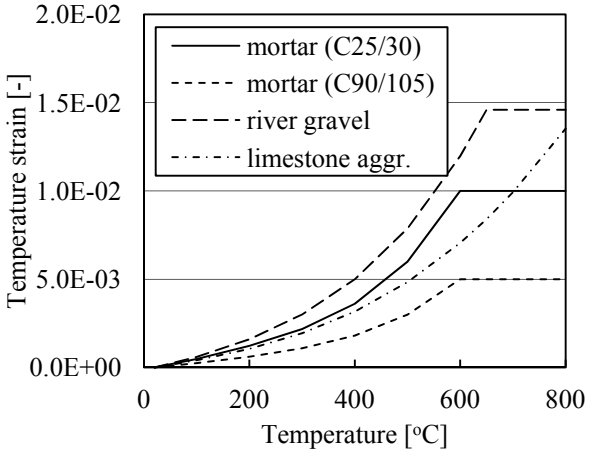

Fig. 9.13 *River gravel reflects the highest temperature strains* (Flynn, 1999) *whereas the expansion of limestone* (Khoury, 2006a) *is similar to the C25/30 mortar* (Diederichs, et al., 1987; Cruz & Gillen, 1980). *The mortar of C90/105 is assumed to have a lower thermal expansion.*

Measurements of the temperature dependence of Young's modulus for river gravel and limestone aggregate suggest only limited influence with the former assumed stiffer (Yang, et al., 1995; Dmitriyev, et al., 1969/1972). Both stiffnesses are therefore assumed constant, neglecting the possible influence of the α-quartz to β-quartz inversion and the decarbonation processes that develop at high temperatures. Temperature independence is also assumed to hold for the tensile strengths for which reference values are obtained from (Zhu, 2012; Giaccio & Zerbino, 1998).

Internal loading is mainly characterised by the temperature strain that develops due to the elongation of the material. This property is investigated experimentally and in literature various normal strength cement paste and mortar results are found with the constant elongation at temperatures higher than 600 ^{o}C commonly reported (Diederichs, et al., 1987; Cruz & Gillen, 1980). However, the influence of the mortar strength class on the temperature strain is at the moment not sufficiently clear. In this thesis it is assumed that shrinkage of the cement paste due to dehydration (Diederichs, et al., 1987; Cruz & Gillen, 1980) has a higher influence on the temperature strain development in case of the denser microstructure of C90/105. Furthermore, thermal dilatometry measurements indicate that river gravel has a markedly higher expansion than limestone (Flynn, 1999; Khoury, 2006a) as seen in Fig. 9.13.

The anisotropic FEM definition is also governed by Poisson's ratio (Timoshenko & Goodier, 1970). This property is occasionally investigated for concrete (RILEM TC-HTC, 2004), but the presence of cracks makes statement of the temperature dependence difficult. In this thesis it is assumed that all components have the same Poisson's ratio, constant with temperature, and defined equal to the reference value of concrete (Eurocode 2, 2011a). Finally, the interfacial zones are especially in NSC less well developed and consequently weaker (Müller & Rubner, 1994). This is expressed by the ratios governing Young's modulus and the tensile strength stated in Table 9.2. For the C90/105 mortar a limited reduction is considered for both material properties. Temperature strain and pressure-induced stress are assumed not affected.

Ratio of properties interfacial zone to mortar		
Strength class	C25/30	C90/105
E_{itz}'/E_m'	**0.7**	**0.9**
$f_{t_{itz}}'/f_{t_m}'$	**0.4**	**0.8**
$\varepsilon_{T_{itz}}'/\varepsilon_{T_m}'$	1.0	1.0
$\sigma_{P_{itz}}'/\sigma_{P_m}'$	1.0	1.0

Table 9.2 *Ratios of the mechanical properties between the interfacial zone and the mortar, dependent on the strength class.*

9.6.3 Validation of static equilibrium by comparison of displacements and stresses

The anisotropic FEM definition has a different basis than the 2D triangular elements used in the previous chapter. It is therefore considered prudent to again asses the numerical approximation of static equilibrium in case of using three 1D bars. For a homogeneous cross-section several loading scenarios are used to examine the numerical approximation of the displacements at the top support and the global stresses. The axial force and moment imposed at both supports are the same as in chapters 5 and 8. However, the reduction of the cross-sectional height affects the level of restraint by the springs based on the deformations at the support. In order to maintain the in-plane stresses the spring constants are multiplied by a factor of 1.67, representing the height reduction from 1000 mm to 600 mm. This ensures that the axial elongation strain and curvature are the same for both discretisations.

The reference schematisation used reflects the 1D bars based on either a plane stress or a plane strain assumption with the latter defined by Eq. (9.4). Through restraint of the out-of-plane extensional stress the plane stress equivalent of the anisotropic definition can be obtained. This particular in-plane schematisation is also used in combination with Bernoulli-Euler beams to determine the influence of local bending using the factor defined in Eq. (9.53).

Constant temperature scenarios		
Calculation	**9.1A**	**9.1B**
Reference temperature	20 °C	20 °C
Material (homogeneous)		
Strength class	C25/30	C25/30
Aggregate type	independent	independent
Boundary conditions		
Axial force	-2.0 kN	-2.0 kN
Moment	-0.05 kNm	-0.05 kNm
Axial spring stiffness	6.7 kN/mm	6.7 kN/mm
Rotational spring stiffness	33 kNm/rad	33 kNm/rad
Characterisation of bending		
Type of 1D elements	bars	bars + beams
Bending factor		0.2 / 0.4 / 0.6 / 1.0

Table 9.3 *Validation of the anisotropic FEM definition based on a uniform in-plane temperature, using both 1D bars separately or in combination with 1D beams.*

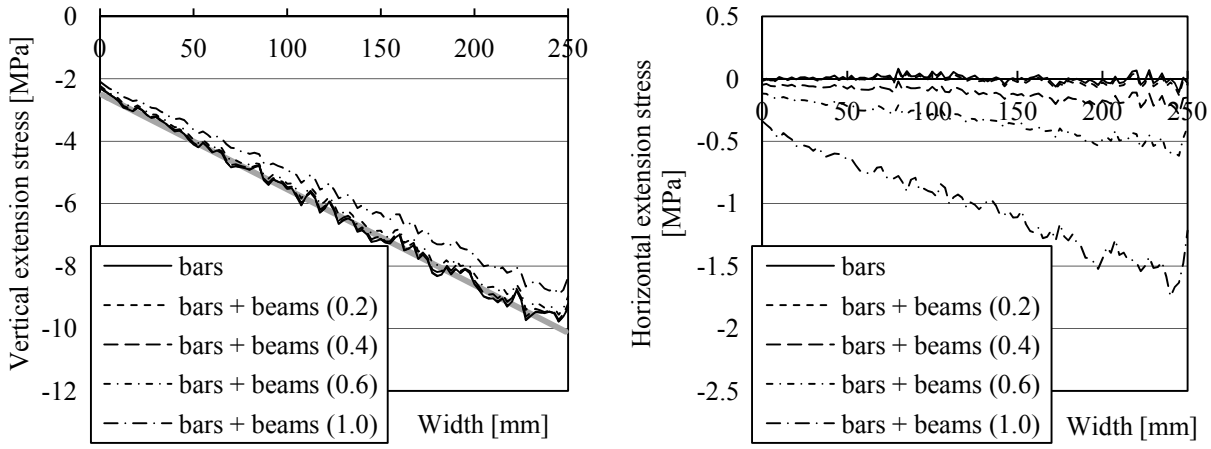

Fig. 9.14 *Vertical stresses in the cross-section are sufficiently approximated by using three 1D bars to schematise the plane stress continuum (left). Introduction of Bernoulli-Euler beams causing horizontal stresses to develop (right).*

Constant temperature in the cross-section

The first loading scenario only includes external partial restraint and forces without imposing temperature strains. The temperature in the homogeneous cross-section remains at reference conditions, only governed by the strength class of the concrete as stated in Table 9.3. Both the plane stress and the plane strain approximation by the 1D bars is sufficient to represent the principal stresses acting across the width of the cross-section as shown in the left graph of Fig. 9.14. However, compared to the isotropic continuum, elaborated in chapter 8, a larger variation of the vertical stresses is approximated. This is attributed to the uncoupled definition of the hinged bars, each governing only two of the element nodes as illustrated by Fig. 9.8.

By extending the element schematisation to include local bending the overall stiffness of the cross-section increases. This is investigated through variation of the bending factor governing the influence of the Bernoulli-Euler beams. The principal stresses remain mostly unaffected as seen in the left graph of Fig. 9.14. However, in the horizontal direction a linear stress state develops, governed by the level of bending considered as observed from the right graph in Fig. 9.14. This is attributed to partial restraint of the nodal rotations by the introduced bending stiffness. The deformations imposed by the external forces are mitigated, causing stresses in the initially unrestrained lateral direction. The addition of 1D beams thus affects the approximation of the global strains, reflecting a stiffening effect in the mechanical response.

Linear temperature in the cross-section

In order to determine the approximation of the imposed strains a linear distribution with a maximum temperature of 800 ^{o}C at the left edge is used. The aggregate type assumed for the homogeneous material schematisation governs the temperature strain development. An overview of the various parameters is provided in Table 9.4.

Both the plane stress and plane strain cross-sectional schematisations are sufficiently approximated by only considering the 1D bars. In the left graph of Fig. 9.15 the main vertical stress state is seen to increase by around 20 percent in case of a plane strain approximation. This tendency was also observed in chapter 8 for the isotropic continuum.

Linear temperature scenarios (I)		
Calculation	**9.2A**	**9.2B**
Maximum temperature (left edge)	**800 °C**	**800 °C**
Material (homogeneous)		
Strength class	C25/30	C25/30
Aggregate type	RG	RG
Boundary conditions		
Axial spring stiffness	6.7 kN/mm	6.7 kN/mm
Rotational spring stiffness	33 kNm/rad	33 kNm/rad
Characterisation of bending		
Type of 1D elements	bars	bars + beams
Bending factor		0.2 / 0.4 / 0.6 / 1.0

Table 9.4 *A linear temperature distribution is used to validate the schematisation by 1D bars and to assess the influence of local bending on the softening behaviour.*

By addition of Bernoulli-Euler beams the level of bending considered again governs the horizontal stresses acting across the width of the cross-section. Larger deformations at the top support also develop, especially in case of the highest bending factor. In Table 9.5 displacements and forces, based on a plane stress assumption, are both seen to increase. The influence of the temperature strains is overestimated based on the 1D beams mitigating the local element deformations.

The various results reflect that by introducing additional stiffness, in this case bending, the displacements and stresses are affected. The global strains are already sufficiently approximated by the 1D bars. No addition to the FEM definition is required, implying that every stiffness increase will affect the anisotropic material schematisation. However, these results also suggest that by using a bending factor smaller than 0.5, the influence on the structural behaviour is limited. This allows to consider a bending contribution to the anisotropic continuum in order to redistribute the fracture forces.

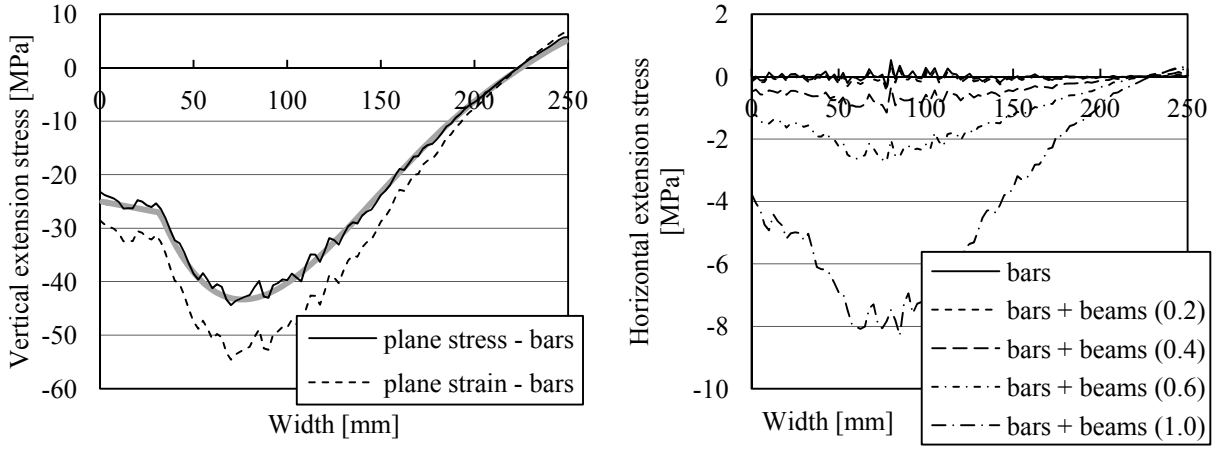

Fig. 9.15 *Schematisation by 1D bars developing similar vertical stresses as determined for the isotropic continuum (left). The addition of Bernoulli-Euler beams governing the horizontal stresses based on the bending factor (right).*

Deformation at top support					
Calculation	Reference	Plane stress	Plane strain	Plane stress	Plane stress
Type of 1D elements		bars	bars	bars + beams	bars + beams
Bending factor				0.4	1.0
Maximum temperature = 800 °C					
Vertical displacement	8.8E-1 mm	8.7E-1 mm	1.1E0 mm	8.8E-1 mm	9.9E-1 mm
Rotation	-6.6E-3 rad	-6.5E-3 rad	-8.0E-3 rad	-6.6E-3 rad	-7.8E-3 rad
Axial force	-5.9 kN	-5.8 kN	-7.1 kN	-5.9 kNm	-6.6 kN
Moment	0.2 kNm	0.2 kNm	0.3 kNm	0.2 kNm	0.3 kNm

Table 9.5 *Displacements and forces at the top support based on a linear temperature distribution, reflecting the influence of the in-plane schematisation and the introduction of local bending.*

Incremental development of displacements and stresses

The final aspect to validate is the incremental development of the displacements and stresses. However, compared to the isotropic FEM definition the displacements are considered to influence the static equilibrium conditions. This geometric non-linearity is included in the anisotropic FEM definition based on the elongation and rotation of the normal force acting in each bar. For this purpose the length and the angle of the 1D element axes are updated. The incremental procedure is validated by using the same linear temperature distribution as previously defined. Only the plane stress schematisation by 1D bars is considered, extended by two different levels of local bending as shown in Table 9.6.

The resultant vertical stresses acting across the width are shown in Fig. 9.16 and reflect mainly dependence on the number of load steps. This behaviour was already observed in chapter 8 and is caused by the softening of the material at temperatures higher than 500 °C.

Linear temperature scenarios (II)		
Calculation	**9.3A**	**9.3B**
Reference temperature	20 °C	20 °C
Maximum temperature (left edge)	800 °C	800 °C
Number of incremental load steps	1 X, 16 X, 64 X	1 X, 16 X, 64 X
Material (homogeneous)		
Strength class	C25/30	C25/30
Aggregate type	RG	RG
Boundary conditions		
Axial spring stiffness	6.7 kN/mm	6.7 kN/mm
Rotational spring stiffness	33 kNm/rad	33 kNm/rad
Characterisation of bending		
Type of 1D elements	bars	bars + beams
Bending factor		0.4 / 1.0

Table 9.6 *Validation of the incremental definition and assessing the influence of local bending based on a linear temperature scenario and the number of load steps.*

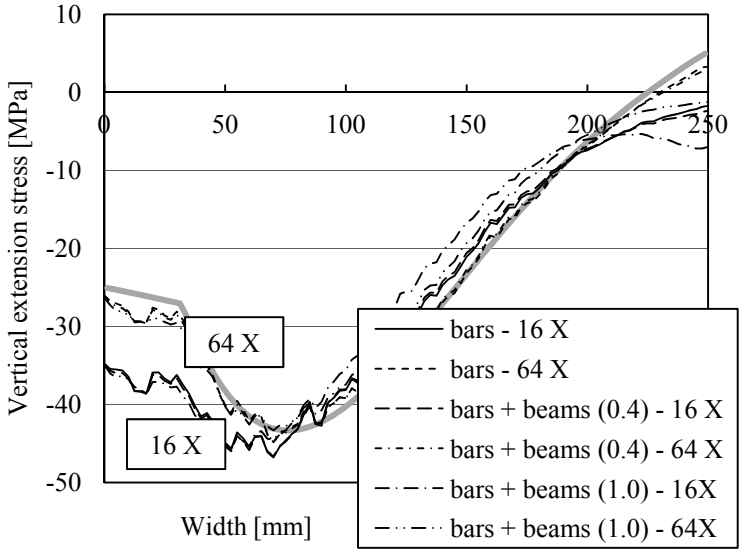

Fig. 9.16 *Main vertical stresses affected by the number of load steps with only small variations due to the bending factor.*

A similar behaviour is also observed in the development of the horizontal stresses, considering the level of bending included in the FEM definition. The various calculations indicate that by consideration of a bending factor of 0.4, under plane stress conditions, the displacements and stresses still reflect the main structural behaviour. The plane strain assumption is believed to lead to similar results, considering the limited Poisson's ratio.

From the previous results it was also concluded that in case of converged global displacements and stresses no significant changes compared to the instant loading case are present. This conclusion was also drawn for the isotropic continuum and holds true as well in case of a non-cracked system of 1D bars. The geometric non-linearity only becomes apparent in case of relatively large and localised deformations, such as occur during crack opening.

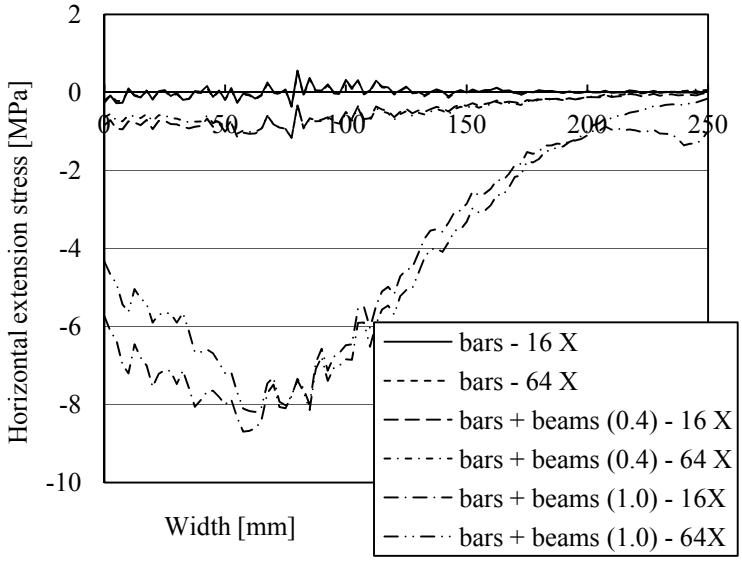

Fig. 9.17 *Horizontal stresses reflecting the influence of the incremental procedure and especially the level of bending.*

Conclusions regarding the FEM definition

The validation by numerical results allows the following conclusions:

- The FEM definition and element discretisation are sufficiently accurate to approximate in-plane static equilibrium in the cross-section.

- By including local bending a stiffening effect in the material response is imposed. The 1D Bernoulli-Euler beams partially restrain the nodal rotations which causes the development of horizontal stresses in the cross-section. However, using a bending factor of 0.4 still leads to a satisfactory approximation of the structural behaviour.

- Geometric non-linearity is considered in relation to the localised deformations that occur during the removal of the 1D bars. This second order behaviour has a limited influence on the incremental displacements as determined for non-cracked concrete.

9.7 Cracking in concrete exposed to a fire based on temperature

The remainder of this chapter focuses on the fracture mechanics behaviour of fire exposed concrete. For this purpose the heterogeneous material schematisation shown in Fig. 9.11 is used. The focus is not only on the fracture mechanics behaviour of fire exposed concrete, but to also assess the numerical stability. The simulations presented are all based on a plane strain approximation governing the discretisation of the structural element by the 1D bars. Furthermore, only the progress of thermal energy across the heterogeneous material is considered using the FEM temperature and pore pressure model stated in chapter 7. The coupling reflects the development of the temperature distribution, imposed in accordance with the incremental load step size.

In this paragraph first the influence of the 1D Bernoulli-Euler beams is investigated. Several possibilities are considered, characterised by the level of nodal rotational restraint defined by the bending factor. In the subsequent sections the material-based fracture of the cross-section is discussed. Of interest is especially the localisation of deformations due to opening of the cracks. The influence of the stresses acting in the cross-section is to be considered in relation to the estimated level of damage. Subsequently the influence of structural restraint is examined, observing for the first time the development of thermal instabilities in the heated surface layer.

9.7.1 Influence of the level of bending included by the Bernoulli-Euler beams

The Bernoulli-Euler beams are considered to stabilise the fracture mechanics behaviour by redistribution of the incremental fracture forces. This traditional lattice approach (Schlangen, 1993; Vervuurt, 1997) extends the anisotropic FEM definition by including local partial restraint governing the nodal rotations. However, in the previous paragraph it was already argued that including additional bending stiffness affects the approximation of the global strains. The capability to deform the three triangularly orientated 1D bars is reduced by the definition of local bending. The initially assumed hinged nodes are partially restrained, causing a stiffening effect throughout the cross-section.

Fire scenarios (I)			
Calculation	**9.4A**	**9.4B**	**9.4C**
Reference temperature	20 ^{o}C	20 ^{o}C	20 ^{o}C
Duration	1200 sec	1200 sec	1200 sec
Incremental time step size	0.5 sec	0.5 sec	0.5 sec
Incremental load step size	5 sec	5 sec	5 sec
Material (heterogeneous)			
Strength class	C25/30	C25/30	C25/30
Aggregate type	RG	RG	RG
Boundary conditions			
Fire scenario	ISO 834	ISO 834	ISO 834
Convective heat transfer coeff.	25 W/m^{2}K	25 W/m^{2}K	25 W/m^{2}K
Axial spring stiffness			
Rotational spring stiffness			
Characterisation of the cracks			
Bending factor	**0.2**	**0.4**	**0.6**

Table 9.7 *Variation of the factor governing the bending stiffness defining the Bernoulli-Euler beams in order to assess the numerical stability.*

The extend of the Bernoulli-Euler beam action included in the FEM definition is governed by the bending factor, reducing the internal height governing the bending stiffness as stated in Eq. (9.53). The validation of the structural response indicated that a bending factor larger than 0.5 caused horizontal stresses to develop across the width of the cross-section. This additional stress state reflected the reduction in the lateral deformations and becomes more predominate by increasing the bending factor. In this section therefore three different levels of bending stiffness are considered, as indicated in Table 9.7, with the maximum defined by a factor of 0.6. The lowest bending factor considered reflects only 20 % of internal height. The fracture mechanics behaviour with no addition of Bernoulli-Euler beams is not presented, since the overall response of the material was found to be too soft. The imposed nodal fracture forces mainly caused the adjacent bars to deform, enabled by the hinged connection. Instead of distributing the forces along part of the crack edges, the displacement was mainly concentrated in the loaded nodes. This destabilised the overall deformations by causing locally too large deformations. In some cases the remaining bars deformed significantly while no longer representing the initial local triangular material description.

The influence of the bending factor is best illustrated by comparing the crack patterns in the C25/30 cross-section that have developed after 1200 seconds of exposure to a standard fire. The crack patterns are based on a bending factor of 0.2 and 0.6 as reflected by the left and right picture of Fig. 9.18 respectively. With respect to these results the cubic relationship for the moment of inertia is to be considered which defines that the largest bending factor represents a 18 times higher bending stiffness as compared to the lower factor. This was already observed to influence the stresses developing in the cross-section as discussed in the previous paragraph. From the crack patterns presented it is observed that the bending factor also influences the crack pattern which varies in distribution as well as in opening.

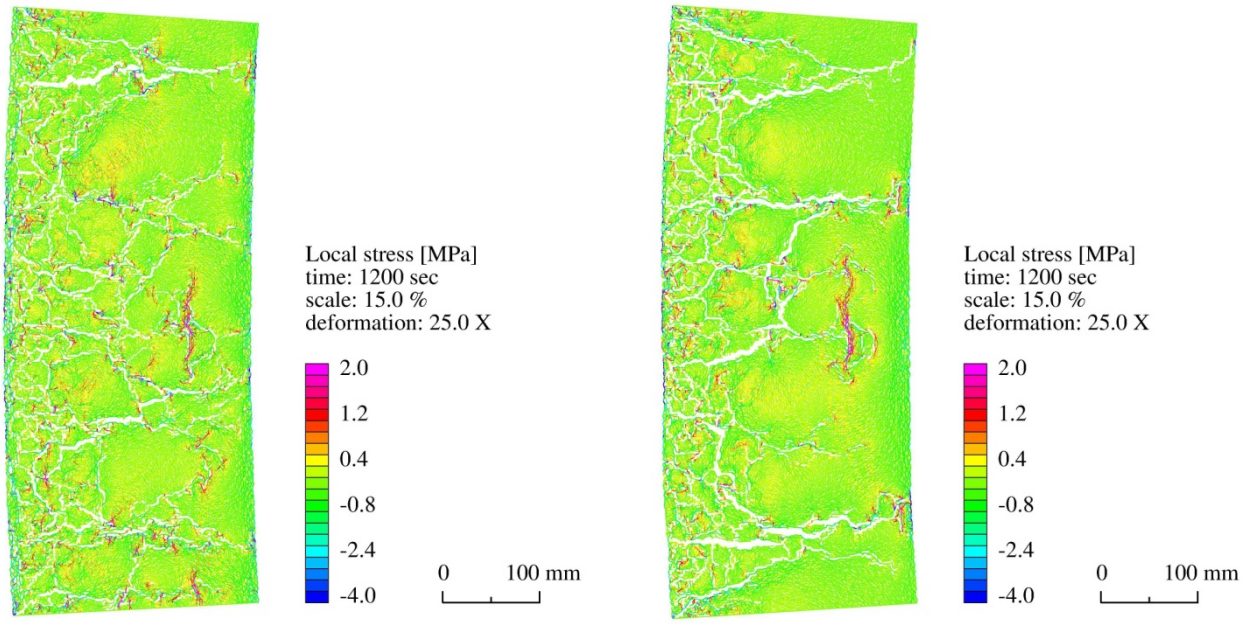

Fig. 9.18 *Cracks in the C25/30 cross-section after 1200 seconds of exposure to an ISO type of fire, reflecting the influence of the bending factor defined as 0.2 (left) and 0.6 (right).*

This is firstly attributed to the adopted fracture mechanics approach. Initial fracture defines the location of the peak tensile stresses and thus the orientation and propagation of the crack. It is therefore logical that the crack patterns are not equal, but only reflect a similar tendency. Furthermore, this fracture mechanics approach is also dependent on the mesh. Changing the 1D element discretisation and/or the properties of the components will influence the results.

The second factor contributing to the development is the bending factor in relation to the previously observed stiffening effect. For higher bending factors not only are the stresses affected, but also the rotational capacity along the crack edges increases. The incremental fracture forces are transmitted across a larger width and consequently a larger area. This can be observed by comparison of the crack patterns, for which several larger cracks develop in the unheated centre of the cross-section characterised by the largest bending factor. A similar trend in the fracture behaviour is also observed for a bending factor of 0.4 as seen in Fig. 9.19.

Conclusions regarding the crack development

Considering this discussion and the numerical results are the following conclusions made:

- The bending factor, governing the Bernoulli-Euler beams, influences the location of the crack initiation through the stresses. Redistribution is based on the partially restrained nodal rotations, allowing to spread the incremental fracture forces along both crack edges.

- By considering 40 % of the internal height to define the bending stiffness sufficient redistribution capabilities along the crack edges are combined with limited influence on the overall stresses. In the remainder of this thesis the bending factor is assumed constant and defined as 0.4.

9.7.2 Crack development based on the concrete strength class

The first aspect about the fracture mechanics behaviour of fire exposed concrete to be examined is the development of the crack pattern. The first simulation therefore reflects the C25/30 cross-section made with RG exposed to an ISO type of fire, as previously discussed. The plane strain cross-section is characterised by a bending factor of 0.4 with the remaining parameters according to Table 9.7. This fire scenario was indicated in chapters 5 and 8 to cause stress levels which are sufficient for cracking. This is confirmed by the crack pattern in Fig. 9.19, formed after 1200 seconds of fire exposure. Especially in the heated surface layer a distributed pattern of small cracks is seen to develop. In the unheated centre of the cross-section several larger, horizontal cracks are observed.

The reduced tensile strength of the interfacial zones combined with the relatively high temperature strain development of river gravel characterises this fracture mechanics behaviour. Cracks in the heated surface layer originate from the interface of the aggregates and propagate based on the continued fire exposure. Opening of the cracks, especially surrounding the particles, allows for sufficient deformations to almost completely relax the compressive stresses. The cross-sectional restraint still results in sufficient tensile loading to induce cracking in the unheated centre of the cross-section. The formation and opening of these horizontal cracks consumes the stored elastic strain energy, relaxing the stresses. Throughout the cross-section the pattern reflects a tortuous, distributed network with cracks intersecting as well as branching off into various directions.

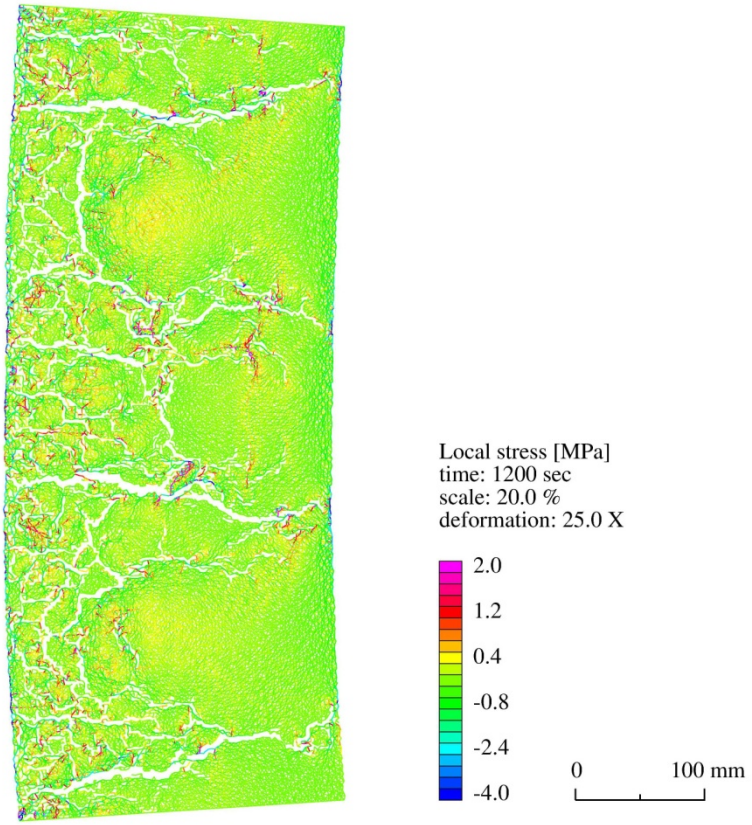

Fig. 9.19 *Stresses acting in the 1D bars causing cracking, especially in the heated surface layer of the unrestrained C25/30 cross-section during exposure to an ISO fire.*

Fire scenarios (II)		
Calculation	**9.5A**	**9.5B**
Reference temperature	20 °C	20 °C
Duration	**480 sec**	**1200 sec**
Incremental time step size	0.5 sec	0.5 sec
Incremental load step size	5 sec	5 sec
Material (heterogeneous)		
Strength class	**C25/30**	**C90/105**
Aggregate type	RG	RG
Boundary conditions		
Fire scenario	HC	HC
Convective heat transfer coeff.	50 W/m^{2}K	50 W/m^{2}K
Axial spring stiffness		
Rotational spring stiffness		

Table 9.8 *Examination of the material-based crack development by exposure of the cross-section to a HC-based fire scenario, characterised by the concrete strength class.*

Increasing the level of imposed thermal energy by exposure to a HC type of fire causes more cracking. This is investigated by also considering the concrete strength class as indicated by the fire scenarios stated in Table 9.8. Both concrete mixtures are composed with river gravel and the structural element is again considered unrestrained. This causes the development of thermal stresses without taking, for the moment, the structural influence into account.

As expected does the C25/30 cross-section reflect a higher level of cracking. Not only the crack pattern in the heated surface layer is extended, but two dominating cracks at the top and bottom edges develop. These cracks already formed at the onset of fire exposure and can be seen in the left picture of Fig. 9.20 to have opened considerably. Even in these unrestrained conditions are the self-equilibrating thermal stresses sufficient to seriously damage the cross-section. With respect to these results it is recalled that the in-plane schematisation affectively assumes that the cracks are constant in depth direction, without allowing for any form of redistribution. Considering this, the type of crack formation and the observed continued opening indicates that this cross-section could ultimately be unable to withstand this thermal impact. Under these circumstances failure of the cross-section could occur.

The case of a C90/105 cross-section is observed in the right picture of Fig. 9.20. The crack pattern in the heated surface layer still reflects a distributed pattern, based mainly on the aggregates. However, in the centre of the cross-section the cracks are less tortuous and less distributed. Deformations are localised in several larger cracks with limited branching off into smaller cracks observed. These cracks also tend to pass around the aggregates, not through the particles. Due to the large temperature strain development the highest thermal loads are locally imposed by the river gravel particles, causing the peak stresses to be situated in the surrounding dehydrating mortar. Furthermore, relaxation of stresses throughout the cross-section is estimated. The level of damage sustained due to fire exposure is sufficient to again raise the question of cross-sectional integrity.

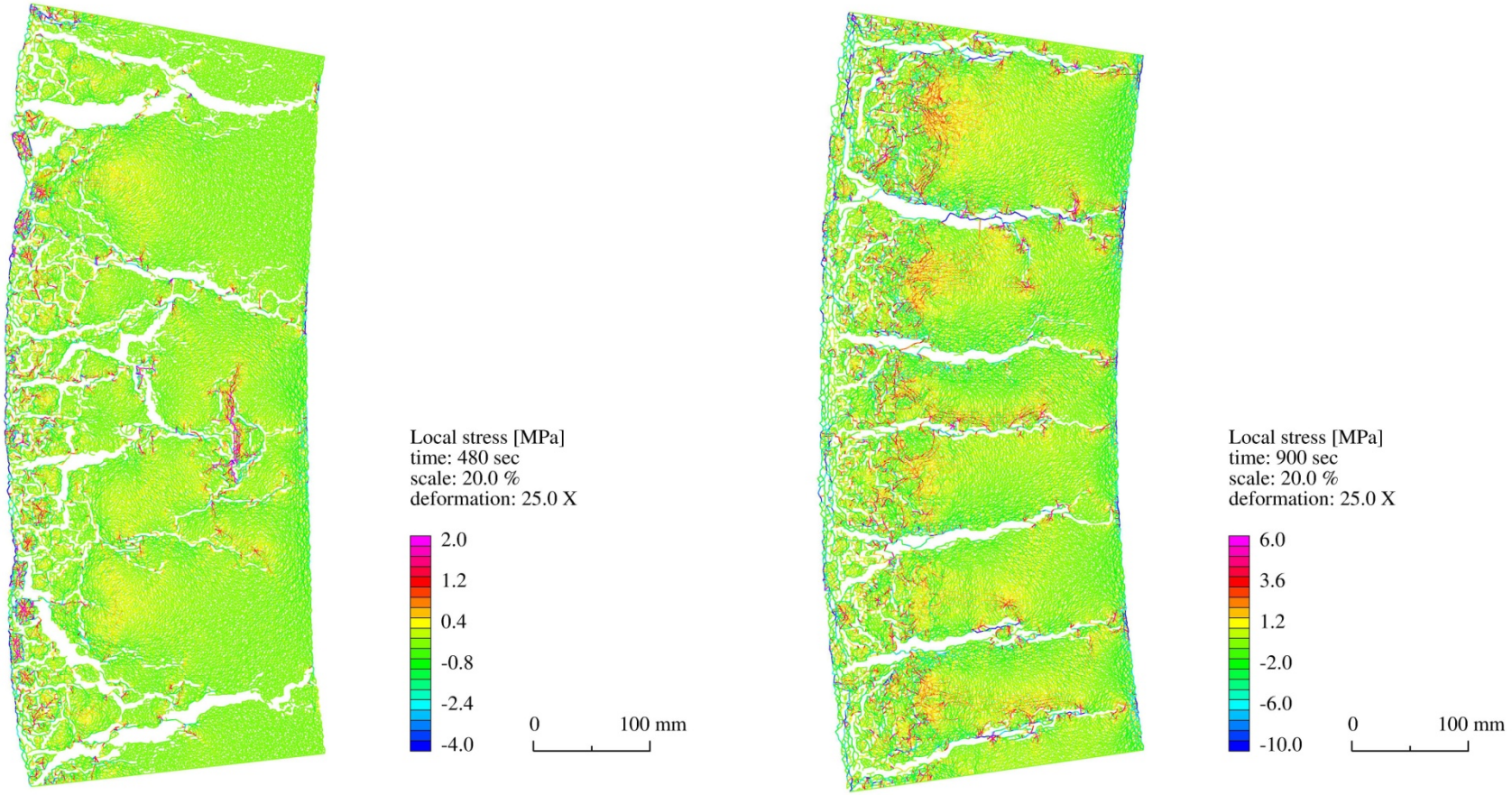

Fig. 9.20 *Exposure to a HC type of fire representing a substantial thermal loading for both C25/30 (left) and C90/105 (right), even in unrestrained conditions. Extensive cracking and possible failure of the cross-sectional integrity is found to develop.*

Finally, with respect to both crack patterns presented it is also mentioned that some pieces are observed to have almost completely separated from the cross-section. This is caused by the fracture process in which removal of 1D elements separates the material (Schlangen, 1993; Vervuurt, 1997). The cracks form discontinuities in the discretisation with nodes at both crack edges having no connection in the system matrix. In this FEM model closure of a crack is not assumed to cause contact or force transfer such as aggregate interlocking (Walraven, 1980).

9.7.3 Infuence of the level of structural restraint

The extensive crack development observed during a HC type of fire exposure coincides with increased thermal deformations. However, in buildings and tunnels these deformations are probably restrained, giving rise to additional stresses. For this purpose several investigations are conducted, reflecting variation of the imposed heating rate, the concrete strength class and the aggregate type. Structural restraint is represented by axial and rotational spring constants as previously defined. Imposing partial restraint on the C25/30 cross-section made with RG during exposure to both a standard and a HC type of fire is first examined according to Table 9.9. The results discussed hereafter will indicate a different fracture mechanism as previously observed, providing first evidence of a possible spalling mechanism.

After 1800 seconds of fire exposure the crack pattern shown in Fig. 9.21 has developed in the C25/30 cross-section. Compared to the previous results several aspects are observed. First, in the heated surface layer still compressive stresses act, causing the development of relatively small vertical cracks. These cracks are caused by the tensile stresses that develop perpendicular to the heated surface, governed by the cross-sectional restraint and Poisson's ratio. Furthermore, several horizontal cracks appear with a smaller opening than compared to unrestrained conditions. These reflect the reduced thermal deformations and are caused by the tensile stress levels that develop in the unheated part of the cross-section. Finally, a relatively large vertical crack has formed which already indicates a change in the fracture behaviour.

Fire scenarios (III)		
Calculation	**9.6A**	**9.6B**
Reference temperature	20 ^{o}C	20 ^{o}C
Duration	**1800 sec**	**600 sec**
Incremental time step size	0.5 sec	0.5 sec
Incremental load step size	5 sec	5 sec
Material (heterogeneous)		
Strength class	C25/30	C25/30
Aggregate type	RG	RG
Boundary conditions		
Fire scenario	**ISO 834**	**HC**
Convective heat transfer coeff.	**25 W/m^{2}K**	**50 W/m^{2}K**
Axial spring stiffness	6.7 kN/mm	6.7 kN/mm
Rotational spring stiffness	33 kNm/rad	33 kNm/rad

Table 9.9 *The influence of structural restraint, investigated by exposing the C25/30 cross-section made with RG to two different types of fire curves.*

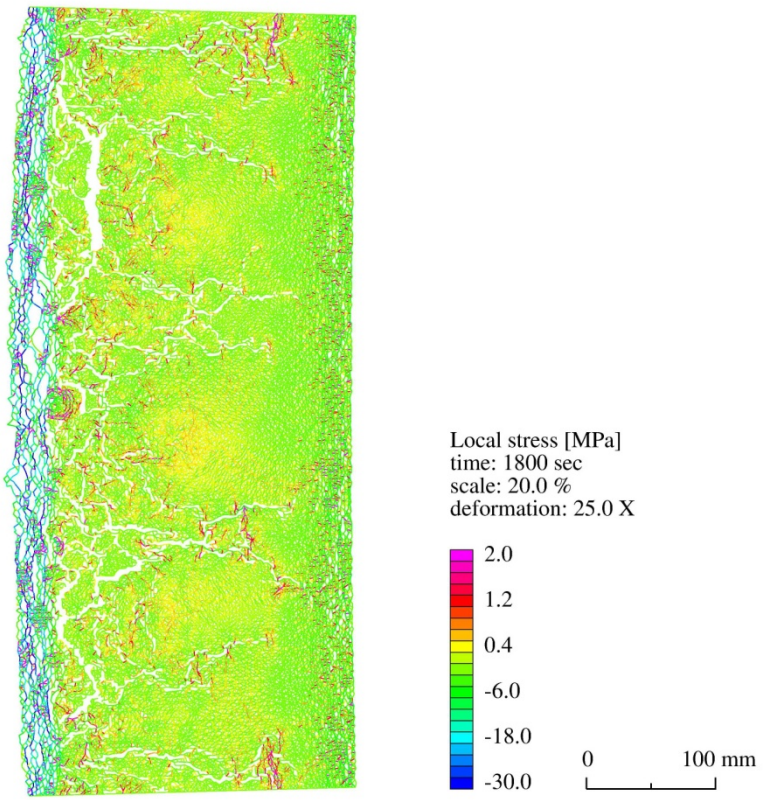

Fig. 9.21 *Overview of the crack pattern that has developed in the partially restrained C25/30 cross-section made with RG during exposure to an ISO-based fire.*

Increasing the imposed thermal energy to represent a HC type of fire influences considerable the rate at which cracks develop. Already after 180 seconds of fire exposure the crack pattern seen in Fig. 9.23 has developed. The coinciding averaged global stresses in the cross-section are shown in Fig. 9.22 and reflect a continued development. In the heated surface layer a compressive peak develops. In both the horizontal and vertical directions, especially in the centre of the cross-section, the tensile stresses are relaxed based on opening of the cracks.

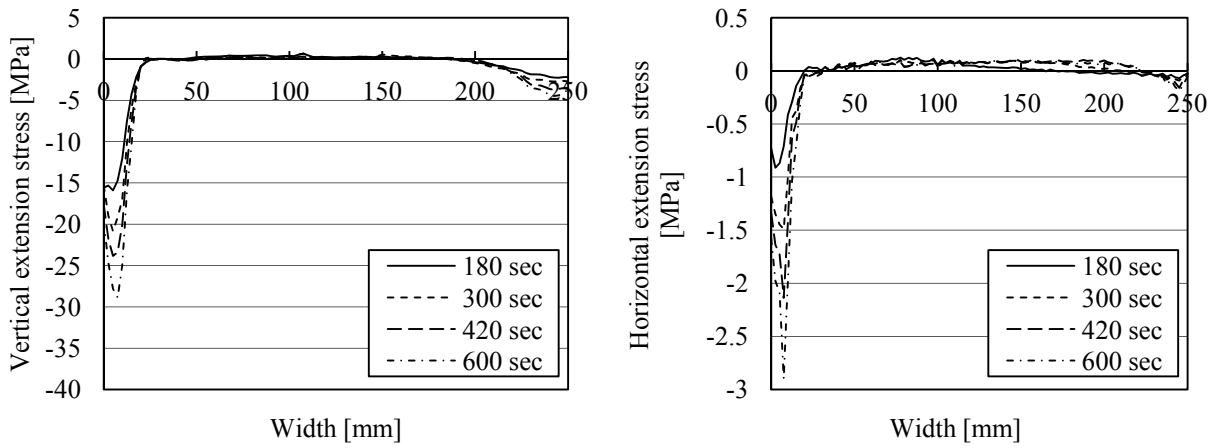

Fig. 9.22 *The vertical compressive stresses are found to remain present in the heated surface layer by adding restraint to the C25/30 cross-section (left). Opening of cracks relaxes the tensile stresses throughout the cross-section (left and right).*

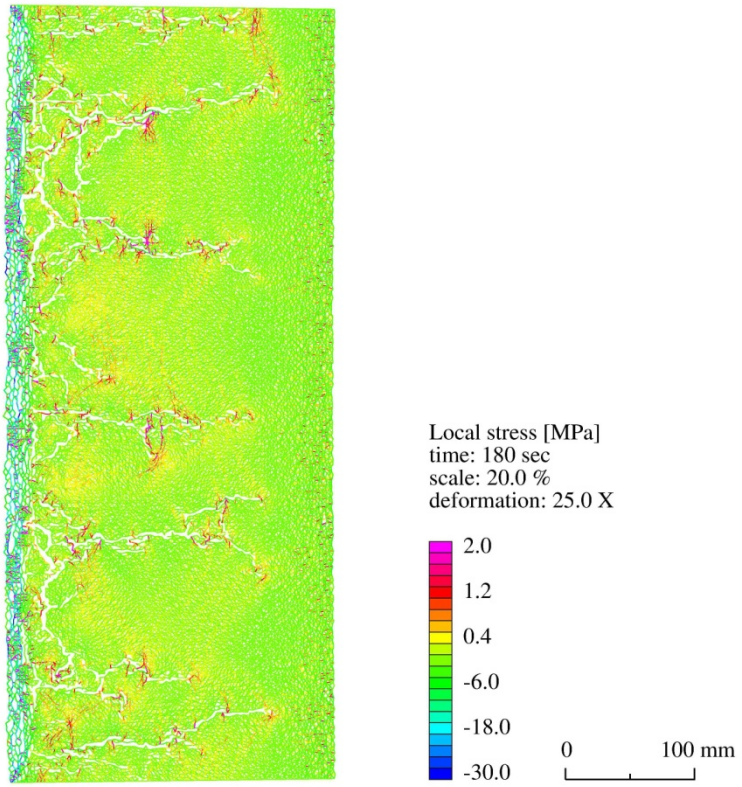

Fig. 9.23 *Severe fire exposure causing cracking in the restrained C25/30 cross-section already after 180 seconds. Cracking in the transition zone between both stress states forms the starting point in the formation of thermal instabilities.*

Continued fire exposure increases the level of cracking in the cross-section. However, as observed from Fig. 9.24 a different fracture mechanics behaviour develops. The addition of structural restraint, ensuring that the compressive stresses remain present, changes the crack pattern. Extensive cracking occurs, especially in the transition zone with the unheated centre of the cross-section (Lottman, et al., 2011). Inclined cracks are seen to develop, reflecting the steep gradient in the thermal stresses (Lottman, et al., 2011). It is also observed that various cracks are seen to intersect, contributing to the formation of a fracture surface along the rear of the heated surface layer. Progressive development of the temperature gradient will coincide with the increasing compression load and extend this crack pattern.

Between 300 and 600 seconds of fire exposure several parts of the heated surface layer are observed to detach from the cross-section. These layers have a length comparable to the width of the cross-section and exhibit curved deformations. The thickness of the compression loaded layer is around 30 mm with the temperature after 300 seconds varying from 310 ^{o}C at the surface to 65 ^{o}C at the opposite side. In the time interval shown the maximum compressive stress increase from 20 MPa to around 30 MPa. These compressive stresses are, especially at the start of these deformations, lower than the temperature-dependent compressive strength of C25/30 (RILEM TC-HTC, 2004). Furthermore, a distinctive curvature shaped fracture surface develops with several pieces of concrete being dislodged in the before mentioned transition zone. These also reflect the tendency to continuously displace towards the fire.

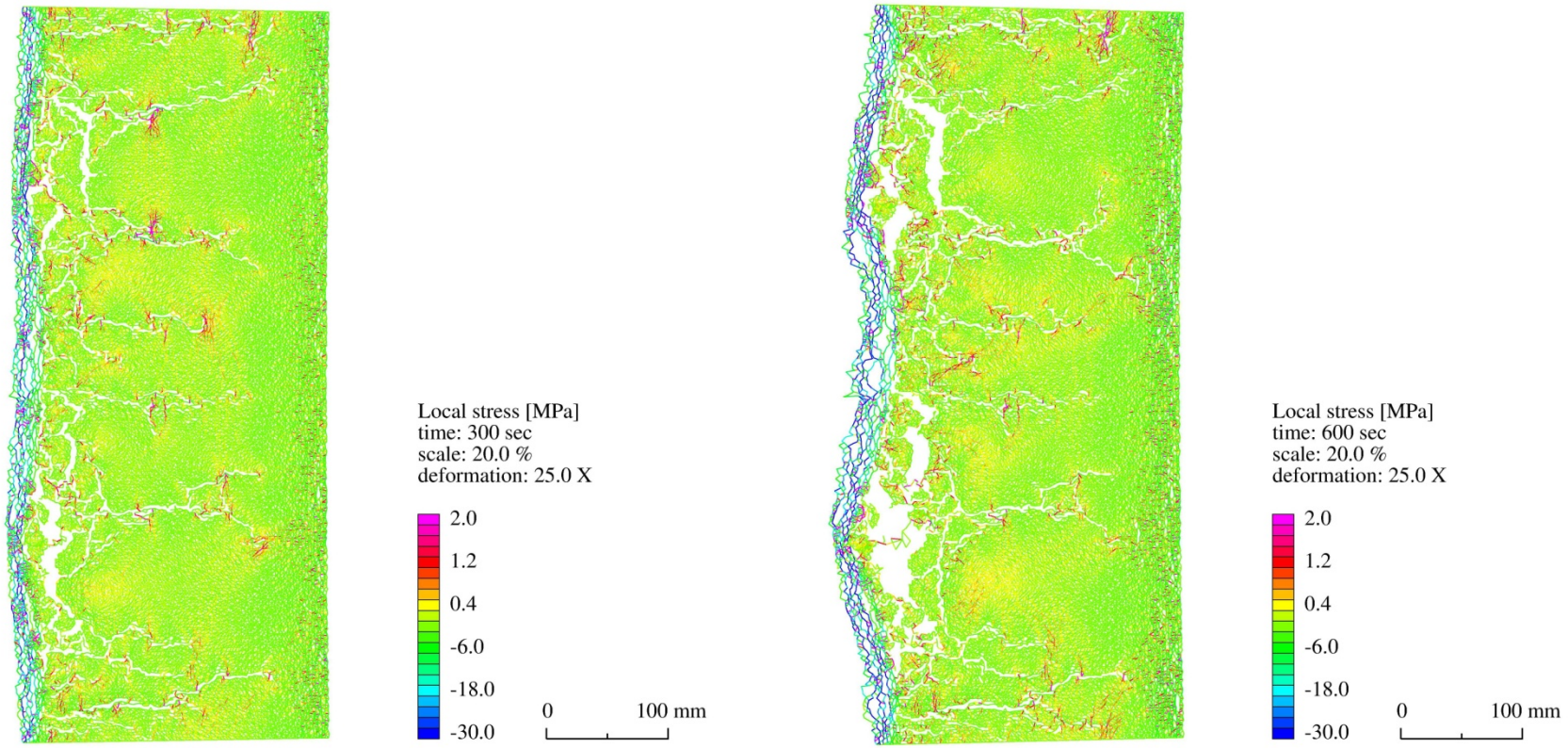

Fig. 9.24 *During fire exposure cracks propagate in the transition zone with the unheated part of the C25/30 cross-section, eventually forming unstable layers. The presence of a compression load and curved deformations suggests a form of thermal buckling.*

The formation and continued deformation of seemingly unstable surface layers represents a different failure mechanism for the cross-section. In fact, the presence of compressed, relatively slender surface layers could suggest that a form of thermal buckling develops. Moreover, it could also be argued that these results are one of the first numerical approximations of a spalling mechanism. In doing so, it has to be considered that despite the geometrical non-linear 1D bars, the mechanical basis remains static equilibrium of forces. The deformations only consider local extension with some level of bending. No accelerations of masses or inertia terms, as present in a dynamic FEM model, are included (Zienkiewicz, et al., 2005). In real life circumstances these deformations would therefore develop much faster with the release of the stored elastic strain energy observed as spalling events.

Increasing the concrete strength class to reflect a C90/105 cross-section influences the formation of the unstable surface layers. Compared to C25/30 not only the tensile strength of the mortar and especially the interfacial zones is higher, also the temperature strain development is lower as elaborated in the previous paragraph. Both simulations are indicated in Table 9.10 while considering two different aggregate types to account for a possible beneficial influence. The structural restraint is the same, governed by the spring constants, which due to the higher stiffness of the cross-section have a reduced influence.

In Fig. 9.25 are the thermal instabilities indicated to have developed after 600 seconds in the heated surface layer. Compared to the C25/30 simulation several differences are observed. First, the fracture surface is more uniform. This is attributed to the higher tensile strength and the resultant limited cracking in the transition zone between both stress states. This also governs the delay in time after start of the simulated fire test and reflects the larger capacity of the material. In this respect it also needs to be considered that the reduced temperature strain development of the mortar increases the imposed loading by the aggregates. Both aspects cause more slender layers to be formed, making them more prone to unstable deformations.

Fire scenarios (IV)		
Calculation	**9.7A**	**9.7B**
Reference temperature	20 ^{o}C	20 ^{o}C
Duration	**1200 sec**	**1800 sec**
Incremental time step size	0.5 sec	0.5 sec
Incremental load step size	5 sec	5 sec
Material (heterogeneous)		
Strength class	C90/105	C90/105
Aggregate type	**RG**	**LS**
Boundary conditions		
Fire scenario	HC	HC
Convective heat transfer coeff.	50 W/m^{2}K	50 W/m^{2}K
Axial spring stiffness	6.7 kN/mm	6.7 kN/mm
Rotational spring stiffness	33 kNm/rad	33 kNm/rad

Table 9.10 *Structural restraint examined by varying the aggregate type in the C90/105 cross-section exposed to a fire according the HC curve.*

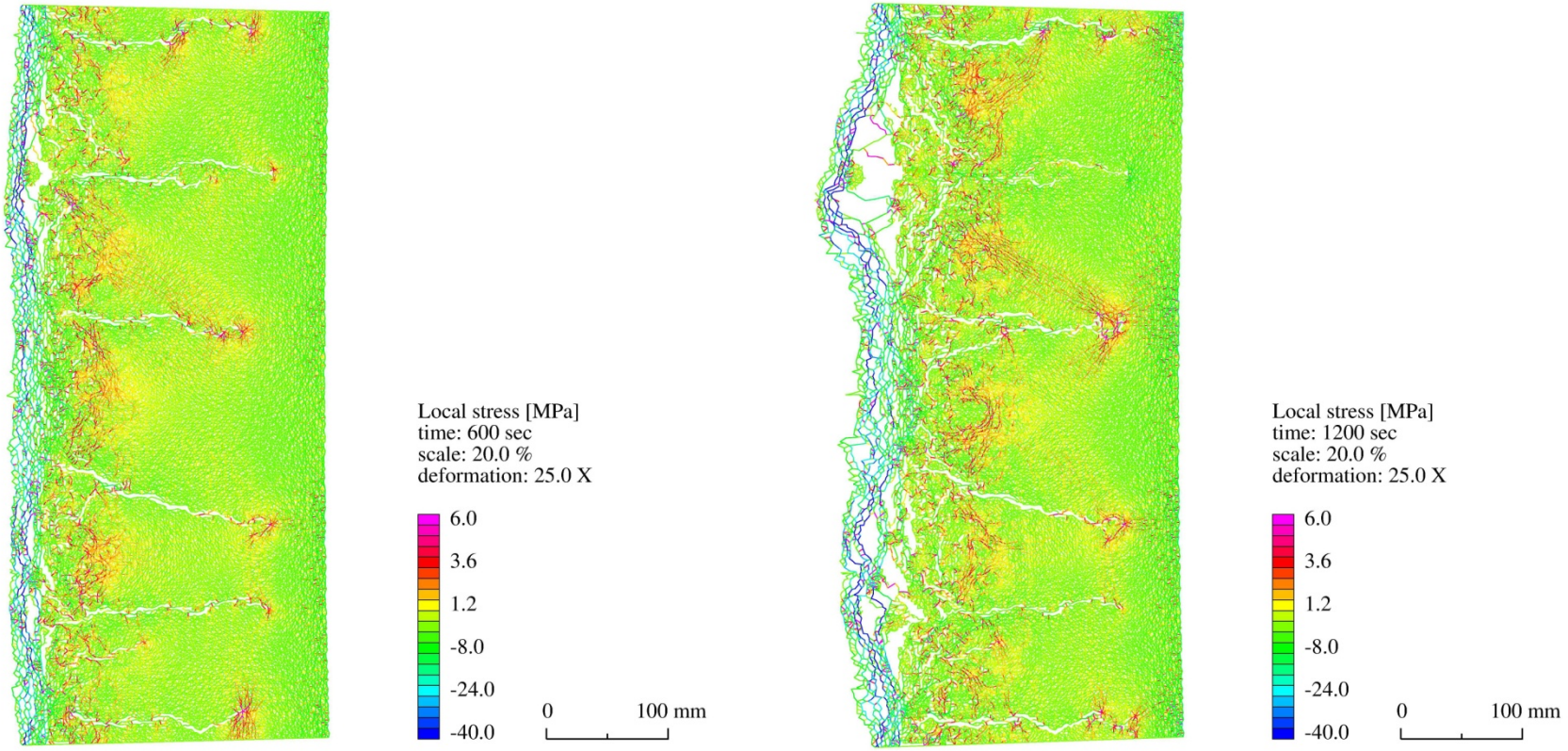

Fig. 9.25 *The formation of thermally unstable surface layers takes longer for the restrained C90/105 cross-section to develop. The level of damage mainly reflects the heated surface layer, making the instabilities more slender and the cross-section more susceptible.*

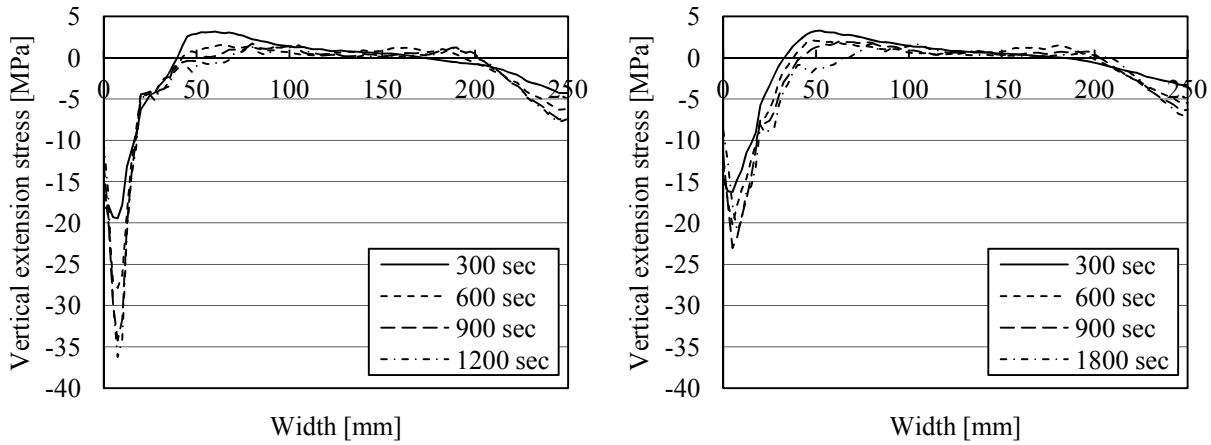

Fig. 9.26 *Reduction of the main vertical stress state in the partially restrained C90/105 cross-section by changing from RG (left) to LS (right).*

A second aspect is illustrated by the averaged vertical stresses as shown in the left graph of Fig. 9.26. Compared to the C25/30 cross-section only a small increase in the compressive stresses is observed. This further supports the premises that the observed instabilities could be related to a form of thermal buckling since the resultant compression force is lower than the temperature-dependent strength of C90/105 (Phan, 1996). Furthermore, this reduced compression also governs the lower rate at which these instabilities develop in this static FEM model. In real life circumstances would these slender layers deform more abruptly.

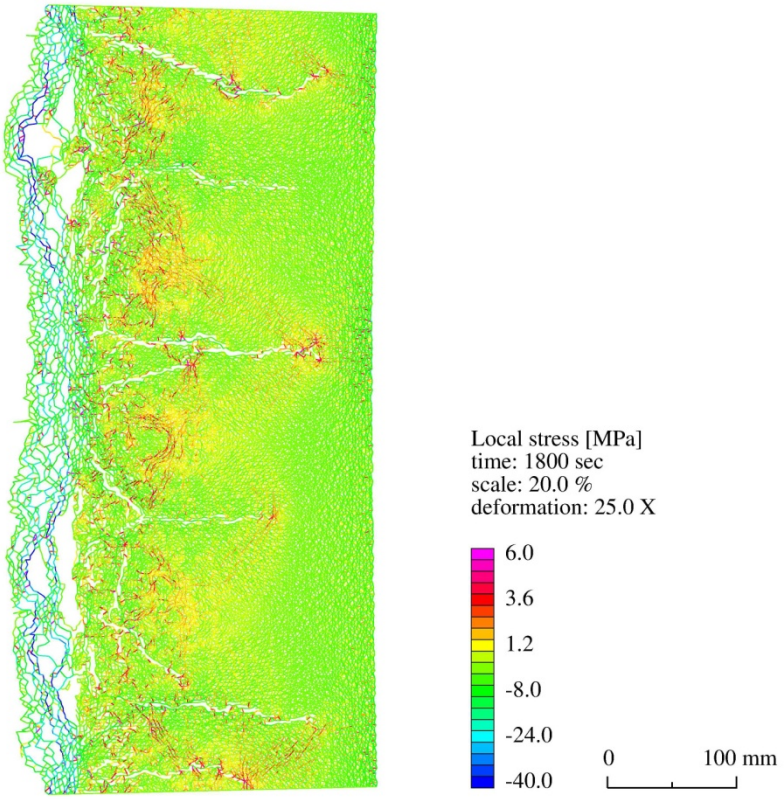

Fig. 9.27 *The reduced thermal elongation of the LS particles in the C90/105 cross-section is not sufficient to overcome the tendency of the thin surface layers to deform.*

Investigation of the possible beneficial influence of using an aggregate type with a lower thermal expansion is the focus of the second C90/105 simulation. Compared to the previous C90/105 cross-section the stress level in the heated surface layer is further reduced as indicated in the right graph of Fig. 9.26. However, the instabilities still develop, but reflect a reduced deformational characterisation. After 1800 seconds of exposure to the HC fire curve the crack pattern shown in Fig. 9.27 has developed.

Especially these last two results indicate that the problem appears to be the presence of the compression force rather than the attained maximum values. Combined with the slenderness of the formed layers the stiffness of the dehydrated concrete is insufficient to withstand the continued thermal exposure. In this respect is failure of the cross-section characterised by a more local phenomenon, However, it is to be noted that the potential arises for more damage to the cross-section. After part of the heated surface layer has spalled, the remaining cross-section is exposed to the full thermal impact of the fire. This is not considered in this FEM model, but could cause additional instabilities to develop.

9.8 Cracking in fire exposed concrete based on temperature and pore pressure

The indicated formation of thermal instabilities in the heated surface layer are based on considering only temperature strains as internal loading. However, the question remains about the possible contribution of the pore pressure in this failure mechanism. For this purpose the FEM temperature and pore pressure model is extended to include both the solid and porous material descriptions. Coupling with the FEM fracture mechanics model consists of imposing both temperature strains as well as pressure-induced stresses. The reverse coupling represents the crack pattern, gradually implemented in the element mass flux definitions as elaborated in chapter 7. The maximum crack width included is 0.25 mm in order to maintain numerical stability. Furthermore, the results presented in this paragraph first focus on the general observed behaviour caused by exposure to a fire according to the ISO curve. Subsequently the simulations from the previous paragraph are recalculated using the pore pressure as additional loading. The aim is to estimate if the pore pressure can develop in the cracked heated surface layer and still contribute to the formation of the instabilities.

With respect to the simulations presented in this paragraph it has to be considered that combination of both FEM models, including all the possible couplings, requires the largest calculation times. On average the simulations required between 2 and 7 days, using a more than average personal computer. Most of the time was spend on the fracture process, dependent on the chosen strength class and type of fire exposure. However, the time step size and the rate of convergence also reduced by including the pore pressure in these simulations.

9.8.1 Forced drying of the cross-section during fire exposure

Before addressing the stability of the heated surface layer first the cross-section is exposed to a more moderate type of fire. This allows to focus on the forced drying of the material and the resultant pore pressure development. The simulations shown in Table 9.11 first reflects the same calculation as formed the starting point in the previous paragraph. The C90/105 simulation is aimed at reducing the level of cracking, promoting the gas pressure to develop.

Fire scenarios (V)		
Calculation	**9.8A**	**9.8B**
Reference temperature	20 °C	20 °C
Reference RH	80 %	80 %
Duration	**1200 sec**	**1800 sec**
Incremental initial time step size	0.2 sec	0.2 sec
Incremental load step size	5 sec	5 sec
Material (heterogeneous)		
Strength class	**C25/30**	**C90/105**
Aggregate type	**RG**	**LS**
Initial saturation level	**58 %**	**85 %**
Boundary conditions		
Fire scenario	ISO 834	ISO 834
Convective heat transfer coeff.	25 W/m^{2}K	25 W/m^{2}K
Exterior vapour pressure (dry)	1000 Pa	1000 Pa
Convective mass transfer coeff.	0.03 m/s	0.03 m/s
Axial spring stiffness	6.7 kN/mm	6.7 kN/mm
Rotational spring stiffness	33 kNm/rad	33 kNm/rad

Table 9.11 *Forced drying of the cross-section, first investigated by exposure of both C25/30 and C90/105 to a fire corresponding to the ISO 834 curve.*

The addition of structural restraint ensures that during fire exposure of the C25/30 cross-section the compressive stresses remain active in the heated surface layer. This causes a pattern of relatively small vertical cracks to develop parallel to the heated surface. In the unheated centre of the cross-section again several horizontal cracks are seen to develop in the left picture of Fig. 9.28.

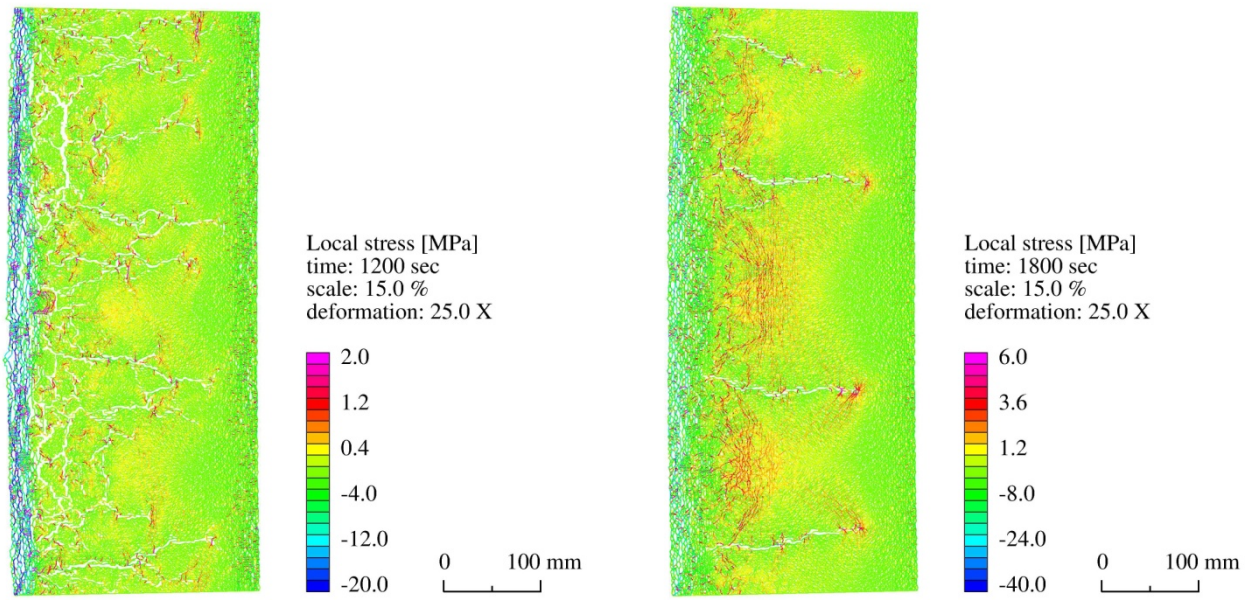

Fig. 9.28 *Overview of the crack patterns for C25/30 made with RG (left) and C90/105 made with LS (right) during prolonged exposure to a standard fire.*

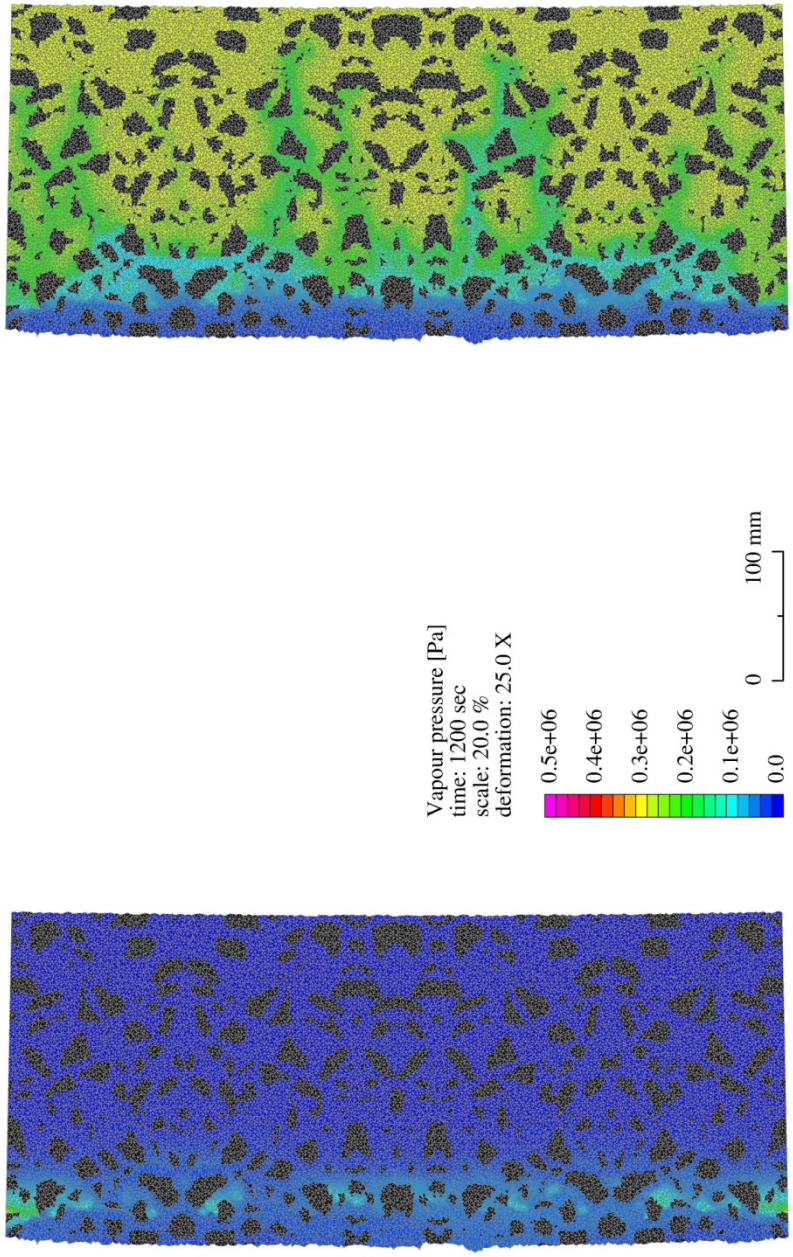

Fig. 9.29 *Gas pressures, found to largely be reduced due to the development of the cracks in the C25/30 cross-section. Especially in the heated surface layer and along the cracks extending into the cross-section the drying process is observed to develop.*

With respect to this distribution it is recalled that the crack width is determined for each fractured 1D element based on the incremental local horizontal nodal displacements, considering also the geometric non-linearity. The overall characterisation of the crack pattern indicates relatively small openings with no substantial localisation to indicate the formation of thermally unstable layers. This crack pattern is used to characterise the permeability which defines the mass flux definitions as elaborated in chapter 7. Each element stiffness is governed by the largest crack width present, defining the orientation and opening.

Including the crack pattern in especially the heated surface layer has a considerable influence on the forced drying process. This dense pattern of small cracks is sufficient to mitigate the gas pressures. After 1200 seconds of fire exposure the gas pressures are indicated to not exceed 0.2 MPa as is shown in Fig. 9.29. In comparison, the maximum gas pressure reached in non-cracked circumstances was found in chapter 7 to be around 1.0 MPa. Furthermore, some small pressure variations are indicated, reflecting the influence of a nearby aggregate particle or the distance to a crack edge. It has to be considered that the estimated gas pressures are only governed by the vapour phase in order to improve the numerical stability. This omits the dry air phase in ensuring that the atmospheric pressure is at least maintained.

Drying of the cross-section by reduction of the saturation level is also seen in Fig. 9.29. Across the heated surface layer most of the liquid water is evaporated (Lottman, et al., 2015) which based on the assumed thermodynamic equilibrium defines the low vapour pressures. As already mentioned in chapter 7, again drying of the concrete along the crack paths extending into the cross-section is observed (Lottman, et al., 2015). Some differences between the crack pattern and the progress of the drying process are observed, but these are caused by the gradual implementation of permeability.

The C90/105 simulation reflects a more moderate fracture behaviour caused by the chosen LS aggregate type. The pattern shown in the right graph of Fig. 9.28 reflects only limited cracking in the heated surface layer. In the unheated centre of the cross-section several horizontal crack develop, but compared to the C25/30 simulation the overall damage is substantially lower. The corresponding influence on the forced drying process is shown in Fig. 9.30 and reflects a more continuous gas pressure development across the height of the cross-section. The gas pressure still reduces to an average of 0.25 MPa for which in non-cracked circumstances 2.5 MPa was found in chapter 7. Several localised peak pressures remain which represent a small additional internal loading for the C90/105. However, compared to the tensile strength, even at increased temperatures, these only constitute a minor stress contribution and could be considered as of limited relevance.

The progress of the drying front into the cross-section reflects the combination of both limited cracking and the presence of aggregate particles. The distribution of the saturation level shown in Fig. 9.30 reflects still a predominately uniform front. Several of the small cracks in the centre of the cross-section are not sufficiently connected to the heated surface layer. This limits the possibility for drainage of the water phases towards the exterior environment and only partial drying along these cracks is found to develop.

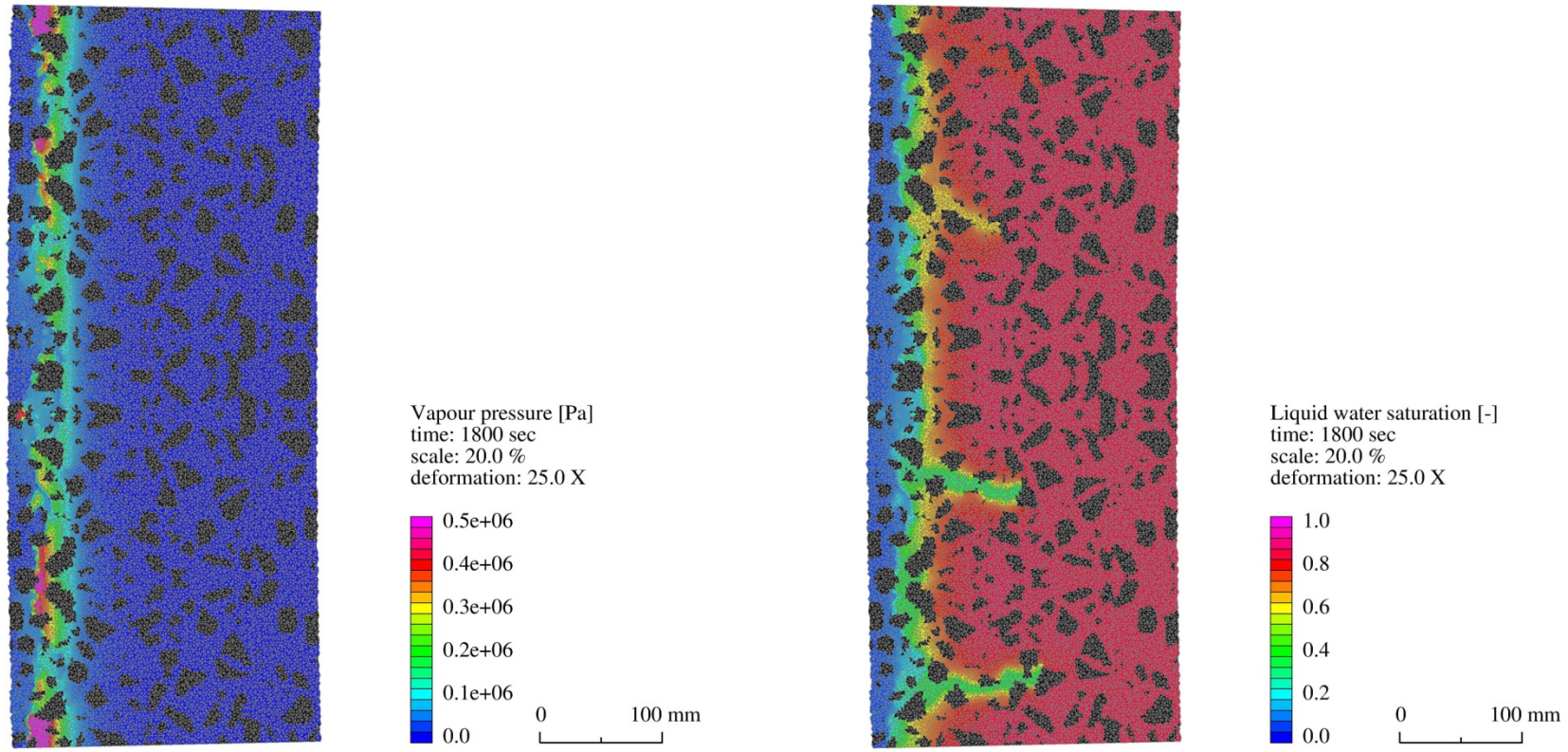

Fig. 9.30 *Drying of the C90/105 cross-section, reflecting only some localised vapour pressure peaks. The level of cracking in the heated surface layer is sufficient to reduce the overall pressure with only limited drying along cracks in the centre of the cross-section.*

This is also reflected in the progress of the thermal energy. The temperature gradient develops almost uniform across the height of the cross-section with limited influence by the limestone particles. Some small temperature changes develop due to drying along the cracks, attributed to the more moderate fire exposure in combination with the relatively small cracks. This simulation also indicates that the distribution or spacing of the cracks seems more important than the actual opening as was also found in chapter 7.

Both these results seem to indicate that the only possibility for the gas pressure to still increase is to reach material with less cracks. This implies passing through the heated surface layer and penetrating into the unheated centre of the cross-section. However, this seems unlikely to occur since the progress of the drying front and the coinciding gas pressure is closely related to the temperature. Gas pressures remain part of the heated surface layer in which the temperature gradient will most likely cause a form of thermal cracking to develop.

9.8.2 Reduced pore pressures with limited influence on the thermal instabilities

The previous results indicate that gas pressures are mainly reduced in fire exposed concrete. However, the possibility exists that a higher thermal exposure combined with a C90/105 still could give rise to gas pressure development. This is the aim of the simulations shown in Table 9.12, reflecting also a C25/30 as a reference. With respect to both concrete strength classes the formation of instabilities in the heated surface layer was already observed. Furthermore, the possibility for fire exposure of the newly formed boundaries, between the destabilised layers and the remaining cross-section, is not included. This is observed in the forced drying distributions presented which reflect a continuous material.

Fire scenarios (VI)		
Calculation	**9.9A**	**9.9B**
Reference temperature	20 ^{o}C	20 ^{o}C
Reference RH	80 %	80 %
Duration	720 sec	1020 sec
Incremental initial time step size	0.2 sec	0.2 sec
Incremental load step size	5 sec	5 sec
Material (heterogeneous)		
Strength class	**C25/30**	**C90/105**
Aggregate type	RG	RG
Initial saturation level	**58 %**	**85 %**
Boundary conditions		
Fire scenario	HC	HC
Convective heat transfer coeff.	50 W/m^{2}K	50 W/m^{2}K
Exterior vapour pressure (dry)	1000 Pa	1000 Pa
Convective mass transfer coeff.	0.03 m/s	0.03 m/s
Axial spring stiffness	6.7 kN/mm	6.7 kN/mm
Rotational spring stiffness	33 kNm/rad	33 kNm/rad

Table 9.12 *Investigation of the possibility to develop gas pressures during severe fire exposure in relation to the formation of thermal instabilities.*

The extensive crack pattern that has formed in the C25/30 cross-section is sufficient to slow down the gas pressure development (Lottman, et al., 2015). From Fig. 9.31 it is observed that a limited pressure peak develops which progresses faster into the cross-section than under ISO conditions. This reflects the higher thermal energy input by exposure to a more severe fire scenario. Moreover, these pressures are of a minor contribution especially considering the definition of local pressure-induced stresses relative to atmospheric conditions.

The progress of the drying front is reflected in the distribution of the saturation level as can be seen in Fig. 9.32. Exposure to a fire according to the HC curve increases the rate at which the cross-section dries. Comparing the temperature and saturation distributions indicates that the drying front coincides with the progress of the heated surface layer. This reflects the strong influence of the crack pattern and also the resultant low vapour pressures. The mainly vertically orientated compression cracks, parallel to the heated surface, are still sufficient. Along the crack paths, extending into the cross-section, drying of the surrounding material is again found to develop. The continued mass fluxes of both vapour and liquid water towards the exterior environment affect the development of the temperature in the heated surface layer. Liquid water is evaporated to ensure that thermodynamic equilibrium is maintained. This consumes thermal energy and mitigates the temperature development. Considering the limited pressures this cooling effect is believed to govern the observed delay in time during which the instabilities developed. Furthermore, along the crack paths also some temperature development is indicated, reflecting the condensation of water vapour.

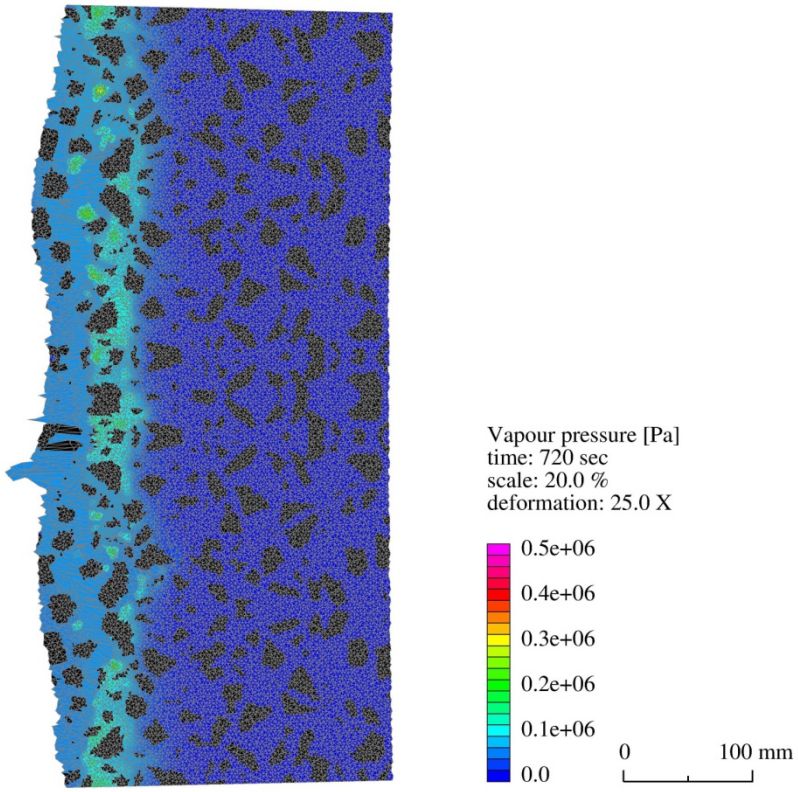

Fig. 9.31 *Exposure of C25/30 made with RG to a severe fire causing drying at a higher rate, reflected by the depth at which the limited pore pressure peaks are situated.*

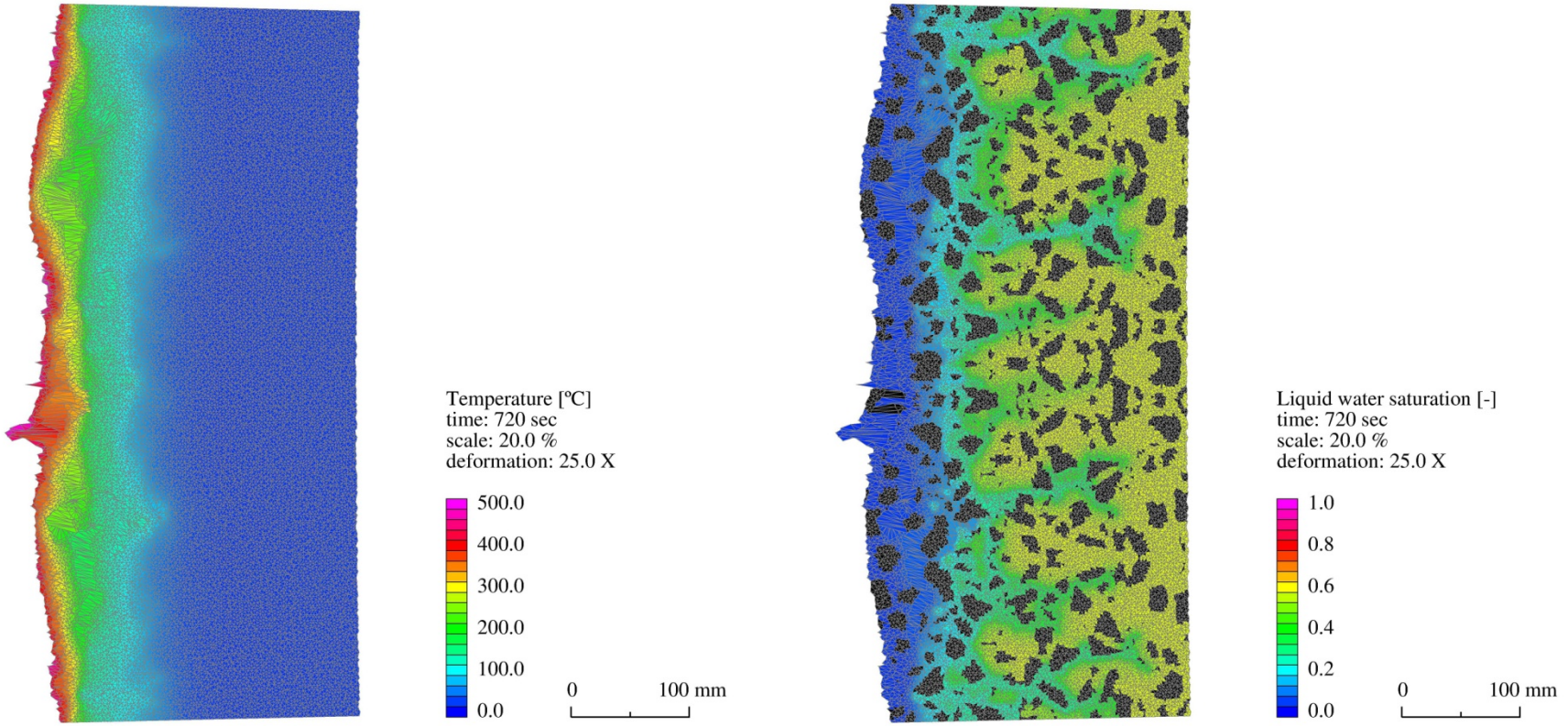

Fig. 9.32 *The drying front in C25/30 in progress through the heated surface layer, extending along the cracks deeper into the cross-section. The continued drainage of vapour and liquid water mitigates the development of the temperature gradient.*

By increasing the concrete strength class to represent a C90/105 the density of the microstructure increases. This increases the strength and stiffness which both govern the formation of the instabilities. However, the reduced permeability is only partially reflected by the gas pressure development as observed in Fig. 9.33. Compared to C25/30 the mitigation of the gas pressure is less uniform with at some locations still a limited increase estimated to develop. The highest gas pressures attained are around 0.4 MPa which is considerably lower than the estimated 4.0 MPa in uncracked circumstances. The distribution of the saturation level also indicates that the heated surface layer dries faster because of the cracks. The overall permeability is sufficient to ensure that drying occurs at lower temperatures and corresponding lower pressures. However, compared to C25/30 drying still develops slower, reflecting the influence of permeability as well as crack spacing and opening.

Deeper into the cross-section the relatively low permeability of C90/105 governs the ability to extend the drying process from the crack edges. Due to the larger crack spacing and the higher initial saturation level marked differences are observed in Fig. 9.34 between dried and still partially saturated material. Vapour and liquid water are levelled off gradually into the crack, before it can be driven towards to heated surface. Furthermore, the distribution of the capillary pressure is also provided to reflect the interaction between the cracks and the exterior environment. From these results it also seems possible that for cracks with sufficient length the drying process could reach the opposite, not fire exposed, surface. Since at this edge also Neumann boundary conditions are imposed, vapour and liquid water could escape.

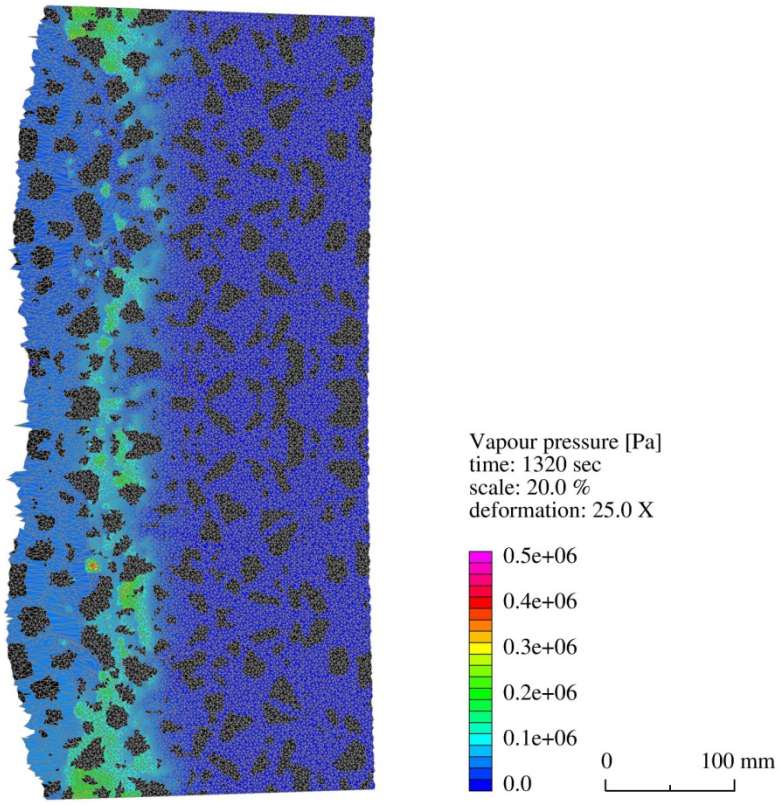

Fig. 9.33 *Reduction of gas pressures in the C90/105 cross-section made with RG caused by the fire-induced crack pattern after 1320 seconds of exposure.*

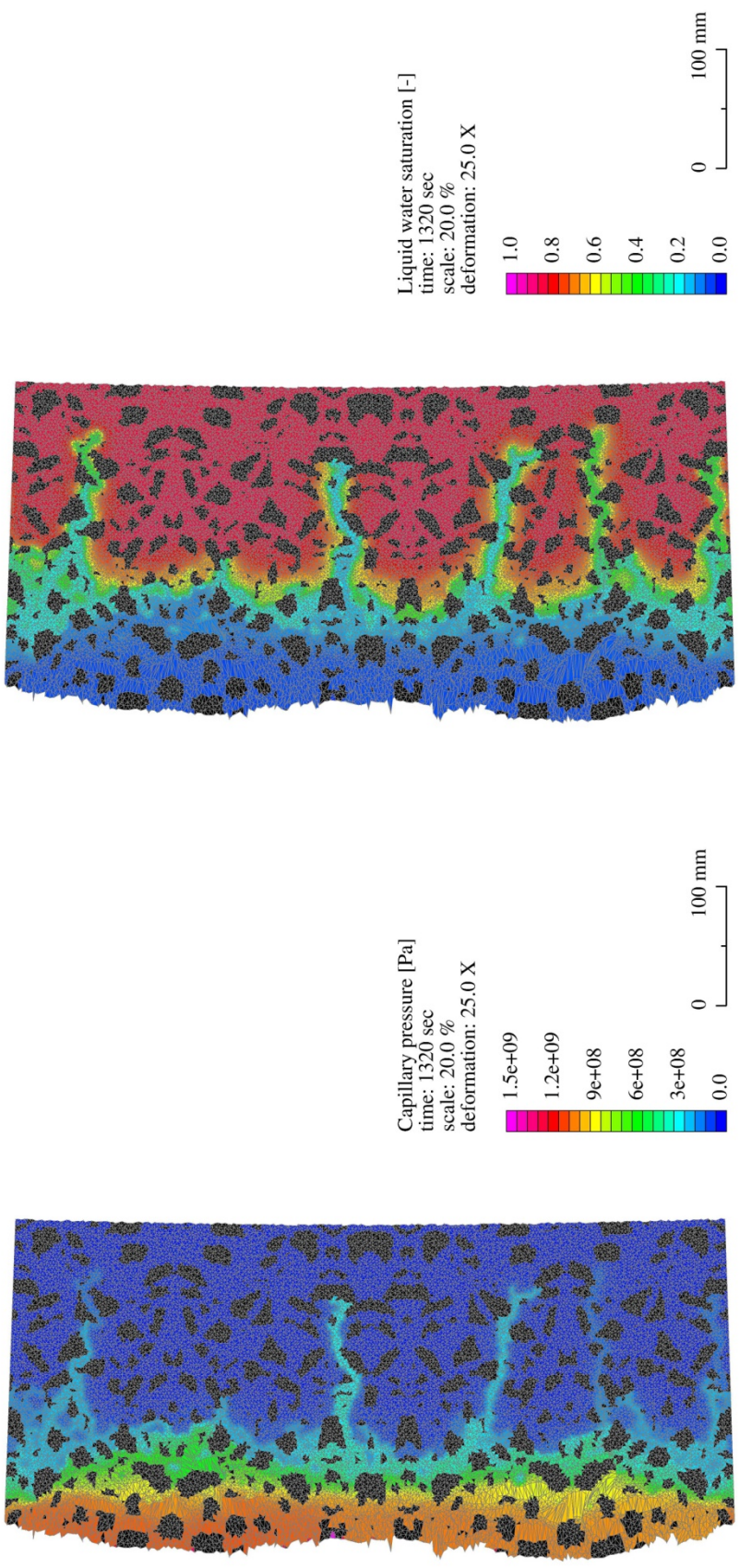

Fig. 9.34 *A steep capillary pressure gradient extending from the exterior environment through the dried surface layer along the cracks into the cross-section. The reduced permeability of C90/105 governs the ability to level off the water phases into the cracks.*

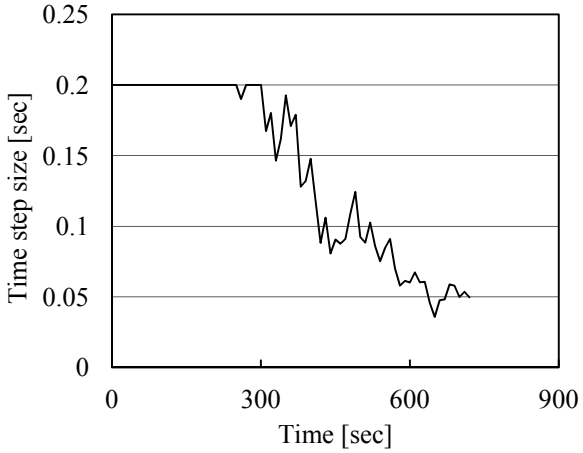

Fig. 9.35 *Development of the incremental time step size during the C25/30 simulation, reflecting the influence of the crack pattern.*

9.8.3 Numerical stability during the simulations

Both simulations proved the most challenging with respect to the numerical stability, representing the level of discontinuity included in the FEM definition. For the FEM temperature and transport model stability is governed by the larger crack openings, especially in case of the C90/105 simulation. The convergence of the solution was also found to be related to opening of the current crack pattern and the number of cracked 1D elements introduced at the same time increment. As a result the incremental time step reduced as seen in Fig. 9.35 for the C25/30 simulation. The FEM fracture mechanics model seemed to be influenced by the formation of the crack pattern. The C25/30 simulation, being more susceptible for cracking, experienced under these circumstances the largest calculation times. However, for both concrete strength classes it was found that especially the deformation of the instabilities reduced the rate of convergence.

For both it is noted that convergence of the solution is closely related to the variations that develop in each time and crack increment across the variables in the domain. Increasing the level of discontinuity diminishes the uniformity in the system matrix and hence influences the rate of convergence. In this respect a heterogeneous cross-section is more time consuming to solve than a homogeneous cross-section. The same reasoning holds true for the cracks, reflecting sudden and localised changes in the material discretisation and variables development. Using a Jacobi preconditioned system matrix increased the rate of convergence for both FEM models (van Kan, et al., 2008). However, alternative conditioning techniques could be used (van Kan, et al., 2008) with also the possibility of parallel computation as an option to consider (Zienkiewicz, et al., 2005). In the latter the problem across the domain is divided into smaller sub-domains which can be solved separately and subsequently combined.

9.8.4 Global behaviour imposed through the anisotropic FEM definitions

A final aspect to elaborate is the influence of the crack pattern on both FEM models. However, as observed from Fig. 9.36 and Fig. 9.37 a strong directional dependence or anisotropy is included (Lottman, et al., 2015). First, it is recalled that the permeability is included in the FEM transport and pore pressure model through a second order tensor (Bear,

1972/1988; Zienkiewicz, et al., 2005). This is reflected by the global permeability's being expressed in the global coordinates axes. These distributions are also affected by the large differences in permeability between cracks of various openings and especially the surrounding material. The remaining 1D bars in the FEM fracture mechanics model approximate the global stiffnesses through a fourth order tensor (Felippa, 2004a; Zienkiewicz, et al., 2005). Stresses are defined in accordance with the coordinate axes whereas the stiffness components are expressed in matrix indications.

Extending on these principals it becomes clear that the influence of the local permeability and Young's modulus on the respective FEM models is in fact the opposite (Lottman, et al., 2015). This is illustrated by considering the following:

- The compression loading of the heated surface layer causes cracks to mainly develop in vertical direction. This is represented by the corresponding global permeability. These cracks are initiated by removal of 1D bars in predominately the horizontal direction, reflected by the stiffness reduction.

- In the unheated centre of the cross-section tensile stresses caused various cracks to develop. The largest permeability increase is defined along these crack paths in horizontal direction. However, the largest stiffness reduction is observed in vertical direction, caused by the bars being mainly fractured in this direction.

Some differences with the behaviour described before are observed. These are governed by the orientation of the fractured bars, affecting both the global permeability and the global stiffness. With respect to the global permeability it should also be considered that a small mass flux contribution in the direction perpendicular to the crack is included as stated in chapter 7.

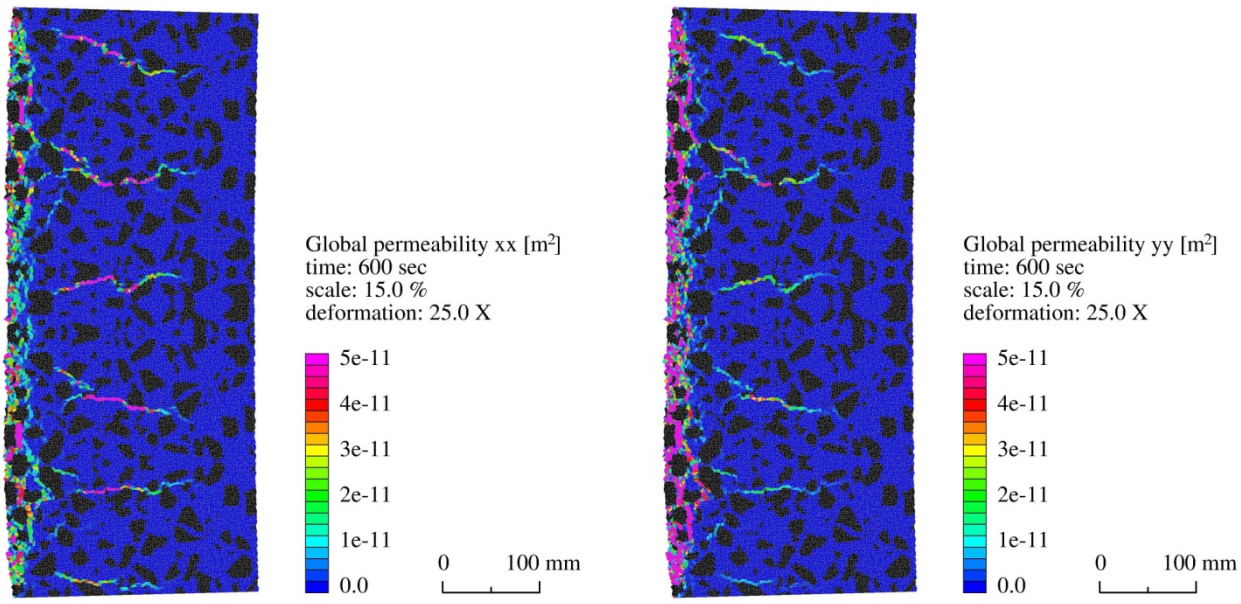

Fig. 9.36 *Distribution of the global permeability in the horizontal (left) and vertical (right) directions, as defined by the orientation of the crack pattern in the C90/105 simulation.*

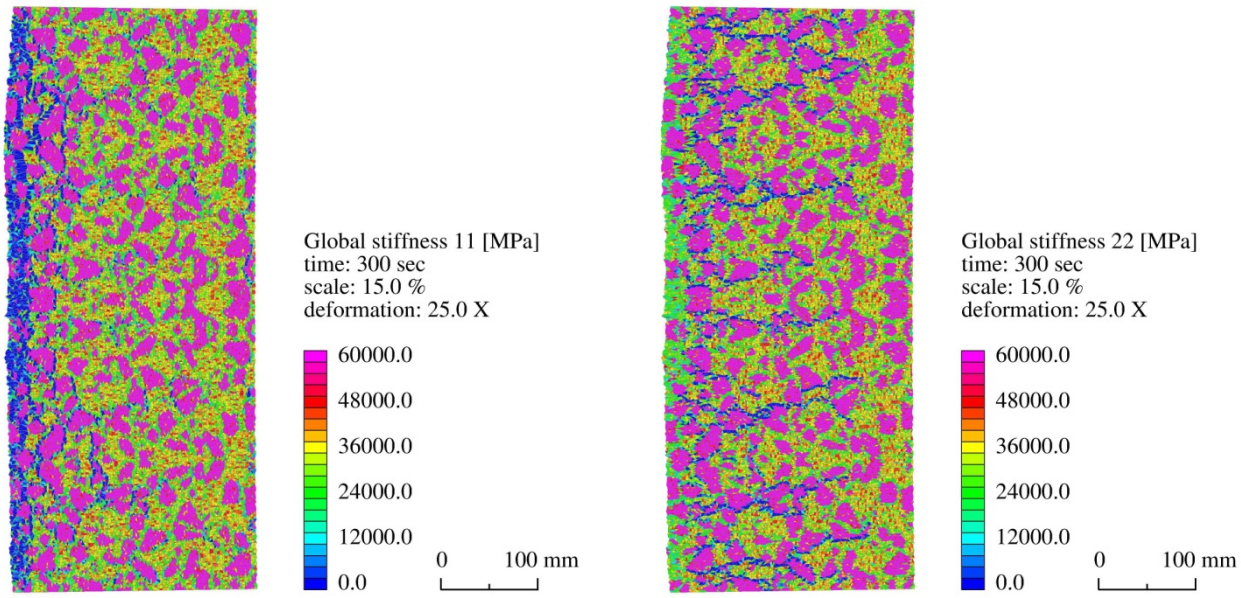

Fig. 9.37 *Distribution of the approximated global stiffnesses, using matrix notation, defined by the remaining fractured 1D bars in the C25/30 simulation.*

The influence of the anisotropic permeability is directly reflected in the temperature and gas pressure distributions as previously shown. However, the anisotropic basis of the FEM fracture mechanic model is commonly characterised by the local stresses and the coinciding crack pattern. The resultant approximation of the global stresses, using the transformation relationship in Eq. (9.57), reflects only contributions by the remaining 1D bars. Examples of the approximated global extensional and shear stresses are shown in Fig. 9.38 for the C90/105 cross-section previously discussed. This simulation is chosen based on the larger, mainly horizontally orientated, cracks distributed in the unheated centre of the cross-section. This localised behaviour is more suited to illustrate the crack influence than the distributed pattern that developed in the C25/30 cross-section. Moreover, the dense pattern of small cracks present in the heated surface layer also makes distinguishing of the global stresses more difficult.

Formation of cracks in the unheated centre of the cross-section causes relaxation of the vertical stresses based on opening. Only at the crack tips some tensile stresses are found whereas the compressive stresses remain present in the heated surface layer and especially in the instabilities that form. Based on the removal of stiffness also shear stresses are observed to develop, especially along inclined cracks. These reflect the rotation of the principal stresses due to crack formation in comparison to the surrounding uncracked material. In this transition zone also horizontal stresses arise. These are caused by parts of the cross-section being partially separated and exhibiting additional displacements and rotations compared to the surrounding material. The shear stresses estimated in the heated surface layer are attributed to the imposed temperature elongations. In case of mixed concrete components or large differences in the averaged temperatures across the 1D bars the thermal strain becomes anisotropic, reflecting also a shear contribution besides both extensional directions.

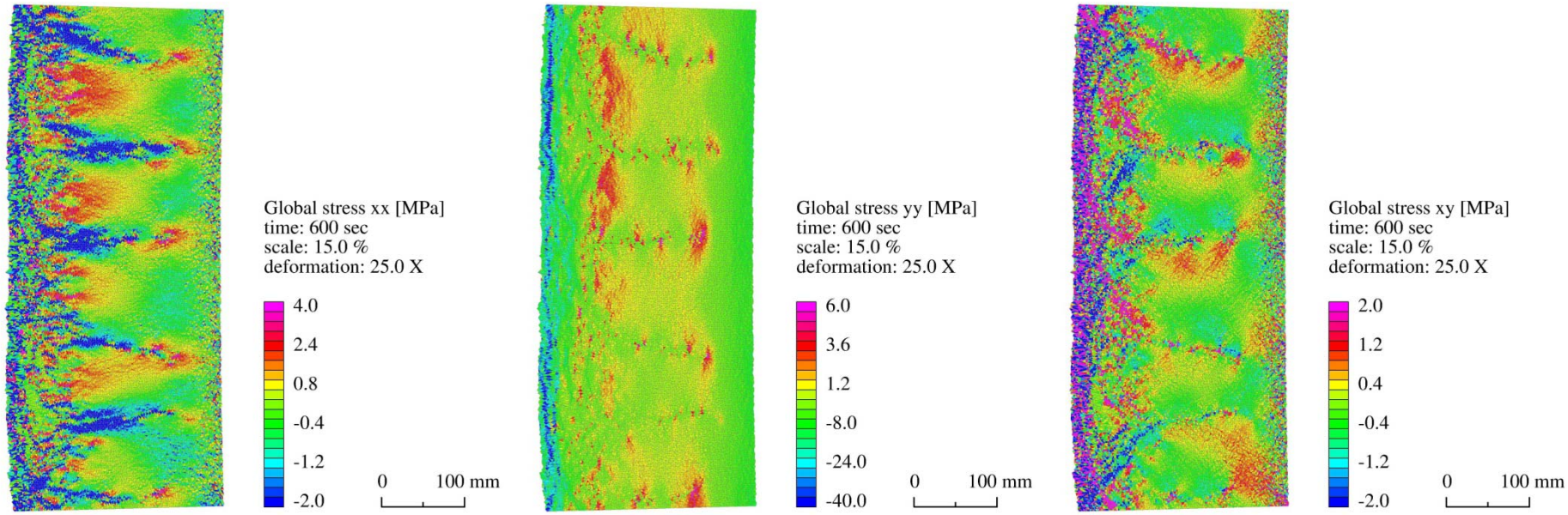

Fig. 9.38 *Approximated global horizontal (left), vertical (middle) and shear stresses (right) in the C90/105 cross-section, reflecting the rotation of stresses based on the removal of 1D bars affecting the anisotropic stiffness definition.*

9.9 Cracking in structural loaded concrete exposed to a fire based on temperature

The final aspect to be considered with respect to the formation of the thermal instabilities is the influence of external loading. During service life conditions the concrete cross-section is most likely not only structurally restrained, but commonly also external forces are imposed. This latter aspect is in this paragraph considered in the simulations presented as stated in Table 9.13. A uniform compression force is imposed at both the top and bottom supports, causing an initial crack pattern to be present in the cross-section. Based on the previous simulations is only the temperature considered as internal loading. Furthermore, fire exposure according to a HC curve is imposed after the initial crack pattern has formed. This affectively causes a new initial equilibrium state to be present in the cross-section.

The initial crack pattern depends on the imposed external compression forces. This is illustrated in Fig. 9.40 by the distributed pattern of relatively small vertical cracks that have been formed in the C25/30 cross-section by imposing the compressive forces of 6 kN. The cracks originate in the weaker interfacial zones surrounding the aggregates and extend in height direction. The deformed cross-section reflects a typical compressed shape with the largest crack openings situated along the left and right outer edges. This coincides with relaxation of the compressive stresses as indicated by the parabolic distribution across the width of the cross-section as shown in the left graph of Fig. 9.39. Furthermore, at the top and bottom edges of the cross-section a distinctive stress reduction is found. This is attributed to the introduction of the external load through the rigid bodies. The imposed Bernoulli hypothesis defines the outer edges to remain plane during deformation. This relaxes the stresses based on the lateral deformations increasing with distance relative to the outer edges. The stress relaxation follows a parabolic shape with the thickness along the centroidal axis being approximately half of the cross-sectional width.

Fire scenarios (VII)		
Calculation	**9.10A**	**9.10B**
Reference temperature	20 ^{o}C	20 ^{o}C
Duration	1200 sec	1200 sec
Incremental time step size	0.5 sec	0.5 sec
Incremental load step size	5 sec	5 sec
Material (heterogeneous)		
Strength class	C25/30	C25/30
Aggregate type	RG	RG
Boundary conditions		
Fire scenario	HC	HC
Convective heat transfer coeff.	50 W/m^{2}K	50 W/m^{2}K
Axial force	**-2.0 kN**	**-6.0 kN**
Moment		
Axial spring stiffness	6.7 kN/mm	6.7 kN/mm
Rotational spring stiffness	33 kNm/rad	33 kNm/rad

Table 9.13 *Examination of the combined influence of structural restraint and external loading on the C25/30 cross-section made with RG exposed to a HC type of fire.*

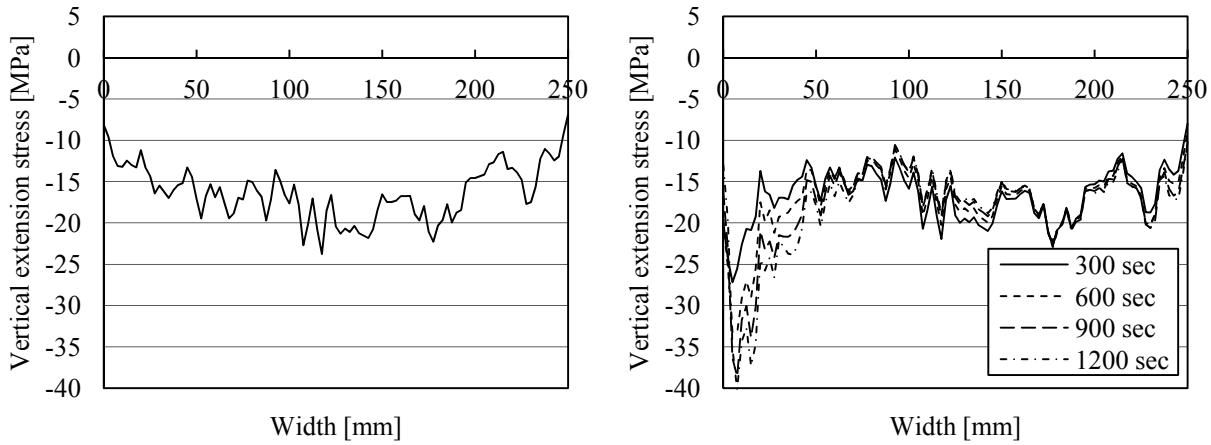

Fig. 9.39 *Vertical stresses in the C25/30 cross-section before (left) and during (right) fire exposure, reflecting the influence of the highest compressive loading level.*

Exposure of the C25/30 cross-section to a HC-based fire mainly extends the initial crack pattern. This holds true for both simulations as shown in Fig. 9.41. The initial vertical cracks form the flaws in which the formation of the instabilities localise. Especially for the highest compression loaded cross-section the damage is seen to extends beyond the previously obtained results. Not only are instabilities formed at the heated surface, but additional layers are seen to develop in the remaining part of the cross-section. At this depth the temperature also increases, but compared to the previous results a compressive stress is already acting.

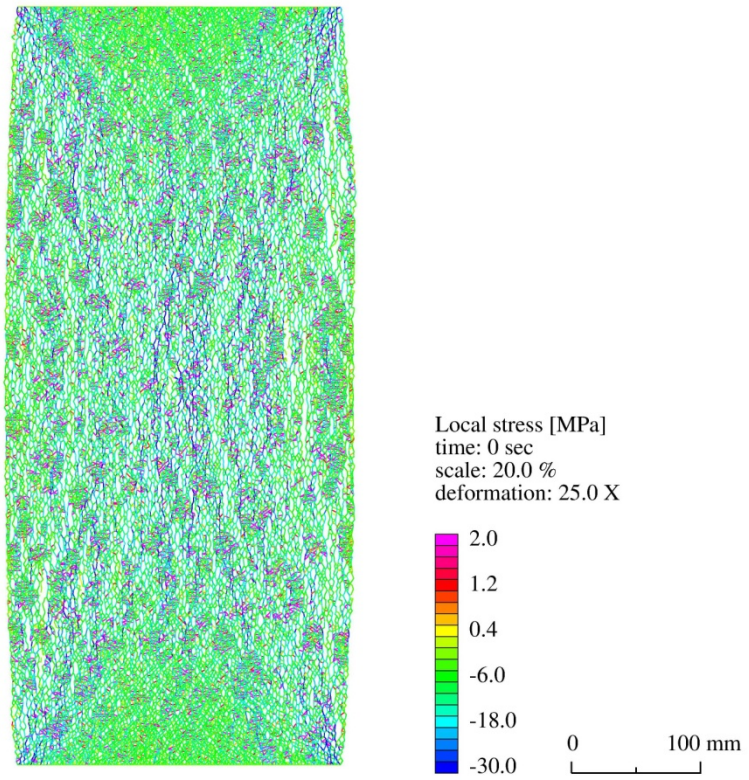

Fig. 9.40 *Deformed and cracked C25/30 cross-section, reflecting the influence of the highest external compression forces before fire exposure.*

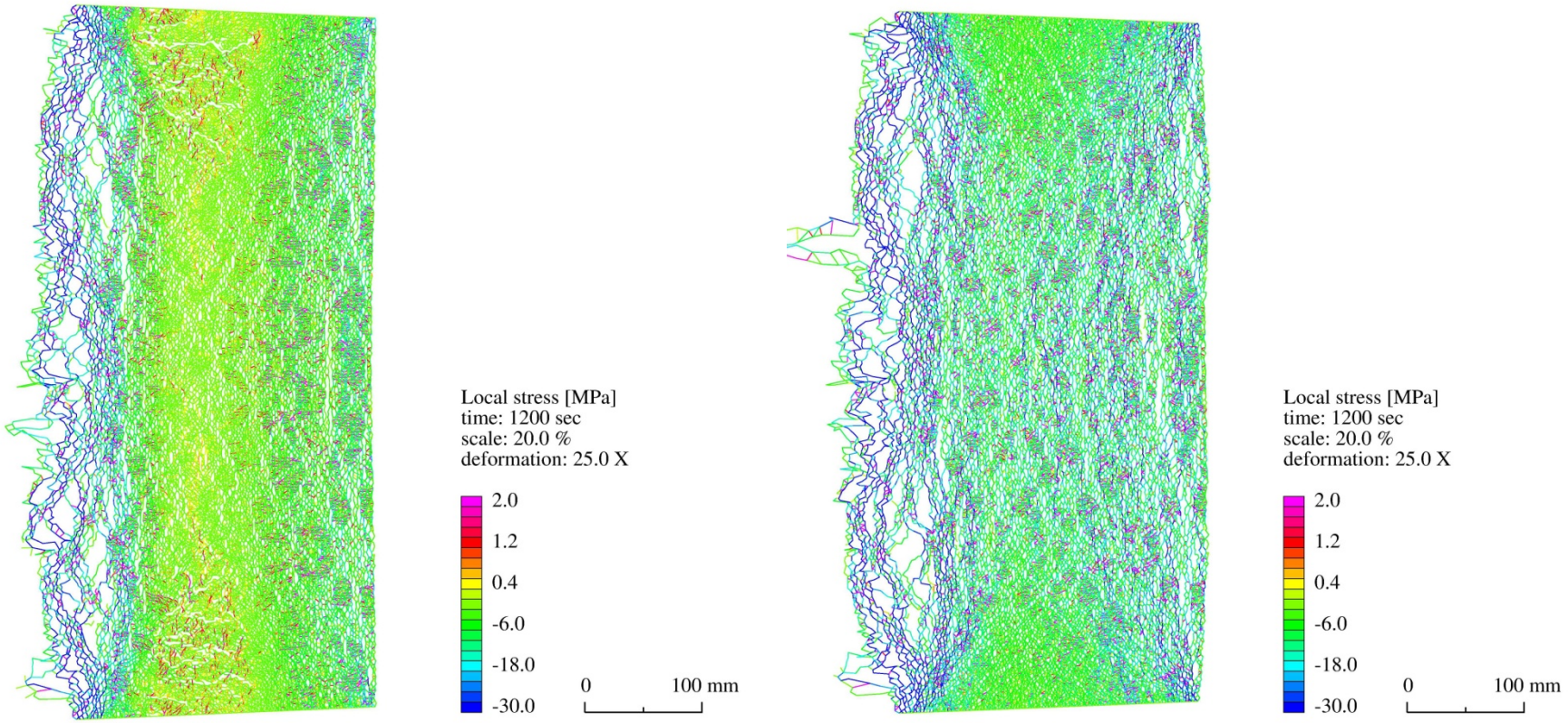

Fig. 9.41 *Increasing the external compressive loading from 2.0 kN (left) to 6.0 kN (right) not only influences the initial crack pattern in the C25/30 cross-section, but also characterises the development during severe fire exposure and the formation of instabilities.*

Both these results provide a first insight into the possible development of a more repetitive type of damage. Returning to the premises of failure by buckling suggests that the presence of the compressed, initially formed, vertical layers makes the cross-section more susceptible to spalling. The compressive stresses acting in the heated surface layer are not only extended by the external loading, but also the fracture process consumes less elastic strain energy. The initial crack pattern needs only to be extended in order for the layers to become separated from the remaining cross-section.

It is also noted that in both these simulations the external load is assumed to remain constant during fire exposure. This is a conservative assumption since during fire exposure of a structure also large redistribution of forces occur based on variation of stiffness and deformations. However, observing the level of damage in especially the highest loaded cross-section and taking into account the continued external and thermal loading again failure could occur. The remaining cross-section is under these circumstances no longer able to withstand the imposed combined load.

9.10 Conclusions with respect to fire exposed concrete

Based on the discussed numerical results the following conclusions are drawn considering only the temperature as internal loading:

- The cracks in the C25/30 simulations are characterised by a tortuous and distributed pattern, influenced by the weaker interfacial zones surrounding the aggregates. The patterns found for the C90/105 simulations reflect larger crack spacings with less branching off into smaller cracks.

- Severe fire exposure of the cross-section in unrestrained conditions causes the development of extensive cracking in C25/30 and C90/105 both made with RG. Opening of the resultant crack pattern relaxes the thermal stresses.

- Addition of structural restraint ensures that the compressive stresses remain active in the heated surface layer. For both concrete strength classes thermal instabilities are found to develop, originating from cracks in the transition zone between the compressive and tensile stress states. Parts of the heated surface layer are separated by the development of the compression load, induced by the continued fire exposure.

- In C25/30 the formed instabilities tend to reflect the compression loaded heated surface layer with additional concrete dislodged by the curved fracture surface extending into the unheated part of the cross-section. A more uniform fracture surface characterises C90/105, causing the separated layers to be more slender and deform under relatively lower compression load levels.

- The curved deformation, the compression loading and the relative slenderness of the separated layers seems to suggest that a form of thermal buckling develops. Furthermore, it could be argued that this represents a possible spalling mechanism.

- Addition of external compression loading causes the cross-section to reflect a distributed pattern of relatively small compressive cracks. The thermal instabilities not only localise in these cracks, but also additional layers are found to develop behind these surface-based deformations.

With respect to the simulations representing both temperature and pore pressure loading the following conclusions are drawn.

- In both ISO 834 and HC fire scenarios (pore) pressures are mainly mitigated by the level of cracking that develops in the heated surface layer. Even for moderate fire exposure it seems unlikely that pressures could, under these circumstances, rise to a sufficiently high level to cause cracking.

- In the C90/105 simulations some small gas pressure peaks are observed to develop. However, compared to the higher tensile strength these are considered to be limited.

- Drying of the cross-section not only develops in the heated surface layer, but also along the crack paths. Especially for C90/105 a sharp moisture front between the cracks and the surrounding material is observed.

- The continued mass fluxes of vapour and liquid water through the cracks towards the exterior environment influence the temperature gradient. This is especially observed for C25/30 and caused a reduced temperature development in the heated surface layer.

Regarding the anisotropic permeability and the approximated stiffness as well as the numerical stability the following is mentioned:

- The influence of a local crack on the global permeability and the global stiffness is opposite. The permeability increase is defined mainly parallel to the crack. In the direction perpendicular to the crack the stiffness reduction is imposed.

- Approximation of the global stresses based on the fractured network of 1D bars reflects overall relaxation. Limited shear stresses develops especially along inclined crack edges, reflecting rotation of the principal stresses.

- Especially the numerical stability of the FEM temperature and transport model for the C90/105 simulation proved to be most challenging. The larger crack openings and spacings proved to impose the highest constraints on the rate of convergence.

- During deformation of the unstable surface layers the calculation times for the FEM fracture mechanics model increased. The higher level of discontinuity governed the rate of convergence.

10 Philosophy, conclusions and recommendations

10.1 Philosophy on the spalling mechanism of fire exposed concrete

In the previous chapter, to the knowledge of the author, for the first time the fire-induced spalling of layers from the surface of the concrete cross-section has been simulated. Through variation of the strength class, type of aggregates, imposed fire scenario and structural loading conditions the concrete cross-section exhibited different types of damage. Under these circumstances spalling was identified as a form of thermal instability that developed in the heated surface layer. This mechanism differed from the more gradual thermal weakening of the cross-section, caused by the material degradation and cracking. Moreover, the fracture mechanics basis enabled the main existing theories on pore pressure development (Harmanthy, 1965) and temperature-induced stresses (Dougill, 1972) to interact. This quantified their contributions and allowed to assess their respective influence on the possible development of spalling. These numerical results and their analyses could thus help to bridge the gap between experimental research into the material behaviour (RILEM TC-HTC, 2004) and the observed spalling events during fire tests (fib WP-4.3-1, 2007).

Reduction of pore pressures

The development of pressures in heated concrete specimens has been experimentally proven using mainly gradual heating rates to reduce the level of thermal cracking (Kalifa, et al., 2000; Phan, 2008; Mindeguia, 2009). Numerical FEM simulations of fire exposed cross-sections, presented in chapter 6, indeed showed significant pressure development, especially in the dense microstructure of C90/105. However, by including an initially crack pattern pressures were reduced in the material as discussed in chapter 7. This behaviour prevailed during the simulations in chapter 9, reflecting fire exposure using the fracture mechanics coupling. Gas pressures were estimated to be reduced across the heated surface layer, remaining well below 1.0 MPa. Comparison to actual fire tests is difficult since mainly temperatures have been measured. However, this tendency was observed for concrete slabs exposed to ISO (Mindeguia, 2008) and RWS (Jansson & Boström, 2008) types of fire curves for which pressure measurements at various depths were conducted as for instance seen in Fig. 2.11.

Pressure reduction seems contradictory to the existing theory (Harmanthy, 1965) since imposing more thermal energy forces the evaporation process to develop at a higher rate. However, pressures arise in concrete based mainly on two aspects in which the temperature increase is the most dominating factor. It is also required that the pore space is sufficiently dense and the permeability limited to ensure that most of the thermal energy is used to increase the temperature. This forces the vapour pressure to develop in order to maintain thermodynamic equilibrium, as assumed present between the water phases (Tenchev, et al., 2001; Gawin, et al., 2003). Both conditions are fulfilled in the microstructure of the cement paste and the exponential pressure build-up is maintained.

During simulations reflecting fire exposure almost immediately cracks were found to develop. The cracks located in the heated surface layer originated from the differences in imposed temperature strains (Diederichs, et al., 1987; Flynn, 1999) between the aggregates and the dehydrating mortar (Alonso & Fernandez, 2004). From a structural point of view these cracks are still considered limited. However, compared to the permeability of the surrounding material even the smallest crack represent a significant improvement in the transport capabilities (Bear, 1972/1988). Under these circumstances the gas pressures from the onset of fire exposure were reduced. Continuation only extended the crack pattern, making the possibility for the pore pressure to still increase less likely. Moreover, the perhaps surprisingly limited influence of the gas pressure could also be argued based on the sudden volume increase at the onset of crack opening (Bažant, 1997) as stated in chapter 4. The scale difference between the pore structure and the crack width is estimated to be sufficiently large to rapidly reduce the gas pressure. Maintaining the pressure by the flow of additional vapour into the crack is impeded by the relatively low permeability of the surrounding material.

This reasoning seems confirmed by the observation of spalling damage after fire testing of an initially predried slab loaded in compression as shown in the right picture of Fig. 2.23 (FSV, 2004). However, spalling is also reported to have not occurred during fire exposure of a dried slab as seen in Fig. 2.27 (Mindeguia, 2009). Analyses of the pore pressure is further complicated by the observation of limited spalling to concrete slabs stored in the ambient air (Mindeguia, 2009) or under water (Horvath, et al., 2004) before exposure to a more moderate ISO type of fire as seen in Fig. 2.24. With respect to drying of slabs it is to be considered that this will cause cracking and take considerable time (FSV, 2004; Mindeguia, 2009).

Crack development due to the temperature gradient

The alleviated gas pressures and the seemingly conflicting results based on initial drying of the concrete slabs prompt the attention on the temperature and the thermal stress theory (Dougill, 1972). The influence of the steep temperature gradient is, as elaborated in chapter 5, based on the development of a distinctive thermal stress state while considering static equilibrium (van Breugel, et al., 1998). Peak compressive stresses in the heated surface layer develop, indicating partially restrained thermal expansion. In the unheated centre of the cross-section deformations are imposed, giving rise to tensile stresses dependent on the structural conditions. The FEM results in chapter 8 reflected these stresses based on assuming linear elasticity without cracking. However, the stress levels were already indicated to be sufficient to cause cracking, especially considering the strength degradation (RILEM TC-HTC, 2004).

From the onset of fire exposure cracks were observed in chapter 9 to develop in the cross-section. Dependent on the structural loading horizontal cracks appeared with the distribution and crack spacing governed by the concrete strength class. The C25/30 simulations reflected a more tortuous and denser pattern of cracks. Continued fire exposure caused these cracks to open, relaxing the stresses in the surrounding material. Especially in unrestrained conditions considerable localised deformations developed. These cracks are found at the concrete surface during fire exposure, as seen in Fig. 2.19, and after testing (FSV, 2004; Horvath, et al., 2004).

The coinciding compressive stresses in the heated surface layer were, especially in unrestrained conditions, estimated to be largely reduced. Extensive cracking in the heated surface layer caused by differences in imposed thermal forces was most prominent in case of the assumed weaker interfacial zones in C25/30 as well as the usage of river gravel. Continued fire exposure extended the crack pattern and caused substantial deformations. Comparing these estimated displacements to measured deformations during fire testing could prove especially valuable. It was also noted that in these unrestrained conditions it is not unlikely that the dehydrated and cracked slabs fail. Fracture or even collapse of relatively thin concrete slabs during fire testing has been reported to have occurred (Horvath, et al., 2004).

Possible spalling mechanism caused by thermal buckling

This specific type of fire-induced damage by fracturing of the slabs is not considered spalling. The violent and explosive nature of this surface-based phenomenon is not present. However, the numerical results presented in chapter 9 also indicated a second type of damage in which part of the heated surface layer seemed to become unstable. Deformations along part of the concrete surface were estimated to increase faster compared to the surrounding cross-section. This particular type of damage is believed to be closely related to the compressive stresses which due to structural restraint remained present. Stress levels were also found to be lower than the compressive strength of the concrete (RILEM TC-HTC, 2004). Considering the shape of the layers and the failure in compression, these results could suggest that spalling represents the ultimate state of a thermal buckling process. Moreover, the sudden nature of buckling (Timoshenko & Gere, 1961/2009) combined with the release of stored elastic strain energy could explain the commonly observed spalling events (FSV, 2004; Mindeguia, 2009).

Finding evidence that the mechanism causing spalling is in fact a form of thermal buckling is not an easy task. However, buckling is closely related to the geometrical dimensions through the bending stiffness and in particular the length (Timoshenko & Gere, 1961/2009). The numerical simulations reflecting partially restrained conditions revealed that the thickness of the spalled layers seemed to be governed by the depth at which various cracks intersected. Continued thermal exposure caused the vertical compressive cracks to combine with the horizontal tensile pattern. Inclined cracks were also observed to develop already after several minutes of simulated fire exposure. This fracture process formed the initial flaws needed for the spalling mechanism. Evidence of this process can for instance be found in the left picture of Fig. 2.22, showing a large opened crack on the concrete slab parallel to the fire exposed surface (Horvath, et al., 2004).

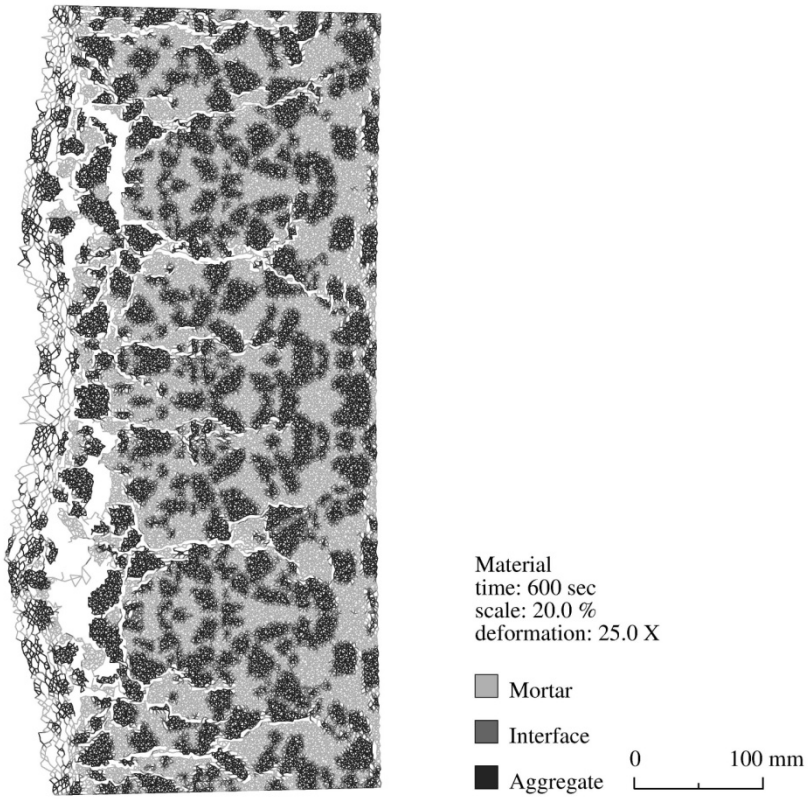

Fig. 10.1 *Formation of thermal instabilities, simulated at the heated surface of the partially restrained C25/30 cross-section made with RG during HC-based fire exposure.*

The numerical results also indicated that the concrete strength influences the geometrical shape of the spalled layers. In case of C25/30 a curved fracture surface formed, extending into the transition zone with the unheated part of the cross-section. The deformed and cracked heterogeneous mesh in Fig. 10.1 illustrates the thermally unstable surface layers with additional material being also ejected outwards. The higher tensile strength and reduced level of cracking in this transition zone determined the damage in case of C90/105. A more uniform fracture surface developed with the layers characterised as more slender which could explain the commonly reported spalling sensitivity for HSC (Khoury & Anderberg, 2000). With respect to these FEM fracture mechanics simulations it should be reminded that only extensional deformation with some level of bending is used the characterise the material.

The premise of thermal buckling also extends to the negative influence of initial loading. By imposing an initial uniform compression load on the cross-section a distributed pattern of cracks developed parallel to the heated surface. Under these circumstances the simulations indicated deformations localising in these cracks, forming the flaws in the spalling process. Spalling of each of these layers would expose the remaining cross-section to the fire which combined with the higher compressive load could allow the mechanism to develop at a higher frequency. This repetitive tendency is for instance reported for loaded concrete slabs (FSV, 2004) and tunnel lining segments (Dehn, et al., 2010). It is noted that loading of fire tested concrete slabs should preferably be done through external forces rather than a post tensioning system to avoid thermal relaxation (Jansson & Boström, 2008).

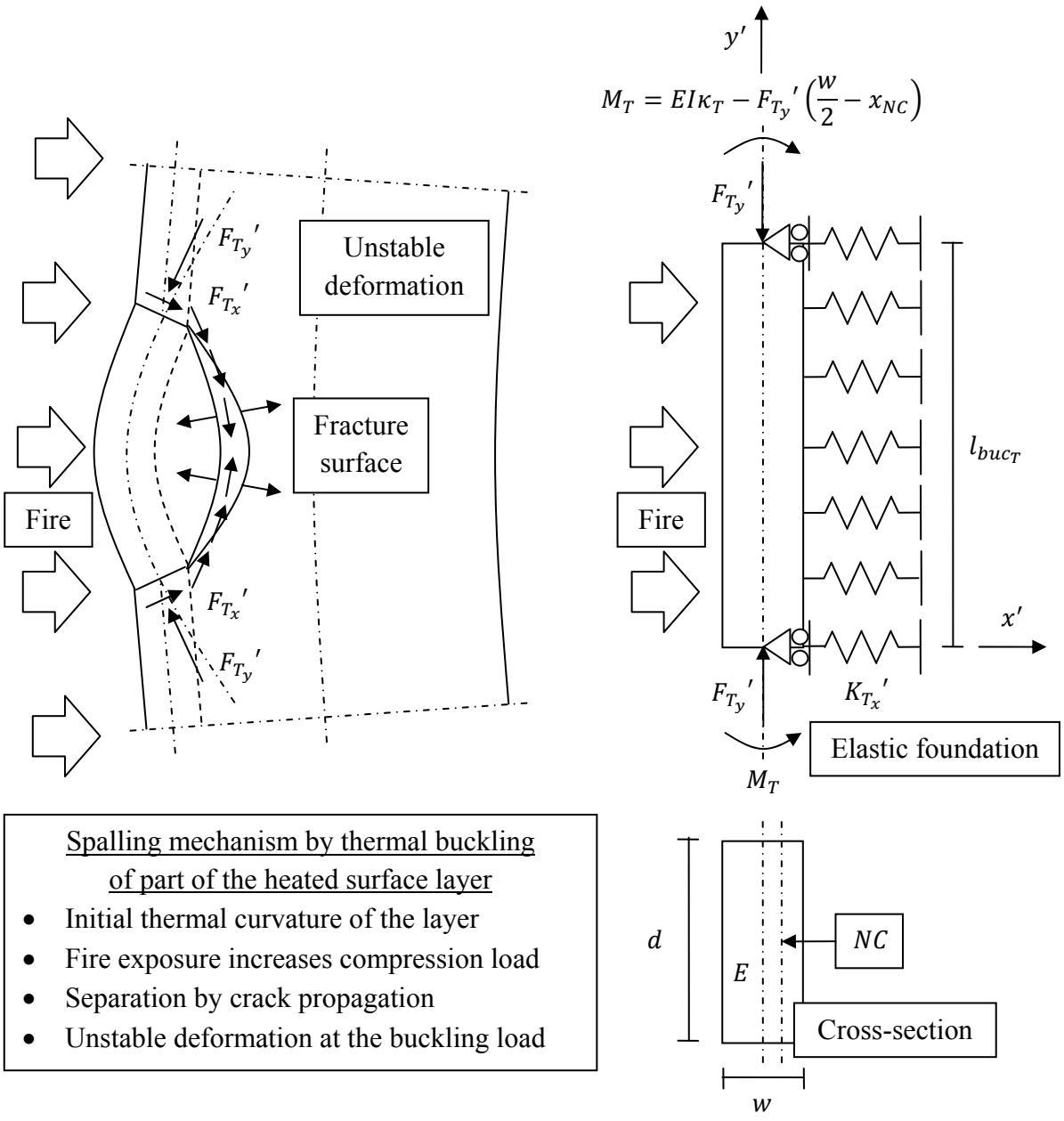

Fig. 10.2 *Schematic overview of fire-induced spalling as thermal buckling of an initially curved concrete layer from the heated cross-section. The layer is supported by an elastic foundation to reflect the surrounding material.*

Thermal buckling of heated surface layers

The proposed spalling mechanism can be illustrated by considering the deformation of the heated surface layer. This process is schematically represented in Fig. 10.2 with the restrained thermal expansion promoting the formation of a crack, leading to separation of a part of the heated surface layer from the cross-section. Propagation of this crack is driven by the imposed thermal energy increasing the compression load whereas separation allows for additional curvature to develop. Both contributions are reflected in the mechanical scheme with an elastic foundation of distributed translational springs governing the crack formation. The cross-section of the spalled layer has a constant width as well as out-of-plane thickness.

The cross-sectional rotation of the layer relative to the surrounding material decomposes the compression forces at the top and bottom edges. The local axial forces still load the layer in compression which, based on the initial curvature of the cross-section, is already directed outwards. An additional moment also develops governed by the thermal degradation of the material stiffness, causing the NC to position asymmetrically with respect to the centroidal axis. With increasing curvature the horizontal forces develop, having to be resisted by the surrounding material. In case of NSC extensive cracking will have weakened this transition zone, causing a curved fracture surface based on the transmission of compression forces. In HSC this fracture surface is considered to be relatively straight which, based on the reduced thickness, should promote the spalling mechanism.

Buckling occurs in outwards direction based on the thermal curvature of the cross-section and in case the crack has sufficiently separated the assumed hinged connected layer, defining the maximum compressive force (Timoshenko & Gere, 1961/2009). The release of the remaining elastic energy stored in the delaminated layer characterises spalling as an ejection of material from the heated surface. However, it needs to be considered that in depth direction, using a plane strain assumption, also a restraining force develops. The layer actually represents a plate loaded in bi-axial compression. Under these circumstances the critical set of buckling forces is determined by the aspects ratios of the plate (Timoshenko & Gere, 1961/2009). Considering that spalling probably reflects a square or rectangular layer, buckling would occur sooner after the start of the fire test than estimated by a 1D approach (Timoshenko & Gere, 1961/2009; Jones, 2006). Estimated spalling times can also increase in case the outer ends of the layer are assumed restrained (Timoshenko & Gere, 1961/2009). In retrospect spalling can take various forms, considering also the dynamic environment in which it develops.

Proof of this failure mechanism is perhaps found in the observed fracture surface and the influence of external loading (Khoury & Anderberg, 2000). The overall cross-sectional reduction was, especially for the loaded C30/37 tunnel lining segment after fire testing, characterised by several distinctive crater shaped pockets of additional damage as seen in Fig. 2.29 (Dehn, et al., 2010). Also the previously mentioned differences in spalling behaviour for initially dried slabs could be considered. Without addition of external loading (Mindeguia, 2009) the level of (micro) cracking caused by the drying shrinkage could reduce the stiffness of the concrete, affecting the ability to develop the compressive stresses. However, addition of sufficient external compression loading (FSV, 2004) could make such a dried concrete slab again more susceptible to spalling.

A particular interesting example represents a gradually heated concrete slab, experiencing a single spalling event (Mindeguia, 2009). The damage to the concrete slab reflected two curved areas, extending across the width as shown in the right picture of Fig. 2.25 (Mindeguia, 2009). The possibility of partial restraint by placing the slab between two refractory concrete blocks could be considered here. Even the cross-sectional thickness represents a form of restraint, increasing the compressive stresses. This could possibly contribute to the observed spalling damage after fire testing of relatively thick concrete slabs (FSV, 2004).

Observations of the spalling damage to C60/75 slabs after fire exposure reflected an almost uniform fracture surface (Mindeguia, 2009). The depth of the damage was after this test approximately the diameter of the largest aggregates. Other examples of HSC slabs with an even fracture surface can be found in (Horvath, et al., 2004) as reflected by Fig. 2.22. A final remark is the geometry of the samples which should preferably not be cubes or cylinders (Brekelmans, et al., 2008), allowing also for a sufficiently large fire exposed area to avoid edge effects.

Effectiveness of measures for spalling mitigation

Understanding the mechanism forms the starting point for reducing the spalling sensitivity through mitigation of the thermal buckling risk. The first possibility is to mitigate the compressive load for which aggregates with reduced thermal expansion are commonly used (FSV, 2004; Jansson & Boström, 2008; Dehn, et al., 2010). In unrestrained circumstances perhaps another possibility involves causing extensive cracking in the heated surface layer. This might seem contradictory, but by using for instance river gravel aggregates the crack pattern was estimated to alleviate the compressive load. However, these aggregates should remain thermally stable in order to avoid additional damage by fracture of particles.

Unrestrained conditions are from a structural point of view less relevant. Structures such as buildings and tunnels are always load bearing. In these restrained and loaded conditions the compressive stress state most probably remains active in the cross-section. In current practise mitigation of temperatures through fire protection measures is still the most common choice. In this respect it could prove beneficial to investigate the fire scenarios relevant for a particular project. Instead of using the provisions established in the regulations (Eurocode 1, 2011a; Eurocode 1, 2011b) a project-based fire curve could be defined using alternate criteria. A reduction or a more gradual thermal exposure could allow the coinciding fire protection measures to become more cost effective. However, it needs to be considered that without fire protection dehydration and thermal cracking will always occur in these circumstances.

Another possibility is to add PP-fibres to the concrete mixture, aimed at pore pressure reduction (Horvath, et al., 2004; Brekelmans, et al., 2008). However, the estimation of limited pore pressure development during fire exposure raises the question for the reason of the commonly reported effectiveness (Horvath, et al., 2004; FSV, 2004). Based on the observed behaviour by the FEM models two possible contributions for melting of the PP-fibres are considered in relation to the proposed spalling mechanism:

- Melting of the PP-fibres increases the quantities of vapour and liquid water being able to escape to the exterior environment. By sustaining higher mass fluxes of both water phases mitigation of the temperature in the heated surface layer could occur. Evidence of these temperature plateau's can be found in gradually heated concrete specimens without PP-fibres (Mindeguia, 2009). Closer examination of temperature measurements in fire exposed tunnel lining segments with PP-fibres reveals similar tendencies (Dehn, et al., 2010). More research into the temperature development during drying is required to validate this concept.

- Another possibility for melting of PP-fibres to contribute to reducing spalling is by extending the level of damage. The network of molten PP-fibres could represent a distributed pattern of small cracks, reducing the stiffness and strength. Both govern the ability of the heated surface layer to maintain the thermal loading and the coinciding compressive stress development. Limited information is found in literature regarding this topic, but measurements of Young's modulus suggested a higher reduction with temperature for concrete with PP-fibres (Hager, 2004). Additional measurements and numerical calculations are required to extent on this concept.

A final possibility commonly used to reduce buckling related problems is reduction of the length. This will prove difficult with respect to heated concrete since the geometrical dimensions for the spalling mechanism are defined through a fracture-based process. However, it could prove insightful to conduct experimental fire tests on concrete slabs which have a modified surface as for instance reported in (Mindeguia, 2009). As an alternative to these tests, several concrete slabs could be cast with a profiled surface as schematically shown in Fig. 10.3.

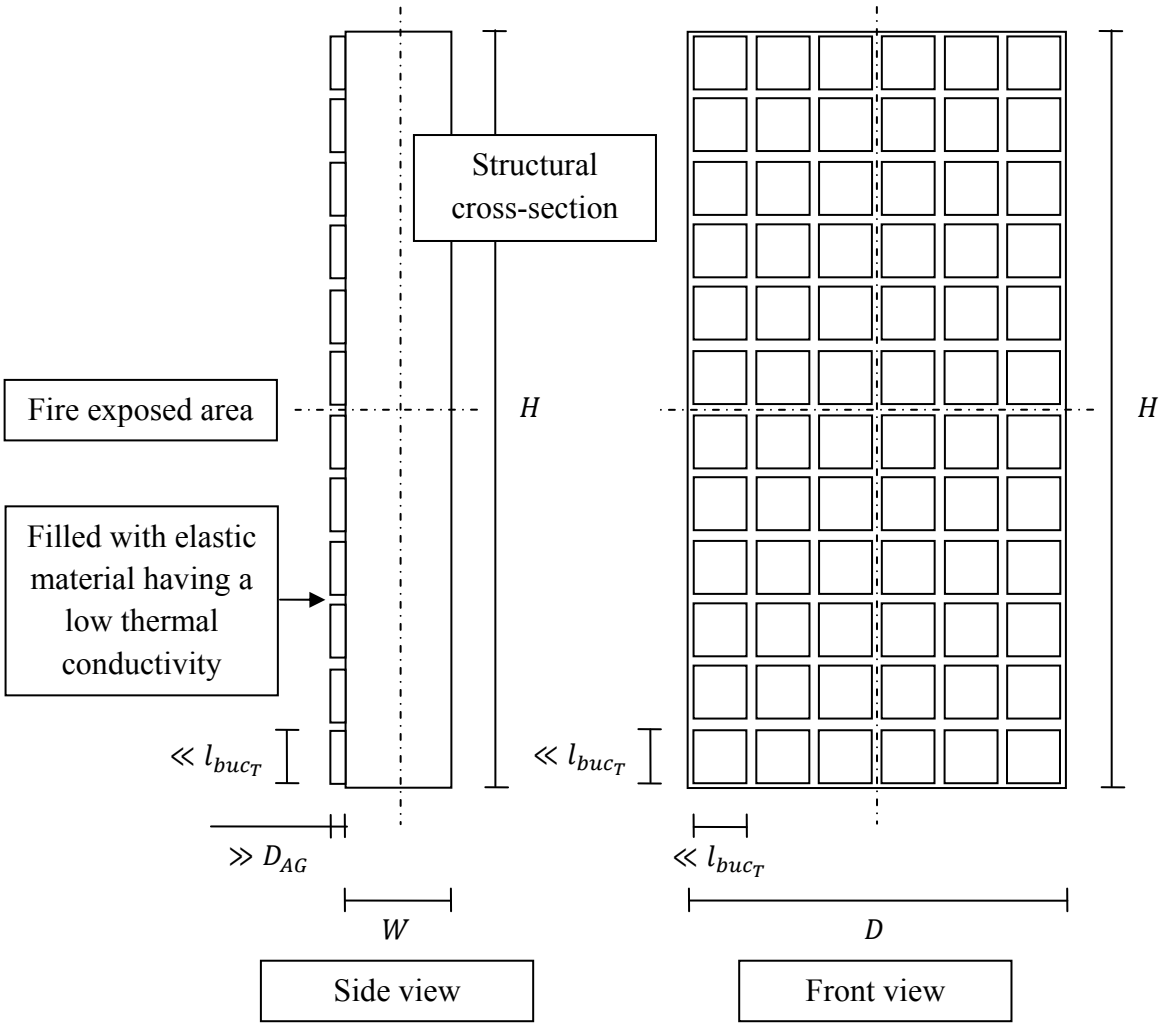

Fig. 10.3 *Schematic overview of a concrete slab having a non-structural profiled surface. The size of the rectangular grid is aimed at reducing the sensitivity to spalling.*

The aim of this non-structural concrete surface is to form a thermal barrier which remains in-place during fire exposure by reducing the spalling sensitivity. The depth of this discontinues grid should be larger than several times the diameter of the largest aggregate particles to ensure that especially the onset of the temperature gradient is situated in this layer. The scale of the blocks is chosen in order to mitigate the spalling sensitivity by only partially sustaining the compression force while also reducing the buckling length. It is important to consider the possibility for additional thermal energy to directly penetrate into the structural cross-section via the space in between the blocks. This could give rise to local variations in temperatures and stresses which could be avoided by using an insulation material. This combines both high elasticity and low thermal conductivity, aiming to maintain the intended surface properties.

10.2 Conclusions

The aim of this thesis was to investigate the fire-induced spalling of concrete. For this purpose a FEM-based model was developed aimed at describing the behaviour of fire exposed concrete. Throughout this thesis intermediate conclusions and remarks were stated based on previous derivations and numerical results. Below an overview of the main conclusions is provided, reflecting the objectives stated in chapter 3.

The first objective: derivation of a conceptual FEM-based model

The temperature and pore pressure development is first addressed in chapter 4 through definition of a closed system. In chapter 6 the isotropic and homogeneous FEM discretisation is derived based on conservation of thermal energy and mass of the water phases. From the derivation and the numerical analyses the following main conclusions were drawn:

- Gas pressure development with temperature in a closed system is mainly characterised by the saturated water vapour pressure. Dependent on the initial saturation level a super heated vapour, a level of partial saturation or a compressed liquid is formed.

- Using this closed system it is demonstrated that also the gas pressure drops in case of the sudden and substantial volume increase upon crack opening. The reduced permeability of concrete is in these circumstances considered insufficient to maintain the pressure.

- Imposing thermal energy and especially drainage of the water phases towards the surrounding environment is best characterised through Neumann boundary conditions. With respect to the former also radiation of thermal energy could be included at the boundary to characterise the type of fire source considered.

- Drying of concrete is characterised by the thermodynamic equilibrium between the water phases as governed by the capillary pressure. Gas pressures in an open system develop with temperature until a minimum saturation level between 0.2 and 0.4 is reached.

- Substantial gas pressures of around 4.0 MPa are reached in case of C90/105, equilibrated at exterior conditions, is exposed to an HC type of fire. Under these circumstances only drying of the almost saturated pore structure is observed to develop.

- Preconditioning of C25/30 at interior conditions reduces the moisture levels. During fire exposure an increase in the saturation level in front of a limited gas pressure peak develops. The same behaviour is to a lesser extent also seen for C90/105.

Thermal mechanical analyses involved derivation in chapter 5 of deformation relationships based on consideration of static equilibrium for a part of a single side heated structural element. In chapter 8 the isotropic and homogeneous FEM discretisation is developed, assuming linear elasticity. The derivation and the numerical results lead to the following main conclusions:

- Single sided fire exposure of the symmetrical structural element causes a constant stress state in height direction. Consideration of in-plane equilibrium of forces reflects a plane stress assumption for the linear elastic continuum.

- Temperature strains are imposed as initial elongation without causing stresses. Pore pressures are, through considering polar linear elasticity, directly related to the stresses.

- The Bernoulli hypothesis is in the FEM discretisation of the structural element imposed along the supported edges based on rigid body conditions. The displacement and rotation along each edge are expressed in the deformations at the support.

- Restrained expansion of the fire exposed surface layer causes compressive stresses, reaching ultimately values of 60 to 100 MPa for C25/30. Imposed deformation of the unheated centre of the cross-section causes the coinciding tensile stresses to exceed 10 MPa. Influencing parameters to be considered are the cross-sectional stiffness, concrete strength class, aggregate type and structural (support) conditions.

- Temperatures higher than 500 ^{o}C cause softening of the material based on reduction of Young's modulus with temperature. As a results compressive stresses are mitigated at the heated surface of the cross-section.

- Thermal stresses can be reduced by using aggregates with a lower thermal expansion. In unrestrained conditions the thermal stresses for NSC and HSC are equal, considering the same temperature strain and stiffness degradation.

The second objective: fracture-based coupling between both FEM models

The FEM temperature and pore pressure model is in chapter 7 extended to reflect a heterogeneous material with an anisotropic mass flux definition for initially a constant crack pattern. The fracture mechanics coupling is presented in chapter 9 and is characterised by a

time-dependent development. Regarding both chapters the following main conclusions are drawn:

- The assumed impermeable aggregates cause gas pressures to increase at the opposite side relative to the fire exposed surface. Only in C90/105 and for the largest aggregate sizes a limited pressure increase is found to develop.

- Continued drying of the material above the critical temperature is ensured through imposing a constant capillary pressure on the heated boundary. For this purpose the density of liquid water at these high temperatures is restated.

- Numerical stability is affected by including the substantial permeability increase caused by opening of the crack. Adaptive time stepping and gradual development are considered as stabilisation measures. The influence of anisotropy is also reduced by allowing for a limited flux perpendicular to the crack.

- The presence of cracks alleviates the gas pressures that develop in severe fire conditions. The permeability of the material surrounding the crack and the crack spacing governs the ability to level off the water phases.

- Drying of the concrete along the crack paths reflects transport of both vapour and liquid phases of water towards the exterior environment. In the heated surface layer the continued evaporation causes a cooling effect whereas in the interior condensation increases the temperature.

The fracture mechanics approach adopted in chapter 9 reflects an anisotropic and heterogeneous FEM discretisation, commonly referred to as a lattice (Schlangen, 1993; Vervuurt, 1997). From the numerical simulations the following main conclusions are drawn:

- The anisotropic discretisation by a triangular orientation of three 1D bars is sufficient to approximate the global strains. Cross-sectional dimensions for the bars are governed by the internal triangular height. Brittle fracture and removal of individual bars govern the crack initiation. Geometrical non-linear effects are considered by alignment of the normal forces with the deformed bars.

- Improved redistribution of incremental fracture forces is obtained by introduction of local curvature deformation. This local bending is defined by 1D Bernoulli-Euler beams characterised by only part of the internal height to mitigate stiffening in the structural response.

- The weaker interfacial zones surrounding the aggregates tend to characterise the crack pattern in C25/30 as more tortuous and distributed. The higher stiffness and especially tensile strength of the mortar and the interfacial zones in C90/105 govern the larger crack spacings and openings.

- Extensive cracking develops in unrestrained and severe fire conditions for both C90/105 and especially C25/30, causing substantial damage to the cross-section. Stresses throughout the material are relaxed by opening of the cracks.

- In partially restrained conditions the compressive stresses remain present in the heated surface layer during fire exposure, causing the development of thermal instabilities. Parts of the heated surface layer are separated from the remaining cross-section by cracking, induced by the sustained compression load.

The third objective: dominant processes in the development of the spalling mechanism
The results presented in chapter 9 indicated the development of thermally unstable surface layers which could be identified as a form of fire-induced spalling of concrete. With respect to this mechanism and the philosophical deliberations presented in this chapter the following main conclusions are drawn:

- High temperature exposure will always cause dehydration of the concrete with, dependent on the severity of the heating rate, also cracking.

- The development of cracks from the onset of fire exposure mitigate the gas pressure development in both NSC and HSC. Considering the type of thermal exposure and coinciding cracking does it seem unlikely that the gas pressures could still develop sufficiently to contribute to the formation of the instabilities.

- The presence of the compressive stresses in the heated surface layer are believed to govern the formation of the instabilities. Considering the crack pattern and the stress level it seems possible that thermal buckling of these layers could occur. Under these circumstances the release of stored energy is observed as a spalling event.

- The geometrical dimensions of the spalled layers seemed characterised by the crack development process with the concrete strength as one of the key parameters. The susceptibility of NSC to cracking causes a curved fracture surface which increases the thickness of the spalled material. For HSC this fracture surface tends to be more uniform, making the thermal instabilities more slender while promoting spalling.

- External compression loading defines an initially cracked cross-section, allowing the formed layers to be more prone to spalling. The presence of compression loaded, partially separated layers in the cross-section promotes the occurrence of the spalling mechanism at a possibly higher frequency.

10.3 Recommendations

The coupled behaviour of both FEM models has provided new insights into the behaviour of concrete at elevated temperature. Especially of interest is the possibility to approximate a possible spalling mechanism. However, with respect to the derivation and the numerical performance the following recommendations are given:

- Derivation of a FEM model requires understanding of the theoretical background and the inherent assumptions, considering also the numerical methods employed. It is therefore recommended that such a basis is at least partially present beforehand. Using simplified models to validate a derived FEM model is also strongly recommended.

- The relationship between gas pressure mitigation and cracking could be improved by including larger openings without time-dependent development. A possibility is to investigate the usage of a higher order definition for especially the mass fluxes, considering also the level of anisotropy in the permeability along the cracks.

- The usage of 1D Bernoulli-Euler beams to improve the redistribution of the fracture forces should be further investigated. Consideration of rotational equilibrium of forces in the continuum could provide a basis to extend the anisotropic definition of the bars.

- Numerical investigations into the possibilities to simulate the behaviour of HSC under fire exposure should continue. Various points of interest are the possible transfer of forces through contact between aggregates and especially the cracking of particles.

- Thermal buckling of small concrete layers from the heated cross-section could be further investigated using the proposed mechanism. A simplified model could be constructed, allowing to vary geometrical parameters and the type of fire exposure while considering also the influence of the out-of-plane direction.

The presented thesis reflects a theoretical approach to understanding fire exposed concrete and the observed spalling events. Continuation of this work should rely on both numerical advances as well as experimental research. With respect to the latter the following is stated:

- The possibility to measure simultaneously temperatures and pressures during fire exposure of concrete slabs could be investigated in order to validate the proposed theory. This could require the collaboration of various parties currently active in the field of concrete and fire research.

- Displacements and external forces could be measured in order to validate the fracture mechanics behaviour. At first spalling should be avoided by reduction of the thermal gradient. Furthermore, additional deformation contributions, perhaps time-dependent such as creep and relaxation, could be considered to improve the mechanical model.

- The ability to observe and possible record the spalling events during fire testing could prove particularly useful for understanding the phenomenon. Furthermore, investigation of the crack pattern visible at the sides of the concrete slab during and after fire testing also provides additional information.

- The proposed spalling mechanism could also be the focus for experimental research. Addressing specific aspects of the thermal buckling process, such as modifying the concrete surface, could prove insightful.

Summary

This thesis deals with the observed damage to a concrete element or structure after exposure to a severe fire. Especially the probability of (explosive) spalling, as reported for large scale fires in the tunnels throughout the past decades (CTSA, 1997; BEA-TT & RAIB, 2010), is discussed in detail. Spalling of concrete is characterised by breaking off of layers from the heated concrete surface, where the term "explosive" reflects the sometimes sudden and violent nature of the observed phenomenon (Khoury & Anderberg, 2000). Two main theories prevail that explain spalling, where the first focuses on pore pressures that develop (Harmanthy, 1965) while the second aims at the thermal stresses that arise from the temperature gradient (Dougill, 1972). Actually the relationship between these physical and mechanical processes is not yet fully understood. Moreover, experimental research (RILEM TC-HTC, 2004) and more recently numerical efforts (Tenchev, et al., 2001; Gawin, et al., 2003) were mainly aimed at the behaviour of concrete at elevated temperatures. The actual spalling phenomena are at the time only investigated by conducting fire tests on concrete elements (Dehn, et al., 2010). However, these have proven to be insufficient for identifying the mechanism.

In this thesis a conceptual finite element based spalling model is derived, using a coupled pore pressure and fracture mechanics approach. This relates the local pore pressures and the global structural behaviour to the development of the crack pattern as determined for a single sided fire exposed concrete element. To establish a theoretical basis first the main physical and mechanical processes are illustrated by the derivation of various simplified models. Through the definition of a closed system (Hettema, 1996) the physical relationship between temperature and pore pressure development is clarified. A similar approach allows to quantify the gas pressure reduction based on the sudden volume increase upon crack opening. With respect to mechanics at first the static equilibrium of forces is considered based on the temperature gradient (van Breugel, et al., 1998; Hartsuijker & Welleman, 2007). This defines the compressive stresses in the heated surface layer and the tensile loading of the centre of the cross-section. The thermal expansion of the aggregates is confirmed to be a key material parameter (Eurocode 2, 2011b). Of importance are also the cross-sectional dimensions as well as the structural restraint and loading. Under these circumstances softening of the concrete occurs at temperatures higher than 500 ^{o}C (Dmitriyev, et al., 1969/1972).

Thereafter a continuum-based approach is used for the definition of the partial differential equations governing the physical processes. The temperature and the pore pressure development are characterised by conservation of thermal energy and the mass of the water phases across a representative elementary volume respectively (Bear, 1972/1988; Hassanizadeh & Gray, 1979b). The latter assumes an instantaneous thermodynamic equilibrium between the vapour and the liquid phases (Tenchev, et al., 2001; Gawin, et al., 2003) as defined by a desorption isotherm (Pel & Huinink, 2007). Neumann boundary

conditions reflect the interaction with the surrounding environment (Tenchev, et al., 2001; Gawin, et al., 2003). Some typical time-dependent solutions using the finite difference method are presented. These results reflect forced drying of the cross-section at a constant temperature.

The mechanical continuum is commonly known in civil engineering and only briefly restated, starting with the balance of linear momentum (Spencer, 1980/2004; Wells, 2006). This translational equilibrium condition is extended by assuming linear elasticity and imposing the temperature strain as an initial elongation (Timoshenko & Goodier, 1970). Both the plane stress and plane strain assumptions (Timoshenko & Goodier, 1970) are discussed with the latter assumed appropriate to represent the structural element. This continuum is subsequently restated in polar coordinates to illustrate a simplified relationship between the pressure in a pore and the stress state in the surrounding material (Timoshenko & Goodier, 1970).

In the remainder of this thesis both continuum-based theories are elaborated to form the spalling model. First, the temperature and pore pressure part of the spalling model is derived. Both conservation equations are coupled by including the thermal energy consumption due to evaporation. Subsequent minimisation of energy yields the weak form of this system (van Kan, et al., 2008; Zienkiewicz, et al., 2005). Through Galerkin's method the finite element definition is stated (van Kan, et al., 2008; Zienkiewicz, et al., 2005), assuming the porous material to be characterised as isotropic and homogeneous. Furthermore, for time integration an implicit Euler backward scheme (van Kan, et al., 2008) is used with the variables, temperature and capillary pressure, stated by an incremental definition. Neumann and periodical conditions are defined with the latter imposed along the top and bottom edges to reflect a continuous material (Segal, 2008). Spatial integration is obtained by randomly orientated 2D triangular elements having a linear basis (Felippa, 2004a).

Before calculating the various fire scenarios first the finite element model is validated. Good agreement is found by comparing separately determined temperature and capillary pressure distributions with results obtained by means of the finite difference method. Subsequently the influence of the concrete strength class, type of fire exposure and the environmental conditions is investigated. The highest gas pressures, reaching values of about 4.0 MPa, are found for concrete C90/105 exposed to a hydrocarbon type of fire. Evidence of the commonly mentioned moisture clog (Harmanthy, 1965; Zeiml, et al., 2006) is mainly observed for normal strength concrete, like C25/30, initially exposed to interior conditions. The same conditions also indicate a small increase of the saturation level in front of the pore pressure peak for C90/105. A final important observation is that in an open system the highest gas pressures are attained for a minimal saturation level between 0.2 and 0.4.

The temperature and pore pressure model is subsequently extended to reflect an anisotropic and heterogeneous material. Both solid and porous material schematisations are defined with the former reflecting the aggregate particles. The aggregates are assumed impermeable which affectively introduces material discontinuities at the particle edges. The porous material, representing the mortar and the interfacial zones with the aggregate particles, is characterised by the process of forced drying and remains isotropic until a crack develops. After that the

flow through the cracks is described regarding a substantial increase of permeability related to crack opening and orientation (Bear, 1972/1988). Both are to be determined by fracture mechanics coupled to the physical parameters. This causes discontinuities in the material discretisation, affecting the numerical stability. Adaptive time stepping (Söderlind & Wang, 2006) and including a mitigation of the level of anisotropy along the cracks are introduced to increase the rate of convergence. Above the critical temperature of water a further stabilisation ensures that the drying process continues.

Both aspects are investigated by exposing a heterogeneous concrete cross-section to several fire scenarios. The influence of including the aggregate particles is limited and only observed in case of a concrete strength class of C90/105 and for the largest particle diameters. Under these circumstances the gas pressure is estimated to increase at the side opposite to the fire exposed surface. However, including an initial crack pattern with a constant opening influences the forced drying process. The results obtained indicate that besides the transport capabilities of the cracks also the permeability of the surrounding material governs the influence. The simulations for C90/105 show that the more dense microstructure imposes higher restrictions on the flow of the water phases into the cracks.

The second part of the spalling model focuses on the mechanical behaviour of fire exposed concrete. At first for the mechanical continuum, through minimisation of energy, the weak form of the partial differential equation is established (van Kan, et al., 2008; Zienkiewicz, et al., 2005). The finite element definition is obtained by means of Galerkin's method (van Kan, et al., 2008; Zienkiewicz, et al., 2005), assuming the material initially as isotropic and homogeneous. The structural behaviour is approximated assuming plane strain (Timoshenko & Goodier, 1970) and rigid bodies (Hartmann & Katz, 2007) defined along the top and bottom edges to impose Bernoulli's hypothesis (Hartsuijker & Welleman, 2007). The latter introduces geometric non-linearities which requires the variables, horizontal and vertical displacements, to be stated in incremental form. Dirichlet and Neumann boundary conditions govern the central supports, both based on a fixed horizontal displacement and structural interaction using springs and forces (Bouma, 2000). Spatial integration is obtained by means of similar 2D triangular elements.

The finite element discretisation is validated by comparing the stresses in the cross-section and the displacements at the top support with results based on static equilibrium. A satisfactory approximation is found by considering a plane stress assumption. By using a plane strain schematisation the stresses are found to increase by around 20 percent. The incremental definition of the variables is also validated, reflecting besides additional temperature strains also redistribution of stresses based on stiffness variations. Several numerical results indicate the influence of the main parameters with special consideration of the imposed rigid bodies. For C25/30 the ultimate compressive stress can reach values between 60 to 100 MPa, dependent on the material properties, geometry, fire curve and structural conditions.

The fracture mechanics model has a different basis and discretises a part of the structural element through an anisotropic and heterogeneous material. Three triangularly orientated 1D bars together approximate the global strains (Prezemieniecki, 1968/1985; Blaauwendraad, 2004; Felippa, 2004a) with their cross-sections defined by the internal height. A linear elastic material definition, considering both the temperature strains and the pressure-induced stresses, is combined with the structural boundary conditions. These 1D bars are also considered to be geometrically non-linear, allowing the incremental deformations to influence the static equilibrium conditions (Bathe, 1986; Gavin, 2014). The fracture mechanics approach subsequently assumes the initiation and propagation of the cracks by the brittle fracture of the 1D bars (Schlangen, 1993; Vervuurt, 1997). However, it was found that redistribution of the incremental fracture forces requires additional curvature deformations to be included, obtained by definition of 1D Bernoulli-Euler beams, which creates a traditional lattice (Schlangen, 1993; Vervuurt, 1997).

In validation of the anisotropic finite element model a sufficiently accurate approximation by the 1D bars for various basic load cases is found. With respect to including the 1D beams it is observed that a stiffening effect could develop in the mechanical response in case a too high bending stiffness is included. After that, the fracture mechanics behaviour is elaborated by first only considering the temperature strains as internal loading. Under these circumstances it was found that the level of structural restraint is of key importance. Without restraint the heterogeneous cross-section experiences, especially under hydrocarbon fire exposure, severe cracking. The level of cracking and especially crack opening is sufficient to relax the thermal stresses. However, addition of structural partial restraint changes the fracture behaviour and thermal instabilities occur at the concrete surface. Locally curved deformations develop based on the compressive stresses which still act in the heated surface layer. Analysed are the influence of the concrete strength class, the type of fire exposure and the possibility for external compressive loading. These are found to determine the crack pattern in the fire exposed cross-section as well as the shape of the surface-based instabilities. These results are therefore of significant value to numerically analyse the spalling mechanism.

Extending the coupling between both models to include pressure-induced stresses also reveals the influence of the cracks on the process of forced drying. The level of cracking in the heated surface layer is sufficient to ensure that only limited gas pressures develop. Only in concrete of a strength class C90/105 some pressure peaks are present, but their contribution to the local stresses is considered minor. The forced drying process is also found to extend through the cracks into the cross-section. This is attributed to the capillary pressure gradient, driving the liquid water towards the exterior environment while affecting the temperature increase by continued evaporation. Especially in the dense microstructure of a concrete C90/105 sharp edges develop between the dried cracks and the surrounding still partially saturated material.

The final part of this thesis consists of a philosophy for fire-induced spalling, analysing the possibility of a thermal buckling mechanism (Timoshenko & Gere, 1961/2009) based on the numerical results presented. Compression of the heated surface layer, by (structural) restraint, causes cracks to develop in the transition zone with the unheated part of the cross-section.

Under these circumstances of continued fire exposure a layer is gradually separated by the formation of a fracture surface, making it susceptible to unstable deformations. Spalling is suggested to occur in case the compression force reaches the buckling load for a particular layer, causing the stored elastic energy to be suddenly released. These deliberations are illustrated by schematisation of a conceptual thermal buckling model. Reflected are key aspects such as the time-dependent compression force, the structural level of restraint and the thermal curvatures.

Several key features commonly observed for spalling (fib WP-4.3-1, 2007; Khoury & Anderberg, 2000) are subsequently discussed based on the premise of the thermal buckling mechanism. The sensitivity of high strength concrete to spalling is considered by the more uniform fracture surface, causing the thickness of a layer to reduce thereby increasing the buckling risk. External compressive loading is considered to also increase the risk of spalling by the formation of an initial crack pattern parallel to the heated surface. A final contribution discusses several possibilities to mitigate spalling with an alternative reasoning for the beneficial influence of adding polypropylene fibres to the concrete mixture. Also a modification of the surface of a concrete element is described and illustrated, aimed at reducing the sensitivity for the described buckling mechanism.

Samenvatting

Dit proefschrift heeft als onderwerp de na een ernstige brand waargenomen schade aan een betonelement of betonconstructie. Vooral de mogelijkheid tot het optreden van (explosief) spatten, als beschreven voor grootschalige branden in de tunnels gedurende de afgelopen decennia (CTSA, 1997; BEA-TT & RAIB, 2010), is in detail besproken. Spatten van beton kenmerkt zich door het afbreken van lagen aan het verhitte betonoppervlak, waar de term "explosief" duidt op het soms plotselinge en heftige karakter van het waargenomen fenomeen (Khoury & Anderberg, 2000). Algemeen gesteld zijn er twee hoofdtheorieën die het spatten verklaren, waarbij de eerste zich richt op het ontstaan van de poriëndrukken (Harmanthy, 1965) terwijl de tweede uitgaat van de thermische spanningen die ontstaan ten gevolge van de temperatuurgradiënt (Dougill, 1972). Op dit moment is de relatie tussen deze fysische en mechanische processen onvoldoende bekend. Bovendien, experimenteel onderzoek (RILEM TC-HTC, 2004) en recentelijke numerieke analyses (Tenchev, et al., 2001; Gawin, et al., 2003) waren voornamelijk gericht op het gedrag van beton bij verhoogde temperaturen. Het daadwerkelijke spatten wordt op dit moment alleen onderzocht door het doen van brandproeven op betonelementen (Dehn, et al., 2010). Echter, deze bleken onvoldoende te zijn om het mechanisme te identificeren.

In dit proefschrift is een conceptueel, op eindige elementen gebaseerd, spatmodel afgeleid dat gebruik maakt van een gekoppelde benadering tussen de poriëndruk en de breukmechanica. Voor een eenzijdig door brand belast betonelement wordt een verband gelegd tussen de lokale poriëndrukken, het globale constructieve gedrag en de ontwikkeling van het scheurpatroon. Om een theoretische basis te leggen zijn eerst de fysische en mechanische hoofdprocessen inzichtelijk gemaakt door afleiding van verschillende eenvoudige modellen. Door middel van de definitie van een gesloten systeem (Hettema, 1996) is de fysische relatie tussen temperatuur en poriëndruk ontwikkeling verduidelijkt. Een vergelijkbare benadering staat toe om de reductie van de gasdruk te kwantificeren, gebaseerd op de plotselinge toename van het volume gedurende de scheuropening. Ten behoeve van de mechanica is eerst het statische evenwicht van krachten gebaseerd op een temperatuurgradiënt (van Breugel, et al., 1998; Hartsuijker & Welleman, 2007). Hiermee worden de drukspanningen in de opgewarmde oppervlaktelaag en de trekbelasting in het midden van de doorsnede bepaald. De thermische uitzetting van het toeslagmateriaal wordt daarbij bevestigd als een belangrijke materiaal parameter (Eurocode 2, 2011b). Ook van belang zijn de doorsnede dimensies als mede de constructieve verhindering en belasting. Onder deze omstandigheden treedt een verzwakking van het beton op bij temperaturen hoger dan 500 ^{o}C (Dmitriyev, et al., 1969/1972).

Daarna is een op de continuïteit gebaseerde benadering gebruikt voor de definitie van de partiële differentiaalvergelijkingen die de fysische processen beschrijven. De ontwikkeling van de temperatuur en de poriëndruk zijn gekenmerkt door de conservering in een

representatief elementair volume van de thermische energie en de massa's van de water fasen respectievelijk (Bear, 1972/1988; Hassanizadeh & Gray, 1979b). Dit laatste gaat uit van een instantane ontwikkeling van een thermodynamisch evenwicht tussen de gas- en de vloeistof fasen (Tenchev, et al., 2001; Gawin, et al., 2003) als gedefinieerd door een desorptie isotherm (Pel & Huinink, 2007). Neumann randvoorwaarden beschrijven de interactie met de omliggende omgeving (Tenchev, et al., 2001; Gawin, et al., 2003). Verscheidene typerende en tijdsafhankelijke oplossingen worden bepaald met behulp van de eindige differentie methode. Deze resultaten illustreren het geforceerde drogen bij een constante temperatuur.

Het mechanische continuüm is algemeen bekend in de civiele techniek en derhalve alleen kort samengevat, beginnend met de balans van het lineaire moment (Spencer, 1980/2004; Wells, 2006). Deze translatie evenwichtsvergelijking is uitgebreid met de aanname van lineaire elasticiteit en het opleggen van de temperatuurrek als initiële verlenging (Timoshenko & Goodier, 1970). Zowel de aanname van een toestand met vlakke spanningen als vlakke rekken (Timoshenko & Goodier, 1970) worden besproken, waar het laatste wordt geacht van toepassing te zijn voor het constructieve element. Dit continuüm is daarna opnieuw gedefinieerd in polaire coördinaten om een simpele relatie tussen de druk in een porie en de spanningstoestand in het omringende materiaal te illustreren (Timoshenko & Goodier, 1970).

In het vervolg van dit proefschrift zijn beide continuüm-gebaseerde theorieën aangevuld om het spatmodel te vormen. Ten eerste is de temperatuur en de poriëndruk als deel van het spatmodel afgeleid. Beide conserveringsvergelijkingen zijn gekoppeld door de consumptie van thermische energie ten behoeve van de verdamping. Vervolgens wordt door minimalisatie van energie de zwakke vorm van dit systeem verkregen (van Kan, et al., 2008; Zienkiewicz, et al., 2005). Door Galerkin's methode ligt de eindige elementen definitie vast (van Kan, et al., 2008; Zienkiewicz, et al., 2005), met als aanname dat het poreuze materiaal zich kenmerkt als isotroop en homogeen. Voorts maakt de tijdsintegratie gebruik van een impliciete Euler achterwaartse methode (van Kan, et al., 2008) met de variabelen, temperatuur en capillaire druk, vastgelegd met een incrementele definitie. Neumann en periodieke randvoorwaarden worden gedefinieerd, waarbij de laatste zijn opgelegd langs de boven- en onderkant om een continu materiaal te verkrijgen (Segal, 2008). Ruimtelijke integratie maakt gebruik van willekeurig georiënteerde 2D driehoekige elementen met een lineaire basis (Felippa, 2004a).

Voor de berekening van de verschillende brandscenario's is eerst het eindige elementen model gevalideerd. Een goede overeenkomst is gevonden bij vergelijking van de afzonderlijk bepaalde temperatuur- en capillaire drukverdelingen met resultaten verkregen door middel van de eindige differentie methode. Daarna is de invloed van de betonsterkteklasse, het type brandbelasting en de omgevingsomstandigheden onderzocht. De hoogste gasdrukken, die een waarde bereiken van ongeveer 4.0 MPa, zijn gevonden voor beton C90/105 blootgesteld aan een koolwaterstofbrand. Bewijs van de vaak genoemde verstopping door vochtophoping (Harmanthy, 1965; Zeiml, et al., 2006) is alleen gevonden voor voornamelijk normale sterkte beton, zoals C25/30, initieel onderworpen aan een binnenklimaat. Dezelfde omstandigheden geven ook een kleine toename aan in de verzadigingsgraad aan de voorzijde van de poriëndrukgolf in C90/105. De laatste belangrijke observatie is dat in een open systeem de hoogste gasdrukken worden bereikt bij een minimale verzadigingsgraad tussen 0.2 en 0.4.

Het temperatuur- en gasdrukmodel is vervolgens uitgebreid om een anisotroop en heterogeen materiaal te verkrijgen. Zowel dichte- als poreuze materiaal schematiseringen zijn gedefinieerd waarbij de eerste het toeslagmateriaal beschrijft. De stenen zijn benaderend als ondoorlatend geschematiseerd, hetgeen eigenlijk materiaal discontinuïteiten introduceert aan de randen van de korrels. Het poreuze materiaal, dat de mortel en het grensvlak met het toeslagmateriaal beschrijft, wordt gekenmerkt door het proces van geforceerd drogen en blijft isotroop totdat zich een scheur ontwikkelt. Daarna wordt de stroming door de scheuren beschreven door middel van een substantiële toename van de permeabiliteit die is gerelateerd aan de opening en de richting (Bear, 1972/1988). Beide dienen te worden bepaald door breukmechanica gekoppeld aan de fysische parameters. Dit leidt tot materiaal discontinuïteiten in de beschrijving, welke de numerieke stabiliteit beïnvloeden. Variërende tijdstappen (Söderlind & Wang, 2006) en het invoegen van een vermindering van het anisotropische niveau langs de scheuren zijn gebruikt om de snelheid van de convergentie te verhogen. Boven de kritische temperatuur van water zorgt een verdere stabilisatie ervoor dat het droogproces continueert.

Beide aspecten zijn onderzocht door het blootstellen van een heterogene betondoorsnede aan verschillende brandscenario's. De invloed van het toevoegen van het toeslagmateriaal is beperkt en is alleen waargenomen bij een betonsterkteklasse C90/105 en voor de grootste korreldiameters. Onder deze omstandigheden wordt de gasdruk geschat toe te nemen aan de tegenoverliggende zijde van het brand belaste oppervlak. Echter, het meenemen van een initieel scheurpatroon met een constante opening beïnvloedt het geforceerde droogproces. De verkregen resultaten geven aan dat naast de transportmogelijkheden van de scheuren ook de permeabiliteit van het omliggende materiaal de mate van invloed bepaald. De simulaties voor C90/105 laten zien dat de dichtere microstructuur hogere beperkingen oplegt aan de stroming van de water fasen naar de scheuren.

Het tweede gedeelte van het spatmodel richt zicht op het mechanische gedrag van op brand belast beton. Eerst is voor het mechanische continuüm, door middel van energie minimalisatie, de zwakke vorm van de partiële differentiaalvergelijking bepaald (van Kan, et al., 2008; Zienkiewicz, et al., 2005). De eindige elementen definitie is verkregen door middel van Galerkin's methode (van Kan, et al., 2008; Zienkiewicz, et al., 2005), waarbij het materiaal initieel als isotroop en homogeen is gedacht. Het constructieve gedrag is benaderd door een vlakke rek toestand (Timoshenko & Goodier, 1970) met starre lichamen (Hartmann & Katz, 2007) gedefinieerd langs de boven- en onderkant om Bernoulli's hypothese (Hartsuijker & Welleman, 2007) op te leggen. Dit laatste introduceert geometrische niet-lineariteiten hetgeen vergt dat de variabelen, horizontale en verticale verplaatsingen, in incrementele vorm moeten worden gedefinieerd. Dirichlet en Neumann randvoorwaarden beschrijven de centraal geplaatste opleggingen, beiden gebaseerd op een vaste horizontale verplaatsing en constructieve interactie door veren en krachten (Bouma, 2000). Ruimtelijke integratie is verkregen door vergelijkbare 2D driehoekige elementen toe te passen.

De eindige elementen discretisatie is gevalideerd door vergelijking van de spanningen in de doorsnede en de verplaatsingen van de bovenste oplegging met de op het statisch evenwicht

gebaseerde resultaten. Een afdoende benadering is gevonden bij inachtneming van een toestand van vlakke spanningen. Op basis van de aanname van een toestand met vlakke rekken zijn de gevonden spanningen ongeveer 20 procent hoger. De incrementele definitie van de variabelen is ook gevalideerd, waarbij naast de bijkomende temperatuurrekken ook de herverdeling van de op stijfheidveranderingen gebaseerde spanningen worden beschouwd. Verschillende numerieke resultaten geven de invloed van de hoofdparameters weer met speciale aandacht voor de opgelegde starre lichamen. Voor C25/30 kan de uiterste drukspanning variëren tussen 60 en 100 MPa, bepaald door de materiaal eigenschappen, geometrie, brandcurve en constructieve omstandigheden.

Het breukmechanica model heeft een andere basis en discretiseert een deel van het constructieve element door een anisotroop en heterogeen materiaal. Drie driehoekig georiënteerde 1D staven benaderen samen de globale rekken (Prezemieniecki, 1968/1985; Blaauwendraad, 2004; Felippa, 2004a) waarbij hun doorsneden worden gedefinieerd door de interne hoogte. Een lineair elastische materiaal definitie, met in acht neming van zowel de temperatuurrekken als de door druk geïnitieerde spanningen, is gecombineerd met de constructieve randvoorwaarden. Deze 1D staven worden ook beschouwd als geometrisch niet-lineair, waardoor de incrementele vervormingen de statische evenwichtsvergelijkingen beïnvloeden (Bathe, 1986; Gavin, 2014). Bij de breukmechanica benadering wordt vervolgens aangenomen dat de initiatie en ontwikkeling van de scheuren ontstaat door het bros breken van de 1D staven (Schlangen, 1993; Vervuurt, 1997). Echter, gevonden werd dat voor herverdeling van de incrementele breukkrachten aanvullende gebogen vervormingen dienen te zijn inbegrepen, opgelegd door de definitie van 1D Bernoulli-Euler liggers, hetgeen leidt tot een traditioneel staafmodel (Schlangen, 1993; Vervuurt, 1997).

Bij validatie van het anisotrope eindige elementen model is een voldoende accurate benadering voor verschillende basis belastingsgevallen door middel van de 1D staven gevonden. Ten aanzien van het introduceren van de 1D liggers is waargenomen dat een verstijvend effect kan ontstaan in de mechanische respons in het geval dat te veel buigstijfheid is toegevoegd. Daarna is het breukmechanica gedrag uiteengezet door eerst alleen de temperatuurrekken als interne belasting te beschouwen. Onder deze omstandigheden werd gevonden dat het niveau van de constructieve verhindering uitermate belangrijk is. Zonder verhindering ervaart de heterogene doorsnede, vooral ten tijde van een koolwaterstof brandbelasting, heftige scheurvorming. Het niveau van de scheuren en vooral de scheuropening is voldoende om de thermische spanningen daarbij te relaxeren. Echter, toevoeging van constructieve partiële verhindering verandert het breukgedrag en thermische instabiliteiten ontstaan aan het betonoppervlak. Gelokaliseerde gebogen vervormingen ontstaan hetgeen gebaseerd is op de drukspanningen die aanwezig blijven in de opgewarmde oppervlaktelaag. Geanalyseerd wordt de invloed van de betonsterkteklasse, het type brandbelasting en de mogelijkheid tot externe drukbelasting. Het is gevonden dat deze het scheurpatroon in de aan brand bloot gestelde doorsnede als ook de vorm van de aan het oppervlak gesitueerde instabiliteiten bepalen. Deze resultaten zijn derhalve van significante waarde voor het numeriek analyseren van het spatmechanisme.

Uitbreiding van de koppeling tussen beide modellen om de door druk geïnitieerde spanningen toe te voegen onthult ook de invloed van de scheuren op het proces van geforceerd drogen. Het niveau van de scheurvorming in de opgewarmde oppervlaktelaag is voldoende om er voor te zorgen dat zich slechts beperkte gasdrukken ontwikkelen. Alleen in beton met als sterkteklasse C90/105 zijn verschillende drukpieken aanwezig, maar hun bijdrage aan de lokale spanningen kan worden beschouwd als gering. Ook is gevonden dat het geforceerde droogproces zich uitbreidt door de scheuren de doorsnede in. Dit wordt toegeschreven aan de capillaire drukgradiënt, welke het vloeibare water naar buiten drijft hetgeen de temperatuurstoename beïnvloedt door de zich continuerende verdamping. Vooral in de dichte microstructuur van een beton C90/105 ontstaan scherpe overgangen tussen de droge scheuren en het omringende nog steeds gedeeltelijk verzadigde materiaal.

Het laatste deel van dit proefschrift bestaat uit een filosofie omtrent het door brand geïnitieerde spatten, waarbij op basis van de gepresenteerde numerieke resultaten de mogelijkheid tot een thermisch knikmechanisme (Timoshenko & Gere, 1961/2009) is geanalyseerd. Samendrukking van de opgewarmde oppervlaktelaag, door (constructieve) verhindering, leidt tot scheurontwikkeling in de overgangszone naar het onverhitte deel van de doorsnede. Onder deze omstandigheden zal gedurende een brandbelasting een laag zich gedeeltelijk afscheiden door de vorming van een breukvlak, waardoor deze gevoelig wordt voor instabiele vervormingen. Spatten wordt verondersteld te gebeuren als de drukkracht de knikkracht bereikt voor deze specifieke laag, waardoor de opgeslagen elastische energie plotseling vrijkomt. Dit wordt onderbouwd door de schematisering van een conceptueel thermisch knikmodel. Weergegeven worden belangrijke aspecten, zoals de tijdsafhankelijke drukkracht, het niveau van de constructieve verhindering en de thermische krommingen.

Verschillende hoofdkenmerken, vaak waargenomen bij spatten (fib WP-4.3-1, 2007; Khoury & Anderberg, 2000), worden vervolgens besproken met het thermische knikmechanisme als uitgangspunt. De gevoeligheid van hoge sterkte beton voor spatten hangt samen met het vlakkere breukvlak, dat leidt tot een reductie van de dikte van een laag hetgeen het risico tot knikken vergroot. Een externe drukbelasting wordt ook geacht het risico op spatten te verhogen door de vorming van een initieel scheurpatroon parallel aan het verhitte oppervlak. Een laatste bijdrage bespreekt verschillende mogelijkheden spatten te verminderen met een alternatieve redenering omtrent de positieve invloed van de toevoeging van polypropylene vezels aan het betonmengsel. Ook beschreven en geïllustreerd wordt het effect van een aanpassing van het oppervlak van een betonelement om de gevoeligheid voor het beschreven knikmechanisme te verminderen.

References

Alonso, C. & Fernandez, L., 2004. Dehydration and rehydration processes of cement paste exposed to high temperature environments. *Journal of materials science,* 39(9), pp. 3015-3024.

Anderberg, Y. & Thelandersson, S., 1976. *Bulletin 54 - Stress and deformation characteristics of concrete at high temperatures - 2: experimental investigation and material behaviour model.* Lund, Sweden: Lund Institute of Technology - division of Structural Mechanics and Concrete Construction.

Bachmat, Y. & Bear, J., 1986. Macroscopic modelling of transport phenomena in porous media 1: the continuum approach. *Transport in Porous Media,* 1(3), pp. 213-240.

Baroghel-Bouny, V., 1994a. *Caractérisation microstructurale et hydrique des pâtes de ciment et des bétons ordinaires et á très hautes performances (in French).* Paris, France: PhD thesis École Nationale des Ponts et Chaussées.

Baroghel-Bouny, V., 1994b. *Caractérisation des pâtes de ciment et des bétons - méthodes, analyse, interprétations (in French).* Paris, France: Laboratoire Central des Ponts et Chaussées.

Baroghel-Bouny, V., Mainguy, M., Lassabatere, T. & Coussy, O., 1999. Characterization and identification of equilibrium and transfer moisture properties for ordinary and high-performance cementitious materials. *Cement and Concrete Research,* 29(8), pp. 1225-1238.

Barrett, R. et al., 1994. *Templates for the solution of linear systems: building blocks for iterative methods.* second edition red. Philadelphia, United States of America: Society for Industrial and Applied Mathematics.

Bastian, P., 2014. *Lecture notes - scientific computing with partial differential equations.* Heidelberg, Germany: Interdisciplinary Center for Scientific Computing - University of Heidelberg.

Bathe, K. J., 1986. *Lecture notes - finite element procedures for solids and structures, non linear analysis (reorder nr. 73-2200).* Cambridge, United States of America: Department of Mechanical Engineering - Massachusetts Institute of Technology.

Bažant, Z. P., 1997. *B. 10 - Analysis of pore pressure, thermal stress and fracture in rapidly heated concrete.* Gaithersburg, United States of America, NIST Special Publication 919 - Proceedings of the International Workshop on Fire Performance of High-Strength Concrete.

Bažant, Z. P., Chern, J. C. & Thonguthai, W., 1981. Finite element program for moisture and heat transfer in heated concrete. *Nuclear Engineering and Design,* 68(1), pp. 61-70.

Bažant, Z. P. & Oh, B. H., 1983. Crack band theory for fracture of concrete. *Matériaux et Constructions,* 16(3), pp. 155-177.

Bear, J., 1972/1988. *Dynamics of fluids in porous media.* New York, United States of America - New York, United States of America: Original published by American Elsevier Publishing Company, Inc. - republished by Dover Publications, Inc..

Bear, J. & Bachmat, Y., 1986. Macroscopic modelling of transport phenomena in porous media 2: applications to mass, momentum and energy transport. *Transport in Porous Media,* 1(3), pp. 241-269.

BEA-TT & RAIB, 2010. *Technical investigation report concerning the fire on Eurotunnel freight shuttle 7412 on 11 September 2008.* La Défense cedex, Paris, France / Derby, United Kingdom: Bureau d'enquêtes sur les accidents de transport terrestre / Rail Accident Investigation Branch.

Bentz, D. P., 2000. Fibers, percolation and spalling of High-Performance Concrete. *ACI Materials Journal,* 97(3), pp. 351-359.

Biersma, R., 2000. Profiel - Tunnel, veiligheid - Bij brand: windkracht zeven (in Dutch). *NRC Handelsblad - online version 1995-2001 - retro.nrc.nl*, 15 June.

Biot, M. A., 1965. *Mechanics of incremental deformations.* New York, United States of America: John Wiley & Sons Inc..

Blaauwendraad, J., 2003. *Lecture notes CT3130 - plates and slabs, volume 1: theory.* Delft, the Netherlands: Faculty of Civil Engineering and Geosciences - Delft University of Technology.

Blaauwendraad, J., 2004. *Lecture notes CT3130 - plates and slabs, volume 2: numerical methods.* Delft, the Netherlands: Faculty of Civil Engineering and Geosciences - Delft University of Technology.

Blom, C. B. M., 2009. *Practical FEM program coding.* Delft, the Netherlands: Concept.

Both, C., 2001. *TNO rapport 2001-CVB-R03264 - Brawat 3: Onderzoek naar afspatgedrag van een op druk belaste wand in afgezonken tunnels (in Dutch).* Rijswijk, the Netherlands: TNO Bouw.

Bouma, A. L., 2000. *Mechanica van Constructies: elasto-statica van slanke structuren (in Dutch).* Delft, the Netherlands: Delft University Press.

Bouwbesluit 2012, 2011. *Staatsblad van het Koninkrijk der Nederlanden, jaargang 2011 - 416: Besluit van 29 augustus 2011 houdende vaststelling van voorschriften met betrekking tot*

het bouwen, gebruiken en slopen van bouwwerken (in Dutch). the Netherlands: Ministerie van Binnenlandse Zaken en Koninkrijksrelaties.

Bouwdienst Rijkswaterstaat, 2003. *Tunnels in Nederland - Een nieuwe generatie - editors: J. van Beek, N. M. Ceton-O'Prinsen and G. L. Tan (in Dutch)*. Emmeloord, the Netherlands: Drukkerij Feiko Stevens.

Brekelmans, J. W. P. M., Breunese, A. J. & Vervuurt, A. H. J. M., 2008. *TNO report - Research on spalling of concrete during fire - 2007-D-R1329/B - part 1: test set-up, 2007-D-R1330/B - part 2: preparation of test specimen, 2007-D-R1331/B - part 3: fire tests, 2007-D-R1332/B - part 4: analysis.* Delft, the Netherlands: TNO Built Environment and Geosciences.

Breunese, A., 2001. *Tensile properties of concrete during fire.* Delft, the Netherlands: MSc thesis TU Delft.

Carré, H. et al., 2013. *Effect of compressive loading on the risk of spalling.* Paris, France, Proceedings of the 3rd International Workshop on Concrete Spalling due to Fire Exposure.

Castellote, M. et al., 2004. Composition and microstructural changes of cement pastes upon heating as studied by neutron diffraction. *Cement and Concrete Research,* 34(9), pp. 1633-1644.

Castillo, C. & Durrani, A. J., 1990. Effect of transient high temperature on high strength concrete. *ACI Materials Journal,* 87(1), pp. 47-53.

CBBN fire proofing int., 2005. *Fire resistant plaster coating protects bored tunnels - 04.2005/BJ/500.* Zwijndrecht, the Netherlands: CBBN fire proofing int..

Černý, R. et al., 2003. Thermal and hygric properties of Portland cement mortar after high-temperature exposure combined with compressive stress. *Cement and Concrete Research,* 33(9), pp. 1347-1355.

Clement, F., 2010. *Fire protection options for concrete tunnel linings.* Frankfurt am Main, Germany, Proceedings of the fourth International Symposium on Tunnel Safety and Security.

Copier, W. J., 1979. The spalling of normalweight and lightweight concrete on exposure to fire. *Heron,* 24(2).

Çopuroğlu, O. & Schlangen, E., 2008. Modeling of frost salt scaling. *Cement and Concrete Research,* 38(1), pp. 27-39.

COT, 2008. *Brand bij bouwkunde (in Dutch) - COT report.* The Hague, the Netherlands: Institute for safety and crisis management.

Couture, F., Jomaa, W. & Puiggali, J. R., 1996. Relative permeability relations: a key factor for a drying model. *Transport in porous media,* 23(3), pp. 303-335.

Cruz, C. R. & Gillen, M., 1980. Thermal expansion of Portland cement paste, mortar and concrete at high temperatures. *Fire and materials,* 4(2), pp. 66-70.

CTSA, 1997. *Inquiry into the fire on Heavy Goods Vehicle shuttle 7539 on 18 November 1996.* London, United Kingdom: Channel Tunnel Safety Authority.

Dal Pont, S., 2004. *Lien entre la perméabilité et l'endommagement dans les bétons à haute température (in French).* Champs-sur-Marne, France: PhD thesis Ecole Nationale des Ponts et Chaussees.

Davey, N. & Ashton, L. A., 1953. *NBS research paper No. 12 - Investigations on building fires - part V: fire tests on structural elements.* London, United Kingdom: National Building Studies.

Davie, C. T., Pearce, C. J. & Bićanić, N., 2006. Coupled heat and moisture transport in concrete at elevated temperatures - effects of capillary pressure and adsorbed water. *Numerical Heat Transfer, Part A: Applications,* 49(8), pp. 773-763.

Davie, C. T., Pearce, C. J. & Bićanić, N., 2010. A fully generalised, coupled, multi-phase, hygro-thermo-mechanical model for concrete. *Materials and Structures,* 43(1), pp. 13-33.

de Borst, R., 1986. *Non-linear analysis of frictional materials.* Delft, the Netherlands: PhD thesis TU Delft.

de Borst, R., 1991. Simulation of strain localization: a reappraisal of the Cosserat continuum. *Engineering computations,* 8(4), pp. 317-332.

de Borst, R. & Sluys, L. J., 1991. Localisation in a Cosserat continuum under static and dynamic loading conditions. *Computer methods in applied mechanics and engineering,* 90(1-3), pp. 805-827.

de Feijter, M. P. & Breunese, A. J., 2007. *Efectis rapport 2007-Efectis-R0894 - Onderzoek brand parkeergarage Lloydstraat, Rotterdam (in Dutch) - Client: Safety Region Rotterdam-Rijnmond, Departement of Public Safety.* Rijswijk, the Netherlands: Efectis the Netherlands BV.

Dehn, F. et al., 2010. *Bast Heft B73 - Brand- und Abplatzverhalten von Faserbeton in Straßentunneln (in German) - Gesellschaft für Materialforschung und Prüfungsanstalt für das Bauwesen, Leipzig, Germany.* Bergisch Gladbach, Germany: Bundesanstalt für Straßenwesen.

den Drijver, K. J. et al., 2003. *Document 6917-2003-0034 - Aanvullend advies tunnel technische installaties Betuweroute (in Dutch).* Utrecht, the Netherlands: Bouwdienst Rijkswaterstaat.

Diederichs, U. et al., 1987. *Sonderforschungsbereich 148: Brandverhalten von Bauteilen - Teilprojekt B3: Hochtemperaturverhalten von Festbeton - Arbeitsbericht 1984-1986 (in German).* Braunschweig, Germany: TU Braunschweig.

Dmitriyev, A. P., Kuzyayev, L. S., Protasov, Y. I. & Yamshchikov, V. S., 1969/1972. *NASA technical translation - NASA TT F-684: physical properties of rocks at high temperatures.* Moscow, Russia / Washington D.C., United States of America: "Nedra" Press / National Aeronautics and Space Administration.

Dos Reis, F. & Ganghoffer, J. F., 2011. *Advanced Structured Materials 7 - Mechanics of Generalized Continua, editors: H. Altenbach, G. A. Maugin, V. Erofeev - Chapter 9, construction of micropolar continua from the homogenization of repetitive planar lattices.* Berlin, Germany: Springer Verlag.

Dougill, J. W., 1972. Modes of failure of concrete panels exposed to high temperatures. *Magazine of Concrete Research,* 24(79), pp. 71-76.

Dullemond, K. & Peeters, K., 1991-2010. *Introduction into tensor calculus.* Heidelberg, Germany: Institute of Theoretical Astrophysics - Heidelberg University.

Edvardsen, C. K., 2004. *Deterioration modelling model verification through in-situ tests Great Belt Link tunnel (Denmark).* Prague, Czech Republic, Proceedings of the 1st International Symposium on Safe & Reliable Tunnels, Innovative European Achievements.

Emperger, F., 1921. *Handbuch für Eisenbetonbau - zweite neuarbeitete Auflage, achter Band: Feuersicherheit, Bauunfälle (in German).* Berlin, Germany: Verlag von Wilhelm Ernst & Sohn.

England, G. L. & Khoylou, N., 1995. Moisture flow in concrete under steady state non-uniform temperature states: experimental observations and theoretical modelling. *Nuclear Engineering and Design,* 156(1-2), pp. 83-107.

Erich, S. J. F. et al., 2008. Validation of FEM models describing moisture transport in heated concrete by Magnetic Resonance Imaging. *Heron,* 53(4), pp. 225-246.

Eurocode 1, 2011a. *Actions on structures - part 1-2: General actions - actions on structures exposed to fire - NEN-EN 1991-1-2+C1: 2011 - NL version (in Dutch).* Brussels, Belgium: European Committee for Standardization.

Eurocode 1, 2011b. *National annex to NEN-EN 1991-1-2+C1: 2011 - NL version (in Dutch).* Brussels, Belgium: European Committee for Standardization.

Eurocode 2, 2011a. *Design of concrete structures - part 1-1: General rules and rules for buildings - NEN-EN 1992-1-1 + C2: 2011 - NL version (in Dutch).* Brussels, Belgium: European Committee for Standardization.

Eurocode 2, 2011b. *Design of concrete structures - part 1-2: General rules - structural fire design - NEN-EN 1992-1-2+C1:2011 - NL version (in Dutch).* Brussels, Belgium: European Committee for Standardization.

Feenstra, P. H., 1993. *Computational aspects of biaxial stress in plain and reinforced concrete.* Delft, the Netherlands: PhD thesis TU Delft.

Feldman, R. F. & Sereda, P. J., 1968. A model for hydrated Portland cement paste as deduced from sorption-length change and mechanical properties. *Matériaux et Constructions,* 1(6), pp. 509-520.

Felicetti, R. & Gambarova, P. G., 1998. On the residual tensile properties of High Performance Siliceous Concrete exposed to high temperature. *Special volume in honour of Z.P. Bazant's 60th anniversary - Prague, March 27-28 - Ed. Hermes (Paris, France),* pp. 167-186.

Felicetti, R., Lo Monte, F. & Pimienta, P., 2012. *The Influence of pore pressure on the apparent tensile strength of concrete.* Zurich, Switzerland, Proceedings of the 7th International Conference on Structures in Fire.

Felippa, C. A., 2004a. *Lecture notes course ASEN 5007 - introduction to finite element methods.* Boulder, United States of America: Department of Aerospace Engineering Sciences and Center for Aerospace Structures - University of Colorado.

Felippa, C. A., 2004b. *Appendices course ASEN 5007 - introduction to finite element methods.* Boulder, United States of America: Department of Aerospace Engineering Sciences and Center for Aerospace Structures - University of Colorado.

Felippa, C. A., 2014. *Lecture notes course ASEN 6107 - non linear finite element methods.* Boulder, United States of America: Department of Aerospace Engineering Sciences and Center for Aerospace Structures - University of Colorado.

Fellinger, J. H. H., 2004. *Shear and anchorage behaviour of fire exposed hollow core slabs.* Delft, the Netherlands: PhD thesis TU Delft - Delft University Press.

Fellinger, J. H. H. & Breunese, A. J., 2005. *TNO report 2005-CVB-R0299 - Evaluation of the fire test procedure for the spalling behaviour of concrete.* Delft, the Netherlands: TNO Building and Construction Research.

FHWA, 2006. *Report FHWA-PL-06-016 - Underground Transportation Systems in Europe - Safety, Operations and Emergency Response.* Washington, United States of America: Federal Highway Administration.

fib WP-4.3-1, 2007. *Fire design of concrete structures: materials, structures and modelling - Working Party, state of art report.* Lausanne, Switzerland: International Federation for Structural Concrete (fib).

Fischer, T. E., 2009. *Materials science for engineering students.* Amsterdam, the Netherlands / Waltham, United States of America: Elsevier / Academic press.

Flynn, D. R., 1999. *NIST GCR99-767 - Response of high performance concrete to fire conditions: review of thermal property data and measurement techniques.* Millwood, United States of America: United States Department of Commerce - Technology Administration - National Institute of Standards and Technology.

FSV, 2004. *Brandbeständigkeit von Faser-, Stahl- und Spannbeton - Schriftenreihe Straßenforschung - heft 544 (in German).* Vienna, Austria: Österreichische Forschungsgemeinschaft Straße und Verkehr, Republik Österreich, Bundesministerium für Verkehr, Innovation und Technologie, Bundesstraßenverwaltung.

Gavin, H. P., 2014. *Lecture notes course CEE 421L - matrix structural analysis, geometric stiffness effects in 2D trusses.* Durham, United States of America: Department of Civil and Environmental Engineering - Duke University.

Gawin, D., Majorana, C. E. & Schrefler, B. A., 1999. Numerical analysis of hygro-thermal behaviour and damage of concrete at high temperature. *Mechanics of cohesive-frictional materials,* 4(1), pp. 37-74.

Gawin, D., Pesavento, F. & Schrefler, B. A., 2003. Modelling of hygro-thermal behaviour of concrete at high temperature with thermo-chemical and mechanical material degradation. *Computer Methods in Applied Mechanics and Engineering,* 192(13-14), pp. 1731-1771.

Gawin, D., Pesavento, F. & Schrefler, B. A., 2006. Towards prediction of the thermal spalling risk through a multi-phase porous media model for concrete. *Computer Methods in Applied Mechanics and Engineering,* 195(41-43), pp. 5707-5729.

Genuchten, M. T., 1980. A closed form equation for predicting the hydraulic conductivity of unsaturated soils. *Soil Science Society of America Journal,* 44(5), pp. 892-898.

Giaccio, G. & Zerbino, R., 1998. Failure mechanism of concrete - combined effects of coarse aggregates and strength level. *Advanced Cement based Materials,* 7(2), pp. 41-48.

Granger, R. A., 1985/1995. *Fluid mechanics.* New York, United States of America - New York, United States of America: Original published by Holt, Rinehart and Winston - republished by Dover Publications Inc..

Gray, W. G. & Schrefler, B. A., 2001. Thermodynamic approach to effective stress in partially saturated porous media. *European Journal of Mechanics - A/Solids,* 20(4), pp. 521-538.

Gross, H., 1973. *On high temperature creep of concrete.* Berlin, Germany, Proceedings of the 2nd International Conference on Structural Mechanics in Reactor Technology - vol. 3 - part H 6/5.

Haack, A., 2002. Current safety issues in traffic tunnels. *Tunnelling and Underground Space Technology,* 17(2), pp. 117-127.

Hager, J. G., 2004. *Comportement à haute température des bétons à haute performance - évolution des principales propriétés mécaniques (in French).* Champs-sur-Marne, France: PhD thesis Ecole Nationale des Ponts et Chaussées.

Harmanthy, T. Z., 1965. Effect of moisture on the fire endurance of building materials. *ASTM Special Technical Publication 385,* pp. 74-95.

Hartmann, F. & Katz, C., 2007. *Structural analysis with finite elements.* Berlin Heidelberg, Germany: Springer-Verlag.

Hartsuijker, C. & Welleman, J. W., 2006. *Engineering mechanics - volume 1 - equilibrium.* Dordrecht, the Netherlands: Springer.

Hartsuijker, C. & Welleman, J. W., 2007. *Engineering mechanics - volume 2 - stresses, strains, displacements.* Dordrecht, the Netherlands: Springer.

Hassanizadeh, M. & Gray, W. G., 1979a. General conservation equations for multi-phase systems 1: averaging procedure. *Advances in Water Resources,* Volume 2, pp. 131-144.

Hassanizadeh, M. & Gray, W. G., 1979b. General conservation equations for multi-phase systems 2: mass, momenta, energy and entropy equations. *Advances in Water Resources,* Volume 2, pp. 191-203.

Hassanizadeh, M. & Gray, W. G., 1980. General conservation equations for multi-phase systems 3: constitutive theory for porous media flow. *Advances in Water Resources,* 3(1), pp. 25-40.

Heijboer, J., van den Hoonaard, J. & van de Linde, F. W. J., 2004. *The Westerschelde tunnel - Approaching limits.* Lisse, the Netherlands: Swets & Zeitlinger B.V..

Herrmann, H. J. & Roux, S., 1990. *Statistical models for the fracture of disordered media.* North-Holland: Elsevier Science Publishers B.V..

Hettema, M. H. H., 1996. *The thermo-mechanical behaviour of sedimentary rock: an experimental study.* Delft, the Netherlands: PhD thesis TU Delft.

Hettema, M. H. H., Wolf, K.-H. A. A. & de Pater, C. J., 1998. The influence of steam pressure on thermal spalling of sedimentary rock: theory and experiments. *International Journal of Rock Mechanics and Mining Sciences,* 35(1), pp. 3-15.

Hillerborg, A., Modéer, M. & Petersson, P. E., 1976. Analysis of crack formation and crack growth in concrete by means of fracture mechanics and finite elements. *Cement and Concrete Research,* 6(6), pp. 773-782.

Horvath, J., Schneider, U. & Diederichs, U., 2004. *Heft 11 - Beiträge zum Abplatzverhalten von Hochleistungsbetonen (in German).* Vienna, Austria: TU Vienna, Institute for Building Materials, Buildings Physics and Fire Protection.

Ichikawa, Y. & England, G. L., 2004. Prediction of moisture migration and pore pressure build-up in concrete at high temperatures. *Nuclear Engineering and Design,* 228(1-3), pp. 245-259.

IREX, 2005. *Synthèse des travaux du projet national BHP 2000 sur les bétons à hautes performances - editor: Presses de l'Ecole Nationale des Ponts et Chaussées (in French).* Paris, France: Institut pour la Recherche appliquée et l'Expérimentation en génie civil.

Jansson, R. & Boström, L., 2008. *SP report 2008:52 - Spalling of concrete exposed to fire.* Borås, Sweden: SP Technical Research Institute of Sweden.

Jones, R. M., 2006. *Buckling of bars, plates and shells.* Blackburg, United States of America: Bull Ridge Publishing.

Kalifa, P., Chéné, G. & Gallé, C., 2001. High-temperature behaviour of HPC with polypropylene fibres - From spalling to microstructure. *Cement and Concrete Research,* 31(10), pp. 1487-1499.

Kalifa, P., Mennetau, F. D. & Quenard, D., 2000. Spalling and pore pressure in HPC at high temperatures. *Cement and Concrete Research,* 30(12), pp. 1915-1927.

Kelly, P., 2008. *Lecture notes - Solid Mechanics, part 1 - an introduction to solid mechanics, version 4.* Auckland, New Zealand: Faculty of Engineering - University of Auckland.

Khoury, G. A., 2006a. Strain of heated concrete during two thermal cycles - part 1: strain over two cycles, during first heating and at subsequent constant temperature. *magazine of Concrete Research,* 58(6), pp. 367-385.

Khoury, G. A., 2006c. Strain of heated concrete during two thermal cycles - part 3: isolation of strain components and strain model development. *magazine of Concrete Research,* 58(7), pp. 421-435.

Khoury, G. A., 2008a. Passive fire protection of concrete structures. *Structures & Buildings,* 161(3), pp. 135-145.

Khoury, G. A., 2008b. Polypropylene fibres in heated concrete part 2: pressure relief mechanisms and modelling criteria. *Magazine of Concrete Research,* 60(3), pp. 189-204.

Khoury, G. A. & Anderberg, Y., 2000. *Fire Safety Design - concrete spalling review.* Sweden: Report submitted to the Swedish National Road Administration.

Khoury, G. A. & Willoughby, B., 2008. Polypropylene fibres in heated concrete part 1: molecular structure and materials behaviour. *Magazine of Concrete Research,* 60(2), pp. 125-136.

Koenders, E. A. B., 1997. *Simulation of volume changes in hardening cement-based materials.* Delft, the Netherlands: PhD thesis TU Delft.

Koenders, E. A. B. & Pel, L., 2004. *Explosive spalling of concrete: towards a model for fire resistant design of concrete elements - Application document for funding by the Dutch Technology Foundation STW.* Delft, the Netherlands - Eindhoven, the Netherlands: Delft University of Technology, Eindhoven University of Technology.

Kordina, K., 1963. *Heft 2 - Das Verhalten von Stahlbeton- und Spannbetonbauteilen unter Feuerangriff (in German).* Braunschweig, Germany: Institut für Baustoffkunde und Stahlbetonbau der Technischen Hochschule Braunschweig.

Kordina, K. E. H. & Klingsch, W., 1983. *CIDECT- Report nr. 15 C1/C2-83/27 - Fire resistance of composite columns of concrete filled hollow sections - Part I: Report, Part II: Documentation.* Ascot, United Kingdom: Information Centre The Steel Construction Institute.

Kordina, K., Ehm, H. & von Postel, R., 1975. *Heft 230 - Erwärmungsvorgänge an balkenartigen Stahlbetonbauteilen unter Brandbeanspruchung (in German) - Deutscher Ausschuss für Stahlbeton.* Berlin, Germany: Wilhelm Ernst & Sohn.

Kotz, J. C., Treichel, P. M. & Townsend, J. R., 2009. *Chemistry and chemical reactivity.* Belmont, United States of America: Thomson, Brooks/Cole.

Krebs, R. E., 2003. *The basics of earth science.* Westport, United States of America: Greenwood Press.

Lagace, P. A., 2001. *Lecture notes MIT-16.20 - Aeronautics and Astronautics - Structural Mechanics, unit 9 - effects of the environment.* Cambridge, United States of America: Massachusetts Institute of Technology.

Lemaire, A. D. & Meeussen, V. J. A., 2008. *Efectis rapport - 2008-Efectis-R0425 - Effects of water mist on real large tunnel fires: experimental determination of BLEVE-risk and tenability during growth and suppression, sponsor: TNO and Rijkswaterstaat.* Rijswijk, the Netherlands: Efectis the Netherlands BV.

Liu, X., 2006. *Microstructural investigation of Self Compacting Concrete and High Performance Concrete during hydration and after exposure to high temperatures.* Tongji, China - Gent, Belgium: PhD thesis - Tongji University, University Gent.

Li, Z., 2011. *Advanced concrete technology.* Hoboken, United States of America: John Wiley & Sons.

Lönnermark, A., 2005. *On the characteristics of fires in tunnels.* Lund, Sweden: PhD thesis Lund University.

Lottman, B. B. G., 2007. *Fire in bored tunnels - structural behaviour, during fire conditions, of bored tunnels made with a concrete segmental lining.* Delft, the Netherlands: MSc thesis TU Delft.

Lottman, B. B. G. et al., 2008. Brand in boortunnels, constructief gedrag van boortunnels tijdens brand (in Dutch). *Cement,* Issue 2, pp. 70-73.

Lottman, B. B. G., Koenders, E. A. B., Blom, C. B. M. & Bouwman, V., 2007. *A model for the structural behaviour of bored tunnels during fire.* Coimbra, Portugal, Proceedings of the workshop Fire Design of Concrete Structures.

Lottman, B. B. G., Koenders, E. A. B., Blom, C. B. M. & Walraven, J. C., 2013. *Spalling of concrete due to fire exposure: a coupled fracture mechanics and pore pressure approach.* Paris, France, Proceedings of the 3rd International Workshop on Concrete Spalling due to Fire Exposure.

Lottman, B. B. G., Koenders, E. A. B., Blom, C. B. M. & Walraven, J. C., 2015. *Spalling of fire exposed concrete based on a coupled material description: an overview.* Leipzig, Germany, Proceedings of the 4th International Workshop on Concrete Spalling due to Fire Exposure.

Lottman, B. B. G., Koenders, E. A. B. & Walraven, J. C., 2009. *Towards a model for fire resistant design of concrete elements.* Leipzig, Germany, Proceedings of the 1st International Workshop on Concrete Spalling due to Fire Exposure.

Lottman, B. B. G., Koenders, E. A. B. & Walraven, J. C., 2011. *Macro-scale spalling model: a fracture mechanics versus pore pressure approach.* Delft, the Netherlands, Proceedings of the 2nd International RILEM Workshop - Concrete Spalling due to Fire Exposure.

Mehta, P. K. & Monteiro, P. J. M., 2006. *Concrete: microstructure, properties and materials.* New York, United States of America: McGraw-Hill.

Meyer-Ottens, C., 1972. *Zur Frage der Abplatzungen an BetonBauteilen aus NormalBeton bei Brandbeanspruchung (in German).* Braunschweig, Germany: PhD thesis TU Braunschweig.

Meyer-Ottens, C., 1975. *Heft 248 - Zur Frage der Abplatzungen an Bauteilen aus Beton bei Brandbeanspruchungen (in German) - Deutscher Ausschuss für Stahlbeton - Technische Universität Braunschweig.* Berlin, Germany: Verlag W.Ernst & sohn.

Mindeguia, J. C., 2008. *Caractérisation thermo-hydrique et comportement au feu de deux bétons: analyse des risques d'instabilités (in French).* Nancy, France, Proceedings of the 26th Rencontres Universitaires de Génie Civil.

Mindeguia, J. C., 2009. *Contribution expérimentale a la compréhension des risques d'instabilité thermique des bétons (in French).* Pau, France: PhD thesis l'université de Pau et Pays de L'Adour.

Mindeguia, J. C., Carré, H., La Borderie, C. & Pimienta, P., 2012. *Analyse expérimentale du risque d'instabilité thermique des bétons en situation d'incendie (in French).* Chambéry, France, Proceedings of the 30st Rencontres Universitaires de Génie Civil.

Moran, J. M. & Shapiro, H. N., 2004. *Fundamentals of Engineering Thermodynamics - 5th Edition.* Hoboken, United States of America: John Wiley & Sons Inc..

Müller, H. S. & Rubner, K., 1994. *High-strength concrete - microstructural characteristics and related durability aspects.* Vienna, Austria, Proceedings of the International RILEM workshop on Durability of High Performance Concrete, editor: H. Sommer.

Nakamura, H. et al., 2011. *Simulation about effect on explosion spalling of thermal stress and vapor pressure.* Delft, the Netherlands, Proceedings of the 2nd International RILEM workshop on Concrete Spalling due to Fire Exposure.

Nakayama, Y. & Boucher, R. F., 1998/2000. *Introduction to fluid mechanics (revised).* Tokyo, Japan - Oxford, United Kingdom: Original published by Yokendo Co. Ltd (in Japanese). - republished by Butterworth-Heinemann (translated to English).

Neuzil, C. E. & Tracy, J. V., 1981. Flow through fractures. *Water resources research,* 17(1), pp. 191-199.

Noda, N., Hetnarski, R. B. & Tanigawa, Y., 2003. *Thermal stresses.* New York, United States of America: Taylor & Francis.

Ožbolt, J., Bošnjak, J., Periškić, G. & Grosse, C., 2011. *Numerical simulation of concrete exposed to high temperature-damage and explosive spalling.* Delft, the Netherlands, Proceedings of the 2nd International RILEM workshop on Concrete Spalling due to Fire Exposure.

Pel, L. & Huinink, H., 2007. *Lecture notes course 3F250 - Transport in porous media.* Eindhoven, the Netherlands: TU Eindhoven, Department of Applied Physics.

Phan, L. T., 1996. *NIST report NISTIR 5934 - Fire Performance of High-Strength Concrete: a report of the State-of-the-Art.* Gaithersburg, United States of America: National Institute of Standards and Technology.

Phan, L. T., 2008. Pore pressure and explosive spalling in concrete. *Materials and Structures,* 41(10), pp. 1623-1632.

Pimienta, P., 2001. *Cahiers du CSTB, nr. 3353 - Études et Recherche - Évolution des caractéristiques des BHP soumis à des températures élevées, résistance en compression et modules d'élasticité (in French).* Paris, France: Centre Scientifique et Technique du Bâtiment.

Pimienta, P. et al., 2010. *Fire protection of concrete structures exposed to fast fires.* Frankfurt am Main, Germany, Proceedings of the 4th International Symposium on Tunnel Safety and Security.

Poděbradská, J., Pavlík, J., Toman, J. & Černý, R., 2003. *Specific heat capacity of cementitious composites in high-temperature range.* Kočovce, Slovakia, Proceedings of Thermophysics.

Poyet, S., 2009. Experimental investigation of the effect of temperature on the first desorption isotherm of concrete. *Cement and Concrete Research,* 39(11), pp. 1052-1059.

Prezemieniecki, J. S., 1968/1985. *Theory of matrix structural analysis.* New York, United States of America - New York, United States of America: Original published by McGraw-Hill Book Company, Inc. - republished by Dover Publications, Inc..

Probst, E., 1917. *Vorlesungen über Eisenbeton - erster Band (in German).* Berlin, Germany: Verlag von Julius Springer.

Promat International N.V., 2003. *Technical note on the fire protection of tunnel structures and services - 11/2003.* Tissel, Belgium: Promat International N.V..

Rastiello, G., Boulay, C. & Dal Pont, S., 2013. *Real-time evolution water permeability of a localized crack in concrete under loading.* Toledo, Spain, Proceedings of the 8th International Conference on Fracture Mechanics of Concrete and Concrete Structures, FraMCos-8.

Richter, E., 1993. *Heißgasentwicklung bei Tunnelbränden mit Straßen- und Schienenfahrzeugen - Vergleich gemessener und in Vorschriften enthaltener Temperatur-Zeit-Verläufe (in German).* Hamburg, Germany, Proceedings of the STUVA Tagung '93.

Richter, R. et al., 2013. *Measurement systems to detect the time-dependent development of concrete spalling under fire exposure.* Paris, France, Proceedings of the 3rd International Workshop of Concrete Spalling due to Fire Exposure.

RILEM TC-HTC, 2004. *Behaviour of concrete at high temperatures - Technical Committee, state of art report - part 1 - ordinary concrete.* Bagneux, France: RILEM publications S.A.R.L..

Robertson, E. C., 1988. *USGS - Open-File Report 88-441 - Thermal properties of rocks.* Reston, United States of America: United States Department of the Interior Geological Survey.

Rots, J. G., 1988. *Computational modeling of concrete fracture.* Delft, the Netherlands: PhD thesis TU Delft.

Roylance, D., 2001. *Transformation of stresses and strains.* Cambridge, United States of America: Department of Materials Science and Engineering, Massachusetts Institute of Technology.

RWS, 2011. *Richtlijn Ontwerp Kunstwerken - ROK versie 1.0 (in Dutch).* Utrecht, the Netherlands: Rijkswaterstaat Dienst Infrastructuur.

Saito, H., 1965. *Explosive spalling of prestressed concrete in fire.* Braunschweig, Germany, Proceedings of a Symposium on Fire Resistance of Prestressed Concrete.

Schlangen, E., 1993. *Experimental and numerical analysis of fracture processes in concrete.* Delft, the Netherlands: PhD thesis TU Delft.

Schlangen, E. & Garboczi, E. J., 1997. Fracture simulations of concrete using lattice models: computational aspects. *Engineering Fracture Mechanics,* 57(2/3), pp. 319-332.

Schneider, U., 1979. *Ein Beitrag zur Frage des Kriechens und der Relaxation von Beton unter hohen Temperaturen (in German).* Braunschweig, Germany: Habilitation TU Braunschweig.

Schneider, U., 1982. *Heft 337 - Verhalten von Beton bei hohen Temperaturen, Behaviour of concrete at high temperatures (in German, in English) - Deutscher Ausschuss für Stahlbeton - Technische Universität Braunschweig, Braunschweig, Germany.* Berlin, Germany: Verlag W.Ernst und sohn.

Schneider, U., 1991. Introduction into fire safety in Nuclear Power Plants. *Nuclear Engineering and Design,* 125(3), pp. 289-295.

Schneider, U., Diederichs, U. & Rosenberger, W., 1980. *Sonderforschungsbereich 148, Brandverhalten von Bauteilen - Arbeitsbericht 1978-1980 - teil II: Hochtemperaturverhalten von Festbeton (in German).* Braunschweig, Germany: TU Braunschweig.

Schrefler, B. A., Khoury, G. A., Gawin, D. & Majorana, C., 2002. Thermo-hydro-mechanical modelling of high performance concrete at high temperatures. *Engineering Computations,* 19(7), pp. 787-819.

Segal, A., 2008. *Lecture Notes J.M. Burgerscentrum, Research School for Fluid Mechanics - finite element methods for the incompressible Navier-Stokes equations.* Delft, the Netherlands: Faculty of Electrical Engineering, Mathematics and Computer Science - Delft University of Technology.

Shorter, G. W. & Harmathy, T. Z., 1961. Discussion: the fire resistance of prestressed concrete beams - paper No. 6444 - vol. 17, 1960. *Proceedings Institute of Civil Engineers,* 20(2), pp. 313-315.

Söderlind, G. & Wang, L., 2006. Adaptive time-stepping and computational stability. *Journal of Computational and Applied Mathematics,* 185(2), pp. 225-243.

Spencer, A. J. M., 1980/2004. *Continuum mechanics.* Essex, United Kingdom - New York, United States of America: Original published by Longman Group UK limited - republished by Dover publications, Inc..

Taerwe, L., 2007. *From member design to global structural behaviour.* Coimbra, Portugal, Proceedings of the International Workshop Fire Design of Concrete Structures.

TCRP & NCHRP, 2006. *Making transportation tunnels safe and secure - TCRP report 86, volume 12 / NCHRP report 525, volume 12.* Washington, United States of America: Transit Cooperative Research Program / National Cooperative Highway Research Program.

Tenchev, R. T., Li, L. Y. & Purkiss, J. A., 2001. Finite element analysis of coupled heat and moisture transfer in concrete subjected to fire. *Numerical Heat Transfer, Part A: Applications,* 39(7), pp. 685-710.

Thelandersson, S., 1971. *Effect of high temperatures on tensile strength of concrete.* Lund, Sweden: Lund Institute of Technology - division of Structural Mechanics and Concrete Construction - Neostyled pp. 27.

Thomas, F. G. & Webster, C. T., 1953. *NBS research paper No. 18 - Investigations on building fires - part VI: the fire resistance of reinforced concrete columns.* London, United Kingdom: National Building Studies.

Timoshenko, S. P. & Gere, J. M., 1961/2009. *Theory of elastic stability, second edition.* New York, United States of America and London, United Kingdom - Minealo, New York, United States of America: Original published by McGraw-Hill Book Company, Inc. - republished by Dover publications, Inc..

Timoshenko, S. P. & Goodier, J. N., 1970. *Theory of Elasticity.* Singapore: Mcgraw-Hill Book Company.

Ulm, F. J., Acker, P. & Lévy, M., 1999b. The "Chunnel" fire II: analysis of concrete damage. *Journal of Engineering Mechanics,* 125(3), pp. 283-289.

Ulm, F. J., Coussy, O. & Bažant, Z. P., 1999a. The "Chunnel" fire I: chemoplastic softening in rapidly heated concrete. *Journal of Engineering Mechanics,* 125(3), pp. 272-282.

van Breugel, K., Braam, C. R., van der Veen, C. & Walraven, J. C., 1998. *Betonconstructies onder temperatuur- en krimpvervormingen BP2 (in Dutch).* Boxtel, the Netherlands: Aeneas.

van der Heijden, G. H. A., 2011. *NMR imaging of moisture inside heated porous building materials.* Eindhoven, the Netherlands: PhD thesis TU Eindhoven.

van Kan, J., Segal, A. & Vermolen, F., 2008. *Numerical methods in scientific computing.* Delft, the Netherlands: VSSD.

van Mier, J. G. M., 1997. *Fracture processes of concrete - assessment of material properties for fracture models.* Boca Raton, United States of America: CRC Press Inc..

Vermolen, F., 2005. *Lecture notes WI4012TA - version 1.1 - Introduction into Numerical Modelling: the Finite Element Method.* Delft, the Netherlands: Department of Applied Earth Sciences - Delft University of Technology.

Vervuurt, A. H. J. M., 1997. *Interface fracture in concrete.* Delft, the Netherlands: PhD thesis TU Delft.

Vonk, R. A., 1992. *Softening of concrete loaded in compression.* Eindhoven, the Netherlands: PhD thesis TU Eindhoven - Wibro dissertatiedrukkerij.

Walraven, J. C., 1980. *Aggregate interlock: a theoretical and experimental analysis.* Delft, the Netherlands: PhD thesis TU Delft - Delft University Press.

Waubke, N. V., 1966. *Heft 6 - Transportphänomene in Betonporen (in German).* Braunschweig, Germany: Institut für Baustoffkunde und Stahlbetonbau der Technischen Hochschule Braunschweig.

Wells, G. N., 2006. *Lecture notes course CT5123 - the finite element method: an introduction.* Delft, the Netherlands: Faculty of Civil Engineering and Geosciences - Delft University of Technology.

Whitten, K. W., Davis, R. E., Peck, M. L. & Stanley, G. G., 2010. *Chemistry.* Belmont, United States of America: Brook/Cole, Cengage Learning.

Wright, R., 2008a. Channel tunnel fire loss 'minimal'. *Financial Times - online version - www.ft.com*, 9 October.

Wright, R., 2008b. Workers battle to meet Channel tunnel repair deadline after fire. *Financial Times - online version - www.ft.com*, 11 December.

Yang, C. C., Huang, R., Yeih, W. & Sue, I. C., 1995. Aggregate effect on elastic moduli of cement based composite materials. *Journal of Marine Science and Technology,* 3(1), pp. 5-10.

Zeiml, M., Lackner, R., Leithner, D. & Eberhardsteiner, J., 2008a. Identification of residual gas-transport properties of concrete subjected to high temperatures. *Cement and Concrete Research,* 38(5), pp. 699-716.

Zeiml, M., Lackner, R., Pesavento, F. & Schrefler, B. A., 2008b. Thermo-hydro-chemical couplings considered in safety assessment of shallow tunnels subjected to fire load. *Fire Safety Journal,* 43(2), pp. 83-95.

Zeiml, M., Leithner, D., Lackner, R. & Mang, H. A., 2006. How do polypropylene fibers improve the spalling behavior of in-situ concrete?. *Cement and Concrete Research,* 36(5), pp. 929-942.

Zhang, Q., 2013. *Microstructure and deterioration mechanisms of Portland cement paste at elevated temperature.* Delft, the Netherlands: PhD thesis TU Delft.

Zhukov, V. V., 1975. *Explosive failure of concrete during a fire (in Russian) - Translation No. DT 2124.* Borehamwood, United Kingdom: Joint Fire Research Organisation.

Zhukov, V. V., 1976. Reasons of explosive spalling of concrete by fire. *Beton i zhelezobeton (Concrete and Reinforcement Concrete),* Issue 3.

Zhu, T., 2012. *Fact sheets - some useful numbers on the engineering properties of materials (geological and otherwise) - GEOL 615.* Stanford, United States of America: Stanford University.

Zienkiewicz, O. C., Taylor, R. L. & Zhu, J. Z., 2005. *The finite element method: its basis and fundamentals (sixth edition).* Oxford, United Kingdom: Elsevier Butterworth-Heinemann.

A. Vector fields and tensors

Notations

The adopted mathematical notations are based on definition of scalars and vectors as well as matrices and tensors (van Kan, et al., 2008; Wells, 2006; Felippa, 2004b).

- A scalar is defined as a single value using an italic character:

$$a \tag{A.1}$$

- A vector is commonly indicated by a lowercase bold character with a single index and represents a directional field in the 2D or 3D Euclidean space, denoted as $\mathbb{R}^2$ or $\mathbb{R}^3$ respectively:

$$\boldsymbol{a} = \begin{bmatrix} a_1 \\ a_2 \end{bmatrix} \qquad \boldsymbol{a} = \begin{bmatrix} a_1 \\ a_2 \\ a_3 \end{bmatrix} \tag{A.2}$$

- The unit outward normal vector defines the direction perpendicular to the surface:

$$\boldsymbol{n} = \begin{bmatrix} n_1 \\ n_2 \end{bmatrix} \qquad \boldsymbol{n} = \begin{bmatrix} n_1 \\ n_2 \\ n_3 \end{bmatrix} \tag{A.3}$$

- A matrix is generally indicated by uppercase bold character and can be square or rectangular respectively. Two indexes, reflecting the row and column, are used:

$$\boldsymbol{A} = \begin{bmatrix} A_{11} & A_{12} & A_{13} \\ A_{21} & A_{22} & A_{23} \end{bmatrix} \qquad \boldsymbol{A} = \begin{bmatrix} A_{11} & A_{12} & A_{13} \\ A_{21} & A_{22} & A_{23} \\ A_{31} & A_{32} & A_{33} \end{bmatrix} \tag{A.4}$$

- The identity matrix can take various forms with only contributions on the diagonal:

$$\boldsymbol{I} = \begin{bmatrix} 1 & 0 \\ 0 & 1 \end{bmatrix} \qquad \boldsymbol{I} = \begin{bmatrix} 1 & 0 & 0 \\ 0 & 1 & 0 \\ 0 & 0 & 1 \end{bmatrix} \tag{A.5}$$

Tensors are defined as geometrical objects describing linear relationships between scalars, vectors and other tensors, independent of the coordinate system (Dullemond & Peeters, 1991-2010). The order or sometimes called rank of the tensor refers to the number of indices needed to define the relationship (Dullemond & Peeters, 1991-2010).

- A second order tensor, represented as a matrix, expresses the relationship between two first order tensors or vectors (Dullemond & Peeters, 1991-2010):

$$\boldsymbol{b} = \boldsymbol{C}\boldsymbol{a} \tag{A.6}$$

- A fourth order tensor governs the relationship between two second order tensors, using four indices and the trace (Dullemond & Peeters, 1991-2010; Wells, 2006):

$$\boldsymbol{B} = \boldsymbol{C} : \boldsymbol{A} \tag{A.7}$$

Basic calculus definitions for vectors and matrices

Mathematical manipulations are based on several definitions, reflecting basic vector and matrix calculus with the latter also applying to second order tensors (van Kan, et al., 2008; Wells, 2006; Spencer, 1980/2004; Felippa, 2004b).

- A column vector can also be transposed which defines a row vector as stated by:

$$\boldsymbol{a^T} = [a_1 \quad a_2 \quad a_3] \tag{A.8}$$

- Transposition of a matrix interchanges the rows and columns which mirrors the off diagonal terms as reflected by:

$$\boldsymbol{A^T} = \begin{bmatrix} A_{11} & A_{21} & A_{31} \\ A_{12} & A_{22} & A_{32} \\ A_{13} & A_{23} & A_{33} \end{bmatrix} \tag{A.9}$$

- For both vector and matrix transpositions the following also holds true:

$$\left(\boldsymbol{a^T}\right)^{\boldsymbol{T}} = \boldsymbol{a} \qquad\qquad \left(\boldsymbol{A^T}\right)^{\boldsymbol{T}} = \boldsymbol{A} \tag{A.10}$$

- Addition or alternatively subtraction of two vectors is relatively straightforward. In case of the same order an approach comparable to scalars is used:

$$\boldsymbol{a} + \boldsymbol{b} = \boldsymbol{b} + \boldsymbol{a} = \begin{bmatrix} a_1 + b_1 \\ a_2 + b_2 \\ a_3 + b_3 \end{bmatrix} \tag{A.11}$$

- Two matrices of similar order are added according to the rows and columns:

$$\boldsymbol{A} + \boldsymbol{B} = \boldsymbol{B} + \boldsymbol{A} = \begin{bmatrix} A_{11} + B_{11} & A_{12} + B_{12} & A_{13} + B_{13} \\ A_{21} + B_{21} & A_{22} + B_{22} & A_{23} + B_{23} \\ A_{31} + B_{31} & A_{32} + B_{32} & A_{33} + B_{33} \end{bmatrix} \tag{A.12}$$

- The dot product of two vectors is also based on summation, leading to a scalar:

$$\boldsymbol{a} \cdot \boldsymbol{b} = \boldsymbol{a^T b} = a_1 b_1 + a_2 b_2 + a_3 b_3 \tag{A.13}$$

- Since the dot product of these two vectors defines a scalar, the following holds true:

$$\boldsymbol{a} \cdot \boldsymbol{b} = \boldsymbol{a^T b} = \boldsymbol{b^T a} = \boldsymbol{b} \cdot \boldsymbol{a} \tag{A.14}$$

- In addition, the dyadic product of both vectors forms a matrix:

$$\boldsymbol{a} \otimes \boldsymbol{b} = \boldsymbol{a b^T} = \begin{bmatrix} a_1 b_1 & a_1 b_2 & a_1 b_3 \\ a_2 b_1 & a_2 b_2 & a_2 b_3 \\ a_3 b_1 & a_3 b_2 & a_3 b_3 \end{bmatrix} \tag{A.15}$$

- However, the dyadic product of these vectors cannot be interchanged as stated by:

$$\boldsymbol{a}\otimes\boldsymbol{b} = \boldsymbol{a}\boldsymbol{b}^{\boldsymbol{T}} \neq \boldsymbol{b}\boldsymbol{a}^{\boldsymbol{T}} = \boldsymbol{b}\otimes\boldsymbol{a} \tag{A.16}$$

- The trace of a matrix defines a scalar based on summation along the diagonal:

$$tr(\boldsymbol{A}) = A_{11} + A_{22} + A_{33} \tag{A.17}$$

- The trace between two matrices of the same order also leads to a scalar, using an approach similar to the dot product of two vectors:

$$\boldsymbol{A} : \boldsymbol{B} = tr\left(\boldsymbol{A}^{\boldsymbol{T}}\boldsymbol{B}\right) = A_{11}B_{11} + A_{12}B_{12} + A_{13}B_{13} + (\cdots) + A_{31}B_{31} + A_{32}B_{32} + A_{33}B_{33} \tag{A.18}$$

- The product of both these matrices, with the number of columns for the former and the number of rows for the latter equal, leads to a matrix:

$$\boldsymbol{AB} = \begin{bmatrix} A_{11}B_{11} + A_{12}B_{21} + A_{13}B_{31} & A_{11}B_{12} + A_{12}B_{22} + A_{13}B_{32} & A_{11}B_{13} + A_{12}B_{23} + A_{13}B_{33} \\ A_{21}B_{11} + A_{22}B_{21} + A_{23}B_{31} & A_{21}B_{12} + A_{22}B_{22} + A_{23}B_{32} & A_{21}B_{13} + A_{22}B_{23} + A_{23}B_{33} \\ A_{31}B_{11} + A_{32}B_{21} + A_{33}B_{31} & A_{31}B_{12} + A_{32}B_{22} + A_{33}B_{32} & A_{31}B_{13} + A_{32}B_{23} + A_{33}B_{33} \end{bmatrix} \tag{A.19}$$

- The product of a matrix and a vector, observing again the column and row equality, leads to a vector as for instance indicated by:

$$\boldsymbol{Ab} = \begin{bmatrix} A_{11}b_1 + A_{12}b_2 + A_{13}b_3 \\ A_{21}b_1 + A_{22}b_2 + A_{23}b_3 \\ A_{31}b_1 + A_{32}b_2 + A_{33}b_3 \end{bmatrix} \tag{A.20}$$

- Various transposition rules, representing vectors and matrices respectively, are used:

$$(\boldsymbol{Ab})^{\boldsymbol{T}} = \boldsymbol{b}^{\boldsymbol{T}}\boldsymbol{A}^{\boldsymbol{T}} \qquad (\boldsymbol{AB})^{\boldsymbol{T}} = \boldsymbol{B}^{\boldsymbol{T}}\boldsymbol{A}^{\boldsymbol{T}} \qquad \left(\boldsymbol{ba}^{\boldsymbol{T}}\right)^{\boldsymbol{T}} = \boldsymbol{ab}^{\boldsymbol{T}} \tag{A.21}$$

Special matrix properties

In the definition of second order tensors various special matrix properties are commonly exploited (van Kan, et al., 2008; Wells, 2006; Dullemond & Peeters, 1991-2010).

- The product of a matrix and its inversion leads to the identity matrix:

$$\boldsymbol{A}\boldsymbol{A}^{-\boldsymbol{1}} = \boldsymbol{I} \tag{A.22}$$

- A matrix is symmetrical if transposition produces the same matrix. This implies symmetry with respect to the diagonal as stated by:

$$\boldsymbol{A}^{\boldsymbol{T}} = \boldsymbol{A} \tag{A.23}$$

- A matrix is orthogonal if the transpose equals the inverse. Orthogonality refers to the perpendicular basis of two Euclidean vectors or vector systems. This property is particular useful in order to remove the inverse of a matrix from an equation using:

$$\boldsymbol{A}^{\boldsymbol{T}} = \boldsymbol{A}^{-\boldsymbol{1}} \tag{A.24}$$

B. Vector and tensor derivatives

First order derivatives

Derivatives of scalars, vectors and tensors take various forms as defined by the divergence and the gradient (van Kan, et al., 2008; Wells, 2006; Spencer, 1980/2004; Bastian, 2014). The choice for a particular form depends on the material characterisation required.

The divergence summarises the partial derivatives and is measure for the total directional change (van Kan, et al., 2008).

- Summation of partial derivatives defines the divergence of a vector, for instance in $\mathbb{R}^3$, obtaining a scalar:

$$\boldsymbol{\nabla} \cdot \boldsymbol{a} = \frac{\partial a_1}{\partial x} + \frac{\partial a_2}{\partial y} + \frac{\partial a_3}{\partial z} \tag{B.1}$$

- The divergence of a second order tensor in $\mathbb{R}^3$ defines a vector of partial derivatives:

$$\boldsymbol{\nabla} \cdot \boldsymbol{A} = \begin{bmatrix} \frac{\partial A_{11}}{\partial x} + \frac{\partial A_{12}}{\partial y} + \frac{\partial A_{13}}{\partial z} \\ \frac{\partial A_{21}}{\partial x} + \frac{\partial A_{22}}{\partial y} + \frac{\partial A_{23}}{\partial z} \\ \frac{\partial A_{31}}{\partial x} + \frac{\partial A_{32}}{\partial y} + \frac{\partial A_{33}}{\partial z} \end{bmatrix} \tag{B.2}$$

In addition, also the gradient can be stated using the partial derivatives, obtaining a measure for the variation in each direction (van Kan, et al., 2008).

- The gradient of a scalar leads to a vector in $\mathbb{R}^3$ based on the partial derivatives:

$$\boldsymbol{\nabla} a = \begin{bmatrix} \frac{\partial a}{\partial x} \\ \frac{\partial a}{\partial y} \\ \frac{\partial a}{\partial z} \end{bmatrix} \tag{B.3}$$

- The gradient of a vector leads to a second order tensor based on separate definition of the partial derivatives as indicated in $\mathbb{R}^3$:

$$\boldsymbol{\nabla a} = \begin{bmatrix} \frac{\partial a_1}{\partial x} & \frac{\partial a_1}{\partial y} & \frac{\partial a_1}{\partial z} \\ \frac{\partial a_2}{\partial x} & \frac{\partial a_2}{\partial y} & \frac{\partial a_2}{\partial z} \\ \frac{\partial a_3}{\partial x} & \frac{\partial a_3}{\partial y} & \frac{\partial a_3}{\partial z} \end{bmatrix} \tag{B.4}$$

- A special derivative is the symmetric gradient of a vector, for example in $\mathbb{R}^3$, which also leads to a second order tensor. The off diagonal terms consist of two contributions, representing derivatives with respect to perpendicular axes:

$$\boldsymbol{\nabla^s a} = \frac{1}{2}\left(\boldsymbol{\nabla a} + (\boldsymbol{\nabla a})^T\right) = \begin{bmatrix} \frac{\partial a_1}{\partial x} & \frac{1}{2}\left(\frac{\partial a_1}{\partial y} + \frac{\partial a_2}{\partial x}\right) & \frac{1}{2}\left(\frac{\partial a_1}{\partial z} + \frac{\partial a_3}{\partial x}\right) \\ \frac{1}{2}\left(\frac{\partial a_2}{\partial x} + \frac{\partial a_1}{\partial y}\right) & \frac{\partial a_2}{\partial y} & \frac{1}{2}\left(\frac{\partial a_2}{\partial z} + \frac{\partial a_3}{\partial y}\right) \\ \frac{1}{2}\left(\frac{\partial a_3}{\partial x} + \frac{\partial a_1}{\partial z}\right) & \frac{1}{2}\left(\frac{\partial a_3}{\partial y} + \frac{\partial a_2}{\partial z}\right) & \frac{\partial a_3}{\partial z} \end{bmatrix} \tag{B.5}$$

Second order derivatives

Combination of the divergence and the gradient allows to form second order partial derivatives, obtaining the Laplacian operator (van Kan, et al., 2008; Wells, 2006; Spencer, 1980/2004; Bastian, 2014).

- The Laplacian of a scalar is governed by the divergence and the gradient, leading to a scalar characterised by second order partial derivatives in for instance $\mathbb{R}^3$:

$$\boldsymbol{\nabla} \cdot \boldsymbol{\nabla} a = \boldsymbol{\Delta} a = \frac{\partial^2 a}{\partial x^2} + \frac{\partial^2 a}{\partial y^2} + \frac{\partial^2 a}{\partial z^2} \tag{B.6}$$

- Similarly, the Laplacian of a vector in $\mathbb{R}^3$ is governed by the second order partial derivatives defined as a vector:

$$\boldsymbol{\nabla} \cdot \boldsymbol{\nabla a} = \boldsymbol{\Delta a} = \begin{bmatrix} \frac{\partial^2 a_1}{\partial x^2} + \frac{\partial^2 a_1}{\partial y^2} + \frac{\partial^2 a_1}{\partial z^2} \\ \frac{\partial^2 a_2}{\partial x^2} + \frac{\partial^2 a_2}{\partial y^2} + \frac{\partial^2 a_2}{\partial z^2} \\ \frac{\partial^2 a_3}{\partial x^2} + \frac{\partial^2 a_3}{\partial y^2} + \frac{\partial^2 a_3}{\partial z^2} \end{bmatrix} \tag{B.7}$$

Combination of derivatives

First and second order derivatives are also used in combination as reflected by the following product rules using the previous stated relationships (van Kan, et al., 2008; Vermolen, 2005; Segal, 2008).

- The divergence of the product of a scalar and the gradient of a scalar is decomposed into two contributions. A scalar is defined by the dot product and the Laplacian operator:

$$\boldsymbol{\nabla} \cdot (a\boldsymbol{\nabla} b) = \boldsymbol{\nabla} a \cdot \boldsymbol{\nabla} b + a\boldsymbol{\nabla} \cdot \boldsymbol{\nabla} b = \boldsymbol{\nabla} a \cdot \boldsymbol{\nabla} b + a\boldsymbol{\Delta} b \tag{B.8}$$

- In addition, the divergence of the tensor-vector product also forms a scalar based on the dot product and the trace:

$$\boldsymbol{\nabla} \cdot (\boldsymbol{Ab}) = \boldsymbol{\nabla} \cdot \boldsymbol{A} \cdot \boldsymbol{b} + \boldsymbol{A} : \boldsymbol{\nabla b} \tag{B.9}$$

Gauss' divergence theorem

In continua, Gauss' divergence theorem is commonly used to relate domain and boundary integrals (van Kan, et al., 2008; Wells, 2006; Spencer, 1980/2004; Bastian, 2014). This fundamental relationship states that the change across the domain equals the outwards orientated removal along the boundary (van Kan, et al., 2008).

- The domain integral of the divergence of a vector is redefined based on the integral along the boundary using the unit outward normal vector:

$$\int_{\Omega} \boldsymbol{\nabla} \cdot \boldsymbol{a} d\Omega = \int_{\Gamma} \boldsymbol{a} \cdot \boldsymbol{n} d\Gamma \tag{B.10}$$

- Similar considerations allow to relate the domain and boundary integrals of a second order tensor, using the unit outward vector:

$$\int_{\Omega} \boldsymbol{\nabla} \cdot \boldsymbol{A} d\Omega = \int_{\Gamma} \boldsymbol{A}\boldsymbol{n} d\Gamma \tag{B.11}$$

Surface-based integrals

The previous relationships are commonly exploited to impose Neumann's boundary conditions (van Kan, et al., 2008). In case of only considering outwards contributions, perpendicular to the surface, can the following be stated for both scalar or vector gradients along the boundary respectively:

$$\int_{\Gamma} \boldsymbol{\nabla} a \cdot \boldsymbol{n} d\Gamma = \int_{\Gamma} \frac{\partial a}{\partial n} d\Gamma \qquad \int_{\Gamma} \boldsymbol{\nabla}\boldsymbol{a}\boldsymbol{n} d\Gamma = \int_{\Gamma} \frac{\partial \boldsymbol{a}}{\partial n} d\Gamma \tag{B.12}$$

About the author

Bas Lottman was born on the 16th of December 1980 in Zwolle, the Netherlands. After the elementary school in Hattem, he attended the higher secondary school in Heerde from which he graduated in 1998. During the next two years he acquired his pre-university education at the same school. His interest is civil engineering lead to the choice of following this particular bachelor study at Windesheim graduate school in Zwolle. During the last two years of this study he was part of a dual learning program for which he worked at the civil engineers company Witteveen+Bos, Department of hydraulic structures in Deventer. He graduated in 2004 and received for his bachelor work "*Brug over het Johan van Hasseltkanaal*" a honourable mention at that years Dutch steel price for students. Having collaborated in the design of various bridges and other structures prompted him to extend his knowledge by a master study at Delft University of Technology, Faculty of Civil Engineering and Geosciences. After a transition program and two years of study he graduated in 2007 with the master thesis "*Fire in bored tunnels, structural behaviour during fire conditions of bored tunnels made with a concrete segmental lining*". For this work he was awarded with the 2007 Dutch concrete price for students. During the final months of his master study Prof. Joost Walraven encouraged him to continue on this topic as part of a promotion study.

He started his promotion at the group of Concrete Structures at Delft University of Technology, Faculty of Civil Engineering and Geosciences in September of 2007. His work was part of a joint research project with Eindhoven University of Technology, funded by the Dutch National Science Foundation (STW) and aimed at the explosive spalling of concrete. This Dutch research project consisted of three PhD students with the others mainly focused on the experimental research into the dehydration processes and the moisture movement respectively. The aim for the author was to develop a conceptual spalling model. During his first year he visited several institutes in the Netherlands and abroad, specialising in experimental research and testing of concrete in fire. In the years that followed he derived both finite element models, simulating and coupling the temperature and (pore) pressure development as well as the structural fracture mechanics behaviour. For this he had to broaden his knowledge into (fracture) mechanics, but also extend his research into the field of applied physics. The chosen finite element method also required to explore numerical approximation techniques. The progress of his work was published and presented especially during the international workshops on concrete spalling due to fire exposure, held in this period every two years. After many years of research he was one of the first to numerically approximate the spalling mechanism of fire exposed concrete.

Publications

- *Fire in bored tunnels - structural behaviour, during fire conditions, of bored tunnels made with a concrete segmental lining*
  B.B.G. Lottman
  MSc thesis TU Delft (2007)

- *A model for the structural behaviour of bored tunnels during fire*
  B.B.G. Lottman, E.A.B. Koenders, C.B.M. Blom & V. Bouwman
  Proceedings of the workshop Fire Design of Concrete Structures
  Coimbra, Portugal (2007)

- *Brand in boortunnels, constructief gedrag van boortunnels tijdens brand (in Dutch)*
  B.B.G. Lottman, C.B.M. Blom, E.A.B. Koenders, V. Bouwman & J.C. Walraven
  Cement, Issue 2, pp. 70-73 (2008)

- *Towards a model for fire resitant design of concrete elements*
  B.B.G. Lottman, E.A.B. Koenders & J.C. Walraven
  Proceedings of the 1st International Workshop on Concrete Spalling due to Fire Exposure
  Leipzig, Germany (2009)

- *Macro-scale spalling model: a fracture mechanics versus pore pressure approach*
  B.B.G. Lottman, E.A.B. Koenders & J.C. Walraven
  Proceedings of the 2nd International Workshop on Concrete Spalling due to Fire Exposure
  Delft, the Netherlands (2011)

- *Spalling of concrete due to fire exposure: a coupled fracture mechanics and pore pressure approach*
  B.B.G. Lottman, E.A.B. Koenders, C.B.M. Blom & J.C. Walraven
  Proceedings of the 3rd International Workshop on Concrete Spalling due to Fire Exposure
  Paris, France (2013)

- *Spalling of fire exposed concrete based on a coupled material description: an overview*
  B.B.G. Lottman, E.A.B. Koenders, C.B.M. Blom & J.C. Walraven
  Proceedings of the 4th International Workshop on Concrete Spalling due to Fire Exposure
  Leipzig, Germany (2015)

- *Spalling of fire exposed concrete (in preparation)*
  B.B.G. Lottman, E.A.B. Koenders, C.B.M. Blom & J.C. Walraven
  Heron, Issue , pp. (estimated 2017)